MANTLE RESERVOIRS AND MAFIC MAGMATISM ASSOCIATED WITH THE BREAK-UP OF GONDWANA - THE BALLENY PLUME AND THE AUSTRALIAN-ANTARCTIC DISCORDANCE

U-Pb ZIRCON DATING OF A PROTEROZOIC MAFIC DYKE SWARM IN THE VESTFOLD HILLS, EAST ANTARCTICA

by

Ruth Lanyon BSc. (Hons) La Trobe University

Submitted in fulfilment of the requirements
for the degree of Doctor of Philosophy (Geology)
University of Tasmania, Hobart
Original Submission - January, 1994
Revised Version - September 1994

STATEMENT

This thesis comprises research performed by the author in the Geology Department at the University of Tasmania, and in the Research School of Earth Sciences (RSES) at the Australian National University from January 1990 to December 1993.

The preliminary results of Chapters 3 and 4 have been published as:
Lanyon R., Varne R. and Crawford A.J. 1993 Tasmanian Tertiary basalts, the Balleny Plume, and opening of the Tasman Sea (southwest Pacific Ocean). *Geology.*, 21: 555-558.

Chapter 9 has been published as:
Lanyon R., Black L.P. and Seitz H.-M. 1993 U-Pb zircon dating of mafic dykes and its application to the Proterozoic geological history of the Vestfold Hills, East Antarctica. *Contributions to Mineralogy and Petrology.*, 115: 184-203.

Chapter 8 has been submitted for publication as:
Lanyon R. and Crawford A.J. (submitted - August 1994) Westward migration of Pacific Ocean upper mantle into the Southern Ocean region between Australia and Antarctica. *Geology.*

This thesis contains no material which has been accepted for the award of any other degree or diploma in any tertiary institution and, to the best of the author's knowledge and belief, this thesis contains no material previously published or written by another person, except where due reference is made in the text of the thesis.

Ruth Lanyon
University of Tasmania
September, 1994

AUTHORITY OF ACCESS

This thesis may be made available for loan and limited copying in accordance with the *Copyright Act 1968.*

Ruth Lanyon
University of Tasmania
September, 1994

ABSTRACT

Part 1:

Within the recent literature, the isotopic heterogeneity of ocean island basalts (OIB) is generally ascribed to mixing between any two or more of four isotopically distinct mantle end-member components - DMM, HIMU, EMI and EMII - the origin and precise location of which are still the subject of much debate. An attempt is made here to constrain the geochemical characteristics of these end-member components using literature-derived end-member OIB data. This has confirmed the presence of consistent trace element differences and also suggested certain major element distinctions, which are interpreted to reflect diverse end-member mantle source compositions rather than differences in the pressure and temperature of melting involved in OIB production.

EMI basalts, which extend to the lowest $^{143}Nd/^{144}Nd$ values of all OIB, were found to possess the most distinctive major element characteristics, the latter evident as higher SiO_2 and lower FeO*, CaO, TiO_2, P_2O_5 and K_2O values than both HIMU and EMII OIB. However, EMI basalts have the least well defined trace element systematics. In contrast, HIMU and EMII basalts, previously characterised by the highest Pb isotope ratios and the highest $^{87}Sr/^{86}Sr$ values respectively, were found to have overlapping major element abundances but quite distinctive trace element systematics. HIMU basalts have the highest CaO and generally lower LILE/HFSE and LREE/HFSE abundance ratios, intermediate Th/La and Th/Nb, lower Zr/Nb and higher Nb/Pb and Ce/Pb values than either of the EM components. EMII basalts extend to the highest K_2O and TiO_2 values and are characterised by lower Ba/Th, higher Th/La and higher Th/Nb values than EMI OIB.

Previous workers have recognised a regional HIMU radiogenic isotope and trace element signature within Cretaceous to Recent volcanics scattered throughout the dispersed continental fragments of eastern Gondwana and dredged from the Tasman Sea - southwest Pacific Ocean seafloor. This study has ascribed the HIMU nature of continental volcanism in Tasmania, the South Island and offshore islands of New Zealand, and Marie Byrd Land and the McMurdo Volcanic Group of West Antarctica to localised and intermittent periods of tectonically-induced decompression and melting of underplated HIMU material emplaced at the base of the lithosphere by one or more upwelling plume heads prior to or coincident with the onset of continental break-up in this region. Ocean floor HIMU volcanism in the southern Tasman Sea and southwest Pacific Ocean has been attributed to lithospheric plate movement over the persisting plume conduits.

Previous plate-tectonic reconstructions have ascribed a 4000 km long curved chain of seamounts and islands, extending from the western flank of Lord Howe Rise to the Balleny Islands close to the Ross Sea region of the southwest Pacific Ocean, to movement of the Indian-Australian and Antarctic Plates over the Balleny Plume with progressive

continental rifting from ~70 Ma to the present. Scott Island, located further east but at a similar latitude to the Balleny Islands, has an homologous isotopic and trace element signature and therefore appears to be the product of a second and parallel HIMU plume trace, here termed the Scott Plume. The latter is also held responsible for the enriched geochemical features of some Macquarie Island basalts. The Balleny and Scott Plumes appear to have been temporarily trapped by, and to have contaminated the eruptives of, the Southeast Indian and Pacific-Antarctic spreading ridges respectively. This has resulted in the ≤28 Ma (between A8 and the active spreading ridges) seafloor in this region bearing an E-MORB to HIMU-DMM isotopic signature. The fact that samples dredged from virtually zero-age oceanic crust on the southern flank of the SEIR and northwest of the Balleny Islands, also bear this distinctive isotopic and trace element signature implies that the supply of HIMU material to this region of the SEIR has continued until very recently.

Significant contamination of Balleny Plume HIMU volcanics by DMM material, particularly evident in Pb-Pb isotopic space, suggests that the Balleny Plume is a relatively weak plume which entrained large amounts of depleted upper mantle during upwelling. Progressive temporal dilution of the HIMU plume component by DMM material may imply either increasing amounts of upper mantle entrainment, suggesting a gradual weakening of the plume with time, or progressive preferential melting of entrained material within a heterogeneous plume. The Balleny Plume also appears to have slightly higher time-integrated Th/U than other known HIMU sources, resulting in the most radiogenic Balleny Plume samples plotting above the HIMU field in $^{206}Pb/^{204}Pb$-$^{208}Pb/^{204}Pb$ space, and thereby potentially expanding the known range of HIMU isotopic values.

Part 2:

The Southern Ocean between the southern margin of Australia and Wilkes Land in Antarctica hosts an important section of the global mid-ocean ridge system. Other researchers have concluded that the Southeast Indian Ridge (SEIR) in this region experienced a dramatic change in spreading rate at ~44.5 Ma, coincident with a major period of global plate reorganisation. Comparative studies, within the recent literature, of individual fast and slow spreading ridges have revealed distinct morphological and geochemical parameters which have been attributed to different underlying magma chamber processes. An attempt is made here to discern if the geochemical parameters correlated with spreading rate in the literature are also evident with a change in spreading rate along a single segment of mid-ocean ridge. This effort has been concentrated on the chemistry of basalts collected from four Southern Ocean dredge sites north of the SEIR. Two of these sites were located on oceanic crust formed during a period of relatively slow seafloor spreading prior to 49 Ma, whereas the other two correspond to a period of more rapid seafloor spreading after 44.5 Ma. The lack of recognisable and systematic geochemical differences between the SEIR slow and intermediate spreading rate eruptives suggests that the change in spreading rate

at ~44.5 Ma, and the inferred change in underlying mantle processes, may not have been great enough to result in the significant geochemical variations cited in the literature. Alternatively, the off-axis Southern Ocean basalt database may be insufficient to enable the detection of such differences.

The Southern Ocean south of the Great Australian Bight is also host to a globally anomalous region of mid-ocean ridge, known as the Australian-Antarctic Discordance (AAD). In addition to its recognised morphological and geophysical anomalies, the AAD represents the current on-axis location of a proposed isotopic boundary between Indian and Pacific Ocean upper mantle convective regimes, previously defined from analyses of ≤4 Ma MORB dredged from within and adjacent to the AAD. An investigation is undertaken here into the off-axis location of this isotopic boundary, concentrating on radiogenic Pb, Sr and Nd isotope data for ~36-66 Ma seafloor dredged from either side of the northward extrapolation of the AAD. The results show that ≥36 Ma seafloor east of the AAD has an Indian Ocean MORB isotopic signature, thereby implying that the proposed Indian-Pacific Ocean isotopic boundary does not extend directly north of the ridge towards the southern margin of Australia. Progressive westward migration of an arcuate-shaped front of Pacific Ocean upper mantle therefore appears to be a consequence of Australian-Antarctic rifting and Southern Ocean opening, favouring models of active mantle flow outlined in the recent literature such as Pacific Ocean basin shrinkage, convergence of hotspot-driven along-axis asthenospheric flow and/or direct Indian and Pacific Ocean upper mantle convergence.

Part 3:

The Vestfold Hills, one of several Archaean cratonic blocks within the East Antarctic Shield, comprises a high-grade metamorphic basement complex intruded by at least nine generations of Early to Middle Proterozoic mafic dykes. Extensive U-Pb ion microprobe (SHRIMP) analyses of zircons, derived predominantly from late-stage felsic differentiates of the mafic dykes, provide precise crystallisation ages for several dyke generations. These new ages enable constraints to be placed on both the history of mafic magmatism in the Vestfold Hills and the timing of the various interspersed, and already documented, Proterozoic deformation events. In addition to demonstrating the utility of zircons derived from felsic late-stage differentiates for the dating of co-genetic mafic dykes, this study also places doubt on previous whole-rock Rb-Sr dating of mafic dyke suites in this and other areas of East Antarctica.

$^{207}Pb/^{206}Pb$ zircon ages of 2241±4 Ma and 2238±7 Ma for the *Homogeneous* and *Mottled Norites*, respectively, provide a younger emplacement age for associated *Group 2 High-Mg* tholeiite dykes than the whole-rock Rb-Sr date (2424±72 Ma) originally interpreted as the age of all high-Mg intrusives in the Vestfold Hills. Zircon ages of 1754±16 Ma and 1832±72 Ma confirm the previously defined Rb-Sr age of the *Group 2 Fe-rich* tholeiites. Two later dyke generations, the *Group 3* and *4 Fe-rich* tholeiites, distinguished on the basis of

field orientations and cross-cutting relationships, yield zircon emplacement ages of 1380±7 Ma and 1241±5 Ma, which also define minimum ages for two suites of lamprophyre dykes.

Xenocrystic zircons within both felsic segregations and mafic dykes yield zircon ages of 2478±5 Ma to ~2740 Ma, indicating the presence of Archaean crustal source rocks of this antiquity beneath the Vestfold Hills.

TABLE OF CONTENTS

LIST OF TABLES

Chapter 5

Chapter 7

Chapter 8

Chapter 9

LIST OF FIGURES

Chapter 1

Chapter 2

Chapter 3

Chapter 4

Chapter 5

Chapter 7

Chapter 8

Chapter 9

ACKNOWLEDGEMENTS

I wish to express my gratitude to the many people who have provided assistance, advice, support and friendship during the last four years of my life and without whom this research could not have been completed:

First and foremost I thank my supervisor Dr. Tony Crawford for rescuing me from potential project-less oblivion with the offer of the Southern Oceans project, throughout which he has provided invaluable advice and supervision as well as many exciting research opportunities.

Dr. Rick Varne is thanked for helping to provide research funds and ideas for the Balleny Plume project through his Southern Oceans research grant held in conjunction with Dr. Tony Crawford.

Professor David Green is thanked for initiating and funding, through an ASAC grant, one of the greatest experiences of my life - the opportunity to undertake field work in Antarctica. The corresponding SHRIMP analytical work was performed in collaboration with, and under the supervision of, Dr. Lance Black (AGSO) who is thanked for his instruction, long days and nights spent running SHRIMP and performing data reduction, and subsequent collaboration on the writing of the Vestfold Hills manuscript.

For the exciting and stimulating 14 months I spent working at the Research School of Earth Sciences (RSES) at the Australian National University I wish to thank Drs. Tony Crawford, Malcolm McCulloch and Steve Eggins who organised and initiated the collaborative isotopic work I performed there. Dr. Malcolm McCulloch is thanked for providing prolonged access to the clean lab and mass spectrometer facilities and for his enthusiasm and advice about my work.

To Drs. Steve Eggins, Janet Hergt and Jon Woodhead it is impossible to express my gratitude for not only their instruction in isotopic analytical procedures, advice in all aspects of my writing-up, tireless reading and re-reading of my chapters, but also their friendship, pep-talks and shared enthusiasm for Bruno's truffles.

To the many talented people at RSES who provided technical assistance during my time there, including Dr. Graham Mortimer (clean lab), Les Kinsley (mass spectrometer, ICP-MS), Gael Watson and Pat Oswald-Sealy (filament preparation), Nick Ware (electron microprobe), Shane Paxton (sample preparation) and Keith Massey (lapidary) - thank you for helping me obtain the data for my PhD. The wry sense of humour of Dr. Graham Mortimer and the impeccable nature of his clean lab was particularly appreciated during the long months of isotope work. SHRIMP technical assistance and sample preparation was provided by Chris Foudoulis, L.A. Keast, and A. Watson. Ross Wylde-Browne is thanked for his excellent slide making skills.

Enthusiastic and invaluable technical assistance was also provided by many equally talented people at the University of Tasmania, including Phil Robinson (XRF), Wieslaw Jablonski (electron microprobe), Nilar Hlaing (sample preparation), Kathi Stait (rock store), and Simon Stephens, Naomi Deards and Maya Kamenetsky (lapidary).

Helen Waldron from Bequerel Laboratories Pty. Ltd. is thanked for her prompt INAA work and for providing the detailed description of the analytical procedure outlined in Appendix 2.

Many people provided unpublished data for use in my thesis. For their generosity I would like to thank Drs. Malcolm McCulloch, Jon Woodhead, Bill McDonough, Ian McDougall (K-Ar dating), Bob Duncan (Ar-Ar dating), John Richards, John Foden, Rick Varne, Chris Jenkins et al. (Balleny Hotspot manuscript - in prep.) and Clifford Gill and Ken Collerson (Balleny Islands manuscript - in prep.).

The samples analysed during the course of this research derive from many sources (as outlined in Appendix 1). Individuals involved in providing these samples include David Cassidy (Antarctic Marine Geology Research Facility, Florida State University), Drs. Chris Jenkins and Tom Hubble (Ocean Sciences Institute, University of Sydney), Dr. Lin Sutherland (Australian Museum), Dr. Steve Eggins (RSES) and Drs. Tony Crawford and Greg Yaxley (University of Tasmania Geology Department). CSIRO division of Fisheries, the Australian Maritime College and local Tasmanian deep-sea fishermen are thanked for providing Soela Seamount samples. The tireless assistance of Ingvar (the slave) Sigurdsson in the drilling, hammering and carting of the Vestfold Hills dyke samples is greatly appreciated.

The cast and crew of the Australian Geological Survey's *R/V Rig Seismic*, under the supervision of voyage leader Dr. Dave Feary, are thanked for a most enjoyable and productive Southern Oceans cruise (Southern Margins cruise 102). Uwe Rieke is also thanked for generously providing accommodation during a subsequent visit to Canberra.

The Australian Antarctic Division and the crews of the *Aurora Australis* and *Icebird* are thanked for a successful and enjoyable summer field season (1990-1991) in Antarctica. Fellow expeditioners whose company particularly enhanced the time spent both voyaging to and working in Antarctica include Doug Thost, Pete Kinny, Ian (Bunge) Scrimgeour, John Sims, Rod Brown and Warwick Crowe. Dr. Jim Burgess is thanked for "Sunday mass" aboard the *Aurora Australis* and his hospitality at Law Base and subsequently in Canberra, the latter in conjunction with Trish Middleton. Hans Hoek and particularly Ingvar Sigurdsson provided enjoyable companionship and invaluable assistance during fieldwork in the Vestfold Hills. Michael Seitz generously provided pre-Antarctic advice on fieldwork in the Vestfold Hills as well as maps, unpublished data and post-Antarctic collaboration on the Vestfold Hills manuscript.

The continuing friendship and encouragement of Dr. Peter Fleming, my Honours supervisor and mentor from La Trobe University, helped pull me through some of the more difficult PhD patches. A better "drinking partner" is hard to imagine.

Dr. Leonid Danyushevsky is thanked for his patience and time in trying to drum in some of the "finer" points of igneous petrology.

Secretarial staff at the University of Tasmania (Geology Department and CODES) who have provided assistance include Jeanette Hankin, Julie Beattie, Christine Higgins and June Pongratz. Peter Cornish is thanked for being so organised.

Numerous post-doctoral fellows and fellow PhD students at the University of Tasmania (Geology Department and IASOS) provided friendship and support throughout the PhD years. In particular I would like to thank the various people I have shared an office and life with in Hobart: Ingvar Sigurdsson, Massimo Gasparon, Michael Seitz, Greg Yaxley, Geoff Nichols, Fernando Della-Pasqua and Alicia Verbeeten. Drs. Russell Sweeney and Garry Davidson were also brave enough to share houses. Anthea Hill, Kim Hein and Patti Virtue are thanked for keeping me company in the male-dominated world of science. Thanks also to Paul (late night beers) Kitto, Sampan Singharajwarapan, Andrew (Bear) McNeill, Udi Hartono, Marcel Kamperman, Michael Roach, Ai Yang, Steve Hunns and Drs. Bruce Gemmell, Trevor Falloon, Vanessa Guthrie, Joe Stoltz, Wayne Taylor, Vadim (Dima) Kamenetsky and John Sinton.

The many research fellows and PhD students at RSES are thanked for accepting me so readily into their midst. In particular I wish to acknowledge the valued friendship and charming wit of Adam Kent, the "soup and salads" and support of Deb Scott and the late night company over drinks at "Tilley's" with Jurgen Streit. Others who deserve at least a mention include Melita Keywood, James Johnson, Sue Keay, Claudine Stirling, Paul Johnson, Dan Zwartz, Mark Fanning and Drs. Des Patterson, Vickie Bennett, Peter Valbracht, Frank Volker, Bill McDonough, Roberta Rudnick, Alan Nutman, Trevor Ireland, Geoff Davies, Shen-su Sun and Xianhua Li. Dr. Richard Armstrong is thanked for his attempts at saving the rhino and in helping me to make the most important decision of all - the colour of the binding.

Tolerant friends and housemates throughout this period include Chris and Cynthia McVinnish, Russell Fulton, Roger Kirkwood, Helen Elliott, Helena Psotova, Liz Jagodzinski, Ruth Dudgeon and my extremely supportive ex-nursing and ex-La Trobe colleagues. Many fantastic bushwalks and chocolate-eating sessions were shared with Melissa Giese.

Last, but never least, I'd like to thank my family for their on-going support throughout my long years as a student - thanks particularly to my dad for his financial and emotional support in the final months, my mum for her constant support and long-distance telephone chats and Jemma, Janet, John, Ian and Anna just for being there.

PREAMBLE

This thesis is divided into three parts. The first two parts pertain to the evolution of mantle reservoirs associated with the rifting of Australia, Antarctica and New Zealand during the break-up of eastern Gondwana. Part 1 introduces the concept of four isotopically distinct mantle end-member components being involved in the generation of ocean island basalts (OIB) (Chapter 1), and attempts to constrain the major and trace element characteristics of HIMU, EMI and EMII end-member basalts (Chapter 2). Chapters 3, 4 and 5 concentrate on the use of radiogenic isotopes and trace element abundances to trace the widespread influence of at least two HIMU mantle plumes, the Balleny and Scott Plumes, on intraplate oceanic and continental volcanism in the Tasman Sea - southwest Pacific Ocean region. The results of Part 1 are summarised in Chapter 6.

Part 2 is concerned with the composition of ~36 to 66 Ma seafloor dredged from the Great Australian Bight region of the Southern Ocean. A comparison of the geochemistry of mid-ocean ridge basalts (MORB) erupted along the Southeast Indian Ridge (SEIR) during a slow spreading regime, with that produced after the dramatic change in spreading rate at ~44.5 Ma, is designed to test if the geochemical variations which have been correlated with different spreading rates along different mid-ocean ridge systems can be applied to a change in spreading rate along a single ridge system (Chapter 7). These same Southern Ocean MORB samples are used to examine the off-axis relationship between the morphologically and geophysically anomalous Australian-Antarctic Discordance (AAD) region of the SEIR and a proposed isotopic boundary between Pacific and Indian Ocean upper mantle convective regimes whose current on-axis location coincides with the eastern AAD (Chapter 8).

The third, and more minor, part of this thesis involves a study of the applicability of the U-Pb zircon (SHRIMP) dating technique to the problem of mafic dyke geochronology (Chapter 9). The successful dating of magmatic zircons derived from late-stage felsic differentiates within mafic dykes has enabled further constraints to be placed on the Proterozoic history of the Vestfold Hills, East Antarctica.

All acronyms and abbreviations used within the main text of this thesis are listed and defined in Appendix 7.

PART 1

MANTLE RESERVOIRS AND MAFIC MAGMATISM ASSOCIATED WITH THE BREAK-UP OF GONDWANA - THE BALLENY PLUME

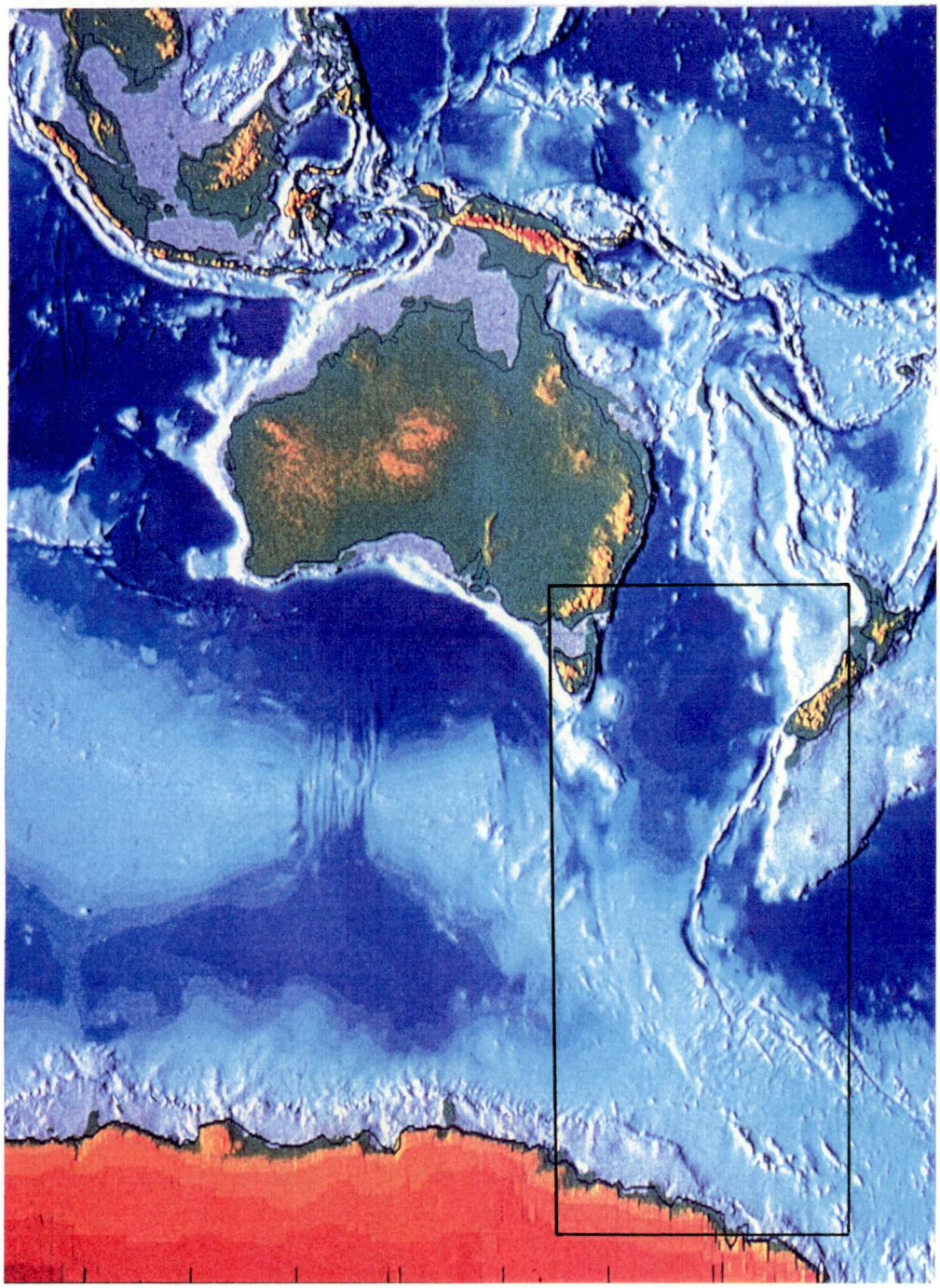

CHAPTER 1

THE ISOTOPIC HETEROGENEITY OF OCEAN ISLAND BASALTS

1.1 INTRODUCTION:

Studies of ocean island basalts (OIB), generally considered to be the products of fixed mantle plumes (Morgan, 1971; 1972), provide an opportunity to constrain the evolution, structure and composition of the Earth's deep mantle. In general terms, OIB possess certain geochemical and isotopic characteristics, including incompatible trace element enrichments (e.g. Sun, 1980; Wood et el., 1981), lower $^{143}Nd/^{144}Nd$ and higher $^{87}Sr/^{86}Sr$ values (e.g. DePaolo and Wasserburg, 1976; Duncan and Compston, 1976; Tatsumoto, 1978), which distinguish them from mid-ocean ridge basalts (MORB). The characteristic features of OIB suggest that they share a common evolutionary history which is distinct from that of other ocean floor basalts. OIB Pb isotope ratios, forming an approximately linear array which extends to the right of the geochron, are generally consistent with the occurrence of one or more ancient (1-2 Ga) mantle differentiation event/s which increased the U/Pb and Th/Pb contents of their mantle reservoirs to values greater than that of bulk Earth (Chase, 1981; Hart, 1984; Zindler and Hart, 1986; Gariépy and Dupré, 1991; McCulloch, 1993). In contrast, the Pb isotope compositions of N-MORB (normal depleted MORB), erupted away from the influence of near-ridge hotspots such as Iceland and the Azores, are far less radiogenic and plot near, or to the left of, the geochron (e.g. Gariépy and Dupré, 1991), indicating time-integrated U/Pb and Th/Pb source contents less than or equal to bulk Earth.

Despite their distinctive characteristics, as compared to other oceanic basalts, it is now well established that OIB are themselves isotopically and geochemically diverse, possibly constituting evidence for large-scale heterogeneities within the mantle (Sun, 1980; Hart, 1984; Hart et al., 1986; Zindler and Hart, 1986). Multiple mantle end-member components have been proposed in order to explain the isotopic heterogeneity of OIB (Zindler et al., 1982; Allègre and Turcotte, 1985; White, 1985; Zindler and Hart,1986; Dupuy et al., 1987); however, the minimum number of components needed, their relative locations within the mantle, and the source of each, are still uncertain. Most of the recent literature

which proposes the existence of these isotopic end-members is in general agreement that mixing between four components, DMM, HIMU, EMI and EMII, can produce the observed spectrum of OIB isotopic and trace element variation (Zindler and Hart, 1986; Hart, 1988; Weaver, 1991) and explain the recurrence of distinctive isotopic patterns at different geographical locations (Gariépy and Dupré, 1991). Although these end-member components possess the extreme Sr, Nd and Pb isotopic compositions necessary to circumscribe the range of observed OIB variations, they do not necessarily reflect physical mantle reservoirs; the latter may actually have intermediate isotopic compositions (Barling and Goldstein, 1990).

This chapter examines the four proposed end-member components on the basis of the radiogenic isotope data available in the literature, with emphasis on the HIMU, EMI and EMII end-members in particular. The ultimate aim is to constrain the isotopic features which distinguish the HIMU component as an introduction to the study of one such HIMU mantle plume, the Balleny Plume (Chapter 3).

1.2 THE ORIGIN OF MANTLE PLUMES:

Much debate still surrounds the subject of mantle plume sources. Plume buoyancy, relative to the surrounding mantle, has been variously attributed to thermal and/or compositional effects, and numerous hypotheses exist as to their spatial origin.

Many researchers now believe that plumes originate from one of two possible thermal boundary layers - the core-mantle boundary, or the 670 km discontinuity. The former, supported by many geophysical observations, suggests that mantle plumes may control heat loss from the core, arising from a thin velocity boundary layer (D") within the thermal boundary layer at the base of a viscously-stratified but wholly convecting mantle (Loper and Stacey, 1983; Davies, 1990; Davies and Richards, 1992). However, the 670 km discontinuity, thought by some to comprise a thermal and convective (mesosphere) boundary layer between upper, depleted, and lower, less-depleted mantle (e.g. Ringwood, 1982; White, 1985), may precipitate the formation of buoyant thermal instabilities, resulting in the upwelling of plumes, due to conductive heating from below (Allègre and Turcotte, 1985; Allègre et al., 1987). A variation on the theme of plumes originating from the 670 km discontinuity proposes that the accumulation and partial melting of subducted lithosphere within the transition zone results in enrichment of the adjacent refractory harzburgite layer (Ringwood, 1982; Ringwood and Irifune, 1988). According to this model, subsequent heating from below, due to rising lower mantle convection currents, results in upper 'fertilised' regions of the boundary layer becoming buoyant and rising into the upper mantle.

Other ideas about plume sources are consistent with models of decoupled mantle convection and plume buoyancy due to compositional anomalies relative to the overlying mantle. These include plume derivation from regions of primitive or relatively undepleted

lower mantle (e.g. Sun and Hanson, 1975a; Dupré and Allègre, 1983), or from small degrees of melting of upper mantle comprising regions of undepleted, less refractory material embedded in a depleted MORB matrix, variously termed "plum-pudding" or "marble-cake" mantle (Morris and Hart, 1983; Allègre and Turcotte, 1986). Anderson (1979; 1982) suggested that plumes derive from partial melting of an upper mantle eclogite layer produced by the accumulation of former oceanic crust between 220 and 670 km depth.

1.3 DEFINITION OF THE MANTLE END-MEMBER COMPONENTS:

Observed variations in the isotopic ratios of oceanic basalts (Figure 1.1), a function of the type and timing of parent/daughter element fractionation processes as well as mixing between these different mantle components, imply that oceanic basalt sources have not evolved as closed systems until the present day. It is, in fact, necessary to invoke ancient (1 to 2 Ga) fractionation events, such as mantle differentiation and continental crust formation, in order to explain the observed isotopic variability of oceanic basalts (e.g. Gariépy and Dupré, 1991).

1.3.1 DMM - Depleted MORB mantle:

DMM or depleted MORB mantle is the best defined of the four end-members. It is generally thought to occupy the uppermost mantle and to represent the depleted residue of the mantle fractionation processes responsible the formation of the Earth's crust (e.g. Hofmann et al., 1986; Zindler and Hart, 1986; Saunders et al., 1988; Gariépy and Dupré, 1991).

There are two alternative isotopic definitions for the DMM end-member. If the shallow mantle is considered to have primary heterogeneities as a result of multiple fractionation events of varying extent (Hart, 1988), DMM can be defined by an 'average' composition (N-MORB), as erupted along bathymetrically 'normal' segments of mid-ocean ridge distant from hotspot activity (Zindler and Hart, 1986; Saunders et al., 1988). In this case, DMM would be characterised by relatively high $^{143}Nd/^{144}Nd$, unradiogenic $^{87}Sr/^{86}Sr$ and $^{206}Pb/^{204}Pb$ values, and incompatible trace element depletions. Alternatively, if the shallow mantle is homogeneous and highly depleted, DMM would be best represented by the most extreme MORB sample/s available, characterised by the lowest $^{87}Sr/^{86}Sr$ (~0.7022), highest $^{143}Nd/^{144}Nd$ (~0.5133) and most unradiogenic $^{206}Pb/^{204}Pb$ (~17.3) values (Hart, 1988), and would plot to the left of the geochron (Figure 1.1b). The latter dictates that MORB which deviate from this extreme composition, including the majority of N-MORB, are the result of subsequent contamination of the DMM end-member component (Zindler and Hart, 1986; Hart, 1988), and that pristine DMM has U/Pb, Th/Pb and Th/U ratios lower than bulk Earth (e.g. Gariépy and Dupré, 1991).

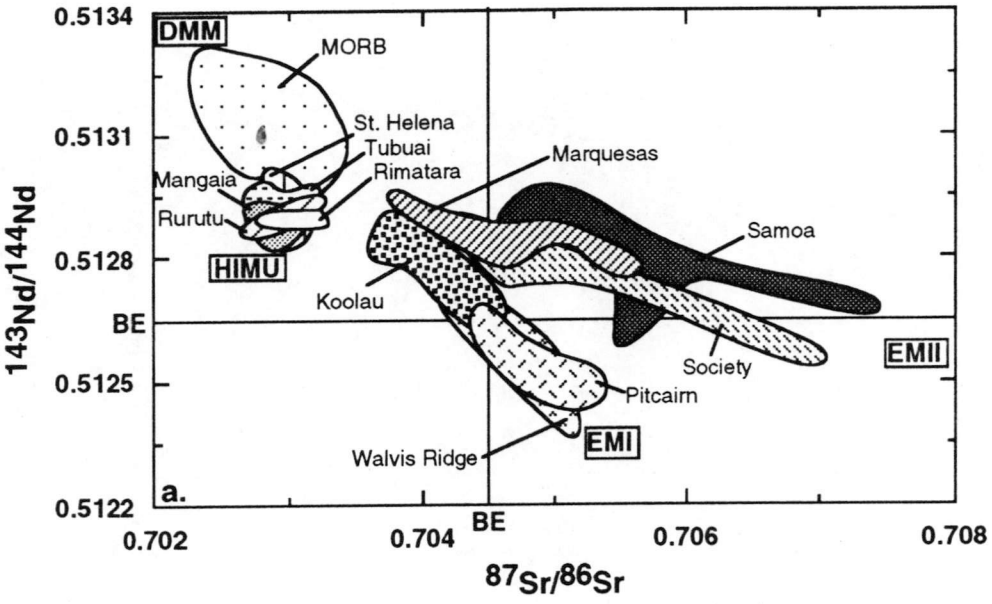
0.5134
0.5131
0.5128
BE
0.5125
0.5122
143Nd/144Nd
DMM
MORB
St. Helena
Tubuai
Rimatara
Mangaia
Rurutu
HIMU
Marquesas
Samoa
Koolau
Society
EMII
Pitcairn
EMI
Walvis Ridge
a.
0.702
0.704
BE
0.706
0.708
87Sr/86Sr

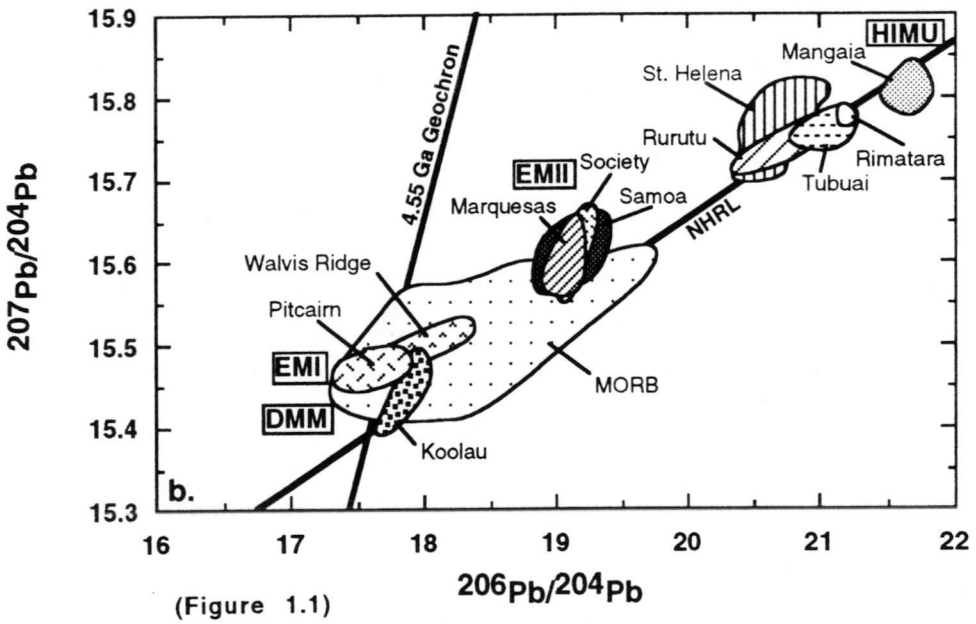
15.9
15.8
15.7
15.6
15.5
15.4
15.3
207Pb/204Pb
4.55 Ga Geochron
HIMU
Mangaia
St. Helena
Rurutu
Rimatara
Tubuai
EMII
Society
Marquesas
Samoa
NHRL
Walvis Ridge
Pitcairn
EMI
MORB
DMM
Koolau
b.
16
17
18
19
20
21
22
206Pb/204Pb

(Figure 1.1)

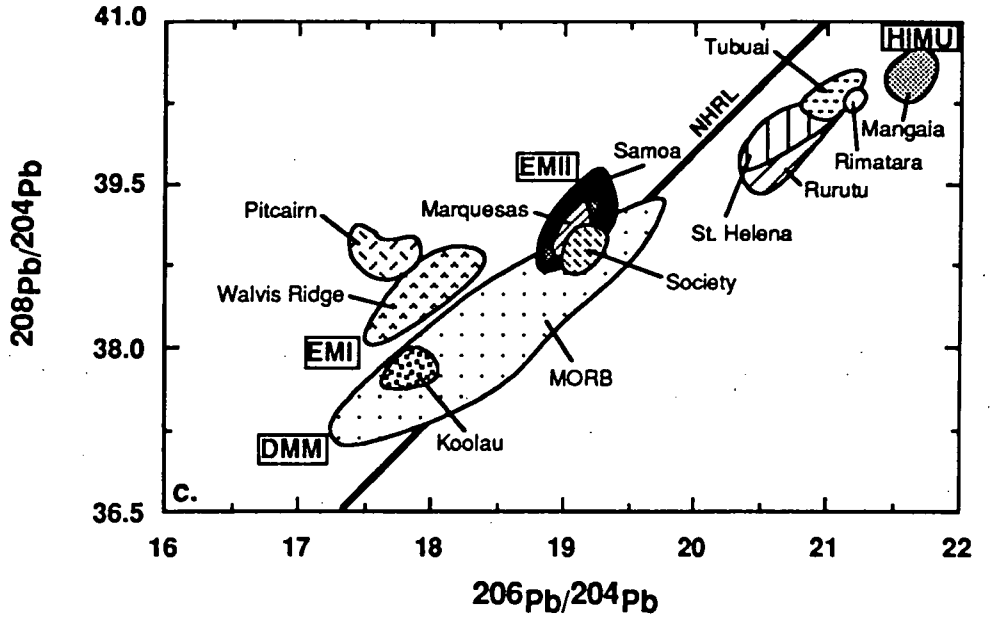
41.0
39.5
38.0
36.5
208Pb/204Pb
16
17
18
19
20
21
22
206Pb/204Pb
HIMU
Tubuai
NHRL
Mangaia
Rimatara
Rurutu
EMII
Samoa
Pitcairn
Marquesas
St. Helena
Society
Walvis Ridge
EMI
MORB
DMM
Koolau
c.

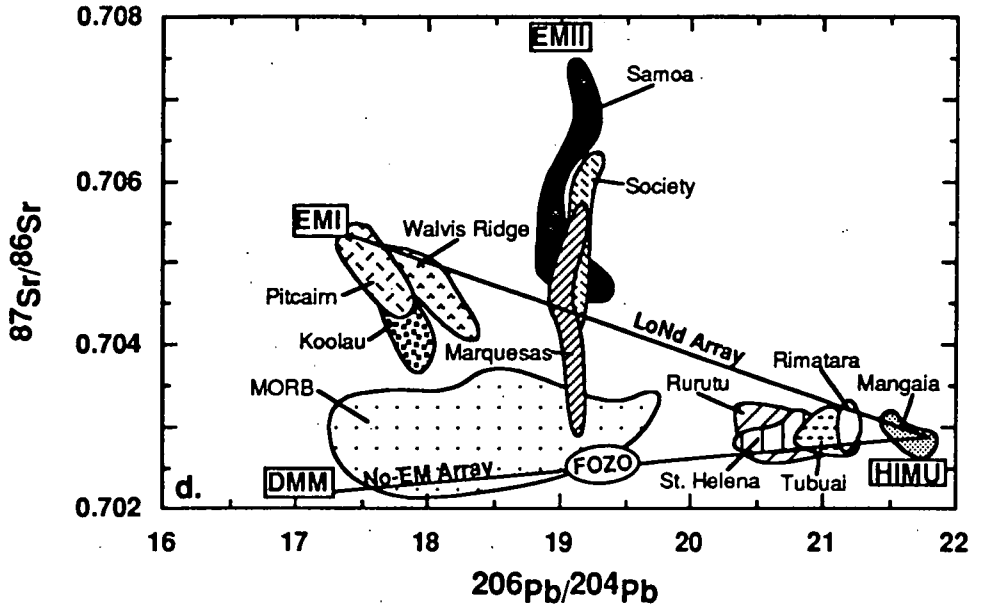
0.708
0.706
0.704
0.702
87Sr/86Sr
16
17
18
19
20
21
22
206Pb/204Pb
EMII
Samoa
Society
EMI
Walvis Ridge
Pitcairn
Koolau
Marquesas
LoNd Array
Rimatara
Mangaia
Rurutu
MORB
No-EM Array
FOZO
St. Helena
Tubuai
HIMU
DMM
d.

(Figure 1.1)

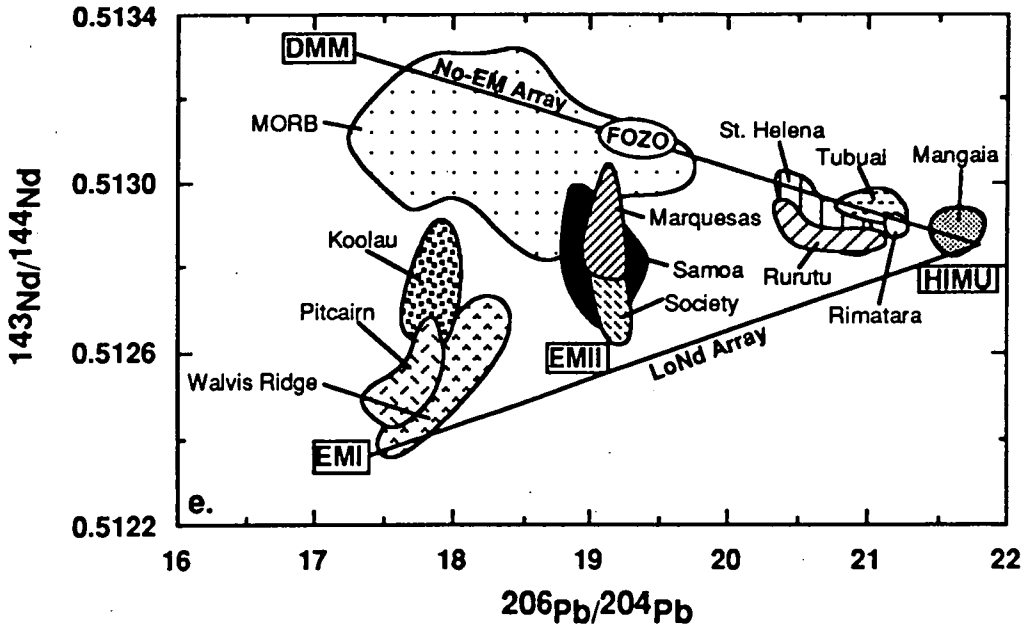

Figure 1.1: Radiogenic isotope plots using data from the following sources: *Cook-Austral Islands (Mangaia, Rimatara, Rurutu and Tubuai)* - Vidal et al. (1984), Palacz and Saunders (1986), Nakamura and Tatsumoto (1988), McDonough and Chauvel (1991), Chauvel et al. (1992) and Hauri and Hart (1993); *Koolau Volcano, Hawaii* - Stille et al. (1983), Roden et al. (1984), Hart (1988) and Roden et al. (in press); *Marquesas Islands (Hatutu, Hiva Oa, Nuku Hiva, Tahuata and Ua Huka)* - Vidal et al. (1984), Dupuy et al. (1987) and Woodhead (1992); *MORB* - Cohen et al. (1980), Dupré and Allègre (1980), Sun (1980), Cohen and O'Nions (1982), White and Hofmann (1982), Dupré and Allègre (1983), Hamelin et al. (1984), Hamelin and Allègre (1985), Hamelin et al. (1986), Macdougall and Lugmair (1986), Michard et al. (1986), Price et al. (1986), Ito et al. (1987), Shirey et al. (1987), White et al. (1987), Dosso et al. (1988) and Mahoney et al. (1989); *Pitcairn Island/Seamounts (Tedside Volcanics, Volcano 2 and Volcano 5)* - Woodhead and McCulloch (1989) and Woodhead and Devey (1993); *Samoan Islands (Manu'a, Tutuila and Upolu)* - White and Hofmann (1982), Newsom et al. (1986), Palacz and Saunders (1986) and Wright and White (1987); *Society slands/Seamounts (Mehetia, Rocard, Tahaa, and Teahitia)* - White and Hofmann (1982), Devey et al. (1990) and Hauri and Hart (1993); *St. Helena* - Sun (1980), Cohen and O'Nions (1982), White and Hofmann (1982), Newsom et al. (1986) and Chaffey et al. (1989); *Walvis Ridge* - Richardson et al. (1982). All $^{87}Sr/^{86}Sr$ data are normalised to $^{86}Sr/^{88}Sr = 0.1194$ and are quoted relative to a value of $^{87}Sr/^{86}Sr = 0.710209$ for the NBS 987 standard (the mean value measured during the course of this study; Appendix 2) where possible, or relative to a value of $^{87}Sr/^{86}Sr = 0.7080$ for the Eimer and Amend $SrCO_3$ standard where NBS 987 standard data are not presented. All $^{143}Nd/^{144}Nd$ data from the literature are normalised to $^{146}Nd/^{144}Nd = 0.7219$ and are quoted relative to a value of $^{143}Nd/^{144}Nd = 0.511897$ for the La Jolla standard (the mean value measured during the course of this study; Appendix 2) where possible, or relative to a value of $^{143}Nd/^{144}Nd = 0.51265$ for the BCR-1 international rock standard where La Jolla standard data are not presented. Bulk Earth (BE) values are $^{143}Nd/^{144}Nd = 0.51265$ and $^{87}Sr/^{86}Sr = 0.70450$; values for the extreme DMM, EMI, EMII and HIMU end-members are from Table 1.1; NHRL calculations are from Hart (1984): $^{207}Pb/^{204}Pb = 0.1084(^{206}Pb/^{204}Pb) + 13.491$; $^{208}Pb/^{204}Pb = 1.2090(^{206}Pb/^{204}Pb) + 15.627$. The geochron (the 4.55 Ga isochron in $^{207}Pb/^{204}Pb$-$^{206}Pb/^{204}Pb$ space which defines the evolution of the Earth as a closed chemical system since its formation) is plotted using 4.55 Ga as the initial age of the Earth and the primordial meteoritic (Canyon Diablo) Pb values of Chen and Wasserburg (1983) as the initial Pb isotope ratios for the Earth. LoNd and No-EM mixing arrays (Hart, et al., 1986; Hart, 1988) in d) and e) are as discussed in the text; approximate location of FOZO from Hart et al. (1992).

Table 1.1: The extreme mantle end-member isotope values used in Figure 1.1 are from the following sources: All $^{87}Sr/^{86}Sr$, $^{143}Nd/^{144}Nd$ and $^{206}Pb/^{204}Pb$ values are from Hart et al. (1992); EMI and EMII $^{207}Pb/^{204}Pb$ and $^{208}Pb/^{204}Pb$ values are from Weaver (1991); HIMU $^{207}Pb/^{204}Pb$ and $^{208}Pb/^{204}Pb$ values are the most radiogenic values for Mangaia from the data set used for Figure 1.1; DMM $^{207}Pb/^{204}Pb$ comprises the least radiogenic value from the data set used in Figure 1.1 and DMM $^{208}Pb/^{204}Pb$ is from Gariépy and Dupré (1991).

	$^{87}Sr/^{86}Sr$	$^{143}Nd/^{144}Nd$	$^{206}Pb/^{204}Pb$	$^{207}Pb/^{204}Pb$	$^{208}Pb/^{204}Pb$
DMM	0.70220	0.51330	17.30	15.42	37.20
HIMU	0.70285	0.51285	21.80	15.84	40.73
EMI	0.70530	0.51236	17.40	15.46	38.00
EMII	0.70780	0.51258	19.00	15.70	39.50

1.3.2 HIMU - High-μ:

The HIMU or high-μ (where $\mu = {}^{238}U/^{204}Pb$) end-member is a relatively uniform component characterised by radiogenic $^{206}Pb/^{204}Pb$ (>20.5), low $^{87}Sr/^{86}Sr$ (~0.7028; less than bulk Earth) and high $^{143}Nd/^{144}Nd$ (~0.51285; greater than bulk Earth) relative to the EM components (Hart, 1988) (Figure 1.1). Its apparent uniformity is based on the limited ranges of $^{87}Sr/^{86}Sr$, $^{143}Nd/^{144}Nd$ and $^{208}Pb/^{204}Pb$ observed in OIB with $^{206}Pb/^{204}Pb$ values greater than 20.5, and the consequent decrease in isotopic data dispersion as this HIMU field is approached (Hart, 1988). The HIMU component is best represented by the island of St. Helena in the southeast Atlantic Ocean, and the Cook-Austral islands of Mangaia, Tubuaii, Rurutu and Rimatara in the south Pacific Ocean (Hart, 1988) (Figure 1.2). As Rurutu also contains young lavas with intermediate HIMU-EM isotopic compositions (Chauvel et al., 1992), only data from this island which have HIMU systematics have been used in Figure 1.1. This includes the $^{87}Sr/^{86}Sr$ and $^{143}Nd/^{144}Nd$ data of Palacz and Saunders (1986) and the corresponding Pb isotope ratios measured, for the same samples, by McDonough and Chauvel (1991).

The paradox of a mantle reservoir with time-integrated high U/Pb values relative to bulk Earth, but low Rb/Sr and Nd/Sm values, appears to be at its most extreme in the HIMU end-member, which has MORB-like $^{87}Sr/^{86}Sr$ but the most radiogenic Pb isotope values known. This is generally known as the "Pb-paradox" and is based on the premise that U, being more incompatible than Pb, should be relatively depleted during mantle differentiation processes, resulting, with time, in unradiogenic Pb isotope ratios which would plot to the left of the geochron (e.g. Newsom et al., 1986). The location of HIMU OIB, far to the right of the geochron in $^{206}Pb/^{204}Pb$-$^{207}Pb/^{204}Pb$ space (Figure 1.1b), indicates that the U/Pb content of their mantle source regions was increased at some time in the past. However, as observed by Hart (1988), their position below the projected extension of the oceanic basalt array in $^{206}Pb/^{204}Pb$-$^{208}Pb/^{204}Pb$ space (Figure 1.1c) implies that HIMU reservoirs possess time-integrated Th/U values less than that of MORB and other OIB sources (Palacz and Saunders, 1986; Chauvel et al., 1992; Vidal, 1992). Although this suggests some degree of U

enrichment relative to Th (e.g. Chauvel et al., 1992), it is still not known whether the actual high-μ signature is a result of U enrichment (e.g. Hart, 1988), Pb depletion (e.g. Vollmer, 1977; Chauvel et al., 1992; Vidal, 1992), or both (e.g. Palacz and Saunders, 1986).

The isotopic decoupling, low $^{87}Sr/^{86}Sr$, high $^{143}Nd/^{144}Nd$ and high Pb isotope ratios, relative to bulk Earth, displayed by many oceanic basalts have stimulated the development of several models for the origin of oceanic basalts in general, and the HIMU source in particular. Most of the current literature proposes long-term isolation of a HIMU source following incorporation into the deep mantle of ancient (1.5-2 Ga) oceanic crust (e.g. Chase, 1981; Hofmann and White, 1982). This recycled oceanic crust may have been subjected to seafloor alteration or hydrothermal processes, increasing its U (e.g. Barnes and Cochran, 1990) or decreasing its Pb content respectively (Chase, 1981; Hofmann and White, 1982; Michard and Albarède, 1985; Palacz and Saunders, 1986), and/or subduction-related processes (Chauvel et al., 1992; Hauri and Hart, 1993) including dehydration (Weaver, 1991; Vidal, 1992) and/or magma extraction (Dupuy et al., 1987).

Recent Re-Os studies of HIMU basalts are compatible with an origin involving crustal recyling. The high $^{187}Os/^{186}Os$ values measured for Mangaia, Tubuai and Rurutu, relative to other oceanic basalts and estimates for the bulk Earth, necessitate a source region with time-integrated high Re/Os, which, along with the other radiogenic isotope characteristics, is consistent with the incorporation of ancient oceanic crust (Hauri and Hart, 1993). Helium isotope ($^3He/^4He$) measurements, expressed here relative to the atmospheric $^3He/^4He$ ratio (R_A) for samples from Tubuai (7.1 R_A) and St. Helena (4.3-5.9 R_A) are lower than MORB values (DMM = 8±1 R_A), and are thought to also be consistent with a recycled origin for HIMU basalts, whereby the recycled material increases the $(U+Th)/^3He$ ratio of the source but has a relatively short storage time in the mantle (<1 Ga) (Graham et al., 1992).

Other ideas have also been proposed for the origin of the HIMU isotopic signature. Lead extraction from the deep mantle into the core via the removal of a sulphide phase after core accretion ('core pumping') (Vollmer, 1977; Vidal and Dosso, 1978; Allègre, 1982) is now largely discredited as a viable option. A lack of systematic variation in the abundances of similarly incompatible chalcophile and siderophile elements relative to lithophile elements (e.g. Mo/Pr and W/Ba, both Mo and W being more siderophile than Pb, and Ce/Pb) over the observed range of Pb isotopic compositions for oceanic basalts (Newsom et al., 1986) argues against continuous core formation, which would be expected to produce correlated mantle depletions in both chalcophile and siderophile elements. Mantle Pb extraction into the core also fails to explain the relative source depletion in Rb necessary to produce the lower than bulk Earth $^{87}Sr/^{86}Sr$ values of HIMU basalts (e.g. Palacz and Saunders, 1986).

Various types of mantle metasomatism have also been invoked to explain the HIMU isotope systematics. Suggested metasomatic origins for HIMU sources include the fluid-related removal of Rb, and possibly Pb, from a portion of the mantle (Hart et al., 1986; Zindler and Hart, 1986; Hart, 1988); the interaction of carbonatitic fluids, enriched in U and Sr and slightly enriched in rare earth elements (REE), with portions of depleted mantle (Nakamura

and Tatsumoto, 1988); and the metasomatism of lithospheric mantle, under oxidising conditions, by carbonatite melts enriched in Nb, Ta and U (as proposed for HIMU-like Christmas Island volcanics; Falloon et al., in prep.). In their study of peridotite xenoliths from Tubuai, Hauri et al. (1993) conclude that the HIMU Pb-Sr-Nd isotopic signature of these rocks is a result of metasomatism of the lithospheric mantle beneath Tubuai by carbonatitic fluids derived from, and bearing the isotopic signature of, the plume itself. They consider the plume to be a product of mixing between peridotite and subducted, volatile-bearing, oceanic crust, thereby invoking a combined recycling/metasomatic origin for the HIMU signature of these xenoliths.

Other proposals for HIMU source production include delamination and reinjection into the mantle of subcontinental lithosphere (McKenzie and O'Nions, 1983); time-integrated U/Pb fractionation between silicate minerals and melt during melt migration in the upper mantle (Halliday et al., 1990); and preferential retention in the mantle of U relative to Pb, primarily in clinopyroxene (Meijer et al., 1990).

A further complication to the HIMU story stems from the suggestion by Vidal (1992) that more than one group of HIMU basalts may exist. Whereas the islands of St. Helena, Mangaia and Tubuai constitute his Group I HIMU basalts, Group II comprises the New England seamounts, the Canary Islands, the Azores and Cape Verde hotspots, Guadalupe, Ua Pou (Marquesas), Muraroa and Fangataufa (Gambiers) and possibly the Pribilof Islands of Alaska. Compared to Group I HIMU basalts, Vidal (1992) proposes that the Group II basalts have lower Pb isotope ratios, although still greater than most other oceanic basalts, are more enriched in the high field strength elements (HFSE) Nb and Ta, and are more depleted in Pb (higher Ce/Pb values). These differences are interpreted to represent a more recent increase (within the last few hundred m.y.) in the μ ratios of Group II source regions due to relatively modern recycling of subducted lithosphere. In contrast, Vidal (1992) interprets Group I HIMU basalts to be the products of a similar lithospheric recycling process during the early to middle Precambrian, entailing substantially higher mantle and lithospheric temperatures, which resulted in some degree of slab melting.

1.3.3 EMI - Enriched Mantle 1:

EMI OIB are characterised by the lowest $^{143}Nd/^{144}Nd$ values of all oceanic basalts (0.5124-0.5125), moderate $^{87}Sr/^{86}Sr$ (0.7050-0.7055) and very unradiogenic $^{206}Pb/^{204}Pb$ (~17.6-17.7) (Hart, 1988). Although EMI is the closest of the four mantle end-members to bulk Earth composition, its isotopic characteristics require a source with time-integrated lower Sm/Nd and U/Pb, slightly lower Th/Pb and higher Rb/Sr values than bulk Earth (Hart, 1988), implying ancient enrichment in Nd/Sm, Rb/Sr and Pb/U (Richardson et al., 1982). Higher Th/U in the EMI source, relative to MORB, is indicated by the location of extreme EMI compositions above the oceanic basalt array in $^{206}Pb/^{204}Pb$-$^{208}Pb/^{204}Pb$ space (Figure 1.1c), defining what some consider to be the most diagnostic feature of the EMI end-member - high $^{208}Pb/^{204}Pb$ at low $^{206}Pb/^{204}Pb$ (J.D. Woodhead, pers. comm., 1993).

Basalts from the aseismic Walvis Ridge in the southeast Atlantic Ocean (Figure 1.2), thought to represent an early trace of the Tristan da Cunha hotspot (e.g. Thompson and Humphris, 1984), are considered characteristic of the EMI end-member. Samples recovered from three Walvis Ridge drillholes define two groups (hole 525A basalts versus hole 527 and 528 samples), and possibly represent variable mixes of the EMI component with more depleted mantle (Thompson and Humphris, 1984).

As Walvis Ridge samples are often altered and data are limited, it is somewhat difficult to assess the uniformity and exact isotopic location of the extreme EMI end-member on the basis of Walvis Ridge basalts alone (Hart, 1988). Other OIB with notable EMI isotopic characteristics include the Koolau tholeiites (Loa group) from the island of Oahu, Hawaii (e.g. Hart, 1988), and volcanics from the Pitcairn Island/Seamount chain (Woodhead and McCulloch, 1989; Woodhead and Devey, 1993) (Figure 1.2). Despite their slightly higher $^{143}Nd/^{144}Nd$ values compared to Walvis Ridge basalts, the Koolau tholeiites define a mixing array with an enriched mantle component (EMI) representing one end-member (Roden et al., 1984; Hart, 1988). This is not evident, however, in Pb-Pb space (Figures 1.1b and c), which may be due to poor definition of the EMI $^{207}Pb/^{204}Pb$ and $^{208}Pb/^{204}Pb$ parameters, based only on the most unradiogenic Walvis Ridge data. The shield-building Tedside Volcanics of Pitcairn Island (Woodhead and McCulloch, 1989) and the younger Pitcairn Seamounts (Woodhead and Devey, 1993) are also considered to represent a mixing array between an EMI plume and a more isotopically depleted component. Of the Pitcairn Seamounts, samples from Volcanoes 2 and 5 possess the most extreme EMI isotopic composition (Woodhead and Devey, 1993) and are therefore included here along with the Koolau and Tedside Volcanics to assist in defining the EMI mantle end-member.

Although the origin of the EMI mantle component is still unresolved, a likely scenario involves subduction and isolation in the mantle of ancient (1.5-2 Ga) oceanic crust accompanied by small amounts (≤5 %: Weaver, 1991; <1 %: Chauvel et al., 1992) of pelagic sediment (Weaver et al., 1986; Weaver et al., 1987; Woodhead and McCulloch, 1989) which has been modified by elemental fractionation (preferential removal of Rb, Sm, and U relative to Sr, Nd and Pb) during subduction (Woodhead and Devey, 1993).

EMI $^{187}Os/^{186}Os$ characteristics are not yet known (Hauri and Hart, 1993). However, a recent oxygen isotope study of the Pitcairn Seamounts has revealed $\delta^{18}O$ values greater than MORB and indicative of the involvement of a small proportion (up to 9 %) of ancient recycled crustal oxygen in their EMI mantle source (Woodhead et al., 1993). Although Graham et al. (1992) consider the $^{3}He/^{4}He$ values of ~4-6 R_A obtained for Tristan da Cunha and Gough Island samples to at least partly reflect an EMI signature, data for seven samples from the Pitcairn Seamounts reveal a greater range of $^{3}He/^{4}He$ (1.9-9.3 R_A; M. Honda, pers. comm., 1993) which overlap with, but extend to lower values than MORB. The range of EMI He isotope values also overlaps with that of the HIMU samples measured by Graham et al. (1992), the latter reflecting increased $(U+Th)/^{3}He$ source contents as a possible consequence of crustal recycling.

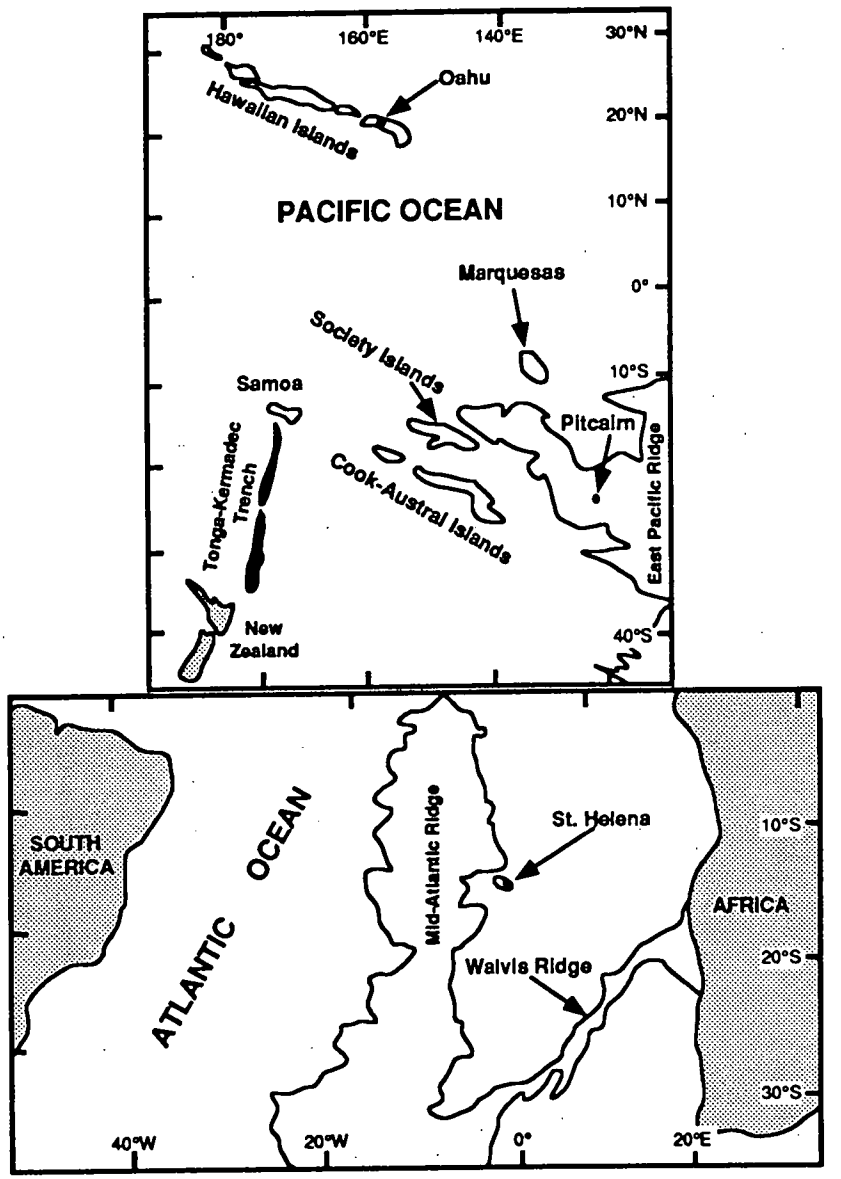

Figure 1.2: Maps showing locations discussed in the text.

As with HIMU, a metasomatic origin for the EMI end-member has also been proposed. This may involve slight modification of a primitive or bulk Earth mantle by small volume melts and CO_2-rich fluids, whereby EMI and HIMU represent the low U/Pb infiltrate and the high U/Pb residue, respectively, of the same metasomatic process (Hart et al., 1986; Zindler and Hart, 1986; Hart, 1988); or partial melting of an enriched (E-type) MORB source with small-scale heterogeneities due to the introduction of small-volume melts and metasomatic fluids (Richardson et al., 1982).

Recent isotopic analyses of MORB dredged from between 39° and 41°E along the Southwest Indian Ridge (SWIR) have revealed unusually low $^{206}Pb/^{204}Pb$ values (16.867-17.449), accompanied by low $^{143}Nd/^{144}Nd$ (0.51244-0.51281) (Mahoney et al., 1992). Whereas this isotopic signature is considered to be unique for MORB, with $^{206}Pb/^{204}Pb$ values even lower than that of the proposed EMI OIB end-member (Table 1.1), no evidence has been found for influence from a near-ridge hotspot in this region. Therefore, Mahoney et al. (1992) have ascribed this isotopic signature to the possible incorporation into the shallow asthenosphere of a portion of Madagascan lithosphere prior to the break-up of Madagascar and Greater India. Recycled lower continental crust or lithosphere have also been suggested as possible EMI sources by Hawkesworth et al. (1984) and Zindler and Hart (1986).

1.3.4 EMII - Enriched Mantle 2:

EMII OIB extend to the highest $^{87}Sr/^{86}Sr$ (>0.7065) values of all oceanic basalts, with $^{143}Nd/^{144}Nd$ (~0.51255) and Pb isotopic ratios intermediate to those of the EMI and HIMU end-members (Hart, 1988; Weaver, 1991). Relative to bulk Earth, the EMII source has higher time-integrated Rb/Sr, U/Pb and Th/Pb, but lower Sm/Nd. The location of the EMII end-member above the NHRL (Northern Hemisphere reference line of Hart (1984) - Section 1.4) indicates a greater Th/U value in its source than in the MORB source.

EMII is the least well-defined isotopically, and possibly the least uniform, of the four mantle end-members. It is the dominant component in Samoa, the Society Islands and the Marquesas archipelago (Hart, 1988). As other mantle components are also represented in these locations, care has been taken to select only those samples with EMII isotopic affinities from these island groups. In the Marquesas for instance, the post-shield alkali volcanics are dominated by an EMII signature whereas the shield-building tholeiites, intermediate between EMII and DMM, have been interpreted to reflect substantial plume contamination by oceanic lithosphere (Woodhead, 1992). Accordingly, Marquesan basalts containing normative hypersthene have been avoided unless stated in the literature to be products of post-shield volcanism. Samples from the island of Ua Pou in the Marquesas have also been excluded due to their HIMU-like isotopic characteristics (Duncan et al., 1986; Dupuy et al., 1987). In contrast, Samoan shield lavas derive from a plume source similar to that of the Society and Marquesan post-shield volcanics, whereas Samoan post-erosional volcanism, superimposed on the shield volcanoes as a consequence of Pacific plate flexure into the Tonga Trench, is derived from mixtures of the EMII shield source and a post-erosional source, the latter interpreted to be the ambient lithosphere or asthenosphere beneath Samoa and characterised by high $^{207}Pb/^{204}Pb$ and $^{87}Sr/^{86}Sr$ and low $^{206}Pb/^{204}Pb$ and $^{143}Nd/^{144}Nd$ (Hofmann and White, 1982; Wright and White, 1987). As no central shield volcano has been formally identified on the Samoan island of Savaii (Wright and White, 1987), no data from this location have been used. Samples excluded from the Society Island/Seamount chain include the evolved trachy-phonolites from Rocard Seamount and all

data from Moua Pihaa; the latter appears to derive from a different (non-EM) source than the rest of the Society chain (Devey et al., 1990).

The linear trends of the plume-derived Marquesan, Society and Samoan samples towards the extreme EMII isotopic composition (Weaver, 1991) are particularly evident on diagrams which show the range of variation in $^{87}Sr/^{86}Sr$ and $^{143}Nd/^{144}Nd$ (Figures 1.1a, d and e). As noted by Hart (1988), these colinear isotopic fields appear to project towards a component intermediate between DMM and HIMU, and located within the MORB field, on all plots in Figure 1.1, rather than toward any of the other recognised end-member components.

The currently popular hypothesis regarding the origin of the EMII mantle end-member proposes subduction and long-term isolation in the deep mantle of ancient (1.5-2 Ga) oceanic crust overlain by a small amount (~5 %; Weaver, 1991) of continental-derived (terrigenous) sediment (White and Hofmann, 1982; Dupuy et al., 1987), possibly accompanied by pelagic sediment (Chauvel et al., 1992). Subsequent remixing with the subducted harzburgitic lithosphere layer has been proposed by Dupuy et al. (1989).

Hauri and Hart (1993) have interpreted their $^{187}Os/^{186}Os$ data for Samoan and Society Island lavas to be similar to peridotite values, and therefore indicative of little, if any, sediment involvement in the EMII source. However, the low Os content of the continental crust, as compared to the mantle (Shirey, 1991), suggests that the incorporation of terrigenous sediment in the mantle could be expected to have little effect on $^{187}Os/^{186}Os$ source values. The high $\delta^{18}O$ values obtained for Society seamount lavas, relative to MORB, imply the involvement of recycled crustal oxygen in the EMII mantle source (Woodhead et al., 1993), and thereby support the subducted sediment hypothesis. Society Seamount samples from Mehetia and Teahitia generally have $^{4}He/^{3}He$ values of ~64,000 (~11 R_A; where $R_A = 1.39 \times 10^{-6}$: Kurz, 1991) and ~90,000 (~8 R_A) respectively (Staudacher and Allègre, 1989), the latter overlapping with MORB values (DMM = 8±1 R_A: Graham et al., 1992). Staudacher and Allègre (1989) interpret the low Mehetia $^{4}He/^{3}He$ values to reflect mixing between upper and lower, relatively undegassed, mantle, whereas high $^{4}He/^{3}He$ in four of their Teahitia samples (142,500-202,000 = 3.5-5 R_A) may be attributed to the presence of subducted material in the source. Graham et al. (1992) propose that EMII basalts may generally have low $^{3}He/^{4}He$ (~3.5-5 R_A) values, based on analyses of Sao Miguel and Shimada Seamount (Graham et al., 1988) samples, consistent with an origin involving the recycling of either sediments with modern day compositions, or upper continental crust.

Other ideas concerning the origin of the EMII end-member include mantle metasomatic enrichment by H_2O-rich fluids, enriched in Rb and U and possibly crustally derived during subduction (Zindler and Hart, 1986); recent (<1.7 Ga) incorporation of subcontinental lithosphere into the suboceanic mantle (Palacz and Saunders, 1986); and short-term storage in the mantle of subducted, recycled continental sediments (Hart, 1988).

1.4 ISOTOPIC MIXING ARRAYS:

Several isotopic mixing arrays have been proposed in an attempt to constrain which of the four mantle end-members are involved in the production of the various OIB suites that do not correspond to the extreme end-member isotopic compositions. The first of these, a planar mantle array in Sr-Nd-Pb (three-dimensional) isotopic space, defined variation among oceanic basalts in terms of mixing between three chemically independent mantle components (Zindler et al., 1982). This concept is now considered to be too simplistic due to the discovery that many EM OIB, including those from Samoa and the Society Islands (White and Hofmann, 1982), Walvis Ridge (Richardson et al., 1982) and Koolau (Stille et al., 1983), plot either above or below the proposed planar mantle array.

Suggested linear mixing arrays include a LoNd array (Hart et al., 1986) and a No-EM array (Hart, 1988), the former reflecting mixing between the EMI and HIMU end-members, and the latter formed by mixing between DMM and HIMU. The No-EM array is considered to lie in the so-called 'reference mantle plane' (Hart, 1988), a two-dimensional projection which parallels the planar mantle array of Zindler et al. (1982) and thereby confirms that the latter did not take either of the EM end-members into account. If the end-member mixing arrays are indeed linear, they imply that the DMM, HIMU and EMI mantle end-members must have similar relative concentrations of Sr, Nd and Pb, resulting in similar values of Sr/Nd, Sr/Pb and Nd/Pb for example (Hart et al., 1986; Hart, 1988). These proposed linear mixing arrays also imply that the EMII end-member is failing to mix with the HIMU and EMI components and may therefore be somewhat physically isolated within the mantle. However, Staudigel et al. (1991), in their study of the oceanic islands and seamounts representing the South Pacific Isotopic and Thermal Anomaly (SOPITA), concluded that the observed isotope systematics of this region are dominated by HIMU-EMII mixing.

Many OIB suites display linear arrays extending from one end-member in isotopic space towards a region intermediate between two other end-member components. The Samoan, Society and Marquesan samples provide a good example, their extreme isotopic ratios define the EMII end-member isotopic composition but their overall arrays extend towards a DMM - HIMU mixing line (Figure 1.1). Zindler and Hart (1986) originally included a fifth mantle end-member component, entitled prevalent mantle (PREMA), which they defined as being isotopically intermediate between HIMU and DMM, but slightly displaced towards EMII. Hart et al. (1992) have redefined this intermediate component or 'missing parent species' as the focal zone (FOZO), characterised by $^{87}Sr/^{86}Sr$ <0.7025, $^{143}Nd/^{144}Nd$ >0.5131, high $^{206}Pb/^{204}Pb$ (19.1 - 19.7) and maybe high $^{3}He/^{4}He$ values. They consider this focal zone to be a possible lower mantle component, incorporated in a great many upwelling mantle plumes (particularly EMII plumes) but rarely, if ever, sampled in a pure form. However, the isotopic overlap between this focal zone and MORB (Figure 1.1d and e) suggests that the former could simply be a product of heterogeneous upper mantle, possibly best defined as E-MORB (enriched MORB contaminated by hotspot emanations

close to ridge crests). The fact that the most extreme EMII end-member basalts known are all located in a similar region of the Pacific Ocean could indicate that their linear isotopic arrays are extending between a pure EMII plume component and an ambient upper mantle in this region which has higher $^{87}Sr/^{86}Sr$, lower $^{143}Nd/^{144}Nd$ and higher Pb isotopic ratios than the most extreme DMM composition and the majority of sampled MORB. Alternatively, as suggested by Woodhead (1992) for the Marquesan basalts, incorporation of an intermediate isotopic component by EMII plumes may be due to lithospheric melting rather than asthenospheric entrainment.

The suggestion that upwelling plumes can melt and incorporate lithospheric material (e.g. Woodhead, 1992) questions the statement by Hart (1988) that the linear LoNd and No-EM arrays are the products of mixing between separate mantle reservoirs, rather than mixing between melts derived therefrom. This may not necessarily be true if plume-derived melts can incorporate DMM material during thermal erosion of MORB lithosphere.

Debate has surrounded the significance of the apparent colinearity of all oceanic basalt data on Pb-Pb plots. Hart (1984) defined a Northern Hemisphere reference line (NHRL) in Pb-Pb space as the line of best fit through data for MORB (both N-MORB and E-MORB), and OIB from Hawaii, Iceland, Azores, Canaries, Cape Verde and the north-east Pacific seamounts. If all oceanic Pb isotope values are the product of a common evolutionary history, this reference line may be interpreted as a secondary isochron in $^{206}Pb/^{204}Pb$-$^{207}Pb/^{204}Pb$ space, whose slope corresponds to an age of ~1.77 Ga (Zindler and Hart, 1986), and would be attributable to a mantle differentiation event which variably increased the U/Pb values of OIB mantle sources (e.g. Chase, 1981) at this time.

However, Chase (1981) also suggested three other possibilities for the origin of the linear array defined by oceanic basalts in Pb-Pb space. One suggestion involves mixing between radiogenic and less radiogenic Pb components, whereby the slope of the line defines the age of their last isotopic equilibration event. Another possibility is that the linear arrays produced in Pb-Pb space by individual islands or island groups may each represent a secondary isochron resulting from a series of secondary enrichment events of a homogeneous primary mantle reservoir after ~1.5 Ga. A third explanation is that the apparent Pb-Pb colinearity displayed by oceanic basalts has no particular age significance and is a result of continuous mantle evolution with changing U/Pb ratios.

1.5 POSSIBLE LARGE-SCALE MANTLE ISOTOPE HETEROGENEITIES:

Hart (1984) proposed the existence of an almost globe-encircling isotopic anomaly in the Southern Hemisphere between the equator and 60°S. As this was based on the original observation of Dupré and Allègre (1983) that Indian Ocean crust constituted a distinct isotopic domain, Hart (1984) coined the term 'Dupal anomaly' to describe the geographical distribution of oceanic regions characterised by high $^{87}Sr/^{86}Sr$ (>0.7035), and

anomalously high $^{207}Pb/^{204}Pb$ and $^{208}Pb/^{204}Pb$ at a given $^{206}Pb/^{204}Pb$ value, the latter expressed as deviations from the NHRL ($\Delta 8/4 > +60$; Hart, 1988). In terms of OIB, this proposed isotopic anomaly pertains to the EM components, precluding them from higher latitudes in the southern hemisphere. Although the apparent absence of EM OIB at high latitudes (Hart, 1988) seems to validate this idea, this may simply be a function of limited sampling in these areas. It is also notable that, in both the Atlantic and Pacific Oceans, HIMU islands may be closely associated with EMI (St. Helena - Walvis Ridge) or intermediate EMI-EMII (Mangaia - Raratonga) components (Hart, 1988). Therefore, the various mantle end-members may in fact be closely related spatially in these areas, repudiating a more distinct and widespread pattern of geographical distribution. It is also notable that EMI OIB are found within the Northern Hemisphere (e.g. Hawaii), and are therefore not restricted to the region between 0° and 60°S.

1.6 ALTERNATIVE EXPLANATIONS FOR OIB HETEROGENEITIES:

Although this chapter has concentrated on the mantle end-member component hypothesis as a possible explanation for the origin of OIB isotopic heterogeneity, not all of the recent literature is in agreement with this idea. For example, studies of Hawaiian basalts by McKenzie and O'Nions (1991) and Watson (1993) suggest that, contrary to the belief that their geochemical variability is a product of several different mantle reservoirs, the degree of melting and processes involved in the transport of the melt may actually be responsible. Watson (1993) claims that only two mantle sources, a primitive source associated with a chemical plume and a depleted source associated with the surrounding thermal plume, plus small variations in the parameters controlling the percolation processes beneath the volcanoes are necessary for the generation of the observed range of intra- and inter-volcano isotopic variations in Hawaii. Despite their corresponding belief that the isotopic compositions of OIB are strongly affected by melt percolation processes, McKenzie and O'Nions (1991) do state that Pb isotopes can still be used for the purposes of defining different mantle reservoirs, due to the fact that all Pb isotopes will be transported by the melt at the same velocity. Therefore, mixing between different reservoirs will produce simple linear mixing relationships in Pb-Pb space (such as that discussed for the Balleny Plume volcanics in Chapter 3), although percolation processes will affect the observed Sr and Nd isotopic ratios.

In their study of the Ninetyeast Ridge hotspot track, Class et al. (1993) argue against the ancient fractionation events and long (1-3 Ga) isolation times required by other researchers to produce the isotopically distinct end-member mantle reservoirs discussed above. They suggest instead that the sources of most plumes are young (<1.2 Ga and probably even <1 Ga) and short-lived (less than a few hundred billion years) due to relatively rapid remixing into the convecting mantle. The isotopic characteristics of their proposed

short-lived plume are a product of a few hundred million year old recycled continental lithosphere, with progressive radioactive decay resulting in a temporal increase in the initial isotopic ratios of samples collected from along the hotspot track.

1.7 SUMMARY:

Recent literature concerning OIB generally explains their isotopic heterogeneity in terms of mixing between four mantle end-member components, DMM (lowest $^{87}Sr/^{86}Sr$, highest $^{143}Nd/^{144}Nd$), HIMU (highest Pb isotopic ratios), EMI (lowest $^{143}Nd/^{144}Nd$) and EMII (highest $^{87}Sr/^{86}Sr$). The processes responsible for the formation of these regions of heterogeneous mantle are still poorly understood. DMM is generally considered to represent a depleted component, located in the uppermost mantle and sampled by both active spreading centres and upwelling mantle plumes. However, both the location and origin of the HIMU, EMI and EMII components involved in the production of OIB are still under debate, with subduction-related and/or mantle metasomatic processes currently the most favoured hypotheses regarding their origin.

These end-member components may not actually reside within physically separate mantle reservoirs (e.g. Barling and Goldstein, 1990). Whereas DMM is usually equated with the upper mantle, Staudigel et al. (1991) and Chauvel et al. (1992), in their studies of South Pacific OIB, suggest that three of the end-member components, HIMU, EMI and EMII may be spatially related within the mantle. Chauvel et al. (1992) favour the idea of a single process producing the observed compositional ranges of oceanic basalts, rather than the proposed end-members representing isolated and independently generated mantle reservoirs.

It is important to be aware that a range of mantle processes of varying extent and timing may be involved in the production of these mantle heterogeneities. As stated by Sun and McDonough (1989), the fact that observed OIB radiogenic isotope variations are a function of parent/daughter ratios and isolation times in the mantle means that the same mantle process/es occurring at different times and resulting in different degrees of elemental fractionation will produce variable but coherent Pb, Sr and Nd isotopic compositions. Their conclusion, that the mantle end-member components should not be expected to possess fixed isotopic compositions, is in accordance, for instance, with the suggestion by Vidal (1992) that more than one group of HIMU basalts may exist.

CHAPTER 2

THE MAJOR AND TRACE ELEMENT HETEROGENEITY OF OCEAN ISLAND BASALTS

2.1 INTRODUCTION:

The DMM, HIMU, EMI and EMII mantle end-members were originally defined in terms of their Sr, Nd and Pb isotopic compositions (Chapter 1), although subsequent research has also revealed the presence of some trace element distinctions (Palacz and Saunders, 1986; Dupuy et al., 1988; Hart, 1988; Dupuy et al., 1989; Sun and McDonough, 1989; Weaver, 1991; Chauvel et al., 1992; Vidal, 1992). Compared to the numerous published studies of OIB isotopic and trace element systematics, however, the examination and interpretation of major element differences between the various OIB end-members remains relatively neglected. Although there is abundant literature pertaining to the major element systematics of MORB (e.g. Klein and Langmuir, 1987; 1989; Niu and Batiza, 1991), derived from the DMM component, no attempt has yet been made to compare the major element compositions of the HIMU, EMI and EMII mantle end-members.

This chapter will examine and compare the major and trace element systematics of HIMU, EMI and EMII end-member basalts with the aim of gaining a better understanding of the petrogenetic conditions involved in their formation. However, it must be kept in mind that, compared to MORB glasses, there are inherent problems associated with attempting a major element comparison of whole-rock OIB samples, including the fact that they are not aphyric, commonly containing phenocrysts and maybe even xenocrysts, and may be altered to varying degrees. This latter point is often particularly difficult to assess when dealing with literature-derived geochemical data, with no opportunity to view the actual rock samples.

2.2 SAMPLE SELECTION:

In attempting to discover consistent major and trace element differences between the HIMU, EMI and EMII mantle end-members, only samples from those localities used to isotopically define each of these components in Chapter 1 will be considered here.

In order to compare the trace element characteristics of magmas derived from the proposed mantle end-members (Section 2.3) and to avoid late-stage fractionation effects, samples from each location which have <5 wt % MgO have been excluded from further consideration. In addition, certain samples with anomalous chemical features compared to other samples from the same locality, are also excluded. These omissions are discussed in more detail throughout this section.

Data for HIMU islands (Mangaia, Tubuai, Rurutu and St. Helena), plotted in Figure 2.1, indicate that olivine and clinopyroxene fractionation were dominant factors in controlling whole rock major element chemistry in these basalts down to ~5 wt % MgO. This is suggested by the decrease in Ni and Cr and the relatively constant CaO which accompanies the decrease in MgO content. The steady increase in Al_2O_3 with decreasing MgO indicates that plagioclase fractionation was not involved. Decreasing CaO, TiO_2, FeO* (where FeO* = (0.9 x Fe_2O_3) + FeO) and P_2O_5 at MgO contents of <5 wt %, consistent with late-stage fractionation of clinopyroxene, Fe-Ti oxides and apatite, is particularly evident in samples from St. Helena. Excluded HIMU data include St. Helena samples 151 (Chaffey et al., 1989), which has lower FeO*, Ni, P_2O_5, TiO_2 and CaO and higher SiO_2, Al_2O_3, K_2O and Na_2O than all other St. Helena samples, and 140 (Chaffey et al., 1989) which has anomalous trace element contents compared to the other St. Helena samples; and Tubuai samples TBA 11 (Chauvel et al., 1992) and 7282 (Dupuy et al., 1989) which have anomalously low CaO contents.

EMI major element data for Walvis Ridge, Koolau Volcano, Pitcairn Island (Tedside Volcanics) and Pitcairn Seamounts (Volcanoes 2 and 5) are plotted in Figure 2.2. Koolau data, in particular, are indicative of a major role for olivine and clinopyroxene fractionation. Excluded Walvis Ridge samples comprise plagioclase cumulates (sample 42.2: Richardson et al., 1984) and altered samples with either anomalously high K_2O contents due to smectite formation (samples 41-2 and 42-1: Humphris and Thompson, 1983 and Richardson et al., 1984 respectively) or very low Rb contents (sample 557-1; Richardson et al., 1984). Compared to other EMI samples, Walvis Ridge basalts are distinguished by a greater range of CaO, P_2O_5 and TiO_2 at a given MgO content. Samples from Volcano 5 of the Pitcairn Seamount chain all have trachytic compositions (Woodhead and Devey, 1993) and are therefore too evolved to be considered further. Koolau samples with very low Rb contents (samples 15, 16, 27, KOO50, KOO52, KOO54 and OH25; Frey et al., in press), possibly due to alteration, have also been excluded from further consideration.

Figure 2.3 shows a series of major element plots for EMII (Marquesas Islands, Samoan Islands and Society Islands/Seamounts) OIB. The observed chemical variations are consistent with olivine and clinopyroxene fractionation, along with an insignificant role for plagioclase fractionation.

For the purposes of examining and comparing the HIMU, EMI and EMII end-members, only those samples with high MgO contents (9.5-12.5 wt %), close to primary compositions, have been used (Section 2.4). Adopting this criterion has meant that no

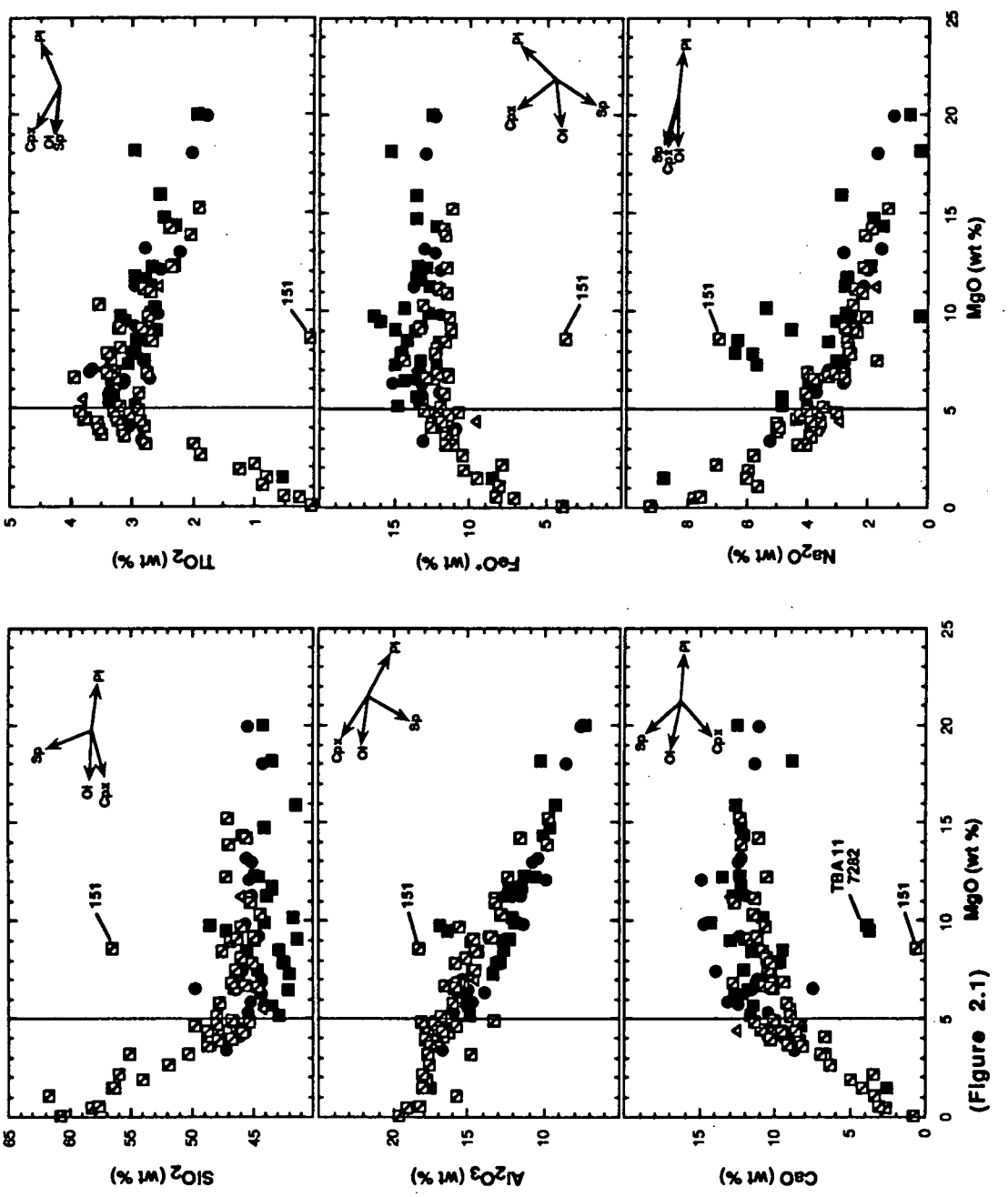
SiO2 (wt %)
Al2O3 (wt %)
CaO (wt %)
TiO2 (wt %)
FeO* (wt %)
Na2O (wt %)
MgO (wt %)
MgO (wt %)
151
TBA11
7282
Pl
Cpx
Ol
Sp

(Figure 2.1)

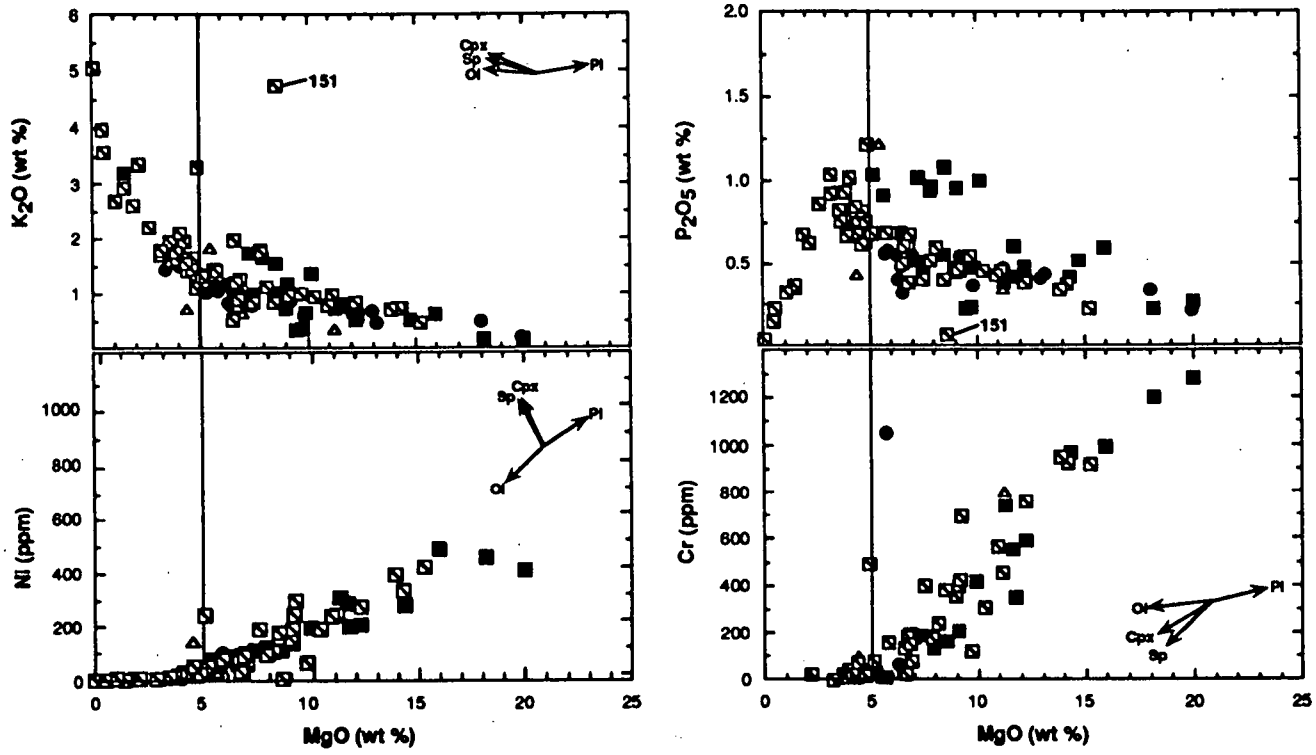

Figure 2.1: MgO versus various major elements, Ni and Cr for HIMU samples from Mangaia (filled circles), Rurutu (open triangles), Tubuai (filled squares) and St. Helena (slashed squares). Data sources include Duncan (1975), Palacz and Saunders (1986), Weaver et al. (1987), Dupuy et al. (1988), Chaffey et al. (1989), Dupuy et al. (1989) and Chauvel et al. (1992). Relative and approximate fractionation trends are plotted as for Figure 3.10.

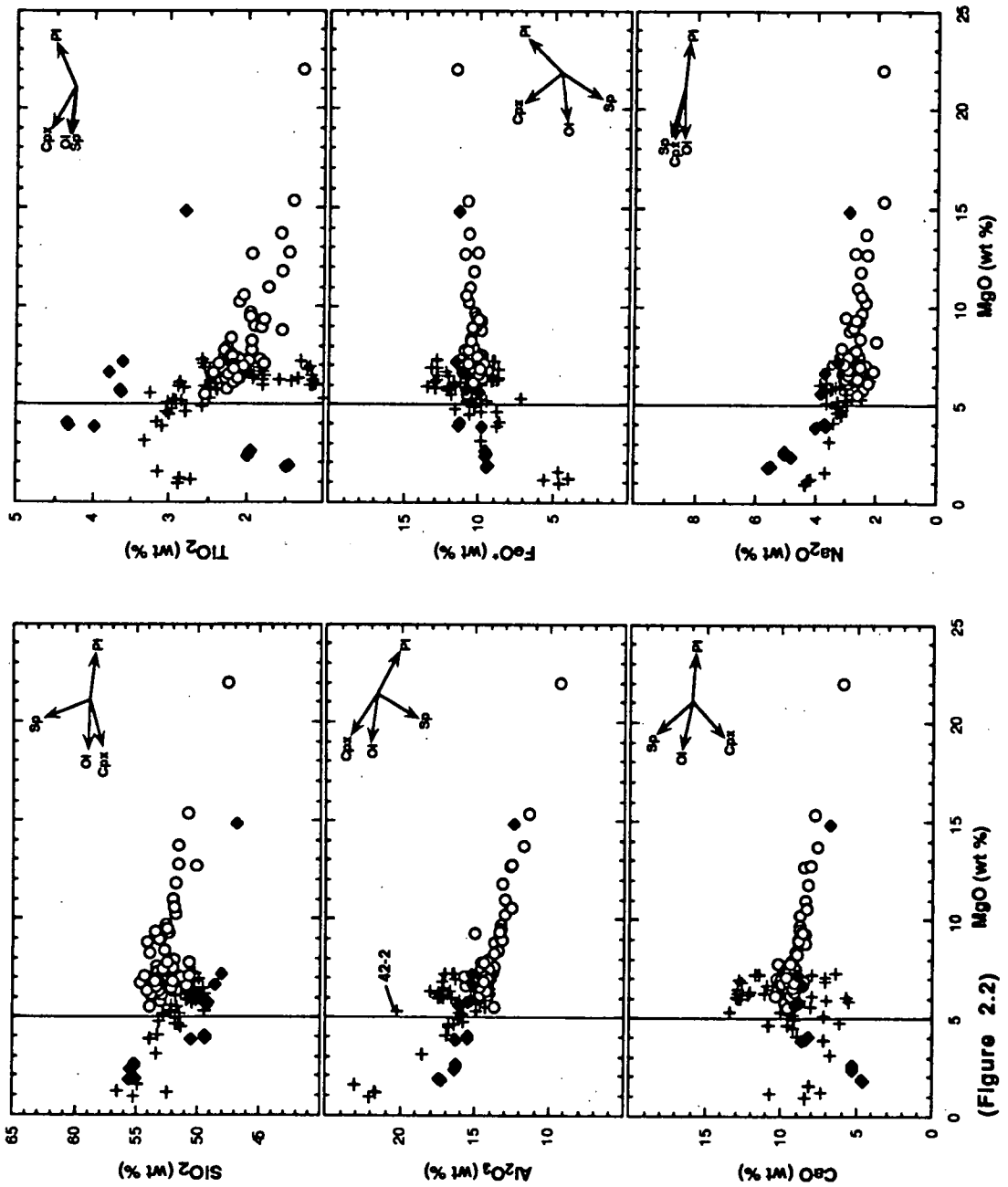
SiO2 (wt %)
Al2O3 (wt %)
CaO (wt %)
TiO2 (wt %)
FeO* (wt %)
Na2O (wt %)
MgO (wt %)
MgO (wt %)
42-2
Pl
Cpx
Ol
Sp

(Figure 2.2)

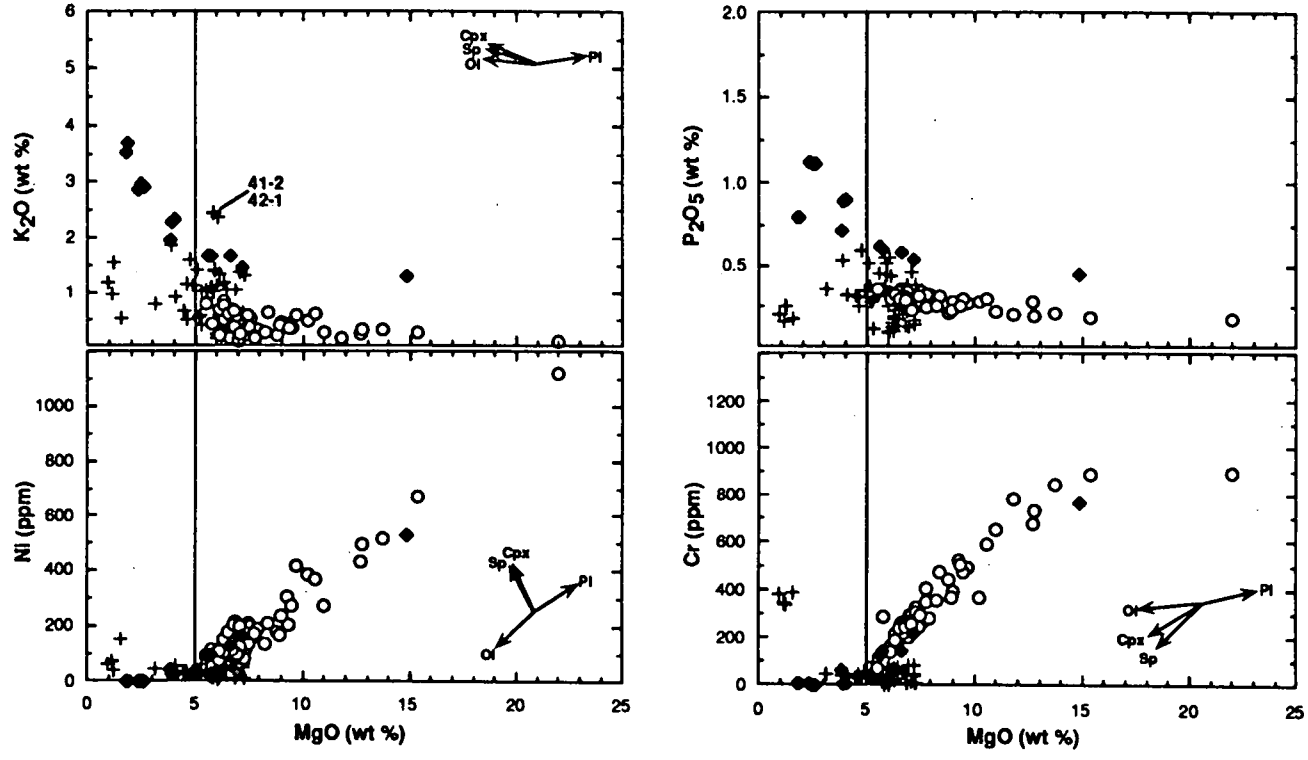

Figure 2.2: MgO versus various major elements, Ni and Cr for EMI samples from Walvis Ridge (crosses), Koolau Volcano (open circles) and Pitcairn Island/Seamounts (filled diamonds). Data sources include Humphris and Thompson (1983), Richardson et al. (1984), Roden et al. (1984), Thompson and Humphris (1984), Budahn and Schmitt (1985), Woodhead and McCulloch (1989), Woodhead and Devey (1993) and Frey et al. (in press). Relative and approximate fractionation trends are plotted as for Figure 3.10.

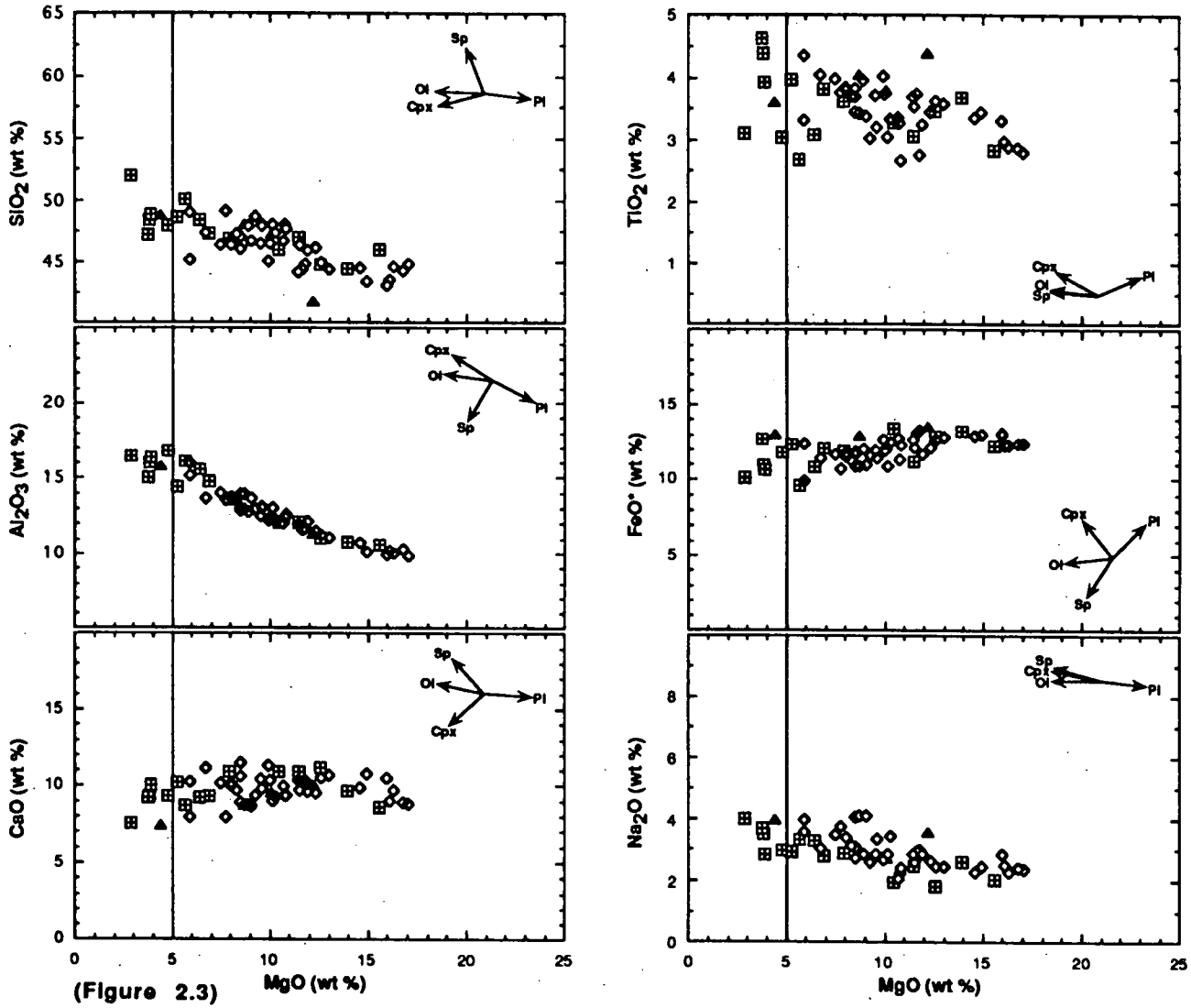
SiO2 (wt %)
Al2O3 (wt %)
CaO (wt %)
TiO2 (wt %)
FeO* (wt %)
Na2O (wt %)
MgO (wt %)
MgO (wt %)
Sp
Ol
Cpx
Pl

(Figure 2.3)

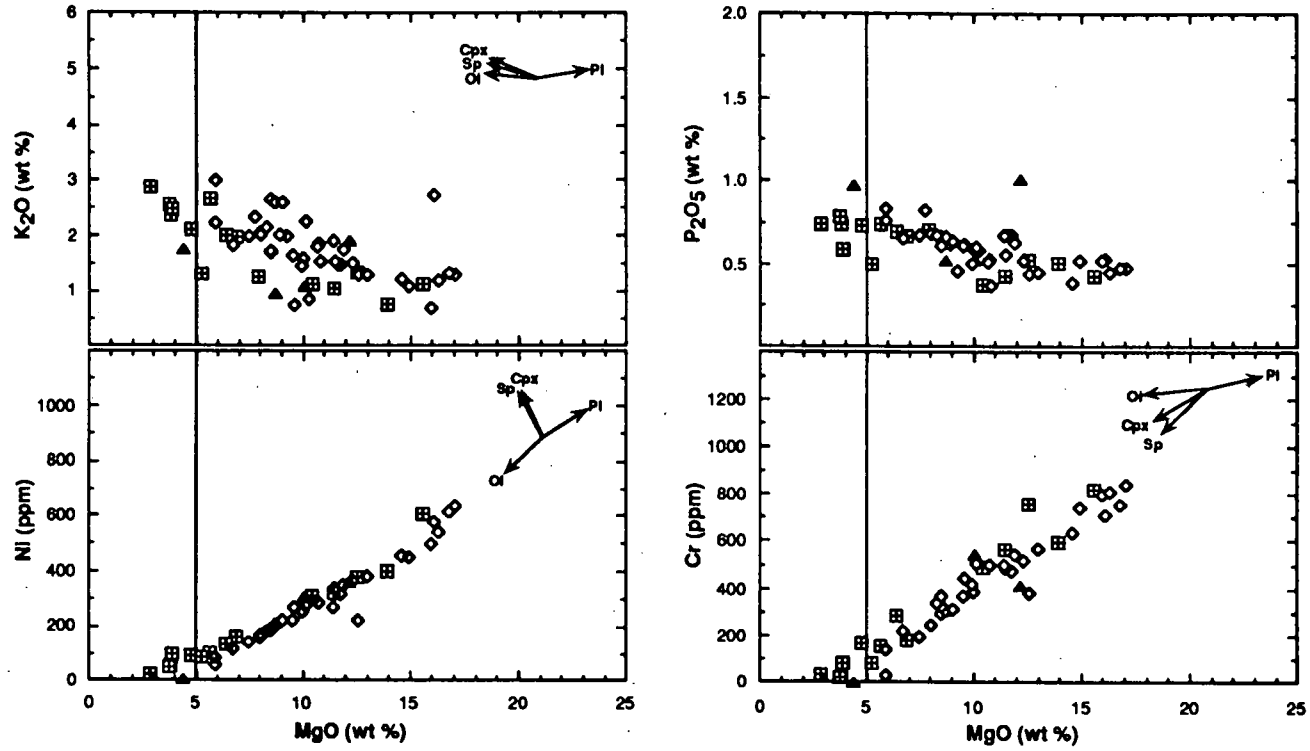

Figure 2.3: MgO versus various major elements, Ni and Cr for EMII samples from the Marquesas (crosses within squares), Samoan (filled triangles) and Society (open diamonds) Islands. Data sources include Duncan, (1975), Dostal et al. (1982), Liotard et al. (1986), Newsom et al. (1986), Palacz and Saunders (1986), Dupuy et al. (1989), Devey et al. (1990) and Woodhead (1992). Relative and approximate fractionation trends are plotted as for Figure 3.10.

Walvis Ridge or Pitcairn data can be included, and discussions of EMI major element data refer exclusively to the Koolau volcanics.

2.3 TRACE ELEMENT SYSTEMATICS OF THE MANTLE END-MEMBER COMPONENTS:

The trace element systematics of various OIB suites have been previously examined in a comparative fashion by a number of researchers (e.g. Palacz and Saunders, 1986; Dupuy et al., 1988; Hart, 1988; Dupuy et al., 1989; Sun and McDonough, 1989; Weaver, 1991; Chauvel et al., 1992; Vidal, 1992), often with conflicting results. Therefore, despite a wealth of studies which attempt to couple OIB radiogenic isotope and geochemical data, the trace element characteristics of the HIMU, EMI and EMII end-member components remain relatively ill-defined.

Studies of OIB trace element systematics have generally assumed that the abundance ratios of highly incompatible elements, which have similar mineral/melt partition coefficients (K_d) with respect to the major high pressure peridotite phases (olivine, pyroxene and garnet), will remain unfractionated during partial melting and fractional crystallisation, and will therefore be representative of source chemistry (e.g. Sun and McDonough, 1989). However, as recently demonstrated by Hoernle and Schmincke (1993) for the island of Gran Canaria, some incompatible elements may be retained by residual accessory mineral phases, such as apatite, zircon, ilmenite and phlogopite, at relatively low degrees of partial melting. Although this observed inter-element fractionation places some doubt on the potential of incompatible element ratios to be used as source tracers in a similar fashion to radiogenic isotope ratios, it is still possible to distinguish some systematic trace element differences between the OIB suites examined here, particularly in terms of the HIMU and EMII end-member basalts.

2.3.1 HIMU Trace Element Compositions:

Examination of the trace element data for basalts from the islands of Tubuai, Rurutu, Mangaia and St. Helena reveals certain distinctive HIMU trace element characteristics. The narrow range and relative consistency of trace element abundance ratios between the various HIMU oceanic islands (Table 2.1; Figure 2.4) also suggests that HIMU mantle sources have more uniform compositions than either of the enriched mantle (EM) sources (Hart, 1988; Weaver, 1991).

In accord with the results of previous studies (e.g. Palacz and Saunders, 1986; Dupuy et al., 1988; Hart, 1988; Dupuy et al., 1989; Sun and McDonough, 1989; Weaver, 1991; Chauvel et al., 1992; Vidal, 1992), the predominant HIMU trace element characteristics (Table 2.1, Figure 2.4) include low LILE/HFSE and LREE/HFSE values, compared to both EMI and EMII basalts. This is most evident in terms of their generally lower

Table 2.1: Trace element abundance ratios for HIMU, EMI and EMII OIB presented as ranges underlain by the mean value ± 1σ error for each locality (numbers in bold type are the most well constrained: σ/mean ≤~10 %); numbers in parentheses indicate the number of analyses used (n) to calculate both the ratio ranges and the mean values. Data sources include: *HIMU* - Palacz and Saunders (1986), Weaver et al. (1987), Dupuy et al. (1988), Chaffey et al. (1989), Dupuy et al. (1989) and Chauvel et al. (1992); *EMI* - Humphris and Thompson (1983), Richardson et al. (1984), Roden et al. (1984), Thompson and Humphris (1984), Budahn and Schmitt (1985), Woodhead and McCulloch (1989), Woodhead and Devey (1993), Frey et al. (in press) and J.D. Woodhead (unpublished data); *EMII* - Dostal et al. (1982), Liotard et al. (1986), Palacz and Saunders (1986), Dupuy et al. (1989), Devey et al. (1990) and Woodhead (1992).

	Rb/Nb	Ba/Rb	Ba/Th	Ba/Nb	Ba/La	Th/U	Th/Nb	Th/La
HIMU								
Mangaia	0.24-0.48 (18)	9.62-22.00 (17)	55-85 (16)	4.63-7.24 (17)	6.67-9.22 (16)	3.39-3.97 (3)	0.081-0.101 (17)	0.103-0.131 (17)
	0.38±0.05	15.74±2.70	**66±7**	**5.88±0.64**	**7.64±0.76**	**3.60±0.32**	**0.091±0.005**	**0.116±0.008**
Rurutu	0.14-0.39 (3)	13.16-50.50 (3)	63-90 (3)	5.07-6.97 (3)	6.76-8.89 (3)	-	0.078-0.084 (3)	0.097-0.109 (3)
	0.27±0.13	29.84±18.99	78±14	6.30±1.07	8.13±1.19	-	**0.081±0.003**	**0.104±0.006**
Tubual	0.15-0.45 (19)	10.72-30.60 (19)	20-83 (11)	1.74-5.23 (19)	2.37-9.34 (18)	3.62-4.46 (11)	0.059-0.124 (11)	0.073-0.167 (10)
	0.32±0.09	14.86±4.78	52±19	4.51±1.01	6.37±1.64	**4.03±0.31**	0.084±0.018	0.121±0.029
St. Helena	0.01-0.39 (22)	1.67-67.00 (22)	64-151 (11)	4.51-10.24 (22)	6.80-15.36 (19)	2.58-9.59 (10)	0.007-0.082 (11)	0.093-0.118 (11)
	0.28±0.11	18.05±11.91	86±26	5.42±1.35	8.45±1.95	4.65±2.38	0.065±0.025	**0.107±0.006**
EMI								
Walvis Ridge	0.15-1.08 (37)	14.08-100.59 (37)	-	10.23-17.60 (38)	14.33-19.11 (6)	-	-	-
	0.57±0.24	32.04±24.47	-	13.75±2.10	16.22±1.93	-	-	-
Koolau	0.14-1.61 (63)	6.67-64.55 (63)	108-475 (53)	5.35-23.33 (71)	2.92-14.20 (57)	0.33-1.67 (3)	0.020-0.095 (49)	0.018-0.062 (53)
	0.62±0.26	20.30±11.21	216±70	10.20±2.60	8.38±2.10	1.07±0.68	0.052±0.013	0.040±0.010
Pitcairn	0.46-0.58 (5)	12.84-16.77 (5)	65-84 (5)	7.10-8.20 (5)	8.93-9.59 (5)	3.78-9.57 (5)	0.085-0.120 (5)	0.110-0.140 (5)
	0.52±0.05	**14.82±1.40**	**72±7**	**7.60±0.40**	**9.26±0.24**	6.09±2.27	0.107±0.014	**0.131±0.012**
EMII								
Samoa	0.58-0.63 (3)	11.09-13.52 (3)	57-67 (3)	6.42-8.75 (3)	7.33-8.59 (3)	-	0.112-0.139 (3)	0.116-0.142 (3)
	0.61±0.04	**12.54±1.28**	**62±5**	7.63±1.17	**8.01±0.64**	-	**0.122±0.015**	**0.129±0.013**
Society	0.31-1.24 (36)	8.76-30.45 (36)	63-80 (9)	8.20-15.57 (36)	8.77-19.62 (30)	3.94-5.13 (4)	0.117-0.168 (9)	0.131-0.183(9)
	0.93±0.19	13.10±4.54	**71±7**	11.51±1.87	12.43±2.87	**4.66±0.51**	**0.145±0.017**	**0.151±0.020**
Marquesas	0.35-1.64 (9)	7.76-30.75 (10)	68-119 (6)	8.62-12.87 (9)	10.02-12.18 (6)	-	0.072-0.159 (6)	0.084-0.179 (6)
	1.01±0.36	12.04±6.74	91±19	10.74±1.32	**11.39±0.80**	-	0.123±0.032	0.131±0.033

Table 2.1: (continued)

	Nb/U	Nb/Pb	K/Nb	La/Nb	Ce/Rb	Ce/Pb	Zr/Nb
HIMU							
Mangaia	37-42 (3) **39±3**	16.9-18.8 (2) **17.9±1.3**	75-292 (18) 141±45	0.72-0.85 (17) **0.78±0.03**	3.76-6.66 (17) 4.47±0.70	27.3-30.2 (2) **28.8±2.1**	3.82-5.49 (18) **4.77±0.50**
Rurutu	- -	10.4-20.8(2) 15.6±7.4	97-157 (3) 119±33	0.75-0.80 (3) **0.77±0.03**	4.30-12.10 (3) 7.67±4.01	17.3-34.5 (2) 25.9±12.2	4.11-5.07 (3) **4.65±0.49**
Tubual	33-76 (11) 50±12	22.3-40.2 (7) 27.5±7.5	25-124 (19) 81±28	0.53-0.80 (18) **0.71±0.07**	3.31-10.04 (19) 5.05±2.30	30.9-54.2 (7) 38.4±10.3	2.67-3.66 (19) **3.10±0.31**
St. Helena	38-143 (8) 69±37	- -	13-266 (22) 136±59	0.07-0.75 (19) 0.59±0.18	0.50-5.27 (19) 4.05±0.99	- -	0.36-4.75 (22) 3.63±1.24
EMI							
Walvis Ridge	- -	- -	172-438 (38) 300±74	0.85-0.97 (6) **0.90±0.05**	1.69-4.08 (6) 2.94±0.78	- -	5.87-11.53 (38) 8.05±1.83
Koolau	- -	- -	77-709 (71) 364±142	1.08-2.00 (53) 1.28±0.15	1.79-20.4 (49) 16.43±4.03	- -	13.75-18.57 (71) **16.19±1.05**
Pitcairn	44-80 (5) 56±15	11.41-12.22 (5) **11.8±0.4**	89-270 (5) 127±80	0.78-0.88 (5) **0.82±0.04**	2.96-3.70 (5) **3.38±0.29**	19.4-21.0 (5) **20.4±0.6**	5.80-6.16 (5) **5.99±0.13**
EMII							
Samoa	- -	10.53-13.26 (3) 12.07±1.40	351-404 (3) **369±31**	0.79-1.19 (3) 0.96±0.21	3.30-3.95 (3) **3.55±0.35**	20.7-31.8 (3) 26.2±5.6	4.63-7.13 (3) 6.21±1.37
Society	26-41 (4) 33±7	4.50-11.33 (13) 7.45±1.78	125-684 (36) 368±94	0.72-1.12 (30) **0.94±0.10**	1.65-7.25 (34) 2.59±1.18	10.7-25.1 (12) 16.6±4.7	5.39-8.68 (36) 7.21±0.81
Marquesas	32-48 (4) 38±7	9.25-10.40 (3) **9.88±0.58**	189-526 (10) 322±90	0.86-1.04 (6) **0.94±0.06**	1.39-5.40 (6) 2.60±1.42	- -	5.52-8.52 (9) 7.04±1.08

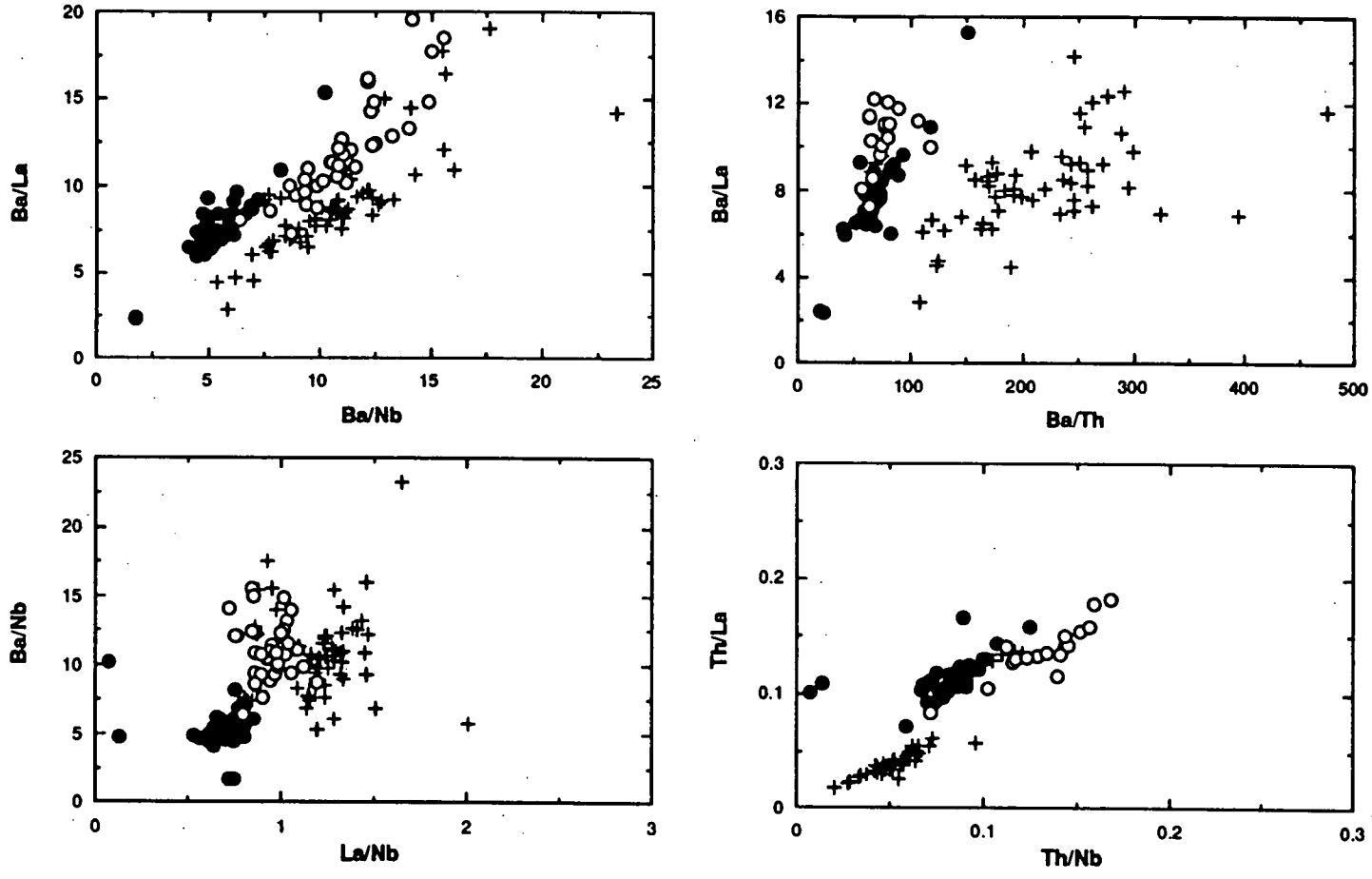

(Figure 2.4)

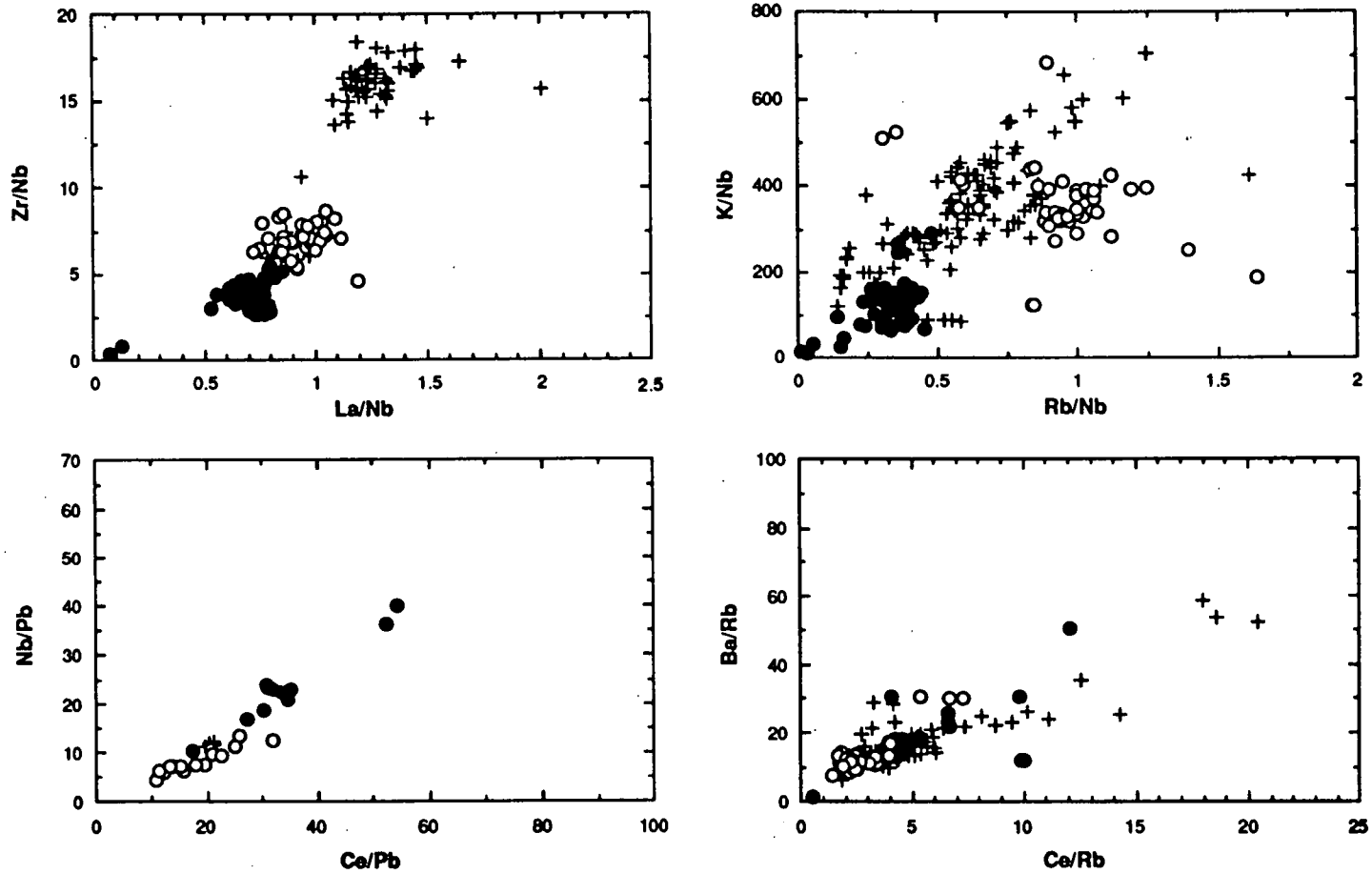

Figure 2.4: Trace element abundance ratio plots for HIMU (filled circles), EMI (crosses) and EMII (open circles) OIB; data sources as for Table 2.1. Note that EMI analyses extend to even higher values than shown in the Ce/Rb versus Ba/Rb diagram.

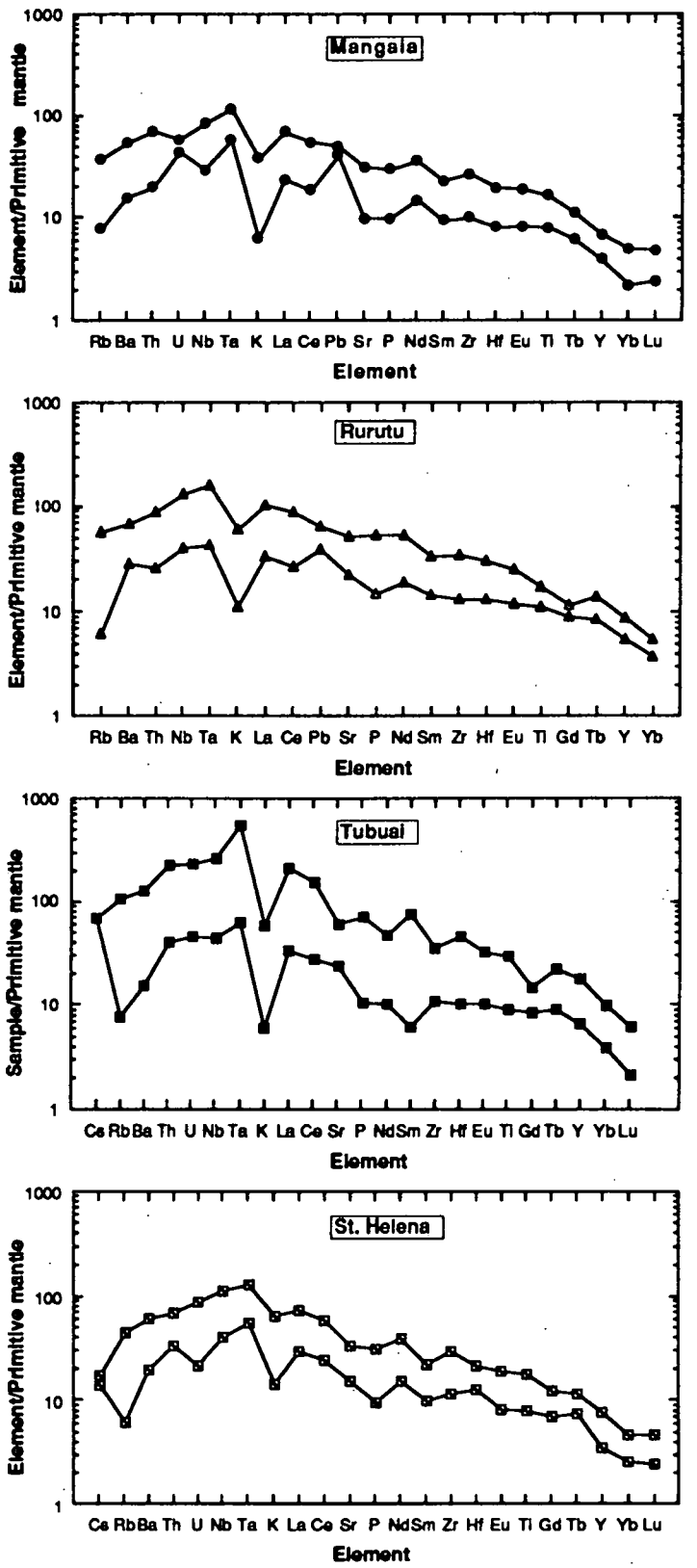

Figure 2.5: Primitive mantle-normalised incompatible element diagrams illustrating the data ranges for the HIMU oceanic islands of Mangaia, Rurutu, Tubuai and St. Helena; data sources are as for Table 2.1. Normalising values are from Sun and McDonough (1989).

Ba/Nb, Rb/Nb (particularly with respect to EMII basalts), K/Nb and La/Nb values. HIMU basalts also have higher Ce/Pb, but no evidence has been found here for the relatively high Ce/Rb values proposed by Vidal (1992) as being representative of HIMU basalts. Their high Nb/Pb and Ce/Pb values, accompanied by a lack of distinction between the HIMU and EM end-members in terms of Nb/U and Th/U, are consistent with the idea (e.g. Chauvel et al., 1992; Vidal, 1992) of Pb depletion rather than U enrichment being responsible for the high-μ characteristics of this mantle source. Other HIMU trace element characteristics include Ba/Th values lower than EMI but similar to EMII basalts, and Th/La and Th/Nb values less than EMII but greater than EMI.

Although Zr/Nb may be affected by partial melting, Nb being more incompatible than Zr, HIMU basalts appear, nevertheless, to have lower Zr/Nb values than both of the EM components. The distinctly higher Zr/Nb values of the Koolau tholeiites are a result of higher degrees of melting, but the fact that the other alkaline EM volcanics also have higher Zr/Nb values than HIMU basalts may be consistent with the idea of relative Nb enrichment in the HIMU source (e.g. Weaver, 1991).

It has been proposed that the incompatible element patterns of HIMU OIB are complementary to those of island arc magmas (e.g. Dupuy et al., 1987; Hart, 1988; Dupuy et al., 1989) and are, therefore, residues of subduction-related processes. The incompatible trace element patterns of Tubuai, Rurutu, Mangaia and St. Helena basalts (Figure 2.5) are characterised by pronounced negative K anomalies and progressively decreasing normalised abundances of LILE more incompatible than Ta. Although these trace element patterns display higher abundances of Nb and Ta with respect to the adjacent LILE, it is debatable as to whether this constitutes a positive anomaly as suggested by Weaver (1991). The plots of Figure 2.5 indicate that this apparent Ta-Nb anomaly is most likely a consequence of relative depletion in the normalised abundances of the adjacent LILE.

All of the HIMU oceanic islands examined here correspond to Group I of Vidal (1992); no attempt has been made to study the characteristics of his proposed Group II HIMU basalts.

2.3.2 EMI Trace Element Compositions:

In terms of their trace element contents, EMI OIB are generally thought to be characterised by higher LILE/HFSE and LREE/HFSE values than other OIB, slightly lower Ce/Pb (~20) than the average value generally assigned to oceanic basalts (Ce/Pb = 25±5; Hofmann et al., 1986), and enrichment in Ba relative to other highly incompatible trace elements (e.g. Weaver et al., 1987; Weaver, 1991; Chauvel et al., 1992).

Their generally higher Ba/Nb and La/Nb values compared to HIMU basalts (Table 2.1; Figure 2.4), may be indicative of LILE and LREE enrichment in the EMI source. However, the ranges of other LILE/HFSE values, such as Rb/Nb and K/Nb, although extending to higher values, do overlap with HIMU values, and considerable overlap also exists between the LILE/HFSE values (Rb/Nb, Ba/Nb and K/Nb) of EMI and EMII OIB. The latter point was emphasised by Woodhead and Devey (1993). who also expressed doubt about the

proposed Ba enrichment of EMI basalts. Despite their relatively high Ba/Th values, EMI basalts have Ba/La values which overlap with HIMU and EMII basalts, and EMI Ba/Nb values are similar to EMII. Therefore, their high Ba/Th may in fact be a consequence of Th depletion in the EMI source, as evidenced by the low Th/Nb and Th/La values of the Koolau tholeiites and the negative Th anomaly of the Koolau incompatible element plot (Figure 2.6). The extension of EMI data to the highest Ba/Rb and Ce/Rb values, and the relative Rb depletions on Walvis Ridge and Koolau incompatible element plots, also suggests Rb depletion in the EMI mantle source. However, the possibility that Rb anomalies may be alteration-related must also be taken into account, despite the exclusion of several Koolau samples with anomalously low Rb contents from Table 2.1 and Figure 2.6.

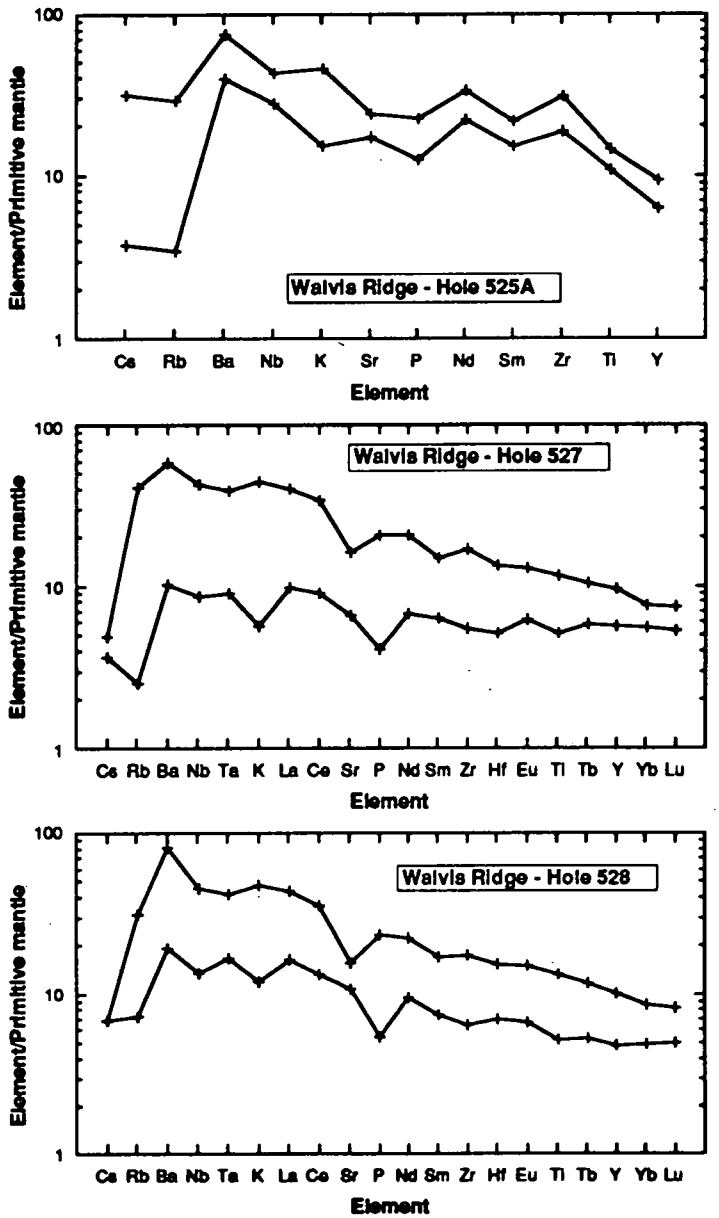

(Figure 2.6)

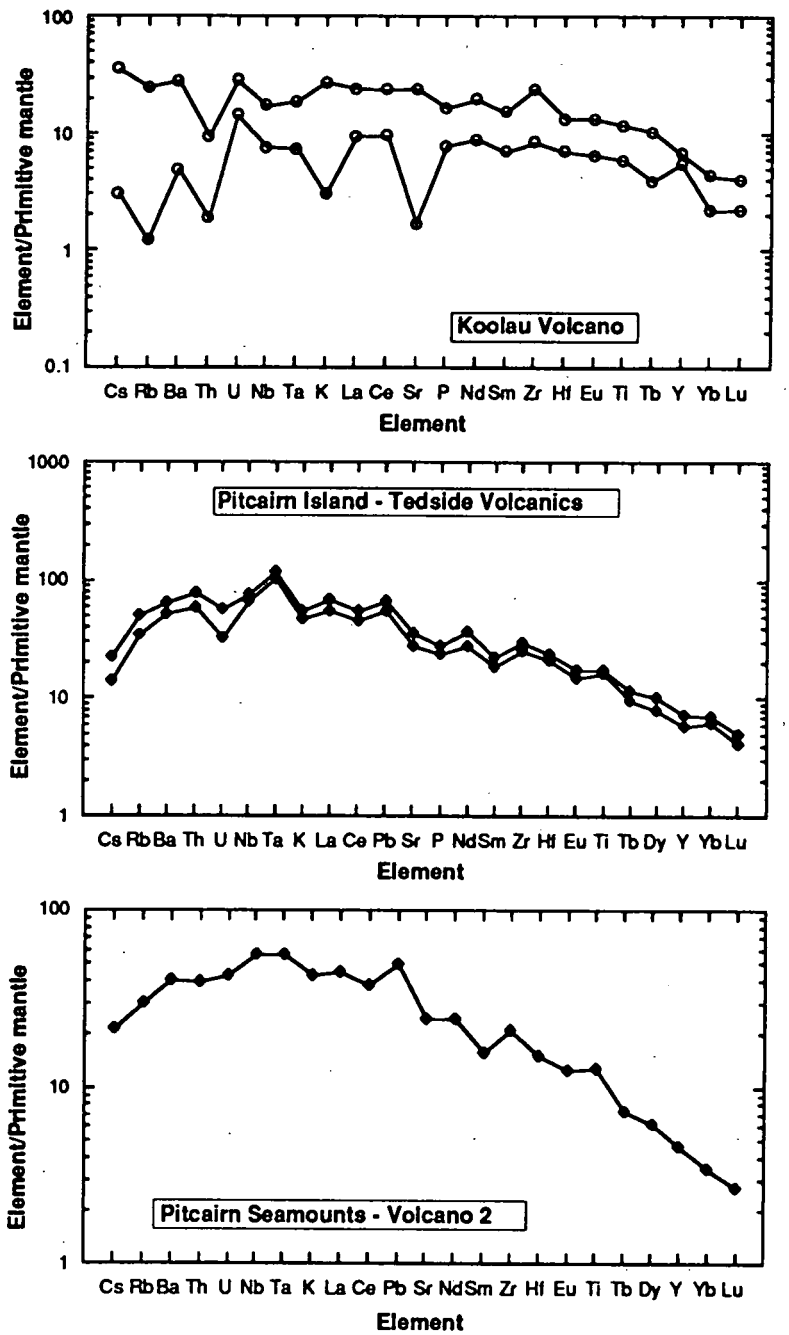

Figure 2.6: Primitive mantle-normalised incompatible element diagrams illustrating the data ranges for EMI basalts from Walvis Ridge (Holes 525A, 527 and 528 are plotted separately for clarity), Koolau, Pitcairn Island (Tedside Volcanics) and Volcano 2 of the Pitcairn Seamounts; data sources are as for Table 2.1. Normalising values are from Sun and McDonough (1989).

Although an apparent positive Ba anomaly is evident in the primitive mantle-normalised incompatible element plots for Walvis Ridge and Koolau (Figure 2.6), this may represent a relative Ba enrichment as a consequence of depletions in the adjacent incompatible elements, Rb and Th in the case of the Koolau tholeiites, Rb and Nb in the case of the Walvis Ridge basalts, rather than the positive Ba spike considered to distinguish the EMI end-member (e.g. Weaver, 1991), or it may be a product of seafloor alteration. Relative Ta and Nb depletions are also evident in the Koolau tholeiites. Pitcairn samples, however, have positive Ta and Nb anomalies and a general decrease in elements more incompatible than Ta, features that are generally considered to distinguish the HIMU basalts. Both the Tedside Volcanics and Volcano 2 display a positive Pb anomaly. Whether or not this Pb anomaly is a characteristic EMI feature is not known as no Pb data are available for either Walvis Ridge or Koolau. However, basalts from the Tasmantid Seamount chain, located in the Tasman Sea parallel to the east coast of Australia, are considered to be derived from an EMI mantle plume (Eggins et al., 1991) and are also characterised by positive Pb anomalies (S.M. Eggins, pers. comm., 1993). EMI source Pb enrichment is consistent with the time-integrated lower than bulk Earth U/Pb and Th/Pb values required to produce the unradiogenic Pb isotope ratios of EMI basalts.

2.3.3 EMII Trace Element Compositions:

EMII OIB are considered to have relatively poorly-defined trace element characteristics compared to the other end-member components, as a consequence of the sparsity of available comprehensive EMII trace element data (Weaver, 1991). However, an examination of basalts from the Samoan, Society and Marquesas island chains indicates that EMII basalts may actually have more distinctive trace element systematics than EMI basalts (Table 2.1; Figure 2.4).

EMII and EMI basalts are similar in that they display LILE/HFSE and LREE/HFSE enrichment relative to the HIMU end-member. Although they overlap with the EMI end-member in terms of their K/Nb and Ba/Nb values, EMII basalts do appear to have lower La/Nb than EMI basalts. It has been proposed that EMII basalts have both higher (Woodhead and Devey, 1993) and lower (Weaver, 1991) Rb/Nb than EMI basalts. Although the EMII data extend to higher Rb/Nb values than EMI basalts in Figure 2.4, it is questionable as to whether these values are distinct enough to assist in constraining the source compositions of the two enriched mantle end-members.

The trace element ratios which appear to best distinguish the EMI and EMII end-members are Ba/Th, Th/La and Th/Nb, the latter two higher in EMII basalts. The fact that EMII Ba/Th values are low, similar to HIMU, whereas Ba/La values are relatively high, suggests that the EMII source is relatively enriched in Th with respect to the EMI source. This requires further testing, however, as available EMI Th data are limited and dominated by the Koolau tholeiites which appear to be Th-depleted.

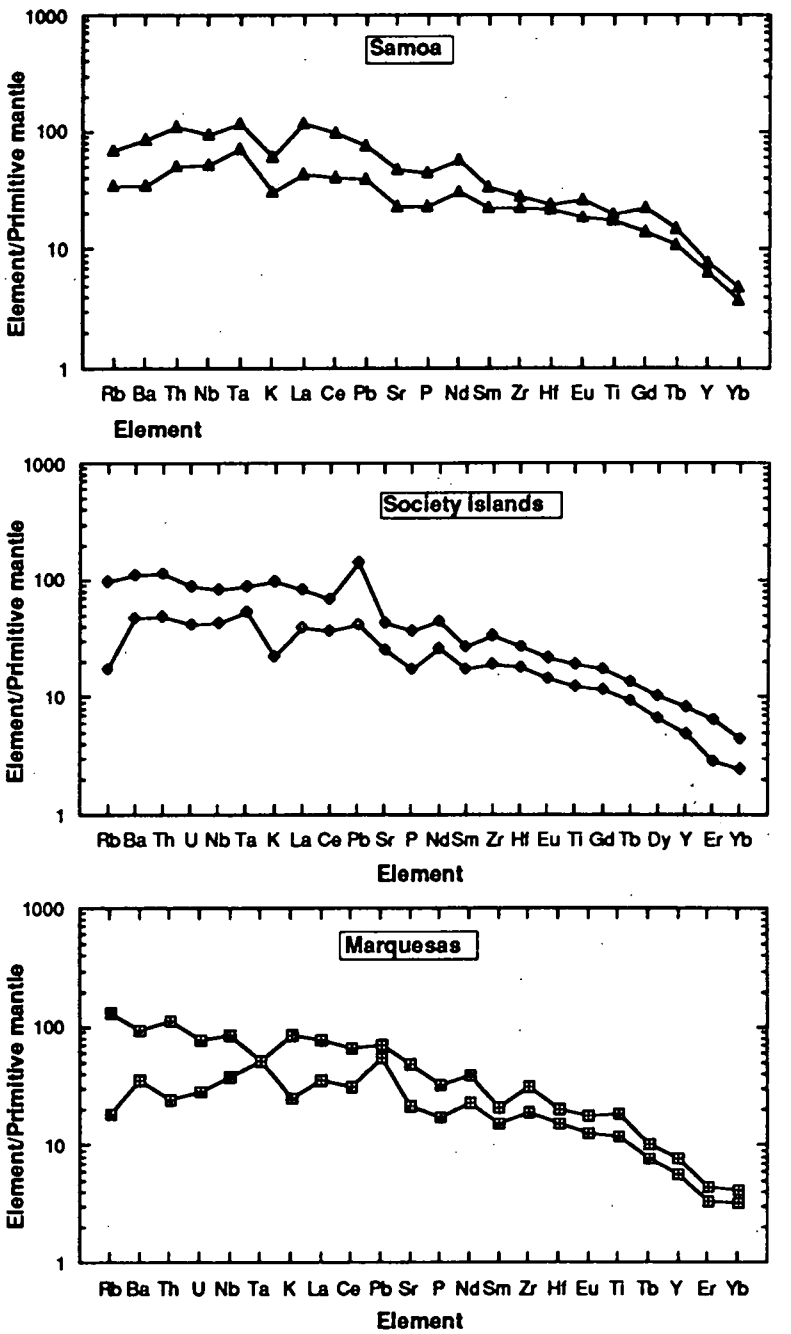

Figure 2.7: Primitive mantle-normalised incompatible element diagrams illustrating the data ranges for EMII basalts from Samoa, the Society Islands/Seamounts and the Marquesas archipelago; data sources are as for Table 2.1. Normalising values are from Sun and McDonough (1989).

Primitive mantle-normalised incompatible element patterns for Samoa, the Society Islands/Seamounts and the Marquesas archipelago are relatively consistent (Figure 2.7). All plots display slight depletions in Sm and P relative to Nd and negative K anomalies. Society and Marquesan basalts also display a degree of Pb enrichment, which is not evident in the Samoan basalts.

2.4 MAJOR ELEMENT SYSTEMATICS OF THE MANTLE END-MEMBER COMPONENTS:

2.4.1 Comparison of OIB End-member Major Element Compositions:

A comparison of end-member major element compositions over a range of whole-rock MgO contents is presented in Figure 2.8. Data for EMI OIB form perhaps the most distinct array, with the highest SiO_2 and lowest FeO*, TiO_2, K_2O and P_2O_5 concentrations over a range of MgO contents. The HIMU and EMII data tend to overlap with each other, but HIMU basalts extend to the lowest SiO_2, and the highest CaO (particularly at >8 wt % MgO), MnO and FeO* values. High FeO at a given MgO value within Mangaia, Rurutu and Tubuai lavas has previously been suggested to represent a possible HIMU geochemical feature (Chauvel et al., 1992; Hauri and Hart, 1993). EMII basalts are distinguished by their high K_2O and TiO_2 values over a range of MgO contents. No significant differences are observed between the three mantle end-members in terms of their Na_2O and Al_2O_3 contents. This might also be concluded for their CaO/Al_2O_3 values, but at MgO content >10 wt % the end-member basalts display quite distinct CaO/Al_2O_3 trends, with HIMU extending to the highest values, EMI to the lowest and EMII intermediate to the other end-members. The trend of decreasing CaO/Al_2O_3 with decreasing MgO at MgO contents >10 wt %, most evident in EMII and HIMU basalts, reflects olivine and clinopyroxene fractionation. End-member CaO/Al_2O_3 variations can be attributed to differences in bulk composition and/or high pressure fractionation processes (e.g. Klein and Langmuir, 1987).

Although major element data for relatively primitive OIB from the regions under examination here are sparse, these same end-member differences do appear to exist at a limited range (9.5-12.5 wt %) of MgO contents (Figure 2.9). The most distinctive major element correlation involves increasing values of FeO* with decreasing SiO_2 from EMI OIB through EMII to HIMU basalts. The resultant trend of decreasing SiO_2/FeO* is accompanied by increasing CaO/Al_2O_3, due predominantly to increasing CaO rather than decreasing Al_2O_3. Other distinct differences between the end-members involve the abundances of TiO_2, P_2O_5 and K_2O, all of which are lowest in the Koolau EMI basalts. Compared to HIMU values, EMII basalts have similar P_2O_5 but higher K_2O and TiO_2. No systematic end-member differences in the values of Na_2O and Al_2O_3 have been found.

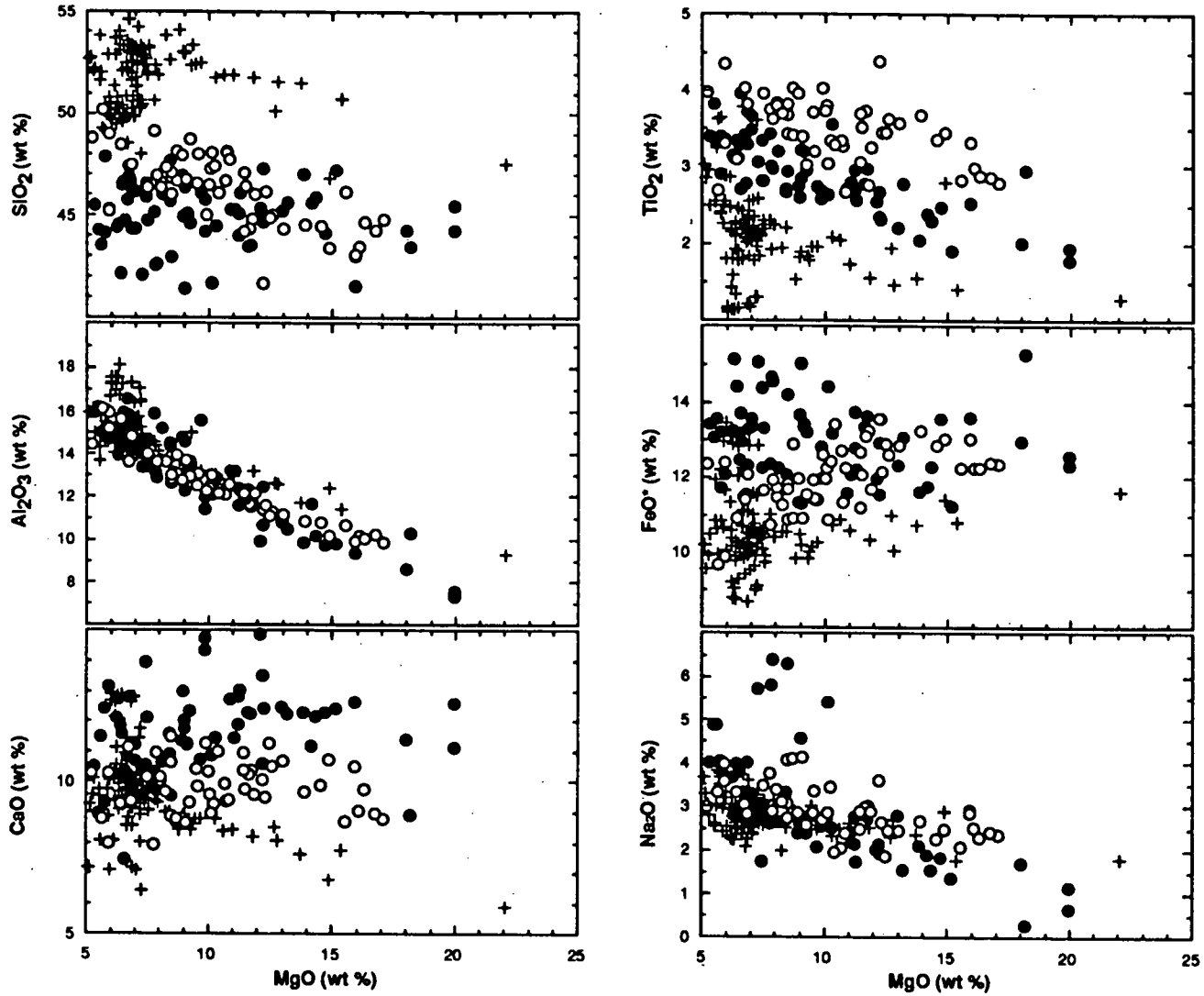

(Figure 2.8)

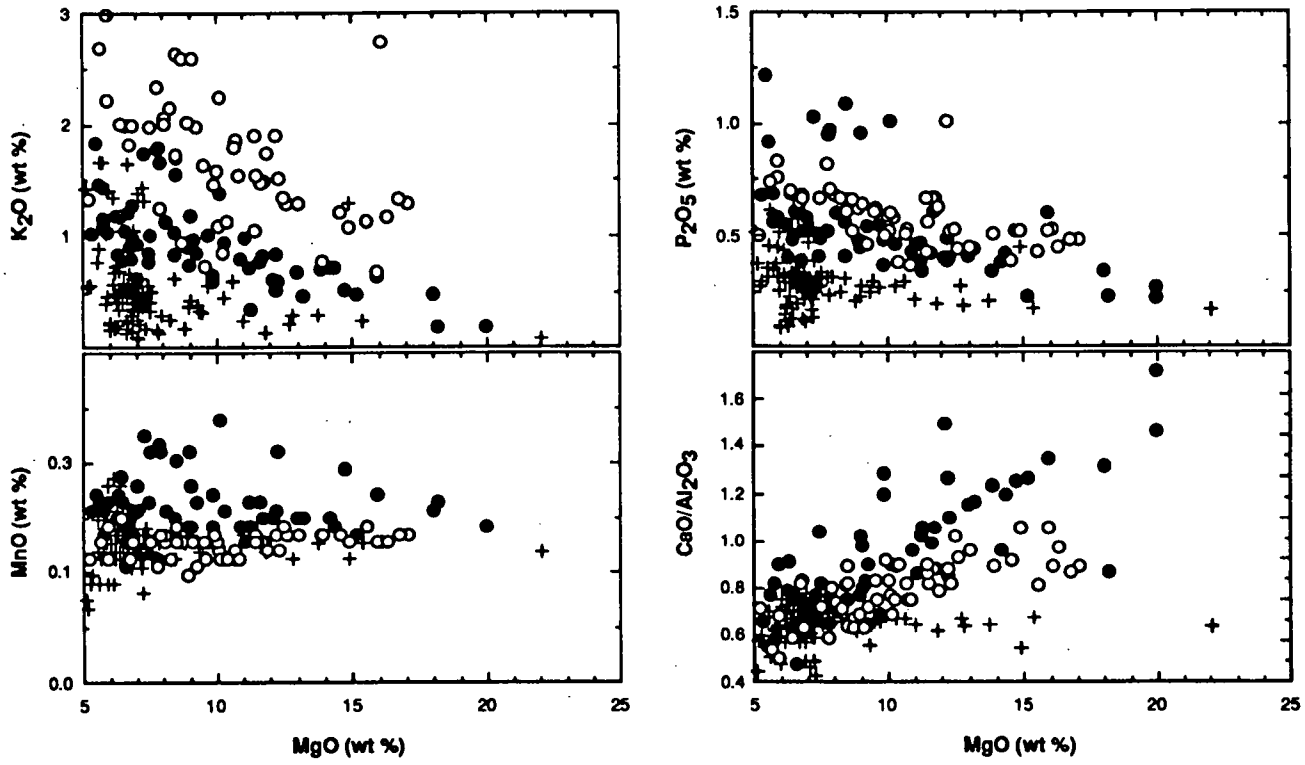

Figure 2.8: MgO versus various major elements for HIMU (filled circles), EMI (crosses) and EMII (open circles) basalts. Data sources include Duncan (1975), Dostal et al. (1982), Humphris and Thompson (1983), Richardson et al. (1984), Roden et al. (1984), Thompson and Humphris (1984), Budahn and Schmitt (1985), Liotard et al. (1986), Palacz and Saunders (1986), Weaver et al. (1987), Dupuy et al. (1988), Chaffey et al. (1989), Dupuy et al. (1989), Woodhead and McCulloch (1989), Devey et al. (1990), Chauvel et al. (1992), Woodhead (1992), Woodhead and Devey (1993) and Frey et al. (in press).

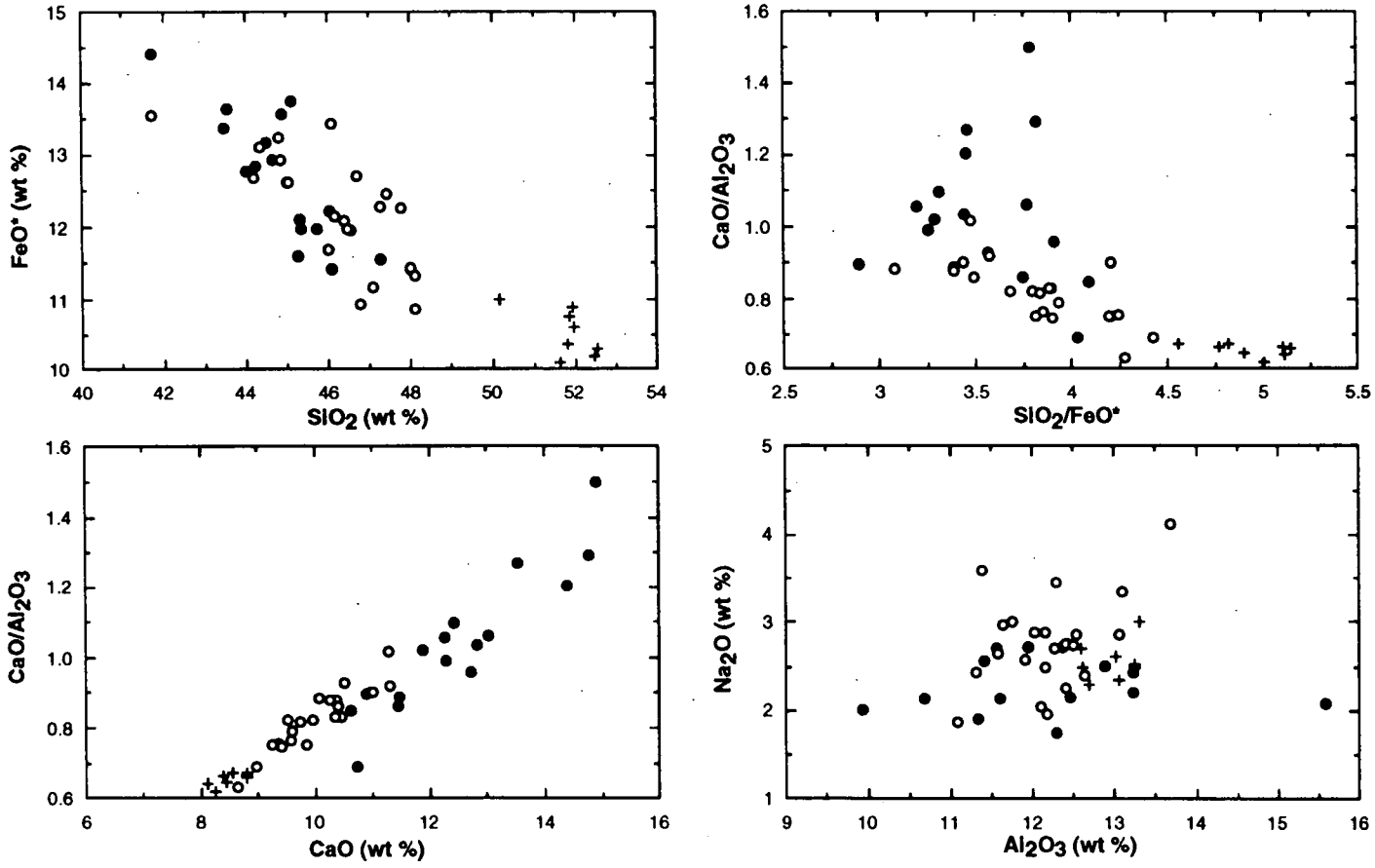
FeO* (wt %)
SiO2 (wt %)
CaO/Al2O3
SiO2/FeO*
CaO/Al2O3
CaO (wt %)
Na2O (wt %)
Al2O3 (wt %)

(Figure 2.9)

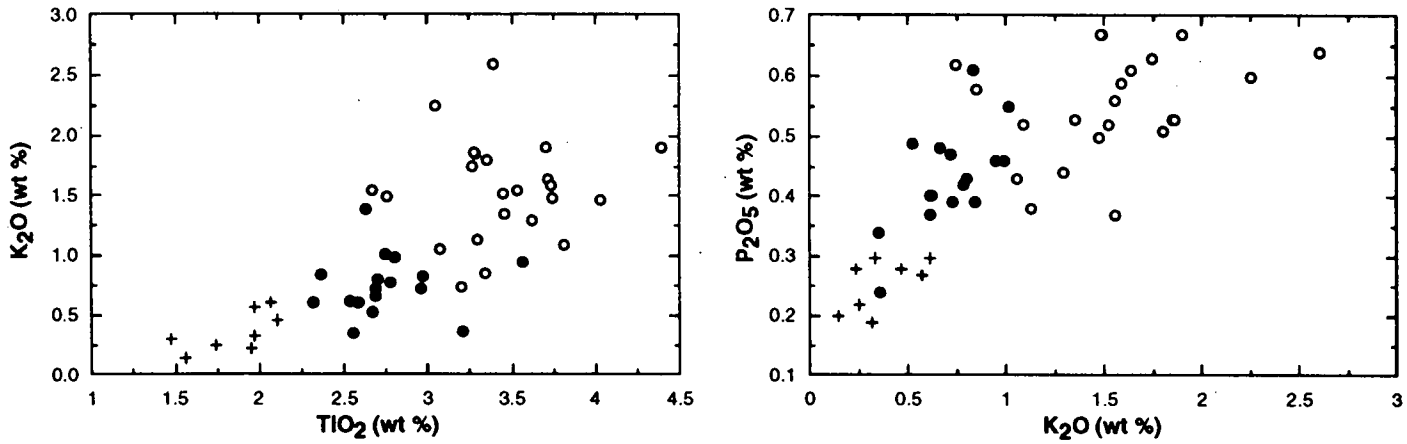

Figure 2.9: Plots of major element oxides and ratios for HIMU (Mangaia, Tubuai, Rurutu and St. Helena - filled circles), EMI (Koolau - crosses) and EMII (Society, Samoan and Marquesas island chains - open circles) OIB with MgO contents between 9.5 and 12.5 wt %. Data sources as for Figure 2.8, minus the Walvis Ridge and Pitcairn references.

2.4.2 Interpretation of OIB End-Member Major Element Differences:

Many experimental and analytical studies have been undertaken involving the partial melting of a spinel lherzolite source to produce MORB (e.g. Fujii and Scarfe, 1985; Falloon and Green, 1987; Klein and Langmuir 1987; Falloon et al., 1988; Niu and Batiza, 1991; Hirose and Kushiro, 1993). However, comprehensive experiments and/or studies of garnet lherzolite melting at the higher pressures required to produce OIB are lacking. Although it is possible to explain some of the major element features noted above in terms of the conclusions drawn from the lower pressure melting studies, there are certain discrepancies which require further investigation.

The trend of increasing FeO* with decreasing SiO_2 from EMI to EMII and HIMU basalts is in keeping with the global MORB trend interpreted to reflect increasing pressures of melting (Klein and Langmuir,1987; Niu and Batiza, 1991). Many peridotite melting studies (e.g. Hirose and Kushiro, 1993) have shown that the SiO_2 content of the melt is strongly pressure dependent, decreasing with increasing pressure, and relatively independent of source composition or the degree of partial melting. Koolau EMI basalts, with the highest SiO_2 and lowest FeO* contents, as compared to HIMU and EMII, may therefore reflect the lowest pressures of melting. The opposite correlation in HIMU basalts, namely low SiO_2 and high FeO* values, suggests melt segregation at a greater pressure than either EMI or EMII basalts.

The trend of increasing CaO/Al_2O_3 from EMI through EMII to HIMU basalts implies that their parental magmas have been produced by different extents of melting (e.g. Niu and Batiza, 1991). The general increase in CaO could be interpreted as reflecting increasing degrees of lherzolite melting prior to clinopyroxene exhaustion (e.g. Fujii and Scarfe, 1985; Klein and Langmuir, 1987), with EMI sources experiencing the lowest extents of melting and HIMU sources the highest.

If the above major element interpretations, based upon extrapolations from MORB studies, are correct, differences between the OIB mantle end-member components may indicate an increase in the extent and pressure of melting from EMI to EMII and HIMU basalt production. This is consistent with the suggestion of Chauvel et al. (1992), based on calculations of P-T melting conditions using the method of Albarede (1992), that HIMU basalts derive from a hotter source that commenced melting deeper in the mantle than either of the EMI or EMII sources.

However, if the HIMU basalts were produced by lherzolite melting just prior to, or during, the exhaustion of clinopyroxene, EM basalts could be the products of increasing, rather than decreasing, degrees of melting of a harzburgitic residue. In this case, the slightly lower CaO values of the EMII basalts, compared to the HIMU basalts, may be a product of further melting, diluting the CaO content of the melt, once all of the clinopyroxene in the source has been melted out, and the EMI basalts, with the lowest CaO values, could reflect even greater degrees of melting and melt CaO dilution. This interpretation is also consistent with the observed end-member differences in terms of the incompatible elements TiO_2, K_2O

and P_2O_5, all of which are at their lowest abundances in the Koolau EMI basalts. If the low CaO/Al_2O_3 values of EMI basalts are a product of low degrees of melting with respect to the other OIB end-members, high abundances of incompatible elements would also be expected. However, the distinctly low values of incompatible minor elements in the Koolau basalts would indicate higher degrees of partial melting in the production of EMI basalts compared to both EMII and HIMU basalts. If this is the case, the EMI basalts reflect a correlation between the lowest pressure of melting and the highest extent of melting relative to the EMII and HIMU sources.

The fact that the EMII basalts have the highest values of TiO_2 and K_2O implies that the EMII source may in fact have experienced lower degrees of partial melting than the HIMU source. This suggests that there is no consistent inverse relationship between pressure of melting and extent of melting in terms of the HIMU and EMII mantle sources.

Although Na_2O is considered to be moderately incompatible with respect to clinopyroxene at low to medium pressures, it has a high solubility in jadeite which is present in both clinopyroxene and orthopyroxene at high pressures (e.g. Klein and Langmuir, 1987) and may establish its own equilibrium with the melt (Langmuir and Hanson, 1980). Therefore, the lack of systematic end-member variation in the abundances of Na_2O and Al_2O_3 suggests that all three sources have residual garnet ($Ca_3Al_2Si_3O_{12}$ - $Mg_3Al_2Si_3O_{12}$) and jadeite ($NaAlSi_2O_6$), consistent with melting of garnet lherzolite or garnet harzburgite.

2.5 MELTING MODELS:

The major element systematics of the basalts examined in Section 2.4 indicate that the main differences between the OIB end-members are the trends of decreasing SiO_2/FeO^* and increasing CaO/Al_2O_3 from EMI to EMII and HIMU basalts accompanied by the lowest abundances of the incompatible elements TiO_2, K_2O and P_2O_5 in the Koolau EMI basalts. An attempt will be made here to understand these major element differences in terms of different pressures and temperatures of melting and source compositions, by comparing the predicted major element systematics associated with three generalised melting models with the observations presented in Section 2.4.

2.5.1 Model 1: Variable Lithospheric Thickness:

The first possibility (Figure 2.10a) involves variable lithospheric thicknesses encountered by upwelling plumes of similar temperature and major element composition. Although these plumes would intersect the mantle solidus at the same pressure and temperature, they would intersect the lithosphere at different pressures. Therefore, assuming that the melting columns extend from the solidus to the base of the lithosphere, the tops of their melting columns would lie at different pressures, and the mean pressure of melting would vary between the plumes. This model would require each of the different end-

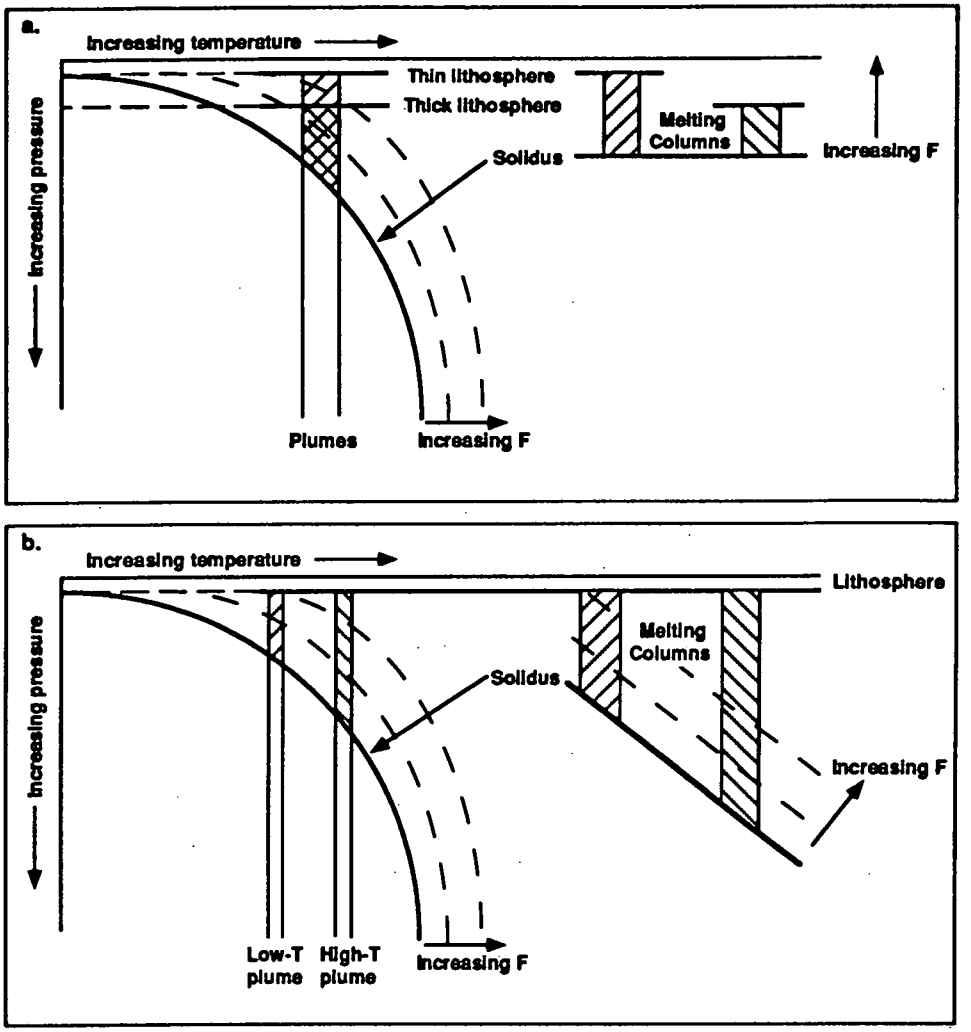

Figure 2.10: Mantle melting models as discussed in the text: a) model 1 involves variable lithospheric thickness at the site of plume intersection; b) model 2 involves variable plume temperatures.

member products to be related to a particular lithospheric thickness and a particular mean pressure of melting. Thinner lithosphere would result in a higher degree of melting (F) at a lower mean pressure and could be correlated with the high SiO_2/FeO^* and low incompatible element abundances of the Koolau EMI basalts. The lower SiO_2/FeO^* and higher TiO_2, K_2O and P_2O_5 of the HIMU and EMII basalts may therefore equate with higher mean pressure and lower degrees of melting at the base of a thicker lithosphere.

In considering this model of variable lithospheric thickness, it is necessary to examine whether there is any evidence for a systematic relationship between the major element characteristics of each of the mantle end-members and lithospheric thickness at the time of plume intersection. In order to calculate lithospheric thickness as a function of age, the base of the lithosphere is here defined in a thermal sense, whereby the oceanic

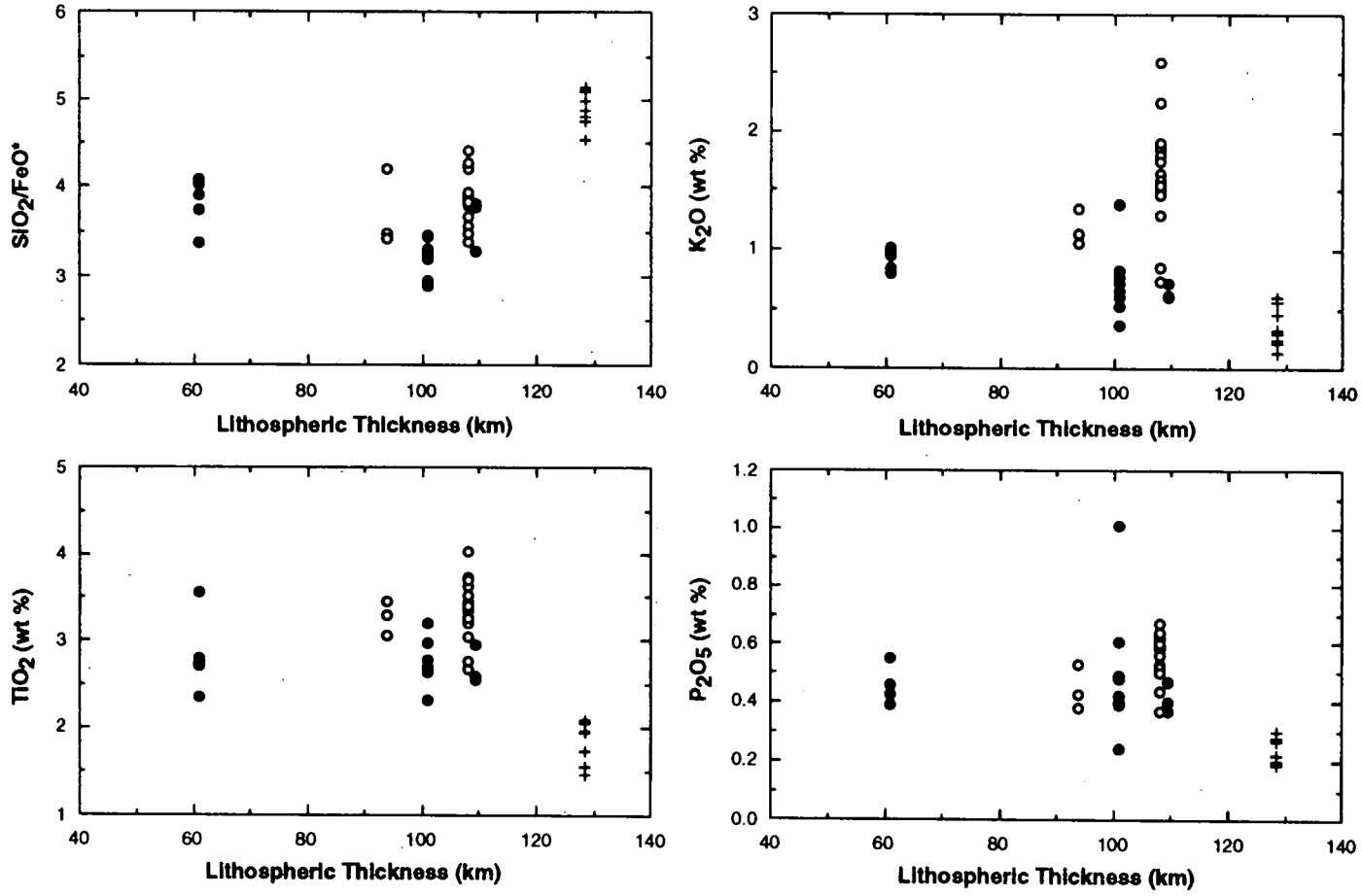

Figure 2.11: Lithospheric thickness (km) versus SiO_2/FeO^*, TiO_2, K_2O and P_2O_5 for HIMU (Mangaia, Tubuai and St. Helena - filled circles), EMI (Koolau - crosses) and EMII (Society and Marquesas island chains - open circles) OIB with > 9.5 wt % MgO. OIB major element data sources as for Figure 2.9. Lithospheric thicknesses as discussed in the text.

lithosphere represents that region between the seafloor and the isotherm which corresponds to 90 % of the upper mantle potential temperature (Turcotte and Schubert, 1982). Lithospheric thicknesses were calculated according to the equation of Turcotte and Schubert (1982): $yL = 2.32 \sqrt{(\kappa t)}$, where yL = lithospheric thickness (m), κ = thermal diffusivity (10^{-6} m^2/s^{-1}), and t = age of lithosphere in years at the time of plume intersection (1 year = 3.2×10^7 s^{-1}). Lithospheric age at the time of plume intersection (t) was calculated by subtracting the age of the island/seamount (oldest dated volcanism) from the age of the surrounding seafloor. Where possible, seafloor age was derived from magnetic lineation information: Marquesas = 57 Ma, Society = 72 Ma, St. Helena = 31 Ma, and Tubuai = 71 Ma (Reinemund, 1984), although Hawaii and Mangaia are located within the Cretaceous Quiet Zone (> 80 Ma), and were therefore ascribed seafloor ages of 100 Ma (Monnereau and Cazenave, 1988) and 90 Ma respectively. Ascribed island/seamount ages are: Mangaia = 19.45 Ma, Marquesas = 4.9 Ma (Hatutu), Society = 3.2 Ma (Tahaa) and Tubuai = 10.70 Ma (Diraison, 1991); Koolau = 2.6 Ma (Doell and Dalrymple, 1973); St. Helena = 9 Ma (Chaffey et al., 1989).

It is evident from Figure 2.11 that no systematic correlation exists between lithospheric thickness and the major element characteristics which define the various end-member components. Although the chemistry of the EMI basalts may appear to relate to plume upwelling under thinner lithosphere, Koolau volcanism is in fact associated with the thickest lithosphere. HIMU and EMII plumes encountered a similar range of lithospheric thicknesses. Therefore, the major element characteristics of the HIMU, EMI and EMII end-members cannot be explained by a model of variable lithospheric thickness.

2.5.2 Model 2: Variable Plume Temperature:

An alternative model (Figure 2.10b) assumes that the different end-members are the product of upwelling plumes with similar compositions, similar pressures of lithosphere intersection (ie. similar lithospheric thicknesses), but different temperatures. Higher temperature plumes would intersect the solidus at greater pressures than lower temperature plumes, resulting in a higher initial pressure of melting, a higher mean pressure of melting (longer melting column) and a higher overall degree of partial melting. Lower temperature plumes would encounter the solidus at a lower pressure, have a lower mean pressure of melting, and undergo a lower degree of partial melting.

Direct geophysical measurement of plume temperature is not possible. However, the buoyancy fluxes of various hotspots (where buoyancy flux is defined as a combination of the source volume flux and the source temperature anomaly: Griffiths and Campbell, 1990) have been calculated (Davies, 1988; Sleep, 1990), predominantly on the basis of seafloor topography (swell magnitude), in an attempt to constrain global plume heat flow and provide an indication of plume magnitude or strength. The assumption that plume buoyancy is a function of the temperature in the originating boundary layer, whereby stronger plumes have higher temperatures, is complicated by factors such as spreading rate and lithospheric

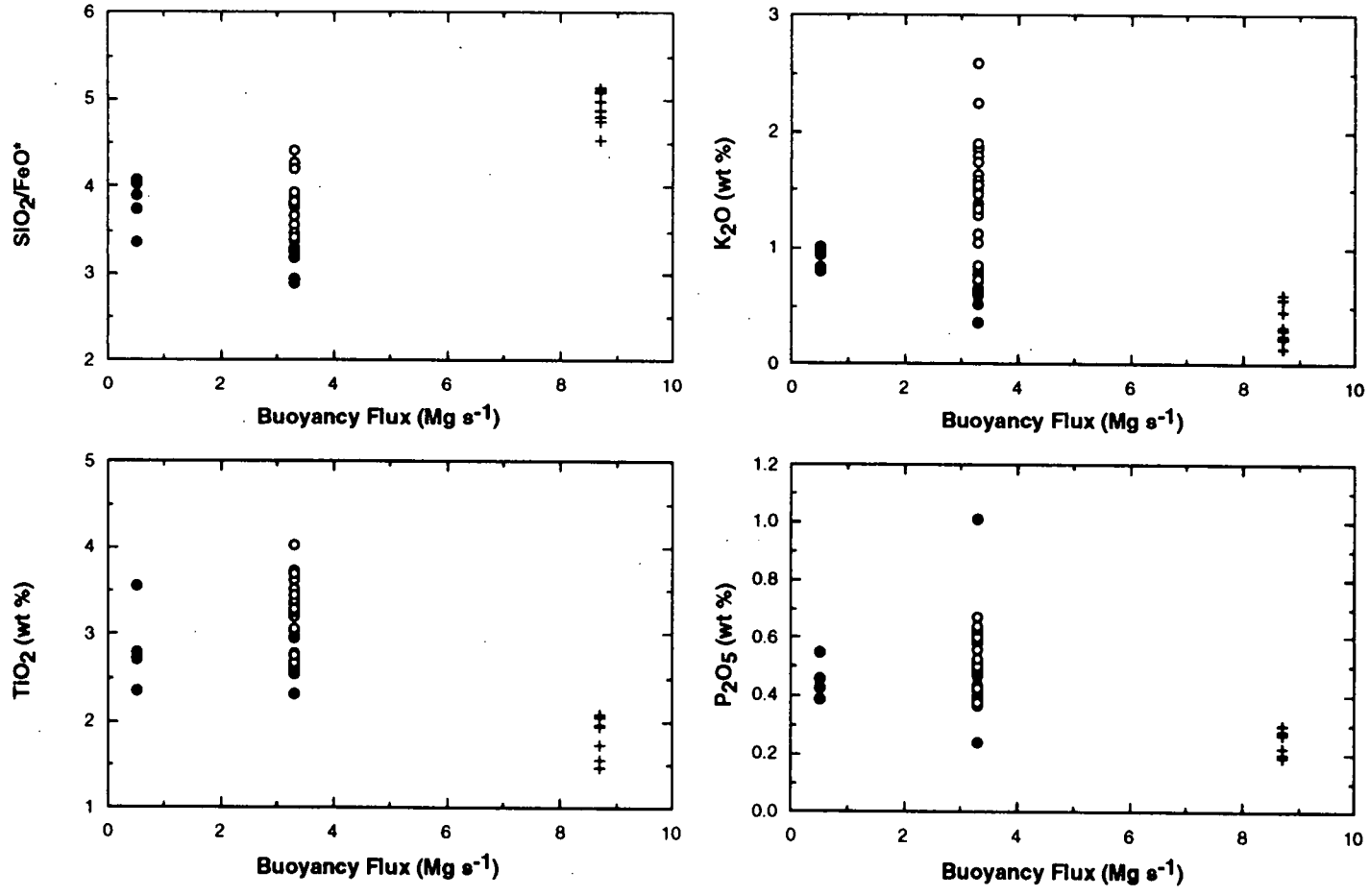

Figure 2.12: Plume buoyancy flux (Mg s^{-1}) versus SiO_2/FeO^*, TiO_2, K_2O and P_2O_5 for HIMU (Mangaia, Tubuai and St. Helena - filled circles), EMI (Koolau - crosses) and EMII (Society and Marquesas island chains - open circles) OIB with > 9.5 wt % MgO. OIB major element data sources as for Figure 2.9; plume buoyancy flux estimates (Sleep, 1990) used include: Macdonald for Mangaia and Tubuai, Hawaii for Koolau, and Tahiti for the Society Islands, as well as St. Helena and Marquesas.

thickness (Sleep, 1990), as well as the influence of ambient cooler mantle entrainment and the greater degree of cooling that would be expected to be associated with the ascent of weaker plumes (e.g. Griffiths and Campbell, 1991). Therefore, the lack of any systematic correlation between plume buoyancy fluxes and end-member major element characteristics (Figure 2.12) does not necessarily negate the possibility that end-member differences are a function of temperature.

However, the expected results in terms of major element systematics would be the opposite to that observed here, namely high SiO_2/FeO^* and high abundances of TiO_2, K_2O and P_2O_5 associated with low temperature plumes and vice versa for high temperature plumes. The major element observations made in Section 2.4 are, therefore, incompatible with this model.

2.5.3 Model 3: Variable Source Composition:

A third proposal involves source major element heterogeneities, producing plumes which have similar pressure-temperature regimes, but possess compositional differences related to their origin as isotopically heterogeneous mantle regions. If, for example, HIMU basalts derive from a fertile and more incompatible element-enriched source, whereas the EMI source is relatively refractory, as suggested for the origin of low $^{206}Pb/^{204}Pb$ MORB along the central Southwest Indian Ridge (Mahoney et al., 1992) and the low $^{206}Pb/^{204}Pb$ signature within the basement lavas of the Ontong Java Plateau (Mahoney et al., 1993), their intersection of the mantle solidus at similar pressures and temperatures would result in different extents of melting and different end-products. Due to its previous melting history, and depletion in the more easily-melted components, the EMI source would melt less and would contain less clinopyroxene than the more fertile source. Once the remaining clinopyroxene had been melted out of this source, leaving a harzburgite residue, the resulting EMI basalts would have low CaO/Al_2O_3 values, consistent with the observations made in Section 2.4. The fact that jadeite would still be present in orthopyroxene at high pressures could account for the lack of lower Na_2O values in EMI basalts. The refractory nature of this source also means that it would be relatively depleted in incompatible elements including TiO_2, K_2O and P_2O_5, consistent with the characteristics of the Koolau basalts. The more fertile source, however, would be relatively enriched in incompatible elements, would have more clinopyroxene in the source and therefore higher CaO/Al_2O_3 values.

Source compositional heterogeneities may also be invoked to explain why the EMII basalts have the highest TiO_2, K_2O and P_2O_5 values, which is difficult to explain by either of the other models.

2.6 SUMMARY:

This chapter has attempted to elucidate the possible major and trace element differences between the isotopically defined HIMU, EMI and EMII mantle end-members. In terms of the major elements, Koolau EMI OIB are the most distinct, possessing the highest SiO_2 and the lowest FeO^*, CaO, TiO_2, P_2O_5 and K_2O values. The HIMU and EMII components overlap somewhat in terms of their major element compositions, although EMII basalts extend to the highest K_2O and TiO_2 values and HIMU basalts have the highest CaO. Although the EMI major element characteristics may be indicative of larger degrees of melting at lower pressures than are involved in the production of either the EMII or HIMU basalts, the models of variable pressure and temperature examined here have failed to explain the observed differences. It seems likely, therefore, that these end-member differences are best explained by variations in mantle source composition, whereby the EMI basalts may derive from a relatively refractory source, and the HIMU basalts from a more fertile source.

Trace element distinctions, indicative of differences in end-member source chemistry, are often less distinct than stated in the literature. Compared to EM basalts, HIMU basalts generally have lower LILE/HFSE and LREE/HFSE abundance ratios, intermediate Th/La and Th/Nb values, lower Zr/Nb and higher Nb/Pb and Ce/Pb values. The latter, accompanied by a lack of distinction between HIMU and EM Nb/U and Th/U values, suggests that Pb depletion rather than U enrichment is responsible for the high-μ signature. EMI and EMII basalts are distinguished predominantly by the lower Ba/Th, higher Th/La and higher Th/Nb values of EMII basalts, suggesting relative Th enrichment in the EMII source. The trace element characteristics of EMI basalts remain particularly enigmatic. Despite these observed end-member differences, Hoernle and Schmincke (1993) suggest that the interpretation of incompatible trace element ratios, particularly in low degree melts, should be treated with caution.

The petrogenesis of the mantle end-member components is no doubt more complicated than any of the models presented in this chapter. For example, the low $^{87}Sr/^{86}Sr$ and high $^{143}Nd/^{144}Nd$ values of HIMU OIB (Chapter 1) require time-integrated low Rb/Sr and Nd/Sm source values, consistent with the relative LILE and LREE depletions which characterise the trace element systematics of HIMU basalts. However, this long-term incompatible element depletion is inconsistent with the proposal that the HIMU major element systematics may be derived from a relatively fertile source as compared to the EM source regions. The apparently contradicting major and trace element systematics of HIMU OIB may therefore imply the involvement of other processes, such as metasomatic enrichment in certain elements subsequent to source formation.

CHAPTER 3

THE BALLENY PLUME

3.1 INTRODUCTION:

Volcanic activity associated with the Balleny Plume is believed to have formed a chain of seamounts and oceanic islands which extend for ~4000 km across the surface of the eastern Indian-Australian and Antarctic plates, spanning a period of at least 70 m.y.. Reconnaissance radiogenic isotope studies of the alkaline volcanics of the Balleny Islands, which represent the youngest, and the only known subaerial expression of this plume, indicate derivation from a HIMU mantle source diluted by depleted upper mantle material (e.g. Hart, 1988; Gill and Collerson, 1992).

This chapter comprises a study of Balleny Plume volcanism, based on the major element, trace element and radiogenic (Pb, Sr and Nd) isotope data obtained for samples dredged from four seamounts along the proposed plume trace and from two sites in the immediate vicinity of the Balleny Islands. The overall aims of this study are as follows:

1. To track the surface expression of the Balleny Plume over the past ~70 m.y., as produced by movement of the Indian-Australian and Antarctic Plates over the plume tail or conduit;
2. To characterise the geochemical and isotopic compositions of the islands and seamounts erupted along the plume trace over this ~70 m.y. period;
3. To examine temporal variations in the chemical composition of the plume tail over the past ~70 m.y.; and
4. To attempt to place further constraints on the geochemical composition of the proposed HIMU mantle end-member component.

3.2 GEOLOGICAL SETTING:

Recent volcanic activity to the northwest of the Antarctic Ross Sea has produced a number of oceanic islands and seamounts, the most prominent of which are the Balleny (Figure 3.1) and Scott (Chapter 5) Islands. The former reflect the current location of the Balleny Plume (Vogt and Johnson, 1973; Vanney et al., 1981), whose activity can be traced

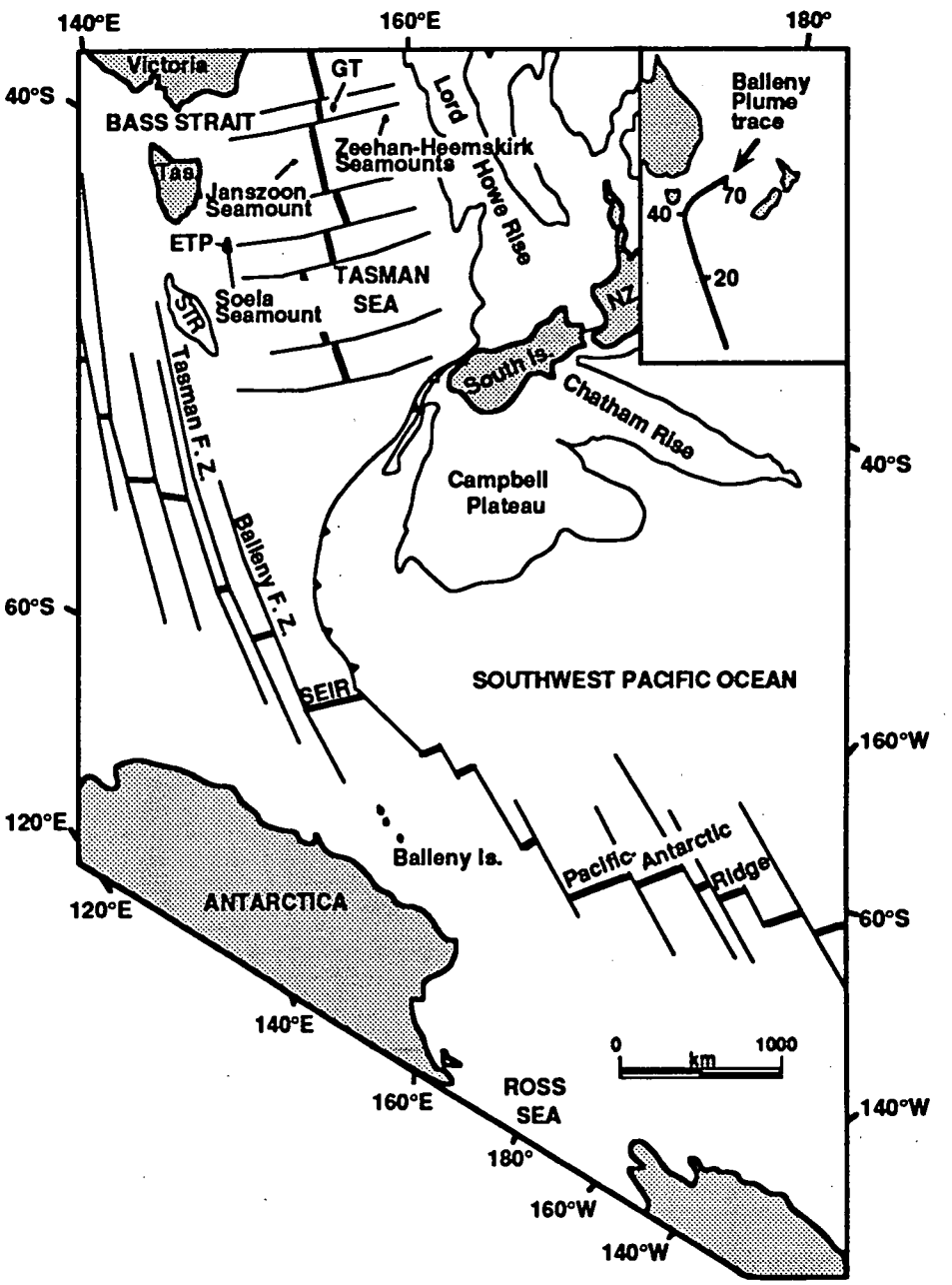

Figure 3.1: Map of the southwest Pacific Ocean region (modified from Reinemund, 1984) showing the location of the Heemskirk, Zeehan, Janszoon and Soela Seamounts and the Balleny Islands, relative to Antarctica, southeastern Australia (Victoria and Tasmania) and New Zealand; SEIR = Southeast Indian Ridge; GT = Gascoyne Tablemount; STR = South Tasman Rise; ETP = East Tasman Plateau. The inset depicts the approximate time progression of the Balleny Plume.

back through time in a north-northwesterly direction, across the present location of the easternmost extension of the Southeast Indian Ridge (SEIR), to the Cascade or East Tasman Plateau (Duncan, 1981; Duncan and McDougall, 1989). Seamounts located on the East Tasman Plateau and the South Tasman Rise (Figure 3.1), plus other more southerly seamounts are thought to represent earlier surface expressions of the Balleny Plume prior to it being over-ridden by the SEIR at ~20 Ma (Duncan and McDougall, 1989), or ~10 Ma , based on the age of the magnetic lineation (A5) closest to the northernmost seamounts in the Balleny group (Green, 1992; Jenkins et al., 1992).

A chain of seamounts extending across the southern Tasman Sea, from the East Tasman Plateau region east of Tasmania to the western flank of Lord Howe Rise (Figure 3.1), age progressively towards the northeast (Jenkins et al., 1992). Assuming that this seamount chain represents the earlier Balleny Plume trace, Yan (1991) suggested that a bend in the chain, located in the vicinity of the East Tasman Plateau and inferred to be ~43 Ma, may correspond to the Hawaiian-Emperor bend (42±1.4 Ma: Dalrymple and Clague, 1976) and thereby reflect the major global reorganisation of plate boundaries at that time.

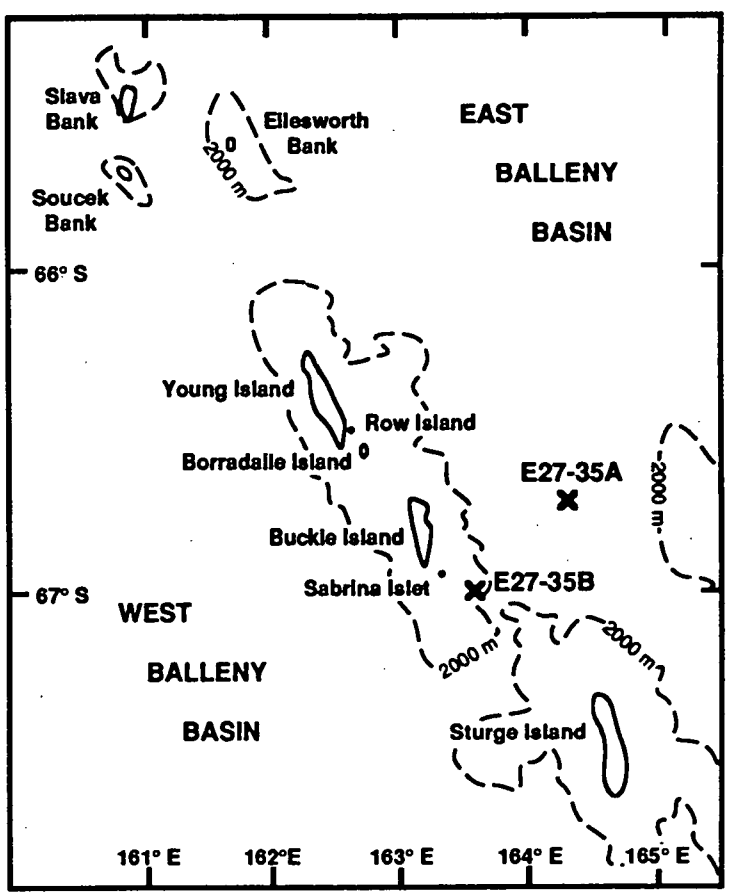

Figure 3.2: Map of the Balleny Island-Seamount chain, modified from Johnson et al. (1982), showing the location of *USNS Eltanin* dredge sites E27-35A and E27-35B (Appendix 1); dashed line marks the 2000 m bathymetric contour.

3.2.1 Southwest Pacific Ocean - Balleny Islands:

The Balleny Islands (66°16'S-67°38'S, 162°15'E-164°44'E), located ~450 km northwest of Cape Adare, Northern Victoria Land, Antarctica, and the more northerly Balleny Seamounts, the Slava, Soucek and Ellesworth Banks (Johnson et al., 1982), extend for ~160 km in a northwest-southeast direction and straddle the Antarctic Circle. This island chain is adjacent to the Antarctic continental rise to the west and located on the southernmost end of a submarine volcanic ridge system which extends in a northwesterly direction and is offset by the SEIR (Johnson et al., 1982; Wright and Kyle, 1990a). The northwest-southeast trend of this island chain is parallel to the fracture zone pattern of the area including the seismic Balleny Fracture Zone (Figure 3.1), a major transform fault which offsets the SEIR near 155°E (Hayes and Conolly, 1972) by approximately 320 km in a dextral sense and parallels the direction of spreading between the Indian-Australian and Antarctic plates (Falconer, 1972). It has been proposed that Balleny Island volcanism is related to the Balleny Fracture Zone (Vanney et al., 1981; Johnson et al., 1982), the latter possibly representing a leaky transform fault (Kyle and Cole, 1974). However, the geochemistry of Balleny Islands samples studied to date is more akin to that of OIB associated with hotspot activity, with >2 wt % TiO_2 and greater enrichment in incompatible elements than the T-type (transitional) MORB usually erupted along oceanic transform faults (Green, 1992). The Balleny Islands and Balleny Fracture Zone are considered to form the western boundary of the East Balleny Basin, which itself contains several islands and seamounts including the Ellesworth, Admiralty, Adare and Amitaka seamounts (Vanney et al., 1981). Although it was originally thought that some of these seamounts may have had a similar origin to the Balleny Islands (Johnson et al., 1982), gravity and bathymetric data indicate no link between them (Jenkins et al., 1992).

The Balleny group (Figure 3.2) comprises three large islands, Young, Buckle and Sturge, and three smaller islands, Row, Borradaile and Sabrina. A number of isolated reefs, rock pinnacles and offshore stacks are also present (Mawson, 1950; Wright and Kyle, 1990a), including the conical Scott stack off the southern end of Buckle Island and the 78 m high Sabrina Monolith, adjacent to Sabrina Island (Lewis, 1984), the latter possibly a volcanic plug or neck (Hatherton et al., 1965). All of these islands comprise interbedded tuff, agglomerate scoria and lava flows, and are bounded by steep cliffs and surmounted by ice caps. Due to their relative isolation, inaccessible morphology, and lack of rock exposure (except on their bounding cliffs) very little systematic geological sampling or fieldwork has ever been undertaken on the Balleny Islands (Wright and Kyle, 1990a).

Magnetic seafloor lineations have been used to infer a maximum age of 10 Ma for the onset of volcanism in the Balleny Island group (Wright and Kyle, 1990a; Green, 1992). Wind-blown rhyolitic glass shards within *USNS Eltanin* deep-sea sedimentary cores suggest that the Balleny Islands experienced both phreatomagmatic and magmatic eruptions during the past 2.5 m.y. (Huang et al,1975). Radiometric dating of Sturge island rocks indicates volcanic activity at 1.91 Ma (Embleton, 1984) and 1.76±0.2 Ma (K-Ar dating - Jenkins et al., 1992).

Recent sightings of volcanic activity on Young and Buckle Islands in 1839 and 1899 (Johnson et al., 1982) remain unconfirmed.

3.2.2 East Tasman Plateau - Soela Seamount:

The Soela or Cascade (Jenkins et al., 1992) Seamount (~43°56'S, 150°25'E), located on the East Tasman Plateau ~290 km southeast of Hobart, Tasmania, is thought to be an earlier product of the Balleny Plume (Duncan and McDougall, 1989). K-Ar dating of a hawaiite pebble from a volcaniclastic conglomerate and an alkali olivine basalt dredged from the flanks of the 660 m deep seamount has provided Mid-Oligocene ages of 31.5±0.5 Ma and 33.4±0.3 Ma respectively (I. McDougall, pers. comm., 1988; 1992 - Appendix 4). Slightly older ages, 35.1±0.4 Ma and 36.4±0.2 Ma were obtained by the $^{40}Ar/^{39}Ar$ step-heating method (R.A. Duncan, pers. comm., 1993 - Appendix 4). Matrix material within volcaniclastic sandstones dredged from the Soela Seamount contain foraminifera ranging from Quaternary to Late Eocene in age (P. G. Quilty, pers. comm., 1992), and Middle to Upper Eocene foraminifera within a volcanic conglomerate provide a minimum Middle Eocene (~36-40 Ma) age for the basaltic clasts (P.G. Quilty, pers. comm., 1992). This is broadly consistent with the suggestion that seamounts south of the South Tasman Rise may range in age from ~36 to 20 Ma (Duncan and McDougall, 1989).

The formation of Soela Seamount at ~40±5 Ma coincides with a marked increase in the spreading rate between Australia and Antarctica (Veevers et al., 1990). Although the East Tasman Plateau is generally believed to be a microcontinental block of similar origin to the larger South Tasman Rise (Figure 3.1) (e.g. Hayes and Conolly, 1972), it may in fact consist of a thick accumulation of basalt related to intense Balleny plume activity at this time of increased seafloor spreading (Lanyon et al., 1993).

3.2.3 South Tasman Sea - Janszoon, Zeehan and Heemskirk Seamounts:

Janszoon Seamount (~39°33'S, 154°20'E), located on ~64 Ma oceanic crust in the south Tasman Sea, is approximately midway between Soela Seamount and the Lord Howe Rise (Figure 3.1). It has been assigned an 'Eocene or older' age (50-60 Ma) based on K-Ar dating of slightly altered basalt, the presence of Late Eocene to Early Oligocene (39-29 Ma) forams within basaltic sand-bearing nanno-foram chalk dredged from a locality close to the summit at a depth of 2012 m, and calculations based on crustal subsidence (Jenkins et al., 1992).

The twin, flat-topped seamounts of Zeehan (~36°17'S, 159°35'E) and Heemskirk (~36°22'S, 159°52'E) rise ~2500 m above the ~78 Ma oceanic crust of the abyssal plain in the southern Tasman Sea, approximately 50 km west of the western flank of Lord Howe Rise (Hubble et al., 1987). K-Ar dating of relatively unaltered mugearites from the flanks of these 2560 and 2400 m deep seamounts gave ages in the range of ~59.1±2.3 to 71.3±2.2 Ma (Jenkins et al., 1992). Unsampled seamounts located on the western flank of Lord Howe

Rise to the east of Heemskirk Seamount may represent even older expressions of the Balleny Plume (Jenkins et al., 1992).

3.3 SAMPLING LOCATIONS:

Submarine Balleny Province samples analysed for major and trace element compositions, mineral chemistry and radiogenic isotope (Pb, Sr and Nd) ratios, were dredged by the *USNS Eltanin* from two sites (E27-35A and E27-35B) in the vicinity of Buckle Island - Sabrina Islet (Figure 3.2). Site E27-35B is located on the submarine volcanic ridge topped by the Balleny Islands, ~20 km southeast of Buckle Island, whereas site E27-35A is located within the adjoining Anare Basin ~50 km east-northeast of Buckle Island. These samples, selected on the basis of their relative freshness and lack of obvious ice-rafted features such as rounding and/or striated surfaces, have a range of compositions, encompassing alkali olivine basalt, basanite, trachybasalt, phonotephrite and trachyte (Figure 3.3).

The exact location of sample sites on the surface of Soela Seamount is unknown, largely as a result of accidental sampling during the course of deep-sea fishing operations. Many of the analysed Soela samples comprise individual clasts within volcanic conglomerates, although basaltic boulders have also been recovered. Soela samples display a narrower compositional range than the Balleny rocks, comprising alkali olivine basalt, trachybasalt and basaltic trachyandesite (Figure 3.3).

The south Tasman Sea seamount samples were recovered during two cruises of the *HMAS Cook*. Basanite and trachybasalt samples were dredged from Janszoon Seamount, trachyandesite from Zeehan Seamount and trachybasalt from Heemskirk Seamount (Figure 3.3).

Details of sampling locations (latitudes, longitudes, water depths) and the sources of samples analysed during this study are listed in Appendix 1 - Table A1.1; bathymetric profiles for the Balleny Province dredge sites are presented in Figure A1.1.

3.4 PETROGRAPHY AND MINERAL CHEMISTRY:

This section discusses the petrography and mineral chemistry of all Balleny Plume samples analysed for whole-rock major and trace element compositions (Sections 3.5 and 3.6). Electron microprobe data for representative silicate and oxide phenocryst and/or microphenocryst phases, are presented in Appendix 3, along with the notation used for mineral chemistry throughout this thesis; microprobe analytical techniques are described in Appendix 2. An attempt has also been made to calculate the compositions of the major phenocryst/microphenocryst phases (olivine, clinopyroxene ± plagioclase) in equilibrium

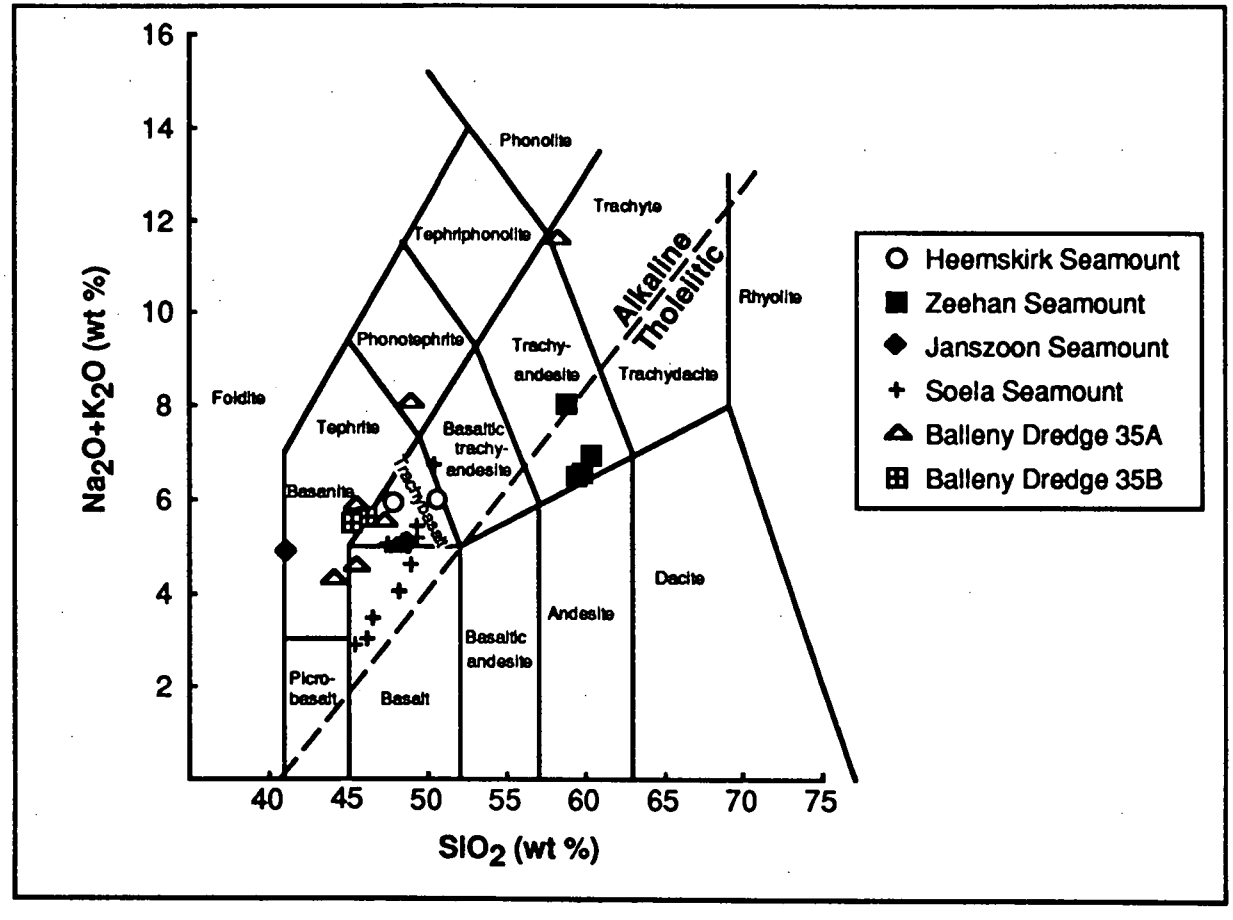

Figure 3.3: Classification of Balleny Plume samples discussed in the text according to the total alkalis versus silica (TAS) diagram of Le Bas et al. (1986) using normalised major element data from Section 3.5; alkaline and tholeiitic fields are separated by the diagonal (dashed) line of Macdonald and Katsura (1964), as defined for the Hawaiian basalts .

with the host whole-rock major element compositions of the various Balleny Plume samples. The results of these calculations are presented in Appendix 3.

3.4.1 Balleny Province:

The petrography and mineral chemistry of nine Balleny Province samples is summarised in Table 3.1. Representative electron microprobe analyses of silicate and oxide minerals are depicted in Figures 3.4 and 3.5.

The range of igneous textures observed in the Balleny Province samples appears to correlate with whole rock composition. Three of the Balleny basanites, 35A-7, 35B-1 and 35B-2, have seriate textures (grainsize from <0.1 to 2 mm) involving the major phenocryst phases - olivine, clinopyroxene ± plagioclase. Where seriate textures are discussed, an arbitrary grainsize classification has been adopted to distinguish phenocryst (>1 mm), microphenocryst (0.2 to 1 mm) and groundmass (<0.2 mm) crystals in order to examine variations in mineral chemistry. The presence of olivine inclusions within both clinopyroxene and plagioclase indicates that these latter phases were co-crystallising whereas olivine was an earlier crystallising phase, possibly co-liquidus with the Cr-rich pleonaste which it commonly encloses. Sample 35A-5, an alkali olivine basalt, also has a seriate texture, with a grainsize range of <0.1 to 6 mm for olivine and clinopyroxene.

Two trachybasalt samples (35A-4 and 35A-6) have porphyritic/glomeroporphyritic textures, with polymineralic aggregates comprising clinopyroxene, plagioclase and spinel. No fresh olivine crystals are visible, but patches of carbonate and clay may be the product of complete olivine alteration in both of these samples. The porphyritic texture of basanite sample 35A-3 is similar to that of the Balleny trachybasalts rather than to the other basanites.

Sample 35A-1, a phonotephrite, is distinguished by its hypocrystalline texture, lack of clinopyroxene, and fine grainsize (0.1 to 0.3 mm). The most evolved Balleny Province dredge sample (35A-2), a porphyritic trachyte, is dominated by aligned phenocrystal and groundmass feldspar.

Within the basanites (samples 35A-7, 35B-1 and 35B-2), olivine microphenocrysts generally overlap with the phenocryst (up to Mg#86.8) compositional range but contain less Cr-rich spinel inclusions. Progressive spinel crystallisation is accompanied by decreasing Cr_2O_3 and increasing TiO_2 contents, ranging from Cr-rich pleonaste within early-formed, magnesian olivines through Cr-poor pleonaste microphenocrysts, inclusions of Cr-poor pleonaste, Cr-aluminous titanomagnetite and Mg-aluminous titanomagnetite within olivine microphenocrysts, clinopyroxene and plagioclase, to aluminous titanomagnetite groundmass crystals. Only the most Ti-rich spinels occur as inclusions within plagioclase phenocrysts in sample 35A-7, suggesting that plagioclase was the last phase to crystallise. Clinopyroxene phenocrysts and microphenocrysts generally have diopside to salite compositions (up to $Mg\#_{84.8}$), whereas groundmass-sized crystals extend into the augite compositional field. Progressive clinopyroxene crystallisation is characterised by increasing FeO, and decreasing CaO and MgO contents. The exception is sample 35A-3 which,

Table 3.1: Petrography of submarine Balleny Province samples.
Note for all petrography tables: zoning - N = normal, R = reverse, O = oscillatory, U = unzoned, P = patchy; cpx = clinopyroxene; modal mineralogy, based on the point counting of 1000 points per sample, relates to phenocryst/microphenocryst phases only.

Sample No.	Rock Type	Texture	Modal Mineralogy	Phenocrysts and microphenocrysts	Groundmass
E27-35A-1	Phonotephrite	Hypocrystalline/ Aphyric Slightly vesicular			1) plagioclase (An_{46-53} - labrodorite-andesine): subparallel alignment; rare clots 2) olivine ($Mg\#_{64.6-71.3}$), zoning (N), spinel inclusions (Mg-Al-titanomagnetite) ± cores or zonal inclusions of brown glass 3) spinels (Mg-Al-titanomagnetite) 4) very fine-grained cpx 5) brown glassy matrix
E27-35A-2	Trachyte	Porphyritic	24 % feldspar 5.5 % olivine 1 % cpx <1 % spinel	1) feldspar phenocrysts ($An_{33}Ab_{61}Or_6$-$An_7Ab_{77}Or_{16}$ - andesine-oligoclase-anorthoclase): complex zoning 2) feldspar microphenocrysts ($An_{25}Ab_{68}Or_7$-$An_7Ab_{71}Or_{22}$ - oligoclase-anorthoclase) 3) olivine microphenocrysts ($Mg\#_{21.6-26.3}$): zoning (U, N), spinel (Al-titanomagnetite) inclusions 4) cpx microphenocrysts ($Mg\#_{40.8-48.7}$ - ferrosalite): zoning (R), spinel (Al-titanomagnetite) inclusions 5) spinel (Al-titanomagnetite) microphenocrysts	Subparallel oligoclase-anorthoclase laths ($An_{24}Ab_{69}Or_7$-$An_1Ab_{71}Or_{28}$); olivine ($Fo_{15.4-19.1}$); cpx ($Mg\#_{42.2-42.4}$ - ferrosalite-ferroaugite); Fe-oxides
E27-35A-3	Basanite	Porphyritic Hypocrystalline groundmass Vesicular	9 % olivine 2 % plagioclase 1.5 % cpx	1) olivine microphenocrysts ($Mg\#_{71.5-84.8}$): zoning (N, R), spinel (Cr-pleonaste, Cr-Al-titanomagnetite) + melt inclusions 2) plagioclase phenocrysts (An_{65} - labradorite) 3) cpx microphenocrysts ($Mg\#_{71.6-79.5}$ - salite-augite): simple or sector twinning, zoning (U, N, R), spinel (Mg-Al-titanomagmetite) inclusions 4) rare cpx clots	plagioclase (An_{63-72} - bytownite-labradorite); olivine; cpx; Fe-oxides; brown glassy matrix

Table 3.1: (continued)

Sample No.	Rock Type	Texture	Modal Mineralogy	Phenocrysts and microphenocrysts	Groundmass
E27-35A-4	Trachybasalt	Sparsely porphyritic/ glomeroporphyritic	2 % plagioclase 1 % cpx	1) plagioclase microphenocrysts (An_{61-71} - bytownite-labradorite): zoning (U, N, R) 2) cpx microphenocrysts ($Mg\#_{61.7-75.2}$ - salite): zoning (U, N, R), spinel (Al-titanomagnetite) inclusions 3) rare glomerocrysts: plagioclase; plagioclase + cpx + spinel	plagioclase (An_{51-72} - bytownite-labradorite); cpx ($Mg\#_{64.5-73.2}$ - salite-augite); spinel (Al-titanomagnetite); patches of calcite and smectite (?secondary to olivine)
E27-35A-5	Alkali olivine basalt	Seriate-textured/ sparsely glomeroporphyritic	13 % olivine 1 % cpx <1 % spinel	1) olivine phenocrysts and microphenocrysts ($Mg\#_{76-87}$: cores = $Mg\#_{77.3-87.4}$; rims = $Mg\#_{75.5-84.0}$): zoning (U, N, R), spinel (Cr-pleonaste, pleonaste, titanian picotite) inclusions 2) cpx phenocrysts and microphenocrysts ($Mg\#_{77.0-83.0}$ - diopside-salite) 3) spinel (pleonaste) microphenocrysts 4) rare glomerocrysts: microphenocryst ($Mg\#_{84.4-85.6}$) + groundmass ($Mg\#_{78.7-83.9}$) olivine	olivine ($Mg\#_{71.5-84.4}$); cpx, ($Mg\#_{76.1-77.5}$ - salite-augite); plagioclase (An_{67-76} - bytownite-labradorite); ?devitrified glass
E27-35A-6	Trachybasalt	Porphyritic/ glomeroporphyritic Vesicular		1) glomerocrysts: plagioclase ± cpx ± spinel 2) plagioclase phenocrysts 3) cpx phenocrysts, may be enclosed by plagioclase 3) patches of carbonate + green alteration material - ?secondary to olivine phenocrysts	plagioclase; cpx; ?altered olivine; Fe-oxides
E27-35A-7	Basanite	Seriate-textured/ sparsely glomeroporphyritic	10 % olivine 4 % cpx 2 % plagioclase <1 % spinel	1) olivine phenocrysts ($Mg\#_{74.2-86.7}$): zoning (U, N), spinel (Cr-pleonaste) inclusions 2) olivine microphenocrysts ($Mg\#_{70.4-86.3}$): zoning (U, N, R) 3) cpx phenocrysts and microphenocrysts ($Mg\#_{66.7-81.2}$ - salite, rare diopside cores): zoning (U, N, R, O), inclusions of spinel (pleonaste, Mg-Al-titanomagnetite) + olivine ($Mg\#_{73.2}$) + plagioclase (An_{69} - bytownite) 4) plagioclase microphenocrysts (An_{74} - bytownite): inclusions of olivine ($Mg\#_{76.6-77.5}$) + cpx ($Mg\#_{71.5-72.9}$) + spinel (Al-titanomagnetite) 5) spinel (pleonaste) microphenocrysts 6) glomerocrysts: cpx ($Mg\#_{76.0-76.6}$) + plagioclase (An_{63-76} - bytownite) + olivine ($Mg\#_{75.1-78.1}$) + spinel (Al-titanomagnetite)	cpx ($Mg\#_{51.8-76.0}$ - salite-augite); olivine ($Mg\#_{66.2-78.1}$); plagioclase (An_{69-75} - bytownite-labradorite); spinel (Al-titanomagnetite)

Table 3.1: (continued)

Sample No.	Rock Type	Texture	Modal Mineralogy	Phenocrysts and microphenocrysts	Groundmass
E27-35B-1	Basanite	Seriate-textured	3.5 % olivine 1 % cpx 1 % plagioclase <1 % spinel	1) olivine phenocrysts and microphenocrysts ($Mg\#_{60.1-86.8}$): zoning (U, N), spinel (Cr-pleonaste in phenocrysts; Mg-Al-titanomagnetite in microphenocrysts) + olivine inclusions; 2) cpx phenocrysts and microphenocrysts ($Mg\#_{68.6-84.8}$ - diopside or diopside zoned to salite): zoning (U, N, R), spinel (Mg-Al-titanomagnetite) inclusions, rare sector twinning 3) plagioclase phenocrysts (An_{53-70} - bytownite-labradorite): zoning (R), spinel + fluid inclusions - sieve-like textures 4) spinel (Mg-Al-titanomagnetite) microphenocrysts	olivine ($Mg\#_{58.6-63.9}$); cpx ($Mg\#_{74.2}$ - salite); plagioclase (An_{50-70} - labradorite); spinel (Mg-Al-titanomagnetite)
E27-35B-2	Basanite	Seriate-textured/ Hypocrystalline groundmass	6 % olivine 4 % cpx 2 % plagioclase	1) olivine phenocrysts and microphenocrysts ($Mg\#_{74.1-85.6}$): zoning (U, N, R), spinel (Cr-pleonaste in phenocrysts; pleonaste, Cr-Al- titanomagnetite, Mg-Al-titanomagnetite in microphenocrysts) inclusions 2) cpx phenocrysts and microphenocrysts ($Mg\#_{70.4-82.8}$ - generally salitic, some diopside): zoning (U, N, R); rare clots 3) plagioclase phenocrysts and microphenocrysts (An_{56-72} - bytownite-labradorite): zoning (N) 4) rare clots of olivine + cpx	olivine ($Mg\#_{71.1-82.3}$, predominantly $Mg\#_{81-82}$); cpx ($Mg\#_{57.9-81.4}$ - diopside-salite); fine opaques; plagioclase (An_{46-74} - bytownite-labradorite-andesine); dusty ?devitrified glass

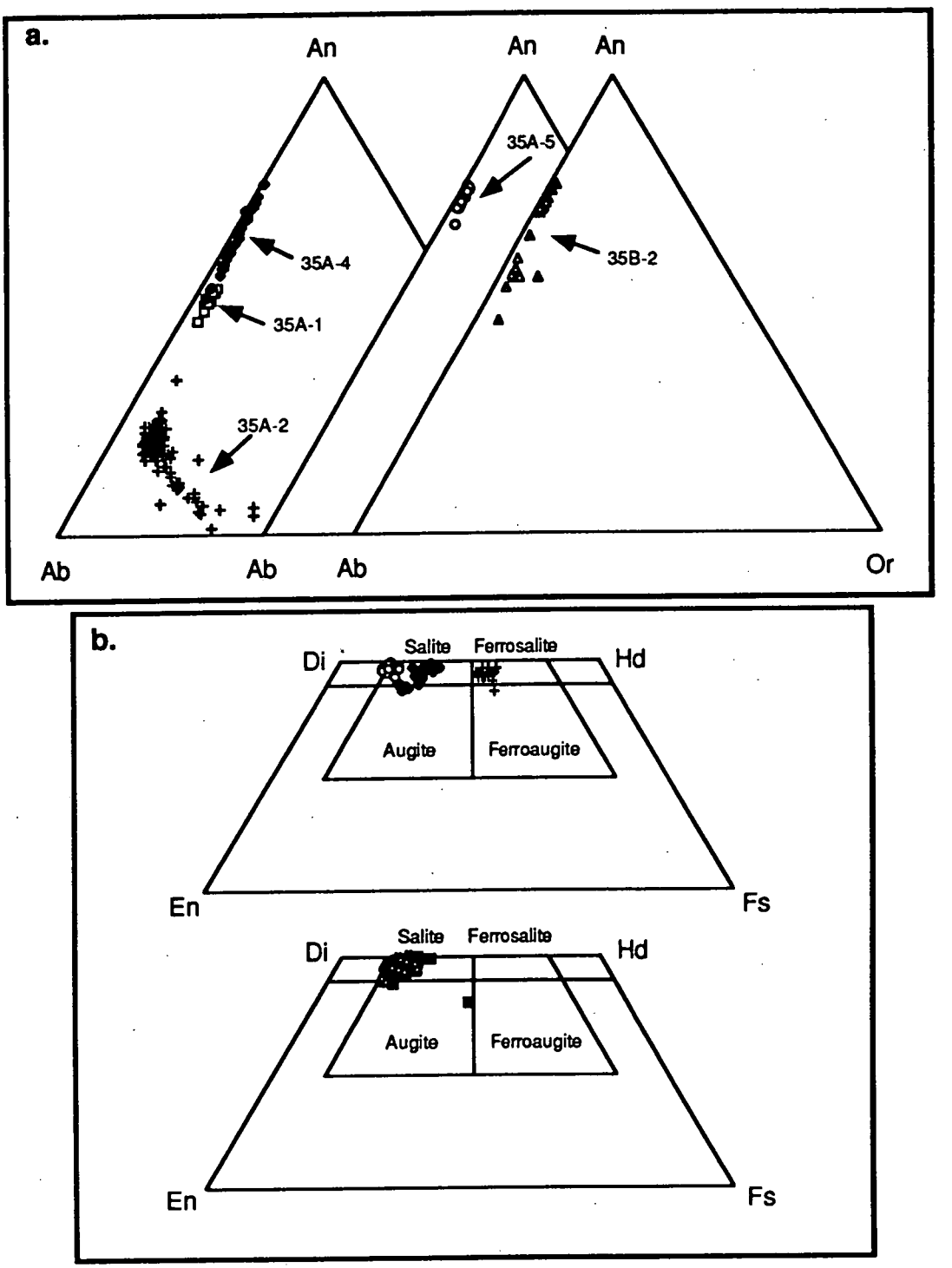

Figure 3.4: Representative electron microprobe analyses of a) feldspar and b) clinopyroxene within submarine Balleny Province samples 35A-1 (open squares - plagioclase only), 35A-2 (crosses), 35A-4 (filled diamonds), 35A-5 (open circles), 35A-7 (filled squares - clinopyroxene only) and 35B-2 (open triangles).

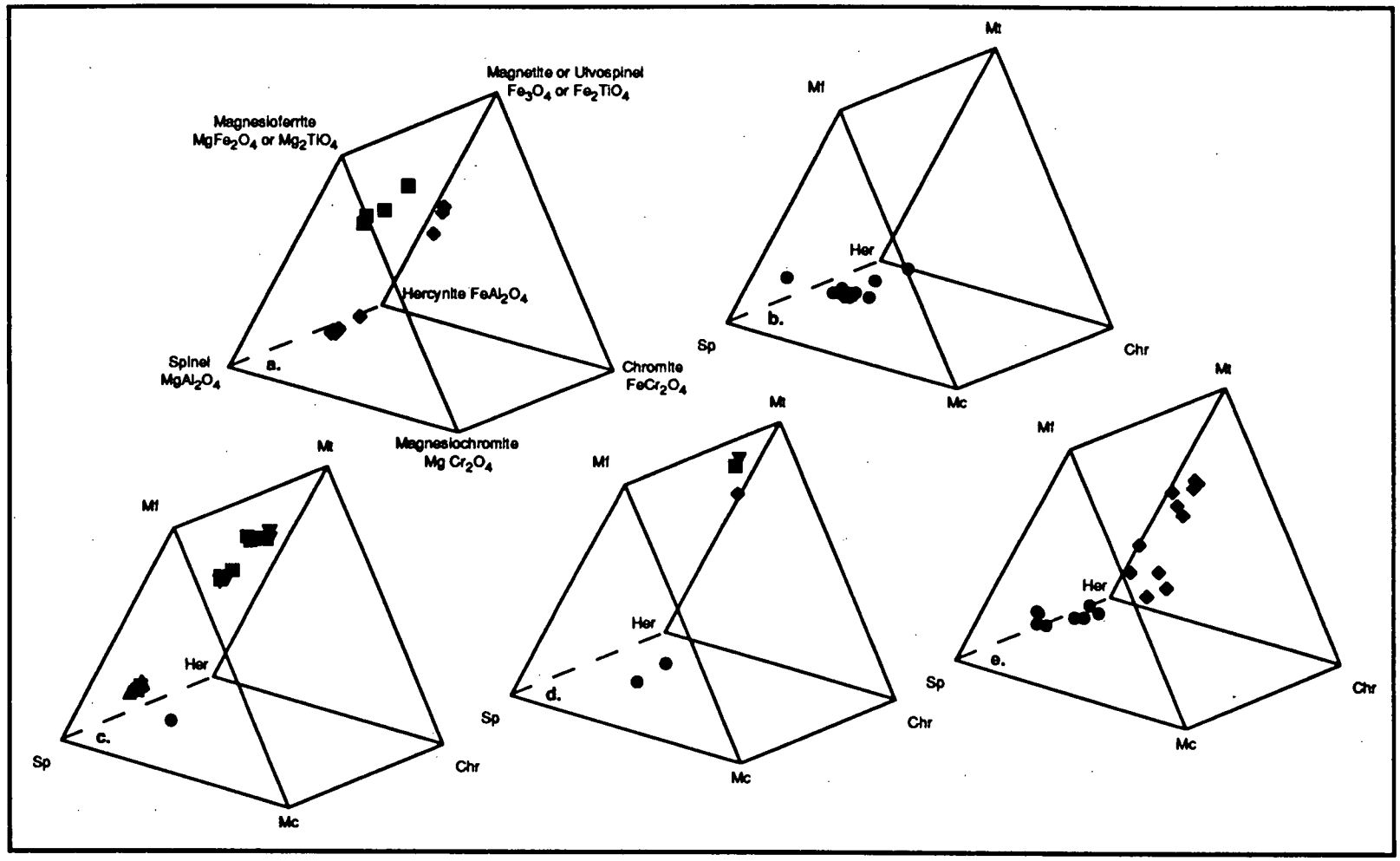

Figure 3.5: Representative electron microprobe analyses of spinel within submarine Balleny Province samples a) 35A-3, b) 35A-5, c) 35A-7, d) 35B-1 and e) 35B-2 plotted on modified Johnston spinel prisms (Deer et al., 1992: p. 560). Symbols used are: inclusion within olivine phenocryst (filled circle), inclusion within olivine microphenocryst (filled diamond), inclusion within clinopyroxene (filled square), microphenocryst (filled triangle), groundmass crystal (inverted filled triangle).

although not the most evolved of the Balleny basanites, has augite microphenocrysts and the least magnesian clinopyroxenes (up to $Mg\#_{79.5}$) of all the basanites. Basanite plagioclase compositions are generally in the bytownite to labradorite fields (up to An_{74}) and may extend to more sodic (andesine) compositions in the groundmass.

Alkali olivine basalt sample 35A-5 has similar clinopyroxene (up to $Mg\#_{83.0}$) compositions to the basanites, the larger crystals comprising either diopside or salite and groundmass-sized crystals extending into the augite field. However, olivine (up to $Mg\#_{87.4}$) is more magnesian than in the basanites. The presence of plagioclase only as a groundmass phase suggests that it was the last phase to crystallise.

In the trachybasalt samples 35A-4 and 35A-6 clinopyroxene is generally salite or augite and less magnesian (up to $Mg\#_{75.2}$) than in the more primitive samples. Plagioclase has a similar compositional range (bytownite to labradorite) to that within the basanite and alkali basalt samples.

Both olivine and plagioclase compositions in phonotephrite sample 35A-1 are similar to the groundmass components of the basanites, 35A-1 plagioclase occupying the more sodic, labradorite to andesine, end of the basanite groundmass range. Olivine and clinopyroxene crystals in trachyte sample 35A-2 are more Fe-rich than in the less evolved Balleny samples, olivine microphenocrysts reaching only $Mg\#_{26.3}$, clinopyroxene (up to $Mg\#_{48.7}$) falling within the ferrosalite compositional field and extending to ferroaugite compositions within the groundmass. Spinel compositions are limited to aluminous titanomagnetite, and feldspar becomes more potassic with progressive crystallisation and finer grainsize.

Disequilibrium textures, visible to varying extents in all of the Balleny Province dredge samples, include rim resorption and reverse compositional zoning of the major mineral phases. Resorption is visible as embayed rims in olivine and clinopyroxene phenocrysts and microphenocrysts and partial to complete rim resorption of plagioclase phenocrysts.

3.4.2 Soela Seamount:

Soela Seamount samples SS1, SS2 and SS4 are poorly-sorted conglomerates comprising a variety of angular to well-rounded volcanic fragments, from <1 mm to 11 cm in diameter, within a bioclastic calcareous matrix. Individual clinopyroxene crystals ($Mg\#_{75.6-84.4}$ - diopside-salite) also occur within the matrix, and sometimes have fine kaersutite inclusions. These three conglomerates are subdivided in Table 3.2 in terms of their constituent clasts. Samples SS3 and SS5 are boulders of volcanic rock. Most of the Soela samples have suffered some degree of alteration, usually evident as carbonate-clay pseudomorphs of olivine and/or yellow-orange clay and Fe-stained material dispersed throughout the groundmass. Representative electron microprobe analyses of silicate and oxide minerals from Soela Seamount samples are plotted in Figures 3.6 and 3.7 respectively.

Table 3.2: Petrography of samples dredged from Soela Seamount. Notation as for Table 3.1.

Sample No.	Rock Type	Texture	Modal Mineralogy	Phenocrysts and microphenocrysts	Groundmass
SS1					
SS1-1	Basaltic trachyandesite	Porphyritic/ glomeroporphyritic Pilotaxitic groundmass Vesicular	6 % plagioclase 2 % altered olivine 2 % cpx	1) plagioclase phenocrysts (An_{52-79} - bytownite-labradorite): zoning (N), spinel (Mg-Al-titanomagnetite) + melt inclusions 2) completely altered olivine phenocrysts 3) cpx phenocrysts ($Mg\#_{75.7-80.0}$ - salite): zoning (N,R), spinel (Mg-Al-titanomagnetite) inclusions 4) glomerocrysts: plagioclase; cpx; plagioclase subophitically enclosed by cpx	plagioclase (An_{50-60} - labradorite); cpx ($Mg\#_{71.5-74.2}$ - salite); spinel (Mg-Al-titanomagnetite); clay - ?altered olivine
SS2					
SS2-4	Alkali olivine basalt	Porphyritic/ sparsely glomeroporphyritic	20 % cpx 15 % altered olivine 2 % unaltered olivine 1 % plagioclase	1) cpx phenocrysts (cores: $Mg\#_{81.8-84.6}$ - diopside; rims: $Mg\#_{75.3-81.0}$ - salite): zoning (N,P), plagioclase + spinel inclusions 2) olivine phenocrysts ($Mg\#_{80-82}$): may be completely altered 3) plagioclase phenocrysts (An_{64-80} - bytownite-labradorite): zoning (U,N,) 4) glomerocrysts: plagioclase; cpx; cpx subophitically enclosing plagioclase; cpx + olivine	plagioclase; cpx; spinel (Mg-Al-titanomagnetite); clay
SS2-6	Alkali olivine basalt	Sparsely glomeroporphyritic Pilotaxitic groundmass Vesicular	6 % altered olivine 3 % cpx 3 % plagioclase	1) completely altered olivine phenocrysts 2) cpx phenocrysts ($Mg\#_{79.3-80.8}$ - salite): zoning (U, N), spinel (Al-Mg-titanomagnetite) + plagioclase (An_{74-77} - bytownite) + kaersutite inclusions 3) plagioclase phenocrysts (An_{54-81} - bytownite-labradorite): zoning (U,N, R), 4) glomerocrysts: cpx; plagioclase; cpx subophitically enclosing plagioclase	plagioclase (An_{29-55} - labradorite-andesine); cpx; spinel (Mg-Al-titanomagnetite); ilmenite; clay alteration-? secondary to olivine
SS3	Alkali olivine basalt	Porphyritic/ slightly glomeroporphyritic	19 % cpx 14 % olivine	1) cpx phenocrysts ($Mg\#_{75.5-81.2}$ - salite; rare augite - $Mg\#_{83.0}$ zoned to salite - $Mg\#_{77.8}$): zoning (N ,R ,P), spinel (Mg-Al-titanomagnetite) + olivine ($Mg\#_{77.7}$) + plagioclase (An_{76} - bytownite) + devitrified melt inclusions, sector or simple twinning 2) olivine phenocrysts ($Mg\#_{71.2-81.4}$): cpx ($Mg\#_{76.5}$ - salite) + spinel (Ti-chromite, Al-chromite, Cr-titanomagnetite, Mg-Al-titanomagnetite) inclusions, zoning (U, N) 3) glomerocrysts: cpx ± olivine	plagioclase (An_{58-69} - bytownite-labradorite) microlites; altered olivine; cpx; Fe-oxides

Table 3.2: (continued)

Sample No.	Rock Type	Texture	Modal Mineralogy	Phenocrysts and microphenocrysts	Groundmass
SS4					
SS4-1	Alkali olivine basalt	Porphyritic/ glomeroporphyritic	24 % altered olivine 0.5 % unaltered olivine 15.5 % cpx <1 % plagioclase	1) olivine microphenocrysts ($Mg\#_{63-82}$): zoning (U, N), spinel (Mg-Al-chromite, titanian picotite, Mg-Al-titanomagnetite) inclusions 2) cpx phenocrysts ($Mg\#_{73.2-81.9}$ - salite; or cores: $Mg\#_{81.9-82.9}$ - diopside and rims: $Mg\#_{79.1-79.5}$ - salite) and microphenocrysts ($Mg\#_{73.4-81.3}$ - generally salite, may have augite cores): zoning (U, N, R, P), spinel (Mg-Al-titanomagnetite) + olivine + plagioclase + kaersutite inclusions, simple twinning 3) plagioclase microphenocrysts (An_{64-81} - bytownite-labradorite) 4) glomerocrysts: cpx; plagioclase; cpx + plagioclase	plagioclase (An_{53-61} - labradorite); cpx ($Mg\#_{71.6-73.7}$ - salite); spinel (Mg-Al-titanomagnetite); partly altered olivine ($Mg\#_{55}$)
SS4-2	Alkali olivine basalt	Porphyritic/ glomeroporphyritic Pilotaxitic groundmass	16 % cpx 7 % altered olivine 1 % plagioclase	1) cpx phenocrysts and microphenocrysts ($Mg\#_{70.1-82.7}$ - diopside, salite, or dipside cores with salite rims): zoning (U, N, O, P), simple twinning, plagioclase (An61 - labradorite) + spinel (Mg-Al-titanomagnetite) inclusions 2) completely altered olivine phenocrysts and microphenocrysts 3) plagioclase phenocrysts and microphenocrysts (An_{64-82} - bytownite-labradorite): zoning (N, R), cpx ($Mg\#_{75.0}$ - salite) + spinel inclusions 4) glomerocrysts: plagioclase; cpx; cpx + altered olivine	plagioclase (An_{59-67} - labradorite); cpx ($Mg\#_{71.6-73.3}$ - salite); spinel (Mg-Al-titanomagnetite)
SS4-3	Trachybasalt	Porphyritic		1) plagioclase phenocrysts: spinel inclusions 2) cpx phenocrysts; rare clots 3) ?altered olivine phenocrysts and microphenocrysts	plagioclase; cpx; spinel; altered olivine
SS4-4	Trachybasalt	Aphyric Vesicular			1) plagioclase (An_{44-55} - labradorite-andesine) 2) cpx ($Mg\#_{66.3-76.3}$ - salite), spinel (Mg-Al-titanomagnetite) inclusions 3) spinel (Mg-Al-titanomagnetite) 4) yellow smectite patches
SS4-5	Alkali olivine basalt	Porphyritic/sparsely glomeroporphyritic		1) glomerocrysts: cpx 2) cpx phenocrysts: spinel + kaersutite inclusions 3) clay-carbonate patches ?secondary to olivine	plagioclase; cpx; Fe-oxides; clay
SS4-6	Trachybasalt	Porphyritic/ glomeroporphyritic		1) glomerocrysts: cpx ± plagioclase ± altered olivine 2) cpx microphenocrysts: zoning (P) 3) plagioclase microphenocrysts: sieve-like textures 4) clay-carbonate patches ?secondary to olivine	plagioclase; cpx; Fe-oxides; clay

Table 3.2: (continued)

Sample No.	Rock Type	Texture	Modal Mineralogy	Phenocrysts and microphenocrysts	Groundmass
SS4					
SS4-7	Trachybasalt	Slightly porphyritic		rare plagioclase microphenocrysts	plagioclase - some parallel alignment; cpx; Fe-oxides
SS4-8	Alkali olivine basalt	Porphyritic/ glomeroporphyritic Vesicular		1) glomerocrysts: cpx; cpx subophitically enclosing plagioclase 2) cpx microphenocrysts: zoning (P), simple twinning 3) ?altered olivine microphenocrysts	plagioclase - some alignment; cpx; Fe-oxides; clay
SS5	Trachybasalt	Sparsely porphyritic/ glomeroporphyritic Pilotaxitic groundmass Slightly vesicular	4 % cpx 2 % altered olivine 1.5 % plagioclase <1 % spinel	1) cpx microphenocrysts ($Mg\#_{71.7-79.4}$ - salite): twinning, spinel (Al-Mg-titanomagnetite) inclusions, zoning (U, N) 2) Fe-stained clay-carbonate patches - secondary to olivine: rare spinel (Cr-Mg-Al-titanomagnetite, Mg-Al-titanomagnetite) inclusions 3) rare plagioclase microphenocrysts (An_{64-68} - labradorite) 4) spinel (Mg-Al-titanomagnetite) microphenocrysts 5) glomerocrysts: cpx; cpx + plagioclase	plagioclase (An_{51-65} - labradorite); cpx ($Mg\#_{71.6-79.4}$ - salite-augite); spinel (Mg-Al-titanomagnetite); alteration material

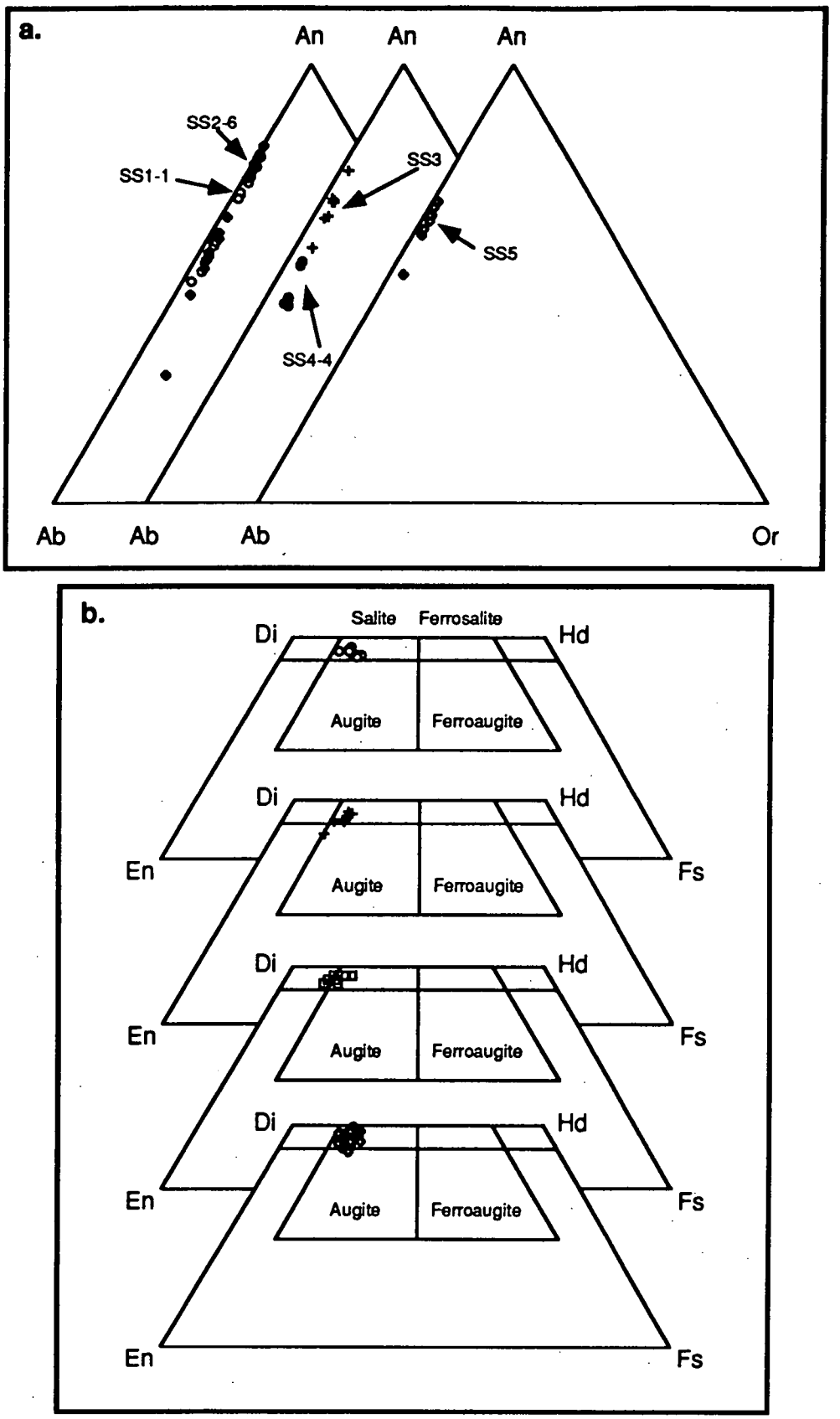

Figure 3.6: Representative electron microprobe analyses of a) plagioclase and b) clinopyroxene within Soela Seamount samples SS1-1 (open circles), SS2-4 (open squares - clinopyroxene only), SS2-6 (filled diamonds - plagioclase only), SS3 (crosses), SS4-4 (filled circles - plagioclase only) and SS5 (open diamonds).

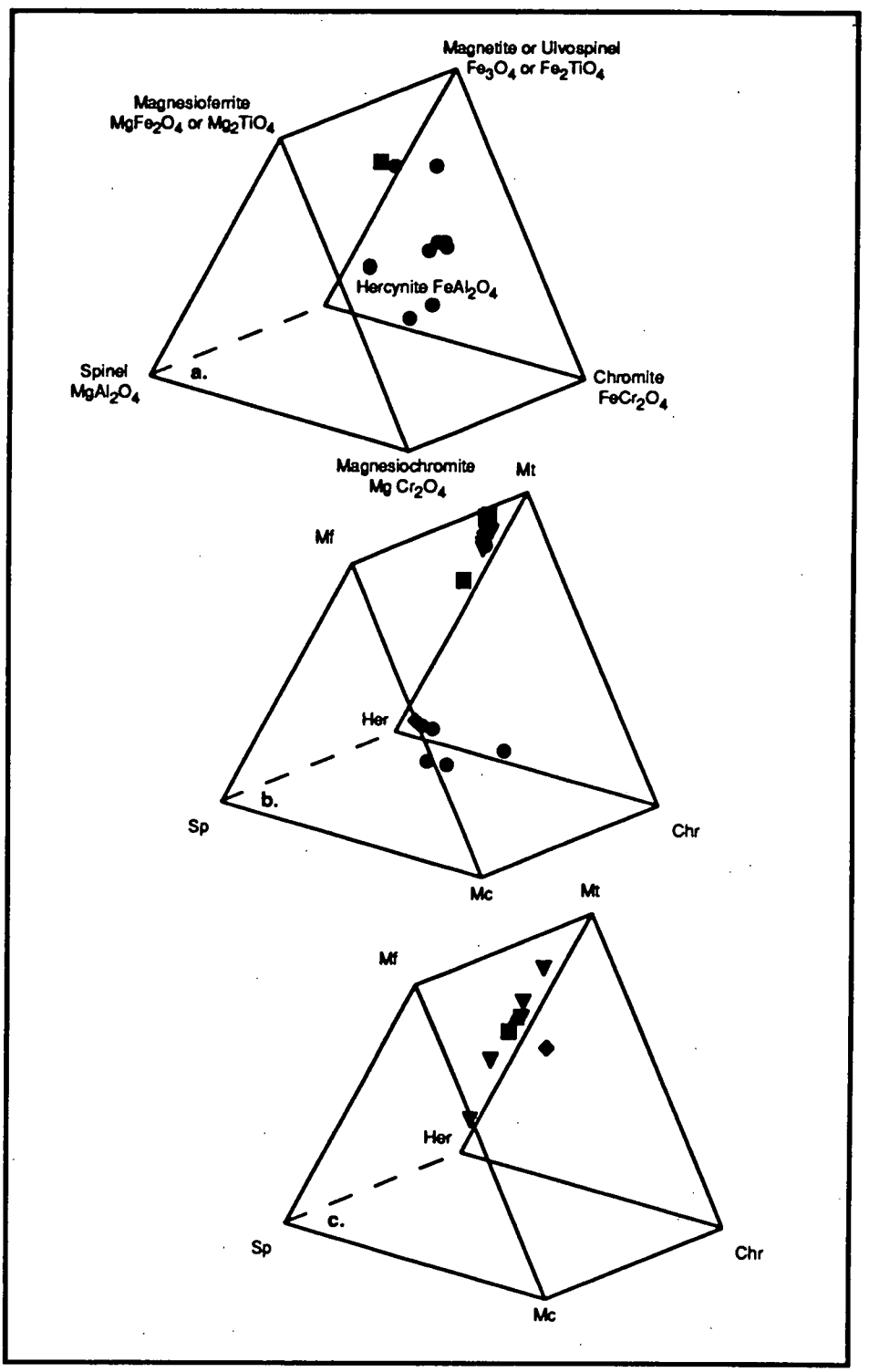

Figure 3.7: Representative electron microprobe analyses of spinel within Soela Seamount samples a) SS3, b) SS4-1 and c) SS5 plotted on modified Johnston spinel prisms (Deer et al., 1992: p. 560). Symbols used are: inclusion within olivine phenocryst (filled circle), inclusion within olivine microphenocryst (filled diamond), inclusion within clinopyroxene (filled square), microphenocryst (filled triangle), groundmass crystal (inverted filled triangle).

Most of the Soela Seamount samples are porphyritic to glomeroporphyritic with a plagioclase-phyric groundmass, the latter commonly characterised by a pilotaxitic arrangement. Possible disequilibrium textural features include crystal rim resorption and reverse compositional zoning. The seven Soela alkali olivine basalts generally display these features, and all contain phenocrysts of olivine and clinopyroxene, the latter commonly enclosing olivine, plagioclase, and kaersutite. Although plagioclase is present as a groundmass phase within all of the alkali olivine basalts, it is absent as a phenocryst/microphenocryst phase in both SS3 and SS4-5. Groundmass olivine has not been observed within all of the samples, however, alteration material, predominantly clay, may represent altered olivine.

The five Soela trachybasalt samples and the basaltic trachyandesite (SS1-1) are also characterised by similar porphyritic to glomeroporphyritic textures. The trachybasalts are distinguished by a rarity, or lack, of olivine in the groundmass, and although olivine is present in SS1-1 as both a phenocryst and groundmass phase, it is completely altered.

Soela Seamount alkali olivine basalts have similar compositional ranges for their major phenocryst phases. Olivine phenocrysts (up to $Mg\#_{82}$) are less Mg-rich than their most magnesian Balleny counterparts (up to $Mg\#_{87.4}$ in Balleny sample 35A-5). Clinopyroxene phenocrysts are generally either of homogeneous salite composition or comprise rims of salite around cores of either augite or diopside which are as magnesian as $Mg\#_{84.6}$ (SS4-2), but more commonly range up to only $Mg\#_{82}$. Spinel inclusions within olivine phenocrysts and/or microphenocrysts are generally Cr-rich. By comparison, spinel inclusions in both clinopyroxene and plagioclase have a similar Mg-aluminous titanomagnetite composition. Where present, plagioclase phenocrysts have a similar compositional range, generally $\sim An_{64-82}$, and rarely extend to compositions as sodic as An_{54}. Alkali basalt groundmass phases include salite ($Mg\#_{71.6-74.2}$), plagioclase (generally An_{53-69}, but may be as sodic as An_{29}), Mg-aluminous titanomagnetite ± olivine.

Clinopyroxene phenocrysts within the Soela trachybasalts are of salite composition (up to $Mg\#_{79.4}$), and plagioclase microphenocrysts are of similar composition (An_{64-68}) to those within the Soela alkali basalts. Olivine microphenocrysts, where present, are completely altered. Groundmass plagioclase is more sodic (An_{44-64}), and groundmass clinopyroxene ($Mg\#_{66.3-79.4}$) less calcic and magnesian, than the corresponding phenocryst phases.

Within the most evolved Soela sample (SS1-1), plagioclase and clinopyroxene display a similar compositional range to the less evolved Soela samples.

3.4.3 South Tasman Sea Seamounts:

Samples dredged from all three south Tasman Sea seamounts display at least some degree of alteration, particularly evident as partial to complete olivine alteration and the devitrification and/or alteration of groundmass glass. Electron microprobe mineral chemistry data have therefore proved difficult to obtain. The petrography of samples analysed for major

Table 3.3: Petrography of samples dredged from the Janszoon, Zeehan and Heemskirk Seamounts. Notation as for Table 3.1.

Sample No.	Rock Type	Texture	Modal Mineralogy	Phenocrysts and microphenocrysts	Groundmass
Janszoon Seamount:					
C1/84(2) 2DB 10	Trachybasalt	Sparsely porphyritic Hypocrystalline/pilotaxitic groundmass Sparsely vesicular	3 % altered olivine 1 % plagioclase <1 % spinel	1) altered olivine phenocrysts and microphenocrysts: Fe-oxide inclusions; rare clots 2) plagioclase microphenocrysts 3) spinel phenocrysts	plagioclase (An_{49-65} - labradorite); altered olivine; Fe-oxides; altered glass (?celadonite); smectite
C1/84(2) 2DB 14	Basanite	Porphyritic Hypocrystalline groundmass Sparsely vesicular		1) altered olivine phenocrysts and microphenocrysts: Fe-oxide inclusions 2) plagioclase microphenocrysts	plagioclase; altered olivine; Fe-oxides; altered glass; smectite
Zeehan Seamount:					
C17/86 8DB 2/1	Trachyandesite	Sparsely porphyritic/ glomeroporphyritic Hypocrystalline groundmass	5 % plagioclase 1 % olivine 1 % cpx	1) plagioclase phenocrysts and microphenocrysts (An_{35-42} - andesine): cpx + spinel + olivine inclusions, sieve-like textures 2) olivine microphenocrysts ($Mg\#_{31.8-34.1}$): spinel inclusions, zoning (U, R) 3) cpx phenocrysts and microphenocrysts ($Mg\#_{39.0-50.8}$ - cores: salite-ferrosalite, ferroaugite or augite; rims: ferrosalite or ferroaugite): spinel (Mg-Al-titanomagnetite) inclusions, zoning (R) 4) glomerocrysts: olivine + cpx + plagioclase + spinel	plagioclase; cpx; altered olivine; Fe-oxides; devitrified glass
C17/86 8DB 2/2	Trachyandesite	Sparsely porphyritic/ glomeroporphyritic Pilotaxitic groundmass	2 % plagioclase 1 % cpx 1 % olivine <1 % Fe-oxides	1) plagioclase phenocrysts (An_{36-42} - andesine): zoning (N) 2) cpx phenocrysts and microphenocrysts ($Mg\#_{40.8-52.6}$ - salite-ferrosalite-ferroaugite): zoning (R), simple twinning, spinel inclusions 3) olivine phenocrysts and microphenocrysts ($Mg\#_{29.2-36.4}$): zoning (N, R), spinel (Mg-Al-titanomagnetite) inclusions 4) spinel phenocrysts and microphenocrysts 5) glomerocrysts: cpx + olivine ± plagioclase	plagioclase; cpx ($Mg\#_{47.0-50.0}$ - augite-ferroaugite); altered olivine; Fe-oxides
C17/86 8DB 2/5	Trachyandesite	Sparsely porphyritic/ glomeroporphyritic Pilotaxitic groundmass	4 % plagioclase <1 % cpx <1 % olivine <1 % Fe-oxides	1) plagioclase phenocrysts (An_{33-45} - andesine) 2) cpx microphenocrysts ($Mg\#_{53.2-54.9}$ - augite-salite): zoning (N) 3) olivine microphenocrysts ($Mg\#_{31.8-33.1}$): zoning (N,R) 4) Fe-oxide phenocrysts and microphenocrysts 5) rare glomerocrysts: cpx + olivine ± plagioclase	plagioclase (An_{37-39} - andesine); cpx; altered olivine; Fe-oxides

Table 3.3: (continued)

Sample No.	Rock Type	Texture	Modal Mineralogy	Phenocrysts and microphenocrysts	Groundmass
Zeehan Seamount:					
C17/86 8DB 3/4	Trachyandesite	Sparsely porphyritic/ glomeroporphyritic Irregular pilotaxitic groundmass	3 % plagioclase 1 % spinel <1 % olivine <1 % cpx	1) plagioclase phenocrysts and microphenocrysts (An_{35-46} - andesine): zoning (N, R) 2) spinel (Mg-Al-titanomagnetite) phenocrysts 3) olivine phenocrysts and microphenocrysts ($Mg\#_{29.4-35.8}$): zoning (U, N, R), cpx ($Mg\#_{52.6}$ - salite) + spinel (Mg-Al-titanomagnetite) inclusions 4) cpx phenocrysts and microphenocrysts ($Mg\#_{39.7-53.3}$ - ferroaugite-ferrosalite): zoning (N, R), spinel (Al-titanomagnetite) inclusions 5) glomerocrysts: cpx + olivine + plagioclase + Fe-oxides	plagioclase (An_{30-38} - andesine); cpx ($Mg\#_{46.4-50.3}$ - augite-ferroaugite) microlites; olivine ($Mg\#_{30.1-31.0}$); spinel (Al-titanomagnetite)
Heemskirk Seamount:					
C17/86 7DB 1/10	Trachybasalt	Hypocrystalline/ sparsely porphyritic Vesicular	<1 % plagioclase	rare partly resorbed plagioclase phenocrysts	1) plagioclase laths 2) completely altered olivine 3) Fe-oxides 4) devitrified brown glassy matrix
C17/86 7DB 1/13	Trachybasalt	Aphyric Vesicular		-	1) plagioclase (An_{39-45} - andesine) 2) cpx ($Mg\#_{54.5-62.3}$ - augite) 3) completely altered olivine 4) Fe-oxides

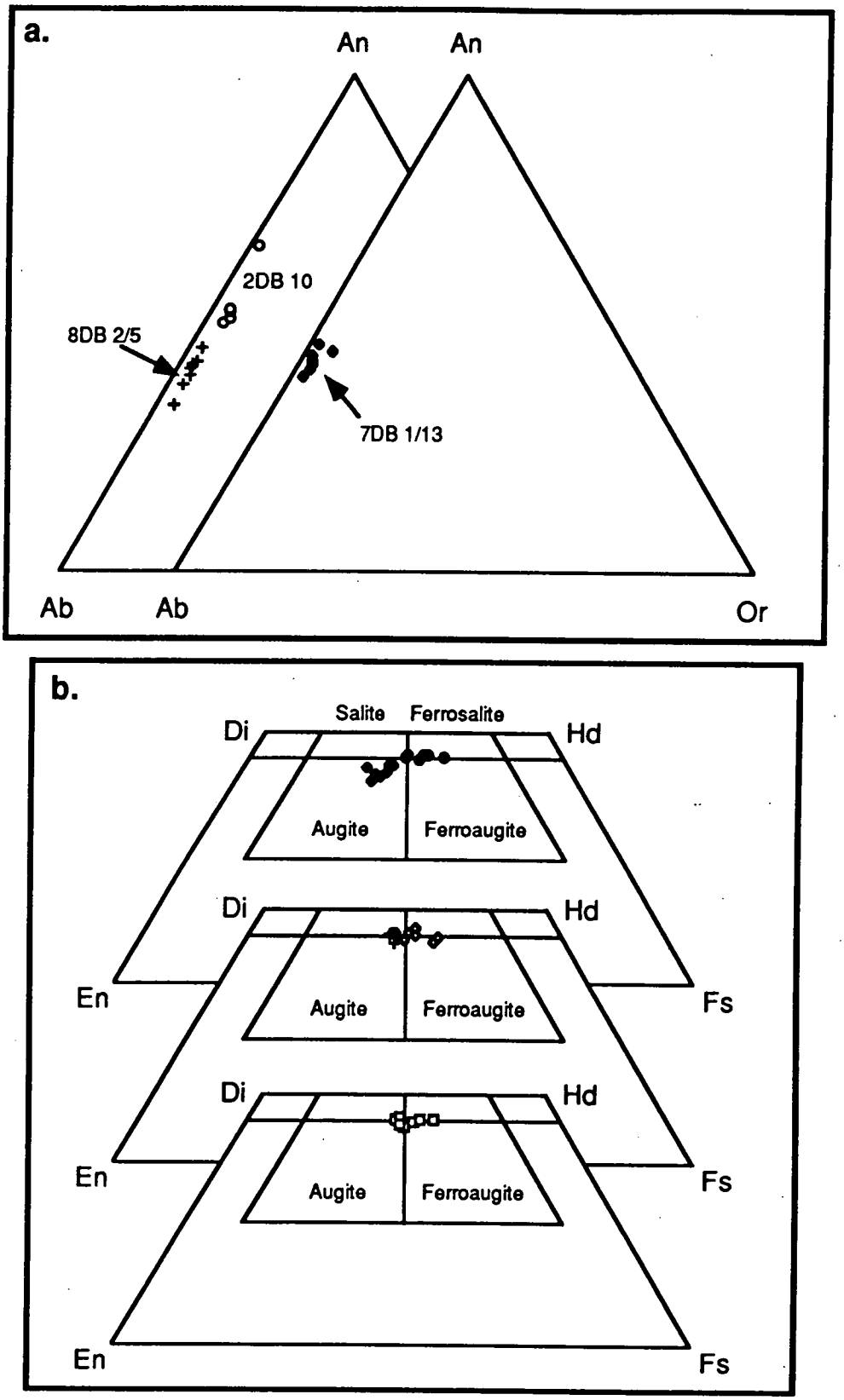

Figure 3.8: Representative electron microprobe analyses of a) plagioclase and b) clinopyroxene within samples from Janszoon Seamount - 2DB 10 (open circles - plagioclase only), Zeehan Seamount - 8DB 2/1 (filled circles - clinopyroxene only), 8DB 2/2 (open squares - clinopyroxene only), 8DB 2/5 (crosses), 8DB 3/4 (open diamonds - clinopyroxene only) and Heemskirk Seamount - 7DB 1/13 (filled diamonds).

and trace element compositions is summarised in Table 3.3. Representative silicate mineral analyses are presented in Figure 3.8.

The basanite and trachybasalt samples from Janszoon Seamount have similar petrographic textures, dominated by elongate and partially aligned plagioclase laths. Phenocrystic and groundmass olivines are completely altered to Fe-stained clay pseudomorphs which exhibit extensive rim resorption. No clinopyroxene is visible in either sample and interstitial glass is completely altered.

The four trachyandesite samples recovered from Zeehan Seamount have similar sparsely porphyritic/glomeroporphyritic textures. The major phases, olivine, clinopyroxene, plagioclase and Fe-oxides, occur as isolated phenocrysts and/or microphenocrysts within the groundmass, and have similar compositions in all four samples. Olivine ($Mg\#_{29.2\text{-}36.4}$) and clinopyroxene (up to $Mg\#_{54.9}$) phenocrysts and microphenocrysts have limited compositional ranges, the latter defining a small field which overlaps the salite, augite, ferrosalite and ferroaugite compositional boundaries. Spinel phenocrysts and microphenocrysts have similar Mg-aluminous titanomagnetite compositions to inclusions within both olivine and clinopyroxene. Plagioclase also has a limited (andesine) compositional range ($An_{33\text{-}46}$) and may contain inclusions of all other mineral phases. The groundmass of Zeehan sample 8DB 2/1 is dominated by devitrified glass and lacks the plagioclase-phyric texture of the other trachyandesites.

The trachybasalts from Heemskirk Seamount are both extremely vesicular. Sample 7DB 1/13, the less altered of the two, is very fine-grained (≤0.1 mm) and plagioclase-phyric. Sample 7DB 1/10 is less plagioclase-phyric, comprising fine plagioclase laths (up to 0.1 mm in length) scattered through a groundmass dominated by finely divided Fe-oxides and altered glass. Fine-grained olivine is completely altered and partly resorbed in both samples.

3.5 MAJOR ELEMENT GEOCHEMISTRY:

The major element compositions of the Balleny Province and Soela Seamount samples were determined by X-ray fluorescence (XRF) spectrometry (Philips PW 1410 spectrometer). The major element compositions of the south Tasman Sea seamount samples were determined by either XRF (Philips PW 1480 spectrometer) or Ir strip electron microprobe analysis (as indicated in Table 3.6). Analytical procedures are discussed in Appendix 2. Throughout this thesis whole-rock Mg-value or $Mg\# = \frac{100 \text{ atomic Mg}}{(Mg + Fe^{2+})}$ where $FeO = \frac{FeO^*}{1 + (0.9 \times \frac{Fe_2O_3}{FeO})}$ and $FeO^* = FeO + (0.9 \times Fe_2O_3)$ assuming $\frac{Fe_2O_3}{FeO} = 0.2$, unless otherwise stated.

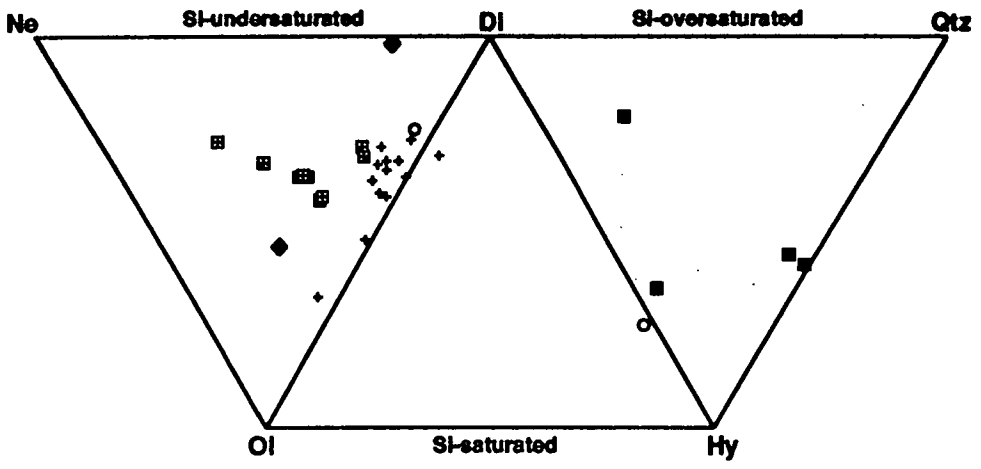

Figure 3.9: Projection of the normative basalt tetrahedron (Yoder and Tilley, 1962) for samples dredged from the Heemskirk (open circles), Zeehan (filled squares), Janszoon (filled diamonds) and Soela (crosses) seamounts and submarine Balleny Province samples (crosses within squares); $\frac{Fe_2O_3}{FeO}$ = 0.2 for CIPW normative (wt %) calculations; mineral abbreviations: Ne - nepheline, Ol - olivine, Di - diopside, Hy - hypersthene, Qtz - quartz.

3.5.1 Balleny Province:

Submarine Balleny Province samples have alkaline affinities and define a SiO_2-undersaturated (Figure 3.9) fractionation trend from basanite and alkali olivine basalt through trachybasalt to phonotephrite and trachyte compositions (Table 3.4; Figure 3.3). Fractionation is controlled predominantly by olivine and accessory Cr-rich spinel, as evidenced by the decrease in Ni and Cr with decreasing MgO content (Figure 3.10). The relatively constant CaO and FeO* contents down to ~5 wt % MgO are consistent with clinopyroxene fractionation, whereas the steady increase in Al_2O_3 and Na_2O with decreasing MgO content indicates an insignificant role for plagioclase fractionation. The two most evolved Balleny samples (35A-1 and 35A-2) have relatively high Na_2O, K_2O and Al_2O_3, consistent with feldspar accumulation, whereas the low FeO* and TiO_2 contents of trachyte sample 35A-2 imply significant titanomagnetite fractionation. In contrast, trachybasalt sample 35A-4 has high FeO* and TiO_2 relative to the trend defined by the other Balleny samples, and basanite sample 35A-7 has high FeO*, relative to rocks of similar MgO content such as sample 35B-2.

If the strict definition of Frey et al. (1978: whole-rock atomic Mg#≥68; Ni ≥320 ppm) is used to distinguish primary melts, none of the Balleny Province samples studied here can be considered as such. This is particularly true if the whole-rock Mg-values of these samples are influenced by cumulate phases; disequilibrium textures (Section 3.4) and equilibrium mineral

Table 3.4: Major and trace element compositions of submarine Balleny Province samples. Note for all major element tables: LOI = Loss on Ignition.

Sample No:	E27-35A-1	E27-35A-2	E27-35A-3	E27-35A-4	E27-35A-5	E27-35A-6	E27-35A-7	E27-35B-1	E27-35B-2
Major Elements (wt %):									
SiO_2	48.38	56.90	45.32	45.96	44.80	45.99	43.37	45.87	43.98
TiO_2	2.58	0.36	2.83	3.54	2.82	2.81	2.86	2.73	2.81
Al_2O_3	17.31	18.40	15.82	14.77	15.35	15.88	14.47	16.30	15.06
Fe_2O_3	11.80	7.65	12.16	14.44	11.64	12.12	13.44	13.08	11.72
FeO	0.00	0.00	0.00	0.00	0.00	0.00	0.00	0.00	0.00
MnO	0.19	0.24	0.20	0.20	0.16	0.16	0.18	0.19	0.16
MgO	3.66	0.64	8.00	4.21	9.85	5.00	9.94	6.88	9.18
CaO	7.01	2.75	9.39	9.40	10.17	10.10	10.35	9.55	9.58
Na_2O	5.67	7.89	4.17	3.89	3.30	3.57	3.16	4.19	3.90
K_2O	2.35	3.44	1.64	1.50	1.22	1.25	1.05	1.40	1.46
P_2O_5	1.01	0.35	0.80	0.70	0.66	0.51	0.75	0.68	0.60
LOI	0.00	0.79	0.19	1.37	0.19	2.59	0.63	-0.50	1.53
Total	99.96	99.41	100.52	99.98	100.16	99.98	100.20	100.37	99.98
Mg#	42.02	16.35	60.59	40.52	66.41	49.08	63.35	55.14	64.67
FeO*	10.62	6.88	10.94	12.99	10.47	10.91	12.09	11.77	10.55
Trace Elements (ppm):									
Ba	599	761	463	391	355	349	314	408	390
Rb	63	124	39	36	29	26	19	35	34
Nb	126	203	89	70	67	53	59	75	68
Sr	956	653	786	563	668	571	651	689	616
Zr	468	835	298	278	214	214	200	249	238
Y	39	46	34	38	29	30	30	34	30
Ni	23	3	126	11	233	50	255	106	170
Cr	22	<2	168	5	378	80	300	149	286
V	105	5	214	327	240	308	226	202	236
Sc	11	1	24	22	28.5	26.5	27	23.5	28
Zn	116	137	98	129	91	103	97	93	85
Cu	31	5	42	20	66	111	68	62	55
Cs	1.07	0.85	0.52	<1	<1	<1	<1	<1	<1
Hf	9.91	16.44	6.42	6.25	4.84	5.00	4.86	5.56	5.35
Ta	8.66	14.95	5.81	4.91	4.48	3.44	3.90	5.00	4.61
Th	12.42	25.39	7.11	5.37	5.09	3.78	4.12	5.99	6.14

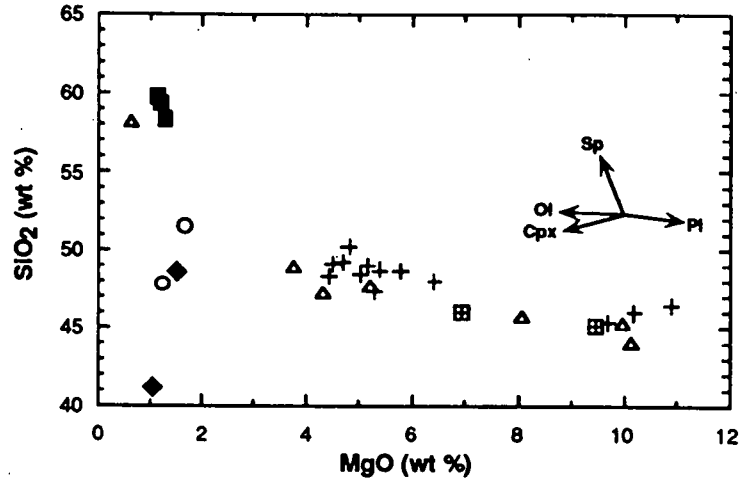
SiO2 (wt %)
MgO (wt %)
Sp
Ol
Cpx
Pl

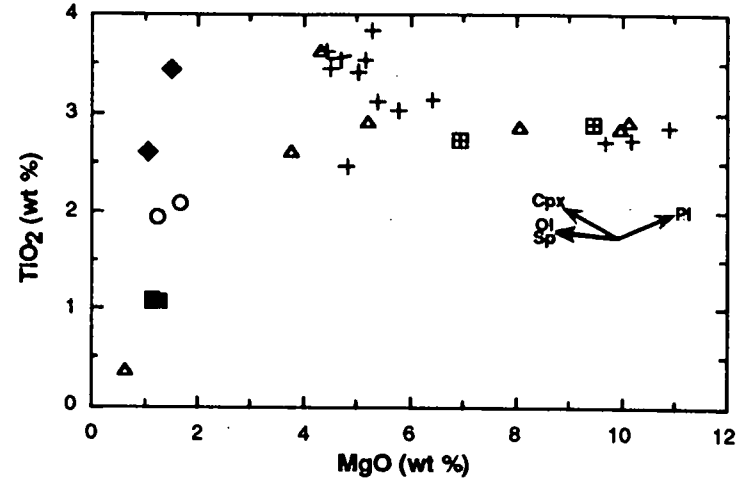
TiO2 (wt %)
MgO (wt %)
Cpx
Ol
Sp
Pl

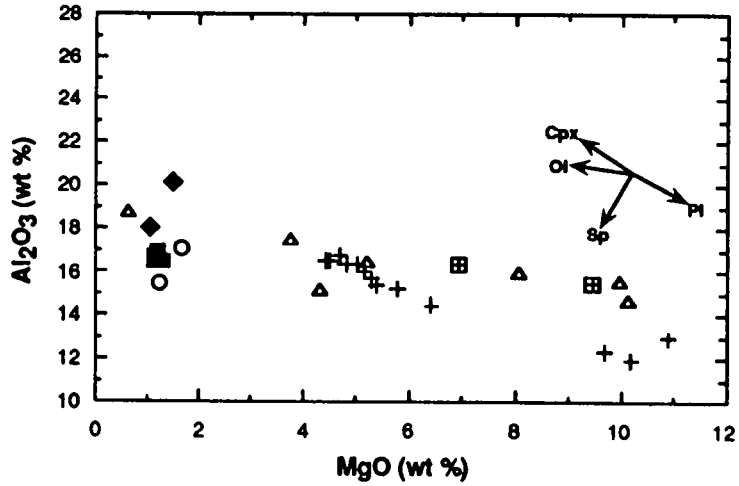
Al2O3 (wt %)
MgO (wt %)
Cpx
Ol
Sp
Pl

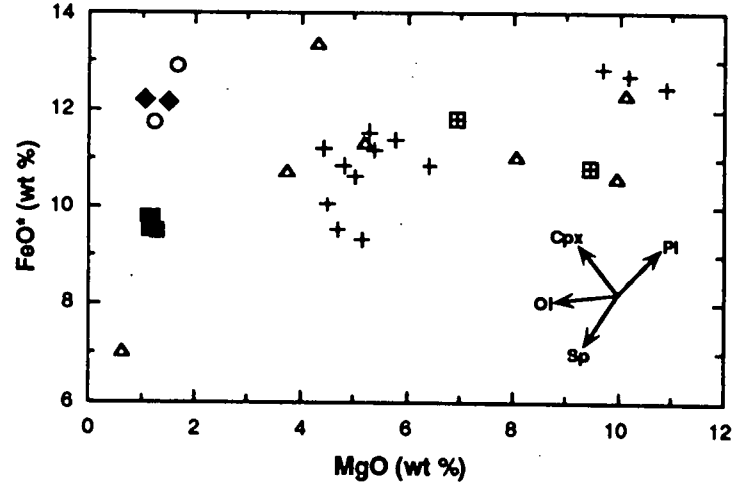
FeO* (wt %)
MgO (wt %)
Cpx
Ol
Sp
Pl

(Figure 3.10)

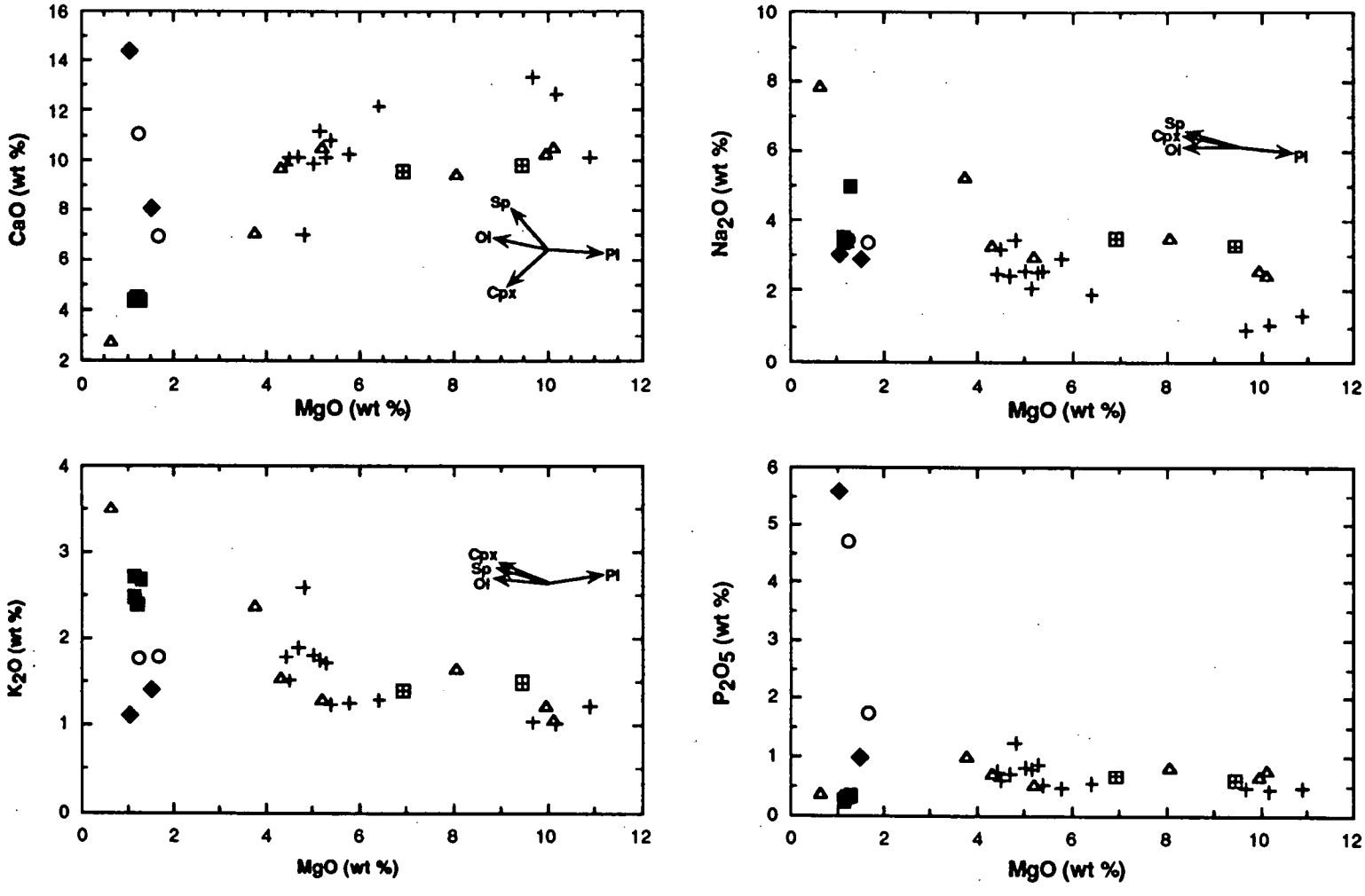
CaO (wt %)
MgO (wt %)
Sp
Ol
Pl
Cpx
Na2O (wt %)
MgO (wt %)
Sp
Cpx
Ol
Pl
K2O (wt %)
MgO (wt %)
Cpx
Sp
Ol
Pl
P2O5 (wt %)
MgO (wt %)

(Figure 3.10)

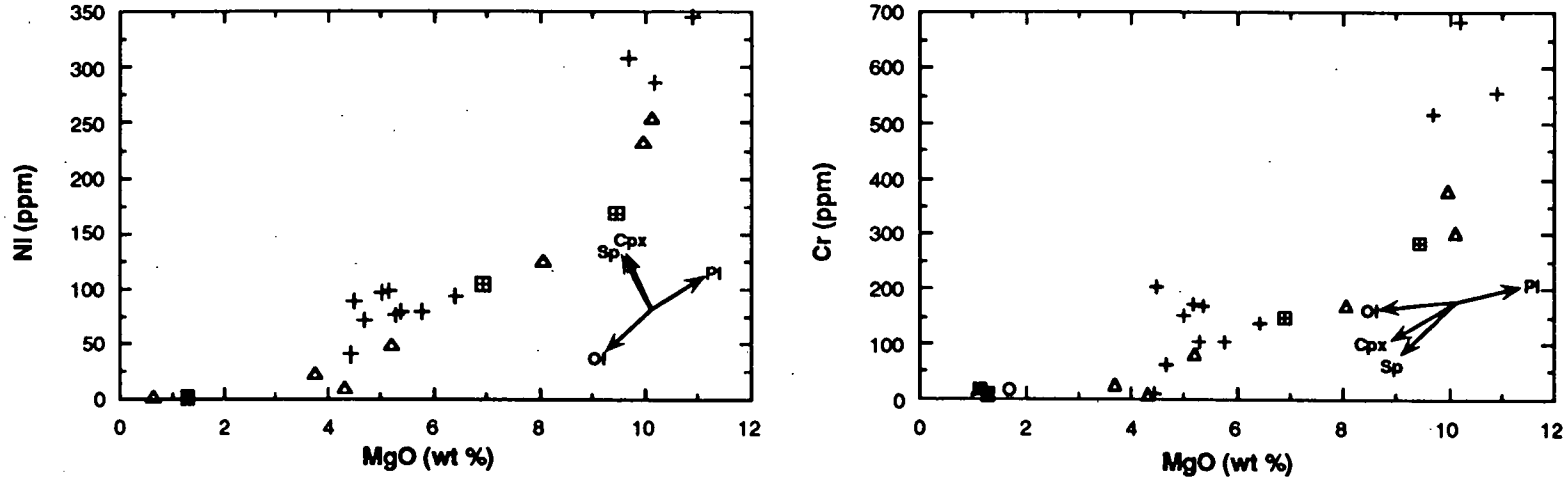

Figure 3.10: MgO (wt %) versus major elements plus Ni and Cr for submarine Balleny Province (dredge 35A - open triangles; dredge 35B - crosses within squares), Soela Seamount (crosses), Janszoon Seamount (filled diamonds), Zeehan Seamount (filled squares) and Heemskirk Seamount (open circles) samples. Relative fractionation vectors were plotted from a point intermediate to the positions of samples 35A-5 and 35A-7 (MgO ~10 wt %) in each diagram, using the following mineral compositions: SS4-1 olivine (Ol) - Table A3.3, analysis 3; SS4-1 clinopyroxene (Cpx) - Table A3.3, analysis 6; SS2-4 plagioclase (Pl) - Table A3.3, analysis 12; 35A-5 spinel (Sp = pleonaste) - Table A3.2, analysis 5.

calculations (Appendix 3) imply that forsteritic cumulate or xenocrystic olivine may have been incorporated into at least some of the Balleny Province samples and may therefore have enhanced whole-rock Mg#. However, Frey et al.'s (1978) definition is based on the assumption that the source is a 'standard' upper mantle peridotite source, which may not be true in the case of OIB source regions, thought to be located within the deep mantle and influenced by crustal recycling and/or metasomatic processes (Chapter 1).

Previous studies of the geochemistry of rocks collected from Sabrina, Borradaile, Sturge and Buckle Islands, together with samples dredged from the Balleny Islands region (Mawson, 1950; Kempe, 1973; Johnson et al., 1982; Campsie et al., 1983; Green, 1992) have revealed a consistently undersaturated alkaline nature. Although somewhat different rock classification schemes were used by these authors, a total alkali versus silica (TAS) plot (Figure 3.11) indicates a similar fractionation sequence for subaerial Balleny samples - alkali basalt, basanite, trachybasalt and phonotephrite - to the submarine Balleny Province samples studied here.

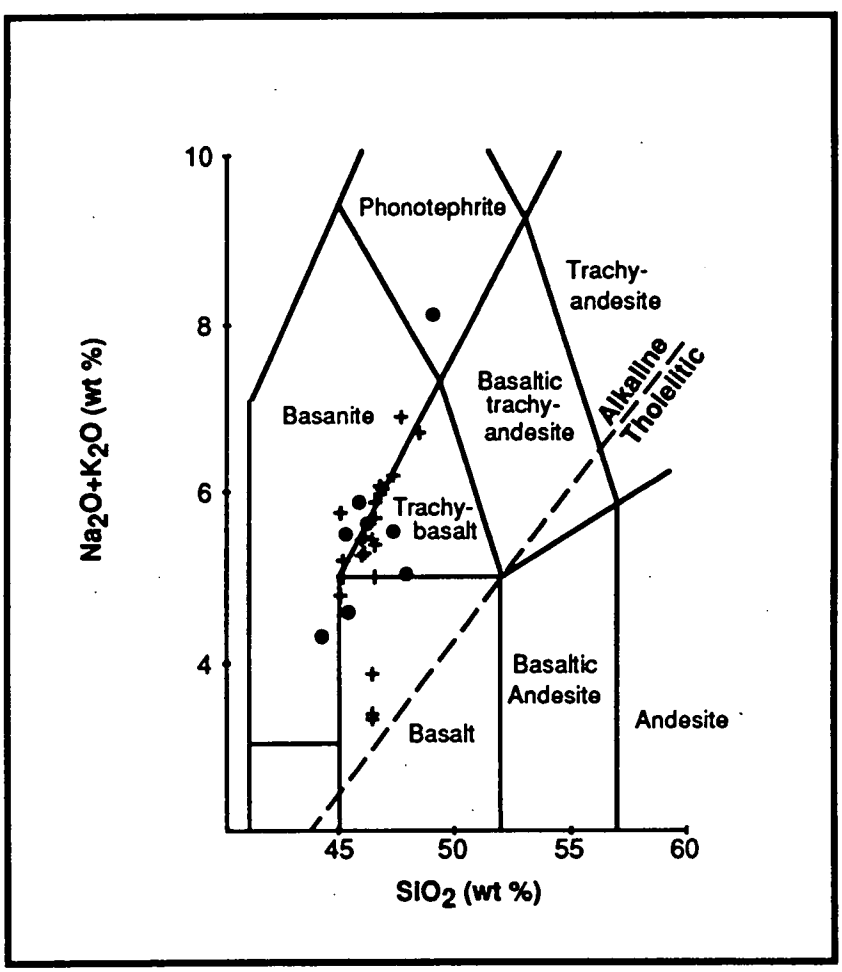

Figure 3.11: TAS diagram of Le Bas et al. (1986) comparing the normalised compositions of the submarine Balleny Province samples examined in this study (circles) with 22 Balleny Islands subaerial samples (crosses). Data sources for the latter are: Mawson (1950), Johnson et al. (1982), Green (1992) and J. Foden (unpublished data). Alkaline and tholeiitic fields are separated by the diagonal (dashed) line of Macdonald and Katsura (1964), as applied to the Hawaiian basalts.

3.5.2 Soela Seamount:

Soela Seamount samples also define an undersaturated (Figure 3.9) fractionation sequence, from alkali basalt through trachybasalt to basaltic trachyandesite (Table 3.5), which parallels the Balleny trend (Figure 3.3). Fractionation is again controlled predominantly by olivine and spinel, resulting in a general decrease in both Ni and Cr with decreasing MgO content (Figure 3.10). The three most primitive Soela samples (alkali basalts SS3, SS4-1 and SS2-4) display a trend of increasing CaO with decreasing MgO, suggesting that they were relatively unaffected by clinopyroxene fractionation. A general decrease in CaO at lower MgO values, however, suggests that the compositions of the more evolved Soela samples were affected by clinopyroxene fractionation. A minor role for plagioclase fractionation is indicated by the general increase in Al_2O_3 and relatively constant Na_2O values which accompany decreasing MgO.

The approximately parallel fractionation trends of the Balleny and Soela samples suggest a similar parental magma composition and evolutionary history. Soela alkali basalt samples SS3, SS4-1 and SS2-4 may represent more primitive melts than any of the Balleny samples, with higher Ni contents and similar MgO contents to the least evolved of the Balleny rocks (samples 35A-7 and 35A-5). All three of these Soela samples have abundant phenocrysts, predominantly olivine and clinopyroxene, which would account for their relatively high MgO, FeO^* and Ni contents. In contrast to the Balleny samples though, these phenocrysts appear to be in equilibrium with their host rock compositions (Appendix 3). Therefore, sample SS3, with 346 ppm Ni and whole-rock $Mg\#_{64.7}$, could represent a primary melt composition from a slightly Fe-enriched source. Inclusions of Cr-rich spinel within olivine phenocrysts/microphenocrysts in these three samples are most likely responsible for their high Cr contents, particularly that of sample SS4-1 with 685 ppm Cr. It must be noted that the spinel fractionation vector of the MgO versus Cr diagram (Figure 3.10) was plotted using a relatively Cr-poor pleonaste composition. A steeper decrease in Cr could therefore be expected from the fractionation of more Cr-rich spinel. The low Na_2O and Al_2O_3 values of these three samples are consistent with their low modal plagioclase contents.

All of the Soela trachybasalts, plus alkali basalt sample SS4-5, have relatively high (>3 wt %) TiO_2 which may be due to greater Ti-substitution within clinopyroxene in these more evolved samples, as well as the possible presence of unobserved ilmenite in the groundmass. Compared to rocks with similar MgO contents, the basaltic trachyandesite (sample SS1-1) has distinctly higher K_2O and lower TiO_2 and CaO values. The latter features may be due to extensive prior clinopyroxene fractionation, or they may indicate that this sample is not simply related to the other Soela samples by crystal fractionation.

Table 3.5: Major and trace element compositions of samples dredged from Soela Seamount.

Sample No:	SS1-1	SS2-4	SS2-6	SS3	SS4-1	SS4-2	SS4-3	SS4-4	SS4-5
Major Elements (wt %):									
SiO_2	47.99	41.87	46.91	45.15	43.24	45.74	46.95	44.12	46.54
TiO_2	2.36	2.50	2.92	2.78	2.56	2.99	3.30	3.58	3.37
Al_2O_3	15.64	11.43	14.70	12.60	11.27	13.79	15.80	14.60	15.26
Fe_2O_3	11.53	13.17	12.19	13.45	13.26	11.48	10.69	11.94	9.85
FeO	0.00	0.00	0.00	0.00	0.00	0.00	0.00	0.00	0.00
MnO	0.15	0.17	0.13	0.18	0.16	0.15	0.11	0.13	0.12
MgO	4.57	8.92	5.56	10.57	9.56	6.08	4.28	4.90	4.88
CaO	6.70	12.30	9.87	9.87	11.90	11.62	9.65	9.41	10.61
Na_2O	3.96	1.71	3.55	2.17	1.89	2.61	3.74	3.08	2.77
K_2O	2.48	0.96	1.21	1.19	0.97	1.23	1.45	1.60	1.67
P_2O_5	1.20	0.43	0.47	0.47	0.41	0.52	0.59	0.81	0.75
LOI	3.27	7.03	2.59	1.19	4.63	2.91	3.20	5.47	3.90
Total	99.85	100.49	100.10	99.62	99.85	99.12	99.76	99.64	99.72
Mg#	48.08	61.28	51.59	64.74	62.75	55.31	48.34	48.95	53.65
FeO*	10.38	11.85	10.97	12.10	11.93	10.33	9.62	10.74	8.86
Trace Elements (ppm):									
Ba		287	305	394	285	323	374	520	508
Rb	63	18	37	30	19	28	28	23	40
Nb	137	40	48	57	44	51	62	85	79
Sr	1014	451	498	532	469	548	641	793	824
Zr	554	185	225	242	192	233	279	331	325
Y	37	23	30	24	23	30	24	32	29
Ni		309	81	346	288	95	90	78	99
Cr		516	102	556	685	138	206	104	173
V		277	273	248	260	309	266	298	248
Sc		29	26	30	33	27	23	15	20
Cs		1.04	2.68	0.86	<0.5	1.28	<0.5		1.09
Hf		3.84	4.89	5.14	4.17	5.28	5.80		6.62
Ta		2.71	2.82	3.38	2.87	2.99	3.44		4.82
Th		2.90	3.66	5.01	3.26	3.95	4.54		5.33

Table 3.5: (continued)

Sample No:	SS4-6	SS4-7	SS4-8	SS5
Major Elements (wt %):				
SiO_2	47.29	46.56	46.77	46.59
TiO_2	3.42	3.50	2.99	3.29
Al_2O_3	16.08	15.93	14.79	15.74
Fe_2O_3	10.20	12.00	11.91	11.36
FeO	0.00	0.00	0.00	0.00
MnO	0.12	0.13	0.13	0.13
MgO	4.48	4.25	5.14	4.80
CaO	9.76	9.44	10.36	9.52
Na_2O	3.12	3.17	3.22	3.21
K_2O	1.82	1.72	1.19	1.74
P_2O_5	0.70	0.73	0.52	0.80
LOI	2.81	2.60	2.66	2.88
Total	99.80	100.03	99.68	100.06
Mg#	50.65	45.28	50.21	49.68
FeO^*	9.18	10.80	10.72	10.22
Trace Elements (ppm):				
Ba	485	485	318	487
Rb	47	50	28	51
Nb	84	76	48	82
Sr	832	768	527	798
Zr	334	319	228	341
Y	28	33	29	30
Ni	73	41	80	98
Cr	60	10	168	152
V	256	284	299	267
Sc	18	15	28	20
Cs	2.05	1.18	0.98	1.62
Hf	6.77	6.33	4.91	6.68
Ta	5.29	4.82	2.80	4.47
Th	5.67	6.10	3.85	6.34

Table 3.6: Major and trace element geochemistry of samples dredged from the Janszoon (C1/84(2) 2DB), Zeehan (C17/86 8DB) and Heemskirk (C17/86 7DB) seamounts.

Sample No:	C1/84(2) 2DB 10	C1/84(2) 2DB 14	C17/86 8DB 2/1	C17/86 8DB 2/2	C17/86 8DB 2/5	C17/86 8DB 3/4	C17/86 7DB 1/10	C17/86 7DB 1/13
Major Elements (wt %):								
	(Ir strip)	(Ir strip)	(Ir strip)	(XRF)	(Ir strip)	(Ir strip)	(Ir strip)	(Ir strip)
SiO_2	47.98	40.31	59.22	56.81	59.56	59.62	47.20	50.69
TiO_2	3.40	2.55	1.08	1.05	1.05	1.10	1.91	2.06
Al_2O_3	19.81	17.64	16.86	16.04	16.60	16.51	15.27	16.82
Fe_2O_3	0.00	0.00	0.00	10.27	0.00	0.00	0.00	0.00
FeO	11.98	11.98	9.75	0.00	9.79	9.54	11.59	12.70
MnO	0.07	0.07	0.19	0.22	0.19	0.20	0.09	0.11
MgO	1.50	1.06	1.19	1.24	1.13	1.13	1.22	1.65
CaO	7.91	14.05	4.54	4.30	4.38	4.41	10.88	6.84
Na_2O	3.57	3.69	4.08	5.37	4.06	4.17	4.07	4.00
K_2O	1.38	1.09	2.38	2.61	2.47	2.71	1.75	1.75
P_2O_5	0.98	5.48	0.31	0.33	0.23	0.26	4.63	1.72
LOI				1.79				
Total	98.58	97.92	99.60	100.03	99.46	99.65	98.61	98.34
Mg#	20.85	15.69	20.43	22.01	19.54	19.95	18.13	21.47
FeO*	11.98	11.98	9.75	9.24	9.79	9.54	11.59	12.70
Trace Elements (ppm):								
Ba				462				
Pb				44.5				
Nb				76.1				
Sr				280				
Zr				602				
Y				77.2				
Ni				2.5				
Cr				3				
V				2				
Sc				13				
Cs								
Hf	7.46			12.40		12.10		7.83
Ta	5.43			4.85		4.60		3.76
Th (XRF)	6.68			7.60		6.77		4.43
Th (INAA)				6.37				
Pb				4.00				

3.5.3 South Tasman Sea Seamounts:

All of the samples dredged from the south Tasman Sea seamounts are very fractionated, with whole-rock Mg# ≤22 (Table 3.6; Figure 3.3). Due to the limited number and evolved nature of the samples available for analysis, very little can be said about the fractionation and/or crystallisation processes responsible for their major element compositions.

SiO_2-undersaturated (Figure 3.9) samples from Janszoon Seamount comprise a basanite and a trachybasalt (Figure 3.3). Basanite sample 2DB 14 has extremely high CaO and P_2O_5 contents (Table 3.6; Figure 3.10) which are alteration-related. Otherwise, the main chemical features which distinguish the two samples are the higher SiO_2, Al_2O_3 and TiO_2 contents of the trachybasalt (2DB 10). The four Zeehan Seamount samples are compositionally very similar hypersthene-normative, SiO_2-oversaturated (Figure 3.9) trachyandesites (Figure 3.3), probably derived from the same volcanic sequence. Heemskirk Seamount trachybasalts (Figure 3.3) have similar chemistry apart from the alteration-related higher CaO and P_2O_5 contents of sample 7DB 1/10 (Table 3.6; Figure 3.10).

Alteration effects, particularly visible in the major element compositions of Janszoon sample 2DB 14 and Heemskirk sample 7DB 1/10 may be responsible for the anomalous data spread of these samples in Figure 3.9.

It is notable that, whereas the Heemskirk and Janszoon Seamount samples have alkaline affinities, Zeehan Seamount samples are hypersthene-normative trachyandesites. The latter may therefore represent the differentiated products of the shield-building tholeiitic phase of hotspot volcanism rather than the pre- or post-shield alkaline phase/s represented by the Heemskirk, Janszoon, Soela and Balleny samples.

3.6 TRACE ELEMENT GEOCHEMISTRY:

Most of the Balleny Province and Soela Seamount trace element abundances were measured by XRF spectrometry (Philips PW 1410 spectrometer); Cs, Hf, Ta and Th abundances were measured by instrumental neutron activation analysis (INAA); south Tasman Sea seamount trace elements were mostly analysed by inductively coupled plasma-mass spectrometry (ICP-MS), due to limited sample size, and INAA (Hf, Ta and Th) although sample C17/86 8DB 2/2 was also analysed by XRF spectrometry (Philips PW 1480 spectrometer). Balleny Province REE concentrations were analysed by ion exchange - XRF spectrometry (Philips PW 1410 spectrometer); Soela Seamount REE concentrations were measured by INAA; and south Tasman Sea seamount REE abundances were measured by INAA and/or ICP-MS. The analytical procedures are discussed in Appendix 2; ICP-MS data are presented in Appendix 5. A comparison of ICP-MS, XRF and INAA REE and trace element data is also presented in Appendix 5.

3.6.1 Balleny Province:

The trace and REE contents of Balleny Province samples are presented in Tables 3.4 and 3.7 respectively.

Submarine Balleny Province samples have similar primitive mantle-normalised incompatible element patterns (Figure 3.12), with the general enrichment in incompatible elements characteristic of OIB (e.g. Sun, 1980; Wood et al., 1981; Sun and McDonough, 1989). Absolute normalised abundances show an overall increase with increasing fractionation, from the lowest abundances in alkali basalt sample 35A-5 to the highest in trachyte sample 35A-2. The predominant features, displayed by all samples regardless of their degree of fractionation, include an overall increase in elemental abundance with increasing incompatibility, a negative K anomaly, greater abundances of the HFSE Nb and Ta relative to the adjacent LILE, a general decrease in the abundance of elements more incompatible than Ta, and a slight Y depletion relative to the heavy REE (HREE). General depletion in the LILE relative to Nb and Ta and the LREE is therefore indicated.

The most primitive samples, 35A-5, 35B-2 and 35A-4 display very similar incompatible element patterns. However, some visible differences may be the product of different extents of crystal fractionation and/or partial melting rather than a reflection of source chemistry. Basanite sample 35B-2 is slightly depleted in P, whereas trachybasalt sample 35A-4 is slightly depleted in both Sr and P with respect to the adjacent REE. The two most evolved samples (35A-1 and 35A-2) display further anomalies. Phonotephrite sample 35A-1 and trachyte sample 35A-2 have negative Ti, P and Sr anomalies with respect to the middle rare earth elements (MREE) and LREE respectively, and relative enrichment in Zr and Hf. Negative Ti and P anomalies may be produced by the fractionation of phases such as titanomagnetite and apatite. Due to their large ionic radii and ionic potential, elements such as Cs, Ba and Rb would be expected to be relatively soluble in aqueous fluids (e.g. Weaver, 1991) and to behave in a mobile fashion during seafloor alteration. This may therefore be responsible for the greatest relative depletion of Ba, in samples 35A-1 and 35A-2, the slight relative Cs enrichment of sample 35A-1 and the relative Rb enrichment of sample 35A-2 compared to the other LILE.

Chondrite-normalised REE patterns for the same five Balleny Province samples (Figure 3.13) are also generally similar. They display LREE enrichment and relative HREE depletion, consistent with small degrees of melting of a source containing residual garnet (e.g. Kay and Gast, 1973; Frey et al., 1978). Overall REE abundances increase with increasing degrees of fractionation, particularly as regards the LREE. A slightly positive Eu anomaly is displayed by all but sample 35A-2 (Figure 3.13). This may be a function of its variable and relatively low precision compared to the other MREE when measured by the ion exchange - XRF method (Robinson et al., 1986). Trachybasalt sample 35A-4 is slightly enriched in HREE compared to the other Balleny Province samples, and the most evolved sample (35A-2) shows a strong increase in $(La/Sm)_n$ and a pronounced flattening of the REE less incompatible than Sm relative to the less fractionated samples. This distinctive REE

Table 3.7: REE contents of submarine Balleny Province samples.

Sample No:	E27-35A-1	E27-35A-2	E27-35A-4	E27-35A-5	E27-35B-2
La	72.70	138.00	44.30	38.00	42.10
Ce	146.00	267.00	98.60	78.60	90.00
Pr	16.70	28.10	11.60	9.19	10.60
Nd	62.80	82.70	47.40	37.60	42.20
Sm	11.30	10.60	9.74	7.68	9.53
Eu	4.03	2.10	3.37	2.83	3.45
Gd	9.73	6.50	9.77	7.21	8.52
Dy	7.62	8.37	7.93	5.65	6.43
Er	3.97	5.38	4.56	2.81	3.42
Yb	3.61	5.12	3.35	2.21	2.63

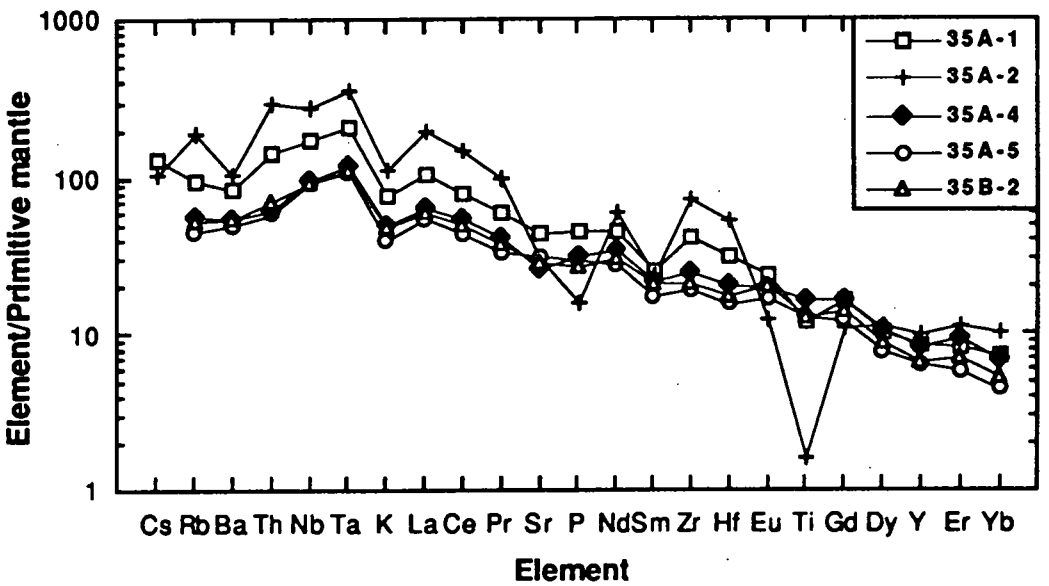

Figure 3.12: Primitive mantle-normalised incompatible element patterns of five Balleny Province samples; data from Tables 3.4 and 3.7; normalising values from Sun and McDonough (1989).

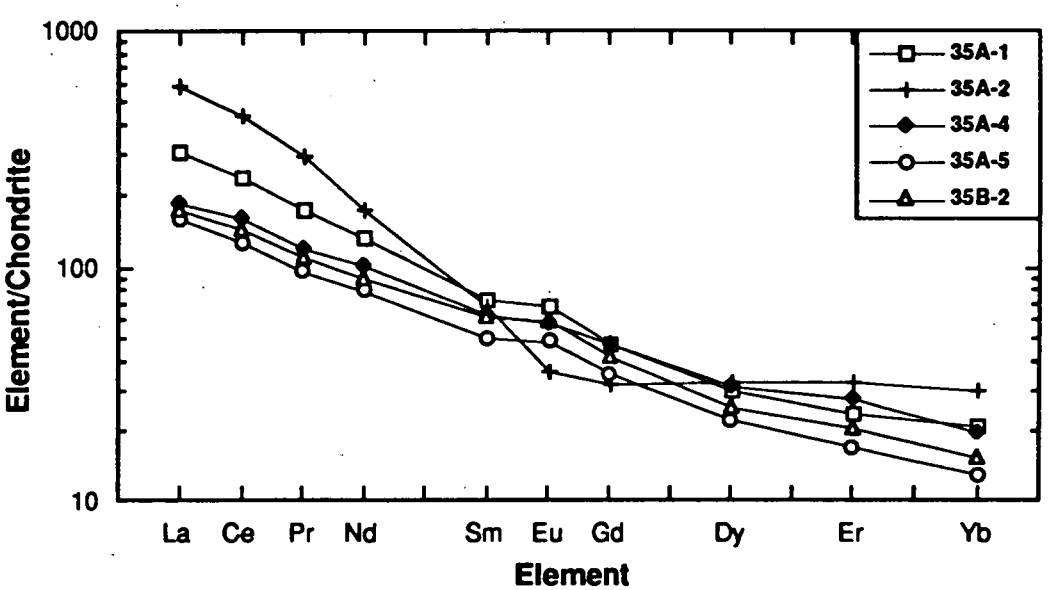

Figure 3.13: Chondrite-normalised REE patterns of five Balleny Province samples; data from Table 3.7; C1 chondrite normalising values from Sun and McDonough (1989).

Table 3.8: Trace element abundance ratios for submarine and subaerial Balleny Province samples, Soela Seamount samples and south Tasman Sea seamount samples presented as ranges underlain by the mean value ± 1σ error (numbers in bold type are the most well constrained: σ/mean ≤~10 %); numbers in parentheses indicate the number of analyses used (n) to calculate both the ratio ranges and the mean values. Data sources for subaerial Balleny Island samples are Green (1992) and J. Foden (unpublished data). Trace element ratio ranges for the HIMU, EMI and EMII mantle end-members are derived from data used to compile Table 2.1; Average N-MORB and OIB ratios were calculated using element concentration data from Table 1 of Sun and McDonough (1989). All south Tasman Sea seamount ratios and Balleny and Soela ratios involving U or Pb were calculated using the ICP-MS data in Appendix 5 for both the numerator and denominator elements; all other ratios were calculated from the XRF and/or INAA data presented in Chapter 3 data tables.

	Rb/Nb	Ba/Rb	Ba/Th	Ba/Nb	Ba/La	Th/U	Th/Nb	Th/La
Average N-MORB	0.24	11.25	53	2.70	2.52	2.55	0.05	0.05
Average OIB	0.65	11.29	88	7.29	9.46	3.92	0.08	0.11
HIMU	0.01-0.48 (62) 0.32±0.10	1.67-67.00 (61) 17.0±9.0	20-151 (41) 68±21	1.74-10.24 (61) 5.31±1.20	2.37-15.36 (56) 7.53±1.74	2.58-9.59 (24) 4.23±1.55	0.01-0.12 (42) 0.08±0.02	0.07-0.17 (41) 0.11±0.02
EMI	0.14-1.61 (105) 0.60±0.25	6.67-100.59 (105) 24.18±17.82	65-475 (58) 203±78	5.35-23.33 (114) 11.27±3.01	2.92-19.11 (68) 9.13±2.99	0.33-9.57 (8) 4.21±3.14	0.02-0.12 (54) 0.06±0.02	0.02-0.14 (58) 0.05±0.03
EMII	0.31-1.64 (48) 0.93±0.24	7.76-30.75 (49) 12.85±4.88	57-119 (18) 76±16	6.42-15.57 (48) 11.12±1.97	7.33-19.62 (39) 11.93±2.8	3.94-5.13 (4) 4.42±0.68	0.07-0.17 (18) 0.13±0.02	0.08-0.18 (18) 0.14±0.03
Submarine Balleny Province	0.32-0.50 (6) 0.44±0.07	11.47-16.53 (6) 12.87±1.92	64-92 (6) 72±11	5.20-6.58 (6) **5.60±0.52**	9.26-9.34 (2)	3.62-4.74 (4) 3.93±0.54	0.07-0.09 (6) **0.08±0.008**	0.13-0.15 (2)
Subaerial Balleny Province	0.38-0.98 (18) 0.52±0.13			5.00-6.40 (10) **5.77±0.50**			0.09-0.15 (8) 0.12±0.02	
Soela Seamount	0.27-0.77 (9) 0.52±0.14	8.24-22.61 (9) 13.34±4.23	77-99 (8) **86±8**	5.94-7.18 (9) **6.49±0.38**	10.50-12.59 (6) **11.38±0.71**	3.16-4.10 (3) 3.70±0.49	0.07-0.09 (8) **0.08±0.007**	0.13-0.15 (6) **0.14±0.008**
Tasman Sea Seamounts	0.11-0.55 (8) 0.42±0.15	9.85-43.04 (8) 16.08±11.25	57-74 (8) **65±6**	4.47-7.38 (8) 5.32±0.90	3.17-7.90 (8) 6.33±1.95	2.56-3.99 (8) 3.45±0.47	0.07-0.10 (8) **0.08±0.009**	0.04-0.13 (8) 0.10±0.04

Table 3.8: (continued)

	Nb/U	Nb/Pb	K/Nb	La/Nb	Ce/Rb	Ce/Pb	Zr/Nb
Average N-MORB	50	7.8	258	1.07	13.39	25	31.76
Average OIB	47	15	250	0.77	2.58	25	5.83
HIMU	33-143 (22) 56±25	10.4-40.2 (11) 23.6±8.3	13-292 (62) 120±52	0.07-0.85 (57) 0.70±0.14	0.50-12.10 (58) 4.69±1.83	17.3-54.2 (11) 34.38±10.51	0.36-5.49 (62) 3.85±1.05
EMI	44-80 (5) 56±15	11.4-12.2 (5) **11.77±0.35**	77-709 (114) 332±132	0.78-2.00 (64) 1.21±0.21	1.69-20.4 (60) 5.83±3.86	19.4-21.0 (5) **20.39±0.65**	5.80-18.57 (114) 13.03±4.32
EMII	26-48 (8) 36±7	4.5-13.3 (19) 8.57±2.37	125-684 (49) 359±91	0.72-1.19 (39) **0.94±0.10**	1.39-7.25 (43) 2.27±1.19	10.7-31.8 (15) 18.48±6.11	4.63-8.68 (48) 7.11±0.91
Submarine Balleny Province	39-82 (4) 60±18	27.5-37.5 (4) 32.47±4.33	148-196 (6) 163±19	0.57-0.62 (2)	2.65-2.71 (2)	32.4-41.9 (4) 36.86±5.0	3.19-4.04 (6) **3.47±0.30**
Subaerial Balleny Province			111-194 (18) 167±21				3.11-4.33 (18) **3.64±0.31**
Soela Seamount	43-54 (3) 50±6	16.8-28.3 (3) 23.8±6.1	156-209 (9) **187±18**	0.56-0.59 (6) **0.58±0.01**	1.62-2.89 (6) 2.33±0.49	22.0-34.8 (3) 30.27±7.17	3.89-4.75 (9) **4.38±0.30**
Tasman Sea Seamounts	25-55 (8) 43±9	2.8-23.5 (8) 13.87±7.28	92-306 (8) 209±72	0.63-2.33 (8) 0.98±0.59	2.66-12.01 (8) 4.37±3.16	5.1-31.8 (8) 19.22±9.89	3.63-7.20 (8) 5.90±1.45

pattern may be due to the late-stage fractionation of amphibole, which has relatively high distribution coefficients for the MREE (e.g. Sm and Eu) (e.g. Cox et al., 1979). The positive Rb anomaly of sample 35A-2, combined with a similar negative K anomaly to the other Balleny Province samples, is consistent with the increase in Rb/K that would be expected with the removal of K during amphibole fractionation.

The trace element abundance ratios of the submarine Balleny Province samples are very similar to those of subaerial samples collected from the Balleny Islands (Table 3.8). However, due to the paucity of Balleny Islands trace element data, only a few ratios are available for comparison. Submarine Balleny Province volcanics, with ≥5 wt % MgO, are characterised by low mean Rb/Nb, Ba/Nb, K/Nb, La/Nb and Zr/Nb relative to the average OIB trace element values of Sun and McDonough (1989). Low Zr/Nb in subaerial Balleny samples has been interpreted to reflect either source geochemistry or a plume-specific metasomatic process (Green, 1992). The other trace element ratio distinctions indicate that the Balleny Province volcanics differ from average OIB in terms of their low LILE/Nb and LREE/Nb values. This is consistent with the general elemental depletions visible in Figure 3.12. Submarine Balleny Province volcanics also have high mean Ce/Pb and Nb/Pb values relative to both average N-MORB and OIB, but similar mean Ce/Rb (Table 3.8). Therefore, although high Nb/Pb could be interpreted as a product of relative HFSE enrichment, the high Ce/Pb content suggests that Pb depletion is responsible instead.

3.6.2 Soela Seamount:

The trace and REE compositions of Soela Seamount samples are presented in Tables 3.5 and 3.9 respectively.

Primitive mantle-normalised incompatible element patterns for Soela Seamount samples (Figure 3.14) are all very similar, displaying typical OIB incompatible element enrichment. Absolute elemental abundances are not strictly related to the degree of fractionation, however, as sample SS3, the least evolved of the Soela samples, does not have the lowest normalised element abundances, and the two trachybasalts, SS2-4 and SS5, have higher absolute element abundances than all of the less fractionated alkali basalts. The general pattern, similar to that of the Balleny Province samples, includes K depletion relative to the adjacent LREE and HFSE, greater abundances of Nb and Ta relative to the adjacent LILE, and a general decrease in the abundances of LILE more incompatible than Nb. The marked Cs enrichment of all Soela Seamount samples also occurs, although to a lesser degree, in Balleny sample 35A-1 (Figure 3.12). Due to the extreme mobility of Cs and the fact that that most samples display evidence of seafloor alteration, these Cs values should be treated with caution. Other general Soela Seamount incompatible element features, which are also evident in at least some Balleny Province samples, include slight relative depletions in Y, Sr and P and slight enrichments in Zr, Hf and Ti.

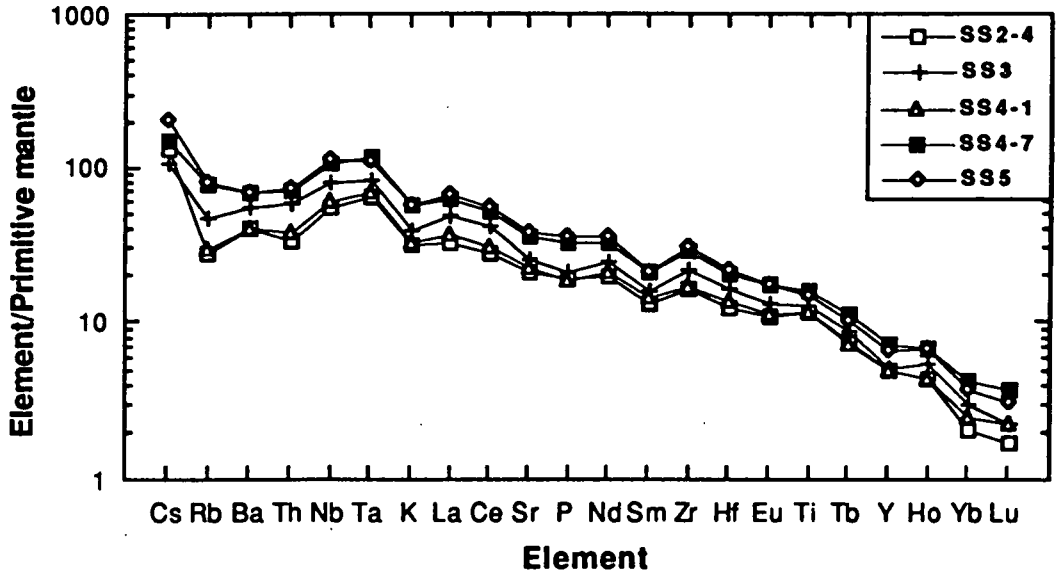

Figure 3.14: Primitive mantle-normalised incompatible element patterns of five Soela Seamount samples; data from Tables 3.5 and 3.9; normalising values from Sun and McDonough (1989).

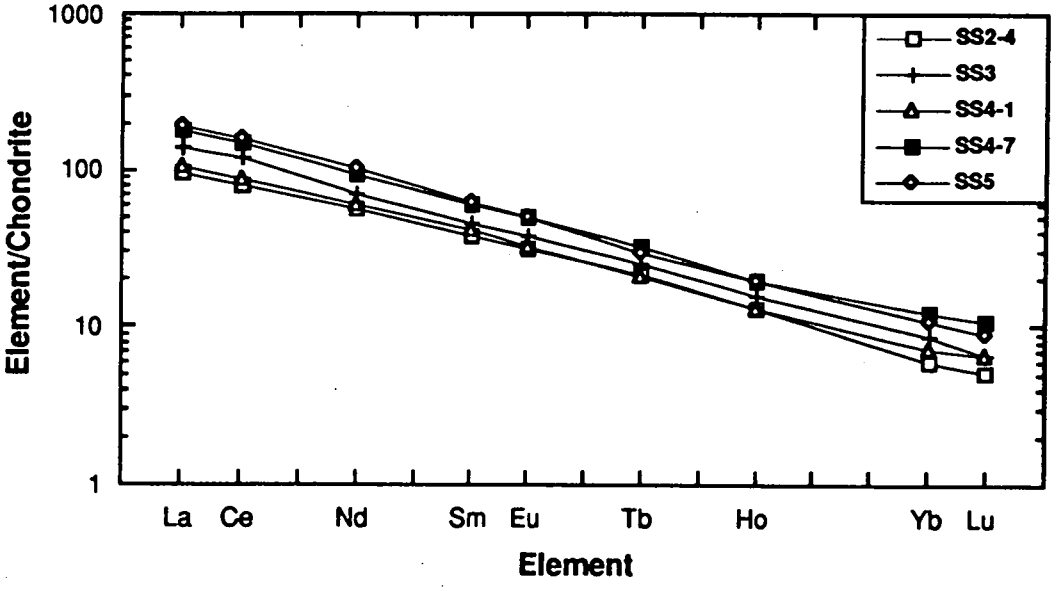

Figure 3.15: Chondrite-normalised REE patterns of five Soela Seamount samples; data from Table 3.9; C1 chondrite normalising values from Sun and McDonough (1989).

Chondrite-normalised REE patterns for the same five Soela Seamount samples (Figure 3.15) are similarly enriched in LREE and depleted in the HREE. The absence of a positive Eu anomaly, as observed in all of the Balleny Province samples, supports the contention that this apparent Eu enrichment in the latter is a function of the ion exchange-

Table 3.9: REE compositions of samples dredged from Soela Seamount.

Sample No:	SS2-4	SS2-6	SS3	SS4-1	SS4-2	SS4-3	SS4-6	SS4-7	SS5
La	22.80	26.80	33.80	25.50	29.40	28.80	41.00	43.90	46.40
Ce	50.10	60.10	74.50	54.90	64.10	63.30	86.80	93.20	98.90
Nd	27.10	32.70	33.70	28.80	33.70	31.60	45.40	44.40	48.00
Sm	5.83	7.25	7.15	6.41	7.82	7.00	8.63	9.34	9.52
Eu	1.85	2.24	2.21	1.88	2.35	2.33	2.76	2.92	2.93
Tb	0.82	0.90	0.96	0.79	1.01	0.96	0.96	1.24	1.12
Ho	0.74	0.93	0.91	0.74	0.92	0.96	1.05	1.11	1.11
Yb	1.03	1.73	1.49	1.25	1.60	1.67	1.73	2.13	1.85
Lu	0.13	0.23	0.17	0.17	0.21	0.21	0.22	0.28	0.23

XRF analytical method (Section 3.6.1), the Soela Seamount REE values having been measured by INAA.

Trace element abundance ratios for Soela Seamount samples, with ≥5 wt % MgO, are listed in Table 3.8. The Soela samples define relatively narrow trace element ratio ranges which are remarkably similar to those measured for the Balleny Province samples. Their Rb/Nb, Ba/Nb, K/Nb and Zr/Nb ranges extend to higher values than Balleny samples, although mean Soela values are within error of the latter and still lower than those of average OIB. Soela Seamount samples may therefore be slightly less depleted in LILE relative to HFSE than the Balleny Province rocks. Mean Soela Ba/La and Ba/Th values are also slightly higher than Balleny values, although Th/Nb and Th/La are virtually identical. This implies a greater degree of Ba depletion relative to the LREE and other LILE in the Balleny source, which is also suggested by the Ba low in the Balleny incompatible element plots of Figure 3.12. However, this may simply be an effect of seafloor alteration. Soela Seamount samples also have mean Ce/Pb and Nb/Pb values slightly higher than average N-MORB and OIB (Table 3.8) but slightly less than Balleny Province volcanics.

3.6.3 South Tasman Sea Seamounts:

The trace element and REE compositions of the south Tasman Sea seamount samples are presented in Tables 3.6, 3.10 and A5.1.

As none of the analysed Tasman Sea seamount samples have ≥5 wt % MgO, it is not possible to filter out the effects of low pressure fractionation by excluding evolved samples, and still make general observations about the trace element characteristics of the source/s of the various seamounts. Therefore, the trace element contents of all Tasman Sea seamount samples will be examined here.

The primitive mantle-normalised incompatible element patterns of four Tasman Sea seamount samples (Figure 3.16) do display similar features to both Balleny Province and Soela Seamount volcanics, including decreasing abundances of elements more incompatible than Nb, K depletion, and high Nb and Ta abundances relative to the adjacent LILE. However, there are some differences which appear to be related to low pressure fractionation and/or seafloor alteration.

Janszoon Seamount sample 2DB 10 has the steepest incompatible element pattern, characterised by the lowest HREE abundances, slight Y depletions, and positive Zr , Hf and Sr anomalies. Apart from the marked Sr enrichment, all of these other features can also be observed in both Balleny Province and Soela Seamount samples, suggesting that they may be related to source chemistry.

Zeehan Seamount samples 8DB 2/2 and 8DB 3/4 have virtually identical incompatible element patterns. Slight depletions in Y and Sr, and enrichments in Zr and Hf are all consistent with observed characteristics of Balleny and Soela rocks. The large Ti and P depletions probably result from the fractionation of titanomagnetite and apatite respectively.

Table 3.10: REE (INAA) geochemistry of samples dredged from the Janszoon (C1/84(2) 2DB), Zeehan (C17/86 8DB) and Heemskirk (C17/86 7DB) seamounts.

Sample No:	C1/84(2) 2DB 10	C17/86 8DB 2/2	C17/86 8DB 3/4	C17/86 7DB 1/13
La	52.80	51.40	51.60	87.60
Ce	108.00	114.00	112.00	88.80
Nd	54.10	61.10	54.30	114.00
Sm	10.30	13.40	13.40	23.40
Eu	3.27	3.99	3.91	7.32
Tb	1.36	2.10	2.18	3.87
Ho	1.57	2.94	2.62	4.92
Yb	2.74	6.50	6.43	14.10
Lu	0.39	0.99	0.93	2.24

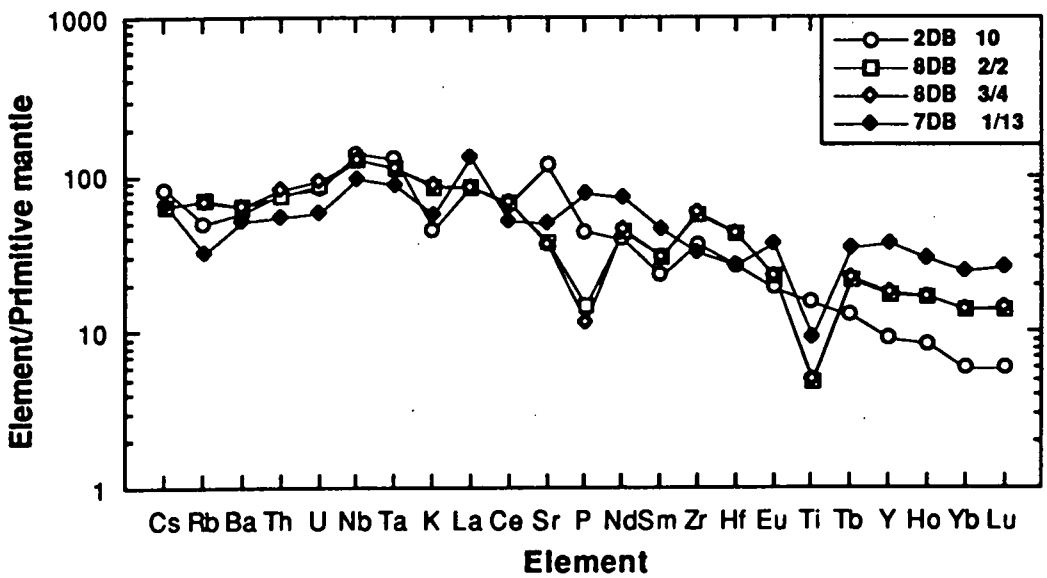

Figure 3.16: Primitive mantle-normalised incompatible element patterns of south Tasman Sea seamount samples using ICP-MS data from Table A5.1; normalising values from Sun and McDonough (1989).

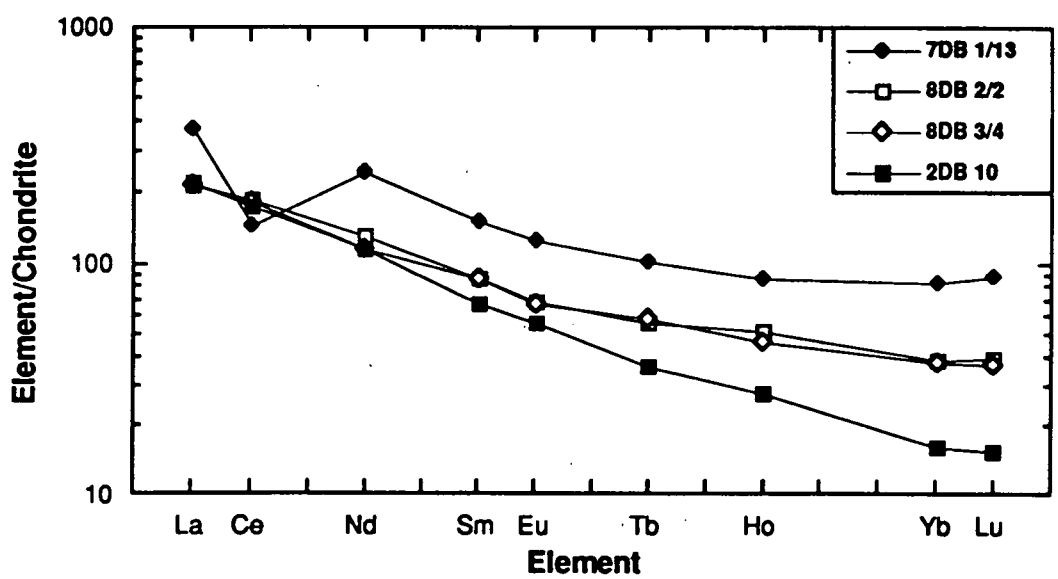

Figure 3.17: Chondrite-normalised REE patterns of south Tasman Sea seamount samples; data from Table 3.10; C1 chondrite normalising values from Sun and McDonough (1989).

Heemskirk Seamount sample 7DB 1/13 has a flatter incompatible element pattern than the other Tasman Sea samples, with relative depletions in Ti, Zr, Hf, Sm, Ce and Sr and a marked positive La anomaly relative to the other LREE, Ta and Nb. Although it has a similar pattern to the Balleny Province, Soela Seamount and other Tasman Sea seamount samples in terms of the most incompatible elements, sample 7DB 1/13 is very different in terms of most other normalised elements.

The chondrite-normalised REE patterns of four south Tasman Sea seamount samples are shown in Figure 3.17. All samples display relative enrichment in LREE, variable degrees of MREE and HREE depletion, a decrease in the gradient of the pattern at the HREE end, and a slight depletion in Eu. Zeehan (dredge 8DB) and Janszoon (dredge 2DB) samples have very similar LREE abundances. Whereas the two Zeehan samples also have very similar MREE and HREE abundances, however, the slightly less evolved Janszoon sample has lower abundances of both. The Heemskirk Seamount trachybasalt sample (dredge 7DB) has a slightly higher MgO content than the other samples, but the highest REE abundances. It is also distinguished by a marked negative Ce anomaly, which is almost certainly alteration-related.

Despite the evolved and often altered nature of the Tasman Sea seamount samples, they have still retained some distinct trace element abundance ratios that are similar to both the Balleny Province and Soela Seamount volcanics (Table 3.8; Figure 3.18). Most samples have low LILE/HFSE and LILE/LREE values, evident as low Rb/Nb, K/Nb and La/Nb. The La enrichment of Heemskirk sample 7DB 1/13 (Figure 3.16) is evident in its low Th/La and Ba/La values and its high La/Nb. Zeehan trachyandesite samples 8DB 2/2 and 8DB 3/4 have high Zr/Nb relative to the other samples analysed during this study. As the latter all have alkaline affinities, it seems likely that the higher Zr/Nb values of the tholeiitic Zeehan samples are a product of higher degrees of partial melting. The slightly higher K/Nb and lower Ce/Pb and Nb/Pb values of the Tasman Sea seamount volcanics, relative to Balleny Province and Soela Seamount basalts, may also be the products of seafloor processes involving the addition of K and Pb.

3.6.4 Trace Element Comparison with the Mantle End-member Components:

The characteristic incompatible element pattern displayed by the Balleny Province, Soela Seamount and south Tasman Sea seamount samples (Figures 3.12, 3.14 and 3.16) is broadly similar to that of the HIMU basalts (Mangaia, Rurutu, Tubuai and St. Helena) discussed in Chapter 2. The main similarities include an apparent enrichment in the HFSE (Nb and Ta) relative to the adjacent LILE, a negative K anomaly and a general depletion in the normalised abundances of elements more incompatible than Ta. Although Balleny Plume basalts lack the positive Pb anomalies evident in the Pitcairn Island/Seamount EMI basalts and some EMII basalts (Figures 2.6 and 2.7 respectively), Pitcairn samples do display similar

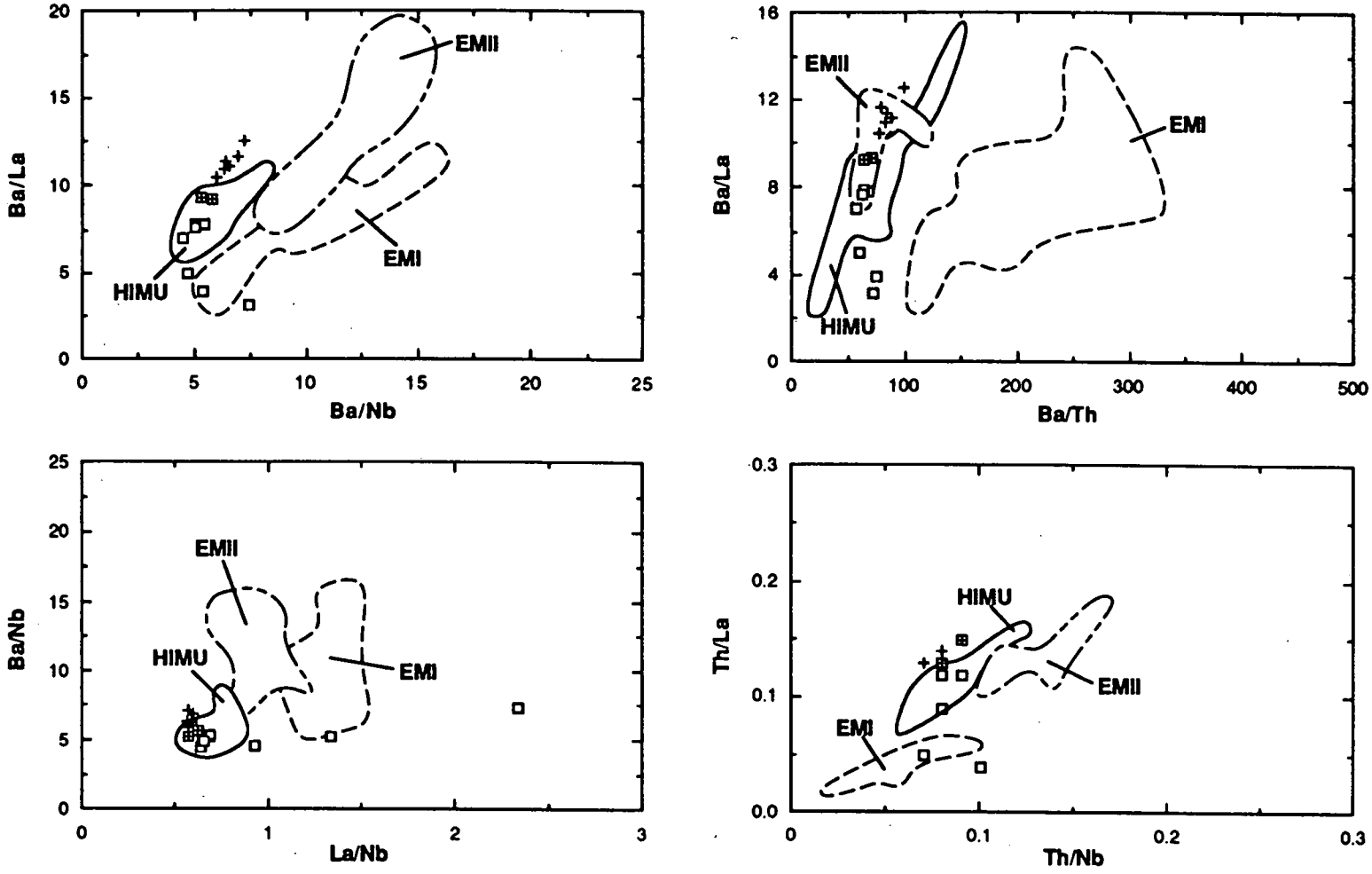
Ba/La
Ba/Nb
EMII
EMI
HIMU
Ba/La
Ba/Th
EMII
EMI
HIMU
Ba/Nb
La/Nb
EMII
HIMU
EMI
Th/La
Th/Nb
HIMU
EMII
EMI

(Figure 3.18)

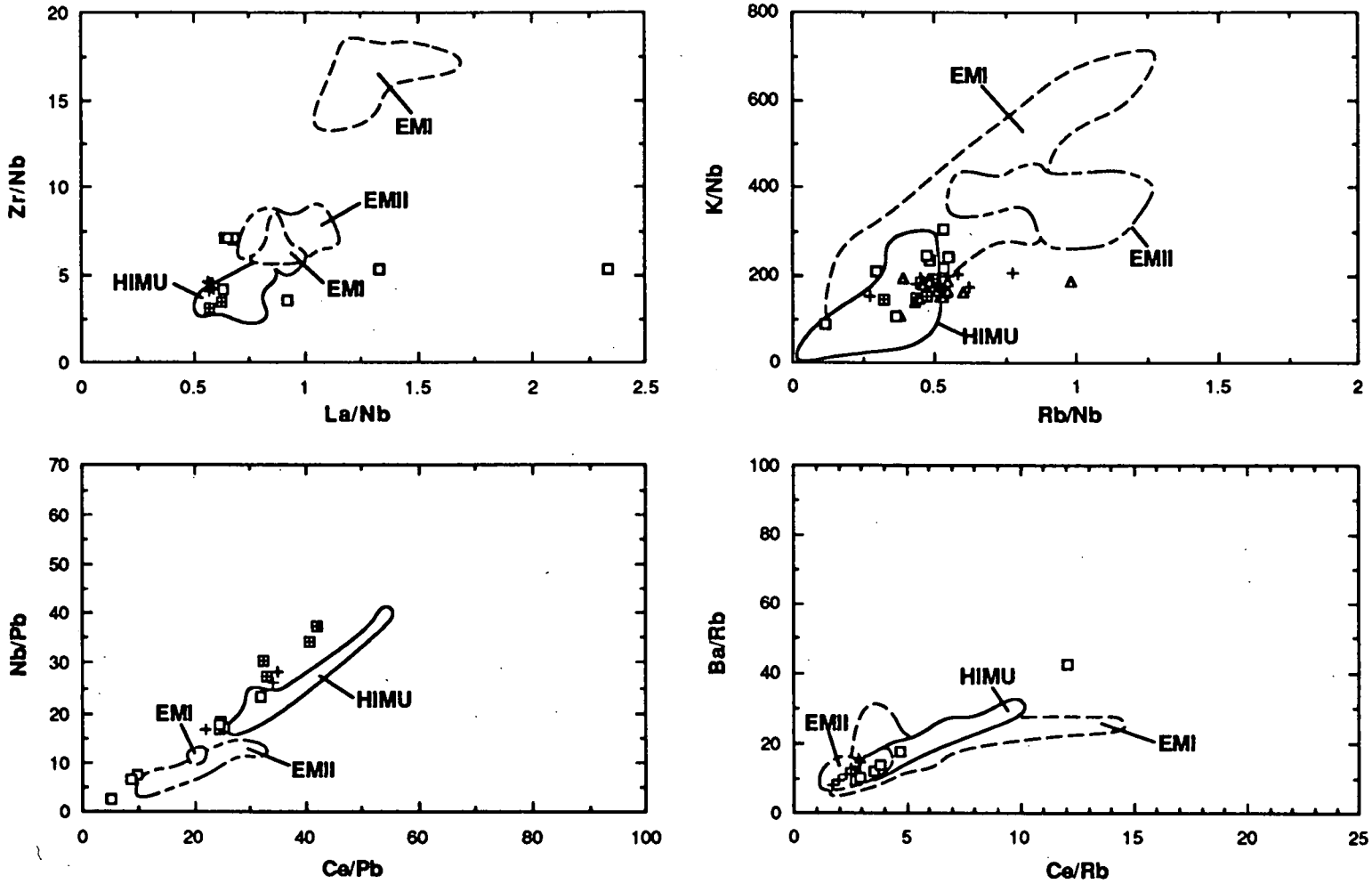

Figure 3.18: Trace element abundance ratios of submarine Balleny Province (crosses within squares), Soela Seamount (crosses) and Tasman Sea seamount (open squares) samples, as used to compile Table 3.8, plotted relative to the HIMU, EMI and EMII OIB fields. The OIB end-member fields have been plotted, using data sources as for Table 2.1, so as to circumscribe the bulk of the data; the complete OIB data sets are plotted in Figure 2.10. Where available, data for subaerial Balleny Island samples (open triangles - Green, 1992 and J. Foden, unpublished data) are also plotted.

relative LILE depletions and Nb-Ta enrichments to the HIMU basalts, indicating that these features are not strictly limited to isotopically-defined HIMU OIB.

The similar trace element abundance ratios of Balleny Province, Soela Seamount and south Tasman Sea seamount samples suggest a similar source chemistry, consistent with the idea that they derive from the same mantle plume source. Compared to those of the DMM (N-MORB), HIMU, EMI and EMII mantle end-member components in Table 3.8 and Figure 3.18, Balleny Plume trace element ratios are generally close to those of the HIMU basalts, characterised by low LILE/HFSE (Rb/Nb, K/Nb and Ba/Nb) and LREE/HFSE (La/Nb) values, compared to the EM OIB and average N-MORB components, as well as low Zr/Nb values and high Ce/Pb and Nb/Pb, indicative of Pb depletion in the source. It should be noted that, although the Zeehan Seamount Zr/Nb values are higher than the other Balleny Plume samples, a probable consequence of higher degrees of melting, they are still lower than those of the EMI Koolau tholeiites (upper field in La/Nb versus Zr/Nb plot of Figure 3.18), consistent with the idea that low Zr/Nb values are a Balleny Plume source feature.

Although Soela Seamount samples are generally similar to the other Balleny Plume and HIMU basalts, their slightly higher Ba/La, Th/La, Ba/Nb and Zr/Nb values plot outside the HIMU field, the former overlapping with EMII end-member basalts, and suggest a possible relative enrichment or slightly lesser depletion in LILE, relative to both LREE and HFSE in the Soela Seamount volcanics.

3.6.5 Summary of Balleny Plume Trace Element Geochemistry:

The Balleny Province, Soela Seamount and Tasman Sea seamount samples have similar trace element characteristics, consistent with a similar source geochemistry and derivation from a common mantle plume. This source, geochemically like other HIMU OIB mantle source regions, is depleted in LILE and LREE relative to the HFSE (Nb and Ta), has low Zr/Nb values and high Ce/Pb and Nb/Pb, indicative of Pb depletion. The apparent slight enrichment in LILE of Soela Seamount rocks, relative to the Balleny Province volcanics, does not appear to represent overall temporal plume evolution due to the lack of similar or greater relative LILE enrichment in the Tasman Sea seamount volcanics. However, due to the degree of alteration of the Tasman Sea seamount samples, and the relative mobility of the LILE, this possibility cannot be completely ruled out.

3.7 RADIOGENIC ISOTOPE CHEMISTRY:

Radiogenic isotope data for all Balleny Plume samples are presented in Tables 3.11 and 3.12; analytical methods are described in Appendix 2. Initial isotopic ratios were calculated using an approximate maximum age for each island or seamount and the equations presented in Appendix 6. The methods used to calculate initial ε_{Nd} and ε_{Sr} values (Table 3.11) as well as μ (Table 3.12) and κ values are also presented in Appendix 6.

In an attempt to negate the effects of seafloor alteration processes on the Sr, Nd and Pb isotopic ratios of the Balleny Plume rocks, samples were acid-leached (as described in Appendix 2) prior to isotopic analysis. However, the effects of acid-leaching on whole-rock elemental concentrations and ratios are relatively unpredictable. To quote Mahoney (1987: p. 212) "...elemental abundances in the [leached] residues therefore do not represent original bulk-rock compositions", and Mahoney and Spencer (1991: p. 200) "...because leaching tends to modify bulk composition, elemental abundances and interelement ratios in leached samples should not be taken as representative of magmatic values...". The main problem with acid-leaching is that it may result in the removal of, in addition to altered portions of a sample, some of the actual unaltered rock. Although the original isotopic ratios should be obtainable after leaching, provided that some of the original sample remains, elemental concentrations, and therefore elemental ratios, will change if some of the unaltered sample is removed during leaching. For this reason, no attempt was made to measure elemental concentrations on the same acid-leached aliquots that were used for isotopic work. Although ICP-MS trace element and REE abundances are available (Appendix 5: Table A5.1) for unleached equivalents of these Balleny Plume samples, the probability that seafloor processes have affected at least some elemental abundances within these rocks dictates that these data may also not be appropriate for the purposes of calculating initial isotopic ratios. In order to circumvent this problem, literature-derived trace and REE data have been used. Therefore, it must be noted that these values do not necessarily represent the correct initial isoptopic ratios for the Balleny Plume rocks, but are the best approximations possible under the circumstances. As a result, some of the ensueing interpretation/s and discussion/s of the Balleny Plume isotopic data may be subject to some debate.

Values used to calculate the initial isotopic ratios of the Balleny Plume samples (Tables 3.11 and 3.12) are derived from ICP-MS analyses of subaerial Balleny Islands samples (Gill and Collerson, in prep.) which are considered to be relatively pristine (ie. unleached and leached samples produced similar Sr isotope ratios). Where possible, data from rocks with comparable major element compositions have been used. However, this was not always possible because no rocks as evolved as the Balleny Province phonotephrite (sample 35A-1) or with tholeiitic affinities, which could be equated with the trachyandesites from Zeehan Seamount, have been located to date on the Balleny Islands. Initial isotopic ratios for Balleny Province samples 35A-1, 35A-4 and 35B-2, Soela Seamount samples SS4-7 and SS5, and all of the Tasman Sea seamount samples have been calculated using the following data (mean ppm concentrations ± standard deviation) for six basanite/trachybasalt samples from Sabrina Island: Rb = 28.38 ± 2.26, Sr = 660 ± 33, Sm = 7.3 ± 0.41, Nd = 35.95 ± 1.66, Pb = 2.48 ± 0.21, Th = 4.72 ± 0.42, U = 1.39 ± 0.12; $^{87}Rb/^{86}Sr$ = 0.1244, $^{147}Sm/^{144}Nd$ = 0.1228, κ = 3.51. Initial isotopic ratios for Balleny Province sample 35A-5 and Soela Seamount sample SS3 were calculated using the following data (mean ppm concentrations ± standard deviation) for three alkali olivine basalt samples from Sturge Island: Rb = 19.25 ± 0.35 (two samples only), Sr = 464 ± 44, Sm = 6.03

± 0.15, Nd = 28.97 ± 0.91, Pb = 1.7 ± 0.20, Th = 2.97 ± 0.06, U = 0.89 ± 0.09; $^{87}Rb/^{86}Sr$ = 0.1200, $^{147}Sm/^{144}Nd$ = 0.1259, κ = 3.45.

The measured and initial radiogenic isotope ratios of the Balleny Plume volcanics are compared in Figure 3.19. The values most affected by age correction are $^{87}Sr/^{86}Sr$, $^{206}Pb/^{204}Pb$ and $^{208}Pb/^{204}Pb$. The $^{207}Pb/^{204}Pb$ values of these rocks vary little with age correction due to the relatively rapid rate of decay of ^{235}U to ^{207}Pb during the early history of the Earth, and its relative depletion and negligible decay over the last billion years (e.g. Gariépy and Dupré, 1991). The small amount of Nd radiogenic growth with time is a function of the relatively low rate of decay of ^{147}Sm to ^{143}Nd, as dictated by the small decay constant (6.54×10^{-12} a^{-1}) and long half life (1.06×10^{11} a) of ^{147}Sm, compared to the other isotopic systems examined here.

3.7.1 Balleny Province:

Although very few isotopic analyses have yet been reported on rocks from the Balleny Province, available data for subaerial Balleny Islands samples (Hart, 1988; Gill and Collerson, 1992; J. Foden, unpublished data) indicate the presence of a distinctive isotopic signature characterised by high $^{143}Nd/^{144}Nd$ (0.51291 - 0.51301) and low $^{87}Sr/^{86}Sr$ (0.70276 - 0.70340) values, similar to MORB. Their negative ε_{Sr} (-15.5 to -24.7) and positive ε_{Nd} (+5.1 to +7.0) values are indicative of derivation from a mantle source with time-integrated low Rb/Sr and Nd/Sm values indicating depletion in the most incompatible elements (LILE and LREE) relative to bulk Earth. The Pb isotopic ratios of subaerial Balleny Island rocks are also distinctive, with high $^{206}Pb/^{204}Pb$ (19.700 - 19.856), $^{207}Pb/^{204}Pb$ (15.520 - 15.605) and $^{208}Pb/^{204}Pb$ (39.399 - 39.850) values (Hart, 1988; Gill and Collerson, 1992), which are intermediate between those of MORB and HIMU OIB and indicative of time-integrated high U/Pb and Th/Pb contents.

The Sr, Nd and Pb isotope ratios of four submarine Balleny Province samples, ranging in composition from alkali olivine basalt through basanite and trachybasalt to phonotephrite, were analysed during the course of this study. All four samples have similar isotope ratios to subaerial Balleny Islands samples (Tables 3.11 and 3.12), with low $^{87}Sr/^{86}Sr$ and high $^{143}Nd/^{144}Nd$ and Pb isotope ratios. Measured negative ε_{Sr} (-20.1 to -23.0) and positive ε_{Nd} (+5.4 to +6.7) values imply similar relative long-term depletions in LILE and LREE to the Balleny Islands samples. A common mantle source for Balleny Province submarine and subaerial samples can therefore be inferred.

3.7.2 Soela Seamount:

Two trachybasalts and an alkali olivine basalt, representing the least altered of the Soela Seamount samples, were analysed for Sr, Nd and Pb isotopes (Tables 3.11 and 3.12). Initial isotopic ratios, calculated assuming an age of 40 Ma for all three samples, are similar to initial ratios calculated for the submarine Balleny Province samples (assumed age = 10 Ma),

Table 3.11: $^{87}Sr/^{86}Sr$ and $^{143}Nd/^{144}Nd$ data for submarine Balleny Province and Soela, Janszoon, Zeehan and Heemskirk Seamount samples; errors ($2\sigma_{mean}$) associated with individual sample measurements indicate within-run precision only.

Sample No.	Age	$^{87}Sr/^{86}Sr$	$\pm 2\sigma$	$(^{87}Sr/^{86}Sr)_i$	εSr_i	$^{143}Nd/^{144}Nd$	$\pm 2\sigma$	$(^{143}Nd/^{144}Nd)_i$	εNd_i
Submarine Balleny Province:									
E27-35A-1	10 Ma	0.702924	21	0.702906	-22.4	0.512977	9	0.512969	6.5
E27-35A-4	10 Ma	0.703083	22	0.703065	-20.2	0.512927	9	0.512919	5.5
E27-35A-5	10 Ma	0.702890	12	0.702873	-22.9	-		-	-
		0.702894	14	0.702877	-22.9	0.512988	8	0.512980	6.7
E27-35B-2	10 Ma	0.702882	12	0.702864	-23.1	0.512992	14	0.512984	6.8
Soela Seamount:									
SS3	40 Ma	0.703216	18	0.703148	-18.5	0.512855	7	0.512822	4.4
SS4-7	40 Ma	0.703171	13	0.703100	-19.2	0.512904	6	0.512872	5.3
		0.703124	17	0.703053	-19.9	0.512886	7	0.512854	5.0
SS5	40 Ma	0.703229	19	0.703158	-18.4	0.512857	7	0.512825	4.4
Janszoon Seamount:									
C1/84 (2) 2DB 10	55 Ma	0.702906	16	0.702809	-23.1	0.512950	11	0.512906	6.4
C1/84 (2) 2DB 14	55 Ma	0.702906	17	0.702809	-23.1	0.512959	15	0.512915	6.5
		0.702910	19	0.702813	-23.0	0.512962	7	0.512918	6.6
Zeehan Seamount:									
C17/86 8DB 2/1	70 Ma	0.703360	14	0.703236	-17.0	0.512911	7	0.512855	5.8
C17/86 8DB 2/2	70 Ma	0.703391	16	0.703267	-16.6	-		-	-
		0.703404	9	0.703280	-16.4	0.512930	4	0.512874	6.1
C17/86 8DB 2/5	70 Ma	0.703391	12	0.703267	-16.6	0.512939	7	0.512883	6.3
C17/86 8DB 3/4	70 Ma	0.703361	19	0.703237	-17.0	0.512923	9	0.512867	6.0
Heemskirk Seamount:									
CK17/86 7DB 1/10	70 Ma	0.703009	14	0.702885	-22.0	0.513131	14	0.513075	10.0
		0.703030	17	0.702906	-21.7	0.513136	20	0.513080	10.1
CK17/86 7DB 1/13	70 Ma	0.702996	19	0.702872	-22.2	0.512963	10	0.512907	6.8

Table 3.12: $^{206}Pb/^{204}Pb$, $^{207}Pb/^{204}Pb$ and $^{208}Pb/^{204}Pb$ data for submarine Balleny Province and Soela, Janszoon, Zeehan and Heemskirk Seamount samples.

Sample No.	Age	μ	$^{206}Pb/^{204}Pb$	$(^{206}Pb/^{204}Pb)_i$	$^{207}Pb/^{204}Pb$	$(^{207}Pb/^{204}Pb)_i$	$^{208}Pb/^{204}Pb$	$(^{208}Pb/^{204}Pb)_i$
Submarine Balleny Province:								
E27-35A-1	10 Ma	36.72	19.743	19.686	15.608	15.605	39.456	39.392
E27-35A-4	10 Ma	36.89	19.849	19.792	15.624	15.621	39.692	39.628
E27-35A-5	10 Ma	34.22	19.698	19.645	15.581	15.579	39.344	39.286
		34.20	19.672	19.619	15.585	15.583	39.329	39.194
E27-35B-2	10 Ma	36.75	19.793	19.736	15.617	15.614	39.492	39.428
Soela Seamount:								
SS3	40 Ma	34.62	20.015	19.799	15.649	15.639	39.856	39.619
SS4-7	40 Ma	37.00	20.029	19.799	15.632	15.621	39.762	39.505
SS5	40 Ma	37.12	20.061	19.830	15.640	15.629	39.898	39.640
Janszoon Seamount:								
C1/84 (2) 2DB 10	55 Ma	37.03	20.021	19.704	15.631	15.616	39.773	39.419
		37.03	20.022	19.705	15.630	15.615	39.777	39.423
C1/84 (2) 2DB 14	55 Ma	37.00	19.966	19.649	15.628	15.613	39.793	39.439
		37.00	19.950	19.633	15.628	15.613	39.776	39.422
Zeehan Seamount:								
C17/86 8DB 2/1	70 Ma	37.20	20.215	19.809	15.649	15.630	39.933	39.480
C17/86 8DB 2/2	70 Ma	37.46	20.360	19.951	15.757	15.738	40.196	39.740
C17/86 8DB 2/5	70 Ma	37.20	20.214	19.808	15.649	15.630	39.929	39.476
C17/86 8DB 3/4	70 Ma	37.23	20.228	19.822	15.662	15.643	39.961	39.508
Heemskirk Seamount:								
CK17/86 7DB 1/10	70 Ma	37.72	20.727	20.315	15.710	15.690	40.466	40.007
CK17/86 7DB 1/13	70 Ma	37.66	20.635	20.224	15.699	15.680	40.406	39.962
		37.64	20.627	20.216	15.692	15.673	40.385	39.927

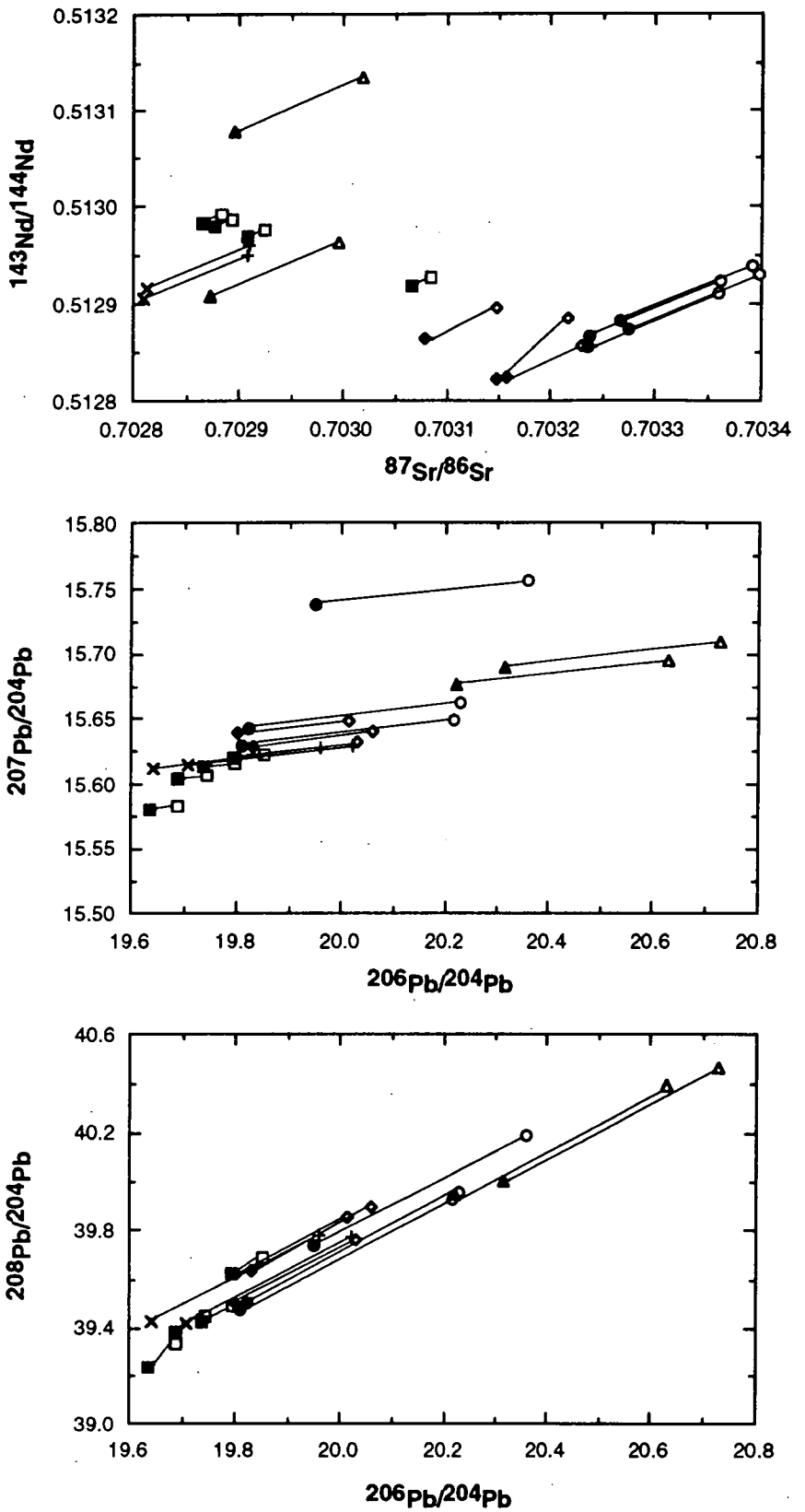

Figure 3.19: Comparison between the measured (open symbols) and initial (filled symbols) isotopic ratios for the Balleny Province (squares), Soela Seamount (diamonds), Janszoon Seamount (crosses - oblique crosses represent the age-corrected data), Zeehan Seamount (circles) and Heemskirk Seamount (triangles) samples analysed during this study; data from Tables 3.11 and 3.12.

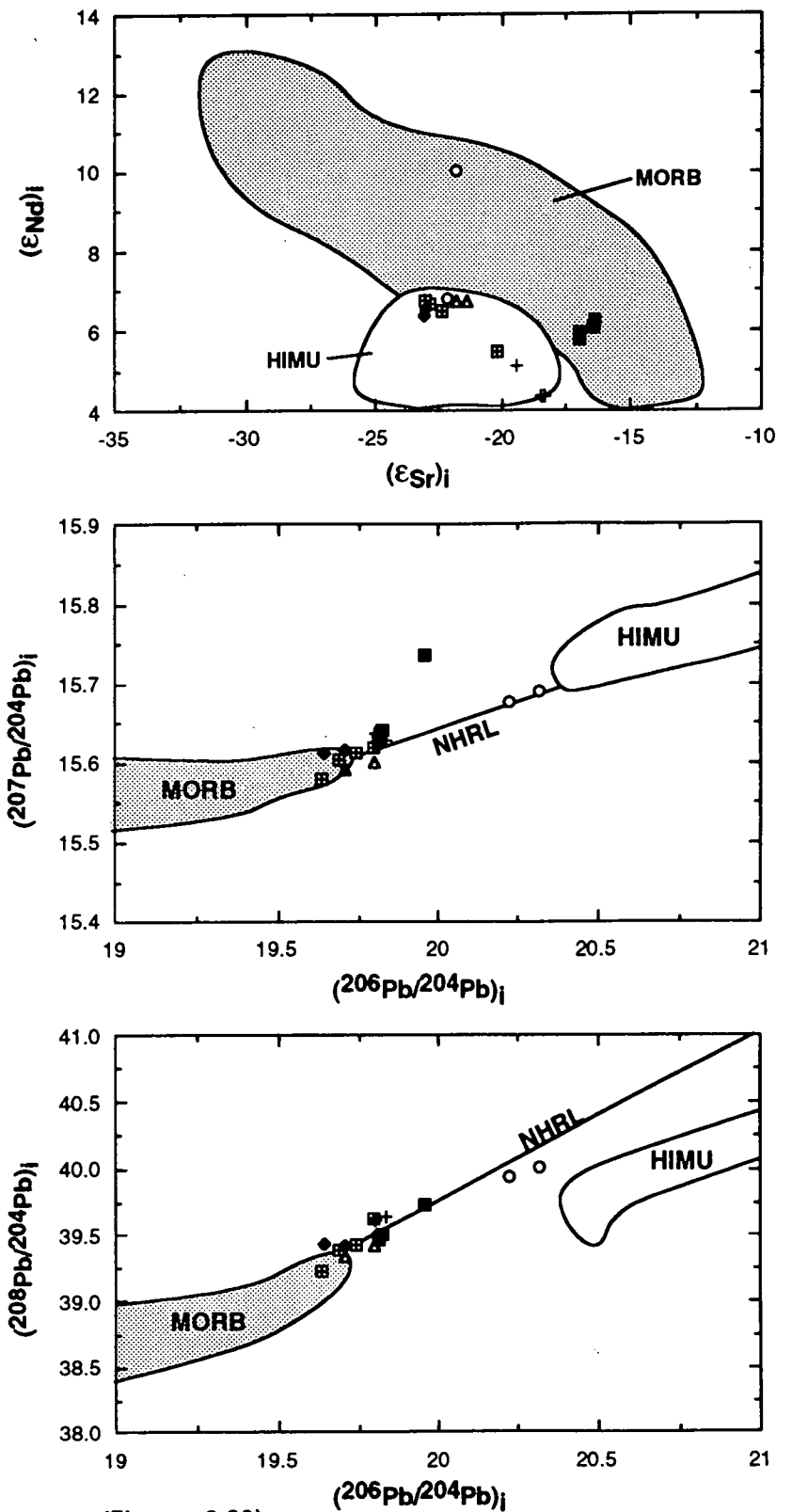
14
12
10
8
6
4
-35
-30
-25
-20
-15
-10
$(\varepsilon_{Nd})_i$
$(\varepsilon_{Sr})_i$
MORB
HIMU
15.9
15.8
15.7
15.6
15.5
15.4
19
19.5
20
20.5
21
$(^{207}Pb/^{204}Pb)_i$
$(^{206}Pb/^{204}Pb)_i$
HIMU
NHRL
MORB
41.0
40.5
40.0
39.5
39.0
38.5
38.0
19
19.5
20
20.5
21
$(^{208}Pb/^{204}Pb)_i$
$(^{206}Pb/^{204}Pb)_i$
NHRL
HIMU
MORB

(Figure 3.20)

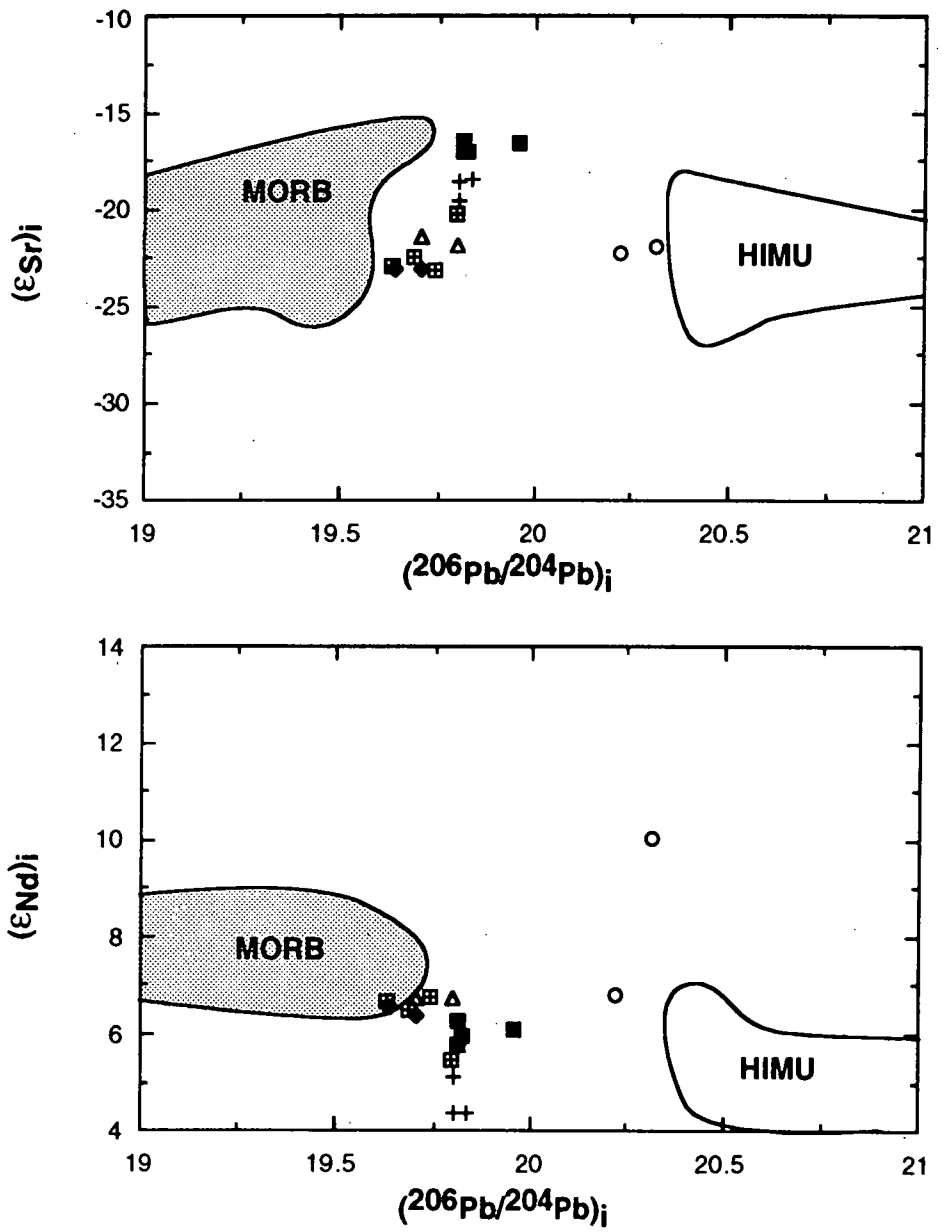

Figure 3.20: Plots of initial radiogenic isotope ratios as calculated for submarine Balleny Province (crosses within squares), Soela Seamount (crosses), Janszoon Seamount (filled diamonds), Zeehan Seamount (filled squares) and Heemskirk Seamount (open circles) samples; data from Tables 3.11 and 3.12 - average values are plotted for duplicate analyses. Two Balleny Islands isotope analyses of Hart (1988) are also included (open triangles): their initial isotopic ratios were calculated using data from Gill and Collerson (in prep.). Data sources for HIMU OIB (Mangaia, Rimatara, Rurutu, Tubuai and St. Helena) and MORB isotopic fields are as for Figure 1.1.

and thereby imply derivation from a similar mantle source. However, the Soela samples extend to slightly higher initial $^{206}Pb/^{204}Pb$, $^{207}Pb/^{204}Pb$, $^{208}Pb/^{204}Pb$ and $^{87}Sr/^{86}Sr$ values, and lower $^{143}Nd/^{144}Nd$ values.

3.7.3 South Tasman Sea Seamounts:

The radiogenic isotope compositions of two Janszoon, four Zeehan and two Heemskirk Seamount samples (Tables 3.11 and 3.12) are also very similar to Balleny Province compositions, with distinctly high $^{143}Nd/^{144}Nd$ and Pb isotope ratios and low $^{87}Sr/^{86}Sr$ values for OIB, implying a similar mantle source. A general increase in initial $^{206}Pb/^{204}Pb$ and $^{208}Pb/^{204}Pb$ values is evident from Janszoon to Zeehan to Heemskirk Seamount, all of which possess initial Pb isotope values which are slightly higher than, or equivalent to, the most radiogenic values of the Balleny Province and Soela Seamount samples. $^{207}Pb/^{204}Pb$ values are less easily interpreted due to considerable overlap between Janszoon and Zeehan samples with the upper end of the Balleny and Soela range. However, rocks from the Zeehan and Heemskirk Seamounts do possess the most radiogenic $^{207}Pb/^{204}Pb$ contents whereas Balleny Province samples extend to the lowest values.

Initial $^{143}Nd/^{144}Nd$ values of Tasman Sea seamount samples are generally slightly lower than those of both submarine and subaerial Balleny samples and overlap with those of Soela Seamount rocks, but show no age progression from one seamount to the next. Initial $^{87}Sr/^{86}Sr$ values generally overlap with the range of the Balleny Province and Soela Seamount samples.

3.7.4 Isotopic Characterisation of the Balleny Plume:

Examination of samples collected along the proposed ~70 m.y. Balleny Plume trace has revealed distinctive isotopic similarities, consistent with the idea of derivation from a common mantle source, the Balleny Plume. According to the analyses performed during this study, the plume is characterised isotopically by low initial $^{87}Sr/^{86}Sr$ (<0.7033) and high initial $^{143}Nd/^{144}Nd$ (>0.5128), somewhat similar to MORB values, plus high initial $^{206}Pb/^{204}Pb$ (≥19.62), $^{207}Pb/^{204}Pb$ (≥15.58) and $^{208}Pb/^{204}Pb$ (≥39.24), compared to all but the HIMU oceanic basalts. These isotopic features, a consequence of the distinct long-term parent/daughter element systematics of the source, indicate low time-integrated Rb/Sr and Nd/Sm values consistent with depletion in the most incompatible elements (LILE and LREE). Negative ε_{Sr} and positive ε_{Nd} values in all Balleny Plume samples signify these incompatible element depletions relative to bulk Earth. However, the high Pb isotopic ratios of the Balleny Plume volcanics are indicative of time-integrated high U/Pb and Th/Pb in the source, inconsistent with the idea of incompatible element depletion unless Pb suffered even greater depletion at some time in the past, thereby producing the relatively high U/Pb and Th/Pb source values.

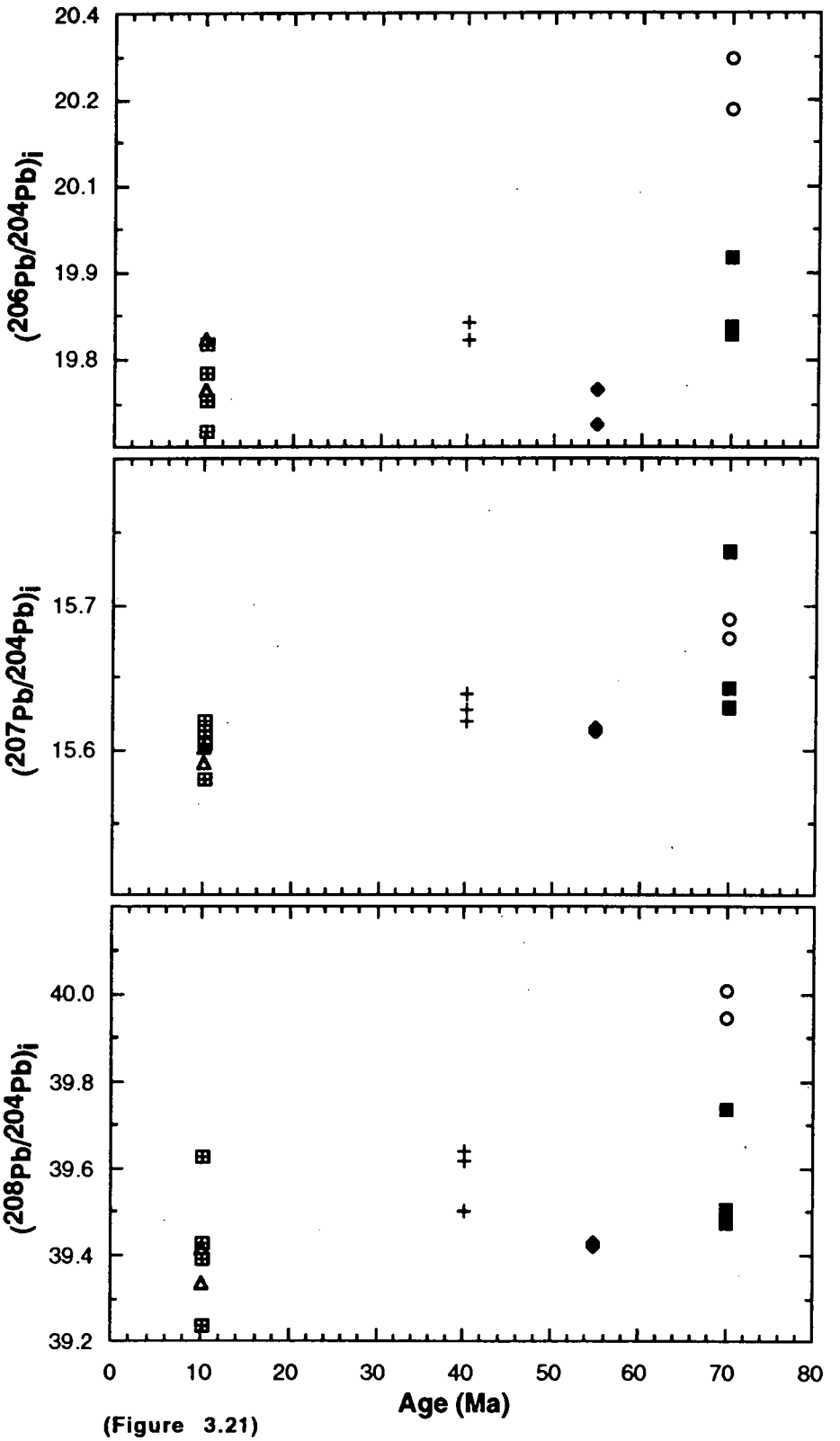
20.4
20.2
20.1
19.9
19.8
(206Pb/204Pb)i
15.7
15.6
(207Pb/204Pb)i
40.0
39.8
39.6
39.4
39.2
(208Pb/204Pb)i
0
10
20
30
40
50
60
70
80
Age (Ma)

(Figure 3.21)

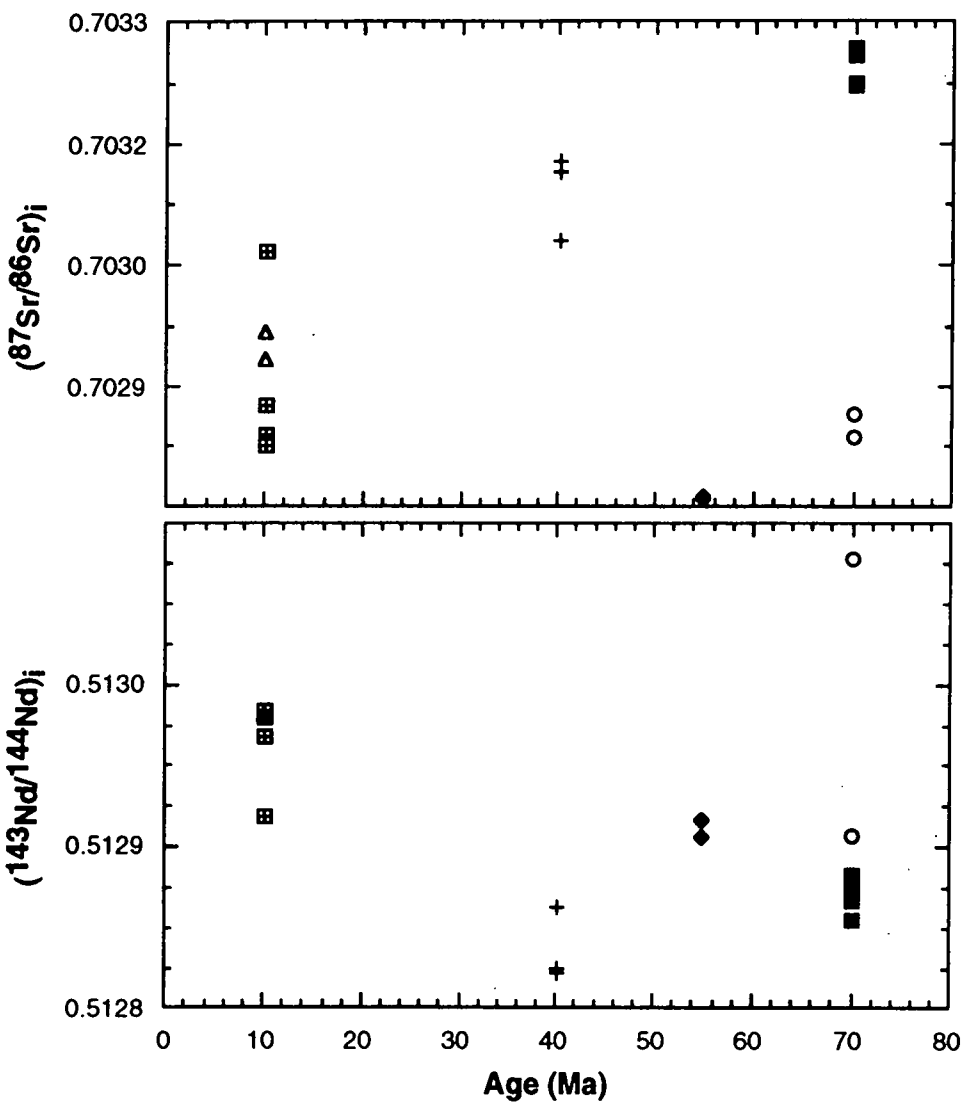

Figure 3.21: Approximate age (Ma) versus initial radiogenic isotope ratios for submarine Balleny Province (crosses within squares), Soela Seamount (crosses), Janszoon Seamount (filled diamonds), Zeehan Seamount (filled squares) and Heemskirk Seamount (open circles) samples plus the two Balleny Islands samples of Hart (1988 - open triangles); isotopic data as for Figure 3.20.

Hart (1988) proposed that the Balleny Islands isotopic signature is a product of mixing between two separate mantle reservoirs. The low $^{87}Sr/^{86}Sr$ and high Pb isotopic ratios of the Balleny rocks are considered to form part of the No-EM array (Figure 1.1), comprising variable mixtures of the DMM and HIMU mantle end-member components (Hart, 1988). The data arrays produced by the range of Balleny Plume samples on Pb-Pb isotope plots (Figure 3.20) are consistent with derivation from mixing between two end-member components, one of which coincides with the MORB field while the other has Pb isotope values similar to those displayed by HIMU OIB. However, the trend displayed by Balleny Plume volcanics as a whole in $^{206}Pb/^{204}Pb$-$^{208}Pb/^{204}Pb$ space (Figure 3.20) indicates that they have slightly higher $^{208}Pb/^{204}Pb$ values than other HIMU OIB, signifying slightly higher Th/Pb in the Balleny Plume source. Whereas HIMU basalts plot below the NHRL of Hart (1984), Balleny Plume samples plot along it. If this NHRL does have an age significance (e.g. Zindler and Hart, 1986), it indicates a similar time-integrated Th/U ratio (~4) for the Balleny Plume and MORB sources, rather than the U/Th enrichment (a possible product of the greater incompatibility of Th) of other known HIMU sources.

3.7.5 Temporal Isotopic Changes in the Balleny Plume:

Temporal isotopic changes in the Balleny Plume, particularly in terms of Pb isotope ratios, do not simply reflect an 'evolving plume source' as proposed for some other hotspot tracks, such as that associated with the Ninetyeast Ridge (Class et al., 1993). Whereas an evolving source could be expected to produce more radiogenic isotope ratios with time due to progressive radioactive decay (Class et al., 1993), Balleny Plume volcanism is characterised by an overall decrease in Pb isotope values with time (Figure 3.21). The Balleny Plume data array on Pb-Pb isotope plots (Figure 3.20) is, in fact, indicative of two end-member mixing, the oldest Heemskirk Seamount samples plotting closest to the most radiogenic end-member, a HIMU-like component enriched in both U/Pb and Th/Pb relative to MORB and other OIB, whereas the youngest Balleny Plume samples, those from the Balleny Islands region, overlap with the most radiogenic MORB (Figure 3.20). This is consistent with the idea that depleted MORB mantle comprises the second end-member mixing component, and indicates that the spread of Balleny Plume Pb-Pb data is a product of mixing and has no overall age significance in terms of secondary isochrons resulting from mantle differentiation event/s.

A decrease in radiogenic Pb, from the Heemskirk Seamount to the Balleny Province samples, is particularly evident in terms of their calculated initial $^{206}Pb/^{204}Pb$ and $^{208}Pb/^{204}Pb$ values (Figure 3.21). Although this does appear to reflect a progressive temporal isotopic change along the length of the Balleny Plume trace, this interpretation is complicated by the relatively low Pb isotope values of the two Janszoon Seamount samples, the latter overlapping with the calculated initial values of the significantly younger Balleny Province rocks. Despite the fact that the Balleny Province samples have the lowest $^{207}Pb/^{204}Pb$ values and Tasman Sea samples have the highest, the range of initial

$^{207}Pb/^{204}Pb$ is relatively narrow (15.579-15.738). Although the Pb isotope ratios of Balleny Plume samples imply time-integrated high U/Pb and Th/Pb values in the source, the greater range of $^{206}Pb/^{204}Pb$ and $^{208}Pb/^{204}Pb$ suggest greater source enrichment in ^{238}U and ^{232}Th relative to ^{235}U. This suggests that the U-Th/Pb enrichment event must have been relatively recent, in keeping with the proposal of reduced ^{235}U and negligible ^{207}Pb production during the last billion years (e.g. Gariépy and Dupré, 1991).

Balleny Plume initial $^{87}Sr/^{86}Sr$ and $^{143}Nd/^{144}Nd$ are more difficult to interpret. Most values plot within, or close to, the field defined by HIMU basalts (Figure 3.20). Excluding Soela Seamount samples, and the anomalously high $^{143}Nd/^{144}Nd$ value of Heemskirk sample 7DB 1/10, the highest $^{143}Nd/^{144}Nd$ values occur within the Balleny Province volcanics and the lowest in the Tasman Sea seamount rocks, consistent with increasing dilution of the plume by a depleted MORB source, with time. However, no correlatable pattern is observed in terms of initial $^{87}Sr/^{86}Sr$, due to the high values calculated for the Zeehan Seamount samples. These high initial ratios may simply be an artifact of the trace element values used (as discussed at the start of Section 3.7), no samples with similar whole-rock chemistry to the Zeehan Seamount samples being available from the Balleny Islands. Due to the fact that the measured trace element abundances (Table A5.1), which are consistent from one Zeehan Seamount sample to the next, produce much higher $^{87}Rb/^{86}Sr$ values (0.4564 - 0.4987), their initial $^{87}Sr/^{86}Sr$ values may in fact be much lower (0.702895 - 0.702937) and thereby closer to the calculated values for the Heemskirk samples. If this is the case, the Soela Seamount samples may actually extend to the highest initial $^{87}Sr/^{86}Sr$ and lowest $^{143}Nd/^{144}Nd$ values, indicative of slightly higher time-integrated Rb/Sr and Nd/Sm values than the other Balleny Plume volcanics.

The higher $^{208}Pb/^{204}Pb$ values, at a given $^{206}Pb/^{204}Pb$ value, of the Balleny Plume volcanics relative to other HIMU OIB make it difficult to define the composition of the Balleny Plume source in terms of the HIMU-like end-member but they may actually expand the HIMU field somewhat in $^{206}Pb/^{204}Pb$-$^{208}Pb/^{204}Pb$ space. Although it is clear that the Balleny Plume volcanics are a product of variable mixing between a HIMU-like plume and depleted MORB mantle, it is not possible to quantitatively evaluate the amount contributed by each of these components. This is particularly true if source mixing rather than melt mixing has occurred, due to the extra difficulties associated with determining source composition as opposed to melt composition, for example the Pb content of the MORB source would not be equivalent to that of the melt represented by an average MORB composition in the vicinity of the hotspot. Despite mixing between these HIMU-like and depleted upper mantle sources, the Balleny Plume volcanics still retain very high present-day μ ($^{238}U/^{204}Pb$) values ($\geq$ 34: Table 3.12) compared to the bulk Earth (9.1) and depleted mantle (4.7 to 5.9) values of Gariépy and Dupré (1991).

Considering each location separately, it is possible to observe what appear to be individual mixing trends in Sr-Nd space (Figure 3.20), particularly for the Balleny Province and Soela Seamount samples. If the most plume-like component at each site is represented

by the sample with the highest $^{87}Sr/^{86}Sr$ and lowest $^{143}Nd/^{144}Nd$ (samples E27-35A-4 and SS3/SS5 respectively), therefore being least like MORB, these lmixing arrays would project towards an extremely depleted DMM end-member. Although constrained by very few data points, the individual Balleny Province and Soela Seamount arrays appear to be continuous and thereby project between the same end-member compositions. Compared to the Soela array, the position of the Balleny array is closer to the DMM end-member implying that different degrees of end-member mixing are involved at the different locations. It is not possible, however, to plot individual mixing arrays for the Tasman Sea seamount samples, due to the small number of data points and their location-based clustering (apart from the apparently anomalous $^{143}Nd/^{144}Nd$ value of Heemskirk sample 7DB 1/10), although they mostly plot close to the mixing trend defined by the Soela Seamount and Balleny Province samples in Sr-Nd space. If the initial Sr isotopic ratios of the Zeehan Seamount samples were closer to those of the Heemskirk Seamount samples, as proposed above, they too would plot close to this array, thereby lending support for the idea that the calculated initial isotopic values for the Zeehan samples (Table 3.11) are incorrect. If this assumption holds true, then the Tasman Sea seamount and Balleny Province samples would have a similar range of initial $^{87}Sr/^{86}Sr$ (Figures 3.20 and 3.21) and the Soela Seamount samples would possess the highest $^{87}Sr/^{86}Sr$ values of all the Balleny Plume eruptives. This suggests that the Soela source may have possessed a slight time-integrated enrichment in Rb/Sr relative to the rest of the plume. An increased incompatible element enrichment of the Soela source is in keeping with the results of the trace element study in Section 3.6, in which Soela Seamount basalts were found to be slightly enriched in LILE compared to other Balleny Plume samples. Possible explanations for these Soela Seamount geochemical deviations will be discussed in the following section.

3.8 MODELLING BALLENY PLUME CHANGES:

The following discussion assumes that there is a progressive temporal isotopic change along the Balleny Plume trace. Temporal changes in the composition of the Balleny Plume, particularly in terms of its decreasing Pb isotope values, appears to be a product of increasing dilution of a HIMU-like plume source by depleted upper mantle material. Entrainment of surrounding mantle by the upwelling head of a starting plume is considered to be related to the buoyancy flux of the plume (Griffiths and Campbell, 1990), whereby those with the largest buoyancy fluxes experience the most rapid ascent and the least dilution through ambient mantle entrainment and subsequent melting. The degree of dilution of the remnant, and often long-lived, vertical plume conduit, following eruption of melts from the plume head to form continental flood basalts or oceanic plateaus, or its attachment to the overlying moving lithosphere, is also thought to be related predominantly

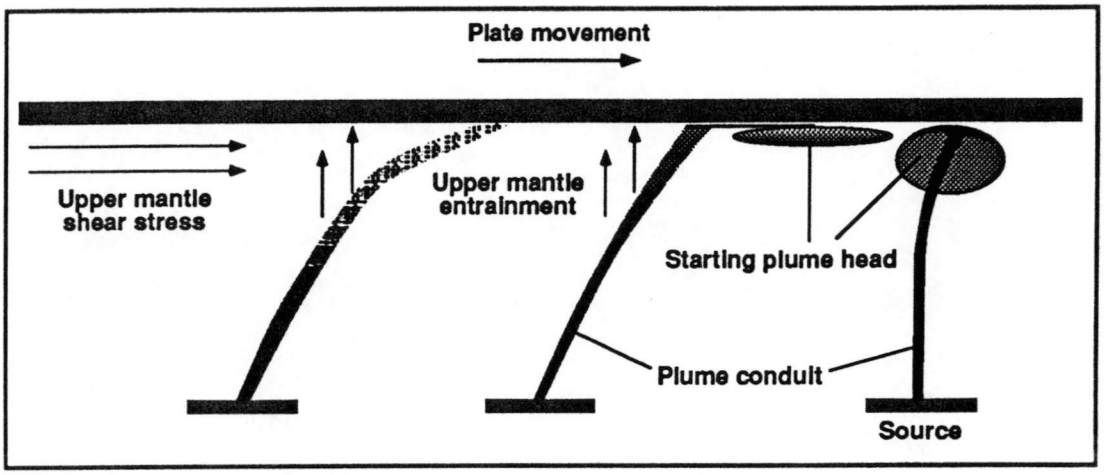

Figure 3.22: Cartoon representation, based on the fluid dynamic experiments of Griffiths and Campbell (1991), of the possible temporal increase in plume conduit inclination and asthenospheric entrainment following detachment of the starting plume head.

to buoyancy flux (Griffiths and Campbell, 1991). The degree of deflection from the vertical of the plume conduit, due to horizontal mantle shear flow produced by overlying plate motion (Skilbeck and Whitehead, 1978; Whitehead, 1982), also contributes, although to a lesser extent, to the degree of overlying mantle entrainment as a result of non-axisymmetric flow within inclined conduits (Griffiths and Campbell, 1991).

As shear stresses are expected to be greatest within the upper mantle, thereby resulting in the greatest degree of conduit inclination in this region (Richards and Griffiths, 1988; Griffiths and Campbell, 1991), entrained ambient material should therefore be dominated by depleted upper mantle. Relatively weak plumes, characterised by the smallest buoyancy flux and greatest horizontal deflection or tilt angle within the upper mantle, are considered likely to entrain the greatest amount, as a fraction of their source flux, of this overlying upper mantle material (Griffiths and Campbell, 1991). Entrainment of depleted upper mantle by the Balleny Plume suggests that it may represent a relatively weak plume in terms of its buoyancy flux. However, in order to avoid excessive dilution and subsequent cooling, whereby ocean floor volcanism is unlikely to occur, the buoyancy flux of the Balleny Plume must have been at least ~10^3 N s^{-1} (~0.3 Mg s^{-1}), equivalent to that of the weakest observed hotspot in terms of seafloor swell topography (Griffiths and Campbell, 1991).

Increasing dilution of the Balleny Plume by overlying upper mantle may reflect a decrease in the buoyancy flux of this plume and/or an increase in the horizontal deflection of the plume conduit with time (Figure 3.22). However, the actual degree of dilution depends on how much of the entrained material is carried by the ascending plume through its mantle solidus, rather than how much material is entrained, the latter resulting in stirring as opposed to compositional mixing (Griffiths and Campbell, 1991). Therefore, the amount of entrained upper mantle material ascending through its solidus may be increasing with time, reflecting

variable zonation within the plume. The apparent temporal dilution of the Balleny Plume is consistent with the thermal plume modelling of Richards and Griffiths (1989). They predict that a horizontally deflected plume will experience strong thermal entrainment of surrounding mantle resulting in strongly diluted material towards the 'upstream' side of the volcanic centre (ie. the youngest hotspot emanations), with the least diluted material occurring in the 'downstream' direction of plate movement (ie. the oldest hotspot volcanism).

The assumption that the Balleny Plume may represent a relatively weak plume, in terms of its buoyancy flux, may assist in explaining several observed anomalies associated with its trace. Lack of evidence for the extensive volcanism which is generally linked to the eruption of melts from a plume head may simply be due to a lack of recognition resulting from the relatively poorly studied nature of the eastern Tasman Sea region and the uncertainty surrounding the exact location of the start of the plume trace. Alternatively, Griffiths and Campbell (1990) suggest that the head of a relatively weak plume (buoyancy flux $<10^4$ N s^{-1}) may become detached from its source during ascent, prior to reaching the lithosphere or even the upper mantle, thereby preventing the occurrence of a major volcanic event at the start of the hotspot track. The relatively intermittent nature of volcanism along the Balleny Plume trace may also be related to a small buoyancy flux, whereby weak plumes are thought to become unstable and highly deflected due to mantle shear, resulting in their subsequent break up into a series of small discrete diapirs which can ascend independently (Skilbeck and Whitehead, 1978; Griffiths and Campbell, 1990). Although Jenkins et al. (unpublished) have ascribed a total of 36 seamounts, as well as the subaerial Balleny Islands, to the Balleny Plume, there are several regions along its trace where no surface expressions of the plume have been recognised. These include a region of the Tasman Sea between seafloor magnetic anomaly 32, east of the (extinct) spreading ridge and anomaly 26 to the west, and from the area just south of anomaly 8 on the Indian-Australian Plate to anomaly 5 on the Antarctic Plate. It is likely however, that these particular eruption-free regions are somehow related to interaction of the plume with a spreading ridge, thought by Sleep (1992) to produce a jump in the plume trace due to temporary capture of the plume by the ridge (Chapter 5).

If the calculated initial Sr isotope ratios of the Zeehan Seamount samples (Table 3.11) are too high, as discussed above, then the high initial $^{87}Sr/^{86}Sr$ values of the Soela Seamount samples imply slightly higher time-integrated Rb/Sr values relative to the other Balleny Plume volcanics. This is not easily explained, particularly given the apparent lack of disturbance of the Soela Pb isotope ratios. One explanation may be that the plume is somewhat heterogeneous in terms of $^{87}Sr/^{86}Sr$, so that a region with relatively high Sr isotope ratios was tapped during the formation of Soela Seamount.

Eruption of the Soela Seamount volcanics may have been influenced by the change of direction in the plume trace at ~43 Ma, the bend in the trace being located close to the East Tasman Plateau. Studies of the Hawaiian-Emperor bend indicate that a strong plume, such as the Hawaiian Plume, is likely to remain stable during a change in the direction of plate

motion, resulting in very little horizontal displacement of the hotspot trace relative to the underlying plume and a sharp bend in the hotspot trace (Griffiths and Richards, 1989). However, Griffiths and Richards (1989) predict that a weak plume, such as the Balleny Plume appears to be, will have a greater angle of tilt, a larger along-track adjustment distance to a change in the direction of plate motion, and greater instability, all of which may result in the conduit breaking up and ascending as discrete diapirs. If Soela Seamount is the product of a such a discrete diapir, due to break up of the plume conduit in the vicinity of the East Tasman Plateau, it is possible that a heterogenous part of the plume, slightly enriched in $^{87}Sr/^{86}Sr$, may have become separated in this region and formed the source of the Soela Seamount.

Alternatively, if the East Tasman Plateau is in fact formed of continental rather than oceanic crust, lithospheric contamination may be the cause of the Soela Seamount isotopic anomalies. Although continental crust contamination could be expected to increase $^{87}Sr/^{86}Sr$ values, as observed in the Soela samples, the greater abundance of Pb in crustal rocks would be expected to shift the Pb isotopes closer to crustal values than either the Sr or Nd isotope ratios (e.g. Gariépy and Dupré, 1991), thereby displacing the Soela Seamount samples from the Balleny Plume linear Pb-Pb mixing trends (Figure 3.20). The apparent lack of influence by a crustal end-member on the Pb isotope compositions of the Soela Seamount samples is difficult to reconcile with a model involving contamination.

3.9 CONCLUSIONS:

The trace of the Balleny Plume has hereto been based primarily on plate tectonic reconstructions and the age progression displayed by a curved chain of seamounts extending from the Balleny Islands region back to the south Tasman Sea. Using Sr, Nd and Pb isotopes and certain trace element ratios as source tracers, the compositions of samples from the Balleny Islands and four seamounts located along the proposed hotspot track are deemed to be consistent with derivation from a single mantle plume source, and with the proposed spatial evolution of the Balleny Plume.

Isotopically, the Balleny Plume is characterised by low $^{87}Sr/^{86}Sr$, high $^{143}Nd/^{144}Nd$, $^{206}Pb/^{204}Pb$, $^{207}Pb/^{204}Pb$ and $^{208}Pb/^{204}Pb$ values, indicative of a source with time-integrated low Rb/Sr and Nd/Sm contents and high U/Pb and Th/Pb values. Although the latter appear to be paradoxical with respect to the LILE and LREE depletions indicated by the $^{87}Sr/^{86}Sr$ and $^{143}Nd/^{144}Nd$ values, this is not the case if the high U/Pb and Th/Pb values are a product of ancient Pb depletion in the source.

Incompatible trace element features of the Balleny Plume volcanics include low LILE/HFSE, LREE/HFSE and Zr/Nb values plus high Nb/Pb and Ce/Pb values compared to MORB and, all but HIMU, OIB. These latter features, along with the similarity of Balleny Plume Nb/U and Th/U values to those of all other oceanic basalts (MORB and OIB), lend support to

the idea that the high U/Pb and Th/Pb responsible for the high Pb isotope values of Balleny Plume volcanics are predominantly a product of time-integrated Pb depletion in the source.

The radiogenic isotope and trace element characteristics of Balleny Plume volcanics indicate a HIMU-like composition for the Balleny Plume. The actual plume end-member composition is unknown due to apparent dilution by depleted upper mantle material (DMM). However, it appears to have a slightly higher time-integrated Th/U value than other known HIMU sources, $^{208}Pb/^{204}Pb$ for the oldest and most radiogenic Balleny Plume samples plotting above the HIMU field in $^{206}Pb/^{204}Pb$-$^{208}Pb/^{204}Pb$ space.

Apart from the trachyandesites of Zeehan Seamount, which may represent a tholeiitic shield-building phase of volcanism, all other samples are SiO_2-undersaturated and define fractionation trends controlled predominantly by olivine, and subordinate clinopyroxene and spinel, from alkali basalt/basanite through to trachyte compositions.

Data arrays defined by Balleny Plume volcanics in Pb-Pb space represent mixing arrays between a HIMU-like plume component and a depleted upper mantle MORB source (DMM). Dilution of the plume source appears to have increased with time, adding a temporal significance to the Pb-Pb mixing arrays. This temporal mixing trend is less clear in Sr-Nd isotopic space, although the Soela Seamount and Balleny Province samples do seem to define a continuous mixing array between a very depleted upper mantle component (DMM) and a HIMU-like plume component, with the Soela Seamount data plotting closest to the plume end-member.

The anomalously high $^{87}Sr/^{86}Sr$ values of the Soela Seamount basalts, assuming that the calculated initial $^{87}Sr/^{86}Sr$ values for the Zeehan Seamount samples are incorrect, suggest time-integrated enrichment in Rb/Sr relative to the other Balleny Plume volcanics. This enhanced incompatible element enrichment is consistent with the slightly greater LILE/HFSE values observed in the Soela trace element abundance ratios, and may be a product of either plume heterogeneity or contamination at this site.

Entrainment of upper mantle material by the Balleny Plume is indicative of a relatively small plume buoyancy flux. Experimental studies suggest that the conduits of weak plumes, such as this, may become inclined due to shear stresses in the upper mantle, resulting in significant entrainment of overlying mantle material. Increasing plume dilution could therefore indicate that the buoyancy flux of the Balleny Plume decreased with time, resulting in a greater horizontal deflection and increasing upper mantle entrainment. Alternatively, some form of zonation may exist within the plume source resulting in an increase in the amount of entrained DMM material which accompanies the plume through the mantle solidus with time.

The fourth aim of this chapter, an attempt to further constrain the characteristics of the HIMU mantle end-member through the study of the Balleny Plume, has proved difficult due to contamination of the HIMU component by depleted upper mantle material. However, the high $^{208}Pb/^{204}Pb$, at similar $^{206}Pb/^{204}Pb$ values, of the south Tasman Sea seamounts relative to other HIMU basalts may serve to expand the previously defined HIMU range in Pb-

Pb space. This study, while confirming the existence of a HIMU mantle plume within the higher latitudes of the southern hemisphere, as opposed to the Cook - Austral Islands and St. Helena at ~10°S to 20°S, also provides a context within which the continental areas surrounding the Tasman Sea - southwest Pacific Ocean can be examined for any evidence of Balleny Plume influence, particularly in relation to the break-up of Gondwana (Chapter 4).

CHAPTER 4

WIDESPREAD INFLUENCE OF THE BALLENY PLUME

4.1 INTRODUCTION:

Despite the degree of mixing with depleted upper mantle that is evident in the radiogenic isotope contents of the Balleny Plume volcanics, the plume itself has a distinctive HIMU-like isotopic signature, with high $^{206}Pb/^{204}Pb$, $^{207}Pb/^{204}Pb$, $^{208}Pb/^{204}Pb$ and $^{143}Nd/^{144}Nd$ values and low $^{87}Sr/^{86}Sr$ (Chapter 3). Balleny Plume volcanics also possess trace element characteristics, including low LILE/HFSE and LREE/HFSE abundance ratios (Chapter 3), typical of other HIMU volcanics (Chapter 2). The aim of this chapter is to use these distinctive HIMU-like isotopic and geochemical features to assess the more widespread influence of the Balleny Plume.

One area of interest involves the effect of the Balleny Plume on continental volcanism peripheral to the proposed plume trace. In this respect, areas of southeastern Australia, predominantly Victoria and Tasmania, are of particular concern as they experienced mafic volcanism prior to, during, and after the period that the East Tasman Plateau region was situated above the Balleny Plume, during which time the Soela Seamount was formed close to the east coast of Tasmania (Chapter 3). Comparison of the radiogenic isotope and trace element signatures of the mafic volcanics of southeastern Australia with those of the Balleny Plume is, therefore, aimed at further confirming the trace of the hotspot, as well as constraining the extent and timing of plume influence on continental volcanism in these regions.

Oceanic intraplate volcanism adjacent to the Balleny Plume trace includes the Tasmantid Seamount chain in the central Tasman Sea basin, and Lord Howe Island, the southernmost outcrop of another hotspot trace located north of the proposed start of the Balleny Plume trace on Lord Howe Rise. The radiogenic isotope compositions of the Tasmantid and Lord Howe hotspot traces, plus those of Macquarie Island, forming part of the complex Macquarie Ridge system in the central southwest Pacific Ocean, will also be examined here because of their relative proximity to the Balleny Plume trace.

Initiation of Balleny Plume volcanism, assumed to coincide with the oldest recognised seamount/s on the flanks of the Lord Howe Rise which can be attributed to the Balleny Plume, is roughly comparable in age to the onset of seafloor spreading in the Tasman Sea and southwest Pacific Ocean (Lanyon et al., 1993). The role of the Balleny Plume in initiating or propagating continental rifting in this region can be examined by studying the temporal and spatial relationships between regions of HIMU-like volcanism in the continental areas surrounding these oceanic basins, and the proposed trace of the Balleny Plume. Areas of particular interest include New Zealand (South Island and offshore islands), southeastern Australia (Tasmania) and West Antarctica (Marie Byrd Land), all of which were juxtaposed prior to the break-up of Gondwana.

The mafic volcanics of the Balleny Islands have been likened to the alkaline volcanic provinces of the McMurdo Volcanic Group (Harrington et al., 1967; Johnson et al., 1982; Campsie et al., 1983), including Ross Island in the western Ross Sea region and the Hallett Volcanic Province of Cape Adare, Northern Victoria Land. To test whether these more southerly regions of volcanism are related to the Balleny Plume, it is necessary to compare their isotopic and trace element systematics, as well as their relative temporal and spatial distributions, with those of the Balleny Plume volcanics.

4.2 BALLENY PLUME INFLUENCE ON CONTINENTAL VOLCANISM IN SOUTHEASTERN AUSTRALIA:

4.2.1 Eastern Australian Cainozoic Volcanism:

Widespread volcanism in eastern Australia over the last 70 m.y. has been subdivided into three distinct volcanic province types (Wellman and McDougall, 1974) on the basis of age, distribution and geochemical constraints. Central volcano provinces comprise predominantly slightly undersaturated to saturated basaltic flows, plus subordinate felsic lava flows and/or intrusions, erupted from well-defined volcanic vents. These provinces display a systematic southward younging which is generally assigned to the northward migration of eastern Australia over one or more upper mantle hotspots, currently located beneath Bass Strait (Wellman and McDougall, 1974; Duncan and McDougall, 1989). In contrast, mafic lava field provinces, dominated by strongly undersaturated basaltic lava flows or piles, have been erupted sporadically throughout the eastern Australian highlands and Tasmania over the last 70 m.y., but particularly between 50 and 30 Ma following the cessation of seafloor spreading in the Tasman Sea (Knutson et al., 1989). Their eruption has been assigned to unspecified intraplate stresses (Wellman and McDougall, 1974), often significantly prior to the formation of central volcano provinces at similar latitudes (Duncan and McDougall, 1989). The third type of volcanism, forming high potassium mafic (Wellman and McDougall, 1974) or leucitite suite provinces (Cundari, 1989), is dominated by minor leucitite-rich intrusions and rare lavas

which are confined to a 90 km-wide strip extending from central New South Wales to north-central Victoria.

The mafic lava field provinces of southeastern Australia, particularly the Victorian Older Volcanics and the Tasmanian Tertiary basalts, are of interest to this study primarily because of their location and timing of eruption, with respect to the Balleny Plume trace, and because they are not easily linked, in a temporal fashion, to the proposed eastern Australian hotspot/s. Day (1983) suggested that Victorian Mesozoic and Cainozoic volcanism may be related more directly to rifting events between Australia, Lord Howe Rise/New Zealand and Antarctica, which is consistent with the idea that the tectonics responsible for the eruption of the eastern Australian mafic lava field provinces as a whole are linked to the continental extension regime associated with the opening of the Tasman Sea (Knutson et al., 1989). Younger mafic lava field provinces, such as the Newer Volcanics of southeast Australia, which are contemporaneous with or younger than central volcano provinces in the same region, may represent eruptions from the marginal parts of the plumes responsible for the latter (Sun et al., 1989). Yet another model proposes that east Australian Cainozoic volcanism is due to plate migration over rift upwellings (Sutherland, 1991). According to this model, Tasmanian Tertiary volcanism is related to five migratory trails originating from Cato Trough-Tasman Sea rifting, whereas migration over the 95 Ma Gippsland-Tasman triple junction is held responsible for the generation of a line of seamounts, including the Janszoon and Soela Seamounts, across the southwest Tasman Sea.

The proposed trace of the Balleny Plume places it under the East Tasman Plateau, southeast of Tasmania, at 40±5 Ma, based on the ages obtained for Soela Seamount volcanism and the inferred ~43 Ma age of the bend in the plume trace (Chapter 3). The proximity of the plume trace to the southeastern continental margin of Australia between the times of eruption of the Janszoon and Soela Seamounts invokes the possibility of a Balleny Plume influence on continental volcanism in Tasmania and Victoria during, and maybe even after, this time, as a result of lateral flow and lithospheric underplating by plume material.

4.2.2 The Victorian Older Volcanics:

The Cretaceous to Tertiary (~95-19 Ma) Older Volcanics of Victoria (Figure 4.1) constitute one of the eastern Australian mafic lava field provinces (Wellman and McDougall, 1974; Day, 1983; 1989). They range in composition from nephelinite to quartz tholeiite basalt and have been subdivided into fifteen volcanic fields on the basis of outcrop distribution, borehole data and petrology (Day, 1989). Four main volcanic groups can be defined, however, on the basis of outcrop age and location alone (Day, 1983; 1989).

Although Day (1983) performed an extensive petrological and major element geochemical study of the Older Volcanics, trace element, particularly REE, data are relatively sparse and no isotope data are available in the literature. For the purposes of this study, samples were collected from each of the four major groups for geochemical and isotopic analyses in an attempt to ascertain whether the Balleny Plume had any significant

geochemical input and if so, when this input occurred. Sampling locations for the six Older Volcanics basalts analysed are detailed in Appendix 1 (Table A1.2). Major and trace element (Table 4.1) and radiogenic isotope (Tables 4.2 and 4.3) data were obtained for two basanite samples (OV2 and OV3) collected from the Group 1 (95-55 Ma; ages of volcanism from Day, 1989) Ballan Graben Province, a transitional alkali basalt* (OV1) from Cape Schank within the Group 2 (59-38 Ma) Flinders Province, quartz tholeiite (OV5) and olivine tholeiite (OV6) basalts from the Group 3 (44-31 Ma) Toombullup Province, and a transitional alkali basalt (OV4) from the Group 4 (29-19 Ma) Melbourne Province (Figure 4.1).

It must be noted, when considering the initial isotopic ratios calculated for the Older Volcanics samples (Table 4.2), that no REE data are available for samples OV2 and OV5. Therefore, Sm and Nd data for samples collected from the same provinces (as stipulated in the caption accompanying Table 4.2) were used to calculate their initial $^{143}Nd/^{144}Nd$ values. As a result, these particular ratios may be somewhat inaccurate.

In terms of their isotopic compositions, particularly $^{87}Sr/^{86}Sr$, $^{206}Pb/^{204}Pb$ and $^{208}Pb/^{204}Pb$, the Older Volcanics samples are relatively diverse (Tables 4.2 and 4.3; Figure 4.2). Considering such factors as the time frame over which they were erupted and their area of outcrop, the latter implying a potential for extensive source heterogeneity and/or differential contamination, this isotopic diversity is not surprising. Despite this, the Older Volcanics are most similar to the EM OIB fields in Figure 4.2, particularly EMII in terms of their Pb isotope values. Sample OV1 is distinct from the other Older Volcanics samples in terms of its low $^{87}Sr/^{86}Sr$ and high $^{143}Nd/^{144}Nd$, similar to the Balleny Plume volcanics. However, OV1 has $^{206}Pb/^{204}Pb$ and $^{208}Pb/^{204}Pb$ values which are significantly lower than Balleny Plume values and indistinct from the other Older Volcanics ratios. The timing of eruption of the Group 2 Flinders volcanic field (49-39 Ma; Day, 1983) does coincide with the location of the Balleny Plume close to the southeast Australian continental margin. Therefore, the isotopic composition of sample OV1 may be indicative of a plume influence in terms of $^{87}Sr/^{86}Sr$ and $^{143}Nd/^{144}Nd$. If this is the case, the low elemental Pb abundances and distinctive Pb isotopic ratios of the Balleny Plume (Table 3.12) may have been swamped by continental crust contamination (current continental crust Pb content is ~8600 ppb: $^{206}Pb/^{204}Pb$ = 18.6-18.9, $^{207}Pb/^{204}Pb$ = 15.58-15.65, $^{208}Pb/^{204}Pb$ = 39.6-39.8; Gariépy and Dupré, 1991) during the eruption of the Flinders volcanic field, resulting in the low $^{206}Pb/^{204}Pb$ and $^{208}Pb/^{204}Pb$ values of sample OV1. There is no other isotopic evidence in the few Older Volcanics samples analysed to suggest any Balleny Plume influence.

***Footnote:** All samples are classified according to the scheme of Le Bas et al. (1986); transitional alkali basalts contain normative hypersthene but plot above the Macdonald and Katsura (1964) line, as defined for Hawaiian basalts, on a TAS classification diagram.

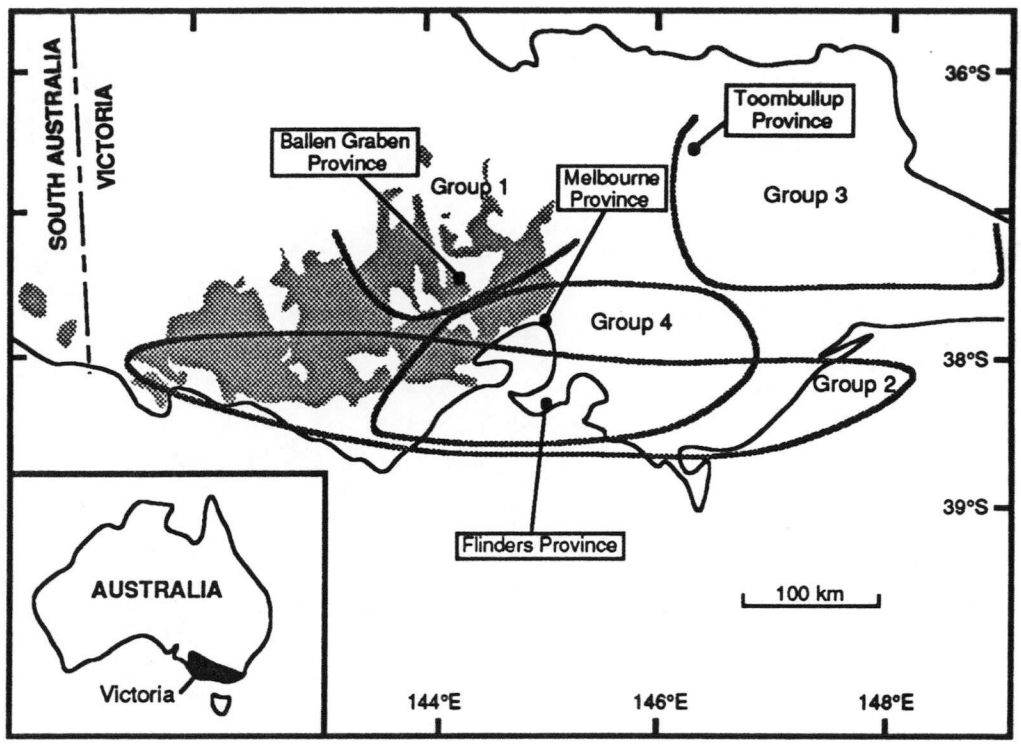

Figure 4.1: Map of Victoria and southeast South Australia (modified from Joyce and Day, 1989), showing the approximate areas of outcrop of the Older (Groups 1 to 4) and Newer (grey crosshatch pattern) Volcanics and the location of Older Volcanics sampling sites (filled circles) discussed in section 4.2.

It is difficult to draw any conclusions about the trace element compositions of the four temporal and geographical Older Volcanics groups due to the small number of samples analysed. Taken as a whole, they tend to overlap with the HIMU and Balleny Province volcanics in terms of their low Ba/Nb, La/Nb and intermediate Th/La and Th/Nb values, but they also extend to values which overlap with the EM OIB fields (Table 4.1; Figure 4.3). The alkaline basalts have low Zr/Nb values but the tholeiites (OV5 and OV6) have high Zr/Nb, suggesting that this may be a function of the degree of partial melting involved, rather than a source feature. Sample OV1 is no more similar to the Balleny Plume volcanics, in terms of the various trace element abundance ratios, than the other Older Volcanics basalts and does in fact have higher LILE/HFSE ratios than most of the other Older Volcanics samples, particularly in terms of Rb/Nb, K/Nb and Ba/Nb (Table 4.1).

The primitive mantle-normalised incompatible element patterns of three Older Volcanics samples (Figure 4.4) are slightly different. Quartz tholeiite sample OV5 has the flattest pattern, relative to the alkaline samples, which is probably due to it having been produced by higher degrees of partial melting. It does, however, still have similar features to basanite sample OV3, in terms of a pronounced negative K anomaly, enrichment in the HFSE Nb and Ta relative to the adjacent LILE, and decreasing normalised abundances of elements more incompatible than Ta. These same features are thought by some (e.g.

Table 4.1: Major and trace element compositions of the Victorian Older Volcanics samples discussed in section 4.2. All analyses were performed by XRF spectrometry (PW 1480 spectrometer) except Hf, Ta, Th (as indicated) and the REE which were analysed by INAA; analytical methods are described in Appendix 2.

Sample No:	OV1	OV2	OV3	OV4	OV5	OV6
Major Elements (wt %):						
SiO_2	45.23	40.23	39.88	49.80	46.88	46.76
TiO_2	1.92	2.69	2.67	2.16	2.57	2.73
Al_2O_3	14.20	12.51	12.47	14.46	13.06	12.75
Fe_2O_3	11.12	13.04	13.04	11.78	17.40	17.75
FeO	0.00	0.00	0.00	0.00	0.00	0.00
MnO	0.16	0.19	0.19	0.14	0.23	0.25
MgO	11.95	10.63	11.20	6.32	5.53	5.65
CaO	8.75	10.85	10.83	8.79	10.06	7.89
Na_2O	2.15	3.73	3.92	3.37	2.10	3.35
K_2O	1.12	0.81	0.94	1.38	0.16	0.12
P_2O_5	0.42	1.08	1.11	0.44	0.26	0.30
LOI	3.44	3.98	3.52	1.28	1.44	2.26
Total	100.46	99.74	99.77	99.92	99.69	99.81
Mg#	71.52	65.58	66.74	55.63	42.62	42.65
FeO*	10.01	11.73	11.73	10.60	15.66	15.97
Trace Elements (ppm):						
Ba	255	688	715	495	54	64
Rb	17	6	8	27	4	3
Nb	29	109	120	33	10	11
Sr	636	1551	1454	542	203	142
Zr	159	282	286	182	157	192
Y	24	31	32	34	50	56
Ni	336	250	250	163	56	46
Cr	477	314	317	313	83	63
V	192	222	224	198	551	557
Sc	24	22	22	21	47	44
Hf	2.93		4.98		4.04	
Ta	1.63		6.15		0.74	
Th (XRF)	2.70	9.10	9.90	4.30	1.60	<1.0
Th (INAA)	2.08		8.78		0.74	
Pb	<1.5	4.10	5.80	2.40	<1.5	<1.5
Rare Earth Elements (ppm):						
La	18.00		68.60		7.87	
Ce	37.20		136.00		22.10	
Nd	21.30		62.10		16.10	
Sm	4.74		10.30		5.56	
Eu	1.58		3.20		1.82	
Tb	0.77		1.22		1.19	
Ho	0.86		1.23		1.69	
Yb	1.79		2.08		4.47	
Lu	0.22		0.24		0.66	
Trace Element Ratios:						
Rb/Nb	0.586	0.057	0.064	0.840		
Ba/Rb	15.27	110.97	92.86	18.07	14.59	23.70
Ba/Th	94.44	75.60	72.22	115.12	33.75	
Ba/Nb	8.95	6.32	5.95	15.18	5.40	5.61
Ba/La	14.17		10.42		6.86	
Th/Nb	0.095	0.084	0.082	0.132	0.160	
Th/La	0.150		0.144		0.203	
Nb/Pb		26.54	20.72	13.58		
K/Nb	326	62	65	351	133	87
La/Nb	0.63		0.57		0.79	
Ce/Rb	2.23		17.66		5.97	
Ce/Pb			23.45			
Zr/Nb	5.58	2.59	2.38	5.58	15.70	16.84

Table 4.2: $^{87}Sr/^{86}Sr$ and $^{143}Nd/^{144}Nd$ data for the Victorian and Tasmanian samples discussed in section 4.2; errors ($2\sigma_{mean}$) associated with individual measurements indicate within-run precision only. Initial isotopic ratios were calculated using the equations in Appendix 6, ICP-MS trace element and REE data where available, and approximate ages from the following data sources: Cape Portland - McDougall and Green (1982); Bream Creek basalt (sample DR13516) - Baillie (1987); Weldborough basalt (sample 2) - Sutherland and Wellman (1986); Older Volcanics ages represent the maximum ages for each of the sampled volcanic fields from Day (1983). XRF Rb and Sr values (Table 4.1) were used to calculate the initial $^{87}Sr/^{86}Sr$ values of samples OV2, OV6, 11 and 13; their initial $^{143}Nd/^{144}Nd$ values were calculated using ICP-MS Sm and Nd data of samples collected from the same localities, namely OV3, OV5 and 10 respectively. Initial ε_{Sr} and ε_{Nd} values were calculated as described in Appendix 6. Analytical methods are described in Appendix 2.

Sample No.	Age	Rb (ppm)	Sr (ppm)	$^{87}Rb/^{86}Sr$	$^{87}Sr/^{86}Sr$	$\pm 2\sigma$	$(^{87}Sr/^{86}Sr)_i$	$(\varepsilon Sr)_i$	Sm (ppm)	Nd (ppm)	$^{147}Sm/^{144}Nd$
Older Volcanics, Victoria:											
OV1	49 Ma	15.65	623.17	0.0727	0.703263	9	0.703212	-17.5	4.90	21.48	0.1379
OV2	79 Ma	6.00	1551.00	0.0112	0.703740	16	0.703727	-9.7			
OV3	79 Ma	6.66	1379.47	0.0140	0.703832	19	0.703816	-8.4	10.59	61.46	0.1042
OV4	22 Ma	27.49	542.90	0.1465	0.704610	11	0.704564	1.3	8.28	36.90	0.1357
OV5	43 Ma	3.28	200.83	0.0473	0.704849	18	0.704820	5.3	5.17	16.57	0.1887
OV6	43 Ma	3.00	142.00	0.0611	0.705033	35	0.704996	7.8			
Cape Portland, Tasmania:											
10	100 Ma	61.54	734.64	0.2424	0.704547	22	0.704203	-2.5	6.35	31.14	0.1233
11	100 Ma	45.00	775.00	0.1680	0.704781	16	0.704542	2.3			
13	100 Ma	91.00	1057.00	0.2491	0.704840	12	0.704486	1.5			
Tasmanian Tertiary basalts:											
DR 13516	58 Ma	24.75	902.88	0.0793	0.703262	9	0.703197	-17.5	6.92	36.78	0.1138
2	46 Ma	23.04	649.57	0.1026	0.703156	15	0.703089	-19.3	6.62	34.38	0.1164

Table 4.2: (continued)

Sample No.	$^{143}Nd/^{144}Nd$	$\pm 2\sigma$	$(^{143}Nd/^{144}Nd)_i$	$(\varepsilon Nd)_i$
Older Volcanics, Victoria:				
OV1	0.513002	13	0.512958	7.2
OV2	0.512869	13	0.512815	5.2
OV3	0.512831	7	0.512777	4.5
OV4	0.512755	12	0.512735	2.2
OV5	0.513056	2	0.513003	8.0
OV6	0.513007	6	0.512954	7.0
Cape Portland, Tasmania:				
10	0.512693	4	0.512612	1.8
11	0.512614	7	0.512533	0.2
13	0.512684	12	0.512603	1.6
Tasmanian Tertiary basalts:				
DR 13516	0.512966	10	0.512923	6.8
2	0.512914	9	0.512879	5.6

Table 4.3: $^{206}Pb/^{204}Pb$, $^{207}Pb/^{204}Pb$ and $^{208}Pb/^{204}Pb$ data for the Victorian and Tasmanian samples discussed on 4.2. Initial isotopic ratios were calculated equations in Appendix 6, the same approximate ages used in Table 4.2, and ICP-MS trace element data where available. The initial isotopic ratios of Cape Portland sample 11 were calculated using the U, Pb and Th abundances of sample 10. Analytical methods are described in Appendix 2.

Sample No.	Age	U (ppm)	Th (ppm)	Pb (ppm)	μ	κ	$^{206}Pb/^{204}Pb$	$(^{206}Pb/^{204}Pb)_i$	$^{207}Pb/^{204}Pb$	$(^{207}Pb/^{204}Pb)_i$	$^{208}Pb/^{204}Pb$	$(^{208}Pb/^{204}Pb)_i$
Older Volcanics, Victoria:												
OV1	49 Ma	0.75	2.26	1.90	25.31	3.25	18.965	18.772	15.578	15.569	38.654	38.454
OV3	79 Ma	2.31	9.93	5.96	25.28	4.44	19.312	19.000	15.617	15.602	39.537	39.097
OV4	22 Ma	0.95	4.25	4.18	14.53	4.62	18.618	18.568	15.599	15.597	38.731	38.658
OV5	43 Ma	0.20	0.77	0.98	13.22	3.98	19.371	19.283	15.560	15.556	39.038	38.926
Cape Portland, Tasmania:												
10	100 Ma	2.55	8.16	7.16	23.02	3.31	19.097	18.737	15.707	15.690	39.016	38.638
11	100 Ma				22.83	3.31	18.720	18.363	15.616	15.599	38.857	38.483
Tasmanian Tertiary basalts:												
DR 13516	58 Ma	1.55	5.93	3.19	31.34	3.95	19.154	18.871	15.569	15.556	38.892	38.536
2	46 Ma	1.42	5.12	2.21	41.44	3.73	19.408	19.111	15.563	15.549	39.204	38.852

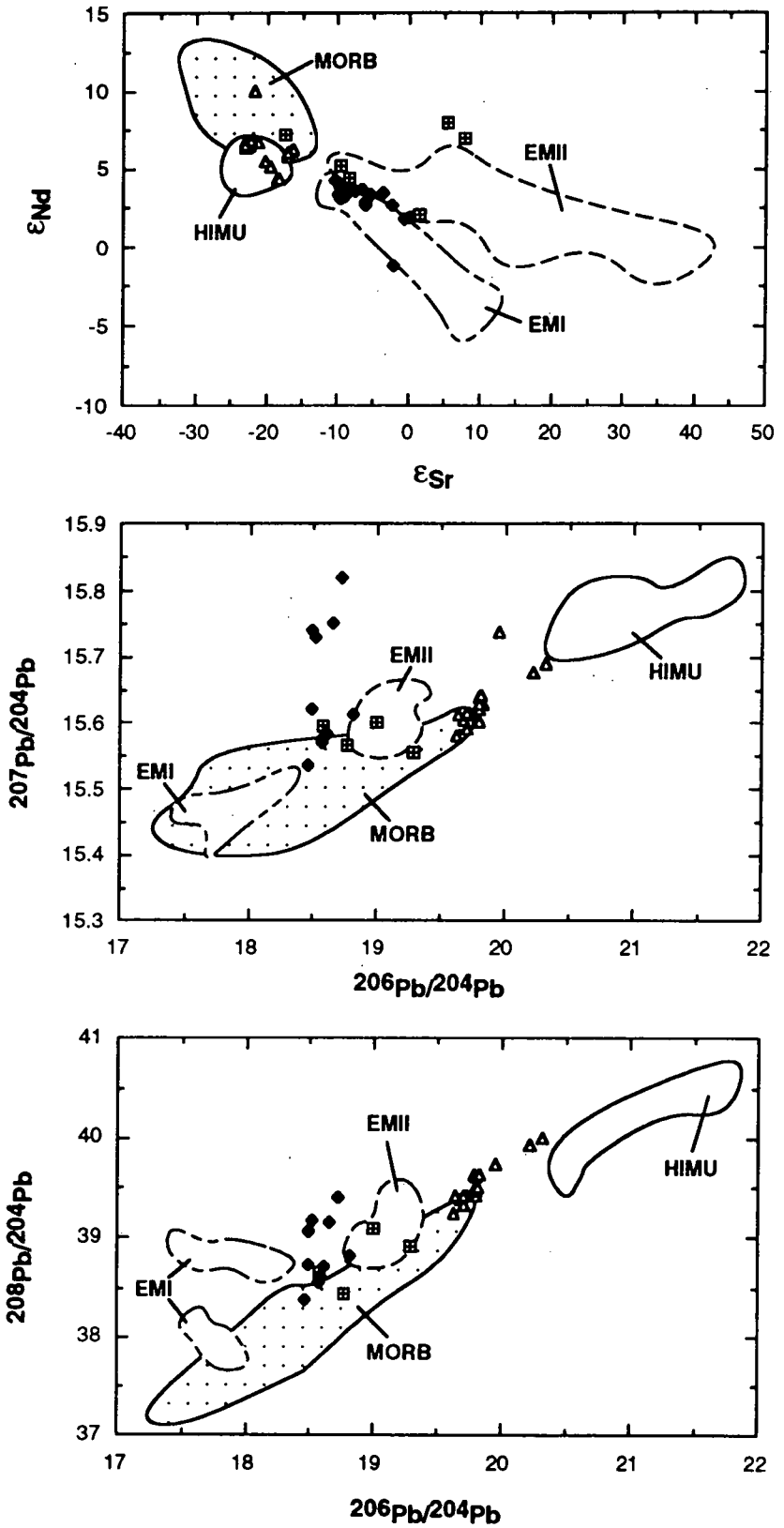

Figure 4.2: Radiogenic isotope plots comparing the southeast Australian Older (crosses within squares) and Newer (filled diamonds) alkaline volcanics with the Balleny Plume volcanics (open triangles) and the HIMU, EMI and EMII OIB and MORB isotopic fields. Data sources for the isotopic end-member fields are as for Figure 1.1; *Newer Volcanics* data sources - Cooper and Green (1969), McDonough et al. (1985) and Ewart et al. (1988). Initial ratios are plotted for all samples measured during the course of this study. Balleny Plume data include the Balleny Islands values of Hart (1988), age corrected as for Figure 3.20; all other literature-derived data are normalised as for Figure 1.1, but are not age-corrected due to the lack of corresponding trace element data.

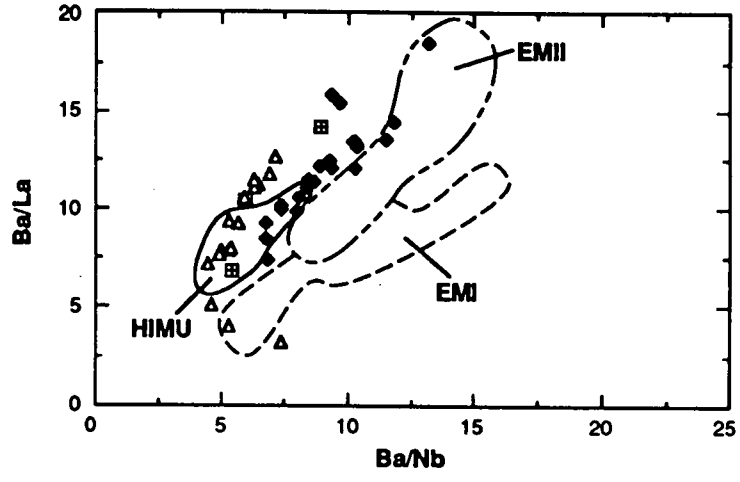
Ba/La
Ba/Nb
EMII
EMI
HIMU
0
5
10
15
20
25

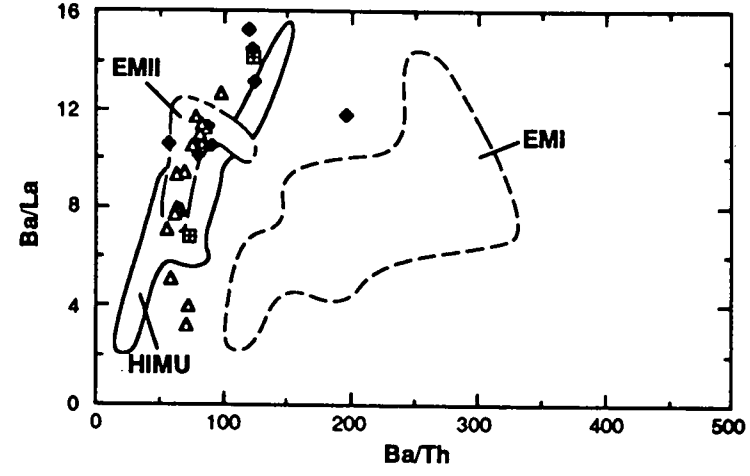
Ba/La
Ba/Th
EMII
EMI
HIMU
0
4
8
12
16
100
200
300
400
500

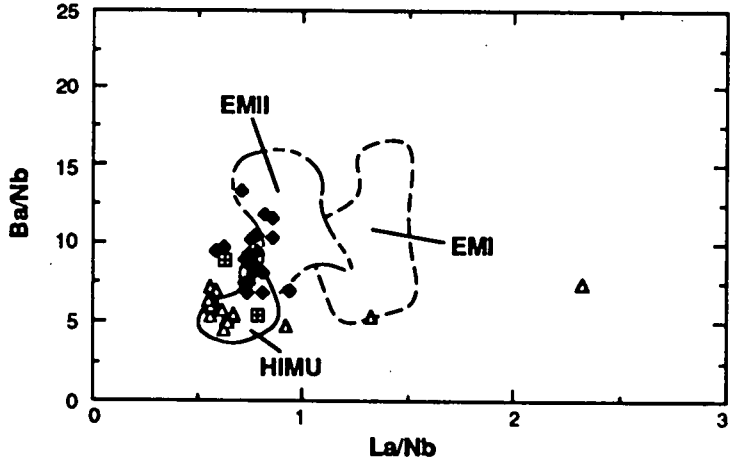
Ba/Nb
La/Nb
EMII
EMI
HIMU
0
5
10
15
20
25
1
2
3

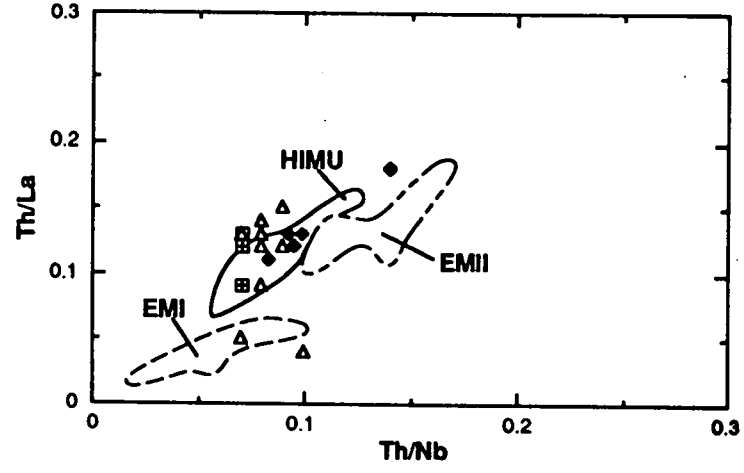
Th/La
Th/Nb
HIMU
EMII
EMI
0
0.1
0.2
0.3

(Figure 4.3)

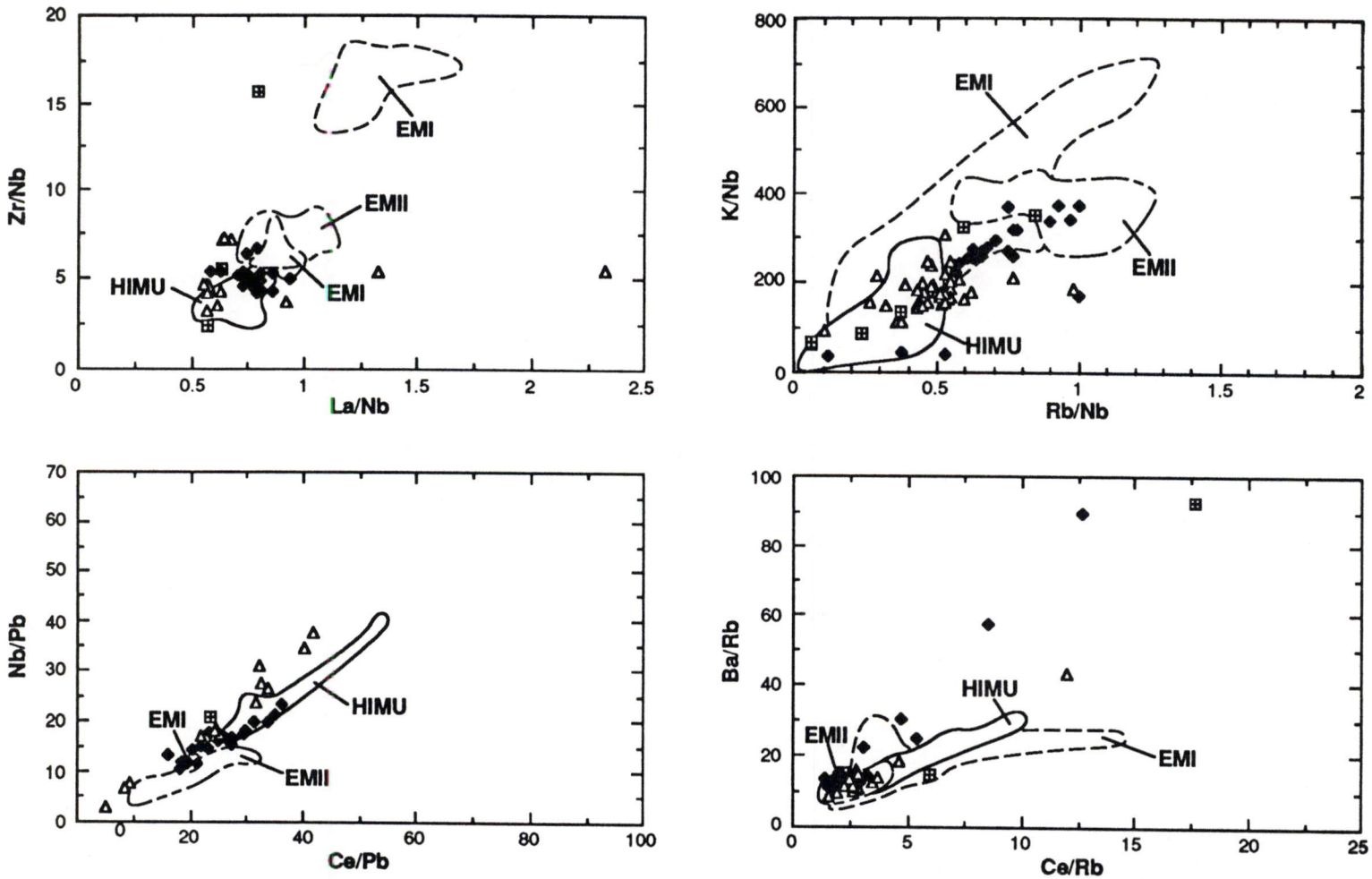

Figure 4.3: Trace element abundance ratio plots comparing the southeast Australian Older (crosses within squares) and Newer (filled diamonds) alkaline volcanics with the Balleny Plume volcanics (open triangles) and the HIMU, EMI and EMII OIB fields; the latter circumscribe the bulk of the end-member data but the complete ranges are shown in Figure 2.10. Data sources include: OIB end-member fields - as for Table 2.1; *Newer Volcanics* - Frey et al. (1978), Ewart et al. (1988) and McDonough et al. (1985); only samples with ≥5 wt % MgO have been used. Balleny Plume volcanics include the Balleny Islands data of Green (1992) and J.Foden (unpublished data).

Weaver, 1991) to be characteristic of HIMU OIB and were observed in the Balleny Plume volcanics (Figures 3.13 and 3.15). However, it should be noted that these features were also observed in some of the EM OIB (e.g. Pitcairn Island/Seamount samples) examined in Chapter 2. The transitional alkali basalt sample OV1 has a similar overall pattern, of increasing normalised trace element abundances with increasing incompatibility, to sample OV3, although the relatively lower abundances in the former reflect slightly greater extents of partial melting. The low LILE/HFSE features of samples OV3 and OV5 are not evident in sample OV1, implying different source chemistry for the latter which is, however, inconsistent with Balleny Plume influence (Chapter 3).

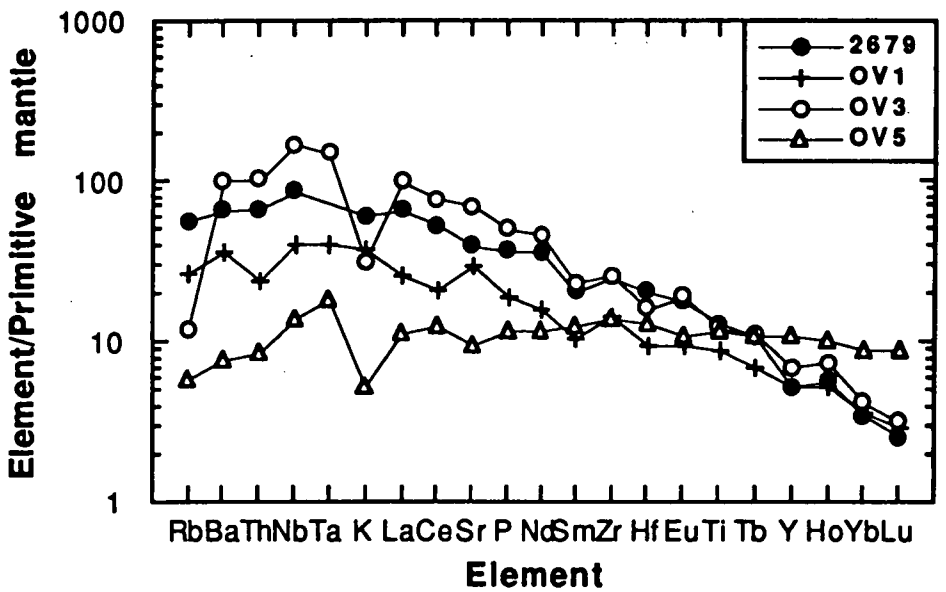

Figure 4.4: Primitive mantle-normalised incompatible element patterns of a basanite (sample 2679; Frey et al., 1978) from the Newer Volcanics mafic lava field province and three Older Volcanics samples (OV1, OV3 and OV5); normalising values from Sun and McDonough (1989).

4.2.3 The Newer Volcanics of Victoria and South Australia:

The Late Tertiary to Holocene (4.5-<0.01 Ma; McDougall et al., 1966; Nicholls and Joyce, 1989) Newer Volcanics outcrop over a 15,000 km^2 area of western and central Victoria and southeast South Australia (Figure 4.1), and comprise a broad range of tholeiitic and alkaline basalt compositions plus minor trachytes (Irving and Green, 1976; McDonough et al., 1985; Nicholls and Joyce, 1989). Only data for Newer Volcanics samples with alkaline affinities will be considered here.

Despite their relative proximity to the proposed Balleny Plume trace, the Newer Volcanics were erupted at a time when the plume itself underlay the Antarctic Plate and was forming the Balleny Islands. In a strict temporal framework therefore, a lack of isotopic

similarity between the alkaline Newer Volcanics and the Balleny Plume volcanics (Figure 4.2) is to be expected. The large ranges in the $^{207}Pb/^{204}Pb$ and $^{208}Pb/^{204}Pb$ contents of the Newer Volcanics overlap with the Balleny Plume and HIMU OIB values, but their $^{206}Pb/^{204}Pb$ values define a limited range, similar, but intermediate to, the EMI and EMII OIB fields. The relatively high $^{87}Sr/^{86}Sr$ and low $^{143}Nd/^{144}Nd$ values of the alkaline Newer Volcanics, compared to the Balleny Plume volcanics, are most similar to EMI OIB.

An isotopic comparison of the Older and Newer Volcanics reveals similar values, in terms of all three isotopic systems, for the Newer Volcanics and the Group 4 Melbourne Province sample (OV4), the youngest of the analysed Older Volcanics. Although the Group 1 Older Volcanics samples (OV2 and OV3) also have similar $^{87}Sr/^{86}Sr$ and $^{143}Nd/^{144}Nd$ values to the Newer Volcanics, sample OV3 has significantly higher $^{206}Pb/^{204}Pb$. In general, the Newer Volcanics have lower $^{206}Pb/^{204}Pb$ plus narrower ranges of $^{143}Nd/^{144}Nd$ and $^{87}Sr/^{86}Sr$ than the Older Volcanics.

In terms of their trace element contents, the alkaline Newer Volcanics have generally higher Rb/Nb, K/Nb, Ba/Nb and La/Nb and lower Nb/Pb at similar Ce/Pb values than the Balleny Plume Volcanics (Figure 4.3). The comparatively lesser depletion of the Newer Volcanics in LILE relative to Nb is also visible in Figure 4.4 in which the normalised abundances of K and LILE more incompatible than Nb are only slightly depleted in the Newer Volcanics basanite (2679; Frey et al., 1978) compared to the Older Volcanics samples (OV3 and OV5). However, sample 2679 does display the same general incompatible element pattern to the Older Volcanics and Balleny Plume samples, as discussed in section 4.2.2.

4.2.4 Tasmanian Cretaceous Igneous Activity:

The trace of the Balleny Plume was originally only projected back from the Balleny Islands to the region east of Tasmania (Duncan, 1981), where minor outcrops of alkaline hypabyssal rocks at Port Cygnet and Cape Portland (Figure 4.5) were thought to reflect earlier loci of Balleny Plume activity at ~100 Ma (Duncan and McDougall, 1989).

Cretaceous alkaline rocks outcropping in the Port Cygnet - Oyster Cove area of southeast Tasmania have been dated at 99 and 109 Ma (Evernden and Richards, 1962) and 98±3 Ma (McDougall and Leggo, 1965), resulting in a preferred age of 99 Ma (Ford, 1989). Ford (1983) measured the $^{87}Sr/^{86}Sr$ values of two Port Cygnet syenite porphyries and two sanidine porphyry dyke samples. Initial ratios (corrected to an age of 95 Ma) range from 0.7036 to 0.7049, significantly higher than Balleny Plume values. Similar Port Cygnet rocks yielded $^{207}Pb/^{204}Pb$ and $^{206}Pb/^{204}Pb$ values of 15.620-15.628 and 18.638-18.650 respectively (J. Richards, unpublished data), the latter significantly lower than Balleny Plume values, but similar to the Tasmanian Jurassic dolerites (Figure 4.6). No $^{208}Pb/^{204}Pb$ values are available for the Port Cygnet samples.

The Cape Portland appinitic suite comprises flows, dykes and plug-like intrusions of andesite, lamprophyre and porphyrite (Ford, 1989), which have been dated at 101.3-

102.3±2.6 Ma (McDougall and Green, 1982). Sampling locations for the three Cape Portland rocks analysed during the course of this study are listed in Appendix 1 (Table A1.2). Radiogenic isotope measurements (Tables 4.2 and 4.3) show that the Cape Portland samples have significantly higher $^{87}Sr/^{86}Sr$ and lower $^{143}Nd/^{144}Nd$, $^{206}Pb/^{204}Pb$ and $^{208}Pb/^{204}Pb$ values than the Balleny Plume volcanics. Therefore, despite their relatively high $^{207}Pb/^{204}Pb$ values, the Cape Portland alkaline intrusives are isotopically unlike the Balleny Plume volcanics (Figure 4.6). Sr and Nd isotope ratios are quite similar to EMI OIB values, whereas Pb ratios are more like EMII OIB. As with the Older Volcanics, trace element and REE data are not available for certain of the Cape Portland samples analysed here for radiogenic isotopes. Therefore, the calculated initial $^{143}Nd/^{144}Nd$ values of samples 11 and 13, plus the Pb isotope ratios of sample 11 (Tables 4.2 and 4.3) may be inaccurate.

The Cape Portland appinites have similar $^{87}Sr/^{86}Sr$ values to the Port Cygnet rocks, and Pb isotope values which plot on either side of the Port Cygnet and Tasmanian Jurassic dolerite values in $^{206}Pb/^{204}Pb$-$^{207}Pb/^{204}Pb$ space. These results suggest that the Cape Portland and Port Cygnet hypabyssal assemblages may have similar isotopic signatures and, combined with age constraints, imply similar sources. However, more isotope data, including $^{143}Nd/^{144}Nd$ and $^{208}Pb/^{204}Pb$ values, are required for the Port Cygnet porphyries.

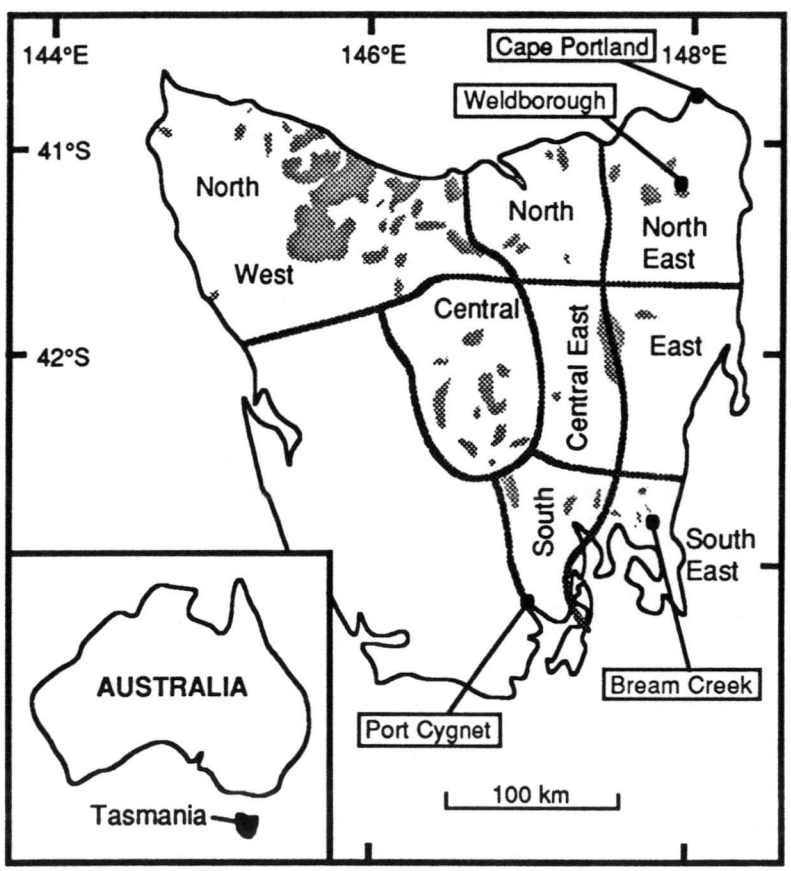

Figure 4.5: Map of Tasmania (modified from Sutherland, 1989) showing the approximate outcrop distribution of the Tertiary volcanics (grey crosshatch pattern), the province subdivisions, and the sampling locations for the Cape Portland, Port Cygnet, Weldborough and Bream Creek samples discussed in section 4.2.

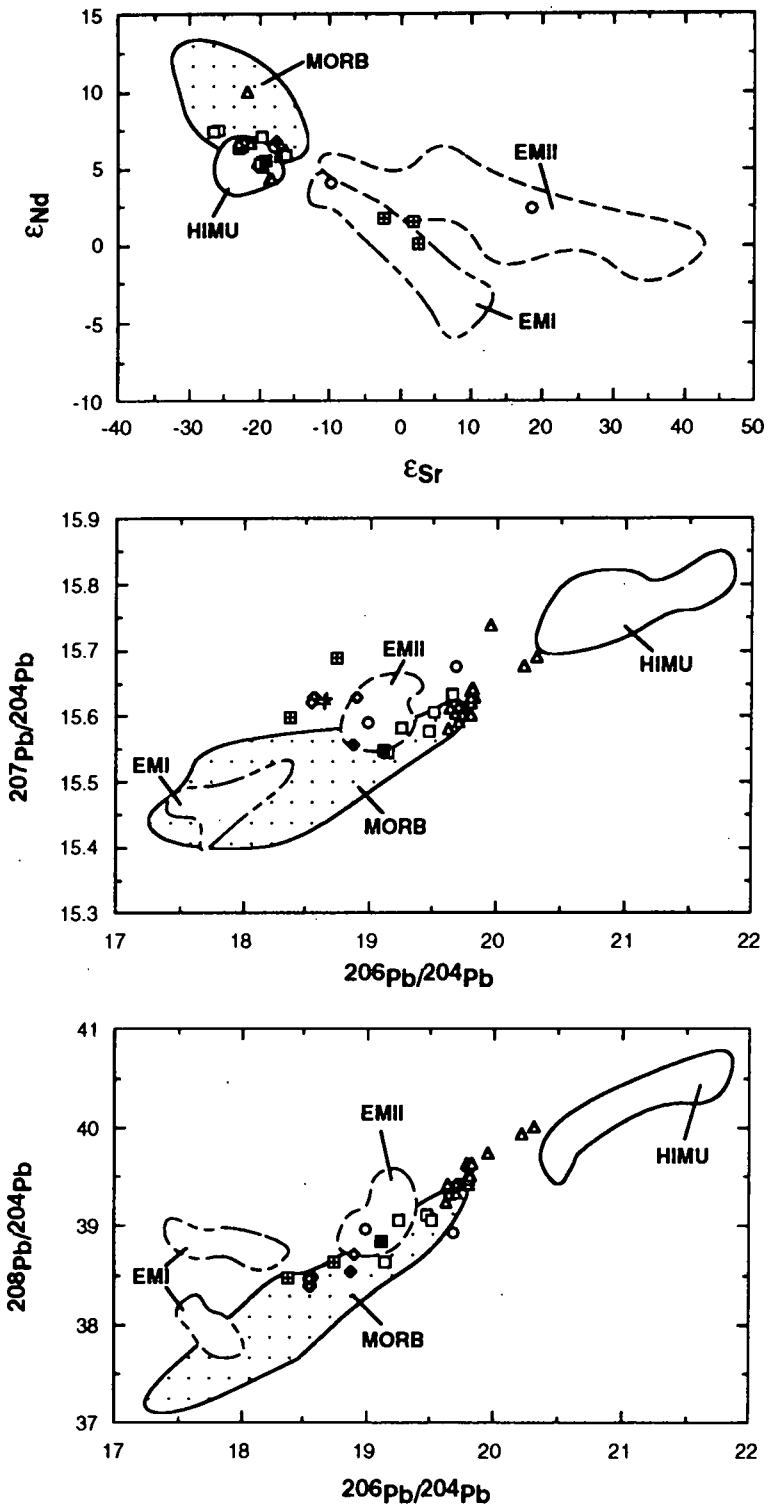

Figure 4.6: Radiogenic isotope plots comparing Cape Portland (crosses within squares) and Port Cygnet (crosses - $^{206}Pb/^{204}Pb$ versus $^{207}Pb/^{204}Pb$ plot only) alkaline hypabyssal rocks, Tasmanian Jurassic dolerites (open diamonds - Pb plots only), Tasmanian Tertiary alkaline volcanics (open squares), including the Bream Creek (filled diamond) and Weldborough (filled square) basalt samples and Tasmanian Tertiary tholeiites (open circles), with the Balleny Plume volcanics (open triangles) and the HIMU, EMI and EMII OIB and MORB isotopic fields. Data sources for the isotopic end-members are as for Figure 1.1. Balleny Plume volcanics include the Balleny Islands ratios of Hart (1988). Other data sources include: *Port Cygnet* Pb data - J. Richards (unpublished data); *Tasmanian Jurassic dolerites* - Hergt et al. (1989a); *Tasmanian Tertiary alkaline volcanics* - McDonough et al. (1985), Ewart et al. (1988) and Varne (unpublished data). Initial ratios are plotted for all samples measured during the course of this study; Tasmanian Jurassic dolerite data are age corrected to 175 Ma; the Balleny Islands data of Hart (1988) are age corrected as for Figure 3.20; other literature-derived data are normalised as for Figure 1.1, but are not age-corrected due to the lack of corresponding trace element data.

4.2.5 Tasmanian Tertiary Volcanism:

Tertiary basalts outcrop as scattered strongly undersaturated alkaline to saturated tholeiitic flows and plugs over a 400 km^3 area of northern and eastern Tasmania (Figure 4.5) (Edwards, 1938; Compston et al., 1968; McDonough et al., 1985; Sutherland, 1989), and comprise the southernmost eastern Australian mafic lava field province (Duncan and McDougall, 1989). Dated samples display an age range of 58 to 8 Ma (Sutherland and Wellman, 1986), although pre-58 Ma transitional to olivine tholeiite basalts have also been recognised (Sutherland, 1989).

Compared to the other eastern Australian Cainozoic volcanics, the Tasmanian Tertiary alkaline volcanics are considered to be quite distinctive, with the highest $^{143}Nd/^{144}Nd$, $^{206}Pb/^{204}Pb$ and $^{208}Pb/^{204}Pb$ and lowest $^{87}Sr/^{86}Sr$ values yet measured for eastern Australian Tertiary basalts (Ewart et al., 1988; Ewart and Menzies, 1989). The low Sr and high Nd isotope ratios suggest long-term depletion of the Tasmanian mantle source region (McDonough et al., 1985), whereas the Pb isotope ratios indicate high time-integrated U/Pb and Th/Pb source values. These same, apparently paradoxical, isotope systematics are displayed by HIMU OIB (Chapter 1) and the Balleny Plume volcanics (Chapter 3), the latter considered to have some influence on the formation of the Tasmanian Tertiary alkaline basalts (Lanyon et al., 1993).

The geochemical (Table 4.4) and radiogenic isotope (Tables 4.2 and 4.3) compositions of two Tasmanian Tertiary basalts (Figure 4.6) were determined during the course of this study; details of sampling locations are listed in Appendix 1 (Table A1.2). The Bream Creek alkali basalt (DR13516) has been dated at 58.5±0.7 Ma (Baillie, 1987) and represents the earliest dated phase of Tasmanian Tertiary volcanism, located in the Southeast Province. Weldborough alkali basalt sample 2 is a product of 46-47 Ma volcanism (Sutherland and Wellman, 1986) in the Northeast Province of Tasmania.

The Weldborough basalt analysed during this study plots in a similar position to other Tasmanian Tertiary alkaline basalts in terms of the isotopic systems depicted in Figure 4.6. However, although the Bream Creek alkali basalt has similar $^{87}Sr/^{86}Sr$ and $^{143}Nd/^{144}Nd$ values to other analysed Tasmanian Tertiary alkaline basalts and the Balleny Plume volcanics, its Pb values are less distinct. Compared to the other Tasmanian Tertiary alkaline basalts, the Bream Creek basalt has slightly lower $^{206}Pb/^{204}Pb$ and $^{208}Pb/^{204}Pb$ values, similar $^{207}Pb/^{204}Pb$, and plots at the least radiogenic end of the approximately linear arrays formed by the Tasmanian and Balleny alkaline volcanics in Pb-Pb space (Figure 4.6). Although the Bream Creek basalt overlaps slightly with the Cape Portland and Tasmanian Jurassic dolerite $^{206}Pb/^{204}Pb$ and $^{208}Pb/^{204}Pb$ values, its higher μ value (31.34) may be indicative of influence from a HIMU source. Interpretation of the isotope systematics of the Bream Creek basalt, the oldest analysed Tasmanian Tertiary basalt, has implications for the timing of Balleny Plume influence on Tasmanian volcanism which will be discussed further in section 4.2.6.

Table 4.4: Major and trace element compositions of the Tasmanian samples discussed in section 4.2. All analyses were performed by XRF spectrometry (PW 1480 spectrometer); the analytical method is described in Appendix 2. Samples RT 56 and K 51 correspond to the base and top of the Benders Hill sequence from which the Bream Creek basalt sample DR 13516 was collected, and these analyses are as reported by Everard (1984).

Location:	Cape Portland, Tasmania:			Tasmanian Tertiary basalts:		
Sample No:	10	11	13	RT 56	K 51	2
Major Elements (wt %):						
SiO_2	50.56	50.14	51.21	45.30	45.12	44.28
TiO_2	0.89	1.45	1.22	1.50	1.60	2.12
Al_2O_3	16.66	13.56	16.82	14.29	14.97	14.94
Fe_2O_3	9.07	10.35	10.10	3.35	2.91	11.81
FeO	0.00	0.00	0.00	7.50	7.89	0.00
MnO	0.18	0.17	0.22	0.15	0.15	0.18
MgO	3.32	7.19	3.77	9.95	10.14	9.73
CaO	6.60	8.82	8.01	10.79	9.59	10.36
Na_2O	3.62	2.49	3.58	2.78	3.43	3.18
K_2O	3.05	1.72	2.78	1.12	1.23	0.99
P_2O_5	0.47	0.66	0.74	1.10	1.03	0.57
LOI	5.45	3.35	2.25	1.99	2.00	1.31
Total	99.87	99.90	100.70	99.82	100.06	99.47
Mg#	46.11	61.89	46.60	66.56	67.00	65.83
FeO*	8.16	9.31	9.09	10.51	10.51	10.63
Trace Elements (ppm):						
Ba	955	789	804	580	590	370
Rb	110	45	91	28	31	20
Nb	36	13	19	68	68	59
Sr	1346	775	1057	1000	990	669
Zr	284	167	261	180	190	226
Y	35	30	34	27	29	29
Ni	16.5	57	7	200	220	200
Cr	18	172	16	330	300	405
V	143	304	196	185	175	212
Sc	10	36	18	26	22	26
Hf						
Ta						
Th (XRF)	13.7	7.6	10.5			5.4
Pb	7.6	8.3	6.3	<4	<4	2.2
Rare Earth Elements (ppm):						
La	50	35	41			43
Ce	98	66	85			80
Nd	46	34	42			36
Trace Element Ratios:						
Rb/Nb	3.06	3.46	4.79	0.41	0.46	0.34
Ba/Rb	8.68	17.53	8.84	20.71	19.03	18.50
Ba/Th	69.71	103.82	76.57			68.52
Ba/Nb	26.53	60.69	42.32	8.53	8.68	6.27
Ba/La	19.10	22.54	19.61			8.60
Th/Nb	0.381	0.585	0.553			0.092
Th/La	0.274	0.217	0.256			0.126
Nb/Pb	4.74	1.57	3.02			26.82
K/Nb	703	1098	1215	137	150	139
La/Nb	1.39	2.69	2.16			0.73
Ce/Rb	0.89	1.47	0.93			4.00
Ce/Pb	12.89	7.95	13.49			36.36
Zr/Nb	7.89	12.85	13.74	2.65	2.79	3.83

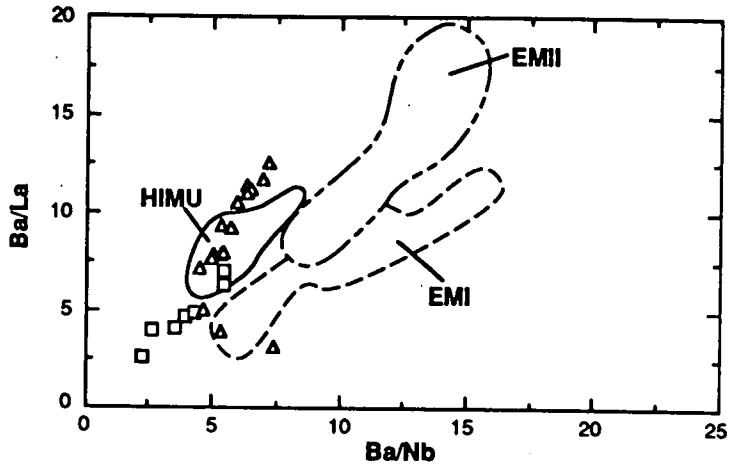
Ba/La
Ba/Nb
EMII
HIMU
EMI
0
5
10
15
20
25

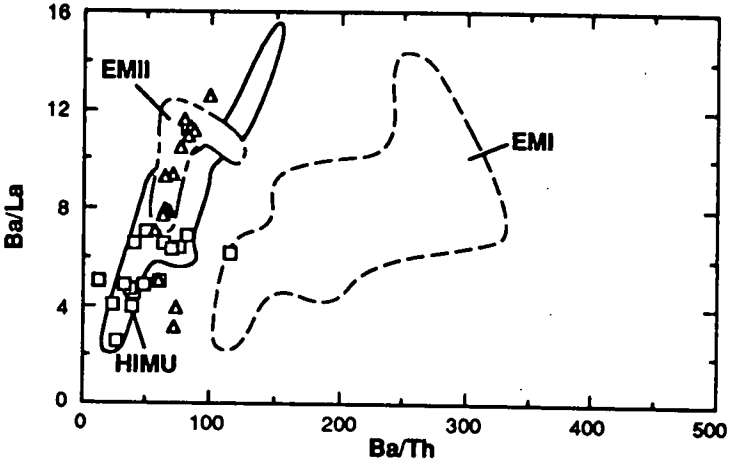
Ba/La
Ba/Th
EMII
EMI
HIMU
0
4
8
12
16
100
200
300
400
500

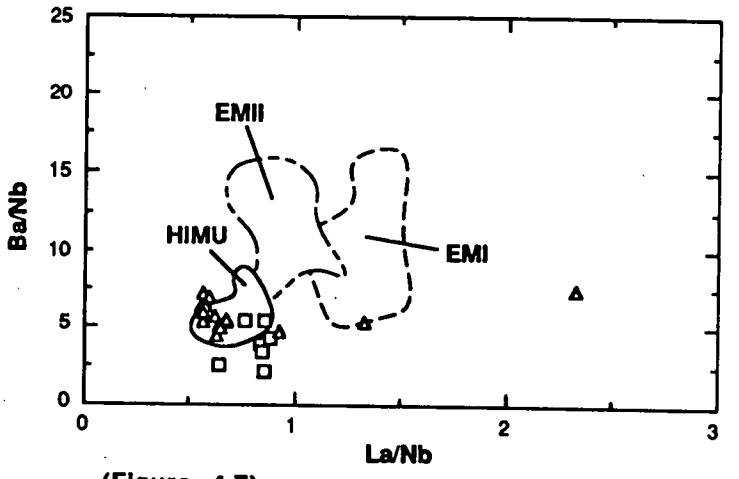
Ba/Nb
La/Nb
EMII
HIMU
EMI
0
5
10
15
20
25
1
2
3

(Figure 4.7)

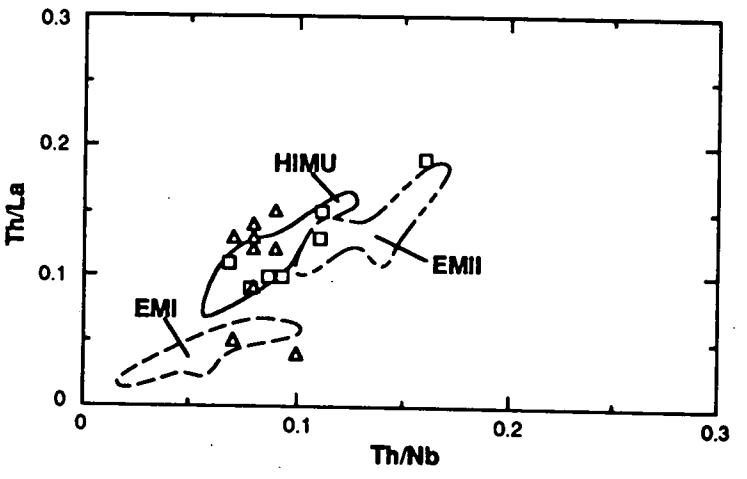
Th/La
Th/Nb
HIMU
EMII
EMI
0
0.1
0.2
0.3

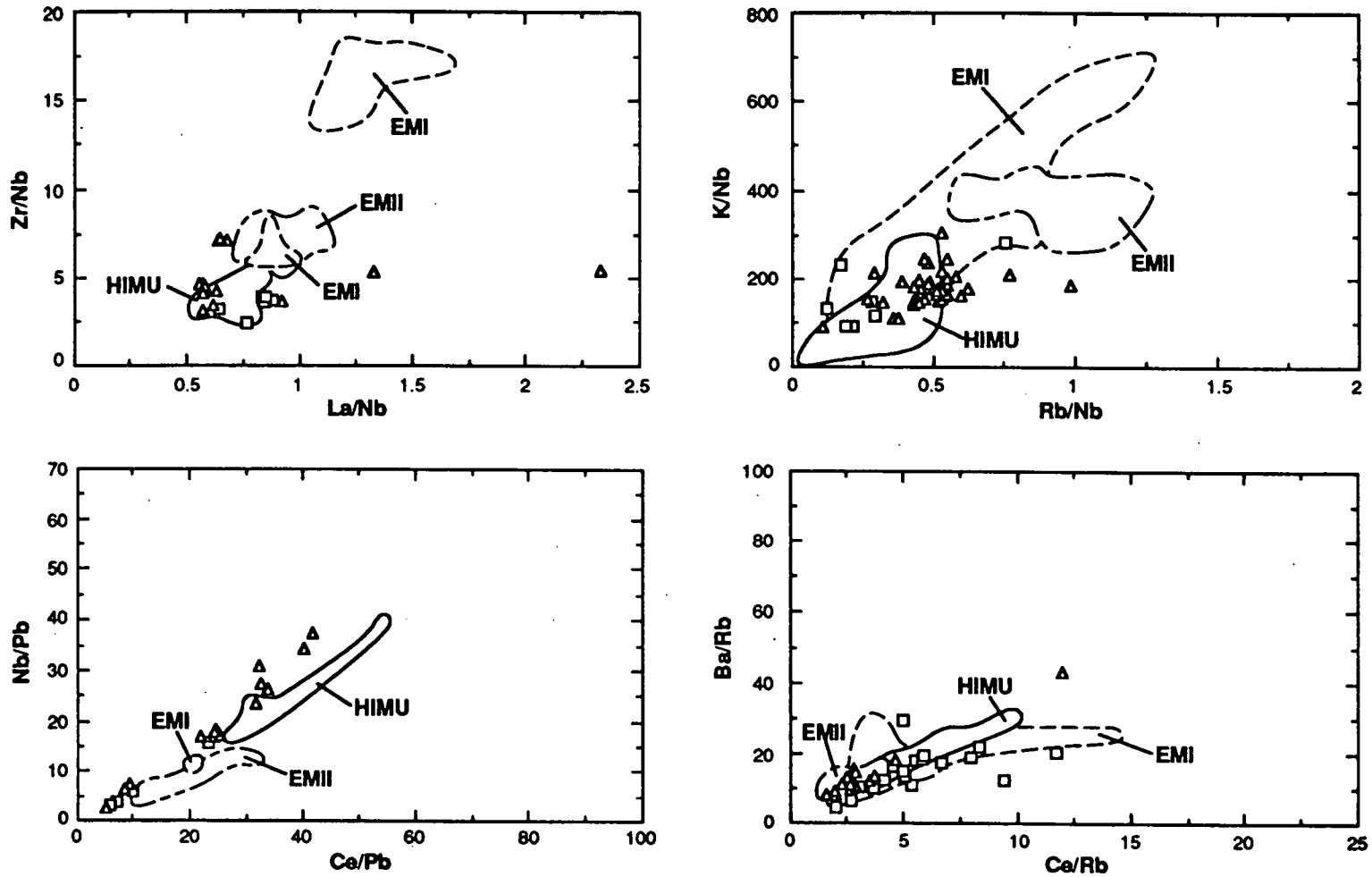

Figure 4.7: Trace element abundance ratio plots comparing the Tasmanian Tertiary alkaline volcanics (open squares) with the Balleny Plume volcanics (open triangles) and the HIMU, EMI and EMII OIB fields. OIB end-member fields as for Figure 4.3; Balleny Plume volcanics include the Balleny Islands data of Green (1992) and J.Foden (unpublished data). *Tasmanian Tertiary alkaline volcanics* data sources - Frey et al. (1978), Ewart et al. (1988) and W.F. McDonough (unpublished data); only samples with ≥5 wt % MgO have been used.

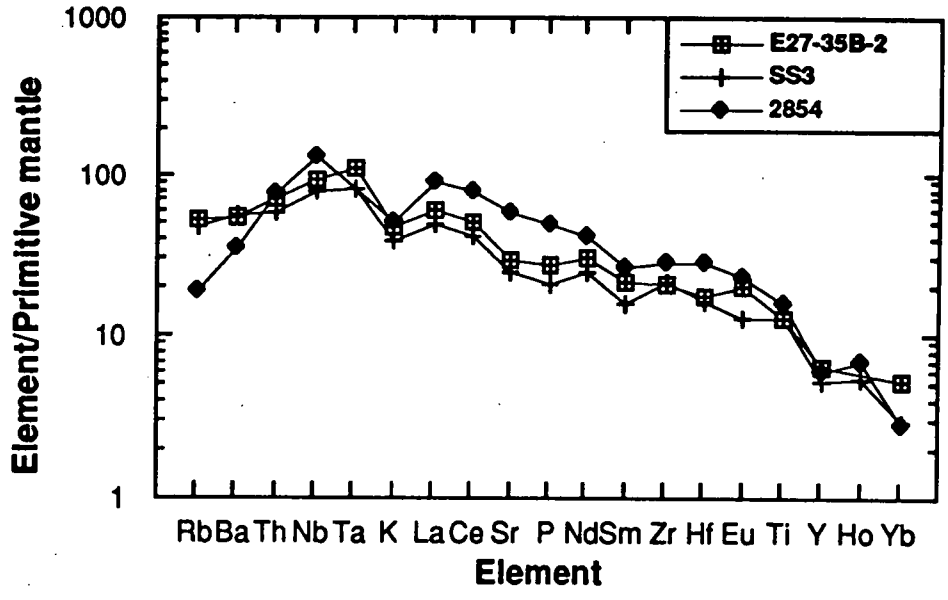

Figure 4.8: Primitive mantle-normalised incompatible element patterns of a Balleny Province basanite (E27-35B-2), a Soela Seamount alkali olivine basalt (SS3) and a Tasmanian Tertiary basanite (2854; Frey et al., 1978); normalising values from Sun and McDonough (1989).

Although there is a relative paucity of isotope data for the Tasmanian Tertiary tholeiitic basalts, they are considered to have generally lower $^{143}Nd/^{144}Nd$ and higher $^{87}Sr/^{86}Sr$ values (Compston et al., 1968; Ewart et al., 1988; Ewart and Menzies, 1989) (Figure 4.6). Two samples analysed for Pb isotope ratios (Ewart et al., 1988; Varne, unpublished data) have higher $^{207}Pb/^{204}Pb$ at similar $^{206}Pb/^{204}Pb$ values to the alkaline basalts, and similar $^{208}Pb/^{204}Pb$ values (Figure 4.6).

Although trace element data for the Tasmanian Tertiary alkaline volcanics are relatively limited, they do display low K/Nb, Rb/Nb, Zr/Nb, La/Nb and Ba/Nb values similar to Balleny Plume and HIMU values (Figure 4.7). Ba/Nb and Rb/Nb are slightly lower in the Tasmanian volcanics, which may be indicative of slightly greater LILE depletion in their source. Nb/Pb and Ce/Pb values in the Tasmanian basalts plot mainly within the lower end of the Balleny Plume array, a possible consequence of Pb addition during contamination of the plume source, particularly if a lithospheric component is involved in the production of the Tasmanian basalts. Slight LREE/LILE and LREE/HFSE enrichment of the Tasmanian alkaline basalts relative to the Balleny Plume volcanics is indicated by the generally higher La/Nb and lower Ba/La values of the former.

The primitive mantle-normalised incompatible element pattern of a representative Tasmanian Tertiary basanite (sample 2854; Frey et al., 1978) displays similar features to both

Balleny Province and Soela Seamount samples (Figure 4.8). The overall pattern is one of increasing elemental abundance with increasing degrees of incompatibility, and a relative depletion in the most incompatible LILE compared to the adjacent HFSE (Nb). As has been discussed previously (e.g. Chapter 2), this overall pattern is typical of many OIB, not only those with HIMU affinities.

4.2.6. Possible Models for the Formation of the Tasmanian Tertiary Basalts:

Frey et al. (1978) suggested that the Tertiary to Recent basalts of Victoria and Tasmania derive from enriched source regions within a heterogeneous upper mantle, similar to those of OIB or continental and rift-valley basaltic provinces. According to this model, differential mantle enrichment is considered to result from migration within the upper mantle of a H_2O/CO_2-enriched melt or fluid. McDonough et al. (1985) proposed that the mixing of two melt components, a mantle plume-derived melt and a lithospheric mantle-derived melt was involved in the production of the southeast Australian Cainozoic basalts, including the Newer Volcanics and the Tasmanian Tertiary volcanics. They proposed that observed isotopic differences between the alkaline and tholeiitic Tasmanian basalts could be due to different degrees of mixing and exchange between the two mantle-melt components involved in their production.

Whereas the HIMU-like isotopic character of the Tasmanian Tertiary alkaline volcanics is considered by some to reflect a lithospheric mantle signature, possibly due to the upwelling of CO_2-rich asthenospheric melts (Sun et al., 1989), Ewart et al. (1988) recognised the involvement of an asthenospheric isotopic end-member component with a composition approaching that of HIMU OIB (St. Helena). Lanyon et al. (1993) pointed out that the distinctive HIMU-like isotopic characteristics of the Tasmanian alkaline volcanics are similar to those of the Balleny Plume volcanics (Figure 4.6). They therefore inferred that horizontal spreading, lithospheric underplating and subsequent melting of Balleny Plume material during the passage of the East Tasman Plateau region of the Indian-Australian Plate over the plume was responsible for Tasmanian Tertiary volcanism.

The Tasmanian Tertiary alkaline volcanics do differ, however, from the Balleny Plume volcanics in that they extend to lower $^{206}Pb/^{204}Pb$ and $^{208}Pb/^{204}Pb$ values, forming an approximately linear array in $^{206}Pb/^{204}Pb$-$^{208}Pb/^{204}Pb$ space, which appears to represent a less radiogenic extension of the Balleny Plume array. They also have slightly higher $^{207}Pb/^{204}Pb$ at similar $^{206}Pb/^{204}Pb$ values compared to the Balleny Plume volcanics (Figure 4.6). These differences could be due to lithospheric contamination of the plume. This seems likely in a scenario where the plume has intersected the base of the lithosphere in the region of the East Tasman Plateau, spread out horizontally beneath Tasmania and eroded the overlying lithosphere, resulting in contamination of a Balleny Plume-derived melt by a sub-Tasmanian lithospheric mantle-derived melt. The most likely contaminant in this case would be the Tasmanian Jurassic dolerite source. Due to the extensive area of outcrop of Jurassic dolerite over ~30,000 km^2, approximately half the area of Tasmania (Hergt et al.,

1989b), it seems likely that some remnant of their source may persist within the lithosphere beneath Tasmania. The position occupied by the Tasmanian Jurassic dolerite field in $^{206}Pb/^{204}Pb$-$^{208}Pb/^{204}Pb$ space (Figure 4.6) could represent one possible end-member of a linear mixing array responsible for the isotopic signature of the Tasmanian Tertiary basalts, with the Balleny Plume representing the other end-member. However, the high initial $^{87}Sr/^{86}Sr$ (0.70940-0.71284) and low initial $^{143}Nd/^{144}Nd$ (0.512156-0.512181) values (not plotted in Figure 4.6) of the Tasmanian dolerites (Hergt et al., 1989a), indicative of continental crustal involvement in their generation (Hergt et al., 1989a; Hergt, 1989b), and their position in $^{206}Pb/^{204}Pb$-$^{207}Pb/^{204}Pb$ space (Figure 4.6) are not consistent with this idea.

Assuming that the Balleny Plume is, in fact, a relatively weak plume in terms of its buoyancy flux, and that it has already entrained a considerable amount of upper mantle material due to substantial horizontal deflection of the ascending plume conduit (Chapter 3), by the time it has intersected and spanned out at the base of the lithosphere in the Tasmanian region its temperature may have been much reduced, resulting in very little lithospheric melting. Therefore, although weaker plumes are generally considered to be subject to greater initial lithospheric entrainment due to the supposition that they fail to penetrate through the lithosphere as easily as stronger plumes (e.g. Woodhead, 1992), the Balleny Plume material interacting with the Tasmanian lithosphere may not have been hot enough to remelt and incorporate Tasmanian dolerite source material, resulting in the lack of isotopic correlation between the Jurassic dolerites and the Tertiary alkaline basalts. An alternative possibility is that lithospheric contamination of the underplating Balleny Plume material was dominated by an isotopic signature similar to depleted MORB mantle, but this seems an unlikely composition for subcontinental lithosphere.

The most likely process responsible for the isotopic deviation of the Tasmanian Tertiary alkaline basalts from the Balleny Plume volcanics appears to be greater incorporation and melting of depleted upper mantle. Although the isotopic compositions of the Tasmanian Tertiary basalts overlap with the lower end of the Balleny Plume range in Pb-Pb space, none of the Tasmanian basalts are as radiogenic as the Janszoon or Soela Seamount samples, suggesting that the plume conduit or diapir (see Chapter 3) was already contaminated by upper mantle material to the extent necessary to produce the Janszoon/Soela Seamount basalts prior to the further contamination required for the Tasmanian Tertiary isotopic signature. This added upper mantle incorporation may have occurred during the period that the Tasmanian lithosphere was underplated by the Balleny Plume, or as a consequence of the actual plume flattening and underplating process. However, it is also possible that the underplating plume material failed to physically entrain any extra upper mantle, but that the already entrained material underwent more, or possibly even preferential, melting during production of the Tasmanian alkaline volcanics, resulting in their slightly more MORB-like isotopic signature.

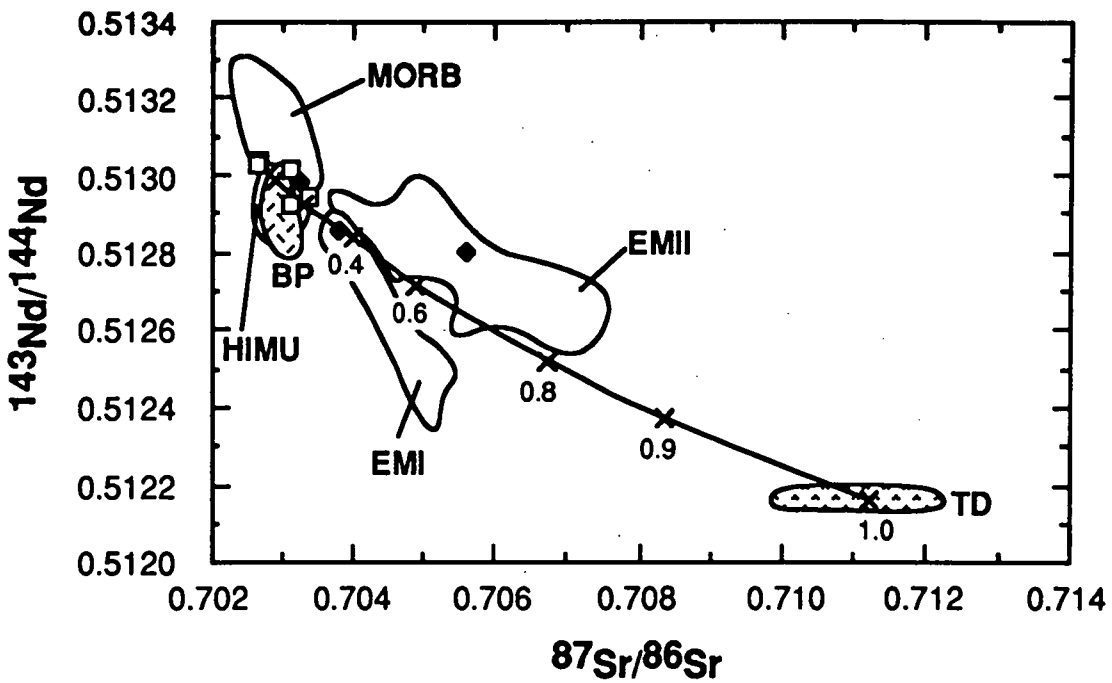

Figure 4.9: $^{87}Sr/^{86}Sr$ versus $^{143}Nd/^{144}Nd$ mixing hyperbola between Tasmanian Jurassic dolerite (TD) and Balleny Plume (BP) end-members in relation to Tasmanian Tertiary alkaline (open squares) and tholeiitic (filled diamonds) volcanics and the HIMU, EMI and EMII OIB and MORB isotopic fields. Data sources include: *Tasmanian Tertiary volcanics* - Compston et al. (1968), McDonough et al. (1985), Ewart et al. (1988), W.F. McDonough (unpublished data) and R. Varne (unpublished data); *Tasmanian Jurassic dolerite field* (TD) - Hergt et al. (1989a); *Balleny Plume field* - Hart (1988) and this study. Tasmanian Jurassic dolerite data are age corrected to 175 Ma; the Balleny Islands data of Hart (1988) are age corrected as for Figure 3.20; other literature-derived data are normalised as for Figure 1.1, but are not age-corrected due to the lack of corresponding trace element data.
Mixing hyperbola equation:

$$(^{143}Nd/^{144}Nd)_M = \frac{(^{143}Nd/^{144}Nd)_A \cdot Nd_A f + (^{143}Nd/^{144}Nd)_B \cdot Nd_B(1-f)}{Nd_A f + Nd_B(1-f)}$$

where f = 1 = pure A (average Tasmanian dolerite: Sr values n=14; Nd values n=12)
and f = 0 = pure B (Balleny Province sample E27-35B-2)
$(^{143}Nd/^{144}Nd)_A = 0.512166$; $Nd_A = 12.51$ $(^{143}Nd/^{144}Nd)_B = 0.512992$; $Nd_B = 37.68$
$(^{87}Sr/^{86}Sr)_A = 0.711191$; $Sr_A = 139.54$ $(^{87}Sr/^{86}Sr)_B = 0.702882$; $Sr_B = 656.61$

Despite the lack of evidence for lithospheric contamination in the Tasmanian Tertiary alkaline volcanics, it may still be a possibility for the production of their tholeiitic equivalents. The scarcity of isotopic data for the Tasmanian tholeiites makes this difficult to assess however, particularly in terms of Pb isotopes. Mixing between Balleny Plume and Tasmanian Jurassic dolerite end-members has therefore been attempted in Sr-Nd space only (Figure 4.9). Two of the three Tasmanian tholeiites plotted do appear to lie along the mixing hyperbola, suggesting increasing degrees of Jurassic dolerite contamination. The third,

however, lies within the EMII field and appears to reflect contamination by something other than Jurassic dolerite. These tentative results suggest that heterogeneous lithospheric contamination may have been responsible for the isotopic differences between the Tasmanian Tertiary alkaline and tholeiitic basalts.

Greater contamination of tholeiitic melts may be a product of the higher temperatures and greater degrees of melting responsible for their production, and/or the more volatile-rich nature of alkaline melts. The latter may result in the more rapid eruption of alkaline volcanics, as compared to pre-eruptive pooling of tholeiitic melts at the base of the crust or lithospheric mantle, where their higher temperature may result in melting and incorporation of overlying material, including the Tasmanian Jurassic dolerite source. The degree of contamination will be constrained by the amount of lithospheric melting and incorporation and the degree of lithospheric heterogeneity encountered.

If the isotopic signature of the Bream Creek alkali basalt is interpreted to reflect influence from the Balleny Plume, as proposed for the younger (≤47 Ma) Tasmanian Tertiary alkaline basalts (Lanyon et al., 1993), the Tasmanian lithosphere must have been underplated by plume material from at least 58 Ma to ~13 Ma (the latter date representing the age of the youngest dated Tasmanian basalt plotted in Figure 4.6: Sutherland and Wellman, 1986) , and maybe even until Tasmanian volcanism ceased at ~8 Ma. Although the younger HIMU-like volcanism could be explained by recurrent melting and eruption of remnant Balleny plume material attached to, or incorporated into, the base of the lithosphere beneath Tasmania, subsequent to the passage of the East Tasman Plateau region over the plume tail, the isotopic systematics of the older Bream Creek volcanism are more difficult to explain. According to the proposed Balleny Plume trace, the plume would have been situated east of Janszoon Seamount at ~58 Ma, too distant from Tasmania to have had a significant effect on continental volcanism in that region. This therefore seems to negate the idea of Lanyon et al. (1993) that the timing of Balleny Plume influence on Tasmanian Tertiary volcanism was coeval with and subsequent to the passage of this region of the Indian-Australian Plate over the plume.

4.2.7 Summary of Balleny Plume Influence on Southeast Australian Volcanism:

The lack of isotopic similarity between the Cretaceous alkaline intrusives of Port Cygnet and Cape Portland in Tasmania and the Balleny Plume volcanics implies that the plume had no influence on the composition of their source, which underlay Tasmania at ~100 Ma. The mafic lava field provinces of Victoria and southeastern South Australia, outcropping as the Older and Newer Volcanics, appear to have derived from EM-like source regions, and also display no signs of significant Balleny Plume input.

However, Tasmanian Tertiary alkaline volcanism, long recognised as being isotopically distinct from volcanism on mainland eastern Australia (e.g. Ewart et al., 1988; Ewart and Menzies, 1989), has a HIMU-like isotopic signature similar to the Balleny Plume

volcanics. A review of Tasmanian alkaline basalts up to ~47 Ma ascribed this distinctive isotopic signature to input from the Balleny Plume as it underlay the region east of Tasmania during the Eocene (Lanyon et al., 1993). However, the discovery that even older Tasmanian volcanism, based on the recent analysis of the ~58 Ma Bream Creek alkali basalt, also bears a similar isotopic signature to the younger Tasmanian and the Balleny Plume volcanics makes it difficult to reconcile the proposed spatial evolution of the Balleny Plume with Tasmanian Tertiary volcanism as proposed by Lanyon et al. (1993). This does not, however, preclude a Balleny Plume influence on Tasmanian volcanism, but the timing must be reconsidered in terms of plume underplating prior to the separation of Australia and Lord Howe Rise/New Zealand. This idea will be examined further in section 4.4.

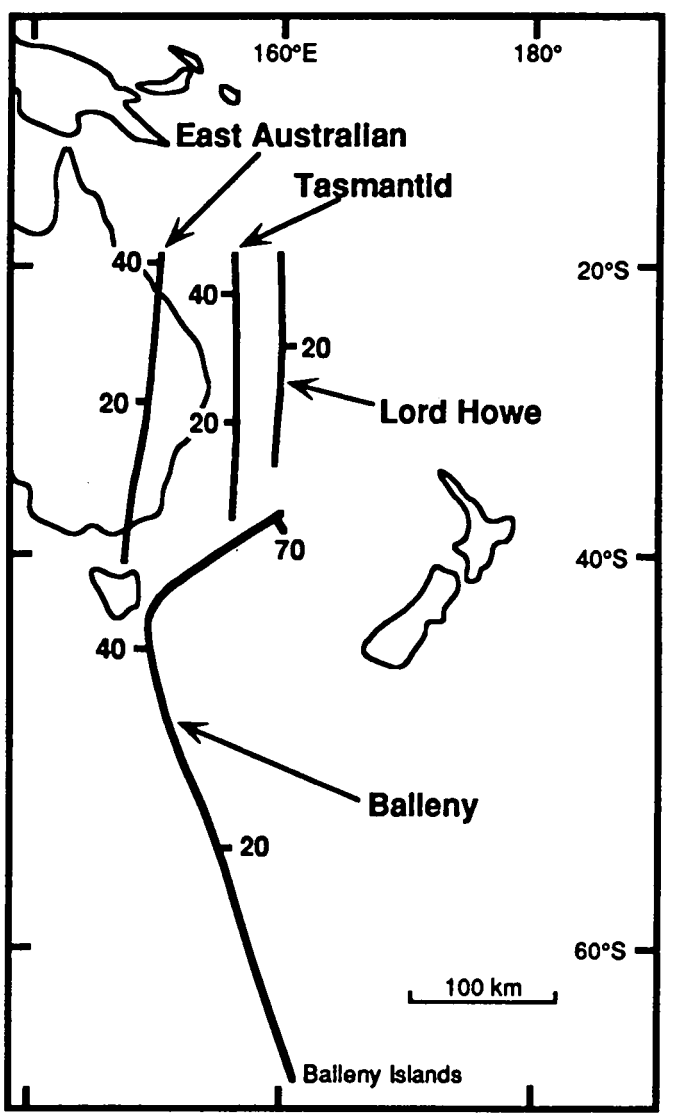

Figure 4.10: Map showing the approximate paths and timing relationships of the eastern Australian, Tasmantid, Lord Howe and Balleny hotspot traces (modified from Duncan and McDougall, 1989 and Jenkins et al., 1992)

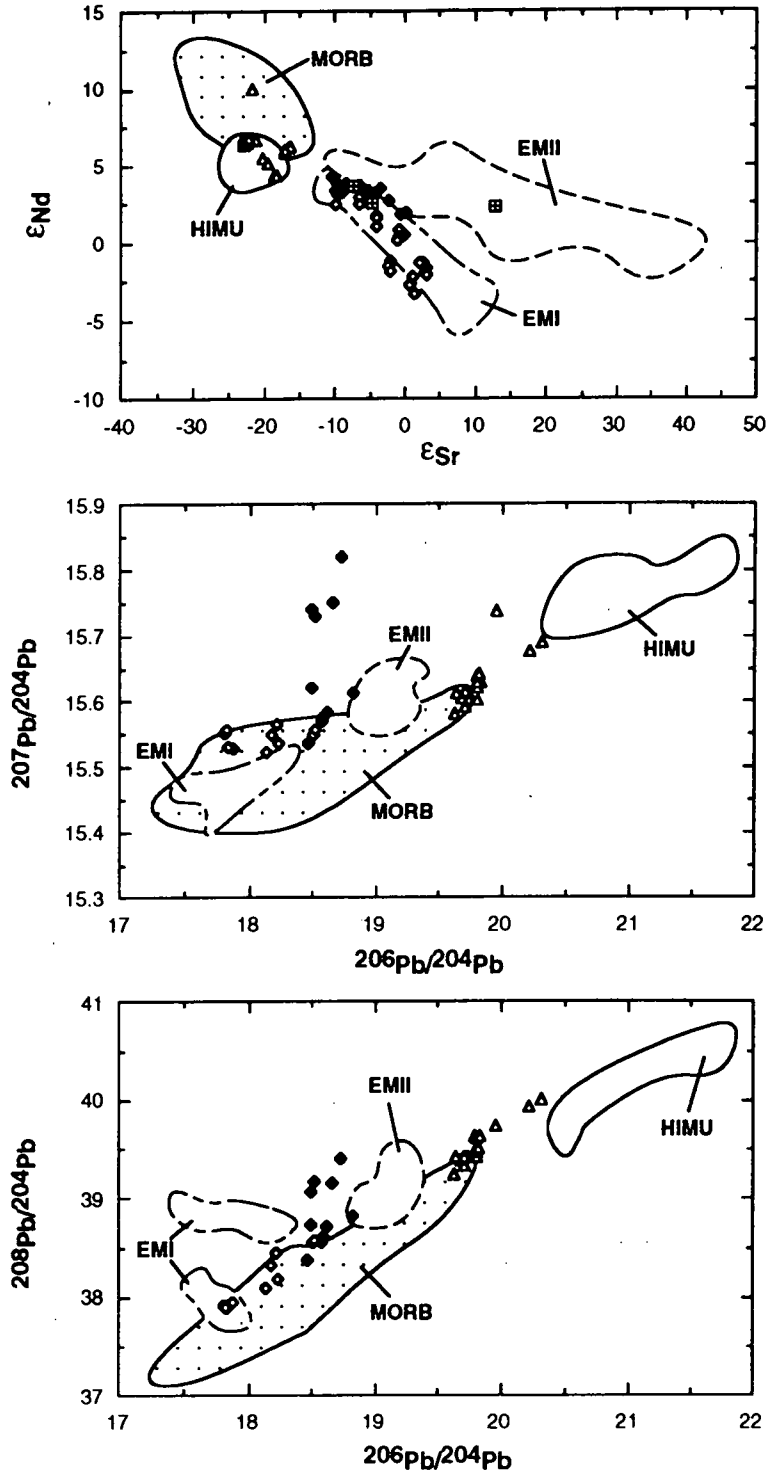

Figure 4.11: Radiogenic isotope plots of the southeast Australian Newer alkaline volcanics (filled diamonds) versus the Tasmantid Seamounts (open diamonds), Lord Howe Island (crosses within squares - $^{87}Sr/^{86}Sr$ versus $^{143}Nd/^{144}Nd$ plot only) and Balleny Plume (open triangles) volcanics and the HIMU, EMI and EMII OIB and MORB isotopic fields. Data sources for the isotopic end-members are as for Figure 1.1. Balleny Plume volcanics include the Balleny Islands ratios of Hart (1988). Other data sources include: *Newer Volcanics* - Cooper and Green (1969), McDonough et al. (1985) and Ewart et al. (1988); *Tasmantid Seamounts* - M.T. McCulloch (unpublished data); *Lord Howe Island* - W.F. McDonough (unpublished data). Initial ratios are plotted for all samples measured during the course of this study; the Balleny Islands data of Hart (1988) are age corrected as for Figure 3.20; other literature-derived data are normalised as for Figure 1.1, but are not age-corrected due to the lack of corresponding trace element data.

4.3 THE BALLENY PLUME AND THE TASMANTID AND LORD HOWE SEAMOUNT CHAINS:

The Tasmantid Seamounts comprise a 1300 km long north-south trending hotspot chain located on Late Mesozoic to Early Tertiary (Palaeocene) oceanic crust in the central Tasman Sea basin (e.g. Vogt and Conolly, 1971; McDougall and Duncan, 1988). They demonstrate a progressive southward decrease in age from 24 to 6.4 Ma (McDougall and Duncan, 1988), consistent with a migration rate of 67±5 mm/year for the Indian-Australian Plate over a fixed mantle plume source, and parallel, both spatially and temporally, the eastern Australian hotspot trace/s as delineated by the central volcano provinces (Figure 4.10). Both the alkali olivine and tholeiitic basalts comprising the Tasmantid Seamounts have significantly higher $^{87}Sr/^{86}Sr$, and lower $^{143}Nd/^{144}Nd$, $^{206}Pb/^{204}Pb$, $^{207}Pb/^{204}Pb$ and $^{208}Pb/^{204}Pb$ values than the Balleny Plume volcanics (Figure 4.11). A study of the Tasmantid Seamounts by Eggins et al. (1991) concluded that their isotope and trace element signatures trend towards the EMI mantle end-member component, resemble some mainland eastern Australian Cainozoic basalts, including the Newer Volcanics, and can therefore be regarded as part of the Dupal anomaly (Chapter 1). Although the youngest (6.4 Ma; McDougall and Duncan, 1988) and most southerly recognised Tasmantid Seamount, Gascoyne Tablemount (Figure 4.12), is located only ~375 km northeast of Janszoon Seamount, the significantly older age of the latter, plus its HIMU-like isotopic and trace element signature (Chapter 3), precludes any possibility of a genetic relationship between these two Tasman Sea seamounts.

Lord Howe Island is also associated with a southward-younging hotspot trace which parallels both the Tasmantid and eastern Australian hotspot paths (Figure 4.10). This 6.7 Ma (McDougall et al., 1981) island lies approximately 500 km directly north of the Zeehan-Heemskirk Seamounts, which represent the eastern most sampled projection of the Balleny Plume trace (Figure 4.10; Chapter 3). Compared to the Balleny Plume volcanics, the few available isotope ratios for Lord Howe Island indicate that the latter has much higher $^{87}Sr/^{86}Sr$ and lower $^{143}Nd/^{144}Nd$, which plot within the EMI-EMII isotopic fields (Figure 4.11). The significant isotopic and age differences between the Lord Howe Island basalts and the Zeehan and Heemskirk Seamount volcanics negates any possibility of a common mantle source.

4.4 BALLENY PLUME INFLUENCE ON THE OPENING OF THE TASMAN SEA - SOUTHWEST PACIFIC OCEAN:

A regional HIMU isotopic signature is present within the Cainozoic continental volcanics of southeastern Australia (Tasmania) the South Island and offshore islands of New Zealand, and Marie Byrd Land in West Antarctica (Figure 4.12) (Coombs et al., 1986; Sun et

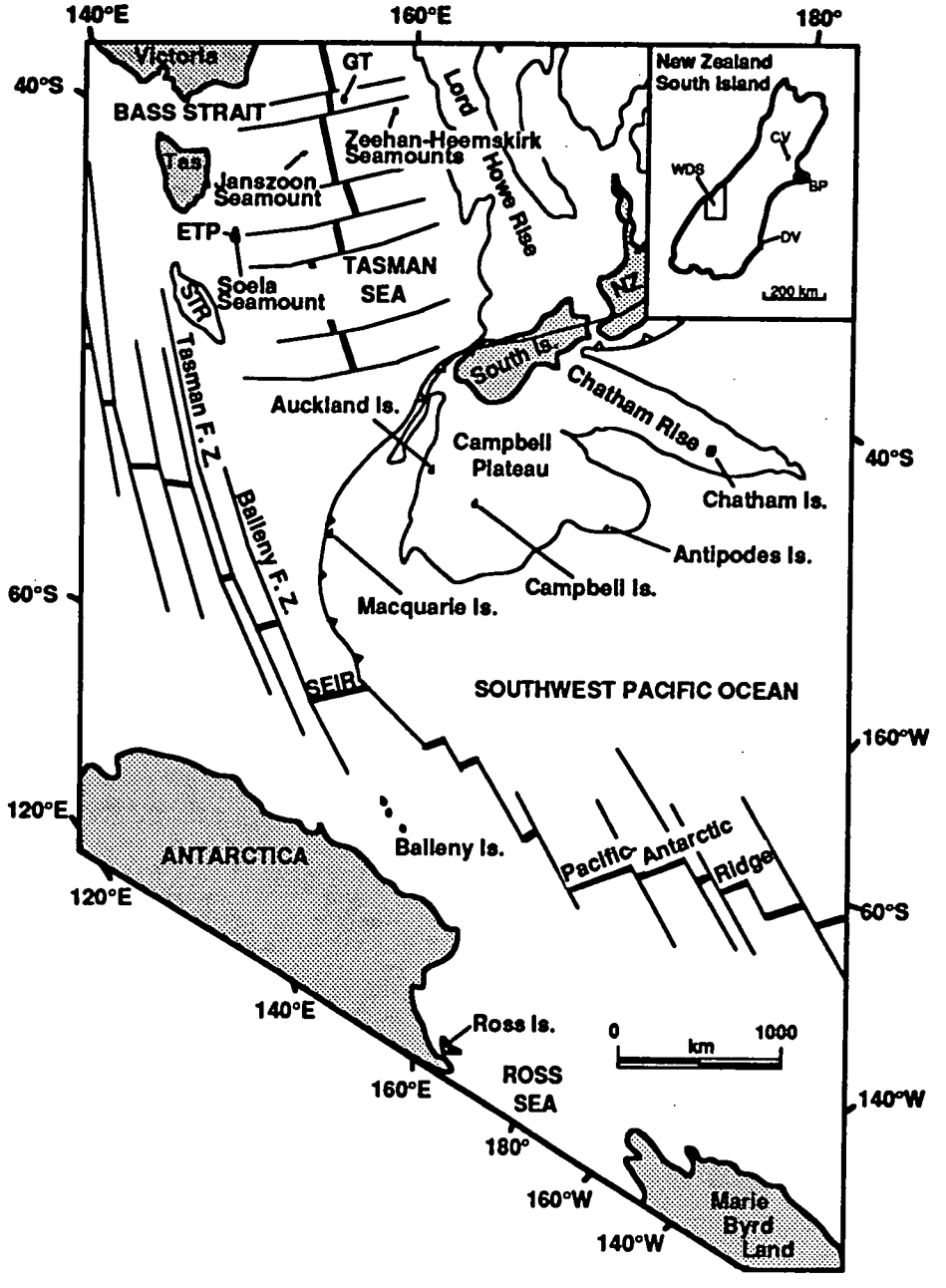

Figure 4.12: Map of the southwest Pacific Ocean (modified after Reinemund, 1984) showing the location of islands and seamounts comprising the Balleny Plume trace (Chapter 3), relative to previously contiguous continental regions of Gondwana (as discussed in Section 4.4), and Macquarie Island (Section 4.5). The inset shows the location of the New Zealand volcanics discussed in Section 4.4.3. Abbreviations inclue SEIR = Southeast Indian Ridge, GT = Gascoyne Tablemount, STR = South Tasman Rise, ETP = East Tasman Plateau, CV = Cookson Volcanics, DV = Dunedin Volcanics, BP = Banks Peninsula, and WDS = Westland and Otago dyke swarm.

al., 1989; Lanyon et al., 1993). Separation of these continental fragments, all of which were juxtaposed prior to the breakup of Gondwana, occurred as a result of opening of the Tasman Sea and southwest Pacific Ocean which commenced during the Cretaceous (e.g. Weissel et al., 1977). The temporal proximity of these rifting events to the possible initiation of the Balleny Plume, the latter distinguished by its HIMU-like isotopic signature (Chapter 3), needs to be investigated in order to establish whether or not these events may be linked.

4.4.1 The Separation of Australia, New Zealand And West Antarctica:

Although rifting between eastern Australia and Lord Howe Rise/New Zealand commenced at ~96 Ma, coincident with the onset of seafloor spreading between Australia and Antarctica (Veevers et al., 1991), the major period of oceanic crust production and development of the Tasman Sea basin occurred between ~82 Ma (A34) (Weissel and Hayes, 1977) and 55.5 Ma (A24) (Veevers et al., 1991). At approximately the same time as significant seafloor spreading commenced in the Tasman Sea, the Campbell Plateau (part of the New Zealand Plateau) and West Antarctica were rifted apart (~81 m.y. ago; Christoffel and Falconer, 1972; Molnar et al., 1975) as a result of the westward propagation of the southwest Pacific-Antarctic Ridge (Bradshaw 1989). The recognition of 90-110 Ma mafic dykes along the coast of Marie Byrd Land (Grindley and Oliver, 1983), however, suggests that continental rifting between Antarctica and the New Zealand Plateau may have commenced at about the same time as Australian-New Zealand and Australian-Antarctic rifting began.

The initiation of Balleny Plume volcanism is also assumed to be roughly comparable in age to the onset of significant seafloor spreading (at ~82 Ma) in the Tasman Sea and southwest Pacific Ocean, based on the proposal by Jenkins et al. (1992) that undated seamounts northeast of Heemskirk Seamount, on the western flank of Lord Howe Rise, most likely represent pre-71 Ma Balleny Plume eruptives.

4.4.2 Tasmanian Tertiary Volcanism:

As discussed in Section 4.2, Tasmanian Tertiary alkaline volcanism bears a distinctive radiogenic isotope and trace element signature which distinguishes it from other eastern Australian Cainozoic volcanism and closely resembles the systematics of the HIMU-like Balleny Plume volcanics. The identification of a HIMU-like signature in the ~58 Ma Tasmanian Bream Creek alkali basalt means that the timing of Tasmanian volcanism cannot, however, be reconciled with the passage of this region of the Indian-Australian Plate over the Balleny Plume as proposed by Lanyon et al. (1993).

Closure of the Tasman Sea would place the Zeehan-Heemskirk Seamount region of the Lord Howe Rise (Chapter 3), and therefore the proposed region of initial surface expression of the Balleny Plume, close to eastern Tasmania prior to the onset of rifting between eastern Australia and Lord Howe Rise and the opening of the Tasman Sea.

Lithospheric intersection and underplating by the Balleny Plume at the time of commencement of significant seafloor spreading in the Tasman Sea (~82 Ma; Weissel and Hayes, 1977) may have resulted in a significant amount of HIMU-like asthenospheric mantle becoming attached to the overlying lithosphere at this time. Lithospheric stresses responsible for the Tertiary volcanism of Tasmania, from ~58 Ma onwards, may have been related to the final stages of Tasman Sea opening. However, Veevers et al. (1991) describe a period of post-breakup extension from ~64 Ma which affected the Tasmanian region, including the South Tasman Rise. These proposed extensional tectonics may have precipitated decompression melting of the underlying HIMU-like material and the subsequent onset of Tasmanian volcanism bearing a Balleny Plume signature while the plume tail was still overlain by the central south Tasman Sea basin.

4.4.3 Cainozoic Mafic Volcanism on the South Island and Offshore Islands of New Zealand:

Outcrops of Cainozoic mafic volcanics scattered throughout the South Island of New Zealand are generally assumed to be of continental intraplate origin and range in age from Lower Eocene to Pliocene (Sewell and Weaver, 1989). Available isotope data for alkaline volcanics and/or intrusives from some of the more major centres (Figure 4.12) are dominated by low $^{87}Sr/^{86}Sr$ and high $^{143}Nd/^{144}Nd$ values (Table 4.5; Figure 4.13), similar to those of the Balleny Plume and Tasmanian Tertiary alkaline volcanics and overlapping with the HIMU OIB isotopic field. New Zealand $^{87}Sr/^{86}Sr$ data do extend to slightly higher values with respect to both the Balleny Plume and Tasmanian Tertiary alkaline volcanics. The only Pb isotope data available for the South Island, from the Westland and Otago lamprophyric dyke swarm (Figures 4.12 and 4.13), comprise a scatter of $^{207}Pb/^{204}Pb$ values, within the Balleny Plume range but apparently extending towards a component with higher $^{207}Pb/^{204}Pb$ than MORB. The slightly higher $^{87}Sr/^{86}Sr$ and higher $^{207}Pb/^{204}Pb$ at similar $^{206}Pb/^{204}Pb$ values of some New Zealand rocks may be due to contamination of a HIMU-like asthenospheric plume component by continental lithosphere in this region, rather than by depleted upper mantle.

The South Island alkaline volcanics also possess similar trace element characteristics to the Balleny plume and Tasmanian Tertiary volcanics (Table 4.6; Figure 4.14). This is particularly evident in terms of their low Ba/Nb, La/Nb, K/Nb, Rb/Nb, Zr/Nb and Ba/Th values, indicating a similar depletion in LILE and LREE relative to Nb to that of the Balleny Plume volcanics. In terms of their trace element abundance ratios, the South Island volcanics consistently overlap with the HIMU field in Figure 4.14.

A low $^{87}Sr/^{86}Sr$ and high $^{143}Nd/^{144}Nd$ signature, similar to that recognised in the South Island volcanics, is also evident in the Late Mesozoic to Cainozoic mafic volcanics of the offshore and sub-Antarctic islands of New Zealand (Table 4.5; Figure 4.13). These HIMU-like volcanics have been recognised on the Chatham, Campbell, Auckland and Antipodes Islands (e.g. Sun et al., 1989; Weaver et al., 1989), located on the continental basement of

Table 4.5: Ranges of measured Sr, Nd and Pb isotope ratios for the Balleny Plume (data from this study only) and HIMU-like alkaline volcanics and intrusives from the South Island and offshore islands of New Zealand, Marie Byrd Land and the Erebus Volcanic Province of West Antarctica, and Tasmania as compared to the extreme HIMU mantle end-member values (Table 1.1); where known, the number of samples analysed is noted in parentheses. Isotope data sources include: *Tasmanian Tertiary volcanics* - Compston et al. (1968), McDonough et al. (1985), Ewart et al. (1988), W.F. McDonough (unpublished data) and R. Varne (unpublished data); *South Island, New Zealand* - Price and Compston (1973), Barriero and Cooper (1987), Coote (1987; cited in Weaver et al., 1989), McDonough et al. (1986); McDonough (1987) and Weaver et al. (1989); *New Zealand offshore islands* - Morris (1985), McDonough et al. (1986) and McDonough (1987), *Marie Byrd Land* - Futa and LeMasurier (1983); *Erebus Volcanic Province* - Sun and Hanson (1975b), Stuckless and Ericksen (1976) and Zhu and Fan (1989). Where possible $^{87}Sr/^{86}Sr$ and $^{143}Nd/^{144}Nd$ data from the literature are normalised as for Figure 1.1. Data sources for ages of volcanism are: Cullen (1969), McDougall and Coombs (1973), Price and Compston (1973), Grindley et al. (1977), Adams et al. (1979), Adams (1980), Price and Taylor (1980), LeMasurier and Rex (1982), Adams (1983), Sutherland and Wellman (1986), Sewell and Weaver (1989) and Zhu and Fan (1989); Balleny Plume ages are as discussed in Chapter 3.

	Age	$^{87}Sr/^{86}Sr$	$^{143}Nd/^{144}Nd$	$^{206}Pb/^{204}Pb$	$^{207}Pb/^{204}Pb$	$^{208}Pb/^{204}Pb$
HIMU OIB		0.70285	0.51285	21.80	15.84	40.73
BALLENY PLUME:						
Balleny Province	≤ 10 Ma	0.70288-0.70308 (4)	0.51293-0.51299 (4)	19.685-19.849 (4)	15.583-15.624 (4)	39.337-39.692 (4)
Soela Seamount	~40 Ma	0.70315-0.70323 (3)	0.51286-0.51290 (3)	20.015-20.061 (3)	15.632-15.649 (3)	39.762-39.898 (3)
Tasman Sea Seamounts	~55-71 Ma	0.70291-0.70334 (8)	0.51291-0.51314 (8)	19.958-20.727 (8)	15.628-15.757 (8)	39.773-40.466 (8)
SOUTHEAST AUSTRALIA:						
Tasmanian Tertiary alkaline	58 - 8 Ma	0.70260-0.70335 (22)	0.51293-0.51304 (22)	19.141-19.656 (5)	15.548-15.633 (5)	38.643-39.336 (5)
Tasmanian Tertiary tholeiitic		0.70324-0.70780 (7)	0.51277-0.51298 (3)	18.994-19.690 (2)	15.591-15.676 (2)	38.935-38.965 (2)
NEW ZEALAND - South Island:						
Westland and Otago lamprophyric dyke swarm	28 - 16 Ma	0.70285-0.70351 (15)	0.51282-0.51291 (15)	19.19-20.59 (13)	15.64-15.71 (13)	39.03-40.42 (13)
Cookson volcanics, Northern Canterbury	Oligocene	0.7029-0.7033 (?)				
Dunedin Volcanic Group	14.4 - 10.1 Ma	0.70265-0.70314 (17)	0.512822-0.512961 (5)			
Akaroa and Lyttleton Volcanoes, Banks Peninsula	12 - 5.8 Ma	0.7029-0.7032 (?)	0.51296 (?)			
NEW ZEALAND - Offshore and sub-Antarctic Islands:						
Chatham Islands	80 - 68 Ma	0.70282-0.70331 (8)	0.51282-0.51291 (5)			
Auckland Islands	25.6 - 12.3 Ma	0.70298-0.70360 (4)	0.51289-0.51294 (3)			
Campbell Island	11.1-6.5 Ma	0.70373 (1)				
Antipodes Islands	< 1 Ma	0.70293-0.70296 (2)	0.51293-0.51294 (2)			
WEST ANTARCTICA:						
Marie Byrd Land	28 - 0.8 Ma	0.70259-0.70322 (12)	0.51286-0.51300 (12)			
Erebus Volcanic Province	≤5 Ma	0.70300-0.70350 (24)		18.741-20.280 (25)	15.595-15.790 (25)	38.332-39.824 (25)

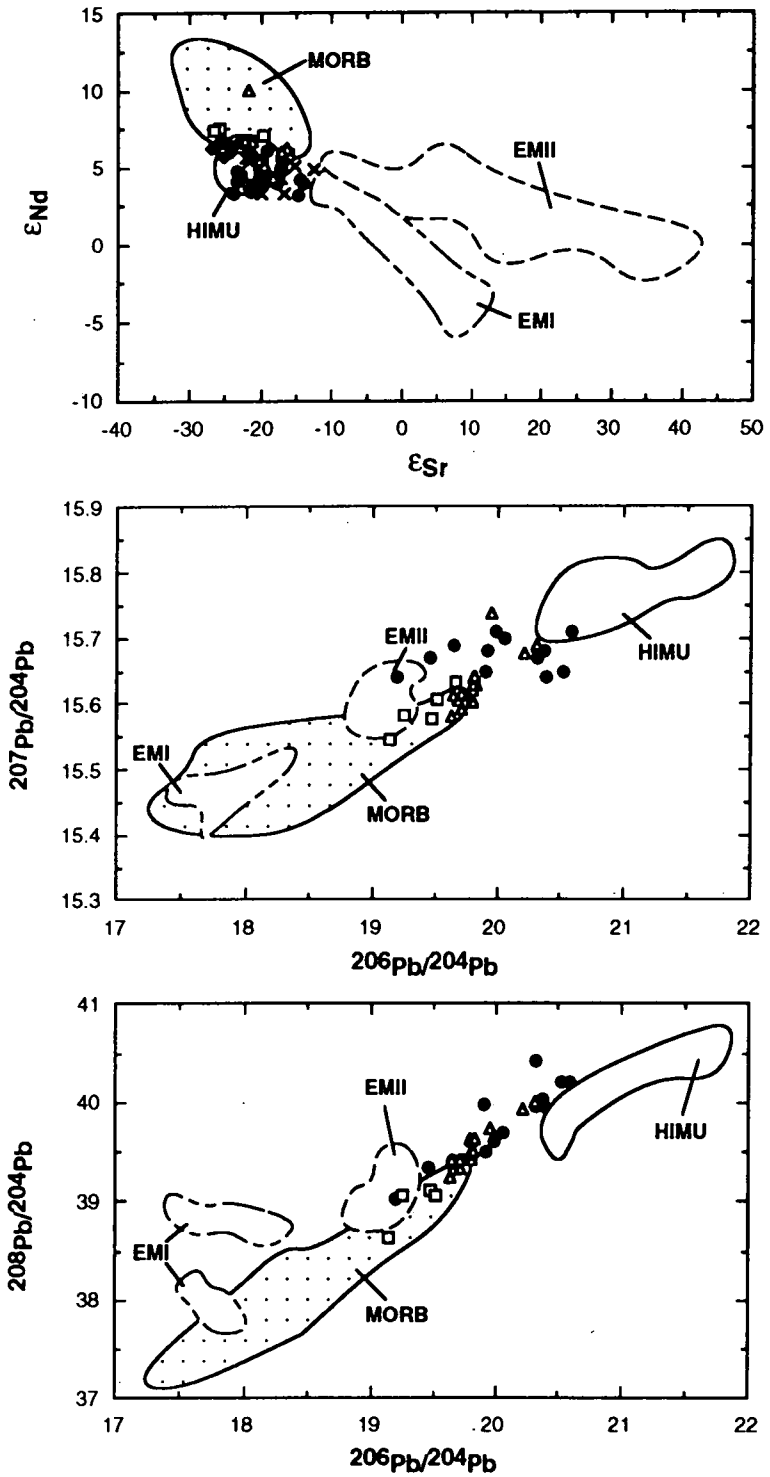

Figure 4.13: Radiogenic isotope plots comparing measured data from the South Island of New Zealand including the Dunedin Volcanics and the Westland and Otago lamprophyric dyke swarm (filled circles), the offshore and sub-Antarctic islands of New Zealand including the Chatham, Auckland and Antipodes Islands (oblique crosses - Sr-Nd plot only), the Marie Byrd Land alkaline volcanics (filled diamonds - Sr-Nd plot only), and the Tasmanian Tertiary alkaline volcanics (open squares) with the Balleny Plume volcanics (initial ratios - open triangles) and the HIMU, EMI and EMII OIB and MORB isotopic fields. Data sources for the isotopic end-members are as for Figure 1.1. Balleny Plume volcanics include the Balleny Islands ratios of Hart (1988), age corrected as for Figure 3.20. Other data sources include: *New Zealand South Island* - Barreiro and Cooper (1987) and McDonough (1987); *New Zealand offshore islands* - McDonough (1987); *Marie Byrd Land* - Futa and LeMasurier (1983).

Table 4.6: Trace element abundance ratios for the alkaline volcanics of the Balleny Plume, Tasmania, the South Island and offshore islands of New Zealand, Marie Byrd Land in West Antarctica and the Erebus, Melbourne and Hallett Volcanic Provinces of the McMurdo Volcanic Group, West Antarctica as discussed in Sections 4.4 and 4.6. Data are presented as ranges underlain by the mean value ± 1σ error (numbers in bold type are the most well constrained: σ/mean ≤~10 %); numbers in parentheses indicate the number of analyses used (n) to calculate both the ratio ranges and the mean values. Sources for data derived from the literature include: *Balleny Plume* - Green (1992) and J. Foden (unpublished data); *Tasmania* - Frey et al. (1978), Ewart et al. (1988) and W.F. McDonough (unpublished data);

	Rb/Nb	Ba/Rb	Ba/Th	Ba/Nb	Ba/La	Th/U	Th/Nb	Th/La
BALLENY PLUME	0.11-0.98 (41) 0.49±0.13	8.24-43.04 (23) 14.17±7.05	57-99 (22) 74±12	4.47-7.38 (33) 5.82±0.72	3.17-12.59 (16) 8.59±2.80	2.56-4.74 (14) 3.62±0.52	0.07-0.15 (30) 0.09±0.02	0.04-0.15 (16) 0.12±0.03
TASMANIAN TERTIARY	0.12-0.75 (7) 0.29±0.21	4.66-29.57 (22) 14.90±5.93	12-114 (22) 48±25	2.20-5.40 (7) 3.90±1.25	2.62-11.25 (18) 5.66±1.84	1.33-11.5 (15) 3.93±2.56	0.07-0.16 (7) 0.10±0.03	0.05-0.43 (18) 0.13±0.08
NEW ZEALAND: South Island								
Westland and Otago lamprophyric dyke swarm	0.22-0.59 (3) 0.37±0.19	10.68-28.58 (4) 17.39±8.19	54-71 (3) 62±9	5.79-6.36 (3) 6.16±0.33	6.92-10.02 (4) 8.41±1.34	3.25-6.0 (3) 4.25±1.52	0.08-0.12 (3) 0.10±0.02	0.10-0.15 (4) 0.13±0.03
Dunedin Volcanic Group	0.18-0.62 (8) 0.48±0.14	11.18-32.33 (8) 16.06±6.92	54-141 (8) 101±27	5.79-8.26 (8) 6.97±0.95	7.92-11.92 (3) 9.61±2.07	1.5-4.0 (8) 3.06±0.82	0.04-0.11 (8) 0.07±0.02	0.09-0.15 (3) 0.12±0.03
Akaroa and Lyttleton Volcanoes, Banks Peninsula	0.26-0.55 (3) 0.44±0.16	7.25-21.43 (3) 13.90±7.13	41-127 (8) 77±25	3.98-8.12 (8) 6.16±1.20	6.55-13.63 (8) 9.09±2.04	2.94-4.20 (6) 3.72±0.42	0.06-0.12 (8) 0.08±0.02	0.10-0.16 (8) 0.12±0.02
NEW ZEALAND - Offshore and sub-Antarctic Islands:								
Chatham Islands	0.24-51 (10) 0.37±0.08	12.84-37.53 (11) 20.09±7.25	22-128 (11) 48±37	4.95-13.87 (10) 7.18±2.75	2.88-21.54 (10) 8.36±5.29		0.05-0.25 (10) 0.13±0.06	0.03-0.30 (10) 0.16±0.09
Auckland Islands	0.31-0.43 (3) 0.36±0.06	12.84-15.85 (3) 14.67±1.61	41-61 (3) 52±10	4.9-5.55 (3) 5.24±0.33	8.58-10.17 (3) 9.15±0.89		0.09-0.12 (3) 0.10±0.015	0.16-0.21 (3) 0.18±0.03
Campbell Island	0.46-0.62 (3) 0.53±0.08	8.06-11.83 (3) 10.27±1.97	42-53 (3) 47±6	5.02-6.04 (3) 5.36±0.59	6.61-8.11 (3) 7.44±0.76		0.09-0.13 (3) 0.11±0.02	0.14-0.17 (3) 0.16±0.016
Antipodes Islands	0.17-0.45 (3) 0.33±0.15	10.98-27.5 (3) 16.92±9.18	37-52 (3) 45±8	4.64-4.94 (3) 4.79±0.15	5.95-8.36 (3) 7.06±1.22		0.09-0.13 (3) 0.11±0.02	0.13-0.19 (3) 0.16±0.03
WEST ANTARCTICA:								
Marie Byrd Land	0.40-0.60 (5) 0.49±0.08	10.81-20.18 (5) 14.01±3.61	46-281 (4) 110±56	5.40-8.54 (5) 6.78±1.35	7.59-12.38 (5) 9.38±1.96	0.50-4.0 (2)	0.02-0.17 (4) 0.11±0.07	0.03-0.27 (4) 0.16±0.10
Erebus Volcanic Province	0.24-0.57 (10) 0.38±0.10	8.49-23.95 (14) 12.16±4.64	42-66 (8) 56±7	2.01-8.57 (9) 4.60±2.21	3.82-9.29 (8) 6.92±1.89	3.82-4.6 (5) 4.23±0.35	0.04-0.10 (8) 0.07±0.02	0.07-0.13 (4) 0.10±0.03
Melbourne Volcanic Province	0.30-0.70 (10) 0.50±0.13	5.58-19.5 (7) 12.32±4.31	57-105 (3) 79±24	1.92-9.13 (7) 5.73±2.63	8.32 (1)	7.0 (2)	0.03-0.09 (6) 0.07±0.03	0.11 (1)
Hallett Volcanic Province	0.39 (1)	12.53 (1)	61 (1)	4.87-21.12 (16) 11.61±4.0	4.24-16.48 (14) 9.29±3.63		0.08 (1)	

Table 4.6: (continued) *New Zealand South Island* - Price and Taylor (1973), Price and Chappell (1975), Irving and Price (1981), Cooper (1986), Sewell and Weaver (1986; cited in Sewell and Weaver, 1989) and Price and Taylor (1980); *New Zealand offshore islands* - Morris (1984), Morris (1985), Gamble et al. (1986), McDonough (1987) and Gamble and Adams (1990); *Marie Byrd Land* - LeMasurier and Rex (1991); *Erebus Volcanic Province* - Goldich et al. (1975), Sun and Hanson (1975b), Kyle and Rankin (1976), Sun and Hanson (1976), Kyle et al. (1979), Kyle (1981), Ellerman and Kyle (1990) and Wright and Kyle (1990b; 1990c); *Melbourne Volcanic Province* - Kyle and Rankin (1976), Kyle (1990b), Kyle and Noll (1990), Schmidt-Thomé et al. (1990) and Wörner and Viereck (1990); *Hallett Volcanic Province* - Hamilton (1972) and Kyle and McIntosh (1990); only samples with ≥5 wt % MgO were included.

	Nb/U	Nb/Pb	K/Nb	La/Nb	Ce/Rb	Ce/Pb	Zr/Nb
BALLENY PLUME	25-82 (14) 48±13	3-37 (14) 20±10	92-306 (41) 179±39	0.56-2.33 (16) 0.78±0.46	1.62-12.01 (16) 3.39±2.40	5.1-41.9 (14) 25.5±11.4	3.11-7.20 (41) 4.22±1.12
TASMANIAN TERTIARY	20-42 (4) 35±10	4-16 (4) 7±6	93-285 (7) 158±73	0.64-0.88 (7) 0.81±0.08	1.98-11.67 (18) 5.63±2.45	5.7-28.83 (13) 14.61±8.18	2.45-4.00 (7) 3.58±0.56
NEW ZEALAND: South Island							
Westland and Otago lamprophyric dyke swarm	30-57 (3) 42±14	9.8-10 (3) 9.9±0.1	90-163 (3) 126±36	0.71-0.84 (3) 0.79±0.07	1.84-5.79 (4) 3.77±1.83	12.9-16.0 (3) 14.52±1.41	3.27-4.19 (3) 3.65±0.48
Dunedin Volcanic Group	31-54 (8) 42±9	13-23 (8) 16.2±3.8	104-226 (8) 181±39	0.66-0.77 (3) 0.71±0.06	2.54-2.87 (2)	19.65-24.38 (2)	3.19-5.1 (8) 3.96±0.53
Akaroa and Lyttleton Volcanoes, Banks Peninsula	25-64 (6) 49±13	6-21 (7) 12.6±5.8	122-257 (8) 184±42	0.60-0.86 (8) 0.68±0.08	2.48-5.28 (3) 3.43±1.60	7.39-29.57 (7) 18.71±8.16	2.97-5.25 (8) 3.84±0.72
NEW ZEALAND - Offshore and sub-Antarctic Islands:							
Chatham Islands			103-215 (10) 175±42	0.39-2.0 (9) 0.96±0.48	2.67-6.84 (10) 5.03±1.37		3.73-6.15 (10) 5.0±0.83
Auckland Islands		21-61 (3) 42±20	144-164 (3) 157±11	0.55-0.61 (3) 0.58±0.03	3.16-4.31 (3) 3.79±0.58	28-82 (3) 56.7±27.2	3.75-4.36 (3) 4.03±0.31
Campbell Island			148-185 (3) 168±19	0.66-0.76 (3) 0.72±0.05	2.12-3.17 (3) 2.79±0.58		3.84-4.43 (3) 4.20±0.31
Antipodes Islands		11-23 (3) 18±6	90-140 (3) 120±26	0.56-0.83 (3) 0.70±0.14	3.47-9.75 (3) 5.78±3.45	18-39 (3) 29±11	3.93-5.91 (3) 4.97±0.99
WEST ANTARCTICA:							
Marie Byrd Land	26-30 (3) 27±2	9-14 (4) 11.3±2.5	159-252 (5) 197±39	0.62-0.92 (5) 0.73±0.11	2.58-5.09 (5) 3.77±0.97	11.2-33.3 (4) 20.5±9.5	3.58-6.0 (5) 4.49±0.96
Erebus Volcanic Province	58-124 (5) 87±26	8-59 (8) 25.9±19.2	98-160 (10) 127±21	0.61-0.66 (3) 0.64±0.03	1.87-4.04 (6) 3.19±0.83	10.9-44.9 (6) 26.4±12.3	2.55-3.93 (6) 2.89±0.52
Melbourne Volcanic Province	93-206 (2)	11-20 (2)	91-226 (10) 152±41	0.68 (1)	3.13 (1)		2.87-5.53 (8) 4.01±0.93
Hallett Volcanic Province		63 (1)	92-277 (16) 166±48	0.90-2.09 (14) 1.37±0.39			1.96-6.55 (16) 2.85±1.13

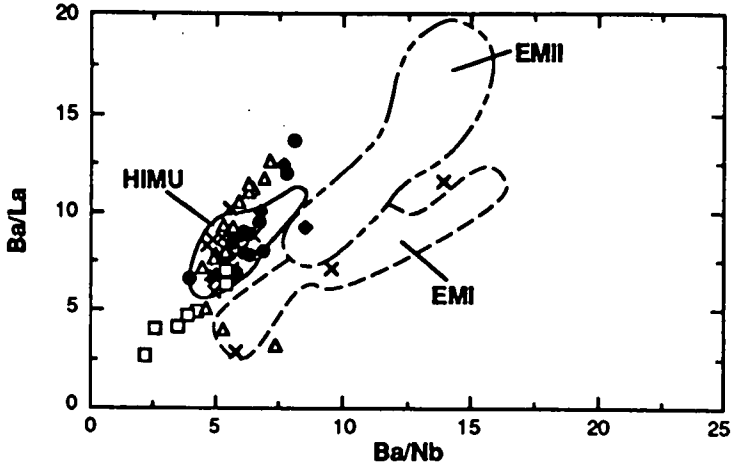
Ba/La
Ba/Nb
EMII
HIMU
EMI
0
5
10
15
20
25

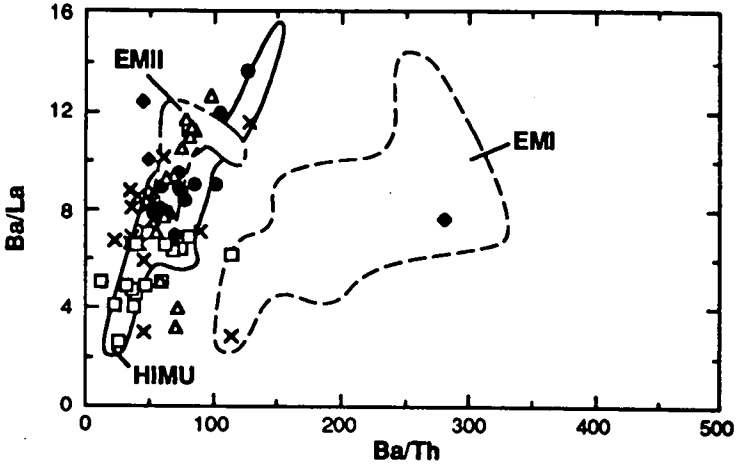
Ba/La
Ba/Th
EMII
EMI
HIMU
0
4
8
12
16
100
200
300
400
500

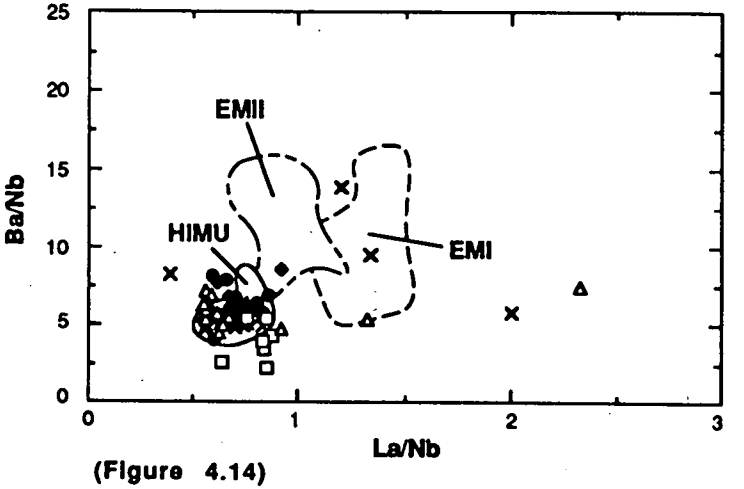
Ba/Nb
La/Nb
EMII
HIMU
EMI
0
5
10
15
20
25
1
2
3

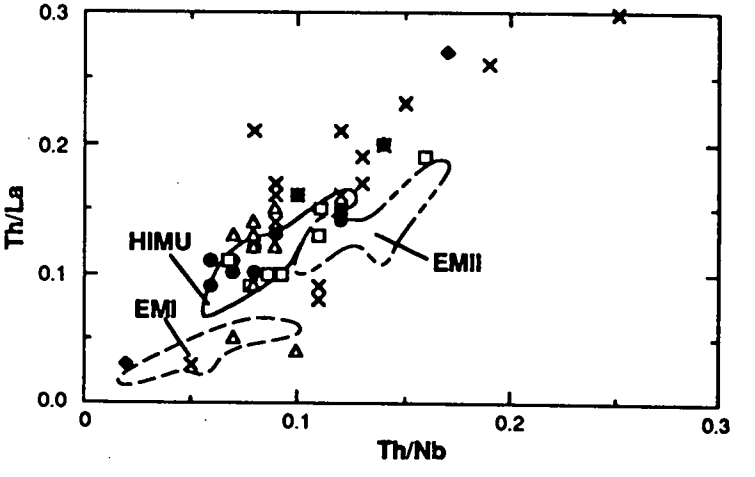
Th/La
Th/Nb
HIMU
EMI
EMII
0.0
0.1
0.2
0.3

(Figure 4.14)

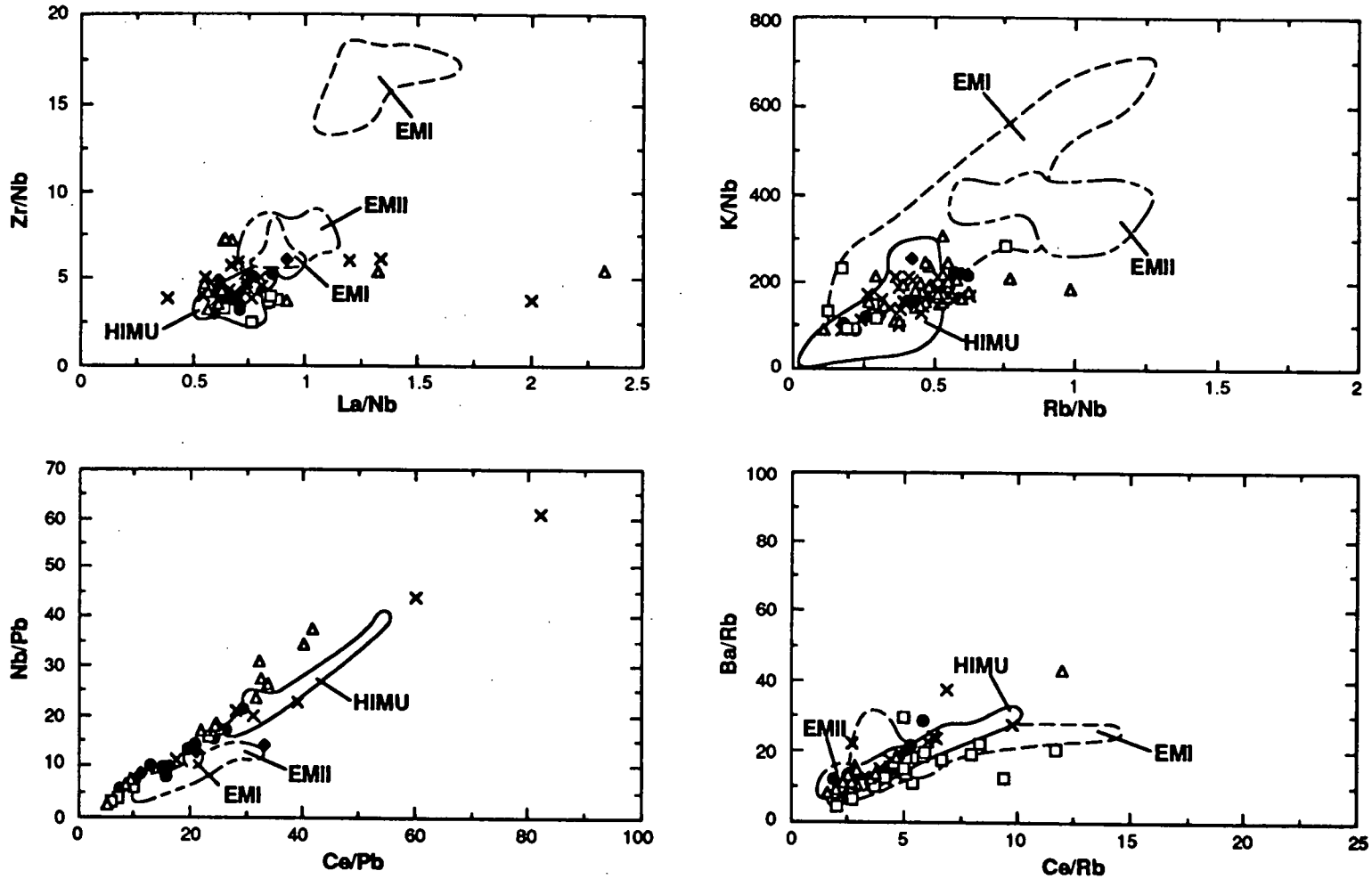

Figure 4.14: Trace element abundance ratio plots comparing data from the South Island of New Zealand including the Dunedin Volcanics, Banks Peninsula and the Westland and Otago lamprophyric dyke swarm (filled circles), the offshore and sub-Antarctic islands of New Zealand including the Chatham, Campbell, Auckland and Antipodes Islands (oblique crosses - Sr-Nd plot only), the Marie Byrd Land alkaline volcanics (filled diamonds - Sr-Nd plot only), and the Tasmanian Tertiary alkaline volcanics (open squares) with the Balleny Plume volcanics (initial ratios - open triangles) and the HIMU, EMI and EMII OIB fields. OIB end-member fields as for Figure 4.3. Data sources as for Table 4.6.

the Chatham Rise and Campbell Plateau south of New Zealand (Figure 4.12). Unfortunately, no Pb isotope data are available for any of these islands.

The trace element systematics of alkaline volcanics from the continental offshore islands of New Zealand display many similar features to the volcanics of the South Island of New Zealand and the Balleny Plume (Table 4.6), which can be considered as HIMU-like (Figure 4.14) in terms of general LILE and LREE depletion. However, there are some obvious variations in trace element chemistry between the various islands. Auckland Islands samples extend to high Ce/Pb and Nb/Pb values, suggesting some Pb depletion relative to the other islands, and samples from the Chatham Islands display the greatest range of Th/Nb and Th/La values, the highest values implying a degree of Th enrichment relative to the LILE, as well as high La/Nb values. Despite these variations, the similarity of the trace element abundance ratios of the offshore islands of New Zealand, coupled with their low $^{87}Sr/^{86}Sr$ and high $^{143}Nd/^{144}Nd$ values, to the South Island, Tasmanian Tertiary and Balleny Plume volcanics, and therefore to HIMU OIB, suggests involvement of a HIMU plume source. Eruption of the offshore island volcanics through the continental lithosphere comprising the Chatham Rise and Campbell Plateau could be the source of the observed inter-island trace element variabilities, particularly considering the likelihood of lithospheric heterogeneities.

Eruption of mafic volcanics on the Chatham Islands at the eastern tip of the Chatham Rise/Campbell Plateau at ~80-68 Ma (Grindley et al., 1977) provides the earliest evidence for influence from a HIMU source in the New Zealand region. The spatial and temporal occurrence of these HIMU-like volcanics suggests a link with the rifting of Campbell Plateau from Marie Byrd Land, which commenced at ~81 Ma (Molnar et al., 1975). However, other recognised areas of HIMU-like volcanism in the South Island and other offshore islands of New Zealand display a range of ages (Table 4.5), inconsistent with lithospheric plate migration over one or more fixed mantle plume sources, although suggestive of underlying HIMU mantle dating back to at least ~80 Ma. The latter again raises the possibility of extensive lithospheric underplating by the Balleny Plume, coincident with the onset of significant rifting between eastern Australia, New Zealand and West Antarctica at ~80 Ma.

4.4.4 Mafic Volcanism in Marie Byrd Land, West Antarctica:

The Late Cainozoic Marie Byrd Land volcanic province outcrops along 800 km of the Pacific coast of West Antarctica (Figure 4.12), overlying a 30-38 km thick basement of continental crust (Futa and LeMasurier, 1983). The volcanic province comprises a basal succession of subhorizontal alkaline basaltic flows surmounted by a series of felsic, predominantly trachytic, central shield volcanoes which are parasitised by alkali basaltic cinder and tuff cones with similar isotopic and geochemical compositions to the basal succession basalts (Futa and LeMasurier, 1983; LeMasurier and Rex, 1989; 1991).

The low $^{87}Sr/^{86}Sr$ and high $^{143}Nd/^{144}Nd$ values of the Marie Byrd Land alkali basalts (Table 4.5; Figure 4.13) are similar to those of the Balleny Plume, Tasmanian Tertiary and New Zealand (South Island and offshore islands) alkaline volcanics, overlapping with the

HIMU OIB isotopic field. No Pb isotope data are available for these samples. The trace element systematics of the Marie Byrd Land alkaline volcanics are also generally consistent with derivation from a HIMU-like source, with low LILE/Nb and LREE/Nb ratios which overlap with fields defined by HIMU OIB and the Balleny Plume volcanics (Table 4.6; Figure 4.14).

Marie Byrd Land volcanism is thought to derive from an asthenospheric mantle plume source underlying the Antarctic Plate, which has undergone little or no chemical interaction with the continental lithospheric mantle or crust (LeMasurier and Rex, 1991). Extensional tectonics within Marie Byrd Land, resulting in lithospheric thinning and fracturing followed by decompression melting of the asthenospheric source and subsequent volcanism, may be related to the West Antarctic intracontinental rift system, the axis of which, in central and eastern Marie Byrd Land, parallels the line of rupture with the Campbell Plateau (LeMasurier and Rex, 1991). The onset of the proposed rift tectonics of Marie Byrd Land is not easily explained, except by thermal processes, presumably the result of mantle plume activity beneath a stationary lithospheric plate (LeMasurier and Rex, 1991), resulting in crustal doming and the observed radial migration of felsic volcanic activity with time (LeMasurier and Rex, 1989).

The suggestion of asthenospheric mantle involvement (LeMasurier and Rex, 1989; 1991), coupled with the observed isotope and trace element systematics of Marie Byrd Land alkaline mafic volcanism, is consistent with derivation from a HIMU-like plume, with similar radiogenic isotope and trace element systematics to the Balleny Plume, located beneath the stationary Antarctic Plate. The idea of extensive lithospheric underplating by the Balleny Plume at the time of onset of Australian-New Zealand-West Antarctic rifting, proposed to explain the temporally diverse HIMU-like mafic volcanism of Tasmania and New Zealand, could also explain the occurrence of HIMU-like volcanics in Marie Byrd Land close to the site of rifting with the Campbell Plateau. However, the possibility of a second HIMU mantle plume will also be considered in the ensuing discussion.

4.4.5 Discussion of a Possible Balleny Plume Influence on Continental Rifting:

The presence of a regional HIMU isotopic and trace element signature, similar to that of the Balleny Plume, in the alkaline mafic volcanics of the continental regions of southeast Australia, New Zealand and West Antarctica, all of which were contiguous prior to the break-up of Gondwana (Figure 4.15), seems far too fortuitous not to be a product of their overall tectonic relationship. Two possible scenarios, alternatively proposing the involvement of one or multiple HIMU mantle plume/s, will be presented in an attempt to explain the widespread spatial and somewhat sporadic temporal occurrence of these HIMU volcanics.

The first scenario involves a widespread influence from a single plume, the Balleny Plume, on both continental and oceanic volcanism in the Tasman Sea - southwest Pacific Ocean region. Whereas the oceanic volcanism is related to the plume tail or conduit (Chapter 3), continental volcanism may be a product of the plume head. The Balleny Plume head is

here assumed to have ascended beneath the region of Gondwana where Tasmania, New Zealand and Antarctica were cojoined prior to the onset of significant continental break-up at ~80 Ma. Upon intersecting the base of the lithosphere, flattening and lateral spreading of the plume head (Griffiths and Campbell, 1990) may have resulted in widespread lithospheric underplating by HIMU-like plume material of this entire region.

Although there are many different ideas in the literature concerning the cause and effect relationship between continental rifting, upwelling mantle plumes and flood volcanism, according to White (1992) impingement of an upwelling plume head on the base of the lithosphere will not in itself cause extensive surface volcanism. The latter would depend on whether or not melting occurred, which in turn is dependent on the temperature of the ascending mantle and the thickness of the lithosphere (Saunders et al., 1992). Both Saunders et al. (1992) and White (1992) believe that lithospheric stretching and thinning must have already taken place in order for flood volcanism to occur. This is summed up in the statement by White (1992: p. 12) that "... without thin lithosphere, melt volumes can only be small". If a starting plume head was particularly 'cool', due to the entrainment of large amounts of surrounding mantle during ascent, and/or it intersected unusually thick lithosphere, plume head material may fail to reach its solidus and melt. In this case, plume head collapse and horizontal flattening would still occur, but a large igneous province (LIP), such as the continental flood basalts and oceanic plateaus attributed to other starting plume heads (e.g. Coffin and Eldholm, 1992), would not.

In Chapter 3, several reasons were proposed as to why Balleny Plume volcanism is likely to represent the trace of a relatively weak, in terms of buoyancy flux, mantle plume. If the upwelling heads of weaker plumes, such as the Balleny Plume, can be expected to entrain more ambient mantle than stronger plumes (Griffiths and Campbell, 1990), they could also be expected to be somewhat cooler upon arriving at the base of the lithosphere, and may therefore fail to undergo substantial melting and to produce surface volcanism. The other factor which may have dictated whether or not melting occurred, namely the thickness of the lithosphere that was intersected by the Balleny Plume head, is difficult to ascertain due to the fact that extension associated with continental rifting may have resulted in subsequent thinning of the lithosphere due to stretching (McKenzie, 1978) or detachment faulting (Wernicke, 1981; 1985; Lister et al., 1986). The current thicknesses of the continental crust comprising Lord Howe Rise and the New Zealand Plateau, the latter a combination of the Chatham Rise and Campbell Plateau (Cullen, 1970), are considered to be 20-25 km (Officer, 1955) and 20±3 km (Adams, 1962) respectively, less than the 30-40 km thick crust of the New Zealand land mass (Thomson and Evison, 1962). Although thinner areas of crust, and hence lithosphere, could be expected to permit extensive surface volcanism during plume head upwelling (Hill, 1991), prior to the production of the oldest seafloor in an area where lithospheric rifting is occurring (White, 1992), the thinner crust of the continental plateaus surrounding New Zealand may be a product of rifting subsequent to the ascent and underplating of the Balleny Plume head. This idea stems from the proposal

that initial lithospheric extension between eastern Australia and Lord Howe Rise involved detachment faulting, whereby the southeast Australian margin is interpreted to be an upper-plate margin whereas the western part of Lord Howe Rise represents the detached and complementary lower plate margin (Etheridge et al., 1989). This means that the lithosphere associated with the eastern Australian margin would probably have been considerably thicker at the time of intersection by the Balleny Plume head.

Although the structure of the conjugate Campbell Plateau-Marie Byrd Land margins has not been studied to the same extent, detachment faulting may also have resulted in lithospheric thinning in this region as submerged continental fragments, such as the Campbell Plateau, are not readily explicable through more symmetrical models of extension (Lister et al., 1986). Therefore, the present-day crustal thickness of the New Zealand Plateau (Chatham Rise and Campbell Plateau) was also probably attained subsequent to underplating by the Balleny Plume. A combination of thick lithosphere, prior to continental rifting between southeast Australia, New Zealand and West Antarctica, plus significant upper mantle entrainment and cooling during the ascent of the relatively weak Balleny Plume head, may therefore have confined its activities at this time to lithospheric underplating rather than melting and extensive surface volcanism.

The actual timing of sub-Gondwana lithospheric intersection by the Balleny Plume is not known, however, plume conduit volcanism appears to have commenced prior to ~71 Ma. This is based on the presumption that the Balleny Plume trace extends northeast, beyond the Zeehan and Heemskirk Seamounts, to even older seamounts located on the western flank of Lord Howe Rise (Jenkins et al., 1992). Plume head upwelling can therefore be inferred to at least coincide with the onset of significant seafloor spreading between the Lord Howe Rise and eastern Australia and between the New Zealand Plateau and Marie Byrd Land at ~80 Ma. However, it is possible that the Balleny Plume head was emplaced beneath this region of Gondwana prior to ~80 Ma, and maybe even prior to or coincident with the commencement of Tasman Sea opening at ~96 Ma (Veevers et al., 1991). Before the onset of significant seafloor spreading within the Tasman Sea basin at ~80 Ma, eastern Australia and the Lord Howe Rise would have been no more than ~200-250 km apart (based on reconstructions performed using Reinemund (1984) and placing Cape Howe in southeast Australia adjacent to the Lord Howe Rise prior to rifting). This short distance, combined with proposals that initial lithospheric extension in this region may have involved detachment faulting, supports the idea that the lithosphere in this region, at the time of Balleny Plume head upwelling, would have been considerably thicker than current estimates.

The thermal effects of an upwelling plume head are considered to include substantial buoyancy-induced uplift and weakening of the overlying lithosphere, due to the presence of additional tensional forces, which may lead to rifting (White and McKenzie, 1989; Hill, 1991). Although the regional uplift produced by the Balleny Plume may well have been largely masked by later tectonic and/or erosional events, precipitation of rifting between the Lord Howe Rise and eastern Australia at ~96 Ma may be a possible

consequence of plume head upwelling, especially when the uncertainty associated with the timing of its initial ascent is taken into account.

The proposal by Hill (1991) that slow continental extension, activated by plate-scale convection, may evolve into full-scale seafloor spreading with the arrival of a plume head may, however, be more pertinent to the opening of the Tasman Sea, where significant seafloor spreading only commenced ~14 Ma after the initial onset of rifting. The arrival of the Balleny Plume head beneath the Tasmania-New Zealand-West Antarctic 'triple point' at ~80 Ma, into a region of already weakened and partially rifted lithosphere, may therefore have resulted in the onset of full-scale seafloor spreading between Lord Howe Rise and southeastern Australia, and between the Campbell Plateau and Marie Byrd Land. This seems more reasonable than proposing that the Balleny Plume actually initiated the 96 Ma onset of Tasman Sea opening, due to the fact that rifting between the southern margin of Australia and Antarctica also commenced at ~96 Ma (Veevers et al., 1991) but was spatially unrelated to the Balleny Plume. In support of the idea that the Balleny Plume may have played a contributing rather than an initiating role for continental break-up in this region, Hill (1991) observed that flood basalt provinces produced by starting plume heads are not always associated with oceanic basins, and therefore that mantle plumes alone are unlikely to initiate continental break-up. White (1992) also concluded that the regional uplift produced by the ascent of a starting mantle plume, particularly in a region where the stress field is such that incipient rifting is likely (White and McKenzie, 1989), may boost rifting but will not necessarily in itself cause continental break-up.

This first scenario, therefore, suggests that the Balleny Plume head ascended at ~80 Ma and had an influence on the break-up of southeast Australia, New Zealand and West Antarctica at this time. Rather than extruding extensive surface flood basalts, possibly due to the relatively weak and cool properties of the plume plus the lithospheric thickness in this region, it underplated the lithosphere of this part of eastern Gondwana during plume head collapse and horizontal spreading, without experiencing substantial melting. Chatham Islands HIMU-like volcanism from ~80 Ma suggests that some melting did occur within the plume head during underplating and the concurrent separation of the Campbell Plateau from Marie Byrd Land. Later sporadic volcanism in the continental regions of Tasmania, New Zealand and West Antarctica occurred in response to more localised extensional tectonic regimes which caused decompression and melting of the Balleny plume material attached, and therefore moving along with, the continental lithosphere in these regions. After plume head underplating and the onset of significant continental break-up, the temporally predictable volcanism associated with the oceanic Balleny Plume trace occurred in response to lithospheric plate movement over the plume conduit still located as a fixed source in the asthenospheric mantle.

A second scenario proposes that more than one HIMU mantle plume is responsible for the regional isotopic and trace element systematics observed in the continental regions bordering the south Tasman Sea and southwest Pacific Ocean. If lithospheric underplating

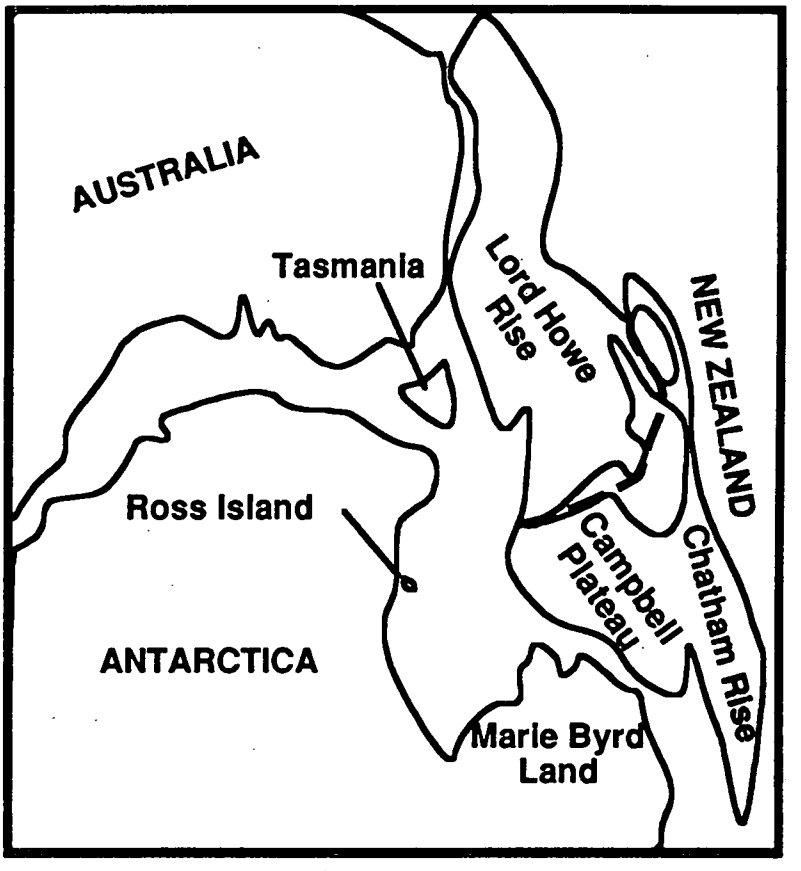

Figure 4.15: Cartoon representation of the morphological reconstruction of eastern Gondwana prior to 96 Ma, modified after Griffiths and Varne (1972).

by the Balleny Plume head at ~80 Ma was confined to the Tasmania-New Zealand region of Gondwana, Marie Byrd Land volcanism could be the product of a second HIMU-like plume, possibly originating from the same region as the Balleny Plume (Lanyon et al., 1993), but intersecting the lithosphere beneath the stationary Antarctic Plate up to ~50 m.y. later. The observation that Marie Byrd Land Quaternary volcanism defines a hotspot with a diameter of 550-650 km, within which all the older areas of volcanism are also contained (LeMasurier and Rex, 1989), plus the hypothesis that the extensional tectonics and resulting volcanism of this region were initiated at ~28 Ma by thermal activity (LeMasurier and Rex, 1991), do appear to be inconsistent with the more long-term and possibly quite diffuse underplating by Balleny Plume material associated with the first scenario. However, the 50 m.y. gap between the proposed initial surface expression of the Balleny Plume head (~80 Ma volcanism on the Chatham Islands) and the onset of Marie Byrd Land crustal doming (LeMasurier and Rex, 1989) and volcanism (~28 Ma; LeMasurier and Rex, 1982) does corresponds to the time lag proposed by Smith and Drewry (1984) for continental uplift following the overiding of hot asthenosphere by a continent. Therefore, if Marie Byrd Land was underplated by a small

amount of hot asthenospheric Balleny plume material at ~80 Ma, with uplift and resultant volcanism delayed by 50 m.y., the need for a second plume may be negated. The fact that this 50 m.y. delay did not occur in Tasmania or New Zealand may be due to extensional events in these areas producing volcanism at an earlier time.

4.5 THE BALLENY PLUME AND MACQUARIE ISLAND:

Macquarie Island (54°35'S, 158°55'E) is a north-northeasterly trending linear feature (~35 km long x <6 km wide) located ~1500 km south-southeast of Tasmania and ~1100 km southwest of the southern tip of New Zealand atop the Macquarie Ridge system (Griffin and Varne, 1980; Duncan and Varne, 1988; Varne, 1989) (Figure 4.12). The latter comprises an arcuate and complex system of ridge, trench and fault morphologies separating the Indian-Australian and Pacific Plates, between the Pacific-Antarctic Ridge and the Alpine Fault of continental New Zealand in the southwest Pacific Ocean (Falconer, 1972; Hayes and Talwani, 1972).

Macquarie Island, considered to comprise blocks of oceanic crust belonging to the Indian-Australian Plate (e.g. Griffiths and Varne, 1972; Varne, 1989), comprises a southern region of extrusive basalts, including pillow lavas, volcanic breccias, hyaloclastites and massive lavas, cut by basaltic dykes, and a northern region of intrusive gabbros and serpentinised peridotites (originally harzburgite and dunite assemblages) cut by a series of dolerite dykes which form a sheeted dyke complex (Varne and Rubenach, 1972; Griffin and Varne, 1980; Varne, 1989). These two regions, separated by a northwest trending fault zone (Varne and Rubenach, 1972), may represent diachronous blocks of oceanic lithosphere which were uplifted and tilted during the formation of the Macquarie Ridge (Duncan and Varne, 1988) due to oblique compression (transpression) between the Indian-Australian and Pacific plates (Williamson, 1988). This transpressional regime, possibly a consequence of the proximity of the Macquarie Ridge to the Indian-Australian - Pacific pole of relative motion (Griffiths and Varne, 1972) is thought to have commenced ~10 m.y. ago following on from earlier strike-slip and extensional regimes (Williamson, 1988).

Radiometric ^{40}Ar-^{39}Ar ages for the Macquarie Island basalts range from 11.5 to 9.7 Ma (Duncan and Varne, 1988). However, a significantly older age of ~27 Ma is assigned to the formation of this section of oceanic crust at the SEIR, based on the magnetic seafloor lineation (A7) observed west of, and interpreted as crossing, Macquarie Island (Williamson, 1988). This latter age is generally consistent with the findings of Quilty et al. (1973) that calcareous *Globigerina* ooze interstitial to, and essentially coeval with, the pillow lavas at the extreme northern end (North Head) of Macquarie Island have an Early to Middle Miocene age. The discrepancy between the radiometric ages and those derived through geophysical and micropalaeontological studies could suggest some volcanic reactivation on Macquarie

Island approximately synchronous with the onset of the transpressional regime along the Macquarie Ridge which was responsible for the uplift of blocks of older oceanic lithosphere.

Six Macquarie Island basaltic (pillow rim) glass samples were analysed during the course of this study for Sr, Nd and Pb isotope ratios; details of sampling localities are listed in Appendix 1 (Table A1.2). Sample compositions range from alkali basalt and trachybasalts to olivine and quartz tholeiites (A.J. Crawford and V.S. Kamenetsky; pers. comm., 1992). The main impetus for performing these isotopic analyses stemmed from the recognition of major and trace element features within Macquarie Island basalts which appeared inconsistent with derivation from a depleted upper mantle MORB source alone (Griffin and Varne, 1980; A.J. Crawford and V.S.Kamenetsky, pers. comm., 1992). Despite the recognition by Varne et al. (1969) that the Macquarie Island basalts are generally similar in composition to Mid-Atlantic Ridge basalts, certain samples were found to have higher Nb and lower Zr/Nb, Y/Nb, Ti/Zr and K/Rb values plus enrichments in K and Sr relative to N-MORB (Griffin and Varne, 1980). The high Nb (20-60 ppm) and low Zr/Nb (3-7) values of these Macquarie Island basalts, prompted the analysis of ~30 more basaltic glasses (>6 wt % MgO) and the subsequent discovery that a positive correlation between K_2O and P_2O_5 trends from depleted N-MORB values to those more typical of enriched OIB sources (1.82 % K_2O, 0.66 % P_2O_5 in trachybasalt sample 47963; A.J. Crawford and V.S. Kamenetsky, pers. comm. 1992).

Sr, Nd and Pb isotope results (Table 4.7; Figure 4.16) indicate a general overlap between the Macquarie Island basalts and Pacific Ocean MORB (see Chapter 8 for a comparison between Pacific and Indian Ocean MORB radiogenic isotopes). However, the Macquarie Island data form a linear array, particularly in Pb-Pb space, which may well represent a mixing line between a depleted upper mantle MORB source and a HIMU-like OIB component, similar in isotopic composition to the Balleny Plume. This array is less obvious on the Sr-Nd plot of Figure 4.16 due to the relatively high $^{87}Sr/^{86}Sr$ value of trachybasalt sample 47978. It should be noted that, as proposed by Jenner (1987; cited in Varne, 1989), the Macquarie Island tholeiites have generally lower $^{87}Sr/^{86}Sr$ and higher $^{143}Nd/^{144}Nd$ values than the alkaline basalts. In terms of Pb isotope ratios, the distinction is slightly less clear. The two trachybasalts possess the highest $^{206}Pb/^{204}Pb$ and $^{208}Pb/^{204}Pb$ contents as well as slightly higher $^{207}Pb/^{204}Pb$ values, although the distinction is very small in terms of the latter ratio, and the olivine tholeiite basalt (sample 47979) has the lowest Pb isotope ratios. Therefore, it appears that, if a HIMU-like OIB source which is isotopically similar to the Balleny Plume is involved, the tholeiites, produced through higher degrees of melting, may be a product of greater upper mantle dilution of the OIB source than the more alkaline samples. This is also consistent with the major element compositions of these six Macquarie Island samples (A.J. Crawford and V.S. Kamenetsky, pers. comm. 1992). All of these samples have K_2O and P_2O_5 contents which are greater than N-MORB values. However, the tholeiites possess significantly lower contents of both elements than the alkali basalt and trachybasalt samples. This relative depletion in incompatible elements such as K and P would be expected with greater degrees of partial melting, as in the case of the tholeiitic

Table 4.7: Sr, Nd and Pb isotope data for Macquarie Island glasses; errors ($2\sigma_{mean}$) associated with individual measurements indicate within-run precision only. Rock types are classified according to the scheme of LeBas et al. (1986) based on the major element compositions determined by A.J. Crawford and V.S. Kamenetsky (pers. comm., 1992); transitional tholeiites refer to basalts with no normative hypersthene, but which plot on or below the Macdonald and Katsura (1964) line, as defined for the Hawaiian basalts. Analytical methods are described in Appendix 2. Present day epsilon values were calculated as described in Appendix 6.

Sample No.	Rock Type	$^{87}Sr/^{86}Sr$	$\pm 2\sigma$	εSr	$^{143}Nd/^{144}Nd$	$\pm 2\sigma$	εNd	$^{206}Pb/^{204}Pb$	$^{207}Pb/^{204}Pb$	$^{208}Pb/^{204}Pb$
47979	Olivine tholeiite basalt	0.702551	10	-27.7	0.513100	6	8.8	18.951	15.528	38.523
25637	Transitional tholeiite	0.702614	13	-26.8	0.513095	15	8.7	19.384	15.562	38.876
38287	Quartz tholeiite basalt	0.702636	7	-26.5	0.513071	4	8.2	19.275	15.559	38.828
25601	Alkali basalt	0.702748	3	-24.9	0.513061	9	8.0	19.294	15.565	38.808
47978	Trachybasalt	0.703315	8	-16.8	0.513040	10	7.6	19.410	15.574	38.927
47963	Trachybasalt	0.702743	14	-24.9	0.513050	9	7.8	19.493	15.589	38.979

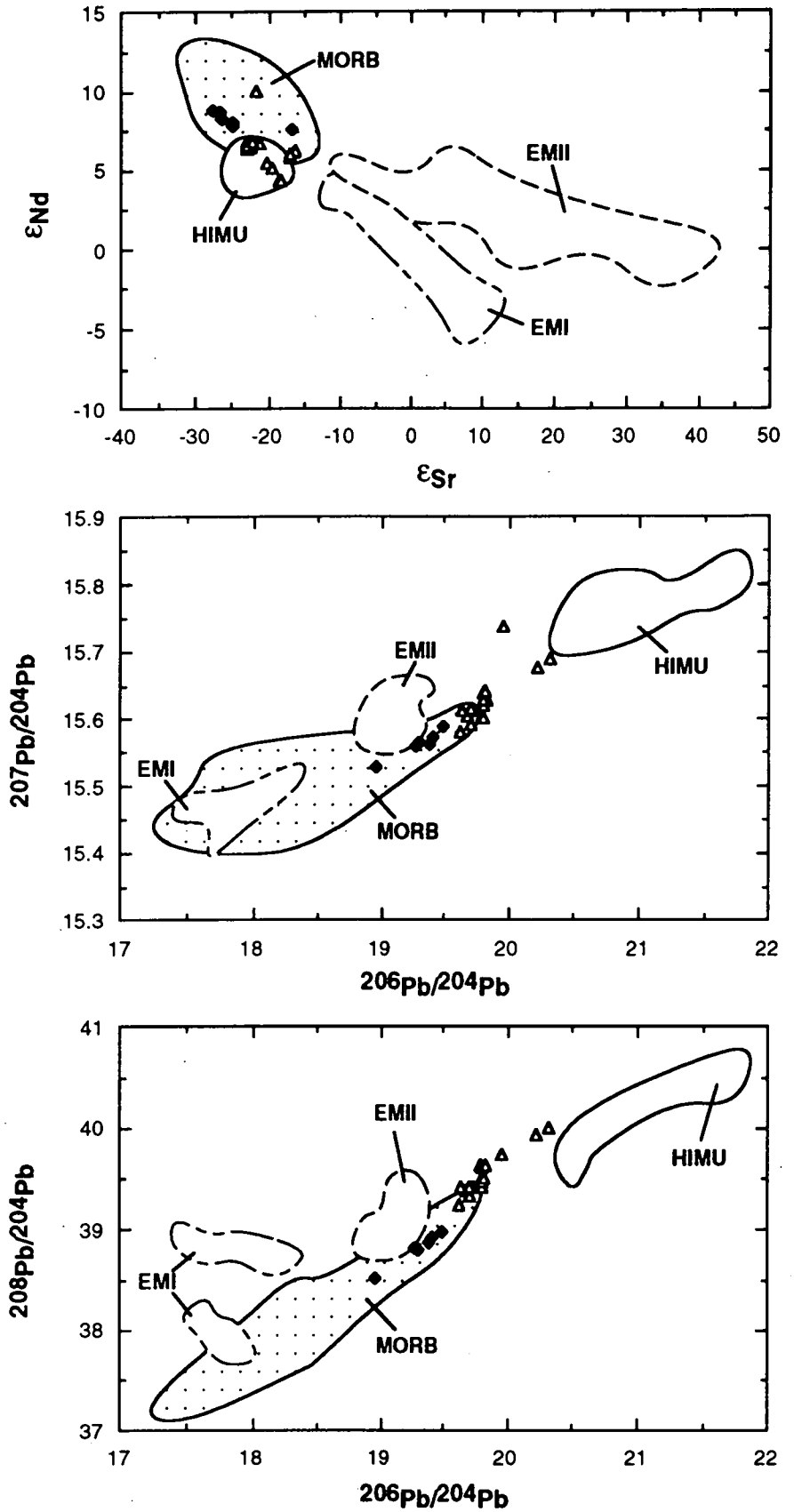

Figure 4.16: Radiogenic isotope plots comparing measured ratios for the Macquarie Island glasses (filled diamonds) with the initial ratios of the Balleny Plume volcanics (open triangles) and the HIMU, EMI and EMII OIB and MORB isotopic fields. Data sources for the OIB and MORB isotopic end-members are as for Figure 1.1. Balleny Plume volcanics include the Balleny Islands ratios of Hart (1988), age corrected as for Figure 3.20.

basalts, but the trend to high OIB-like values also appears to represent a mixing line, whereby greater input from the OIB source is consistent with lower degrees of partial melting.

The Macquarie Island basalts appear to be a product of mixing between two sources, a depleted upper mantle MORB source and an OIB source which is isotopically similar to the HIMU-like Balleny Plume. If Macquarie Island was formed by seafloor spreading at the SEIR in the Late Oligocene to Middle Miocene (Quilty et al., 1973; Williamson, 1988), the younger ^{40}Ar-^{39}Ar basaltic ages (Duncan and Varne, 1988) may reflect volcanic reactivation during the transpressional regime which has dominated the Macquarie Ridge complex during the last ~10 m.y. and resulted in the uplift of the oceanic lithosphere which forms Macquarie Island. Underplating by Balleny Plume material during the passage of the Macquarie Island region of the Indian-Australian Plate over the plume conduit, may have resulted in subsequent volcanism bearing a HIMU-like signature, but diluted by depleted upper MORB mantle. Although this may explain the occurrence of both the depleted MORB and more OIB-like geochemical and isotopic signatures of Macquarie Island basalts, underplating by the plume would have had to extend some 400 km or so from the actual Balleny plume trace. If this explanation for the HIMU-like OIB signature on Macquarie Island is correct, radiometric dating of the island's basement rocks could be expected to yield ages consistent with that of the adjoining magnetic seafloor lineations (A7 and A8 - 28 to 26 Ma) in samples with N-MORB isotopic affinities.

An alternative explanation, but one which does not explain the location of Macquarie Island adjacent to older magnetic anomaly lineations or the calcareous ooze ages derived by Quilty et al. (1973), is that plume contamination occurred during production of the oceanic crust which now comprises Macquarie Island at the time that the Balleny Plume was over-ridden by the spreading ridge, sometime between 10 and 20 Ma (Chapter 3).

Another possible explanation for the isotopic and geochemical systematics of Macquarie Island is that volcanic reactivation in response to the transpressional regime along the Macquarie Ridge Complex was influenced by a second HIMU plume responsible for the formation of Scott Island on the Antarctic Plate (Chapter 5). Further study is required to test which, if any, of these hypotheses is likely to be correct.

4.6 THE BALLENY PLUME AND THE McMURDO VOLCANIC GROUP, WEST ANTARCTICA:

The relative paucity of available radiogenic isotope and trace element data for the McMurdo Volcanic Group severely limits geochemical comparison with the Balleny Plume Volcanics. However, the location of the McMurdo Volcanic Group relative to the Balleny Islands (Figure 4.17), and claims in the literature that some link may exist between the

Balleny and Hallett Volcanic Provinces (e.g. Johnson et al., 1982), prompts this comparative study.

4.6.1 Regional Setting:

The McMurdo Volcanic Group (McMurdo Volcanics) of West Antarctica was originally defined as including all Quaternary and possibly Upper Tertiary volcanics of the Ross Archipelago and other Ross Sea islands, the Balleny and Scott Islands, and the Victoria Land coast (Harrington, 1958; Harrington et al., 1967; Nathan and Schulte, 1968). This 2000 km long region of volcanics, east and northeast of the Transantarctic Mountains, was later subdivided into four volcanic provinces, entitled the Balleny, Hallett, Melbourne and Erebus Provinces (Figure 4.17), all of which comprise Late Cainozoic intraplate, alkaline undersaturated, volcanics (Hamilton, 1972; Kyle and Cole, 1974; Kyle, 1976). However, the Balleny Volcanic Province has since been excluded from the McMurdo Volcanic Group due to its location on oceanic crust with no obvious geographic or tectonic relationship to the other McMurdo volcanic provinces (Kyle, 1990a).

Kyle and Cole (1974) considered volcanism in each of the McMurdo Group provinces to be related to unique structural features. The Balleny Province volcanics, situated at the southern end of the Balleny Fracture Zone, have been likened to the linear Hallett Province volcanics (Harrington et al., 1967; Johnson et al., 1982), due to the suggested alignment of the Balleny Fracture Zone with the Adare Peninsula at the northern end of the Hallett Volcanic Province and the inference that the latter is situated along a continental extension of this fracture zone (Kyle and Cole, 1974; Johnson et al., 1982). However, the proposed relationship between Balleny Island volcanism and a leaky transform fault, the Balleny Fracture Zone (Kyle and Cole, 1974; Vanney et al., 1981; Johnson et al., 1982), has now been superseded by the mantle plume proposal discussed in Chapter 3. Likewise, the distribution of Hallett Province volcanism is now considered to be controlled by the major crustal suture which separates the Transantarctic Mountains from the Ross Embayment (Fitzgerald et al., 1987; Kyle 1990a). The locations of Melbourne Province volcanoes are thought to be controlled primarily by north-northwest trending graben and fault structures, whereas the Erebus Volcanic Province is situated at the southern end of the Terror Rift, in a region marked by flexure in the trend of the Transantarctic Mountain chain and the intersection of several major fault zones (Kyle and Cole, 1974; Kyle, 1990a).

No obvious temporal pattern or migration of volcanic activity has been observed within the McMurdo Volcanic Group (Kyle, 1976). The oldest dated lavas, from Sheridan Bluff, within the Erebus Volcanic Province yielded an age of 19.8 Ma, alkaline intrusives within the Melbourne Volcanic Province range up to 25 Ma, and volcanogenic sediments from drill holes within McMurdo Sound may be ≥35 Ma (Kyle, 1990a). Extensive K-Ar dating by Armstrong (1978) revealed that the majority of McMurdo Group volcanics are, however, <4 Ma.

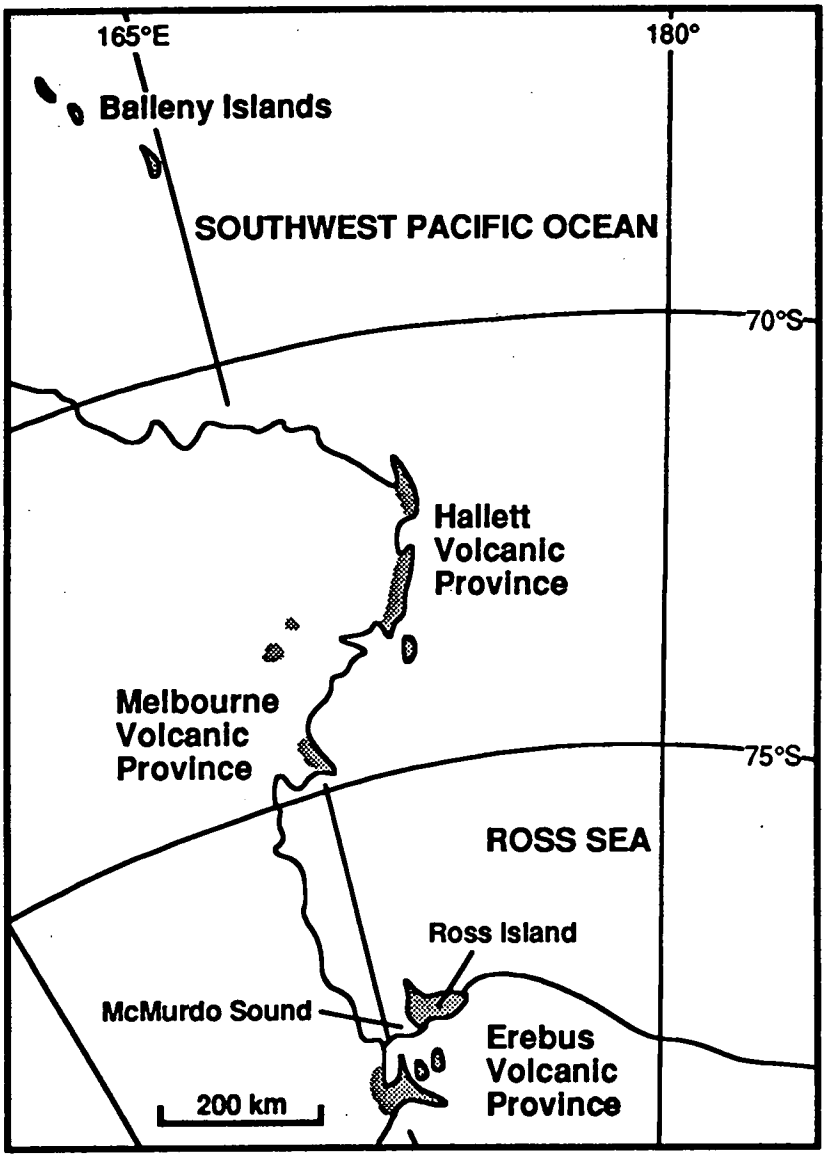

Figure 4.17: Map showing the location of the volcanic provinces comprising the McMurdo Volcanic Group of the Victoria Land - Ross Sea region of West Antarctica relative to the Balleny Islands (modified from Kyle, 1976).

The Transantarctic Mountains - Ross Embayment region is generally considered to have resulted from continental extension during rifting (e.g. Kyle and Cole, 1974; Moore and Kyle, 1987). The Ross Embayment comprises an 800 km wide region of continental crust with an average thickness of ~25 km (Bentley, 1983; McGinnis et al., 1983), a minimum thickness of ~21 km within McMurdo Sound (McGinnis et al., 1985), and a proposed original thickness, prior to rifting, of 35-40 km (Fitzgerald et al., 1987). The Transantarctic Mountains to the west comprise an uplifted region of 40-45 km thick continental crust, step-faulted down towards, and bounded abruptly by, the anomalously thin crust of the Ross Embayment. To the east of the Ross Embayment, the continental crust gradually increases in thickness to 35 km under Marie Byrd Land. The latter area and the Ross Embayment are considered to represent complementary lower and upper plate margins, resulting from detachment faulting (e.g. Lister et al., 1986) during continental rifting, whereas the

Transantarctic Mountains are a product of underplating and uplift of the upper plate margin (Fitzgerald et al., 1987). Extension in the Ross Sea region, interpreted as being spatially continuous with Tasman Sea extension, is thought to have ceased either just before or just after the onset of seafloor spreading in the Tasman Sea (Etheridge et al., 1989).

Several mechanisms have been proposed to explain the occurrence of the McMurdo Group Volcanics. Fitzgerald et al. (1987) believe that McMurdo Group volcanism is related to continental rifting within the Ross Sea Embayment. However, its onset, possibly as early as ~35 Ma, does appear to post-date both rifting and uplift (Kyle, 1981), the latter thought to have commenced at ~50 Ma (Fitzgerald et al., 1987). Smith and Drewry (1984) interpreted Late Cainozoic volcanism and uplift in the Ross Sea - Transantarctic Mountains region of Antarctica as a delayed product of the over-riding of a hot linear asthenospheric source, the site of a former oceanic ridge, by heated lithosphere during Australian-Antarctic separation (Smith and Drewry, 1984). Kyle (1976) concluded that the McMurdo Sound area of the Erebus Volcanic Province overlies two mantle plumes, each of which is responsible for the doming and radial symmetry of both fractures and volcanic vents associated with Mt. Erebus and Mt. Discovery.

4.6.2 Radiogenic Isotope Characteristics of the McMurdo Volcanic Group:

Sr and Pb isotope data are only available for samples from the Erebus Volcanic Province, most of which were collected from various sites on, and in the immediate vicinity of, Ross Island; no $^{143}Nd/^{144}Nd$ data are available. Low $^{87}Sr/^{86}Sr$ and high Pb isotope ratios appear to be a general feature of the alkaline volcanics of this province (Table 4.5; Figure 4.18). Further reports of low Sr isotopic values include an average $^{87}Sr/^{86}Sr$ value of 0.70366±25 for 38 volcanics collected from Ross Island and southern Victoria Land (Jones and Walker,1972) and an average $^{87}Sr/^{86}Sr$ value of 0.70345 for three salt samples collected from the summit of Mount Erebus and considered to represent Sr derived from the exposed summit rocks and the emitted volcanic gases (Jones et al., 1983). Two rock samples with higher $^{87}Sr/^{86}Sr$ values, 0.70480 (trachyte sample 29; Stuckless and Ericksen, 1976) and 0.70453 (tephrite sample CB_2; Zhu and Fan, 1989), interpreted as a product of crustal contamination and input from a Kerguelen-type OIB source respectively, have been omitted from the data sets used here due to their anomalous nature compared to the bulk of Erebus Volcanic Province samples analysed.

The overall isotopic trends displayed by the Erebus Province alkaline volcanics (Figure 4.18) are generally consistent with mixing between a HIMU-like source and a MORB source (DMM). There is considerable overlap with the Balleny Plume volcanics in both the Sr and Pb isotopic systems, although the Erebus Province volcanics extend to values indicative of greater upper mantle contamination. In Pb-Pb space, the Erebus Province volcanics display some anomalous features with respect to the Balleny Plume array. A second linear array, subparallel to the proposed HIMU-DMM array, but comprising higher $^{207}Pb/^{204}Pb$ at similar $^{206}Pb/^{204}Pb$ values, plus the scatter evident within the less

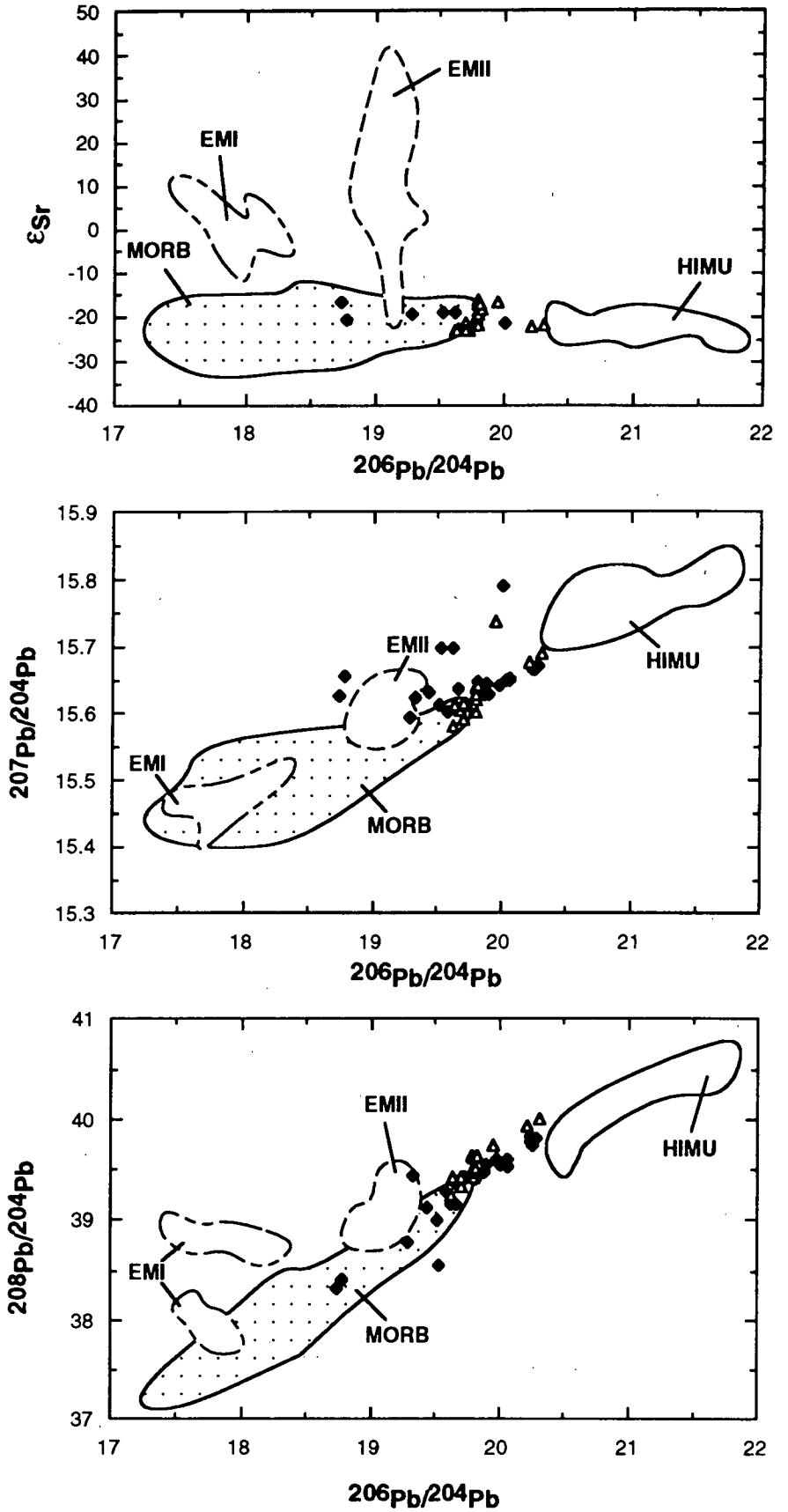

Figure 4.18: Radiogenic isotope plots comparing measured ratios for the Erebus Volcanic Province (filled diamonds) with the initial ratios of the Balleny Plume volcanics (open triangles) and the HIMU, EMI and EMII OIB and MORB isotopic fields. Data sources for the OIB and MORB isotopic end-members are as for Figure 1.1. Balleny Plume volcanics include the Balleny Islands ratios of Hart (1988), age corrected as for Figure 3.20. *Erebus Volcanic Province* data from Sun and Hanson (1975b) and Zhu and Fan (1989) are normalised as for Figure 1.1.

radiogenic end of the $^{206}Pb/^{204}Pb$-$^{208}Pb/^{204}Pb$ array, may be products of crustal contamination during eruption. However, considering the abundance of Ross Island samples which have been analysed for $^{87}Sr/^{86}Sr$, the fact that only two samples have been found to have relatively high values suggests that crustal contamination was minimal, possibly due to rapid eruption through thinned continental crust post-rifting. Despite these features, the Erebus Volcanic Province, and the Ross Island region in particular, has a similar HIMU-DMM isotopic signature to the Balleny Plume volcanics.

4.6.3 Trace Element Characteristics of the McMurdo Volcanic Group:

Trace element data for relatively unevolved samples (≥5 wt % whole-rock MgO) from the McMurdo Volcanic Group, and the Hallett Volcanic Province in particular, are relatively scarce. Therefore, little can be concluded about the trace element systematics of the source/s of the McMurdo Group Volcanics on the basis of the trace element ratio ranges and mean values documented for each of the McMurdo Group provinces in Table 4.6. The Melbourne and Erebus Volcanic Provinces have similar low LILE/Nb, La/Nb and Zr/Nb values to the Balleny Plume volcanics but the available Hallett Province data are characterised by higher mean Ba/Nb and La/Nb values and a greater range of Ba/La values.

4.6.4 Possible Balleny Plume Influence on the McMurdo Volcanic Group:

Based on the HIMU-DMM Sr and Pb isotope characteristics of the Erebus Province alkaline volcanics, it seems likely that their derivation has involved melting of a HIMU-like mantle plume source, similar to the Balleny Plume, and its entrained depleted upper mantle material. However, a more detailed study, involving comprehensive radiogenic isotope and trace element analyses of relatively unevolved alkaline volcanics from all three McMurdo Group provinces, is necessary before any conclusions can be made about the source/s of the McMurdo Volcanic Group as a whole.

The location of the McMurdo Volcanic Group, bordering a region of continental rifting, the Ross Embayment, may be significant when attempting to determine the cause of volcanism and the source of the HIMU-like isotopic signature of the Erebus Volcanic Province. This region of continental extension is thought to have been continuous with Tasman Sea extension (Etheridge et al., 1989) prior to the westward propagation of the Pacific-Antarctic Ridge at ~80 Ma (Bradshaw, 1989). If upwelling of the Balleny Plume head did result in extensive lithospheric underplating by HIMU plume material prior to or synchronous with the onset of significant seafloor spreading in the Tasman Sea at ~80 Ma (Section 4.4.5), it seems likely that the spatially continuous region of West Antarctica at this time would also have been underplated. The fact that rifting within the Ross Sea Embayment is thought to have ceased either just before or just after the onset of seafloor spreading in the Tasman Sea (Etheridge et al., 1989) means that the lithosphere in this region may already have undergone significant thinning prior to plume head underplating, depending on when the latter occurred relative to rifting. Although the intersection of the Balleny plume

head with this thinned lithosphere, as opposed to the pre-rifted lithospheric thickness proposed for the New Zealand region at this time (Section 4.4.5), may be expected to have produced surface volcanism in the Ross Embayment region, sporadic McMurdo Group volcanism is thought to have commenced up to 45 m.y. later (~35 Ma; Kyle, 1990a) in response to more localised stresses (Kyle and Cole, 1974; Kyle 1990a).

4.7 CONCLUSIONS:

A regional HIMU mantle signature, characterised predominantly by low $^{87}Sr/^{86}Sr$, high $^{143}Nd/^{144}Nd$ and high Pb isotope values, is evident in the mafic volcanism of continental regions of southeast Australia (Tasmania), the South Island, offshore and sub-Antarctic islands of New Zealand, and Marie Byrd Land and the Erebus Volcanic Province of West Antarctica. The trace element systematics of these regions are also generally characterised by HIMU-like low LILE/Nb, LREE/Nb and Zr/Nb values, although data are somewhat sketchy. These regional radiogenic isotope, and to a lesser extent trace element, features are similar to those of the Balleny Plume volcanics (Chapter 3). On the basis of the spatial proximity of these continental areas to each other and to the proposed site of initial Balleny Plume upwelling prior to the break-up of Gondwana, they are likely to be related to the same HIMU plume source. This HIMU signature is, however, absent from the Cretaceous hypabyssal rocks of Cape Portland and Port Cygnet in Tasmania and the Cretaceous to Tertiary Older and Newer volcanics of Victoria.

It is here proposed that the head of a relatively weak starting plume, the Balleny Plume, ascended beneath the region of Gondwana defined by the intersection of what were to become, with future rifting, the continental regions of Tasmania (southeast Australia), New Zealand, Marie Byrd Land (Antarctica) and Victoria Land (Antarctica). Entrainment of significant amounts of cooler ambient mantle during ascent, and subsequent intersection with relatively thick continental lithosphere prevented the plume head from melting. Flattening and horizontal spreading of the plume head therefore resulted in extensive lithospheric underplating, unaccompanied by the significant melting and surface volcanism often associated with starting plume heads.

The Balleny Plume head ascended at or prior to ~80 Ma, into a region within which continental rifting had already commenced between Lord Howe Rise and eastern Australia and between Marie Byrd Land and Victoria Land in Antarctica, now represented by the Tasman Sea and Ross Embayment respectively. Plume head interaction with the already weakened lithosphere in these regions may have been responsible for the concurrent onset of seafloor spreading in the Tasman Sea region and the westward propagation of the Pacific-Antarctic Ridge between the Campbell Plateau and Marie Byrd Land at ~80 Ma. Mafic volcanism on the Chatham Islands at this time attests to the presence of a HIMU mantle source in this region. The sporadic nature of subsequent HIMU-like volcanism in the

previously contiguous continental regions of Australia, New Zealand and Antarctica is best explained by decompression, melting and subsequent volcanism of underplated Balleny Plume head-entrained upper mantle material in response to localised tectonic stresses in those regions.

As continental rifting proceeded, movement of the Indian-Australian Plate over the Balleny Plume conduit or tail resulted in the linear hotspot trace described in Chapter 3. The Macquarie Island region of the Indian-Australian Plate may have been contaminated by plume material during its passage close to the plume tail, resulting in subsequent volcanism bearing a HIMU-DMM signature, although it is likely that a second HIMU plume was involved (Chapter 5). Once the SEIR had passed over the plume tail, it was then overlain by the relatively stationary Antarctic Plate. The linear nature of subsequent Balleny Plume volcanism, as defined by the Balleny Island/Seamount chain extending between magnetic anomalies A5 and A6 on the Antarctic Plate and therefore superimposed on 10 to 20 Ma seafloor, suggests however, that some north-northwesterly lithospheric migration must be associated with the Antarctic Plate.

Further, more detailed, studies of these various continental regions should be aimed at relating the isotopic and trace element systematics of mafic volcanism to radiogenic ages, locations and known tensional regimes in order to more precisely define the chain of events resulting in this broad region of HIMU volcanism surrounding the southern Tasman Sea and southwest Pacific Ocean.

CHAPTER 5

SCOTT ISLAND - THE SITE OF ANOTHER HIMU MANTLE PLUME?

5.1 INTRODUCTION:

The model presented in Chapters 3 and 4, whereby the HIMU isotopic and trace element signature which dominates the dispersed fragments of eastern Gondwana and the intervening seafloor in the southwest Pacific Ocean region is ascribed solely to the Balleny Plume, may be somewhat simplistic. The presence of HIMU volcanics in the Scott Island region, located ~650 km east of, but at approximately the same latitude as, the Balleny Islands, may reflect the presence of more than one HIMU mantle plume currently underlying the Antarctic Plate.

Isotopic and geochemical analyses of samples dredged from the Scott Island region, and from four sites located on seafloor northwest of the Balleny Islands and northwest to north-northwest of Scott Island, are aimed at testing for the possible presence of a second HIMU plume in this region and on examining the interaction of both this and the Balleny Plume with volcanism at the Pacific-Antarctic and Southeast Indian spreading ridges respectively. This second HIMU plume may also be the source of the HIMU-DMM signature of the Macquarie Island alkaline volcanics discussed in Chapter 4.

5.2 GEOLOGICAL SETTING:

All samples examined in this chapter are submarine rocks, dredged by the *USNS Eltanin*. Details of sampling locations (latitudes, longitudes, water depths) are listed in Appendix 1 - Table A1.1; bathymetric profiles are presented in Figure A1.1. They will be subdivided in the following sections into Scott Island samples and southwest Pacific Ocean seafloor samples.

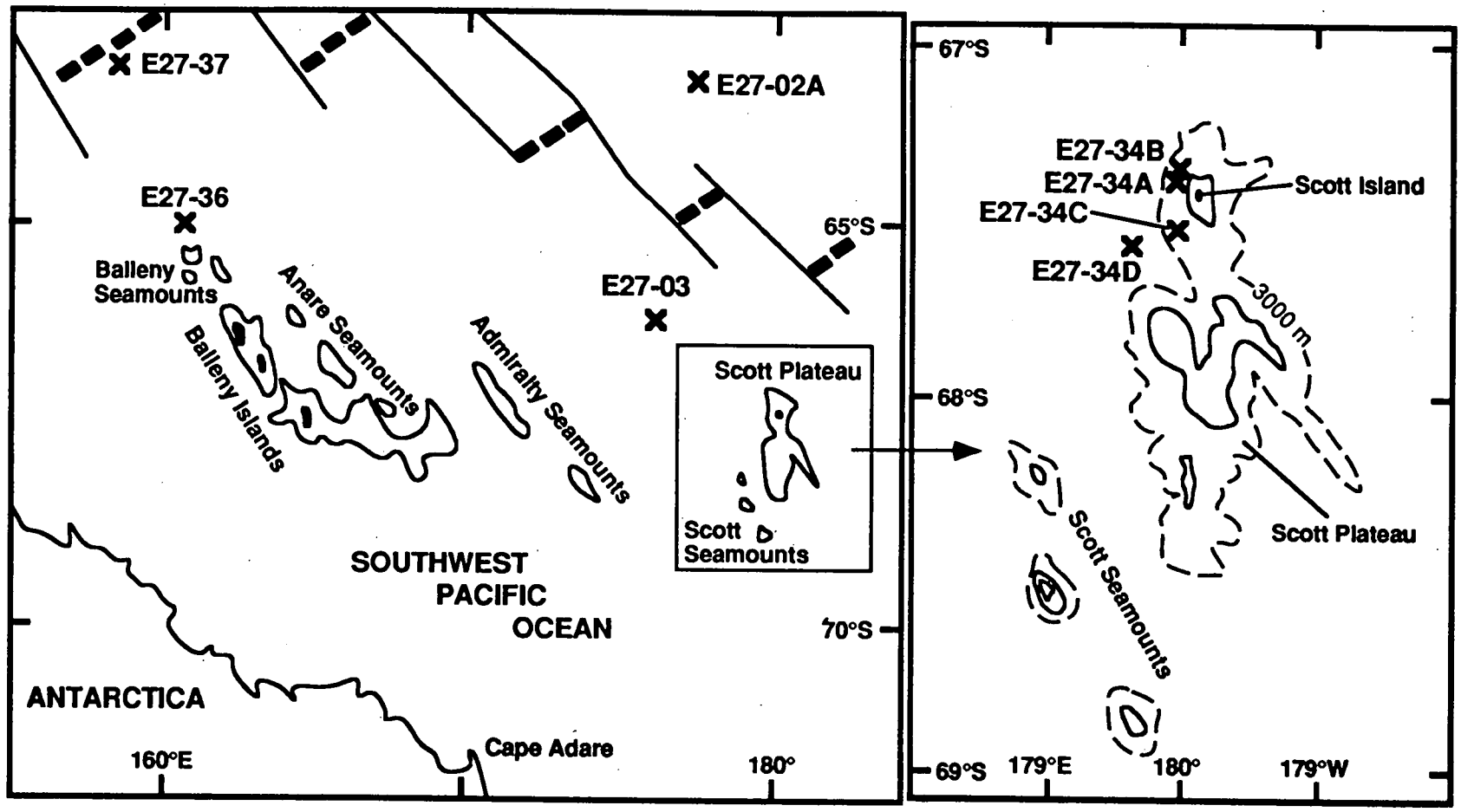

Figure 5.1: Map of the Scott Island region of the Antarctic Plate (modified from Johnson et al., 1982) showing the location of the dredge sites discussed in the text relative to the Balleny Islands and the Pacific-Antarctic Ridge (thick dashed line).

5.2.1 Scott Island:

The Scott Island samples were collected from four dredge sites on and adjacent to the Scott Plateau (Figure 5.1). Samples collected from each location are relatively evolved and fairly uniform in composition, comprising phonolites at three sites (E27-34A, E27-34B and E27-34D) and phonotephrites at site E27-34C (Figure 5.2).

Scott Island (67°30'S 180°00'), a flat-topped island which rises ~100 m above sea level, plus an adjacent isolated rocky pillar known as Haggit's Pillar, are located at the eastern boundary of the Balleny Basin on the northernmost end of the elongate submarine Scott Plateau (Figure 5.1). This 30 km wide plateau extends for ~145 km in a north-south direction along the 180° parallel (Wright and Kyle, 1990d). Three unsampled seamounts, the Scott Seamounts, are situated ~100 km southwest of Scott Island (Johnson et al., 1982). Although the Scott Plateau has a predominant north-south trend, which is inconsistent with the northwest-southeast fracture zone pattern of the region and the trend of the Balleny Islands chain (Vanney et al., 1981; Johnson et al., 1982), it does display northwest-southeast trending features (Figure 5.1b) which parallel the overall alignment of the Scott Seamounts.

No radiometric age data are available for Scott Island or Plateau, but the former is located in the vicinity of magnetic lineation A6 on the Antarctic Plate, atop ~20 Ma seafloor .

5.2.2 Southwest Pacific Ocean Seafloor:

The southwest Pacific Ocean seafloor samples examined in this chapter derive from three dredge sites on the Antarctic Plate and one site on the Pacific Plate north of the Pacific-Antarctic Ridge (Figure 5.1). These samples are all alkaline in nature and display a range of compositions both within and between the various dredge sites (Figure 5.2).

Dredge site E27-02A is located on the Pacific Plate, approximately 150 km north of the Pacific-Antarctic spreading ridge and ~430 km north-northwest of Scott Island. It is also situated north of magnetic lineation A6, on very rugged seafloor >20 Ma, at a depth of 3660 m. Dredge E27-03 was sited on the Antarctic Plate ~120 km southwest of the Pacific-Antarctic Ridge axis and ~200 km northwest of Scott Island. Although located close to the southern ridge flank, at a depth of 3541 m, the seafloor is less rugged than at site E27-02A near the northern ridge flank (Figure A1.1). Site E27-03 is also located on seafloor older than 20 Ma (south of A6).

Dredge sites E27-36 and E27-37 are both located on the Antarctic Plate northwest of the Balleny Islands. Dredge E27-36 was sited ~240 km southwest of the SEIR on 2837 m deep seafloor directly north of the Balleny Seamounts and magnetic lineation A5 (9 Ma). Site E27-37 is situated on the southern flank of the SEIR, ~370 km northwest of Young Island and immediately adjacent to the ridge crest. It has therefore sampled virtually zero-age ridge volcanism.

5.3 PETROGRAPHY AND MINERAL CHEMISTRY:

The petrography and mineral chemistry of the Scott Island and southwest Pacific Ocean seafloor samples which have been analysed for major and trace element chemistry (Sections 5.4 and 5.5), are summarised here. Electron microprobe data for representative silicate and oxide phenocryst/microphenocryst phases are presented in Appendix 3, along with the notation used for mineral chemistry throughout this thesis. Calculated olivine Mg-values (Mg#) in equilibrium with whole-rock compositions are presented in Appendix 3 (Table A3.10).

5.3.1 Scott Island Samples:

The petrography and mineral chemistry of ten submarine Scott Island samples is summarised in Table 5.1. Due to the similarity of samples from each dredge site in terms of igneous textures, mineral components and mineral chemistry, a general description is given for each location. Representative electron microprobe analyses of feldspar crystals are depicted in Figure 5.3.

The phonotephrites from dredge site E27-34C are feldspar-phyric, comprising phenocryst and groundmass-sized plagioclase, olivine, titanomagnetite and very rare kaersutite within an altered glassy matrix. The phonolites (from dredge sites E27-34A, E27-34B and E27-34D) are dominated by a feldspar-rich pilotaxitic groundmass, comprising both elongate laths and more irregularly-shaped interlocking grains, paralleled by tabular microphenocrysts of slightly less potassic feldspar. Titanomagnetite and olivine are present as both microphenocryst and groundmass phases within all but the E27-34A phonolites, from which olivine is absent.

It is interesting to note that the submarine Scott Island phonolites from each of the three dredge sites differ in hand-specimen appearance, ranging from slightly vesicular light greenish-grey rocks at site E27-34A to dark grey or black aphanitic to glassy-looking and conchoidally fractured samples at site E27-34B to the grey 'moth-eaten' and pitted appearance of sample 34D-1. A great range in appearance and colour has also been observed within the subaerial Scott Island phonolites (I.E.M. Smith, pers. comm., 1993).

The phonotephrites (site E27-34C) contain the most anorthitic feldspars (up to An_{55}) and the most magnesian olivines (up to $Mg\#_{59.3}$) of all the submarine Scott Island samples. Phonolites from each of the other three dredges have similar within-site mineral chemistry, but vary slightly between sites. Samples from sites E27-34B and E27-34D show similar ranges in both feldspar and olivine chemistry, although the former extend to slightly more Mg-rich olivine (up to $Mg\#_{20.0}$) compositions and have elongate anorthoclase microlites with bubble-like inclusions and more potassic compositions (up to $An_{15}Ab_{56}Or_{29}$) than sample 34D-1 feldspars. Olivines within E27-34B and E27-34D samples contain ~3 to 4 wt % MnO and ~1 to 2 wt % CaO, but 34D-1 olivines are yellow whereas E27-34B phonolites

Table 5.1: Petrography of submarine Scott Island samples. Notation as for Table 3.1.

Sample No.	Rock Type	Texture	Phenocrysts and microphenocrysts	Groundmass
E27-34A-1 E27-34A-2 E27-34A-4	Phonolite	Microporphyritic/ Pilotaxitic groundmass Slightly vesicular	1) feldspar microphenocrysts ($An_{21}Ab_{72}Or_7$-$An_8Ab_{70}Or_{22}$ - oligoclase to anorthoclase) 2) titanomagnetite microphenocrysts	subparallel anorthoclase to sanidine laths ($An_{18}Ab_{71}Or_{11}$-$An_3Ab_{62}Or_{35}$); fine Fe-oxides
E27-34B-1 E27-34B-2 E27-34B-3 E27-34B-4	Phonolite	Microporphyritic/ Pilotaxitic groundmass	1) feldspar microphenocrysts ($An_{31}Ab_{64}Or_5$-$An_{21}Ab_{70}Or_9$ - andesine-oligoclase): zoning (N,U), olivine inclusions 2) olivine microphenocrysts ($Mg\#_{14.3\text{-}19.5}$): may be enclosed by feldspar 3) titanomagnetite microphenocrysts	subparallel feldspar ($An_{36}Ab_{56}Or_8$-$An_{18}Ab_{67}Or_{15}$ - andesine-oligoclase-anorthoclase) laths; microlites of anorthoclase ($An_{15}Ab_{56}Or_{29}$-$An_{13}Ab_{65}Or_{22}$); olivine ($Mg\#_{18.5\text{-}20.0}$); titanomagnetite; accessory apatite needles
E27-34C-1 E27-34C-2	Phonotephrite	Microporphyritic/ Hypocrystalline Vesicular	1) plagioclase microphenocrysts ($An_{51\text{-}55}$ - labradorite): zoning (N, U) 2) olivine microphenocrysts($Mg\#_{57.0\text{-}59.3}$); melt inclusions 3) titanomagnetite microphenocrysts 4) rare kaersutite microphenocrysts	plagioclase ($An_{40\text{-}54}$ - labradorite-andesine); olivine ($Mg\#_{56.4\text{-}58.5}$); and fine titaniferous magnetites in a dark brown glassy matrix
E27-34D-1	Phonolite	Microporphyritic/ Pilotaxitic groundmass	1) plagioclase microphenocrysts ($An_{30}Ab_{65}Or_5$ - $An_{25}Ab_{70}Or_5$ - andesine-oligoclase); rare anorthoclase ($An_{20}Ab_{67}Or_{13}$) cores: zoning (U, R, N) 2) titaniferous magnetite microphenocrysts 3) olivine microphenocrysts ($Mg\#_{16.1\text{-}18.7}$)	feldspar ($An_{30}Ab_{65}Or_5$ - $An_{12}Ab_{70}Or_{18}$ - andesine-oligoclase-anorthoclase); olivine ($Mg\#_{18.2}$); titaniferous magnetite; accessory apatite crystals

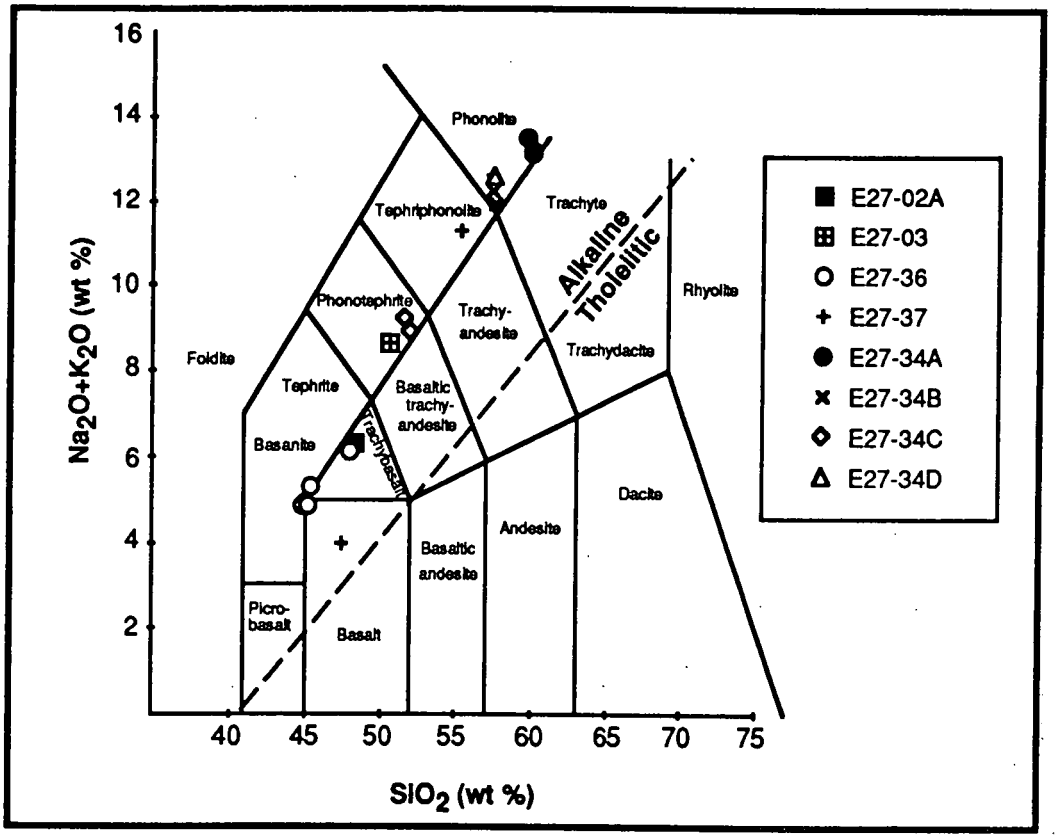

Figure 5.2: Classification of the submarine Scott Island and southwest Pacific Ocean seafloor samples discussed in the text according to the TAS diagram of Le Bas et al. (1986) using normalised major element data from Section 5.4; alkaline and tholeiitic fields are separated by the diagonal (dashed) line of Macdonald and Katsura (1964), as applied to the Hawaiian basalts.

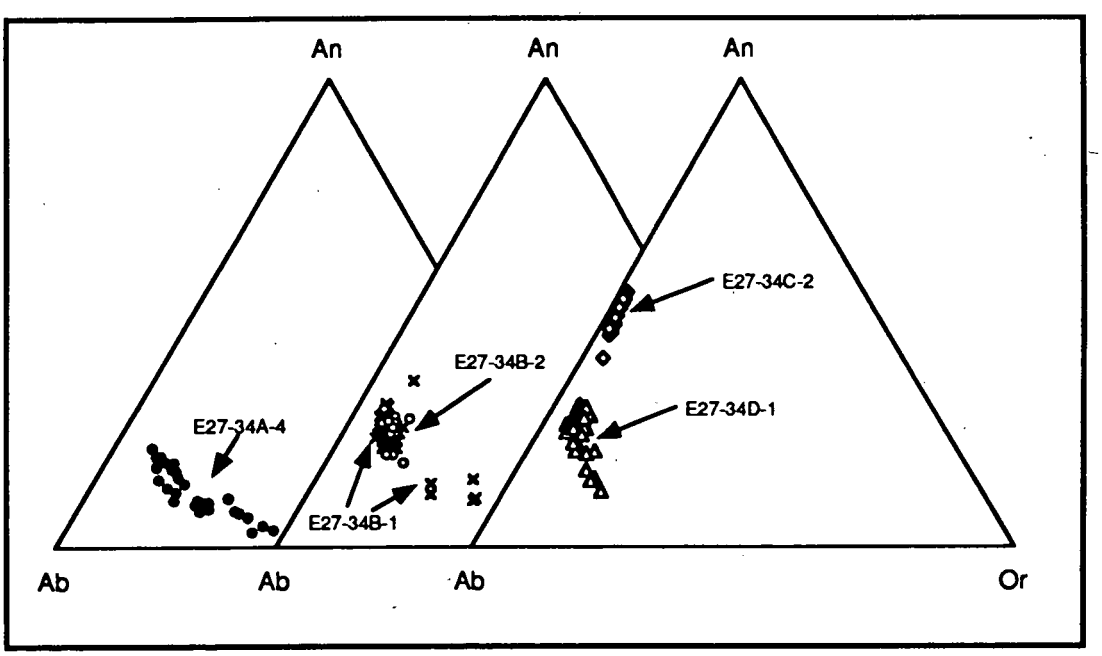

Figure 5.3: Representative electron microprobe analyses of feldspar crystals within submarine Scott Island samples - E27-34A-4 (filled circles), E27-34B-1 (oblique crosses), E27-35B-2 (open circles), E27-34C-2 (open diamonds) and E27-34D-1 (open trangles).

have green glassy olivine crystals. Phonolites from site E27-34A extend to the most potassic feldspar compositions (up to $An_3Ab_{62}Or_{35}$).

Sparse evidence of crystal-liquid disequilibrium is visible as partial resorption of plagioclase microphenocrysts in sample 34C-2 and reverse zoning of some plagioclase microphenocrysts in sample 34D-1. Samples 34C-2 and 34D-1 also contain some olivine crystals (up to $Mg\#_{59.3}$ and $Mg\#_{18.7}$ respectively) which are more Mg-rich than predicted ($Mg\#_{55.1}$ and $Mg\#_{17.0}$ respectively) by the equilibrium whole-rock - olivine calculations of Table A3.10. All of the submarine Scott Island samples are characterised by a lack of clinopyroxene.

5.3.2 Southwest Pacific Ocean Seafloor Samples:

The petrography and mineral chemistry of ten seafloor samples from the four southwest Pacific Ocean dredge sites is summarised in Table 5.2. Representative electron microprobe analyses of silicate and oxide minerals are depicted in Figures 5.4 and 5.5 respectively.

5.3.2.1 Dredge E27-02A:

The single trachybasalt (sample 02A-2) analysed from this locality comprises microphenocrysts of olivine, plagioclase and titanomagnetite within a groundmass composed of the same mineral phases. Microphenocryst and groundmass olivine crystals (up to $Mg\#_{60.5}$) display extensive iddingsite alteration; plagioclase microphenocrysts (up to An_{55}) may be partly resorbed, and groundmass plagioclase occurs as quenched microlites.

5.3.2.2 Dredge E27-03:

Sample 03 is a plagioclase-phyric phonotephrite with scattered plagioclase phenocrysts and microphenocrysts of partially altered olivine, green salite and titanomagnetite. These three microphenocryst phases also occur in the groundmass where they are intergranular to aligned plagioclase laths, and as inclusions within the plagioclase phenocrysts, suggesting that plagioclase was the last phase to crystallise. Olivine (up to $Mg\#_{60.7}$) and plagioclase (up to An_{57}) have similar compositions to those in trachybasalt sample 02A-2 from the previous dredge site, although the latter is distinct in its lack of clinopyroxene.

5.3.2.3 Dredge E27-36:

Of the five samples analysed from dredge E27-36, four are basanites with variable hand-specimen appearances. Most of them are grey to brown, vesicular, and porphyritic to microporphyritic, but sample 36-4 is a rubbly agglomerate of rounded to angular brown vesicular pebbles. Three of the basanites collected from this site (samples 36-2, 36-4 and 36-7) have seriate textures (grainsize from <0.1 to 4 mm) involving anhedral to euhedral and skeletal olivine and clinopyroxene crystals, commonly displaying resorbed rims. Olivine

Table 5.2: Petrography of southwest Pacific Ocean seafloor samples. Notation as for Table 3.1.

Sample No.	Rock Type	Texture	Phenocrysts and microphenocrysts	Groundmass
E27-02A-2	Trachybasalt	Microporphyritic Vesicular	1) plagioclase microphenocrysts (An_{46-55} - labradorite-andesine): zoning (N) 2) olivine microphenocrysts ($Mg\#_{60.5}$): Fe-oxide inclusions 3) Mg-Al titanomagnetite microphenocrysts	olivine; plagioclase; Fe-oxides
E27-03	Phonotephrite	Porphyritic/ Pilotaxitic groundmass Sparsely vesicular	1) plagioclase phenocrysts (An_{43-57} - labradorite-andesine): zoning (N, U, R), olivine ($Mg\#_{35.8-49.0}$), cpx and Fe-oxide inclusions 2) olivine microphenocrysts ($Mg\#_{48.8-60.7}$ - rims: $Mg\#_{48.8-56.8}$, core: $Mg\#_{54.1-60.7}$): zoning (N) 3) cpx microphenocrysts ($Mg\#_{62.4-65.4}$ - salite) 4) Mg-Al-titanomagnetite microphenocrysts	plagioclase (An_{41-52} - labradorite-andesine); olivine ($Mg\#_{49.2-53.0}$); cpx finely divided opaques
E27-36-2 **E27-36-4**	Basanite Basanite	Seriate-textured/ Glomeroporphyritic Vesicular	1) olivine phenocrysts and microphenocrysts ($Mg\#_{70.5-88.1}$): zoning (N, R), inclusions of spinel (Cr-pleonaste and Mg-Al-titanomagnetite in phenocrysts, Cr-pleonaste in microphenocrysts) and cpx ($Mg\#_{72.2-78.6}$ - salite), rare cpx ($Mg\#_{68.3-70.5}$ - salite) overgrowth rims 2) cpx phenocrysts and microphenocrysts ($Mg\#_{65.3-84.3}$ - diopside-salite-augite): zoning (P, O, R), olivine ($Mg\#_{79.3-81.5}$), kaersutite, spinel (pleonaste, Mg-Al-titanomagnetite), and rare diopside ($Mg\#_{84.1}$) inclusions 3) plagioclase phenocrysts (rims: An_{72-75} - bytownite, cores: An_{45-46} - andesine) 4) spinel (Cr-pleonaste, Cr-Al-titanomagnetite, Mg-Al-titanomagnetite) microphenocrysts 5) glomerocrysts: olivine ; cpx ± olivine ± spinel (Mg-Al-titanomagnetite)	olivine ($Mg\#_{66.4-79.4}$); cpx ($Mg\#_{73.4-82.6}$ - diopside-salite-augite); plagioclase (An_{48-74} - bytownite-labradorite); Fe-oxides (magnesioferrite ± ilmenite)
E27-36-5	Basanite	Microporphyritic/ Hypocrystalline groundmass Vesicular	1) olivine microphenocrysts and rare phenocrysts ($Mg\#_{76.2-87.5}$): zoning (N, R), spinel inclusions 2) spinel (pleonaste) microphenocrysts	olivine ($Mg\#_{78.0-87.5}$); plagioclase (An_{68-72} - bytownite-labradorite); cpx ($Mg\#_{70.4-75.2}$ - salite); Al-titanomagnetite; devitrified glass

Table 5.2: (continued)

Sample No.	Rock Type	Texture	Phenocrysts and microphenocrysts	Groundmass
E27-36-7	Basanite	Seriate-textured/ Glomeroporphyritic Slightly vesicular	1) olivine phenocrysts ($Mg\#_{80.7-86.7}$) and microphenocrysts ($Mg\#_{69.1-86.9}$): zoning (N), spinel (Cr-pleonaste, pleonaste Cr-Al-titanomagnetite, Mg-Al-titanomagnetite) inclusions, rare more Fe-rich olivine overgrowth rims 2) cpx phenocrysts ($Mg\#_{70.9-83.5}$ - diopside-salite, may have diopside core and salite rim) and microphenocrysts (rims: diopside or salite - $Mg\#_{72.9-78.8}$, cores: salite - $Mg\#_{66.0-72.7}$, rare apple-green cores of more Fe-rich salite - $Mg\#_{61.8}$): zoning (N, R, P, O), olivine ($Mg\#_{81.5}$) inclusions 3) feldspar phenocrysts (An_{48-49} - andesine; rare cores of andesine - An_{35} zoned to sanidine - $An_8Ab_{54}Or_{38}$) 4) glomerocrysts: olivine ($Mg\#_{79.9-86.9}$); salite ($Mg\#_{72.9-78.5}$); or olivine ($Mg\#_{76.8-84.0}$) surrounded by cpx ($Mg\#_{76.6-82.8}$)	olivine ($Mg\#_{65.5-80.8}$); cpx ($Mg\#_{69.3-81.1}$ - salite); plagioclase (An_{48-61} - labradorite); Mg-Al-titanomagnetite
E27-36-8	Trachybasalt	Seriate-textured/ Glomeroporphyritic	1) olivine phenocrysts and microphenocrysts ($Mg\#_{75.5-87.0}$): zoning (U, N, R), spinel (Cr-pleonaste, Cr-Al-titanomagnetite) inclusions, cpx overgrowths ($Mg\#_{68.6-78.5}$ - salite) 2) cpx phenocrysts and microphenocrysts - predominantly salite ($Mg\#_{68.1-81.3}$), rare diopside ($Mg\#_{83.3-83.9}$), rare apple-green salite cores: zoning (N,R,O), simple or sector twinning, spinel (Cr-pleonaste), olivine ($Mg\#_{79.0-83.4}$) and devitrified melt inclusions 3) rare anorthoclase phenocrysts ($An_{21}Ab_{69}Or_{10}$ to $An_{14}Ab_{71}Or_{15}$): sieve textures due to bands of groundmass and melt inclusions 4) glomerocrysts: cpx ($Mg\#_{69.0-83.6}$ - salite) ± olivine ($Mg\#_{77.0-82.6}$) ± spinel	cpx ($Mg\#_{72.7-80.9}$ - salite); olivine ($Mg\#_{71.5-82.7}$); plagioclase (An_{41-71} - bytownite-labradorite-andesine); spinel (Mg-Al-titanomagnetite,Cr-Al-titanomagnetite)

Table 5.2: (continued)

Sample No.	Rock Type	Texture	Phenocrysts and microphenocrysts	Groundmass
E27-37-2	Alkali olivine basalt	Glomeroporphyritic/ Hypocrystalline Vesicular	1) cpx phenocrysts and microphenocrysts ($Mg\#_{72.6-82.8}$ - diopside-salite): zoning (U, R, P), twinning, plagioclase (An_{73-83} - bytownite) inclusions 2) olivine phenocrysts ($Mg\#_{80.4-85.7}$) and microphenocrysts ($Mg\#_{75.6-79.1}$): spinel (Cr-pleonaste) and diopside ($Mg\#_{82.8-84.2}$) inclusions 3) plagioclase phenocrysts and microphenocrysts (An_{64-86} - bytownite-labradorite): zoning (O, R), plagioclase (An_{81-83} - bytownite) inclusions, sieve-textures 4) glomerocrysts: plagioclase(An_{73-83} - bytownite) ± olivine ($Mg\#_{76.6-77.5}$) ± cpx ($Mg\#_{76.3-79.1}$ - salite)	plagioclase (An58-77 - bytownite-labradorite); cpx (Mg#66.5-87.2 - diopside-salite-augite); completely altered olivine; Mg-Al-titanomagnetite; dusty devitrified brown glass
E27-37-3	Tephriphonolite	Aphyric/Pilotaxitic Vesicular	-	1) plagioclase laths (An_{32-46} - andesine); 2) yellow olivines ($Mg\#_{28.7-33.7}$): zoning (N,R) 3) Al-titanomagnetite 4) intersertal orange-yellow alteration material

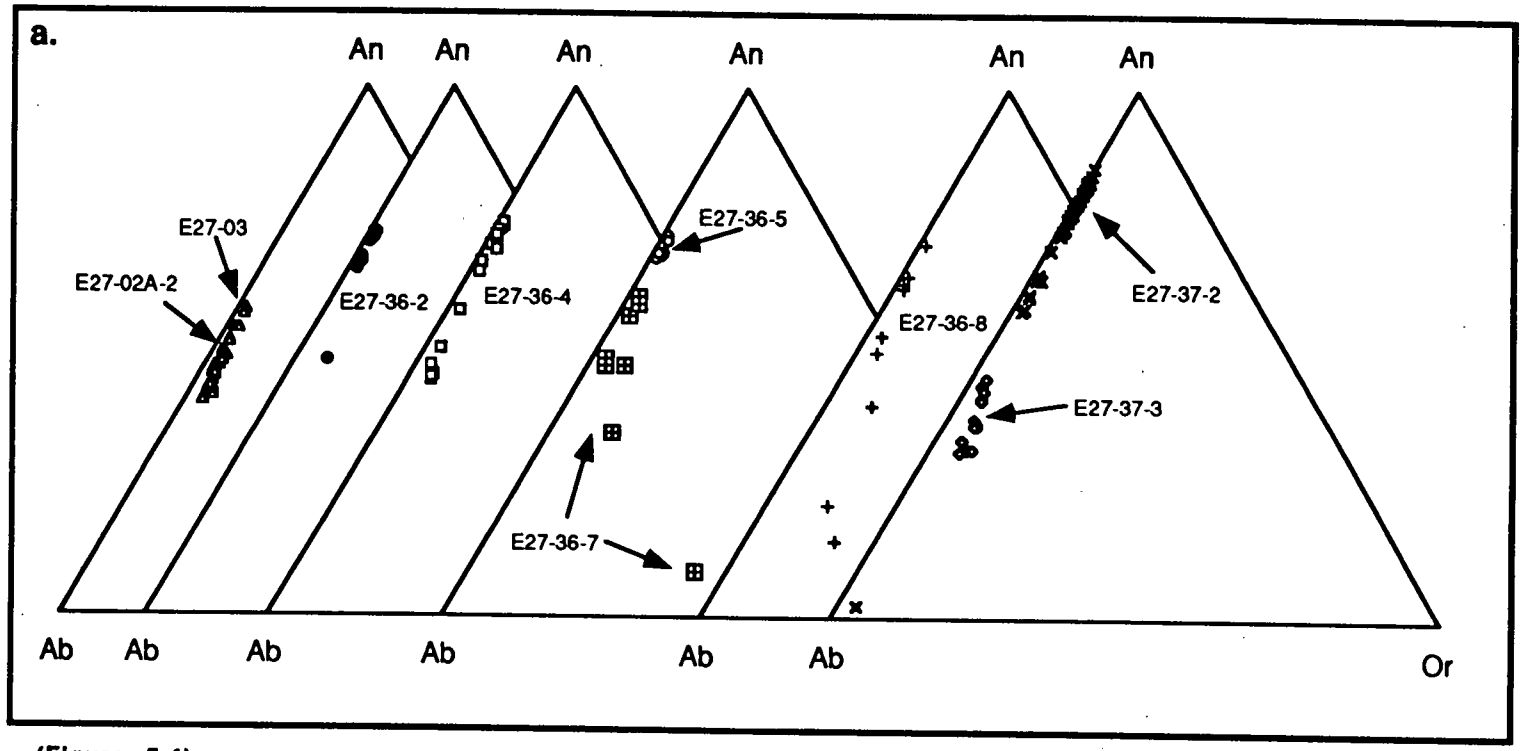
a.
An
An
An
An
An
An
E27-03
E27-02A-2
E27-36-2
E27-36-4
E27-36-5
E27-36-8
E27-37-2
E27-37-3
E27-36-7
Ab
Ab
Ab
Ab
Ab
Ab
Or

(Figure 5.4)

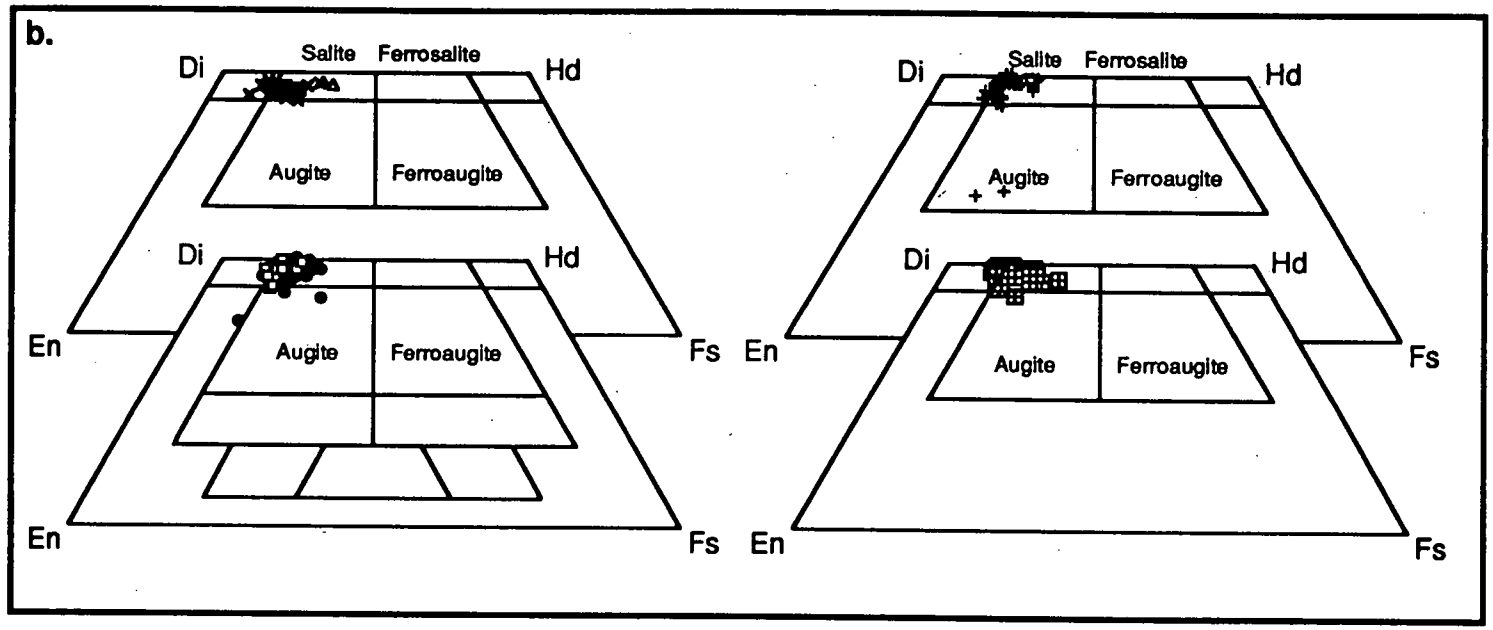

Figure 5.4: Representative electron microprobe analyses of a) feldspar and b) clinopyroxene within southwest Pacific Ocean seafloor samples E27-02A-2 (filled triangles - feldspar only), E27-03 (open triangles), E27-36-2 (filled circles), E27-36-4 (open squares), E27-36-5 (open circles), E27-36-7 (crosses within squares), E27-36-8 (crosses), E27-37-2 (oblique crosses) and E27-37-3 (open diamonds - feldspar only).

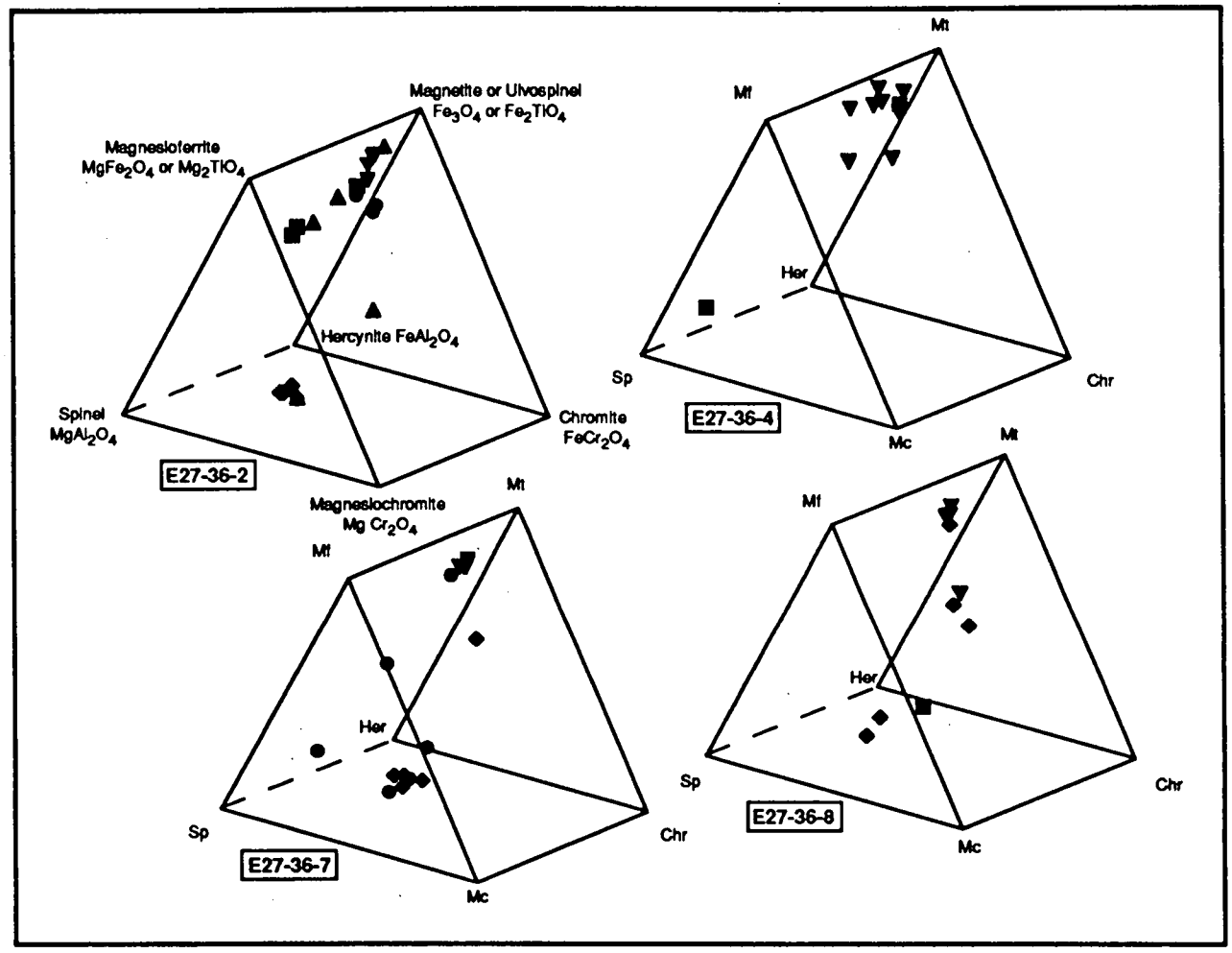

Figure 5.5: Representative electron microprobe analyses of spinel, within four southwest Pacific Ocean seafloor samples, plotted on modified Johnston spinel prisms (Deer et al., 1992: p. 560). Symbols used are: inclusion within olivine phenocryst (filled circle), inclusion within olivine microphenocryst (filled diamond), inclusion within clinopyroxene (filled square), microphenocryst (filled triangle), groundmass crystal (inverted filled triangle).

crystals within sample 36-4 are partially to completely altered. Where seriate textures are discussed, an arbitrary grainsize classification has been adopted to distinguish phenocryst (>1 mm), microphenocryst (0.2 to 1 mm) and groundmass (<0.2 mm) crystals, as used for the Balleny Plume volcanics described in Chapter 3. Plagioclase occurs as phenocryst and groundmass sized crystals only. Monomineralic and polymineralic glomerocrysts of olivine and/or clinopyroxene and spinel are also scattered throughout these rocks.

The fourth basanite (sample 36-5) has rare phenocrysts and slightly more abundant microphenocrysts of pleonaste, and partially to completely altered subhedral, euhedral and skeletal olivine within a hypocrystalline groundmass. The latter, although dominated by devitrified glass, also comprises scattered plagioclase laths, olivine, clinopyroxene and titanomagnetite.

Trachybasalt sample 36-8 has a similar seriate texture and mineralogy to three of the basanite samples from this locality. Olivine displays a range of morphologies, including skeletal, embayed, hollow and rare elongate parallel growth crystals; overgrowth rims of salite are uncommon. Glomerocrysts of olivine and/or clinopyroxene generally comprise groundmass-sized crystals. Rare plagioclase phenocrysts have sieve textures produced by bands of fine melt inclusions.

In terms of their mineral chemistry, basanite samples 36-2 and 36-4 are very similar. Reverse compositional zoning, although a common feature of the olivine (up to $Mg\#_{88.1}$) and clinopyroxene (up to $Mg\#_{84.3}$) phenocryst/microphenocryst phases, is most marked within the plagioclase phenocrysts which have andesine cores (up to An_{46}) and bytownite (up to An_{75}) rims. Groundmass plagioclase compositions overlap with that of the phenocryst rims. Spinel compositions are varied. Cr-pleonaste occurs as microphenocrysts and as inclusions within olivine phenocrysts, suggesting that olivine and spinel were early co-crystallising phases. The occurrence of Cr-aluminous titanomagnetite and Mg-aluminous titanomagnetite microphenocrysts and inclusions within clinopyroxene phenocrysts, and Mg-aluminous titanomagnetite within olivine microphenocrysts, suggest that less Cr-rich spinel was co-crystallising with later-formed clinopyroxene and olivine. The rare occurrence of salitic clinopyroxene overgrowth rims (up to $Mg\#_{70.5}$) around olivine phenocrysts in sample 36-2 and the presence of olivine inclusions within clinopyroxene are also indicative of olivine representing an early crystallisation phase. However, clinopyroxene, with a more Mg-rich composition (up to $Mg\#_{78.6}$) than that rimming olivine, also occurs as inclusions within olivine.

Despite its similar petrographic texture and mineralogy, basanite sample 36-7 has slightly different mineral chemistry to samples 36-2 and 36-4. Olivine (up to $Mg\#_{86.9}$) and clinopyroxene (up to $Mg\#_{83.6}$) extend to slightly less Mg-rich compositions. Feldspar phenocrysts, although still of andesine (up to An_{49}) composition, may be rimmed by sanidine rather than bytownite. Groundmass plagioclase is again more anorthitic (up to An_{61}) than the phenocrysts. Other distinctive features of sample 36-7 include rare more Fe-rich olivine overgrowth rims ($Mg\#_{72.9}$) around olivine phenocrysts ($Mg\#_{79.9}$), and angular apple-

green Fe-rich salite cores ($Mg\#_{61.8}$) with overgrowth rims of less Fe-rich salite ($Mg\#_{77.6}$). Clinopyroxene crystals with homogeneous light-brown to pink cores and slightly lighter coloured rims may have either normal or less marked reverse compositional zoning.

Basanite sample 36-5 has phenocrystic and groundmass olivine with similar compositional ranges (up to $Mg\#_{87.5}$), overlapping with olivine compositions within the other basanites but extending to slightly greater Mg-values than in sample 36-7. Groundmass plagioclase crystals within sample 36-5 are also more anorthitic (up to An_{72}) than in sample 35A-7, but similar to that found in samples 36-2 and 36-4. The most magnesian clinopyroxenes found ($Mg\#_{75.2}$) are more Fe-rich than in the other basanites, and Cr-rich spinel is absent.

Trachybasalt sample 36-8 has similar mineral chemistry to the basanite samples 36-2, 36-4 and 36-7, with which it also displays textural similarites. Olivine (up to $Mg\#_{87.0}$) and predominantly greenish-brown clinopyroxene (diopside and salite up to $Mg\#_{83.9}$), the former sometimes rimmed by the latter, both display reverse compositional zoning and some clinopyroxenes also have sector twinning. As in sample 36-7, angular apple-green clinopyroxene cores may be rimmed with pinkish-brown, more Ti-rich and Fe-poor clinopyroxene, all of which have salitic compositions. Cr-pleonaste occurs as inclusions within both olivine and clinopyroxene, but is absent as a microphenocryst phase; phenocrystic feldspar has a more potassic composition (anorthoclase up to $An_{14}Ab_{71}Or_{15}$) than groundmass plagioclase (An_{41-71}).

Probable textural and compositional disequilibrium features are abundant in the dredge E27-36 rocks. Reverse compositional zoning of olivine, clinopyroxene and plagioclase is commonplace, as are partly resorbed crystal rims in olivine and clinopyroxene. There are olivine phenocrysts and/or microphenocrysts in all of the olivine-bearing samples which have higher Mg-values than predicted to be in equilibrium with their corresponding whole-rock compositions (Table A3.10) and they may therefore represent inherited xenocrystic or cumulate phases. Other possible inherited minerals include the apple-green Fe-rich cores in sample 36-7 and 36-8 clinopyroxenes, and the feldspar phenocrysts or phenocryst cores within samples 36-2, 36-4, 36-7 and 36-8. Medium- to coarse-grained clots of olivine and clinopyroxene up to 1.5 cm in diameter appear to represent inherited material in sample 36-7.

5.3.2.4 Dredge E27-37:

Alkali olivine basalt sample 37-2 comprises phenocrysts and microphenocrysts of clinopyroxene, olivine and plagioclase within a hypocrystalline matrix. Scattered glomerocrysts may be monomineralic or they may comprise any combination of plagioclase, slightly altered subhedral olivine, and greenish-brown subhedral to euhedral clinopyroxene crystals, the latter often partially or completely enclosing plagioclase. Groundmass olivine is completely altered. Tephriphonolite sample 37-3 is aphyric and dominated by a pilotaxitic

arrangement of plagioclase laths with intersertal yellow olivine, cube-shaped Fe-oxides and alteration material.

The mineral chemistry of sample 37-2 is somewhat similar to that of the dredge E27-36 seriate-textured basanites, with phenocrysts of olivine ranging up to $Mg\#_{85.7}$. Olivine microphenocrysts have lower Mg-values (up to $Mg\#_{79.1}$) than the phenocrysts, groundmass clinopyroxene crystals (up to $Mg\#_{87.2}$) extend to higher Mg-values than analysed clinopyroxene phenocrysts and microphenocrysts (up to $Mg\#_{82.8}$), and sieve-textured plagioclase phenocrysts and microphenocrysts extend to more anorthitic compositions (An_{86}) than any of the dredge E27-36 rocks. Disequilibrium features of sample 37-2 include reverse compositional zoning in both clinopyroxene and plagioclase phenocrysts, and more Mg-rich olivine compositions than predicted by whole-rock olivine equilibrium calculations (Table A3.10).

Sample 37-2 contains olivines with homogeneous Fe-rich compositions (up to $Mg\#_{33.7}$), andesine plagioclase laths (up to An_{46}) and aluminous titanomagnetite crystals.

5.4 MAJOR ELEMENT GEOCHEMISTRY:

The major element compositions of the submarine Scott Island and southwest Pacific Ocean seafloor samples (Tables 5.3 and 5.4 respectively) were determined by X-ray fluorescence (XRF) spectrometry (Philips PW 1410 spectrometer) as described in Appendix 2.

5.4.1 Scott Island Samples:

The submarine Scott Island samples are all alkaline and define a SiO_2-undersatured (Figure 5.6) trend from the phonotephrites of dredge E27-34C through the phonolites of dredges E27-34B and E27-34D to the slightly more evolved phonolites of dredge E27-34A (Figure 5.2). This trend is defined in the major element plots of Figure 5.7 by increasing SiO_2, Na_2O, K_2O and Al_2O_3 and decreasing TiO_2, FeO^*, CaO and P_2O_5 with decreasing MgO. The chemical variation of these relatively evolved rocks is consistent with fractionation involving Fe-rich olivine, titanomagnetite, apatite and feldspar.

Previous work on this region was limited to the geochemical analysis of five samples, all of which have similar alkaline affinities to those analysed during the course of this study, and to rocks outcropping at Cape Crozier on Ross Island (Johnson et al., 1982; Campsie et al., 1983). Four of these samples (Campsie et al., 1983) are from the same *Eltanin* dredges and have similar compositions to those analysed herein (Figure 5.8), although what is here classified as a phonotephrite (dredge E27-34C) has been previously described as a ne-mugearite (Wright and Kyle, 1990d). Likewise, a subaerial Scott Island sample (Prior, 1907), described as a phonolite (Wright and Kyle 1990d), is classified here as a tephriphonolite.

Table 5.3: Major and trace element chemistry of submarine Scott Island samples; notation as for Chapter 3 (Section 3.5).

Sample No:	E27-34A-1	E27-34A-2	E27-34A-4	E27-34B-1	E27-34B-2	E27-34B-3	E27-34B-4	E27-34C-1	E27-34C-2	E27-34D-1
Major Elements (wt %):										
SiO_2	58.52	58.40	58.57	56.72	56.52	56.66	56.33	50.67	50.24	56.87
TiO_2	0.10	0.09	0.10	0.34	0.32	0.33	0.31	1.56	1.59	0.35
Al_2O_3	18.99	18.90	18.99	18.59	18.45	18.77	18.40	17.78	17.68	18.67
Fe_2O_3	5.96	5.81	5.65	8.51	8.31	8.43	8.40	10.81	10.94	8.08
FeO	0.00	0.00	0.00	0.00	0.00	0.00	0.00	0.00	0.00	0.00
MnO	0.23	0.20	0.20	0.29	0.30	0.28	0.30	0.28	0.25	0.25
MgO	0.11	0.15	0.23	0.32	0.31	0.32	0.38	2.10	2.03	0.25
CaO	1.55	1.51	1.62	2.58	2.59	2.59	2.58	6.02	5.95	2.65
Na_2O	9.07	8.69	8.67	8.04	8.49	8.06	8.30	6.21	6.38	8.61
K_2O	4.13	4.15	4.11	3.70	3.81	3.65	3.72	2.49	2.56	3.78
P_2O_5	0.11	0.12	0.10	0.22	0.24	0.23	0.24	0.86	0.87	0.22
LOI	0.74	1.78	1.60	0.10	0.07	0.04	0.53	1.14	1.22	0.29
Total	99.51	99.80	99.84	99.41	99.41	99.36	99.49	99.92	99.71	100.02
Mg#	4.13	5.69	8.69	8.08	8.02	8.15	9.56	31.22	30.25	6.74
FeO*	5.36	5.23	5.08	7.66	7.48	7.59	7.56	9.73	9.84	7.27
Trace Elements (ppm):										
Ba	942	964	923	1095	1106	1067		747	704	1168
Rb	121	107	112	101	103	103		52	54	101
Nb	221	216	220	230	230	229		168	170	228
Sr	377	422	384	671	673	672		1104	1114	707
Zr	886	850	871	742	746	748		477	483	733
Y	39	39	38	40	39	40		39	39	40
Ni	3	2	4	2	<1	<1		6	6	<1
Cr	<2	<2	2	<2	<2	<2		3	<2	<2
V	<3	<3	4	<3	<3	4		39	36	<3
Sc	<1	<1	1	1	<1	<1		5	5	2
Zn	167	159	168	161	156	161		137	137	149
Cu	<2	<2	2	5	<2	3		13	11	<2
Cs	1.24	1.07	0.93	1.25	1.06	1.06	1.00	0.79	0.58	1.11
Hf	15.99	14.89	15.39	14.06	13.62	13.52	13.28	9.45	9.20	13.77
Ta	15.79	14.53	15.03	14.66	14.35	14.03	13.94	10.33	10.11	14.25
Th	23.92	22.05	23.02	21.09	20.28	20.33	19.66	12.20	11.84	20.22

This sample is intermediate in composition to the phonotephrites of dredge E27-34C and the phonolites of dredges E27-34B and E27-34D (Figure 5.8).

The rocks of Scott Island and Plateau define a narrow range of evolved major element compositions from phonotephrite through tephriphonolite to phonolite. It has been suggested that they may have evolved by fractional crystallisation from an alkali basalt or basanite similar to that found in the Balleny Islands region (Johnson et al., 1982; Campsie et al., 1983).

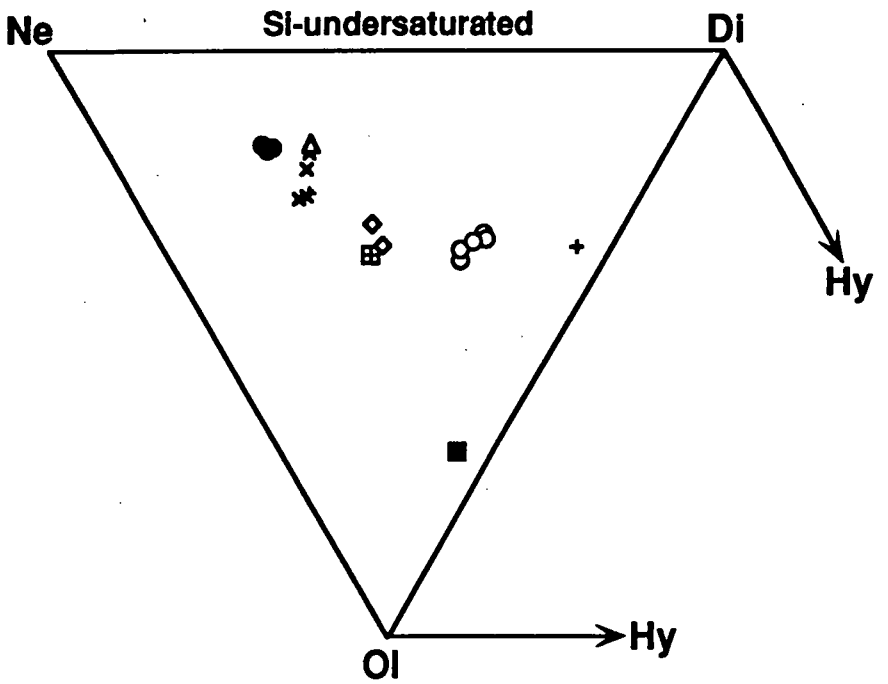

Figure 5.6: Projection of the normative basalt tetrahedron (Yoder and Tilley, 1962) for submarine Scott Island and southwest Pacific Ocean seafloor samples as for Figure 3.9. Dredge symbols are: E27-02A (filled square), E27-03 (cross within square), E27-34A (filled circles), E27-34B (oblique crosses), E27-34C (open diamonds), E27-34D (open triangle), E27-36 (open circles) and E27-37 (crosses).

5.4.2 Southwest Pacific Ocean Seafloor Samples:

5.4.2.1 Dredges E27-02A and E27-03:

Trachybasalt sample 02A-2 and phonotephrite sample 03, although collected from dredge sites ~300 km apart, no less than ~200 km from Scott Island, and on different sides of the Pacific-Antarctic spreading ridge appear to form a less evolved continuation of the fractionation trend displayed by the samples collected from the Scott Island region (Figures 5.2 and 5.7). They are both SiO_2-undersaturated rocks (Figure 5.6) which lack the tholeiitic affinities of N-MORB (Figure 5.2), and are therefore not simply a product of mid-ocean ridge volcanism. They may derive from a similar source to the Scott Island/Plateau rocks.

SiO2 (wt %)
MgO (wt %)
Cpx
Ol
Sp
Pl
Al2O3 (wt %)
MgO (wt %)
Ol
Cpx
Sp
Pl
TiO2 (wt %)
MgO (wt %)
Cpx
Ol
Sp
Pl
FeO* (wt %)
MgO (wt %)
Ol
Sp
Cpx
Pl

(Figure 5.7)

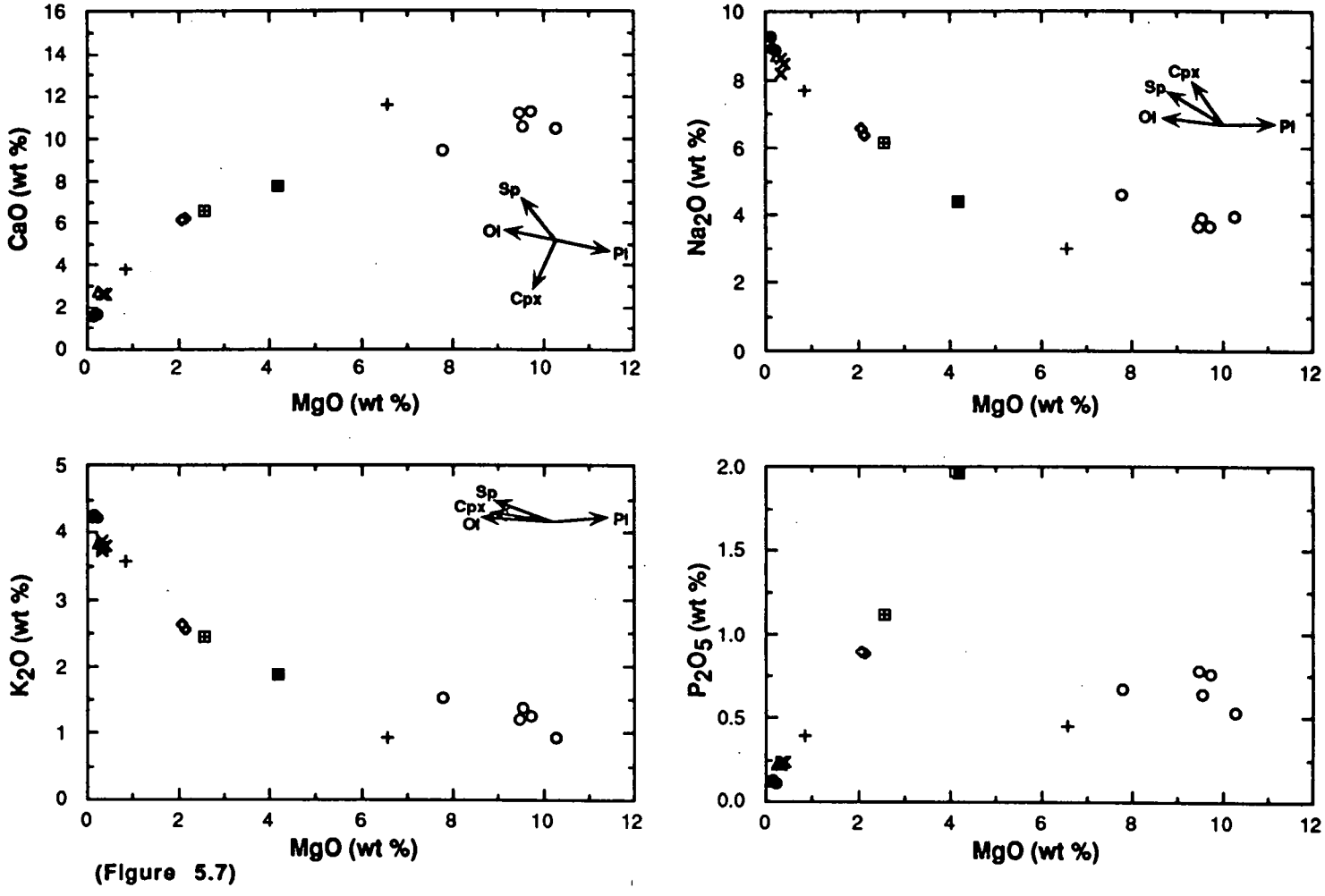
CaO (wt %)
MgO (wt %)
Sp
Ol
Pl
Cpx
Na2O (wt %)
MgO (wt %)
Cpx
Sp
Ol
Pl
K2O (wt %)
MgO (wt %)
Sp
Cpx
Ol
Pl
P2O5 (wt %)
MgO (wt %)

(Figure 5.7)

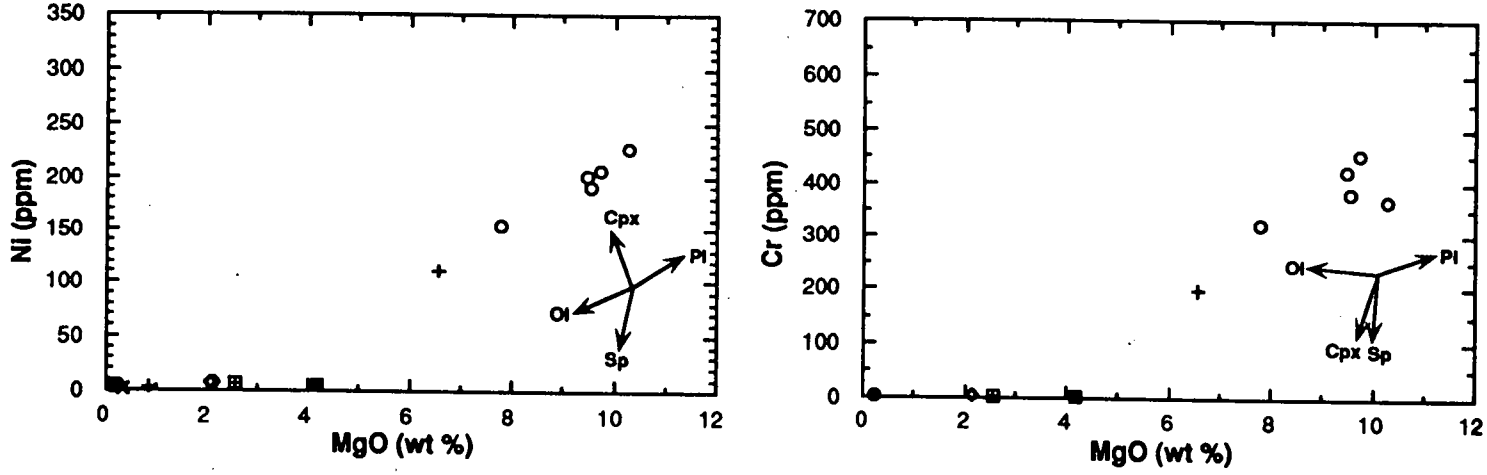

Figure 5.7: MgO (wt %) versus major elements plus Ni and Cr for submarine Scott Island (*USNS Eltanin* dredge E27-34A - filled circles; dredge E27-34B - oblique crosses; dredge E27-34C - open diamonds; dredge E27-34D - open triangle), and southwest Pacific Ocean seafloor (*USNS Eltanin* dredge E27-02A - filled square; dredge E27-03 - cross within square; dredge E27-36 - open circles; dredge E27-37 - crosses) samples. The fractionation vectors relate to the dredge E27-36 samples and were plotted relative to sample E27-36-4 (MgO ~10 wt %) in each diagram, using the following mineral compositions: E27-36-4 olivine (Ol) - Table A3.7, analysis 7; E27-36-4 clinopyroxene (Cpx) - Table A3.7, analysis 26; E27-36-4 plagioclase (Pl) - Table A3.7, analysis 40; E27-36-2 spinel (Sp = Cr-pleonaste) - Table A3.8, analysis 1.

Table 5.4: Major and trace element chemistry of southwest Pacific Ocean seafloor samples; notation as for Chapter 3 (Section 3.5).

Sample No:	E27-02A-2	E27-03	E27-36-2	E27-36-4	E27-36-5	E27-36-7	E27-36-8	E27-37-2	E27-37-3
Major Elements (wt %):									
SiO_2	46.56	49.29	44.35	43.62	44.37	44.67	47.34	46.61	54.34
TiO_2	2.56	1.82	3.03	2.75	2.61	3.01	2.51	2.77	0.67
Al_2O_3	15.38	17.67	13.96	14.32	14.67	14.10	14.85	15.13	18.92
Fe_2O_3	13.45	11.26	12.12	12.24	12.00	12.19	11.35	12.82	9.00
FeO	0.00	0.00	0.00	0.00	0.00	0.00	0.00	0.00	0.00
MnO	0.26	0.22	0.20	0.17	0.18	0.20	0.19	0.17	0.22
MgO	4.01	2.52	9.62	10.03	9.36	9.37	7.70	6.47	0.83
CaO	7.45	6.45	11.11	10.20	10.30	11.02	9.28	11.36	3.77
Na_2O	4.27	5.99	3.60	3.85	3.81	3.62	4.52	2.97	7.54
K_2O	1.81	2.40	1.24	0.90	1.35	1.18	1.51	0.93	3.52
P_2O_5	1.90	1.09	0.75	0.52	0.63	0.77	0.66	0.45	0.39
LOI	2.19	0.85	0.02	1.46	0.23	0.07	-0.23	0.66	1.01
Total	99.84	99.56	100.00	100.06	99.51	100.20	99.68	100.34	100.21
Mg#	41.06	34.34	64.97	65.69	64.57	64.24	61.32	54.11	17.73
FeO^*	12.10	10.13	10.91	11.01	10.80	10.97	10.21	11.54	8.10
Trace Elements (ppm):									
Ba	594	571	431	343	406	452	560	283	714
Rb	40	57	27	24	35	26	45	20	102
Nb	107	98	89	61	76	90	111	43	122
Sr	825	886	782	618	683	775	743	499	703
Zr	349	422	287	217	250	286	361	193	593
Y	45	38	31	30	31	30	32	29	33
Ni	5	5.6	206	227	190	201	153	110	3
Cr	4	3	453	368	379	421	321	197	<2
V	107	49	272	222	223	270	202	297	<3
Sc	20	6	27	30	37	25	20	29	2.5
Zn	138	111	99	88	91	98	103	115	132
Cu	16	25	62	31	54	62	44	66	10
Cs	<1	<1	<1	0.61	<1	<1	<1	<1	1.14
Hf	7.87	9.13	6.59	5.02	5.44	6.39	6.75	5.21	11.09
Ta	7.03	6.91	6.20	4.17	4.92	5.90	6.43	3.03	8.41
Th	7.80	8.78	6.95	4.74	5.96	6.90	7.71	3.59	14.81

5.4.2.2 Dredges E27-36 and E27-37:

Dredge E27-36 and E27-37 samples are alkaline, SiO_2-undersaturated (Figures 5.2 and 5.6), basanites and trachybasalts with MgO contents of ~8-10 wt %. Dredge E27-37 samples have lower MgO contents, and include an alkali olivine basalt and a tephriphonolite. These samples do not appear to lie along the same fractionation trends defined by the dredge samples collected further to the east, in and to the northwest of the Scott Island region (Figure 5.7).

Dredge E27-36 comprises primitive basanites, with whole-rock Mg# up to 65.69 and Ni contents up to 227 ppm (sample 36-4). They are compositionally similar to the least evolved submarine Balleny Province rocks (Figure 5.9), and together with the E27-37 samples, follow similar fractionation trends, controlled predominantly by olivine, clinopyroxene and Cr-spinel down to ~4 wt % MgO.

Importantly, these dredges have not sampled seafloor with MORB-type geochemical features, despite their proximity to the SEIR.

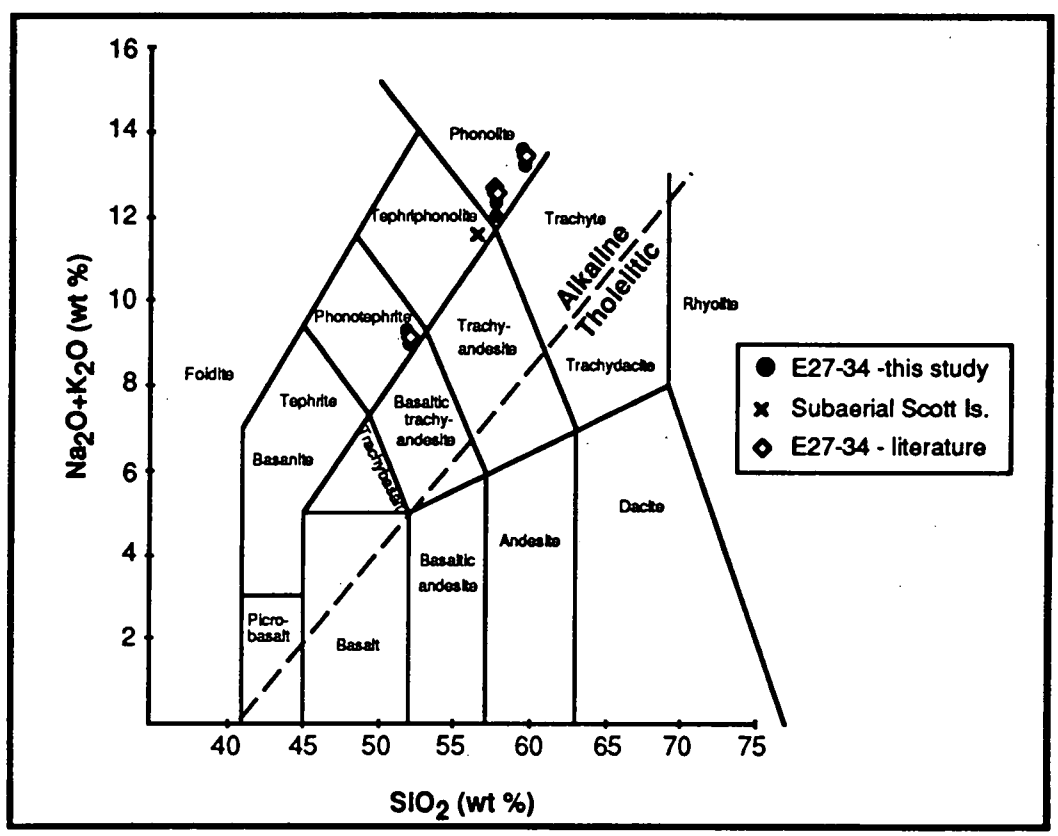

Figure 5.8: TAS diagram of Le Bas et al. (1986) comparing the normalised compositions of the submarine Scott Island samples analysed during this sudy (filled circles) with four submarine samples from the same dredge sites analysed by Campsie et al. (1983) (open diamonds) and one subaerial Scott Island analysis of Prior (1907) (oblique cross). Alkaline and tholeiitic fields are separated by the diagonal (dashed) line of Macdonald and Katsura (1964), as applied to the Hawaiian basalts.

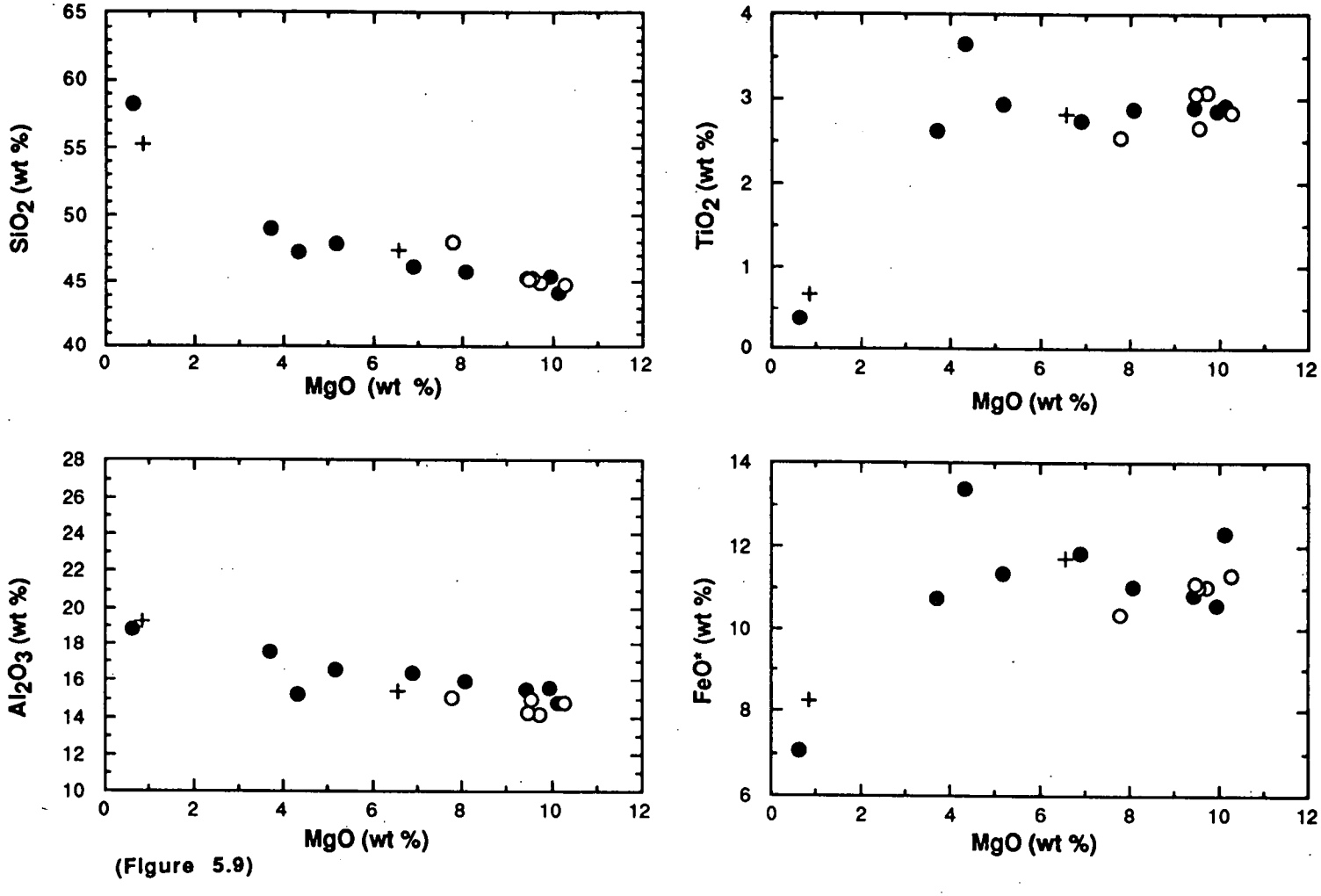

(Figure 5.9)

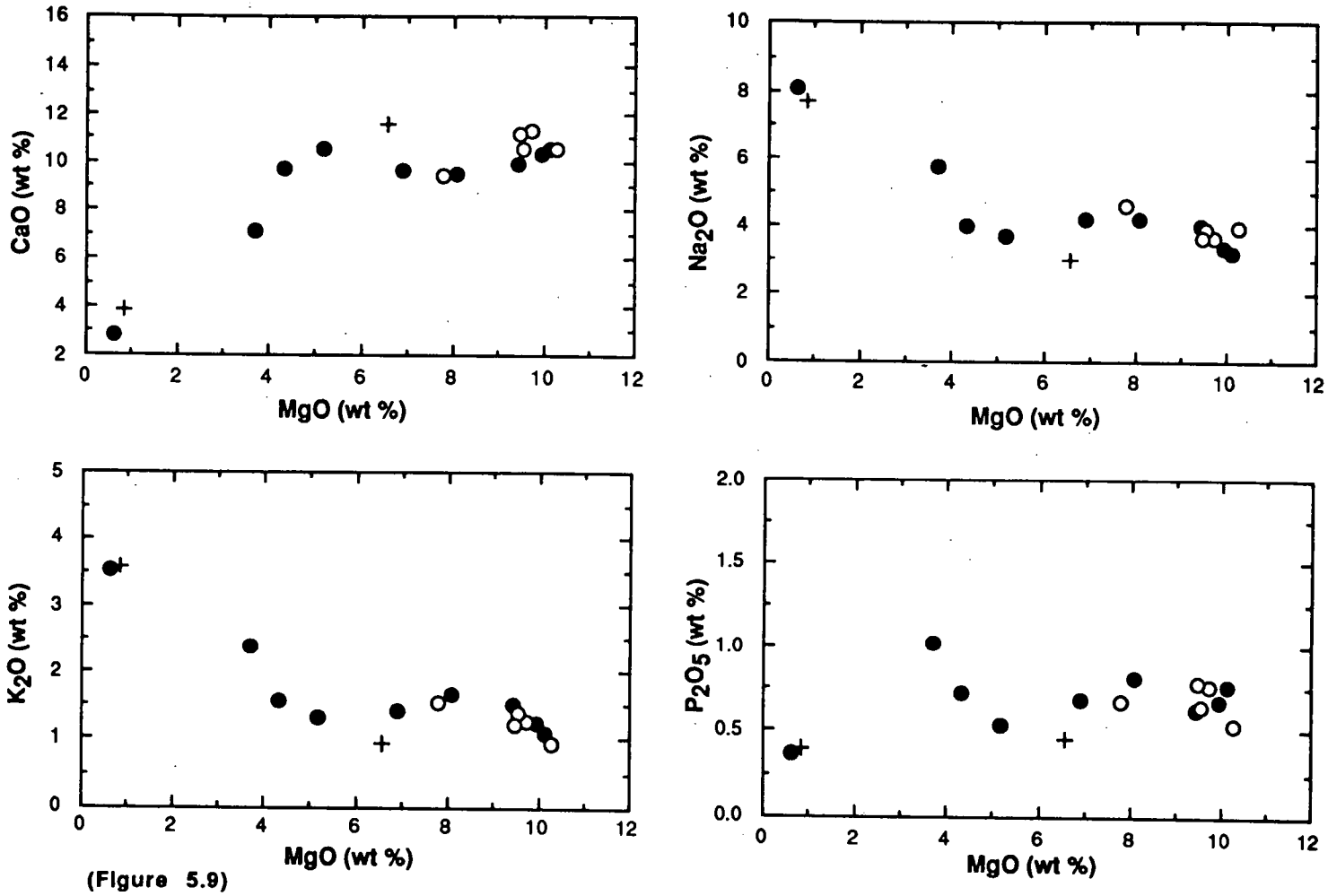

(Figure 5.9)

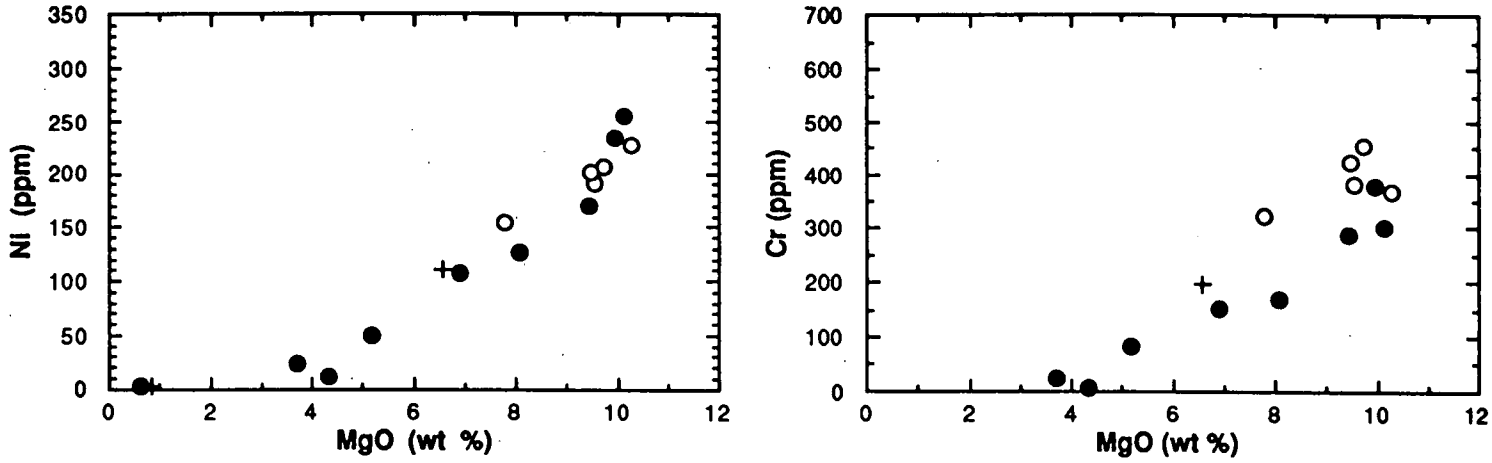

Figure 5.9: MgO (wt %) versus major elements plus Ni and Cr for submarine Balleny Province (dredges E27-35A and E27-35B - filled circles) versus dredge E27-36 (open circles) and dredge E27-37 (crosses) samples.

5.5 TRACE ELEMENT GEOCHEMISTRY:

The trace element abundances of the submarine Scott Island and southwest Pacific Ocean seafloor samples were mostly determined by XRF spectrometry (Philips PW 1410 spectrometer); Cs, Hf, Ta and Th abundances were measured by INAA. REE concentrations were analysed by ion exchange - XRF spectrometry (Philips PW 1410 spectrometer). All analytical procedures are described in Appendix 2.

Table 5.5: Submarine Scott Island REE contents.

Sample No:	E27-34A-4	E27-34B-1	E27-34C-2	E27-34D-1
La	145.00	129.00	95.40	131.00
Ce	256.00	241.00	193.00	254.00
Pr	26.50	25.70	21.60	24.90
Nd	76.00	78.70	79.60	84.30
Sm	9.59	9.63	13.30	12.40
Eu	1.94	2.16	4.42	3.17
Gd	5.05	6.11	9.94	7.06
Dy	6.70	7.37	8.03	7.53
Er	4.49	4.12	4.44	4.22
Yb	4.32	4.03	3.76	3.61

5.5.1 Scott Island Samples:

The trace element and REE contents of the submarine Scott Island samples are presented in Tables 5.3 and 5.5 respectively.

The four Scott Island samples plotted in Figure 5.10 have similar primitive mantle-normalised incompatible element patterns, characterised by a relative enrichment in the most incompatible elements and a progressive increase in elemental abundance with increasing fractionation. The latter feature results in the three phonolites generally plotting above the pattern produced by the slightly less evolved phonotephrite (sample 34C). The main characteristics of these patterns include a negative K anomaly, greater abundances of the HFSE Nb and Ta relative to the adjacent LILE, a general decrease in the abundance of elements more incompatible than Ta, and positive Zr and Hf anomalies. These general features displayed by the incompatible element patterns of the submarine Scott Island samples are extremely similar to those of the Balleny Plume volcanics described in Chapter 3 (Figures 3.13 and 3.15), and are probably source-related. However, the pronounced negative P, Sr and Ti anomalies, which increase from the phonotephrite (34C-2) through the least evolved phonolites (34B-1 and 34D-1) to the most evolved phonolite (34A-4), appear to be produced by protracted fractionation involving feldspar, apatite and titanomagnetite.

The chondrite-normalised REE contents of these same four submarine Scott Island samples display broadly similar patterns of LREE enrichment relative to the MREE and HREE (Figure 5.11). However, all of the phonolites show relatively flat MREE and HREE, most pronounced in the most evolved phonolite (sample 34A-4), and a strong increase in $(La/Sm)_n$ compared to sample 34C-2. This same pattern, evident in the Balleny Province

trachyte sample 35A-2 (Figure 3.14) can be ascribed to late-stage amphibole fractionation (Chapter 3). The slightly positive Eu anomaly of sample 34C-2 may be a product of the ion exchange - XRF technique (chapter 3) and is not evident in any of the other samples.

Despite their evolved nature, the submarine Scott Island samples have retained certain trace element abundance ratios, particularly those comprising more incompatible elements, which probably reflect their source chemistry. It is significant therefore that they possess similarly low LILE/HFSE and LREE/HFSE values to both the Balleny Plume Volcanics and the HIMU OIB fields (Figure 5.12), and that they define a more limited range than the former.

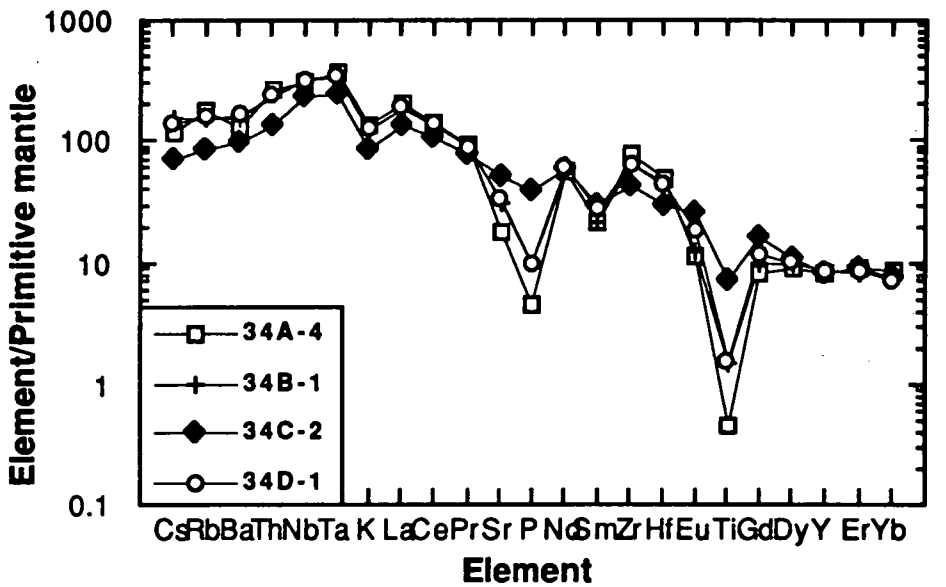

Figure 5.10: Primitive mantle-normalised incompatible element patterns of four submarine Scott Island samples; data from Tables 5.3 and 5.5; normalising values from Sun and McDonough (1989).

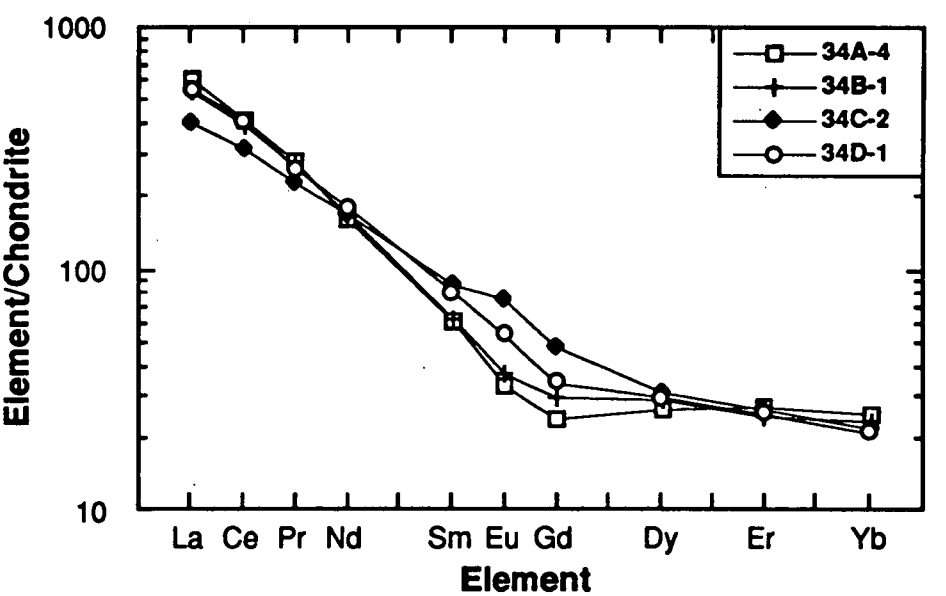

Figure 5.11: Chondrite-normalised REE patterns of four submarine Scott Island samples; data from Table 5.5; C1 chondrite normalising values from Sun and McDonough (1989).

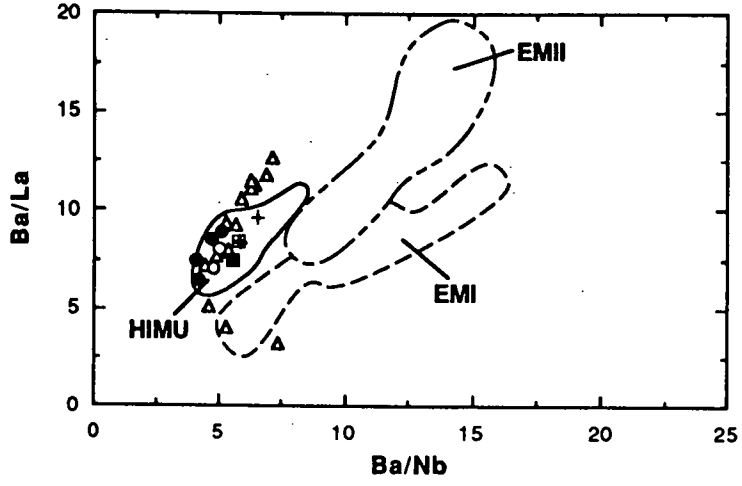
Ba/La
Ba/Nb
EMII
EMI
HIMU
0
5
10
15
20
25

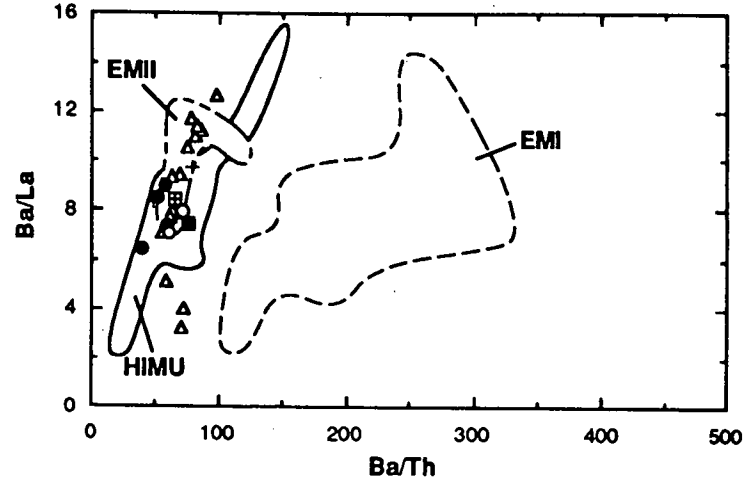
Ba/La
Ba/Th
EMII
EMI
HIMU
0
4
8
12
16
100
200
300
400
500

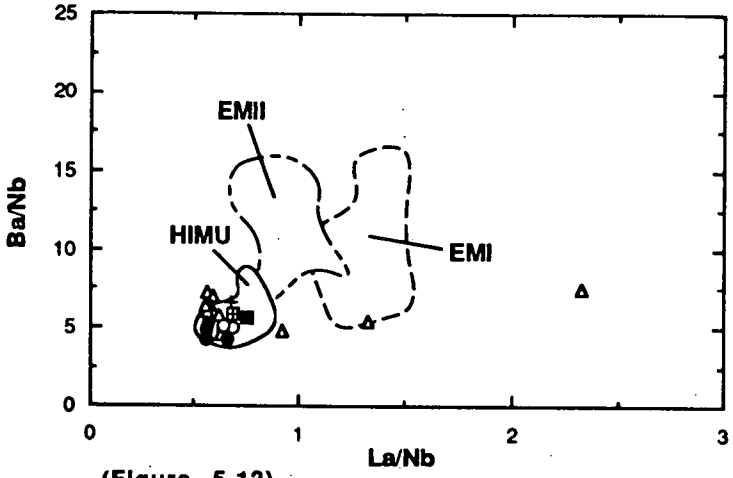
Ba/Nb
La/Nb
EMII
HIMU
EMI
0
5
10
15
20
25
1
2
3

(Figure 5.12)

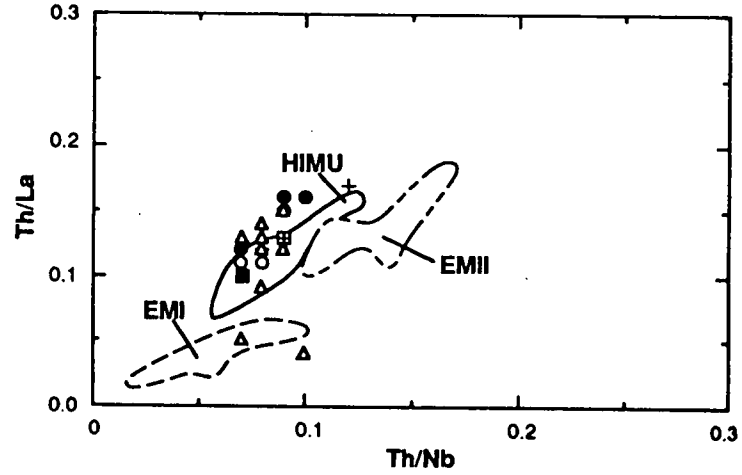
Th/La
Th/Nb
HIMU
EMII
EMI
0.0
0.1
0.2
0.3

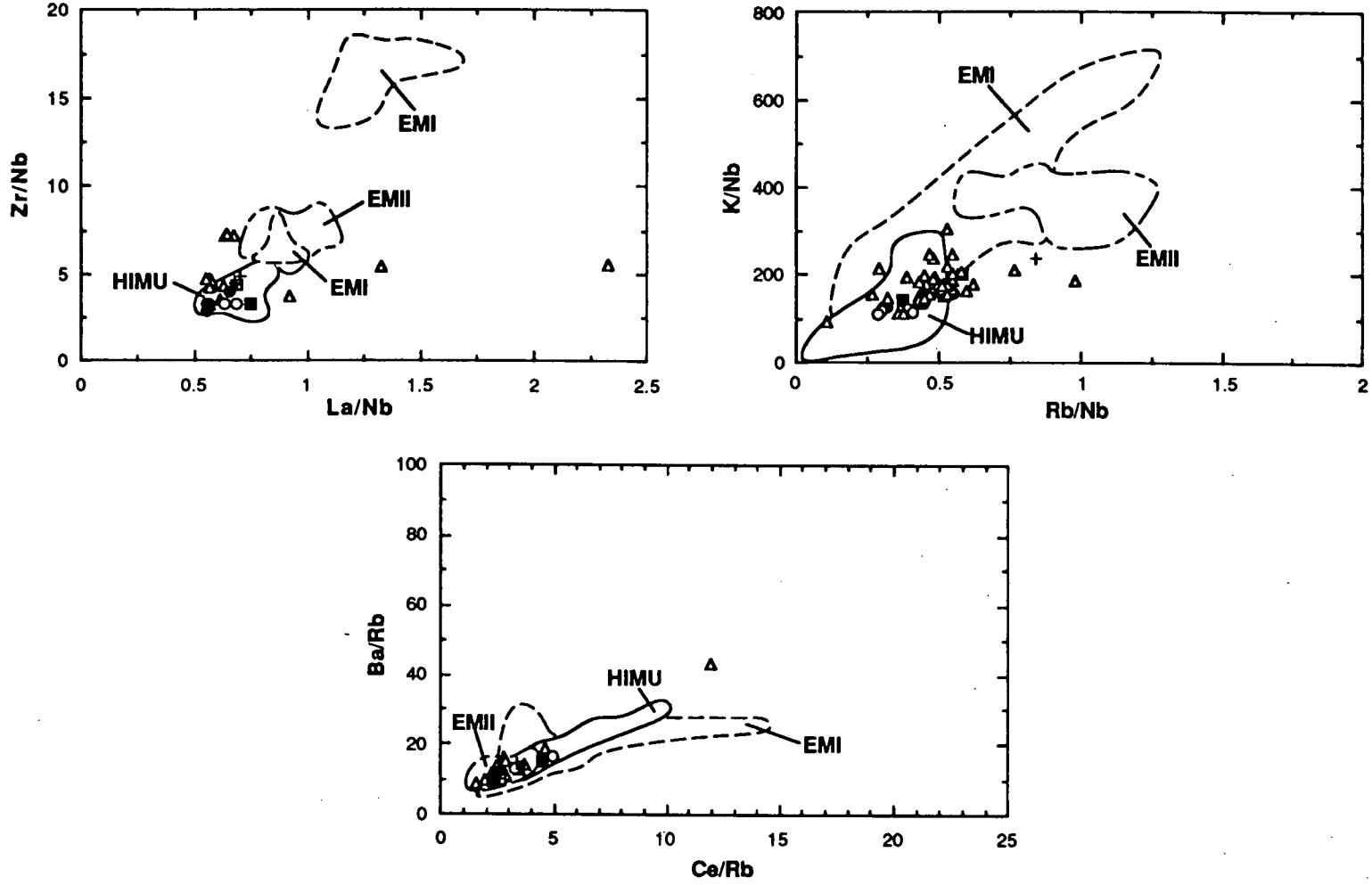

Figure 5.12: Trace element abundance ratio plots of submarine Scott Island (filled circles), and southwest Pacific Ocean seafloor (dredge 02A - filled square, dredge 03 - cross within square, dredge 36 - open circles, and dredge 37 - crosses) samples plotted relative to the HIMU, EMI and EMII OIB fields and the Balleny Plume volcanics (open triangles). The OIB end-member fields have been plotted, using data sources as for Table 2.1, so as to circumscribe the bulk of the data; the complete OIB data sets are plotted in Figure 2.10. Balleny Plume volcanics include data for subaerial Balleny Island samples (Green, 1992 and J. Foden, unpublished data).

Table 5.6: Southwest Pacific Ocean seafloor REE contents.

Sample No:	E27-02A-2	E27-03	E27-36-2	E27-36-8	E27-37-2	E27-37-3
La	80.10	67.80	61.40	70.50	29.30	86.00
Ce	180.00	147.00	134.00	148.00	66.90	168.00
Pr	21.30	16.40	15.00	16.11	8.00	17.20
Nd	84.40	62.70	62.70	62.50	32.20	59.00
Sm	14.10	11.60	13.20	12.00	5.99	9.83
Eu	4.37	3.57	4.70	3.83	2.00	2.90
Gd	12.40	9.31	10.80	9.00	6.58	6.68
Dy	10.40	7.61	7.59	6.87	6.18	6.23
Er	5.12	3.89	3.72	3.46	3.19	3.78
Yb	3.47	3.16	2.58	2.59	2.26	3.39

5.5.2 Southwest Pacific Ocean Seafloor Samples:

The trace element and REE contents of the southwest Pacific Ocean seafloor samples are presented in Tables 5.4 and 5.6 respectively.

The primitive mantle-normalised patterns of all the southwest Pacific Ocean seafloor samples (Figure 5.13) display the general enrichment in incompatible elements characteristic of OIB (e.g. Sun, 1980; Wood et al., 1981; Sun and McDonough, 1989), and are remarkably similar to both the submarine Scott Island (Figure 5.10) and Balleny Plume patterns (Figures 3.13 and 3.15). The predominant features once again include a negative K anomaly, greater abundances of the HFSE Nb and Ta relative to the adjacent LILE, a general decrease in the abundance of elements more incompatible than Ta, and positive Zr and Hf anomalies. Tephriphonolite sample 37-3 appears, at first glance, to be markedly different than the other seafloor samples, but this is in fact a function of its greater degree of fractionation compared to the alkali olivine basalt (37-2) against which it is plotted. This greater fractionation has resulted in sample 37-3 plotting significantly above sample 37-2 and having much more pronounced negative Ti , P and Sr anomalies. The slightly negative Ba anomaly relative to the other highly incompatible LILE may suggest some inter-element fractionation between these elements, or may reflect Ba leaching during seafloor alteration processes.

The chondrite-normalised REE patterns of the southwest Pacific Ocean seafloor samples (Figure 5.14) all display the LREE/HREE enrichment patterns typical of OIB derived from small degrees of melting of a garnet-bearing source (e.g. Kay and Gast, 1973; Frey et al., 1978). Dredge E27-36 samples have small positive Eu anomalies which may be a function of the ion exchange - XRF analytical technique. Tephriphonolite sample 37-3 displays the same pattern of MREE to HREE flattening and the steep trend from Sm to La which is visible in all of the submarine Scott Island phonolites and the Balleny Province trachyte sample 35A-2. This REE pattern is a feature common to the most evolved rocks from this region, and is suggestive of late-stage amphibole fractionation.

In terms of their trace element abundance ratios, the southwest Pacific Ocean seafloor samples are remarkably similar to both the submarine Scott Island and Balleny Plume values, plotting within or close to the HIMU OIB fields in Figure 5.12.

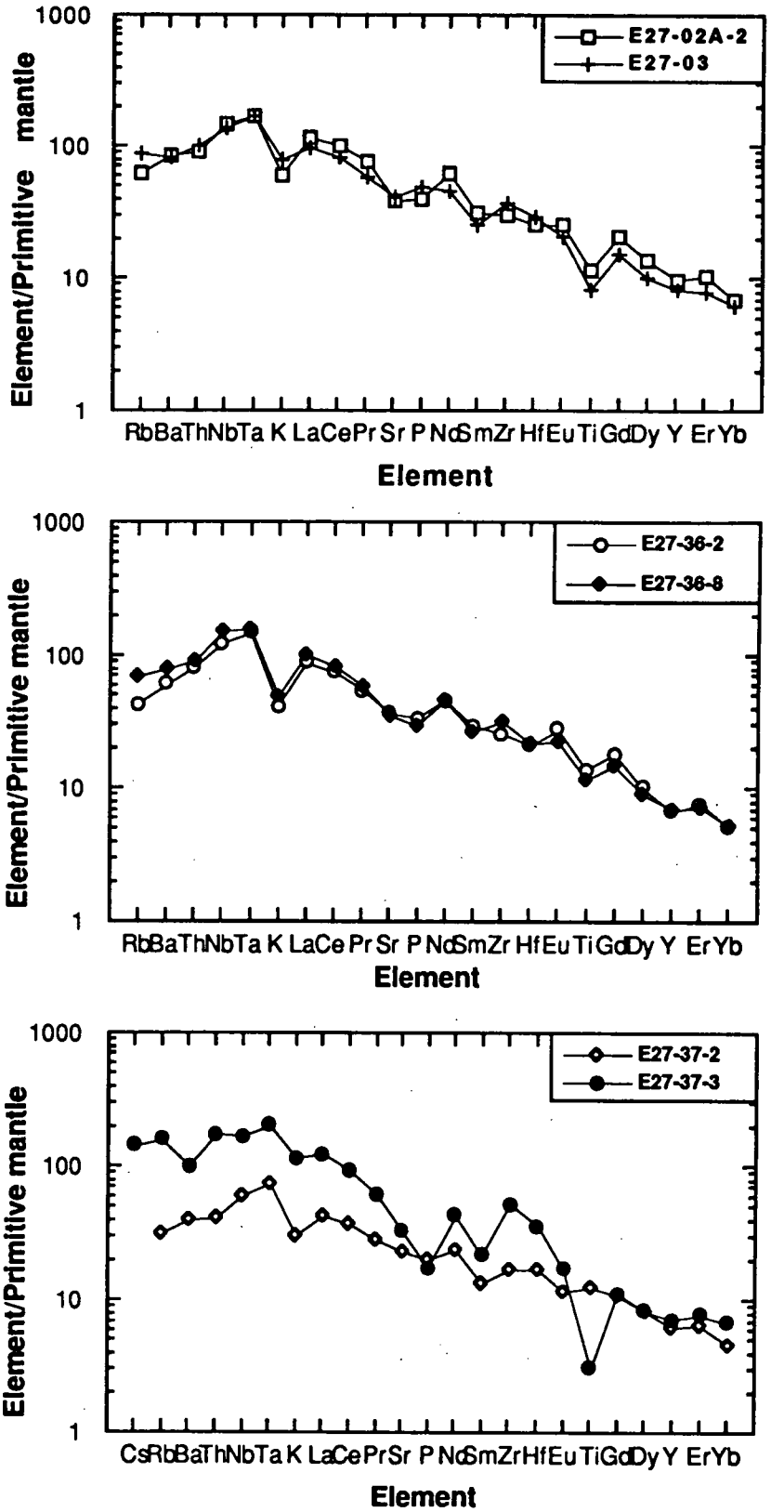

Figure 5.13: Primitive mantle-normalised incompatible element patterns of southwest Pacific Ocean seafloor samples; data from Tables 5.4 and 5.6; normalising values from Sun and McDonough (1989).

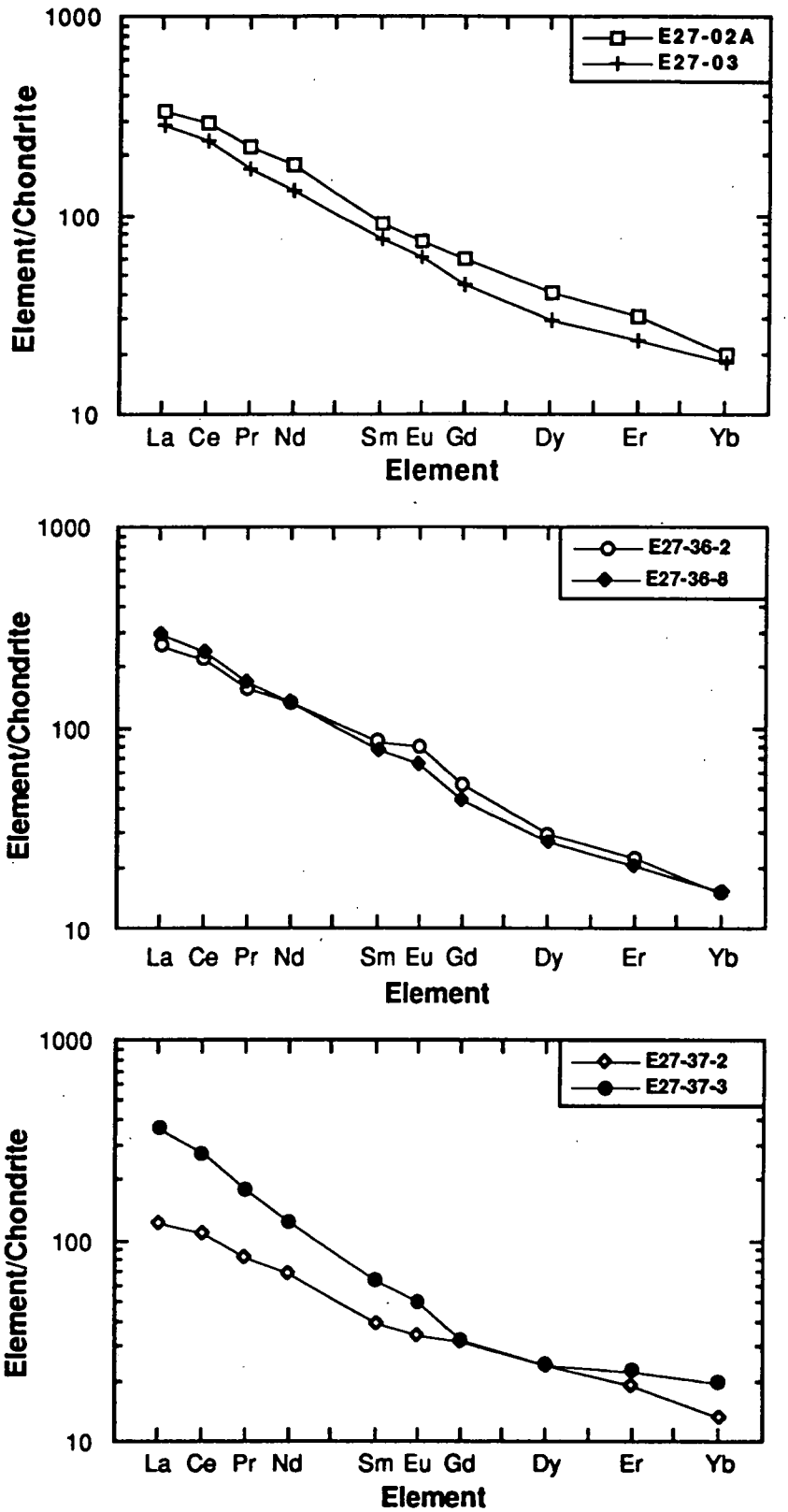

Figure 5.14: Chondrite-normalised REE patterns of southwest Pacific Ocean seafloor samples; data from Table 5.6; C1 chondrite normalising values from Sun and McDonough (1989).

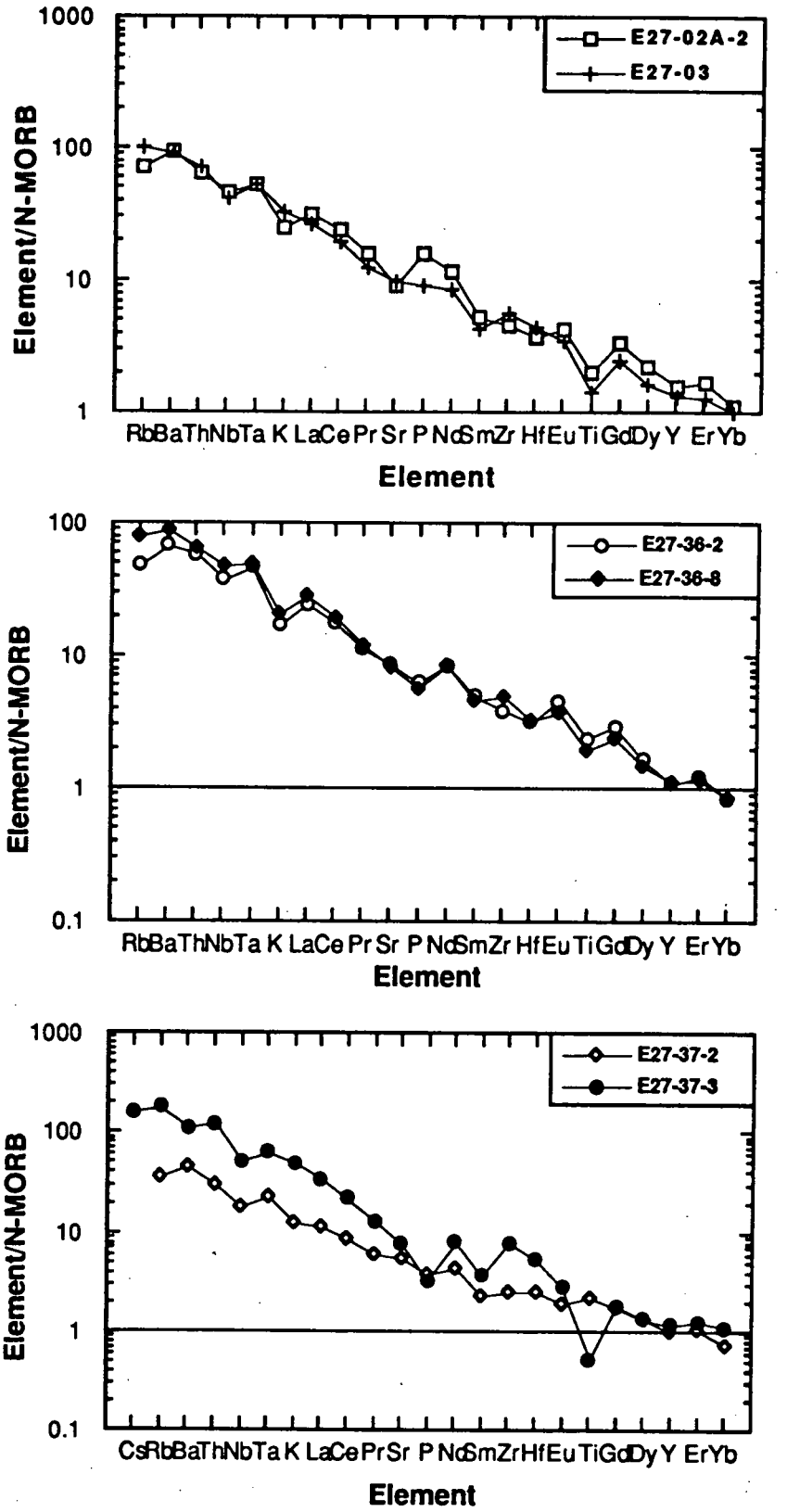

Figure 5.15: N-MORB normalised incompatible element patterns of southwest Pacific Ocean seafloor samples; data from Tables 5.4 and 5.6; normalising values from Sun and McDonough (1989).

To emphasise the fact that the southwest Pacific Ocean seafloor samples examined here are not simply products of mid-ocean ridge volcanism, their incompatible element contents have been normalised to N-MORB values in Figure 5.15. The consistently steep trends of these patterns, with increasing elemental abundances accompanying increasing degrees of incompatibility confirm that seafloor volcanism in these regions has had at least some input from a geochemically enriched source/s.

5.6 RADIOGENIC ISOTOPE CHEMISTRY:

Radiogenic isotope data for the submarine Scott Island and southwest Pacific Ocean seafloor samples are presented in Table 5.7; analytical methods are described in Appendix 2. Due to the complete lack of radiogenic or other age data as well as the lack of U and Pb contents for these samples, initial isotopic ratios have not been calculated.

5.6.1 Scott Island Samples:

Despite the statement by Hart (1988) that Scott Island volcanics have a HIMU Pb isotopic signature similar to that of both the Balleny Islands and Ross Island as well as similar low $^{87}Sr/^{86}Sr$ values to the young basaltic volcanics from Marie Byrd Land, no radiogenic isotope data from Scott Island are available in the literature. However, Sr, Nd and Pb isotope data for three Scott Island samples analysed during the course of this study (Table 5.7; Figure 5.16) do substantiate the claim of Hart (1988).

The submarine Scott Island samples extend to slightly lower measured $^{87}Sr/^{86}Sr$ values than the Balleny Plume volcanics, and overlap with the least enriched ends of the HIMU-DMM mixing trends produced by the Balleny Plume volcanics in Pb-Pb space, a similar position to that occupied by samples from the Balleny Islands region. Isotopically, they therefore appear to be products of mixing between a HIMU plume component, with a similar isotopic composition to that of the Balleny Plume, and DMM material.

5.6.2 Southwest Pacific Ocean Seafloor Samples:

5.6.2.1 Dredges E27-02A and E27-03:

Sample 03 has radiogenic isotope values consistent with derivation from a MORB source enriched by a HIMU component. It plots within both the HIMU and MORB fields in Sr-Nd space and within or adjacent to the most enriched end of the MORB field in Pb-Pb space, along a hypothetical extension of the HIMU-DMM mixing array produced by the Balleny Plume volcanics (Figure 5.16).

Table 5.7: Sr, Nd and Pb isotope data for the submarine Scott Island and southwest Pacific Ocean seafloor samples discussed in the text; errors (2σmean) associated with individual sample measurements indicate within-run precision only. Present-day epsilon values were calculated as described in Appendix 6.

Sample No.	$^{87}Sr/^{86}Sr$	±2σ	εSr	$^{143}Nd/^{144}Nd$	±2σ	εNd	$^{206}Pb/^{204}Pb$	$^{207}Pb/^{204}Pb$	$^{208}Pb/^{204}Pb$
Scott Island:									
E27-34A-4	0.702766	23	-24.6	0.513006	4	6.9	19.731	15.603	39.304
E27-34C-2	0.702815	29	-23.9	0.513019	10	7.2	19.661	15.608	39.229
E27-34D-1	0.702781	21	-24.4	0.513008	8	7.0	19.664	15.603	39.235
Southwest Pacific seafloor samples:									
E27-02A-2	0.703765	11	-10.4	0.512918	6	5.2	19.786	15.654	39.311
	0.703732	21	-10.9	0.512943	11	5.7			
E27-03	0.703079	25	-20.2	0.512965	8	6.1	19.428	15.578	39.230
E27-36-2	0.702917	8	-22.5	0.512994	10	6.7	20.165	15.650	39.674
E27-36-8	0.702945	21	-22.1	0.512989	9	6.6	20.179	15.659	39.698
E27-37-2	0.703117	10	-19.6	0.512964	8	6.1	19.768	15.620	39.622
E27-37-3	0.703113	23	-19.7	0.512981	5	6.5	19.435	15.583	39.253

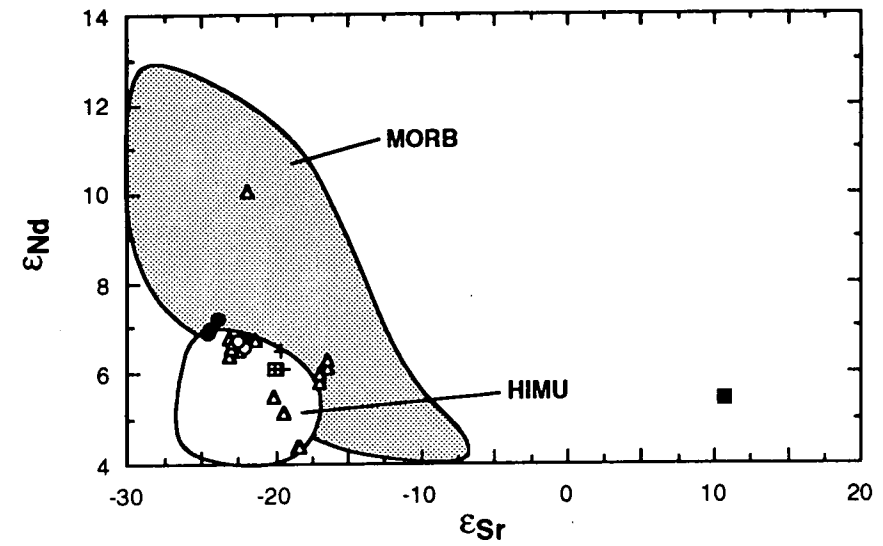
14
12
10
8
6
4
εNd
MORB
HIMU
-30
-20
-10
0
10
20
εSr

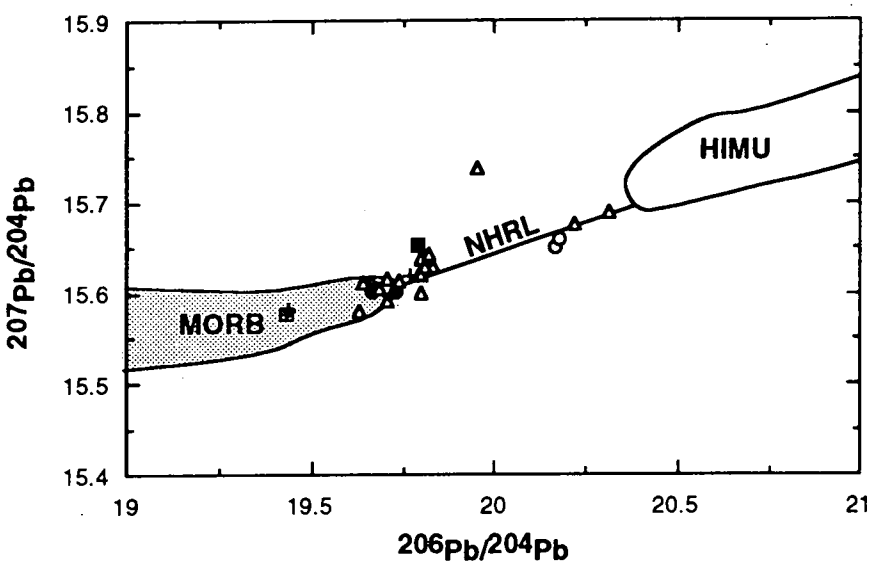
15.9
15.8
15.7
15.6
15.5
15.4
207Pb/204Pb
HIMU
NHRL
MORB
19
19.5
20
20.5
21
206Pb/204Pb

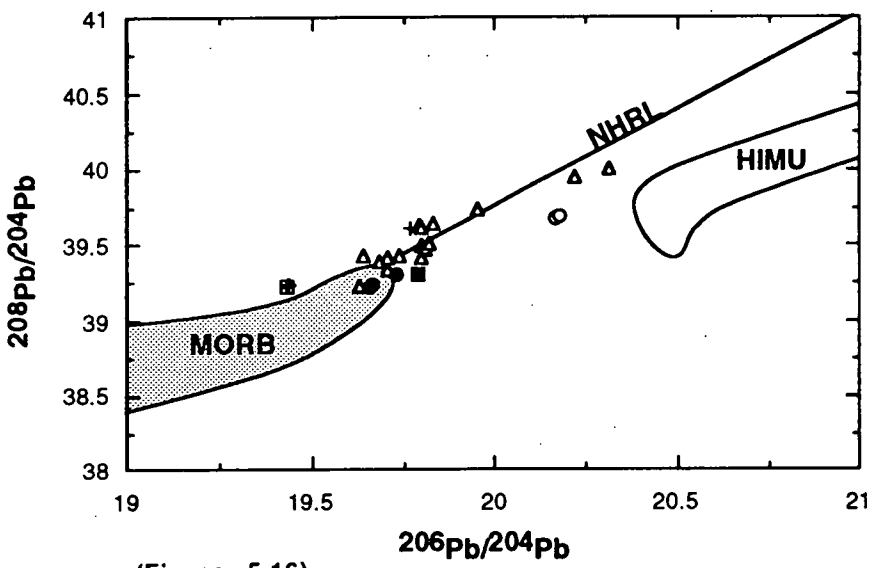
41
40.5
40
39.5
39
38.5
38
208Pb/204Pb
NHRL
HIMU
MORB
19
19.5
20
20.5
21
206Pb/204Pb

(Figure 5.16)

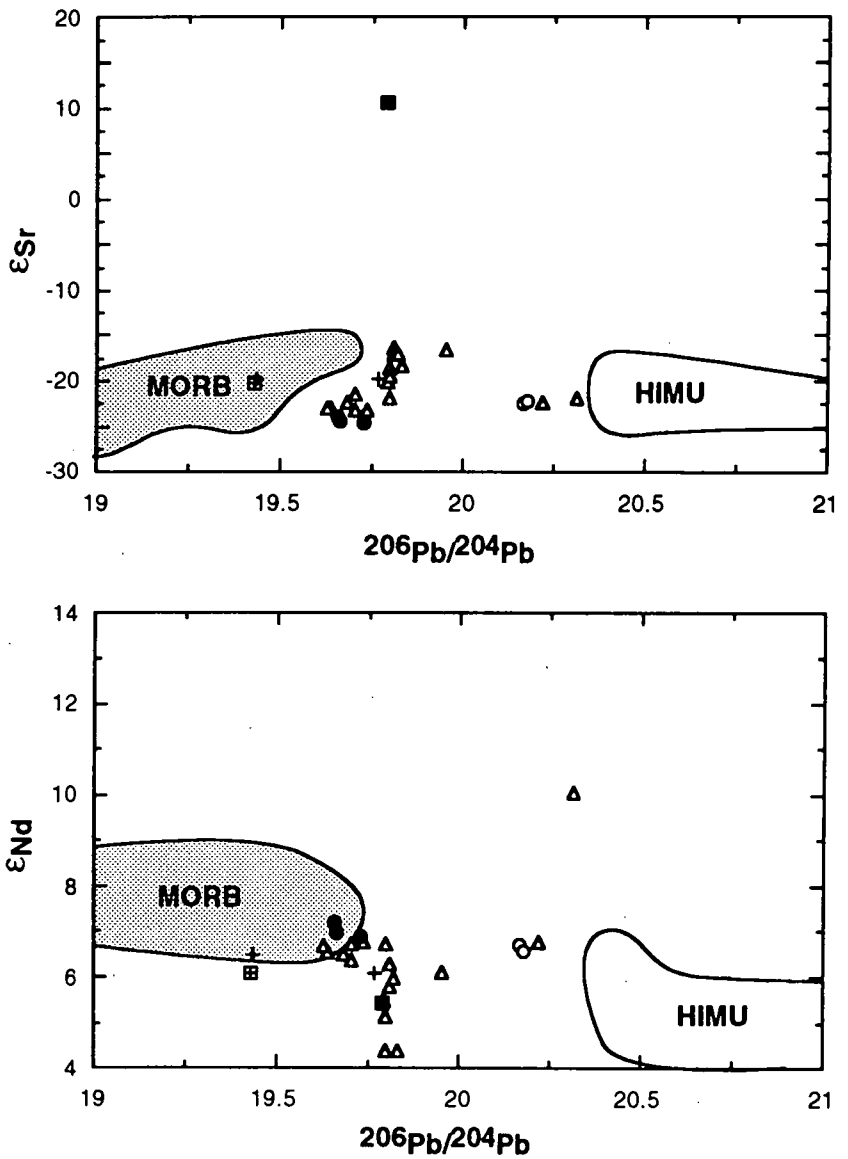

Figure 5.16: Radiogenic isotope plots comparing measured ratios for samples from the Scott Island region (filled circles) and southwest Pacific seafloor dredges E27-02 (filled square), E27-03 (cross within square), E27-36 (open circles) and E27-37 (crosses) with the initial ratios of the Balleny Plume volcanics (open triangles) and the HIMU OIB and MORB isotopic fields. Data sources for the OIB and MORB isotopic end-members are as for Figure 1.1. Balleny Plume volcanics include the Balleny Islands ratios of Hart (1988).

Sample 02A-2 is more difficult to interpret. It has a similar high $^{143}Nd/^{144}Nd$ value to both the HIMU and MORB fields, but significantly higher $^{87}Sr/^{86}Sr$. In Pb-Pb space, sample 02A-2 has similar high $^{206}Pb/^{204}Pb$ to the Balleny Plume volcanics, but slightly higher $^{207}Pb/^{204}Pb$ and slightly lower $^{208}Pb/^{204}Pb$ compared to the Balleny Plume mixing array. This sample is here interpreted to have an isotopic composition produced by HIMU-DMM mixing, but with a contaminated $^{87}Sr/^{86}Sr$ composition. The source of the latter is not known, but the similar $^{87}Sr/^{86}Sr$ data obtained for replicate analyses of leached aliquots suggest that it is unlikely that this sample suffers from the effects of seafloor contamination and/or alteration which are not evident in other samples subjected to the same analytical technique.

5.6.2.2 Dredges E27-36 and E27-37:

In Sr-Nd space, the two samples from dredge E27-36 plot close to the boundary between the MORB and HIMU isotopic fields (Figure 5.16), overlapping with several of the submarine Balleny Province samples. However, both samples have very radiogenic $^{206}Pb/^{204}Pb$ isotope contents, closest to those of the oldest and most radiogenic Balleny Plume seamount, the Heemskirk Seamount. Dredge E27-36 $^{207}Pb/^{204}Pb$ and $^{208}Pb/^{204}Pb$ values are slightly lower, however, the latter plotting well below the NHRL and similar to values for other known HIMU OIB.

Dredge E27-37 samples have similar $^{87}Sr/^{86}Sr$ and $^{143}Nd/^{144}Nd$ values to each other, and to the dredge E27-03 phonotephrite (sample 03) and the Balleny Plume volcanics, once again plotting within both the MORB and HIMU isotopic fields in Figure 5.16. In Pb-Pb space, however, sample 37-3 has virtually identical isotopic values to sample 03, plotting within or adjacent to the enriched end of the MORB field, whereas sample 37-2 has slightly more radiogenic values and plots in a similar position to the submarine Balleny Province data.

5.7 POSSIBLE LINKS WITH THE BALLENY PLUME?:

It is evident from the data presented here that volcanism on the Balleny and Scott Islands has a similar and distinctive geochemical and isotopic composition, consistent with derivation by mixing between HIMU and DMM mantle material. It is also evident that the southwest Pacific Ocean seafloor located between the Balleny and Scott island regions and the Southeast Indian and Pacific-Antarctic Ridges respectively, has a corresponding source signature. The distance of ~650 km between the Balleny Islands, the postulated current site of the Balleny Plume, and Scott Island tends to negate the idea that a single plume could be responsible for both occurrences of HIMU volcanism. However, their similar latitudinal locations on the Antarctic Plate imply that parallel plumes, possibly deriving from the same deep mantle HIMU source region, may be responsible for the Balleny and Scott Island

regions, the latter here termed the Scott Plume. A good example of closely-spaced parallel plume traces is provided by the Tasmantid, Lord Howe and eastern Australian hotspot tracks further north on the eastern edge of the Indian-Australian Plate, all of which appear to bear similar, and predominantly EMI, isotopic signatures.

The alkaline, SiO_2-undersaturated nature, the HIMU-like trace element contents, and the E-MORB to HIMU-DMM isotopic compositions of the southwest Pacific Ocean seafloor samples, combined with their location close to the proposed Balleny and Scott Island plume traces, implies that they too are products of these HIMU plumes. The observed lack of islands or seamounts along the Balleny Plume trace between the region just south of anomaly 8 on the Indian-Australian Plate to anomaly 5 on the Antarctic Plate suggests that the Balleny Plume may have become trapped by the SEIR sometime after ~28 Ma (A8). Sleep (1992) has proposed that the crossing of an upwelling off-ridge plume by a spreading ridge may result in a period during which the top of the plume is entrained by, and supplies material to, the ridge. Once the lower part of the plume conduit is far enough away from the ridge on the other side, its observed surface position would jump off the ridge axis, thereby producing a region on either side of the ridge free of plume-related seamounts and/or islands. This is consistent with both the proposed Balleny and Scott plumes, whereby a period of plume entrainment by the Southeast Indian and Pacific-Antarctic Ridges respectively has resulted in ridge volcanism being contaminated to varying extents by HIMU plume material, and therefore resulting in the HIMU-DMM compositions of the southwest Pacific Ocean seafloor samples examined here. The fact that dredge E27-37 samples, located in virtually zero-age oceanic crust on the southern flank of the SEIR, bear this same isotopic and trace element signature implies that the spreading ridge may still, or has recently been, entraining significant amounts of HIMU plume material.

If there is a separate HIMU Scott Plume, as this study suggests, it could well explain the HIMU contribution to the isotopic composition of the Macquarie Island basalts (Chapter 4). According to the age of the magnetic seafloor lineations adjacent to Macquarie Island, it was produced by seafloor spreading at the Southeast Indian - Pacific-Antarctic Ridge at ~27 Ma. Significantly younger ages (11.5 to 9.7 Ma; Duncan and Varne, 1988) are recorded, however, for the alkaline volcanics of Macquarie Island, shown in Chapter 4 to have HIMU-DMM radiogenic isotope affinities. Temporal projection of the proposed Scott Plume trace would extend it back in a north-nothwesterly direction to the vicinity of Macquarie Island. If the Scott Plume was entrained by, and supplied HIMU material to, the spreading ridge as far back as ~28 Ma, the oceanic crust, which was later uplifted to form Macquarie Island, may have been contaminated and/or underplated by plume material. The lack of radiogenic isotope data for the older basement rocks of Macquarie Island makes this idea difficult to test. However, the HIMU-DMM signature of the younger alkaline volcanics of Macquarie Island may be a product of the remelting of underplated Scott Plume material during the transpressional regime which resulted in the uplift of Macquarie Island.

No attempt has been made to trace the proposed Scott Plume further back in time than Macquarie Island due to the currently poor bathymetric coverage of the south Tasman Sea. However, if this plume trace does parallel that of the Balleny Plume both in time and space, it is possible that it too may have contributed to the lithospheric underplating of eastern Gondwana prior to continental break-up.

CHAPTER 6

HIMU OIB AND THE BALLENY PLUME - A SUMMARY

6.1 THE GEOCHEMISTRY OF HIMU, EMI AND EMII OIB:

Radiogenic isotope ratios are generally favoured as a mantle source-tracing tool due to their non-fractionating behaviour during partial melting and fractional crystallisation, and their subsequent ability to reflect the timing and nature of the processes responsible for the formation of geochemically distinct mantle source regions. As a result, the definition of four mantle end-member components, DMM, HIMU, EMI and EMII, invoked to explain OIB heterogeneity (e.g. Zindler and Hart, 1986; Hart, 1988), has been based primarily on their isotope systematics (Chapter 1), with considerably less emphasis on their comparative major (Chauvel et al., 1992; Hauri and Hart, 1993) and trace element (e.g. Sun and McDonough, 1989; Weaver, 1991) compositions.

An attempt has been made to characterise the major and trace element characteristics which distinguish the HIMU, EMI and EMII mantle end-members (Chapter 2). This has concentrated on an examination of literature-derived data for those OIB which most closely approach the proposed extreme end-member isotope compositions. The propensity for magma major and trace element contents to reflect mantle melting and crystallisation processes, rather than just source geochemistry, has been minimised by the use of samples with ≥5 wt % MgO (thereby avoiding late stage fractionation effects) for trace element comparisons, ratios of incompatible trace elements which are presumed to remain relatively unfractionated, and relatively primitive samples with ≥ 9.5 wt % MgO for major element comparisons. The results indicate that isotopically-defined HIMU, EMI and EMII OIB do possess some distinct major and trace element features.

HIMU OIB, characterised by the highest Pb isotope ratios (Hart, 1988), have lower LILE/HFSE and LREE/HFSE abundance ratios, intermediate Th/La and Th/Nb, lower Zr/Nb and higher Nb/Pb and Ce/Pb values than either of the EM components. EMII basalts, characterised by the highest $^{87}Sr/^{86}Sr$ values (Hart, 1988), have lower Ba/Th, higher Th/La and higher Th/Nb values than EMI OIB. Despite their poorly defined trace element systematics, EMI OIB, characterised by the lowest $^{143}Nd/^{144}Nd$ values (Hart, 1988), have the highest SiO_2 and the lowest FeO*, CaO, TiO_2, P_2O_5 and K_2O values. HIMU and EMII OIB

tend to overlap somewhat in terms of their major element compositions, although EMII basalts extend to the highest K_2O and TiO_2 values and HIMU basalts have the highest CaO.

End-member major element systematics have been interpreted to primarily reflect differences in source chemistry, rather than differences in the pressure and temperature of melting involved in OIB production. However, the supposition that EMI OIB, with their relatively low incompatible major element (e.g. K_2O, P_2O_5 and TiO_2) and CaO abundances, may derive from a more refractory source than HIMU OIB is complicated by the observation that the latter possess lower LILE/HFSE and LREE/HFSE values as well as isotopic ratios which result from time-integrated low Rb/Sr and Nd/Sm, and thereby imply long-term incompatible element depletion. The origin of the observed end-member geochemical distinctions may therefore be more complex than any of the simple models presented in Chapter 2, whereby the apparently contradicting major and trace element systematics of HIMU OIB, for example, may imply the involvement of a range of processes in source formation.

6.2 HIMU PLUME INFLUENCE IN THE TASMAN SEA - SOUTHWEST PACIFIC OCEAN REGION:

HIMU volcanics are widespread throughout the dispersed continental fragments of eastern Gondwana and the Tasman Sea - southwest Pacific Ocean seafloor (e.g. Coombs et al., 1986; Sun et al., 1989; Lanyon et al., 1993). At least two HIMU mantle plumes have been advocated as causing underplating of the lithosphere in this region, as a result of plume head upwelling prior to or coincident with continental break-up, and/or seafloor volcanism in response to lithospheric plate movement over the remaining plume conduits.

The Balleny Plume (Chapter 3), currently located beneath the Balleny Islands in the Ross Sea region of Antarctica, is here assumed to be a relatively weak plume which has been contaminated by significant amounts of depleted upper mantle (DMM) material during upwelling. Although its eruptives are characterised by the low $^{87}Sr/^{86}Sr$, high $^{143}Nd/^{144}Nd$ and Pb isotope ratios, low LILE/HFSE, LREE/HFSE and Zr/Nb values and high Nb/Pb and Ce/Pb values characteristic of HIMU OIB, linear trends in Pb-Pb isotope space are indicative of HIMU-DMM mixing. The Balleny Plume also appears to have slightly higher time-integrated Th/U than other known HIMU sources, resulting in the most radiogenic Balleny Plume samples plotting above the HIMU field in $^{206}Pb/^{204}Pb$-$^{208}Pb/^{204}Pb$ space, and thereby potentially expanding the known range of HIMU isotopic values.

The regional HIMU-DMM signature evident in the mafic continental volcanics of southeast Australia (Tasmania), the South Island, offshore and sub-Antarctic islands of New Zealand, and Marie Byrd Land and the McMurdo Volcanic Group of West Antarctica has been attributed to the Balleny Plume (Chapter 4) on the basis of their spatial proximity, to each other and to the proposed site of initial Balleny Plume upwelling, prior to the break-up of

Gondwana. Although the Balleny Plume head is assumed to have ascended at ~80 Ma into a region within which continental rifting had already commenced between Lord Howe Rise and eastern Australia and between Marie Byrd Land and Victoria Land in Antarctica, the weak nature of the plume is thought to have combined with thick continental lithosphere to prevent the significant melting and surface volcanism generally associated with starting plume heads (e.g. Coffin and Eldholm, 1992). In addition to the extensive lithospheric underplating of these continental regions with HIMU-DMM material, Balleny Plume head interaction with already weakened lithosphere may have been responsible for the concurrent onset of significant seafloor spreading in the Tasman Sea region and the westward propagation of the Pacific-Antarctic Ridge between the Campbell Plateau and Marie Byrd Land at ~80 Ma. Subsequent, and temporally sporadic, HIMU-DMM volcanism in the previously contiguous regions of Australia, New Zealand and Antarctica is here attributed to decompression and melting of underplated Balleny Plume head-entrained upper mantle material in response to localised tectonic stresses.

Continental rifting between eastern Australia, New Zealand and Antarctica resulted in the opening of the Tasman Sea and southwest Pacific Ocean. Progressive younging of a 4000 km long curved chain of islands and seamounts extending from the western flank of Lord Howe Rise to the Balleny Islands (Duncan, 1981; Duncan and McDougall, 1989; Jenkins et al., 1992), as well as a HIMU-DMM isotopic and trace element signature, suggests that their eruption is consistent with movement of the Indian-Australian Plate, and eventually the Antarctic Plate, over the Balleny Plume conduit (Chapter 3).

A temporal significance can also be attached to the linear mixing arrays defined by the Balleny Plume ocean floor volcanics in Pb-Pb space. The progressive dilution of the HIMU plume component by depleted upper mantle (DMM) material with time may imply either increasing amounts of upper mantle entrainment or progressive preferential melting of entrained material. Whereas the former suggests a gradual weakening of the plume, whereby increasing conduit inclination due to upper mantle shear stresses would promote ambient mantle entrainment (Griffiths and Campbell, 1991), the latter implies that the plume is heterogeneous with respect to its inherent and entrained components, so that differential melting is occurring with time.

A second HIMU plume is necessary to explain the apparent parallel trace of HIMU-DMM volcanism extending between Macquarie and Scott Islands in the southwest Pacific Ocean - Ross Sea region (Chapter 5). The location of Scott Island at the same latitude on the Antarctic Plate as the Balleny Islands, but ~650 km further to the east, precludes derivation from the Balleny Plume, despite its remarkably similar isotopic signature. The E-MORB to HIMU-DMM isotopic compositions of samples dredged from the southwest Pacific Ocean seafloor located between the Balleny and Scott island regions and the Southeast Indian and Pacific-Antarctic Ridges respectively implies that the Balleny and Scott Plume conduits may have been trapped by, and supplied HIMU material to, these spreading ridges sometime after ~28 Ma (A8). Scott Plume underplating of the ridge segment which was later uplifted to

form Macquarie Island may also have occurred at this time. The fact that samples dredged from virtually zero-age oceanic crust on the southern flank of the SEIR, northwest of the Balleny Islands, also bear this distinctive isotopic and trace element signature implies that the supply of HIMU material to this region of the SEIR has continued until very recently, and may even be an on-going phenomenon.

PART 2

MANTLE RESERVOIRS AND MAFIC MAGMATISM ASSOCIATED WITH THE BREAK-UP OF GONDWANA - THE AUSTRALIAN-ANTARCTIC DISCORDANCE

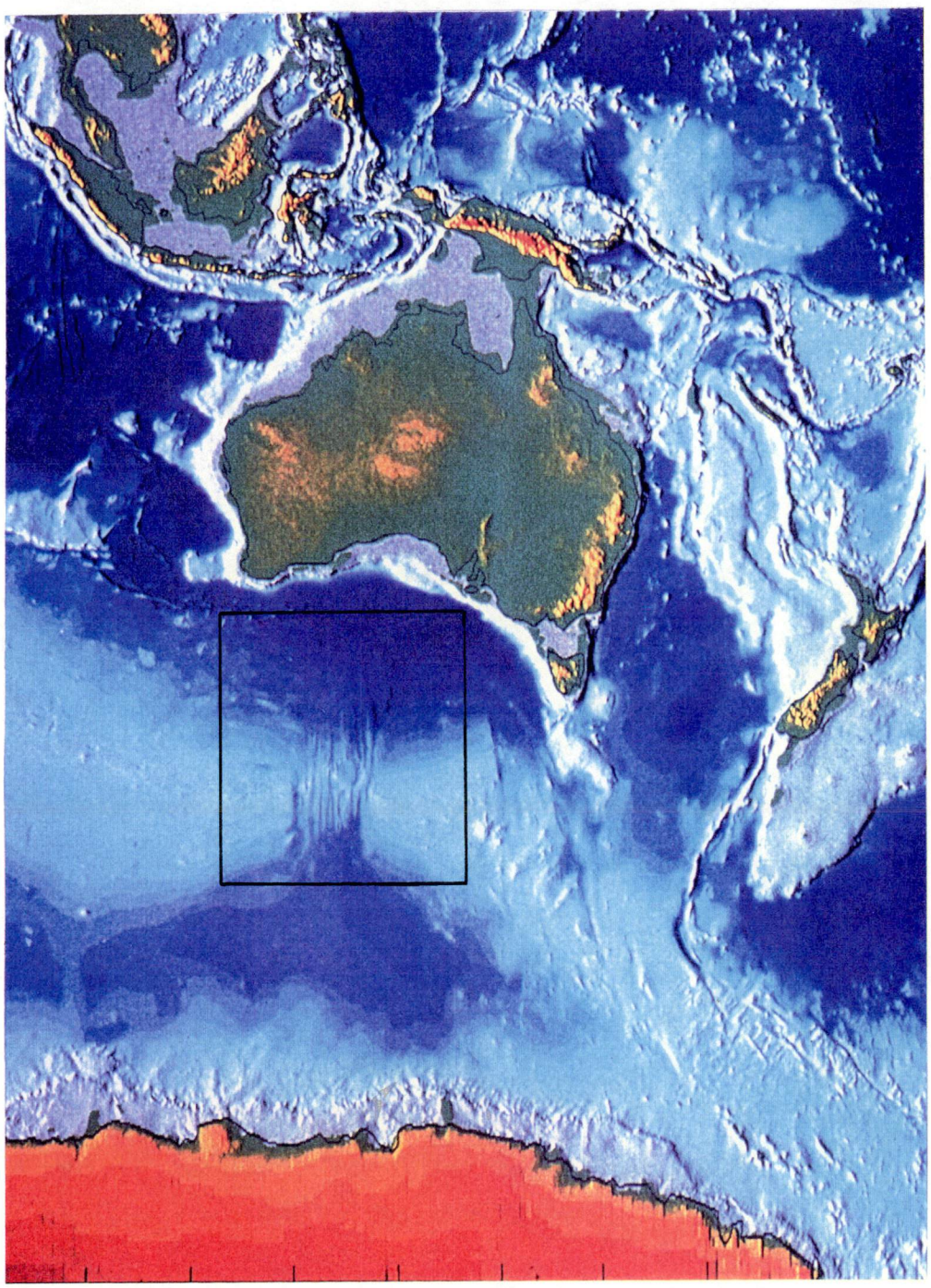

CHAPTER 7

THE EFFECTS OF CHANGING SPREADING RATE ON THE GEOCHEMISTRY OF THE SOUTHERN OCEAN SEAFLOOR

7.1 INTRODUCTION:

The Southern Ocean, extending between the southern margin of Australia and Wilkes Land in Antarctica, comprises a region of seafloor which has the potential to address at least two globally important tectono-magmatic problems:

1. The first of these is related to a major change in seafloor spreading rate along the SEIR at ~44.5 Ma. Although variations in seafloor spreading rates have been correlated with certain mid-ocean ridge morphological and geochemical parameters (e.g. Menard, 1967; Flower, 1981; Macdonald, 1982; Francheteau and Ballard, 1983; Phipps Morgan et al., 1987 Langmuir et al., 1992; Sinton and Detrick, 1992; Niu and Batiza, 1993), comparisons have so far been confined to separate mid-ocean ridge systems, such as that between the fast spreading East Pacific Rise (EPR) and the slow spreading Mid-Atlantic Ridge (MAR). The Southern Ocean seafloor therefore provides a unique opportunity to compare MORB geochemistry resulting from different spreading rates along a single mid-ocean ridge.

An attempt is made in this chapter to find geochemical differences, similar to those described in the literature as correlatable with variations in seafloor spreading rate, between basalts dredged from four Southern Ocean dredge sites north of the SEIR. Two of these sites are located on oceanic crust formed during a period of relatively slow seafloor spreading prior to 49 Ma, the other two correspond to a period of more rapid seafloor spreading after 44.5 Ma.

2. Another globally important feature of the Southern Ocean is the Australian-Antarctic Discordance (AAD). This is an approximately 500 km long region of the SEIR which is markedly different from the adjacent sections of mid-ocean ridge, and apparently unique on a global scale in terms of its geophysical, morphological and geochemical characteristics (e.g. Weissel and Hayes, 1971; Hayes and Conolly, 1972; Klein et al., 1988; Pyle et al., 1992). Mantle flow models invoked to explain the relationship between the observed physical and

geochemical characteristics of this region range from those that suggest these features are intimately related, to others which suggest that they are entirely coincidental. In terms of this particular study (Chapter 8), the most important observation made in relation to the AAD is the presence of an abrupt change in the radiogenic isotope composition of zero-age basalts erupted within it. This suggests that a boundary between distinct Indian (to the west) and Pacific (to the east) Ocean upper mantle isotope reservoirs exists beneath the eastern section of the AAD. Radiogenic isotope and geochemical studies of MORB erupted within this region have so far been confined to 0 to 4 Ma rocks. Therefore, although these studies have helped to constrain the recent history of the AAD, an examination of the more long-term evolution of the proposed isotopic boundary has not been possible until now. Chapter 8 will address this problem using Pb, Sr and Nd isotope data obtained for samples dredged from the four ~36 to 66 Ma Southern Ocean seafloor sites, located on either side of the northward extrapolation of the AAD.

7.2 AUSTRALIAN-ANTARCTIC RIFTING:

Several hundred kilometres (~360 km) of continental extension between Australia and Antarctica commenced during the Jurassic and preceded the mid-Cretaceous (~96 Ma) initiation of seafloor spreading between these continents (Veevers et al., 1990). Based on the revised anomaly identifications of Cande and Mutter (1982), the oldest magnetic anomaly observed south of the Australian margin's Magnetic Quiet Zone is anomaly 34 (82 Ma) which also closely corresponds to the initiation of Tasman Sea opening (~80 to 82 Ma; Hayes and Ringis, 1973; Weissel and Hayes, 1977), the start of seafloor spreading between New Zealand and Antarctica (~81 Ma; Molnar et al., 1975), and a major reorganisation of plate boundaries in the Indian Ocean (80-90 Ma; Norton and Sclater, 1979).

Australian-Antarctic breakup propagated from west to east at a rate of ~2 cm/yr at the end of continental rifting and commencement of seafloor spreading (Mutter et al., 1985). Since the Cretaceous, the Indian-Australian Plate has moved north-northeast (in the hotspot frame of reference) away from the relatively stationary Antarctic Plate, while the SEIR has migrated to the northeast (Minster and Jordan, 1978; Gordon and Jurdy, 1986) by more than 10° latitude (Norton and Sclater, 1979). Breakup is thought to have involved three stages of seafloor spreading. According to Veevers et al. (1990) and Veevers and Li (1991), the full spreading rate from 96 to 49 Ma was ~9 mm/yr. Therefore, following this first period of separation Australia and Antarctica were still only ~500 km apart. The spreading rate then increased to ~20 mm/yr between 49 and 44.5 Ma before a dramatic increase in spreading rate at 44.5 Ma (Veevers et al., 1990) which coincided with a change in spreading direction along the SEIR from north-south to northeast-southwest (N45°E) and a major change in the rate and direction of seafloor spreading along the Southwest Indian Ocean and Central Indian Ocean ridges (Madagascar, Crozet and Central Indian basins) at A19 time (Sclater et

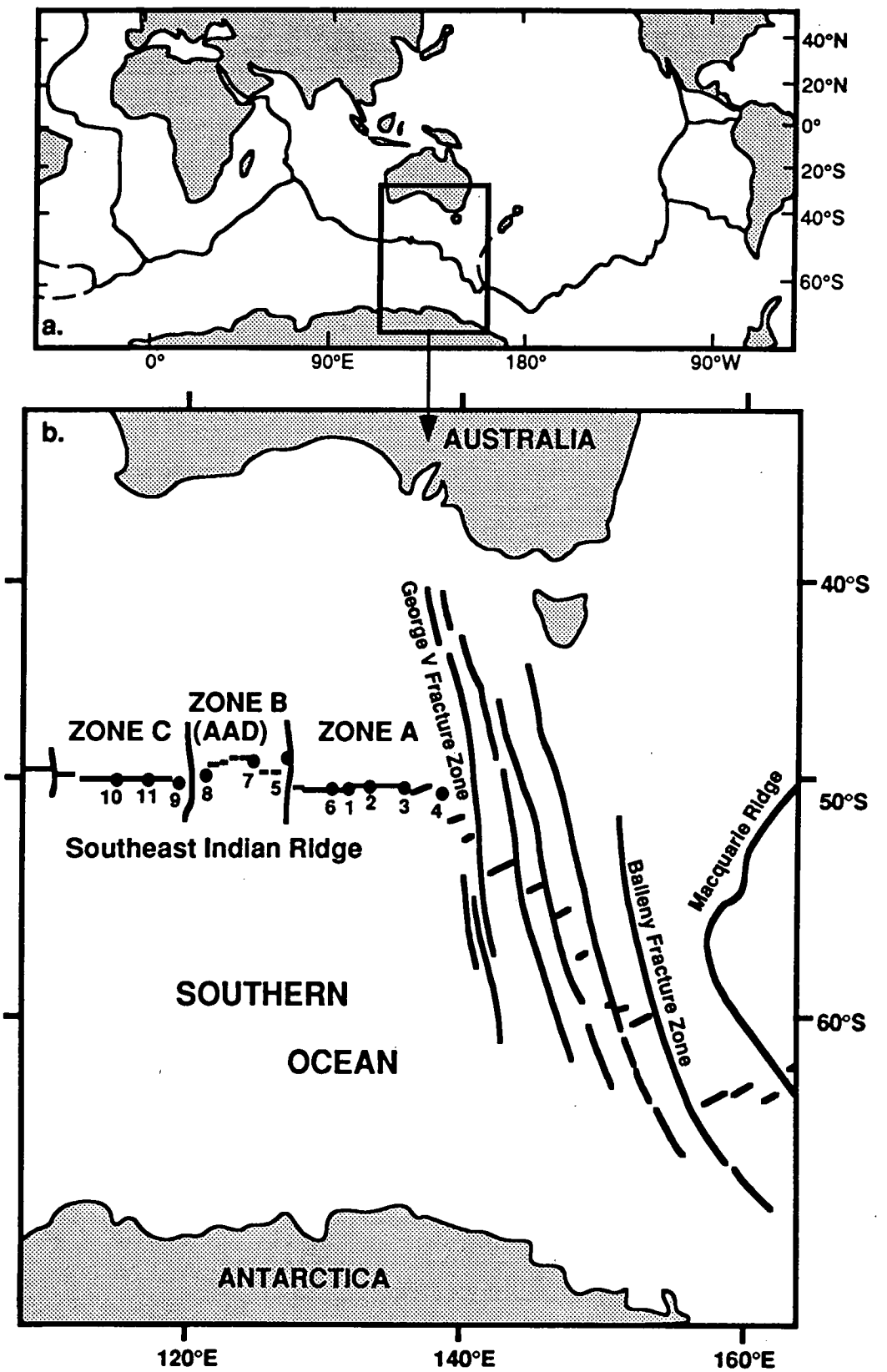

Figure 7.1: a) Map of the Earth showing the location of the Southeast Indian Ridge (modified from Klein et al., 1991) and the outline of the area enlarged in b). The latter depicts the three zones defined by Weissel and Hayes (1971), including zone B, the Australian-Antarctic Discordance (modified from Anderson et al., 1980); filled circles represent *R/V Vema* cruise 33 dredge sites, from which the samples of Anderson et al. (1980), Klein et al. (1988) and Klein et al. (1991) were collected.

al., 1981). It also corresponds closely to the time of Pacific Plate reorganisation, as indicated by the age of the Hawaiian-Emperor bend (42±1.4 Ma: Dalrymple and Clague, 1976).

Seafloor spreading along the SEIR since the dramatic change in spreading rate at 44.5 Ma is generally considered to comprise a full spreading rate (e.g. Macdonald, 1982; Phipps Morgan et al., 1987; Sempéré et al., 1991) of somewhere between 58-59 mm/yr (P. Symonds, pers. comm., 1993), ~62 mm/yr (Royer and Sandwell, 1989) and 74 mm/yr (Palmer et al., 1993). However, Veevers et al. (1990) and Veevers and Li (1991) propose a full spreading rate of only 40 mm/yr from 44.5 Ma to the present day, or at least until ~32 Ma (south of A13), corresponding to the definition of a slow spreading rate (<50 mm/yr: e.g. Macdonald, 1982; Phipps Morgan et al., 1987; Chen and Morgan, 1990; Sinton and Detrick, 1992; Niu and Batiza, 1993; Palmer et al., 1993). Weissel and Hayes (1971) also calculated slower spreading rates of 44 mm/yr to 62 mm/yr between 38 Ma and 10 Ma with an increase to rates in excess of 70 mm/yr from 10 Ma to the present day. Based on the widespread proposals for a spreading rate between 60-74 mm/yr since 44.5 Ma, the SEIR will here be assumed to have had an intermediate (refer to Section 7.6.1) spreading rate since that time.

7.3 MORPHOLOGY OF THE SOUTHEAST INDIAN RIDGE:

The SEIR is an east-west trending mid-ocean ridge which separates the Indian-Australian and Antarctic plates between the Indian Ocean triple junction (central Indian Ocean) and the Macquarie triple junction (southwest Pacific Ocean). Between 105°E and 138°E, the ridge is considered to comprise three distinct morphological and geophysical zones (Weissel and Hayes, 1971) (Figure 7.1). Zone B, an approximately 500 km long, anomalously deep and morphologically complex region of the SEIR located between 120°E and 128°E at a latitude of 48°S to 51°S, was named the Australian-Antarctic Discordance by Hayes and Conolly (1972). It is bounded to both the east and west by major transform faults with >100 km of offset, including 175 km of right lateral offset along the eastern transform (Weissel and Hayes, 1971; 1972; Sempéré et al., 1991; Palmer et al., 1993).

The morphological and geophysical features which serve to differentiate between the AAD and the adjacent regions (zones A and C) of the SEIR will be discussed in greater detail in Chapter 8 (Section 8.2.1). It should be noted here, however, that the well-defined axial rift valley and segmented nature of the AAD are considered more typical of slow spreading centres, rather than the intermediate spreading rate of the SEIR (Phipps Morgan et al., 1987; Sempéré et al., 1991). In contrast, zone A is characterised by a 500 m high axial ridge, considered to be more characteristic of faster spreading centres (Sempéré et al., 1991).

7.4 GEOCHEMICAL FEATURES OF ZERO-AGE BASALTS FROM THE SOUTHEAST INDIAN RIDGE:

Previous geochemical studies of basalts dredged from zones A to C of the SEIR have concentrated on attempting to find differences which could be correlated with along-ridge morphological and geophysical changes and interpreted in terms of variations in the temperature and extent of melting. Therefore, although the findings of these studies will be presented here, the literature-derived interpretations mainly have implications for the models presented in Chapter 8 (Section 8.2.3) concerning the origin of the AAD.

Anderson et al. (1980) discovered anomalously high TiO_2 and FeO whole-rock abundances in lavas dredged from the SEIR axis within zone A east of the AAD. They inferred a positive correlation between whole-rock FeO^*/MgO, % titanomagnetite, magnetic anomaly amplitude, the intensity of natural remanent magnetization, and the variation in depth anomalies along this region of the SEIR.

Christie et al. (1988) found that MORB dredged from the AAD comprise relatively uniform and unfractionated ($Mg\#_{60-71}$) lavas which are distinguished from those of zone A by their higher Na, K, Al and Si abundances and lower Ca, Ti, Fe, and Ca/Al contents at a given MgO content, variations which are also evident in the data of Anderson et al. (1980) and Klein et al. (1991) plotted in Figure 7.2. Based on these along-axis major element differences and the observation that zone A basalts are generally more compositionally varied and more fractionated ($Mg\#_{41-68}$) than samples collected from the AAD, Christie et al. (1988) suggested that a major geochemical boundary, resulting from "discontinuity in the post-melting processes", is coincident with the eastern boundary of the AAD.

Klein et al. (1991) confirmed that zone A basalts have higher TiO_2 and FeO contents than zone B and C lavas (Figure 7.2), but concluded that they were still within the N-MORB compositional range. Based on the proposal that MORB chemistry can be correlated with axial depth, crustal thickness and mantle temperature (Klein and Langmuir, 1987), they noted a correlation between maximum ridge axis depth, lowest CaO/Al_2O_3 and $Fe_{8.0}$ and highest $Na_{8.0}$ and $Si_{8.0}$ (Figure 7.3), which they interpreted in terms of the global component of MORB chemical variability of Klein and Langmuir (1989).

Incompatible element plots of the natural basaltic glass data of Klein et al. (1991) from zones A to C of the SEIR (Figure 7.4) reveal generally flat patterns of the less incompatible elements, from Lu to P, consistent with their classification as N-MORB. However, the LILE and LREE define more irregular patterns in most samples, suggesting variable levels of enrichment in the most incompatible elements. Zone A sample D1-2 is unusual in that it displays a gradual increase in the normalised abundances of elements more incompatible than Sm, but a generally flat pattern in terms of the less incompatible elements, the latter similar to N-MORB. It may therefore be representative of a T-MORB composition, transitional between N-MORB and E-MORB. The other zone A glasses all have similar patterns, characterised by a relative depletion in the most incompatible elements, K, Ba and

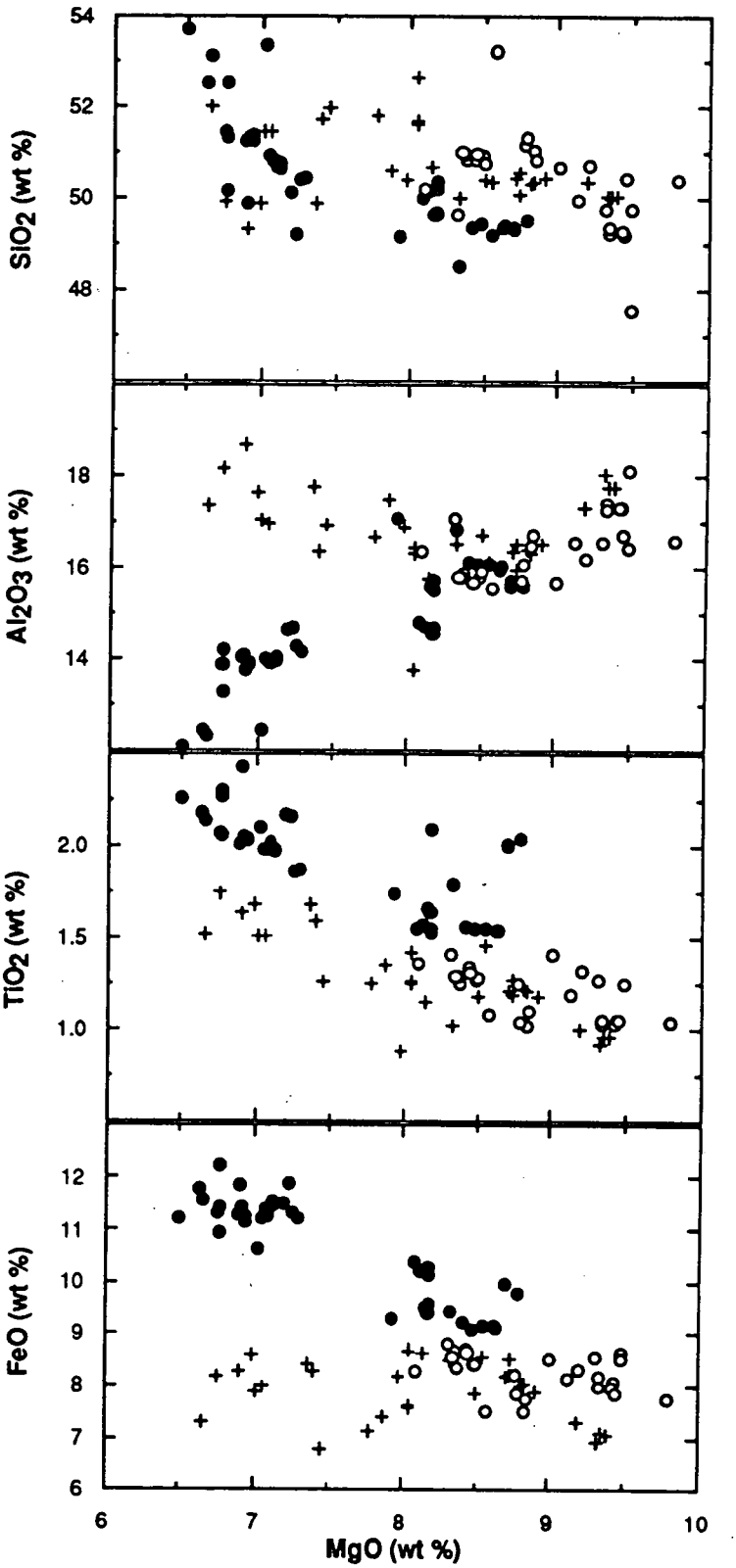
54
52
50
48
SiO2 (wt %)
18
16
14
Al2O3 (wt %)
2.0
1.5
1.0
TiO2 (wt %)
12
11
10
9
8
7
6
FeO (wt %)
6
7
8
9
10
MgO (wt %)

(Figure 7.2)

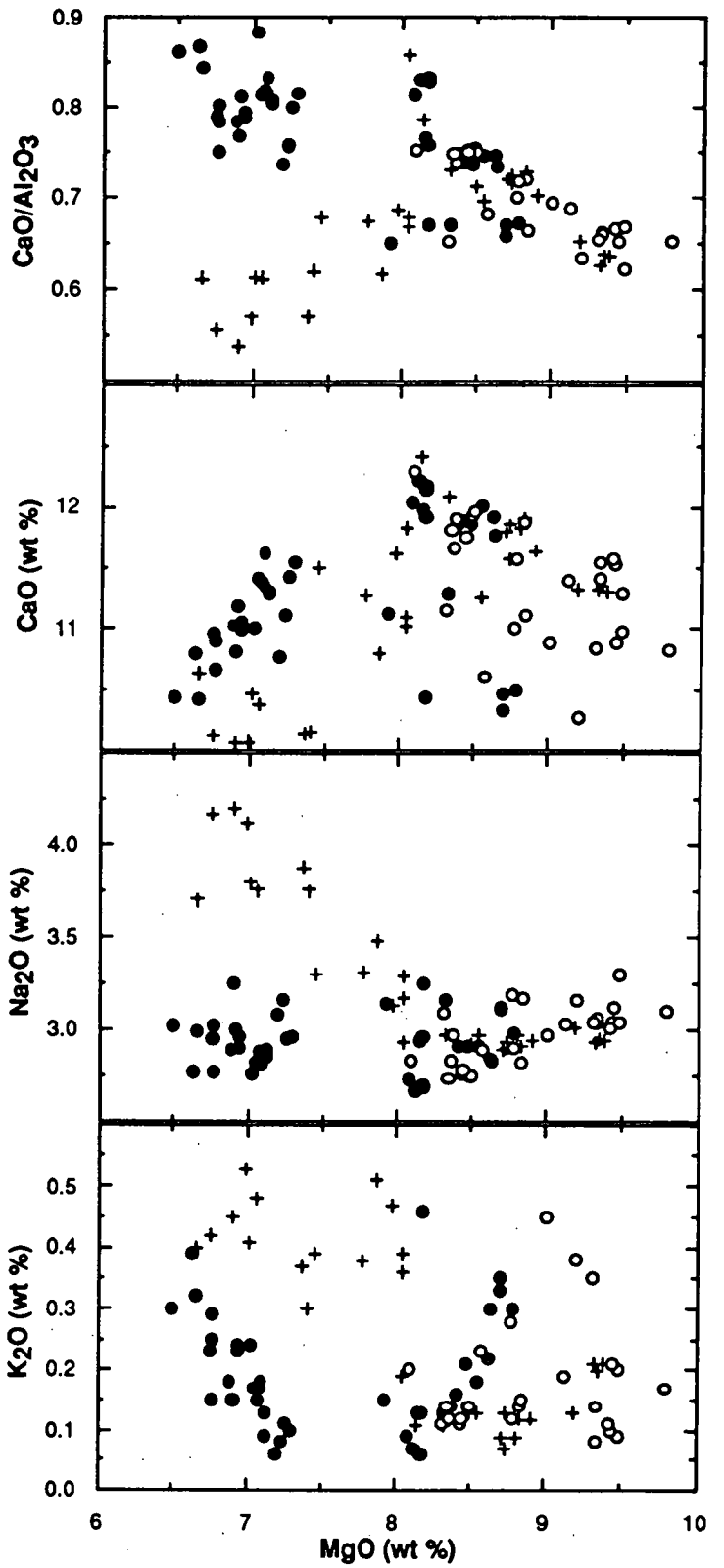

Figure 7.2: Plots of MgO versus major element oxides and ratios using the SEIR data of Anderson et al. (1980) and Klein et al. (1991): zone A (filled circles), zone B or AAD (crosses) and zone C (open circles).

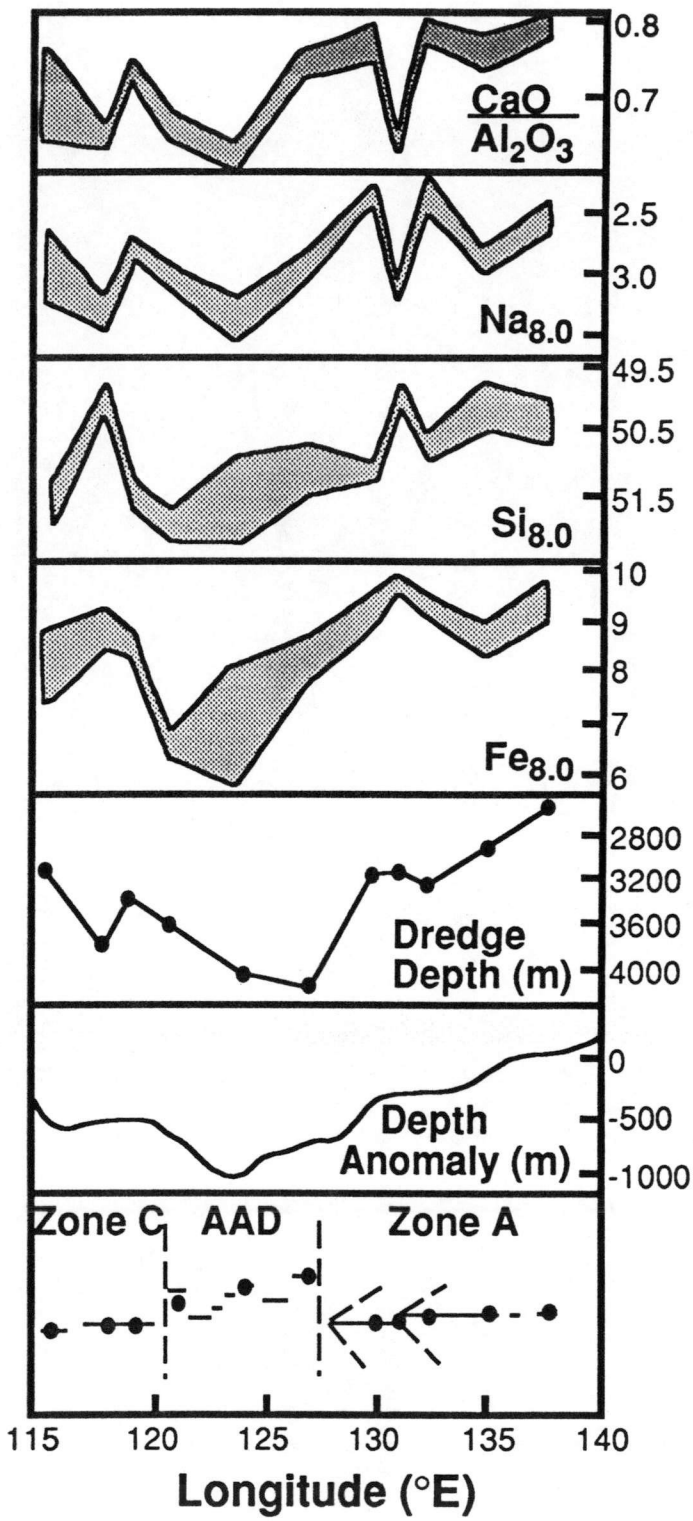

Figure 7.3: Longitude versus axial depth and the locations and depths of the *R/V Vema* dredge sites (small filled circles), within and immediately adjacent to the AAD, are plotted relative to the ranges of whole-rock Na_2O, SiO_2 and FeO normalised to 8 wt % MgO and CaO/Al_2O_3 (modified from Klein et al., 1991).

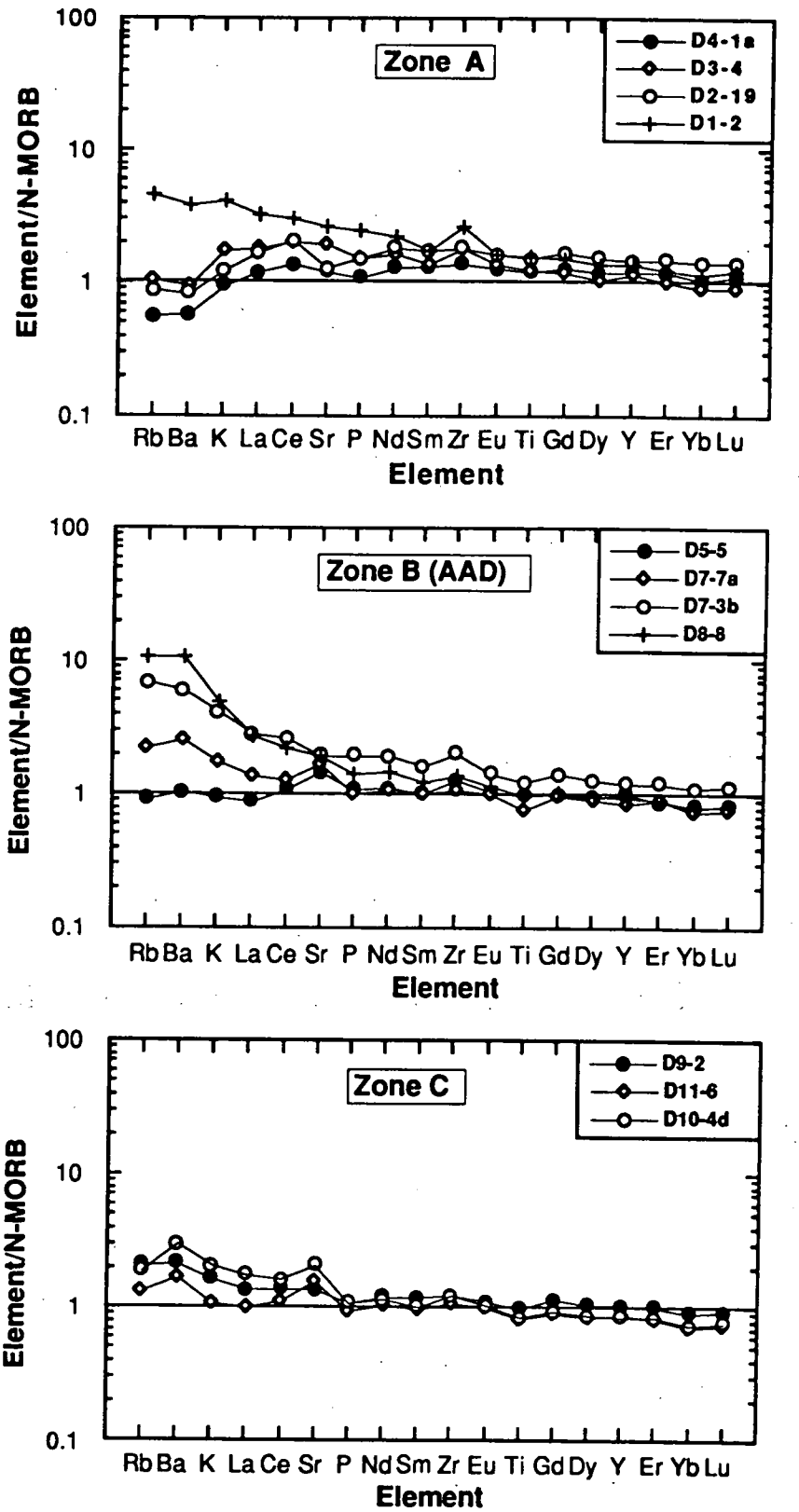

Figure 7.4: Incompatible element patterns of natural basaltic glasses (Klein et al., 1991 - Table 5) dredged from zones A to C of the SEIR and normalised to the N-MORB values of Sun and McDonough (1989).

Rb. The slightly positive Zr anomalies displayed by zone A samples are also present in the zone B glasses, but the latter also possess slight positive Sr and negative Ti anomalies, similar to those of the zone C samples. The lower normalised abundances of Ti in the zone B and C samples are consistent with the observation that zone A basalts have generally higher TiO_2 than those erupted further west along the SEIR (Anderson et al., 1980; Christie et al., 1988; Klein et al., 1991). Apart from sample D5-5, collected from the eastern AAD, zone B samples are characterised in Figure 7.4 by relative enrichments in K, Rb and Ba, quite distinct to samples dredged from further east at sites 5, 2, 3 and 4. Zone B samples D7-3b and D8-8 are also slightly enriched in LREE. Zone C glasses display generally flat incompatible element patterns with less marked Rb and Ba enrichments than the AAD samples.

The flat patterns displayed by the zero-age SEIR glasses in terms of elements less incompatible than Sr (Figure 7.4) suggest that most samples have N-MORB geochemical affinities. However, the enrichment in the most incompatible LILE relative to N-MORB in the zone B (except sample D5-5), and to a lesser extent zone C, samples, plus the distinct pattern of sample D1-2 from zone A suggests that the SEIR may also be erupting some basalts with slightly more enriched (T-MORB) compositions.

7.5 SOUTHERN OCEAN SEAFLOOR SAMPLES:

7.5.1 Sampling Locations:

The sampling locations for the Southern Ocean seafloor samples, dredged during Southern Margins cruise 102 of the *R/V Rig Seismic*, are listed in Appendix 1 - Table A1.1 and depicted in Figure 7.5. All four sites are located on the Southern Ocean abyssal plain at depths in excess of 4000 m. Dredges 102/DR09 and 102/DR10 are located east of the northward extrapolation of the AAD, the former just south of magnetic seafloor lineation A22 (53.5 Ma), the latter just south of A13 (36 Ma). Dredges 102/DR11 and 102/DR13 are located west of the northward extrapolation of the AAD, the former just north of A13 (36 Ma), the latter just south of A29 (66 Ma). Seafloor magnetic lineation ages are from Reinemund (1984).

These Southern Ocean seafloor samples are the products of two different spreading regimes along the SEIR. Those from sites 102/DR09 and 102/DR13 were erupted during the first period of slow spreading between Australia and Antarctica (9 mm/yr full rate; Veevers et al., 1990; Veevers and Li, 1991) prior to 49 Ma. Dredge sites 102/DR10 and 102/DR11 correspond to a period of more rapid seafloor spreading, following the increase in spreading rate along the SEIR at 44.5 Ma (Veevers et al., 1990).

The majority of samples collected from these four sites are extremely altered, many showing signs of hydrothermal activity. Greenschist facies metamorphism is also evident as clinopyroxene uralitisation in some samples from site 102/DR13. However, sixteen samples

with lesser degrees of pervasive microscopic alteration were considered suitable for major and trace element analysis, and 13 were also analysed, following acid leaching, for their radiogenic (Sr, Nd and Pb) isotope compositions (Chapter 8).

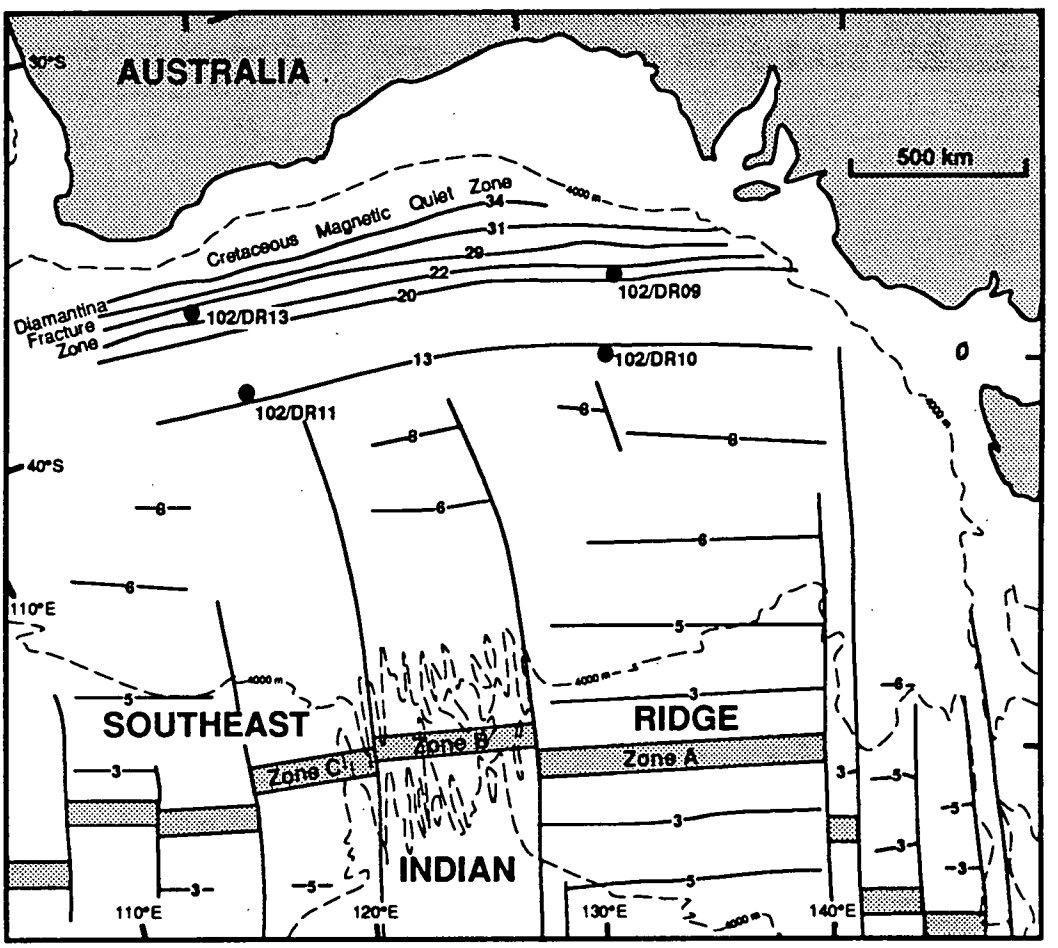

Figure 7.5: Map of the Southern Ocean region between the southern margin of Australia and the SEIR showing the location of the four *R/V Rig Seismic* dredge sites relative to the location of the AAD and recognised magnetic seafloor lineations (modified from Reinemund, 1984).

7.5.2 Petrography:

The Southern Ocean seafloor samples range in grain size from basaltic at dredge sites 102/DR09 and 102/DR11 through doleritic at sites 102/DR10 and 102/DR13 to gabbroic at site 102/DR10. No basalts were dredged from site 102/DR10. The petrography of the samples analysed for major and trace element geochemistry is summarised in Table 7.1.

The basalts are generally characterised by sparsely porphyritic to glomeroporphyritic textures with plagioclase ± clinopyroxene ± olivine phenocrysts and/or microphenocrysts and plagioclase-phryric groundmasses devoid of olivine. Groundmass plagioclase and clinopyroxene may form subophitic textures, or clinopyroxene may infill columnar plagioclase

Table 7.1: Petrography of the Southern Ocean seafloor samples discussed in the text.

Sample No.	Rock Type	Texture	Phenocrysts and microphenocrysts	Groundmass
Dredge 09:				
09-4A	Olivine tholeiite basalt	Subophitic Slightly vesicular	1) plagioclase phenocrysts and glomerocrysts	anhedral to subhedral cpx subophitically enclosing, or intergranular to, plagioclase laths; smectite clots; skeletal to finely disseminated Fe-oxides
09-4B(I)	Transitional tholeiite basalt	Sparsely porphyritic/ glomeoporphyritic Slightly vesicular	1) subhedral to euhedral cpx microphenocrysts 2) elongate plagioclase microphenocrysts 3) plagioclase ± cpx glomerocrysts	plagioclase; cpx - may subophitically enclose plagioclase; skeletal Fe-oxides; clay
09-4B(II)	Olivine tholeiite basalt	Porphyritic/ Glomeroporphyritic Slightly vesicular	1) plagioclase phenocrysts and glomerocrysts	plagioclase laths; cpx may infill columnar plagioclase laths, subophitically enclose plagioclase, or be interstitial to plagioclase laths; fine skeletal Fe-oxides; alteration material
09-4B4	Transitional tholeiite basalt	Sparsely porphyritic/ glomeoporphyritic Slightly vesicular	1) rare plagioclase phenocrysts: some with partly resorbed rims 2) glomerocrysts of clinopyroxene ± plagioclase	plagioclase laths are often columnar and infilled with cpx and finer groundmass; fine Fe-oxides; alteration material
09-4B5	Olivine tholeiite basalt	Sparsely porphyritic/ glomeroporphyritic Vesicular	1) rare plagioclase microphenocrysts 2) glomerocrysts of plagioclase ± cpx	subhedral cpx; plagioclase laths; disseminated Fe-oxides; finer grained than previous samples
09-4C	Transitional tholeiite basalt	Spherulitic Vesicular	1) spherules of plagioclase and partially altered cpx phenocrysts and/or microphenocrysts 2) olivine microphenocrysts completely altered to calcite and smectite 3) Fe-stained elongate feather-like structures overprinting spherulites - ? quenched olivines	Finely divided Fe-oxides; smectite
Dredge 10:				
10-1B	Tholeiitic gabbro	Consertal texture	-	Partially altered anhedral olivine, rimmed by calcite and clusters of fine-grained Fe-oxide; anhedral, partly uralitised cpx; interlocking irregular-shaped plagioclase; coarse Fe-oxides
10-1C	Tholeiitic metagabbro	Consertal texture	-	Interlocking cpx, plagioclase and Fe-oxides; partial cpx replacement by chlorite and fibrous green amphibole

Table 7.1: (continued)

Sample No.	Rock Type	Texture	Phenocrysts and microphenocrysts	Groundmass
Dredge 10:				
10-3A	Tholeiitic metadolerite	Subophitic/sparsely porphyritic	1) plagioclase phenocrysts: anhedral zoned crystals to elongate laths with partly resorbed rims 2) scattered plagioclase glomerocrysts	plagioclase laths may be columnar and infilled with cpx; cpx partially altered to fibrous amphibole may subophitically enclose plagioclase; scattered Fe-oxides
Dredge 11:				
11-2A **11-2A(iv)**	Olivine tholeiite basalt	Hypocrystalline/ subophitic Vesicular	1) microphenocrysts of cpx subophitically enclosing plagioclase	devitrified glass; finely divided Fe-oxides
11-2A(iii)	Olivine tholeiite basalt	Hypocrystalline/ glomeroporphyritic Vesicular	1) glomerocrysts of olivine + cpx + plagioclase 2) plagioclase microphenocrysts: may be hollow and columnar 3) clinopyroxene microphenocrysts: may subophitically enclose plagioclase 4) olivine microphenocrysts	devitrified glass; finely divided Fe-oxides
11-2B	Olivine tholeiite basalt	Porphyritic	1) plagioclase phenocrysts; partly resorbed rims or hollow columnar crystals infilled with cpx 2) olivine microphenocrysts altered to smectite	plagioclase needles infilled with cpx; ?spherulitic structures; fine Fe-oxides
Dredge 13:				
13-3(iii) **13-3D**	Tholeiitic dolerite	Subophitic	-	plagioclase laths subophitically enclosed by cpx partially altered to chlorite and amphibole; scattered Fe-oxides
13-3E	Basalt	Subophitic	-	very fine-grained plagioclase, subophitically enclosed by cpx; fine Fe-oxides

crystals. Most samples from site 102/DR11 have hypocrystalline groundmasses comprising only devitrified glass and finely divided Fe-oxides.

The dolerites and gabbros are more equigranular, the former dominated by subophitic enclosures of plagioclase by clinopyroxene whereas the latter are characterised by consertal intergrowths of the dominant mineral phases.

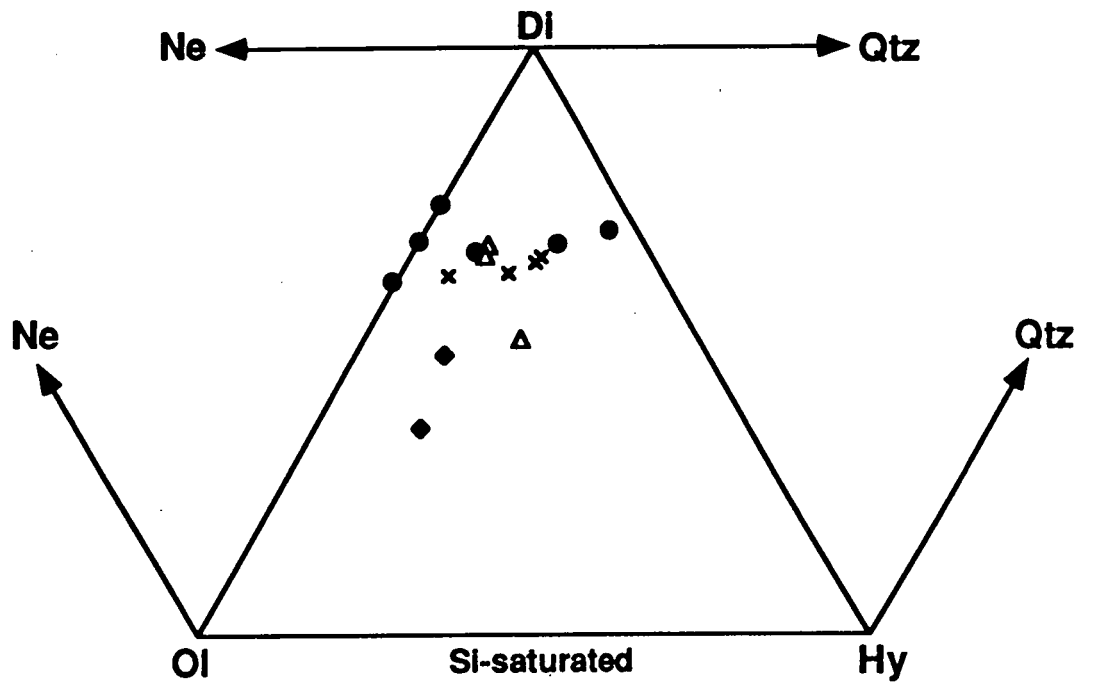

Figure 7.6: Projection of the normative basalt tetrahedron (Yoder and Tilley, 1962) for samples dredged from the Southern Ocean seafloor: dredge 102/DR09 (filled circles), dredge 102/DR10 (open triangles), dredge 102/DR11 (oblique crosses) and dredge 102/DR13 (filled diamonds); notation as for Figure 3.9.

7.5.3 Geochemistry:

The major and trace element compositions of the Southern Ocean seafloor samples (Table 7.2) were determined by X-ray fluorescence (XRF) spectrometry (Philips PW 1480 spectrometer). REE, Hf and Th (as marked) abundances were measured by INAA. Analytical procedures are described in Appendix 2.

Although CIPW norm (wt %) calculations indicate that most of the samples are SiO_2-saturated olivine tholeiites, apart from three transitional tholeiites from site 102/DR09 which plot at the boundary between the SiO_2-saturated and SiO_2-undersaturated fields (Figure 7.6), the pervasive microscopic alteration of these samples means that normative calculations should be considered with caution.

The chondrite-normalised REE plots of basalts from dredge site 102/DR11 (Figure 7.7) display the characteristic concave-upward patterns and relative LREE depletions of N-MORB, produced by relatively large degrees of melting of a depleted source. Despite its lower REE abundances, the similar pattern of gabbro sample 10-1C to the dredge 102/DR11 basalts indicates that the seafloor in the vicinity of dredge site 102/DR10 also has N-MORB

Table 7.2: Major and trace element chemistry of Southern Ocean seafloor samples.

Sample No:	09-4A	09-4B(I)	09-4B(II)	09-4B4	09-4B5	09-4C	10-1B	10-1C	10-3A	11-2A	11-2A(III)	11-2A(Iv)	11-2B	13-3(III)	13-3D
Major Elements (wt %):															
SiO_2	50.22	50.79	51.72	49.78	50.93	48.10	50.26	50.22	49.87	50.45	49.68	50.12	48.11	48.70	50.21
TiO_2	1.91	2.02	2.16	2.07	2.08	1.75	0.59	0.72	1.29	1.36	1.35	1.34	1.39	1.10	0.99
Al_2O_3	15.49	15.63	16.19	14.83	15.85	16.88	16.25	16.11	16.70	15.92	15.76	15.87	17.30	15.72	16.00
Fe_2O_3	10.41	9.26	7.56	12.09	9.14	10.43	6.44	6.54	8.79	9.53	10.30	9.28	10.14	9.38	9.10
FeO	0.00	0.00	0.00	0.00	0.00	0.00	0.00	0.00	0.00	0.00	0.00	0.00	0.00	0.00	0.00
MnO	0.16	0.16	0.14	0.19	0.14	0.14	0.12	0.12	0.15	0.16	0.16	0.15	0.15	0.19	0.18
MgO	5.64	5.14	5.38	4.73	5.17	4.34	9.23	9.01	8.03	6.50	6.71	6.73	5.49	8.48	8.03
CaO	10.56	10.70	10.85	9.73	10.56	9.93	13.69	12.86	11.05	12.00	11.80	11.89	11.63	10.06	7.71
Na_2O	3.65	4.11	3.91	4.00	3.77	3.81	2.50	2.78	3.08	3.10	3.00	3.09	3.04	3.22	4.27
K_2O	0.56	0.51	0.35	0.81	0.57	0.44	0.06	0.07	0.09	0.26	0.27	0.21	0.27	0.18	0.16
P_2O_5	0.23	0.33	0.27	0.26	0.29	0.31	0.06	0.08	0.13	0.18	0.18	0.17	0.17	0.14	0.12
LOI	1.61	1.11	1.76	1.25	1.91	3.63	0.95	1.22	0.81	0.80	0.90	1.04	2.46	2.65	3.02
Total	100.44	99.76	100.29	99.74	100.41	99.76	100.15	99.73	99.99	100.26	100.11	99.89	100.15	99.82	99.79
Mg#	55.87	56.47	62.45	47.77	56.93	49.30	77.01	76.30	68.10	61.45	60.35	62.89	55.85	67.87	67.34
FeO*	9.37	8.33	6.80	10.88	8.22	9.39	5.79	5.88	7.91	8.58	9.27	8.35	9.12	8.44	8.19
Trace Elements (ppm):															
Ba	44	36	36	37	35	26	14	4	7	16	59	19	15	80	99
Rb	15	9	3	23	14	11	1	<1	<1	5	3	4	5	3	2
Nb	5.6	6.2	6.3	5.5	6.6	4.7	0.4	0.4	0.8	3.1	2.9	2.9	3.2	7.9	8.0
Sr	202	226	240	186	231	226	113	155	124	168	153	166	147	184	210
Zr	166	177	178	183	187	156	31	51	85	96	91	96	98	80	98
Y	45	46	49	50	48	44	17	22	32	33	34	33	34	27	26
Ni	54	41	47	27	43	99	162	158	134	71	54	80	62	89	99
Cr	246	171	176	94	171	352	572	1053	261	386	398	378	299	290	309
V	305	296	312	321	284	277	181	200	228	269	286	272	291	249	230
Sc	42	42	48	44	45	43	40	39	31	41	45	43	36	44	41
Hf	3.61	3.85						1.21		2.00		2.03		1.69	2.17
Th (XRF)	<1.0	1.30	<1.0	<1.0	<1.0	<1.0	<1.0	<1.0	<1.0	<1.0	<1.0	<1.0	<1.0	2.10	3.80
Th (INAA)	0.40	0.63						<0.1		0.39		0.29		0.93	2.34
Pb	1.80	<1.5	<1.5	1.50	1.80	1.50	<1.5	<1.5	<1.5	<1.5	<1.5	<1.5	<1.5	<1.5	<1.5
Rare Eath Elements (ppm):															
La	7.03	7.18						1.71		3.90		3.91		6.21	7.92
Ce	18.50	21.40						5.53		11.50		12.00		16.10	19.50
Nd	15.30	17.20						5.28		9.44		10.30		11.00	12.60
Sm	4.98	5.22						2.01		3.30		3.24		3.03	3.13
Eu	1.59	1.76						0.76		1.32		1.20		1.09	1.07
Tb	0.96	1.04						0.47		0.83		0.79		0.66	0.63
Ho	1.30	1.41						0.65		1.20		1.13		0.93	0.93
Yb	3.37	3.52						1.78		2.63		2.73		2.30	2.26
Lu	0.51	0.50						0.23		0.35		0.38		0.34	0.28

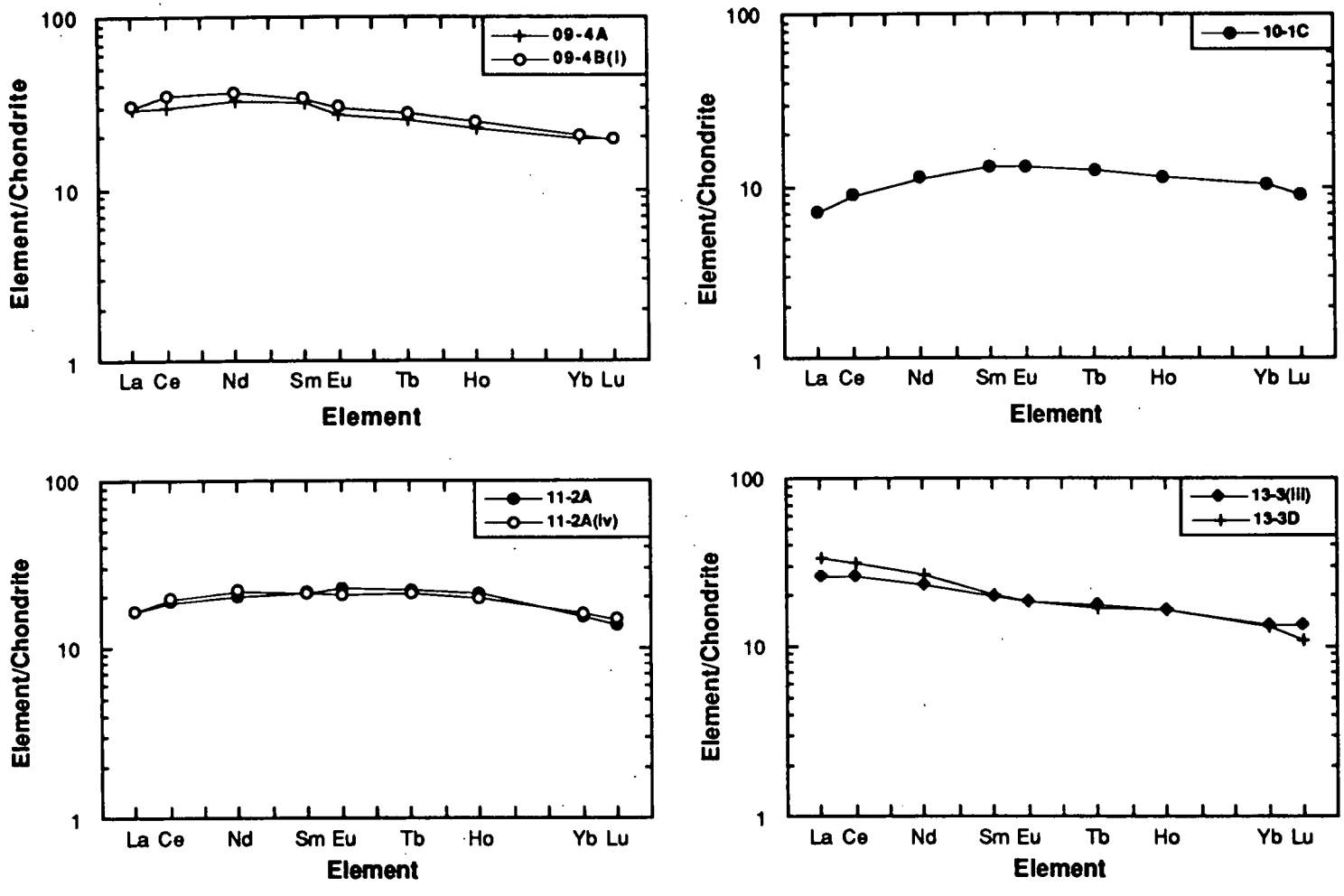

Figure 7.7: Chondrite-normalised REE patterns of the Southern Ocean seafloor samples; data from Table 7.2; C1 chondrite normalising values from Sun and McDonough (1989).

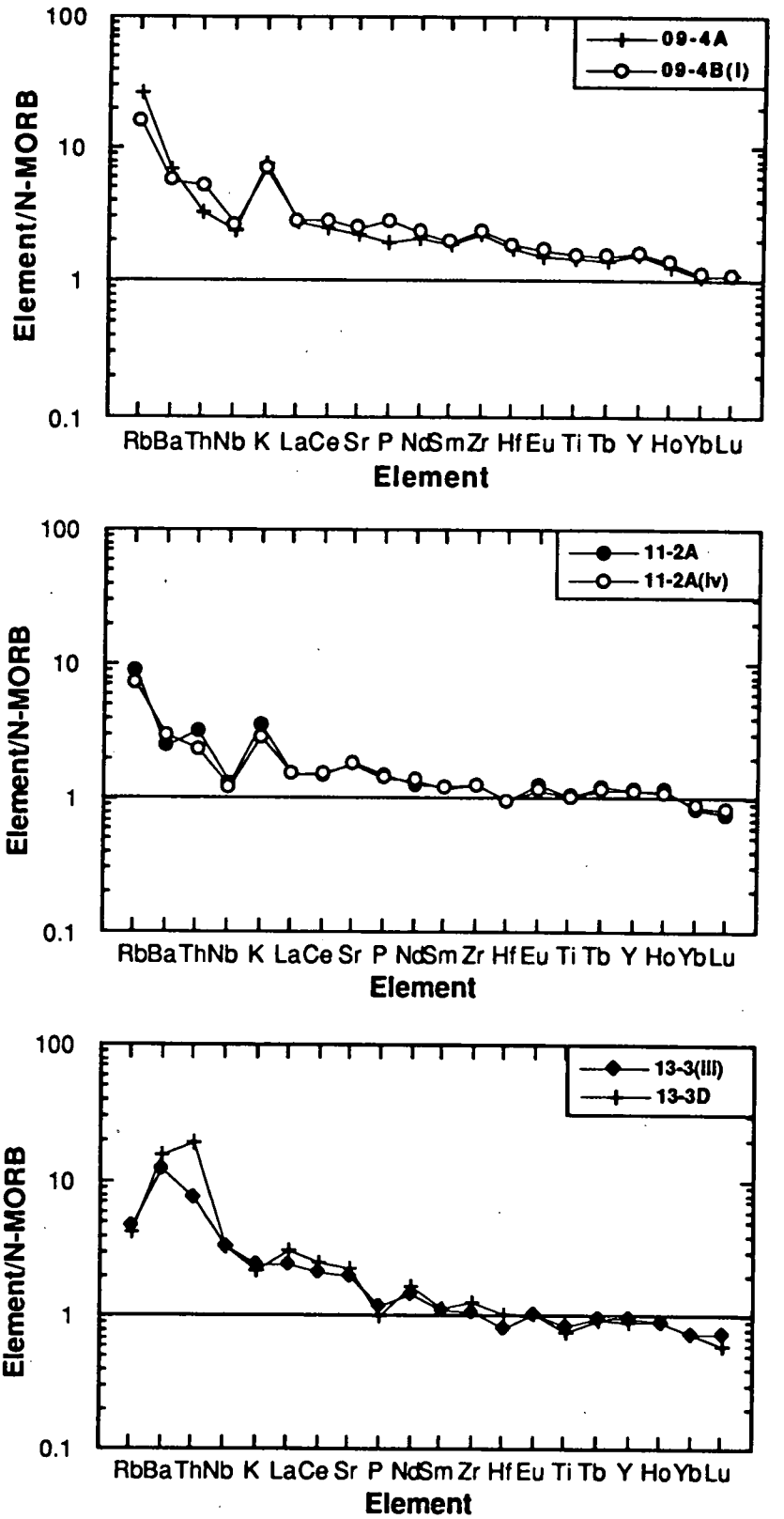

Figure 7.8: Incompatible element patterns of the Southern Ocean seafloor samples normalised to the N-MORB values of Sun and McDonough (1989); raw data from Table 7.2.

affinities; no REE data are available for dolerite sample 10-3A from this same location. However, dredge 102/DR13 and, to a lesser extent, 102/DR09 basalts are more characteristic of T-MORB compositions, displaying slight LREE enrichments, relative to the MREE, and lacking significant HREE depletion.

The N-MORB-normalised incompatible element patterns of the Southern Ocean seafloor basalts are similar in that they display gradually increasing elemental abundances with increasing incompatibility, which is most evident within the dredge 102/DR13 samples (Figure 7.8). The trace element patterns of the Southern Ocean seafloor samples are therefore suggestive of T-MORB rather than N-MORB compositions. Dredge 102/DR09 and 102/DR11 samples have high normalised abundances of the LILE, K, Ba and Rb, relative to the adjoining LREE and Nb, whereas samples from site 102/DR13 lack the positive K spike evident in basalts from the other dredge sites but have very high Ba abundances compared to the adjoining elements.

The mobility of the LILE (e.g. Weaver, 1991) means that they are prime candidates to reflect the effects of seafloor alteration processes. This may well be the case with the Southern Ocean seafloor samples plotted in Figure 7.8, particularly as they all display alteration effects, and the positive K spikes of the dredge 102/DR09 and 102/DR11 samples are absent from the zero-age SEIR glasses (Figure 7.4). However, as most of the samples from sites 102/DR09 and 102/DR11 have relatively low LOI (loss on ignition) measurements (<2 % in all samples plotted in Figure 7.8), the similarity of their incompatible element patterns may reflect some degree of source enrichment in LILE, relative to the other highly incompatible elements. The relatively large LOI values of the site 102/DR13 samples suggest that they may well be more altered than most of the other Southern Ocean dredge samples. This inference does, however, assume that the degree of LOI is a direct reflection of the degree of alteration, which is not necessarily the case. The dredge 102/DR13 basalts are also generally more enriched in incompatible elements. Their extremely high normalised Ba contents (Figure 7.8) may also be due to seafloor alteration, a proposal supported by the unusually high Na_2O and low CaO of sample 13-3D.

The geochemistry of the gabbros from site 102/DR10 will not be included in any further discussions of the Southern Ocean seafloor samples in this chapter due to their probable cumulate origin.

7.6 SLOW VERSUS FAST SPREADING MID-OCEAN RIDGES:

7.6.1 Background:

Spreading rates have been found to vary significantly along the world's mid-ocean ridge system. These variations may be concurrent, occurring either between different ridges, such as the slow spreading MAR and the fast spreading EPR, or along the length of a single ridge, as evidenced by the ultra-fast spreading rate of the southern EPR compared to

the fast spreading rate of the northern EPR (e.g. Sinton and Detrick, 1992), or they may be temporally related such as the change in spreading rate with time along the SEIR (Veevers et al., 1990).

The definition of slow, intermediate and fast spreading rates varies slightly in the literature. Although in general agreement that a full spreading rate of <50 mm/yr constitutes slow spreading, Niu and Batiza (1993) classify fast spreading as >60 mm/yr whereas most other researchers define fast spreading as either >80 mm/yr (Chen and Morgan, 1990; Sinton and Detrick, 1992) or >90 mm/yr (Macdonald, 1982; Phipps Morgan et al., 1987; Palmer et al., 1993).

Despite the lack of consensus over spreading rate classifications, there does appear to be general agreement that ridge axis morphology is a function of spreading rate. Slow spreading ridges are associated with well-developed deep axial rift valleys bounded by mountainous ridge flanks which display rough topography; all features that are absent, or at least far less pronounced, along fast spreading ridges (e.g. Macdonald, 1982; Francheteau and Ballard, 1983; Phipps Morgan et al., 1987). Sinton and Detrick (1992) state that this morphological change occurs over the intermediate spreading rate range of 50-70 mm/yr. Morphological change is accompanied by an abrupt change in gravity signals, from high-amplitude variable signals at slow spreading rates of <70 mm/yr (Chen and Morgan, 1990; Lin et al., 1990; Lin and Phipps Morgan, 1992) to lower-amplitude and more uniform signals with faster spreading >70 mm/yr (Chen and Morgan, 1990; Lin and Phipps Morgan, 1992).

Geochemical differences have also been observed within MORB erupted at various spreading rates along different mid-ocean ridges. Comparisons of major element differences are based on the assumption that the depleted upper mantle source of MORB is homogeneous on a global scale. Flower (1981) proposed that basalts erupted at slow spreading ridges generally define a narrower range of relatively undifferentiated compositions compared to those erupted at faster spreading centres. Sinton and Detrick (1992) compared the Mg-values of glasses erupted at a number of fast, intermediate and slow spreading ridges and concluded that increased fractionation with faster spreading actually begins at intermediate (50-80 mm/yr) spreading rates. Although Langmuir et al. (1992) also agree that more primitive MORB compositions occur at slower spreading rates, they propose that geochemical variability increases with decreasing spreading rate, so that slow spreading ridge eruptives range from very primitive to very differentiated compositions, whereas basalts produced at faster spreading ridges fail to extend to the more primitive compositions but also possess a more limited range of MgO contents. They consider faster spreading ridges to be associated with lower and more limited mantle temperature variations, hence the lower and more homogeneous MgO contents of their eruptives.

There is some debate in the literature as to other possible geochemical effects of variations in spreading rate. Niu and Batiza (1993) have correlated observed geochemical differences between basalts erupted at fast and slow spreading ridges with the proposed global and local MORB trends (Klein and Langmuir,1987; Klein and Langmuir, 1989; Niu and

Batiza, 1991; Langmuir et al., 1992). They observe the global MORB trend, defined by increasing $Fe_{8.0}$ and decreasing $Si_{8.0}/Fe_{8.0}$ with decreasing $Na_{8.0}$ and indicative of a positive correlation between the extent and pressure of melting, at spreading rates in excess of 60 mm/yr, corresponding to the intermediate spreading rates of most other researchers (e.g. Macdonald, 1982; Phipps Morgan et al., 1987; Sinton and Detrick, 1992; Palmer et al., 1993). The local trend, comprising a positive correlation between $Fe_{8.0}$ and $Na_{8.0}$ abundances and indicative of a negative correlation between the extent and pressure of melting, is observed within slow spreading ridge eruptives (Niu and Batiza, 1993). However, Langmuir et al. (1992) state that the global trend is independent of spreading rate, due to the fact that there is no recognisable correlation between $Na_{8.0}$ and spreading rate, except in terms of variability; slow spreading ridges displaying the entire range of $Na_{8.0}$ compositions whereas fast spreading ridges have only intermediate $Na_{8.0}$ values.

Langmuir et al. (1992) suggest that trace element differences can be correlated with the difference in spreading rate between the MAR and the EPR. Segments of the slower spreading MAR, distant to hotspot activity, were found to have lower Ce/Sm values than EPR samples, suggestive of greater incompatible element depletion.

A variety of models proposed to explain the observed differences between fast and slow spreading mid-ocean ridges (e.g. Sleep and Rosendahl, 1979; Chen and Morgan, 1990; Lin et al., 1990; Parmentier and Phipps Morgan, 1990; Lin and Phipps Morgan, 1992), mostly invoke variations in the dynamics of mantle upwelling and/or crustal-level magma chamber processes. One common theme (Lin et al., 1990; Parmentier and Phipps Morgan, 1990; Langmuir et al., 1992; Lin and Phipps Morgan, 1992; Niu and Batiza, 1993) involves the transition between three-dimensional plume-like upwelling beneath slow spreading ridges to more two-dimensional and sheet-like upwelling beneath fast spreading ridges as a consequence of the large horizontal shear stresses produced by rapid overlying plate motion.

Another recent model (Sinton and Detrick, 1992) proposes that fast spreading ridges are associated with steady-state magma chambers comprising narrow sill-like bodies of melt underlain by partially solidified crystal mush and transitional crystalline material forming a low velocity zone (LVZ) which extends to the Moho Discontinuity. According to this model, slow spreading centres, underlain only by a dyke-like crystal mush and transition zone material, are characterised by a lack of steady-state melt lenses. This means that eruptive activity at slow spreading ridges is virtually dependent on the intermittent injection of new and more primitive magma into the crystal mush zone from the underlying mantle, resulting in the observed higher Mg# of these basalts and the often complex chemical trends produced by high pressure and/or polybaric fractionation and magma mixing (Flower, 1981). Sinton and Detrick (1992) suggest that the morphological aspects of slow spreading ridges may also be a product of the lack of steady state eruptable magma bodies in these regions of low magma supply, so that amagmatic extension and the development of graben structures ensue. They propose that simple high-level fractionation trends are more evident in basalts

produced at intermediate and fast spreading centres due to the lack of compositional buffering by magma reinjection which is observed at slower spreading centres.

7.6.2 Southern Ocean Geochemistry Versus Spreading Rate:

In comparing the major element systematics of the Southern Ocean seafloor samples erupted during slow spreading (sites 102/DR09 and 102/DR13) with those erupted during the period of more rapid spreading after 44.5 Ma (sites 102/DR10, 102DR11 and zero-age SEIR samples), samples from dredge sites with similar latitudes and crustal ages will be treated here as individual geochemical groups, despite the fact that they are not necessarily co-magmatic suites. The subdivision of the SEIR into zones A to C will be maintained here due to the suggestion that the well-developed axial morphology observed within zone B (AAD), compared to the adjacent ridge segments, is more like that of a slow than an intermediate spreading ridge (Phipps Morgan et al., 1987; Sempéré et al., 1991). This suggests that the magma chamber processes occurring beneath zone B may also be more similar to those associated with slow spreading ridges, thereby resulting in different major element systematics compared to zone A and C eruptives.

As discussed in the previous section, some of the geochemical differences observed along the world's mid-ocean ridge system have been correlated with variations in spreading rate. One of the main geochemical parameters thought to reflect spreading rate, Mg#, has been plotted against latitudinal location in Figure 7.9a. The off-axis Southern Ocean seafloor samples have ranges of Mg# which overlap with each other and with the zero-age basalts from the SEIR. Consistent with the observation of Christie et al. (1988), zone A basalts display a bimodal distribution of Mg# and extend to the most evolved compositions of the zero-age samples. In contrast, basalts from zones B and C have more restricted ranges of Mg#, with zone B extending to the least fractionated compositions.

If the SEIR assumed an intermediate spreading rate at 44.5 Ma it is surprising that the greater differentiation considered typical of intermediate to fast spreading centres (e.g. Sinton and Detrick, 1992) is expressed only within the zone A eruptives. The fact that zone B samples extend to slightly more primitive Mg-values could be indicative of magma chamber processes generally associated with slower spreading ridges. Although the large range of Mg# in zone B samples is also consistent with slow spreading proposals, zone C basalts display a somewhat similar range.

The suggestion of Langmuir et al. (1992) that lower Ce/Sm abundances are correlated with slow spreading rates is also not evident in the Southern Ocean seafloor samples (Figure 7.9b). Dredge 102/DR13 samples, corresponding to a period of slow spreading and distant from any known hotspot activity, extend to the highest Ce/Sm values, whereas all other samples display similar ranges despite differences in spreading rate at their relative times of eruption.

No significant and consistent differences between the slow and intermediate spreading rate groups are evident in plots of MgO (wt %) versus various major element

oxides (Figure 7.10). However, dredge 102/DR09 and 102/DR13 samples, plus some of the zone B (AAD) basalts, have higher Na_2O values over a range of MgO contents than the other Southern Ocean samples, possibly suggesting lower degrees of melting involved in their production. Dredge 102/DR09 and some of the zone B samples also extend to the highest K_2O contents, although, at least in the off-axis samples, this may be an alteration-related feature.

The proposal by Niu and Batiza (1993) that the observed global and local MORB trends (Klein and Langmuir,1987; Klein and Langmuir, 1989; Niu and Batiza, 1991) are a function of spreading rate is investigated in Figure 7.11 with respect to the SEIR. Sample 13-3D has been excluded due to its anomalously high Na_2O and low CaO values (Table 7.2; Figure 7.10), as discussed in Section 7.5.3. The trends for the off-axis dredge sites, particularly sites 102/DR09 and 102/DR13, are generally fairly ill-defined due to the paucity of geochemical data, and are therefore difficult to interpret. However, they do appear to show a mixture of global and local trends which are not correlated with variations in spreading rate. According to Niu and Batiza (1993), samples from 102/DR09 and 102DR/13, the more northerly dredge sites, would be expected to show the local trends associated with slow spreading. All other samples, except possibly those from zone B with its well-defined ridge axis morphology, would be expected to show the global geochemical trends predicted for spreading rates >60 mm/yr (Niu and Batiza, 1993).

Global MORB trends are evident in Figure 7.11 in terms of the increasing $Fe_{8.0}$ and decreasing $Si_{8.0}/Fe_{8.0}$ which accompanies decreasing $Na_{8.0}$ values within the zone B (AAD) basalts, the opposite to what would be expected if slow spreading magma chamber processes underlie this region. All other zero-age SEIR basalts and samples from sites 102/DR10 and 102/DR11 display local trends on these particular plots, also the opposite to the predictions of Niu and Batiza (1993). The SEIR zero-age rocks generally trend towards increasing $Si_{8.0}$ with decreasing $Na_{8.0}$, another local trend, whereas those from dredge sites 102/DR10 and 102/DR11 display the global trend. Data from dredge 102/DR09 and 102/DR13 samples do not define easily interpretable trends in Figure 7.11.

If the zero-age samples are considered separately, those from zone B (AAD) do appear to differ from both zone A and C basalts in terms their increasing $Fe_{8.0}$ and decreasing $Si_{8.0}/Fe_{8.0}$ with decreasing $Na_{8.0}$, but these are considered to be global trends associated with more rapid seafloor spreading rather than the slower spreading processes predicted by the ridge axis morphology of the AAD.

The results of this study are inconclusive, but they do suggest that the pronounced change in spreading rate along the SEIR at 44.5 Ma cannot be correlated with a systematic change in geochemistry as suggested in the current literature. This may be due to the small data base available here for off-axis Southern Ocean seafloor, or the use of inappropriate algorithms (Figure 7.11 caption) to correct the Southern Ocean data to 8 wt % MgO. The latter is possible due to the fact that the algorithms in the literature are calculated for quite different data sets and any differences between the slopes of the liquid lines of descent

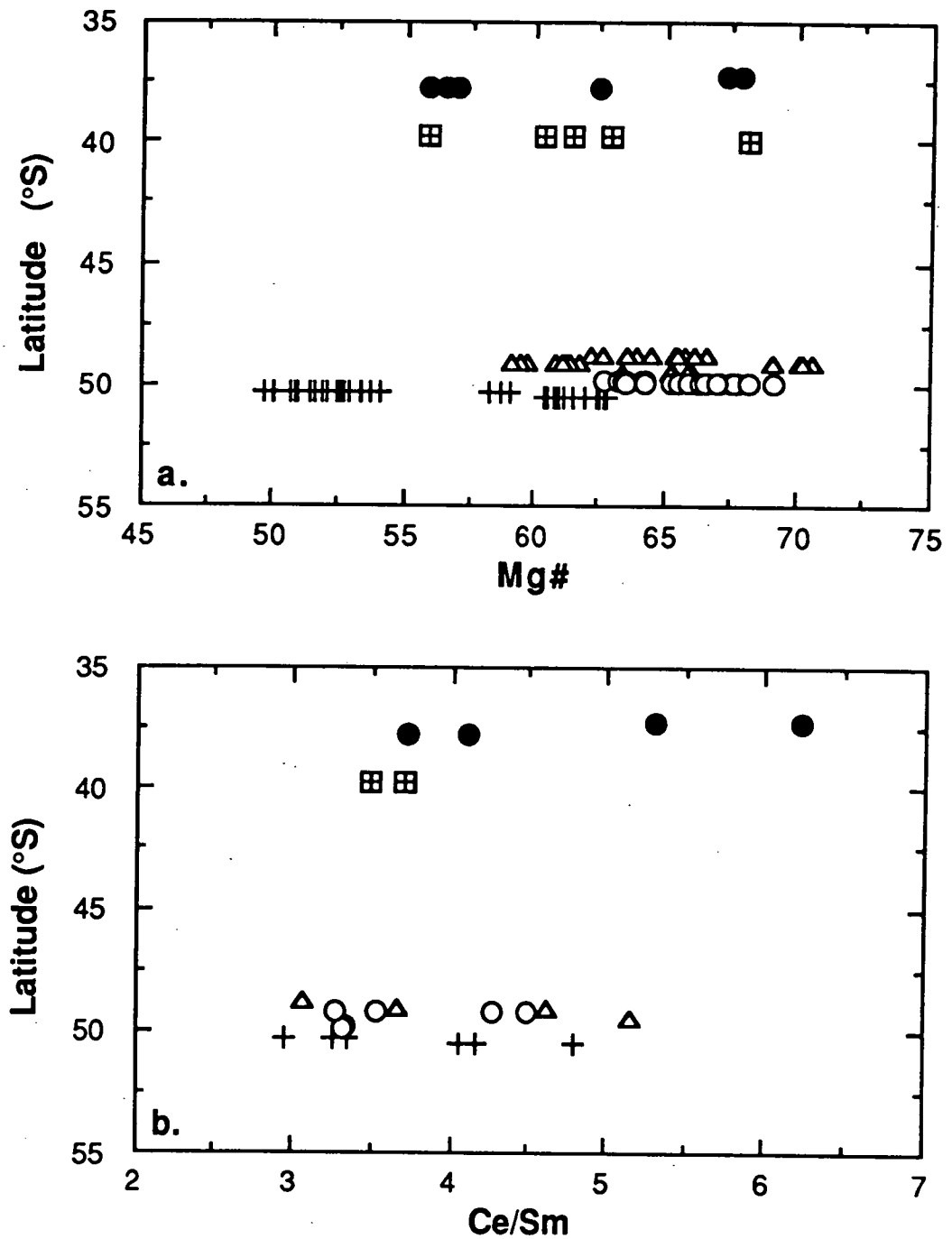

Figure 7.9: Whole-rock a) Mg# and b) Ce/Sm versus latitudinal position for samples from the Southern Ocean dredge sites 102/DR09 and 102/DR13 (filled circles), sites 102/DR10 and 102DR11 (crosses within squares) and zero-age samples from the SEIR: zone A (crosses), zone B (open triangles) and zone C (open circles); only samples with ≥5 wt % MgO are included. SEIR data sources are Anderson et al. (1980) and Klein et al. (1991).

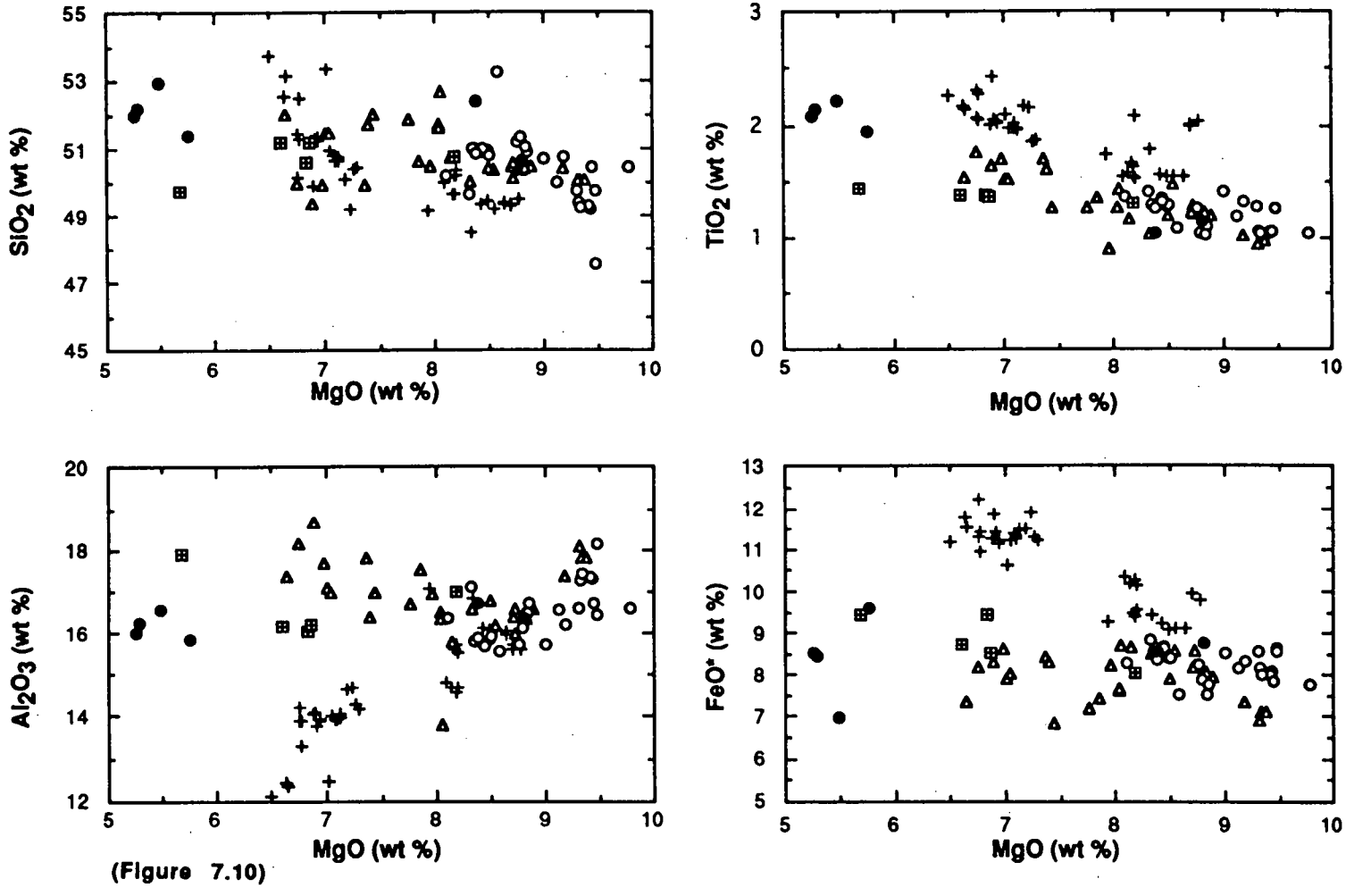

(Figure 7.10)

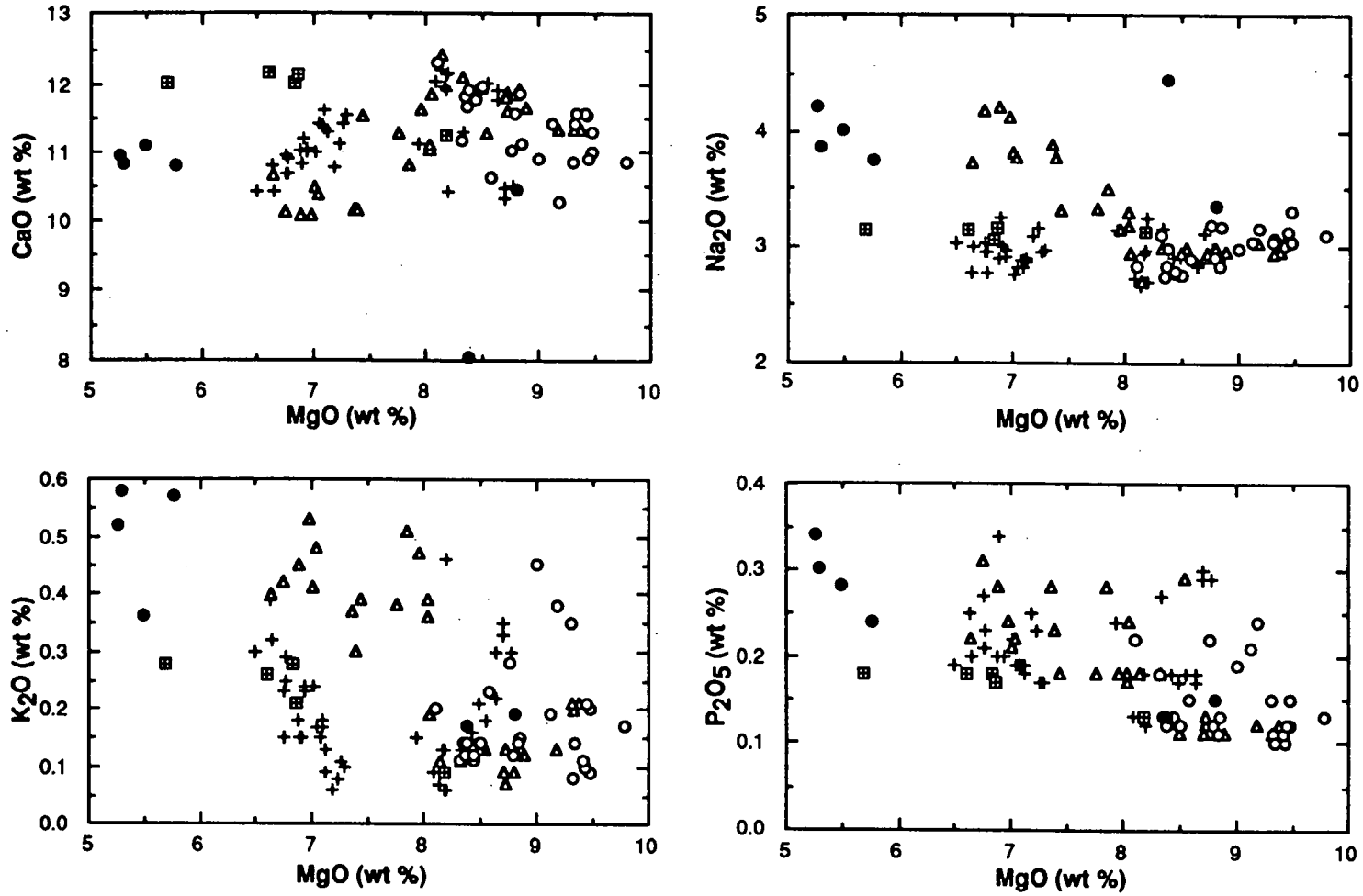

Figure 7.10: Plots of whole-rock MgO (wt %) versus major element oxides for samples from the Southern Ocean dredge sites 102/DR09 and 102/DR13 (filled circles), sites 102/DR10 and 102DR11 (crosses within squares) and zero-age samples from the SEIR: zone A (crosses), zone B (open triangles) and zone C (open circles); only samples with ≥5 wt % MgO are included. SEIR data sources are Anderson et al. (1980) and Klein et al. (1991).

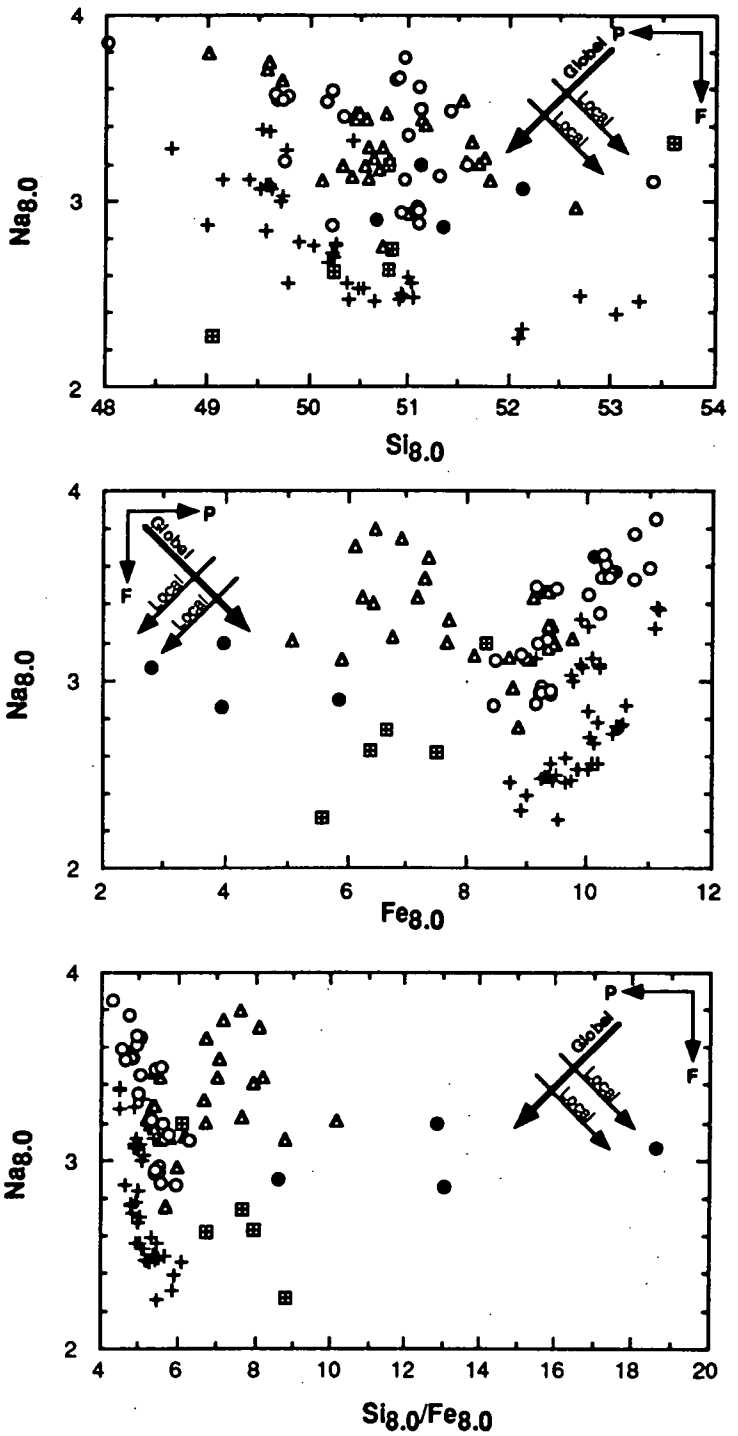

Figure 7.11: Plots of major element oxides and ratios corrected to 8 wt % MgO to compare samples from Southern Ocean dredge sites 102/DR09 and 102/DR13 (filled circles) with sites 102/DR10 and 102DR11 (crosses within squares) and zero-age samples from the SEIR: zone A (crosses), zone B (open triangles) and zone C (open circles); only samples with ≥5 wt % MgO are included. SEIR data sources are Anderson et al. (1980) and Klein et al. (1991). Global and local trend directions are as shown by Klein and Langmuir (1989) and Niu and Batiza (1993) - actual slopes have no significance here. P and F indicate increasing pressures and extents of melting respectively. Na_2O and FeO contents have been normalised to 8 wt % MgO using the algorithms of Klein and Langmuir (1987: Figure 2 caption), while SiO_2 values have been normalised to the same MgO values using the algorithm from Klein and Langmuir (1989: Figure 1 caption) to produce values of $Na_{8.0}$, $Fe_{8.0}$ and $Si_{8.0}$ respectively.

(LLD) used in the algorithms and the LLD slopes of the Southern Ocean data sets may have resulted in the calculation of slightly inaccurate $Si_{8.0}$, $Na_{8.0}$ and $Fe_{8.0}$ values for the Southern Ocean data (Langmuir et al., 1992). This can only be checked, however, once specific algorithms have been calculated for SEIR MORB data.

A third possible explanation for the lack of observed systematic geochemical variations with the change in spreading rate along the SEIR may be due to the fact that although the increase in spreading rate at 44.5 Ma was quite pronounced, from ~20 mm/yr (Veevers et al., 1990) to ≥60 mm/yr (e.g. Royer and Sandwell, 1989; P. Symonds, pers. comm., 1993; Palmer et al., 1993), it only resulted in an intermediate spreading rate rather than a fast spreading rate. If an intermediate spreading rate represents a transitional zone where either slow or fast spreading geochemical correlatives can occur, this may explain the lack of distinction between the Southern Ocean seafloor samples erupted during different spreading regimes.

7.7 CONCLUSIONS:

Although the Southern Ocean seafloor samples examined in this study all display pervasive microscopic alteration effects, their generally low LOI values suggest that their major element compositions can still be used to compare seafloor chemistry at the various dredge sites. Such comparisons have, however, failed to reveal systematic geochemical differences which can be correlated with the pronounced change in spreading rate along the SEIR at 44.5 Ma. Although the well-developed axial morphology of the AAD region of the SEIR appears to be a product of processes associated with slow rather than intermediate spreading rates (Phipps Morgan et al., 1987; Sempéré et al., 1991), it lacks the corresponding major element systematics described in the literature for slow spreading ridges.

These results suggest that the change from slow to intermediate spreading which occurred along the SEIR at 44.5 Ma, and the inferred change in underlying mantle processes, may not have been great enough to result in the significant geochemical variations which have been interpreted by other researchers to correspond with fast versus slow spreading rates along different mid-ocean ridge systems. Alternatively, the off-axis Southern Ocean basalt database may be insufficient to enable the detection of such differences.

CHAPTER 8

RADIOGENIC ISOTOPE SYSTEMATICS OF THE SOUTHERN OCEAN SEAFLOOR NORTH OF THE SOUTHEAST INDIAN RIDGE

8.1 INTRODUCTION:

The Australian-Antarctic Discordance (AAD), zone B of the SEIR, was originally defined as a globally anomalous region of mid-ocean ridge on the basis of its unique morphological and geophysical characteristics (e.g. Weissel and Hayes, 1971; Hayes and Conolly, 1972; Weissel and Hayes, 1972; 1974). However, the eastern AAD was subsequently discovered to represent the current on-axis location of an isotopic boundary between proposed Indian Ocean and Pacific Ocean upper mantle convective regimes (Klein et al., 1988; Pyle et al., 1992). As the recognition of this isotopic boundary has so far been confined to 0 to 4 Ma seafloor, in the immediate vicinity of the SEIR, it is not yet known how long it has existed at its current location in the Southern Ocean. Is it a long term feature intimately associated with the AAD since Australian-Antarctic rifting commenced? Or, does it represent the apex of a progressively westward-migrating Pacific Ocean upper mantle domain, so that its current on-axis position within the AAD is entirely coincidental.

Recent dredging of old (>35 Ma) oceanic crust north of the SEIR, in the Great Australian Bight region of the Southern Ocean, provides an opportunity to investigate one proposal about the longevity of the Indian-Pacific Ocean isotopic boundary, namely that it represents an intimate feature of the AAD which has been in existence since rifting between Australia and Antarctica commenced during the Cretaceous. Comparison of the radiogenic isotope compositions of off-axis Southern Ocean seafloor samples, dredged from either side of the northward extrapolation of the AAD, with literature-derived Pacific and Indian Ocean MORB data and previously analysed 0 to 4 Ma zone A to C SEIR samples is aimed at determining whether or not the proposed Indian-Pacific Ocean isotopic boundary has maintained its present position since at least ~66 Ma.

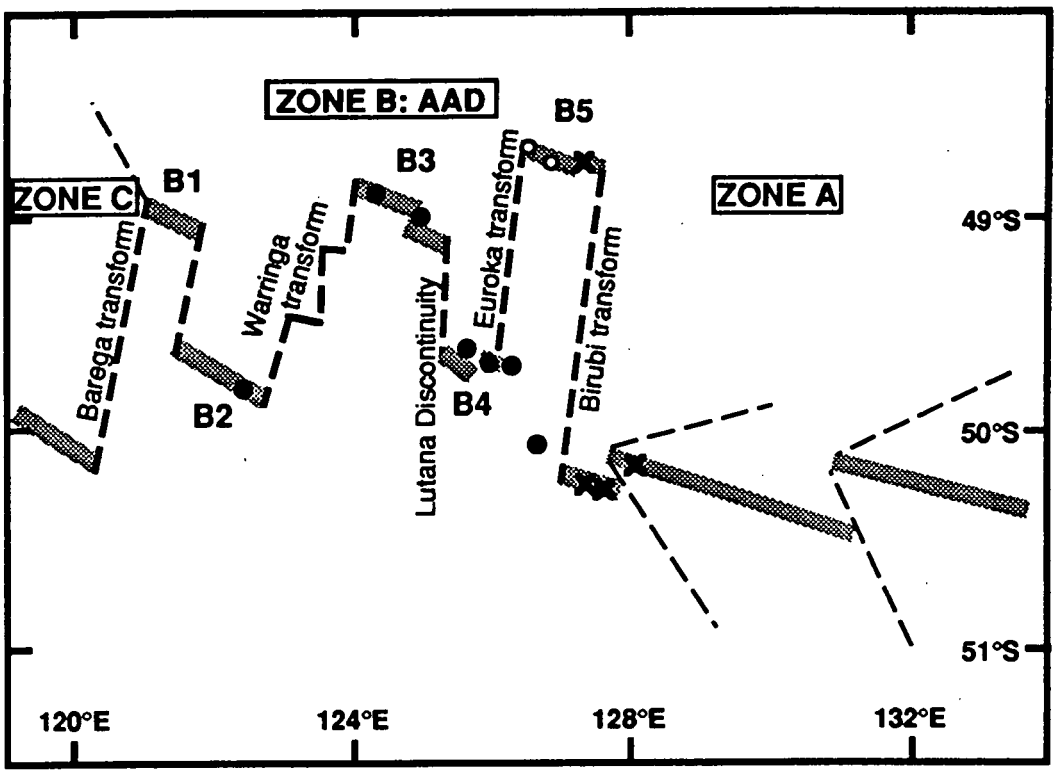

Figure 8.1: Map of the SEIR within, and immediately adjacent to, the AAD (modified from Palmer et al., 1993), showing the major transform faults, the B1 to B5 spreading segments of Vogt et al. (1983) and the location of the *R/V Moana Wave* dredge sites for the samples of Pyle et al. (1992). Dredge site symbols reflect the radiogenic isotope affinities assigned by Pyle et al. (1992): Indian Ocean (filled circles), Pacific Ocean (crosses), transitional (open circles).

8.2 THE AUSTRALIAN-ANTARCTIC DISCORDANCE:

8.2.1 Geophysical and Morphological Features:

The AAD is a highly fractured, seismically active zone of the SEIR (Figure 7.1) with a dominantly north-south physiographic fabric, normal to the ridge system orientation (Hayes and Conolly, 1972). It is characterised by maximum crestal depths (~124°E; Klein et al., 1988) greater than 4000 m (e.g. Weissel and Hayes, 1974), more than 1000 m deeper than the average ~2600 m crestal depth of mature ocean basins ≥75 Ma (Veevers, 1977), and a crenulate geometry. The latter is defined by alternating north and south spreading ridge offsets (Figure 8.1), resulting in five distinct transform-bounded ridge segments (B1 to B5 from west to east) in addition to non-transform discontinuities at 40 to 60 km intervals within the AAD (Vogt et al., 1983; Sempéré et al., 1991; Pyle et al., 1992; Palmer et al., 1993). Ridge flank morphology is extremely rugged compared to the adjacent ridge segments, with high amplitude local topographic relief (~600-1000 m) which becomes more marked in the proximity of the ridge crest (Weissel and Hayes, 1971; Hayes and Conolly, 1972). Other distinguishing features of the AAD include small amplitude magnetic anomalies (Weissel and Hayes, 1972), a negative satellite free-air gravity anomaly (Anderson et al.,1973; Weissel and Hayes, 1974), and a saddle-shaped negative geoid anomaly centred on the ridge axis at

125°E (Marsh et al., 1986). Forsyth et al. (1987) measured significantly faster Rayleigh wave phase velocities in young seafloor (0 -10 Ma) with negative depth anomalies >500 m within the AAD, as compared to normal ocean floor of similar age, and Woodhouse and Dziewonski (1984) found an unusually high seismic wave velocity anomaly at depths of 250 to 350 km beneath this region of the SEIR.

The AAD forms the central and most pronounced area of a 2000 km wide morphotectonic depression (15 x 10^6 km^2) which extends from the southern half of Australia through the Southern Ocean to Wilkes Land, Antarctica (Veevers, 1982) (Figure 8.2a). This depression is up to 1000 m deeper than expected from the empirical age versus depth relationships of other ocean basins (Forsyth et al., 1987). Although this wide regional negative depth anomaly in the Southern Ocean is thought to have existed since at least 30 Ma (Weissel and Hayes, 1974), and probably since rifting of Australia and Antarctica commenced at ~96 Ma (Veevers, 1982), the actual distinctive properties of the AAD are generally confined to crust younger than ~20 Ma (Weissel and Hayes, 1974) to 25 Ma (Vogt et al., 1983).

Hayes (1988) and Marks et al. (1990) have also recognised a large scale residual negative depth anomaly dominating the AAD (Figure 8.2b). This depth anomaly represents a departure of the observed bathymetric depth from that predicted by the depth-age relationship considered necessary to maintain isostatic equilibrium. According to Marks et al. (1990), the depth anomaly is arcuate in shape and roughly symmetrical about the SEIR, trending north-northeast across the Indian-Australian Plate and south-southeast across the Antarctic Plate. It has two prominent lows associated with 15 Ma oceanic crust on either side of the AAD (north flank - 45°S 128°E; south flank - 54°S 125°E), and extends for 1200 to 1700 km east-west and 2500 to 3000 km north-south. Contours of anomalous depth are roughly perpendicular to the ridge axis orientation (Forsyth et al., 1987). Both the trend of the depth anomaly and the prominent 15 Ma lows cross the major transform fault which marks the eastern boundary of the AAD, and are therefore oblique to the spreading direction (Marks et al., 1990). The prominent symmetrical lows at 15 Ma indicate that although the source has varied in strength, it has remained positioned at the ridge axis as the ridge migrated northeastward, whereas the arcuate shape of the depth anomaly suggests a westward migration (~15 mm/yr) of the source along the ridge axis over the last 15 m.y., which may now have ceased.

The actual position of the plate boundaries within the AAD is difficult to ascertain (Weissel and Hayes, 1971) due to the absence of a persistent pattern of magnetic anomalies younger than ~10 Ma (A5) within 350 to 400 km of the ridge crest (Weissel and Hayes, 1972). The position of the ridge axis can however be inferred from an east-west trending band of epicentres between 49°S and 51°S which ends abruptly at the eastern boundary of the AAD (128°E) (Hayes and Conolly, 1972). The diffuse nature of this band of seismic activity is probably indicative of the displacement of short lengths of ridge crest along several small offset transform faults (Weissel and Hayes, 1974). Fingers of the South Indian and

South Australian abyssal plains extend for hundreds of kilometres into the AAD (Hayes and Conolly, 1972). Seismic reflection profiles indicate that the sedimentary cover within the vicinity of the AAD is generally <1000 m thick as compared to the 2000 to 5000 m of sediment in the surrounding regions (Marks et al., 1990).

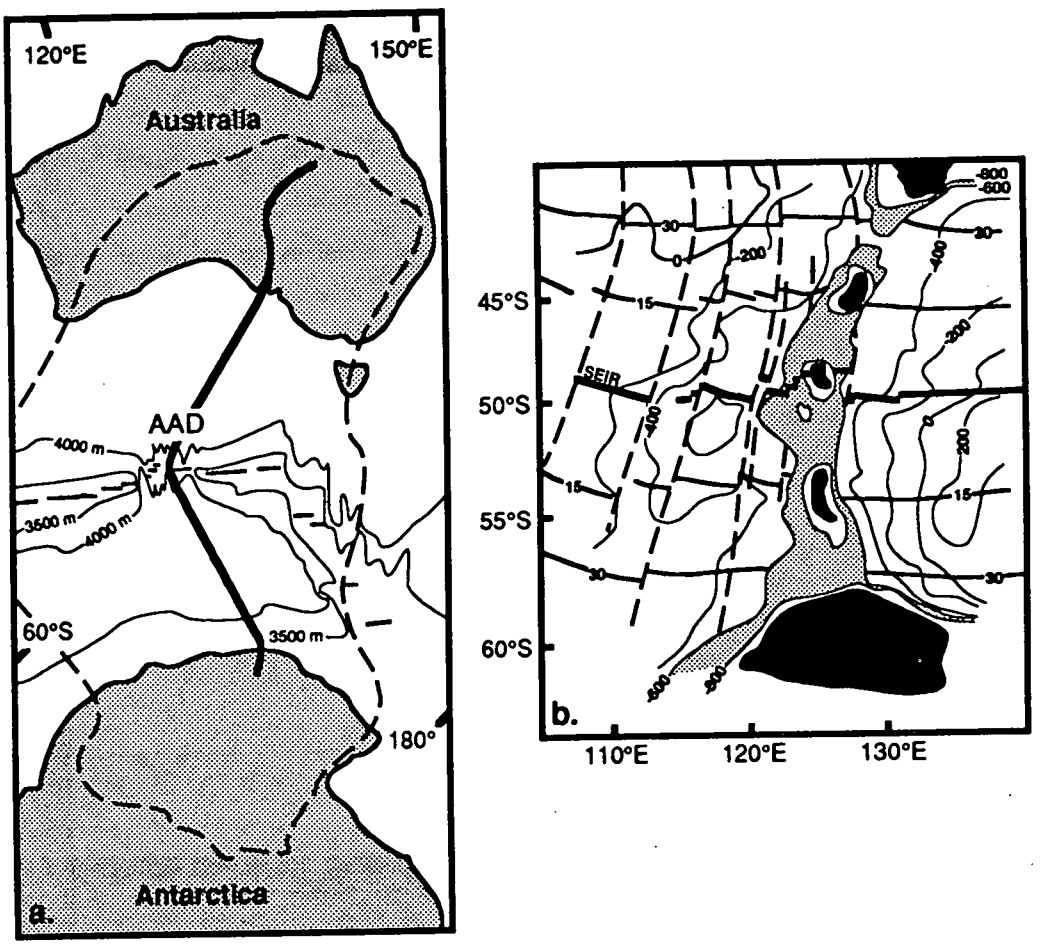

Figure 8.2: Maps of a) the Australian-Antarctic morphotectonic depression of Veevers (1982) - the dashed line depicts the extent of the depression whereas the heavy solid line represents the median morphological axis of the depression; and b) the residual negative depth anomaly of Marks et al. (1990) - solid lines represent depth anomaly contours at 200 m intervals, thin solid lines are key isochrons (Ma), dashed lines are transform faults, and the ridge axis (SEIR) is marked by a thick line.

Weissel and Hayes (1971) describe the ridge within zone A, east of the AAD (138°E to 128°E), as being almost aseismic, owing to a lack of major transform faults, with a morphologically distinct crestal zone, relatively low local topographic relief (~100-200 m), large amplitude magnetic anomalies, and easily recognizable magnetic lineation anomalies both north and south of the spreading ridge. West of the AAD (120°E to 105°E), zone C of Weissel and Hayes (1971), the ridge is once again well developed with local relief similar to that of zone A (generally <200-300 m), less seismic activity than the AAD, normal magnetic anomaly amplitudes, and relatively well defined magnetic anomaly lineations on both ridge flanks. In contrast to the morphological descriptions of Weissel and Hayes (1971), Palmer et

al. (1993) describe zone A as defining an axial high, whereas the ridge crest within zone B (AAD) has a wide deep rift valley more typical of slow spreading centres.

A period of continuous asymmetric spreading in zone A took place between 38 Ma (A13) and 10 Ma. This produced 30 % more oceanic crust on the northern ridge flank of zone A at a time when zones B and C were experiencing symmetrical extension. This differential spreading may explain the ~175 km ridge crest offset of the zone A-B boundary (Weissel and Hayes, 1971; Weissel and Hayes, 1972). Zone B (AAD) may also have experienced asymmetric seafloor spreading from ~10 ma to the present time (Hayes, 1976). Observed zonal differences in magnetic lineation patterns, magnetic anomaly amplitudes, morphology and seismicity may result from changes in the mechanics of crustal accretion along the accreting plate boundary and/or later second order deformation within the plate which has altered the thermal remanent magnetization and caused fracturing of the ridge flanks (Weissel and Hayes, 1971). Weissel and Hayes (1974) also observed that the southern flank of the SEIR between 105°E and 160°E is at least 100 m shallower than the northern flank of comparable age crust for ~900 km on either side of the ridge axis. They consider phenomena such as episodes of asymmetric seafloor spreading and north-south ridge flank depth differences to reflect large differences in physical properties across the accreting plate boundary.

8.2.2 Radiogenic Isotope Characteristics:

Radiogenic isotope studies of zero-age basaltic glasses collected from 11 *R/V Vema* dredge sites along the SEIR (Figure 7.1), within and adjacent to the AAD, indicate an abrupt westward decrease in $^{206}Pb/^{204}Pb$ and $^{208}Pb/^{204}Pb$, an increase in $^{87}Sr/^{86}Sr$, and systematically lower $^{207}Pb/^{204}Pb$ and $^{143}Nd/^{144}Nd$ values west of ~127°E (Figure 8.3) (Klein et al., 1988). These SEIR samples therefore comprise two distinct non-overlapping isotopic groups which correspond to longitudinal location along the ridge axis. The western group samples of Klein et al. (1988) show strong affinities with Indian Ocean MORB (Table 8.1; Figure 8.3). As well as extending to lower $^{206}Pb/^{204}Pb$ values than other MORB, Indian Ocean MORB are characterised by higher $^{87}Sr/^{86}Sr$, lower $^{143}Nd/^{144}Nd$, and higher $^{208}Pb/^{204}Pb$ and $^{207}Pb/^{204}Pb$ at a given $^{206}Pb/^{204}Pb$ value than Pacific and North Atlantic Ocean MORB (e.g. Hedge et al., 1973; Subbarao and Hedge, 1973; Hedge et al., 1979; Dupré and Allègre, 1983; Hart, 1984; Hamelin and Allègre, 1985; Hamelin et al., 1986; Michard et al., 1986; Price et al., 1986; Ito et al., 1987; Dosso et al., 1988; Klein et al., 1988; Mahoney et al., 1989; Storey et al., 1989; Mahoney et al., 1992). The eastern group of Klein et al. (1988), comprising all samples collected east of and including the dredge site (5) at ~127°E in the easternmost AAD, show isotopic affinities with Pacific Ocean MORB (Table 8.1; Figure 8.3). The distinct isotopic compositions of the eastern and western group samples were used to infer the presence of an abrupt boundary between Indian Ocean and Pacific Ocean isotope provinces within a 200 km long zone of ridge crest between ~127°E and 124°E (Klein et al., 1988).

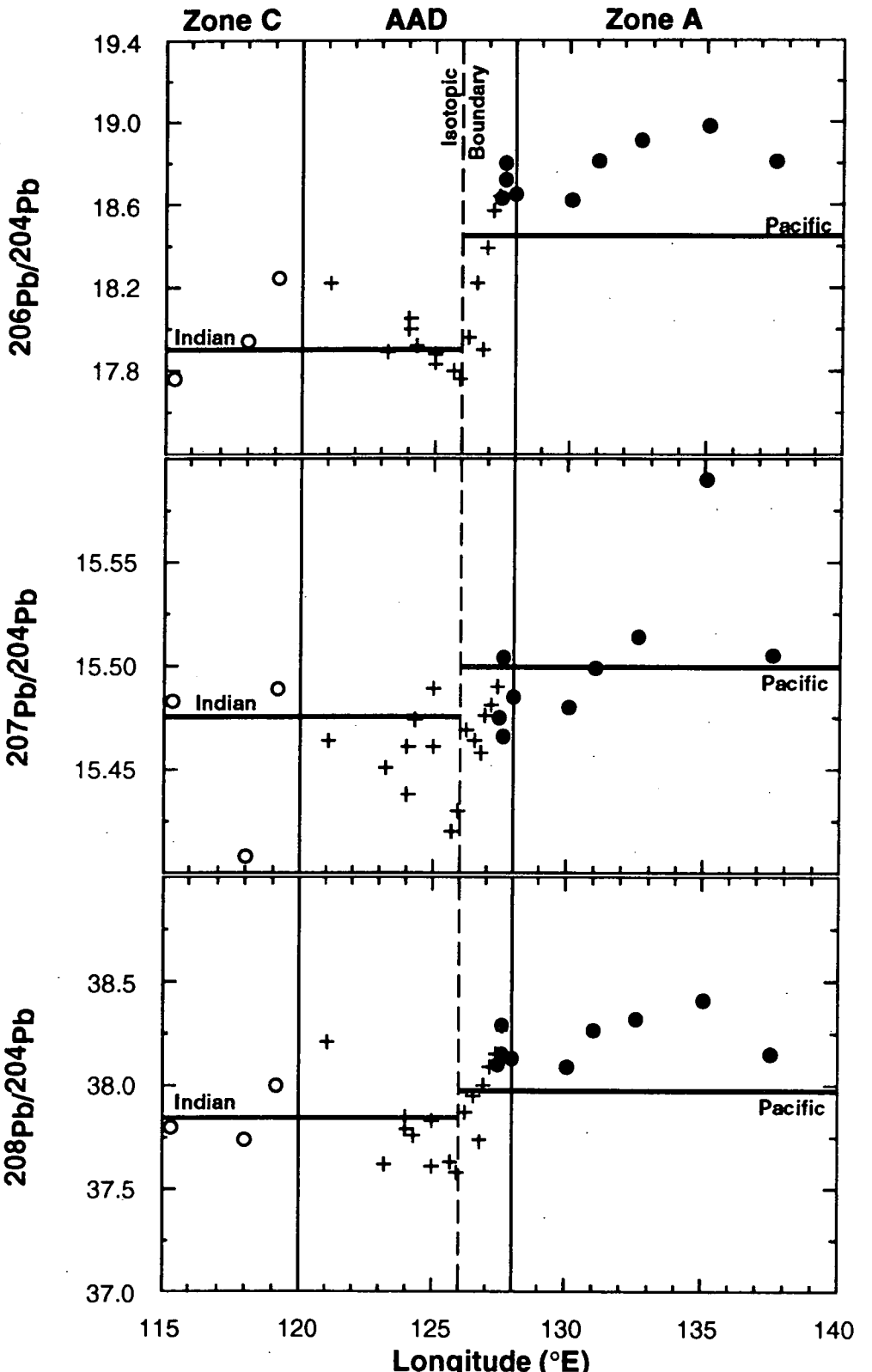
Zone C
AAD
Zone A
Isotopic Boundary
206Pb/204Pb
19.4
19.0
18.6
18.2
17.8
Indian
Pacific
207Pb/204Pb
15.55
15.50
15.45
Indian
Pacific
208Pb/204Pb
38.5
38.0
37.5
37.0
Indian
Pacific
115
120
125
130
135
140
Longitude (°E)

(Figure 8.3)

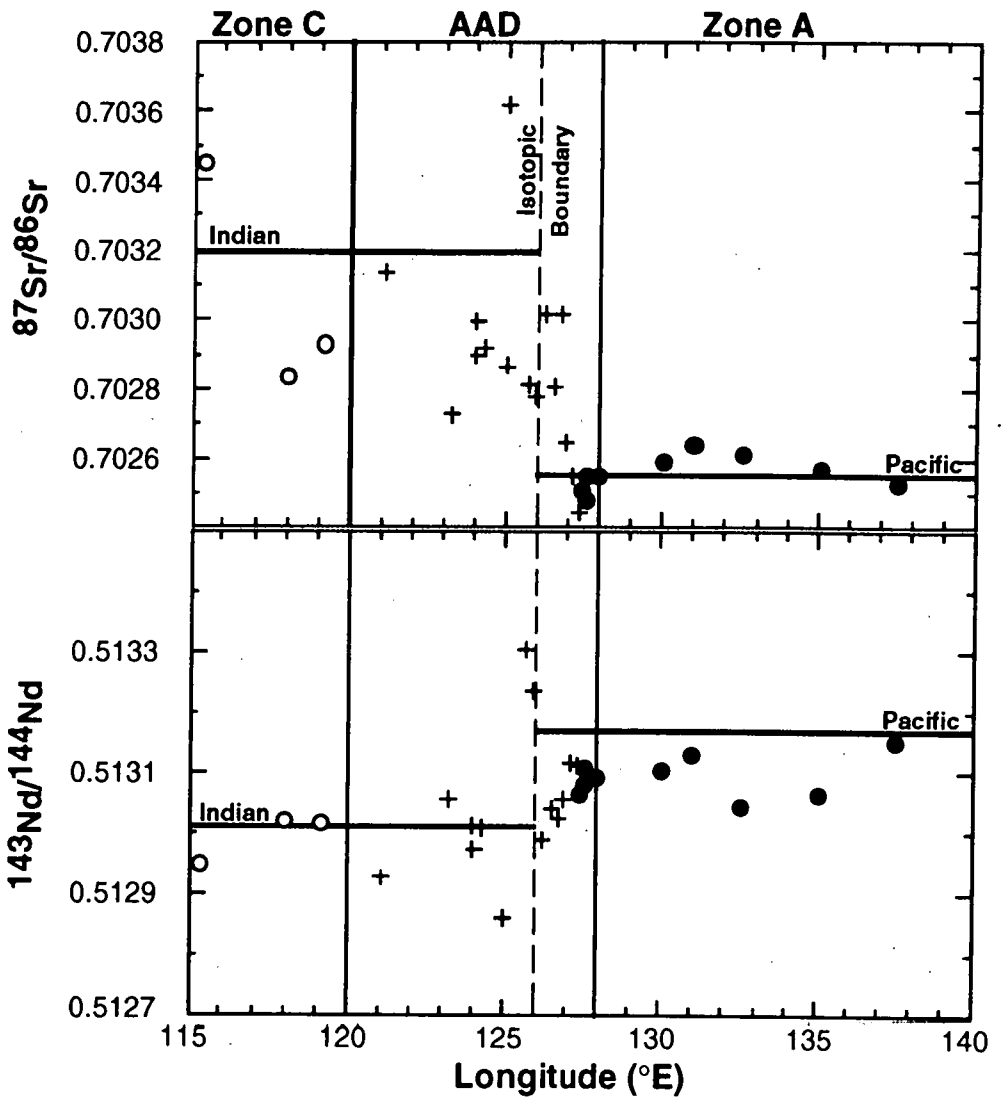

Figure 8.3: Plots of the radiogenic isotope data of Klein et al. (1988) and Pyle et al. (1992) versus longitudinal position along the SEIR: zone A (filled circles), zone B or AAD (crosses) and zone C (open circles). SEIR $^{87}Sr/^{86}Sr$ data are normalised to $^{86}Sr/^{88}Sr = 0.1194$, and are quoted relative to a value of to $^{87}Sr/^{86}Sr = 0.7080$ for the Eimer and Amend $SrCO_3$ standard; SEIR $^{143}Nd/^{144}Nd$ data are normalised to $^{146}Nd/^{144}Nd = 0.7219$, and are quoted relative to a value of $^{143}Nd/^{144}Nd = 0.51265$ for the BCR-1 international rock standard. Thick horizontal lines depict the average values for Indian and Pacific Ocean MORB samples as presented in Table 8.1.

Table 8.1: Radiogenic isotope ratio data for Indian and Pacific Ocean MORB, compiled from the following data sources: Cohen et al. (1980), Sun (1980), Cohen and O'Nions (1982), White and Hofmann (1982), Dupré and Allègre (1983), Hamelin et al. (1984), Hamelin and Allègre (1985), Hamelin et al. (1986), Macdougall and Lugmair (1986), Michard et al. (1986), Price et al. (1986), Ito et al. (1987), White et al. (1987), Dosso et al. (1988), Mahoney et al. (1989) and Mahoney et al. (1992). Indian and Pacific Ocean MORB data used here were selected in an attempt to avoid, where possible, anomalous isotopic ratios and/or the recognised and documented influence of near ridge hotspots. Data are presented as ranges underlain by the mean value ± 1σ error; numbers in parentheses indicate the number of analyses used (n) to calculate both the ratio ranges and the mean values. All MORB $^{87}Sr/^{86}Sr$ and $^{143}Nd/^{144}Nd$ data are normalised as for Figure 1.1.

	Indian Ocean MORB	Pacific Ocean MORB
$^{87}Sr/^{86}Sr$	0.70253-0.70531 (100) 0.70320±61	0.70223-0.70313 (94) 0.70255±15
$^{143}Nd/^{144}Nd$	0.51238-0.51323 (95) 0.51301±17	0.51302-0.51330 (86) 0.51317±5
$^{206}Pb/^{204}Pb$	16.867-18.839 (103) 17.903±393	17.721-19.240 (77) 18.468±253
$^{207}Pb/^{204}Pb$	15.370-15.604 (103) 15.474±43	15.309-15.573 (77) 15.498±45
$^{208}Pb/^{204}Pb$	37.084-39.077 (103) 37.844±402	37.029-38.855 (77) 37.966±345

Consistent with the Sr, Nd and Pb isotope data of Klein et al. (1988), $^{3}He/^{4}He$ measurements performed on the same zero-age basalts indicate a He isotope discontinuity between the eastern and western group samples (Graham et al., 1990). Western group MORB, with Indian Ocean Sr, Nd and Pb isotopic affinities, have lower and more variable $^{3}He/^{4}He$ ratios (6.3-7.3 R_A) compared to the eastern Pacific Ocean-like MORB samples with a narrower range of higher $^{3}He/^{4}He$ values (7.3-7.6 R_A).

More recent Sr, Nd and Pb isotope analyses of zero-age MORB from this region of the SEIR (Pyle et al., 1992) (Figure 8.3) have enabled the Pacific-Indian Ocean isotope transition to be constrained to the B5 spreading segment (the easternmost of the five spreading segments of Vogt et al. (1983): Figure 8.1) between a non-transform discontinuity near 127°E and the 110 km long B4/B5 transform ~40 km to the west. Such a sharp boundary between two such distinct upper mantle isotopic domains is unknown elsewhere along the global mid-ocean ridge system. Ridge axis lavas west of the B4/B5 transform have an Indian Ocean isotope signature, whereas those immediately to the east have a transitional Pacific-Indian Ocean MORB signature (Figure 8.3). The isotopic boundary therefore appears to be located close to the B4/B5 transform at ~126°E within the eastern section of the AAD. Pyle et al. (1992) also discovered that 3-4 Ma seafloor south of the eastern B5 spreading centre has Indian MORB Sr, Nd and Pb isotope ratios, in contrast to the Pacific Ocean MORB isotope characteristics of the eastern B5 axial lavas. They therefore concluded that the isotopic boundary has migrated ~100 km westward during the last 3 to 4 m.y., implying a sub-Pacific Ocean mantle migration rate of ~25 mm/yr. Although this inferred migration rate is ~10 mm/yr faster than the proposed depth anomaly migration rate (Marks et al.,1990), Pyle et al.

(1992) state that if continuous mantle migration has occurred, the existing data allow for rates of between 10 and 40 mm/yr.

8.2.3 Models Proposed for the Origin of the AAD:

The following models, invoked to explain the existence and characteristic features of the AAD, are not necessarily mutually exclusive:

8.2.3.1 Downward Convective Mantle Flow Models:

Proposed hotspots, such as Iceland and the Hawaiian Islands, are associated with regional bathymetric and gravity highs, symptomatic of rising currents within the mantle (Morgan, 1971). Therefore, it has been suggested that regional topographic lows, such as the AAD, could be associated with colder areas of the upper mantle resulting from downward convective flow within the asthenosphere (Hayes and Conolly, 1972; Menard, 1973; Weissel and Hayes, 1974). This downwelling would cause a gradual deepening of the lithospheric isotherms, reaching maximum depths under the AAD and resulting in greater lithospheric thicknesses. Several of the observed geophysical and geochemical features of the AAD have been interpreted as the products of cool asthenosphere beneath this region.

Anderson et al. (1973) infer a positive correlation between free air gravity anomalies and crestal depths within the mid-ocean ridge system, whereby a positive gravity anomaly is indicative of an ascending convective limb. The coexistence of a negative satellite free air gravity anomaly and an extensive morphotectonic depression, centred on the AAD, may therefore suggest that this region is underlain by downward convecting asthenosphere (Veevers, 1982). Unusually fast Rayleigh wave phase velocities in the 0-10 Ma AAD oceanic crust are indicative of high shear wave velocities in at least the upper 30 km, and possibly the upper 150-200 km of mantle beneath this region, consistent with the presence of cooler, more rigid materials (Forsyth et al., 1987). The seismic nature of the discordance zone (e.g. Hayes and Conolly, 1972) is also consistent with underlying relatively cool asthenosphere, as ridge morphology capable of supporting earthquakes is considered to be a product of low magmatic heat input (Phipps Morgan et al., 1987). The correspondence of gravity/geoid and depth anomaly lows associated with the AAD (Marks et al., 1990) and the high calculated geoid/topography ratios for this region are consistent with downwelling mantle convection beneath young lithosphere, and imply an upper mantle temperature ~170° C less than normal (Marks et al., 1991).

Klein and Langmuir (1991) observed correlations between axial depth within the AAD and geochemical parameters which are interpreted, according to the global component of MORB chemical variability (Klein and Langmuir, 1989), to reflect the smallest degree of melting at the lowest mean pressure of melting. These observations, implying that the depth of solidus intersection is shallower beneath the AAD than beneath adjacent warmer sections of mid-ocean ridge, suggest the presence of colder subsolidus mantle beneath the AAD

(Klein et al., 1991) which would therefore intersect the solidus at lower pressure during adiabatic upwelling and melt less on ascent (Klein et al., 1988). Anderson et al. (1980) attributed the Fe-Ti enrichment of zone A lavas to extensive shallow fractionation of plagioclase, clinopyroxene and olivine at unusually low crystallisation temperatures, possibly due to their close proximity to a region of downwelling asthenosphere.

One model which incorporates the idea of downward convective flow, the fixed coldspot model, proposes that the AAD is underlain by a roughly equidimensional (in planform) heatsink or 'coldspot' composed of downwelling convective currents that are cooler than the surrounding upper mantle material and remain fixed in the mantle reference frame (Hayes, 1976). If asymmetric spreading is currently occurring within the AAD, it may be due to this stationary heatsink producing asymmetric temperature contrasts within the lithosphere and upper asthenosphere (Hayes, 1976). Downwelling currents may also inhibit the normal convective transfer of upper mantle material to the ridge, thereby resulting in the observed depletion (~500 km^2/unit length) of igneous material supplied to this region of mid-ocean ridge over the past 10 m.y. (Hayes and Conolly, 1972). However, if there is a fixed mantle coldspot currently positioned at the ridge axis, northeast migration of the SEIR during the past ~45 m.y. (Sclater et al., 1981) would have produced an oblique northeast trend to the residual depth anomaly on the Indian-Australian Plate parallel to the spreading direction rather than the observed trend which crosses the major fracture zones and is therefore oblique to spreading direction (Marks et al., 1990). As the Antarctic Plate has remained virtually stationary since the Cretaceous (Minster and Jordan, 1978; Gordon and Jurdy, 1986), a fixed coldspot could also not have produced the observed depth anomaly on the Antarctic Plate (Marks et al., 1990).

A second downward convective flow model proposes that the AAD is located above the site of convergence of adjoining upper mantle convection cells which are elongated parallel to spreading direction and downwell beneath this region (Hayes, 1988). This idea is in accordance with the results of numerical and laboratory studies (e.g. McKenzie et al., 1973; Richter and Parsons, 1975; Buck, 1985) which can be used to predict the association of negative gravity and depth anomalies, like those associated with the AAD, with areas of downwelling mantle currents. However, the observed pattern of the residual depth anomaly (Marks et al., 1990) is inconsistent with the proposal of Richter and Parsons (1975) that small-scale upper mantle convection involves a series of elongate convection cells which produce a regular pattern of highs and lows (corresponding to the upwelling and downwelling limbs of convection cells) oriented in the direction of absolute plate motion. In addition, the fact that the Antarctic Plate has remained almost stationary (only a small amount of east-northeast movement), since Australian-Antarctic rifting commenced, implies that any longitudinal convective rolls resulting from the shear produced by overlying plate movement would only occur on the north flank of the AAD (Marks et al., 1990).

The 'direct convergence' pattern suggested by Klein et al. (1988) is also related to the idea of convergence and downwelling of adjoining mantle convection cells beneath the

AAD, although it does not attempt to predict the scale of deep mantle convection involved. Klein et al. (1988) suggest that the AAD may be continually supplied with Pacific Ocean mantle by an eastern convective domain and Indian Ocean mantle by a western convective domain. The isotopic boundary may therefore coincide with the position along the ridge axis where the limbs of these two convective regimes converge and descend into the mantle. This model of mantle flow implies the coexistence of deep convective mantle downwelling with the shallow upwelling and melting associated with seafloor spreading beneath the same region of mid-ocean ridge. As the latter is generally assumed to be a passive process, it may be largely unrelated to the larger mantle convection pattern, apart from sampling whatever mantle is overlain by the ridge axis at that time (Klein et al., 1988).

8.2.3.2 Thin Oceanic Crust Model:

Forsyth et al. (1987) suggest that the AAD is underlain by a region of anomalously cool asthenosphere resulting from either the flow of viscous, cool or depleted mantle south from beneath Australia into the AAD and subsequent mixing with normal mantle supplied from along-ridge axial flow, or the presence of asthenosphere depleted in volatiles and lower-melting temperature components. The presence of cool mantle and the subsequent decrease in magma supply to a ridge axis with a constant spreading rate may have resulted in the production of anomalously thick, brittle lithosphere and thin oceanic crust (possibly as thin as 2000 to 3000 m) within the AAD, the latter being isostatically compensated at a greater water depth than the surrounding areas of thicker crust (Forsyth et al., 1987; Palmer et al., 1993).

Although the major element trends (Anderson et al., 1980; Christie et al., 1988; Klein et al., 1991), high shear wave velocities in the upper 150-200 km of mantle below the AAD (Forsyth et al., 1987), and certain morphological characteristics of the AAD, such as its well-developed axial rift valley and highly segmented nature (Sempéré et al., 1991; Palmer et al., 1993) are consistent with the idea of cool asthenosphere, reduced mantle upwelling, and possible thin crust in this region, neither the residual depth anomaly trend nor the available seismic refraction data are in agreement with this idea. If the characteristics of the AAD were simply associated with thinner than normal oceanic crust, and did not involve source migration or strength variability with time, the depth anomaly would be expected to trend at right angles to the ridge, parallel to the spreading direction, with no change in amplitude or orientation with distance from the ridge (Marks et al., 1990). The results of limited seismic refraction experiments along A6 north of the SEIR, indicate that oceanic crustal thicknesses in this region range from ~6 km beneath the maximum depth anomaly to ~9.5-10.5 km further east (Diebold et al., 1977), consistent with or greater than the usual 6 km thickness suggested by Turcotte and Schubert (1982). Geoid/topography ratios calculated for the AAD region are also significantly larger than expected for a depth anomaly resulting from decreased magma supply to the mid-ocean ridge and the production of anomalously thin oceanic crust (Marks et al., 1991).

8.2.3.3 Channelled Asthenospheric Flow Model:

Vogt and Johnson (1973) propose a model of hotspot convergence, whereby subaxial asthenospheric flow, driven by the outpourings of mantle hotspots east and west of the AAD, may converge beneath the AAD and either downwell or mix with cooler upwelling material. The cool source may be either depleted residual mantle which has separated from a down-going circum-Pacific slab and ascended to its present location (Marks et al., 1990), or downwelling currents in the upper mantle (e.g. Hayes and Conolly, 1972; Weissel and Hayes, 1974). The hotspots responsible may include the Amsterdam hotspot to the west and the Tasmantid and Balleny hotspots to the east of the AAD (Vogt and Johnson, 1973). Marks et al. (1990) also suggest involvement of the Indian Ocean Kerguelen hotspot and the 'George V Complex hotspot' south of eastern Australia. The additional output and closer proximity of the eastern plumes, particularly the 'George V Complex hotspot', may result in a higher pressure gradient and therefore a greater driving force from the east than from the more distant hotspots to the west. This could explain the proposed westward migration of the source of the negative depth anomaly, a possible collision zone between east and west asthenospheric flow along the SEIR over at least the last 15 m.y. .

Rifts, driven by sublithospheric flow beneath the ridge axis (Hey and Vogt, 1977), are observed propagating down regional topographic gradients away from shallow seafloor associated with hotspots on the Juan de Fuca Ridge (Johnson et al., 1983) and forming borders for the Easter microplate (Hey et al., 1985). The presence of four propagating rifts approaching the AAD from the east and west down regional topographic gradients towards the deep discordance zone has been cited as support for the channelled asthenospheric flow model (Vogt et al., 1983; Phipps Morgan et al., 1988).

Magnetic anomaly amplitude data indicate that the high amplitudes east of the AAD terminate abruptly against the large offset transform fault which forms the eastern AAD (Marks et al., 1990). As a number of hotspot-dominated spreading axes exhibit unusually high magnetic anomaly amplitude zones, it has been suggested that hotspot flow blocked by a transform fault (thicker lithosphere) would show a similar sharp termination of amplitudes against the fracture zone. High amplitude magnetic anomalies, such as those of zone A east of the AAD, are also frequently located behind propagating rifts (e.g. Marks et al., 1990). Vogt and Johnson (1973) suggest that the complex stresses exerted on the axial lithosphere by the converging flows may give rise to the seismicity, asymmetric spreading and rough bathymetry associated with the AAD. Kuo (1993) also supports a model of converging asthenospheric 'pipe flow' from mantle plumes both east and west of the AAD in order to explain the faster shear wave velocities and a predicted negative temperature anomaly of 80 to 250° C beneath this region.

Although Klein et al. (1988) state that analyses of zero-age rocks east of the AAD indicate that they are all N-MORB, unenriched by hotspot outpourings, a re-examination of the data (Chapter 7) suggests that the SEIR may be erupting some basalts with slightly more enriched (T-MORB) compositions, particularly evident in sample D1-2 (Klein et al., 1991)

from zone A. Although this appears to be consistent with the expectations of the channelled asthenospheric flow model, Pyle et al. (1992) tend to dismiss the model on the basis that the proposed hotspots involved lie up to ~3000 km away from the AAD and would therefore be too distant to have any significant effect.

8.2.3.4 Pacific Basin Shrinkage Model:

This model invokes an influx of Pacific upper mantle into the region south of Australia due to shrinkage, at a current rate of ~0.45 km^2/yr (Garfunkel, 1975), of the Pacific Ocean basin (Alvarez, 1982; 1990). Klein et al. (1988) note that the current Indian Ocean is surrounded by continents which once formed Gondwana. They suggest that upper mantle convection beneath Gondwana may have been decoupled from larger global convection patterns during the Palaeozoic, resulting in the formation of a distinct upper mantle reservoir whose isotopic signature reflects relatively localised events, such as contamination by delamination/subduction and/or input from mantle plumes (e.g. the Kerguelen Plume), during that time. Australian-Antarctic rifting may eventually have formed a corridor, as a result of separation of the South Tasman Rise from the Antarctic continent at ~36 (A13) to 43 (A18) Ma (Royer and Sandwell, 1989) which enabled communication between the Pacific and Indian Ocean upper mantles.

Alvarez (1982; 1990) proposes that upper mantle convection beneath the Pacific Ocean is bounded by a ring of deep sub-continental lithospheric roots, viscously coupled with the tops of lower mantle convection cells. According to this 'continental undertow' hypothesis, only three gaps (the Caribbean Sea, the Drake Passage and the Southern Ocean between Australia and Antarctica) allow upper mantle outflow from the shrinking Pacific basin. This region of Southern Ocean may therefore represent the site of convergence of upper mantle return flow from subduction zones in the Pacific basin and a source area located at the Java-Sumatra trench as the Australian and Antarctic continents are towed apart by diverging lower mantle convection cells. The AAD may represent a zone of low pressure towards which circum-Australia upper mantle flow is moving (Alvarez, 1990). This model incorporates a similar along-axis flow theme to the channelled asthenospheric flow model of Vogt and Johnson (1973), although the source of flow is different in each case.

8.2.4 Possible Relationships Between the AAD and the Proposed Indian-Pacific Ocean Isotopic Boundary:

Although the long-term relationship between the proposed isotopic boundary and the AAD region of the SEIR is not yet understood, the longevity of the Indian-Pacific Ocean upper mantle boundary at its current position beneath the AAD must be a product of the mantle flow dynamics of this region. Pyle et al. (1992) suggest that there are two categories of mantle flow to be considered here - active versus passive flow. They classify passive flow

as that which is occurring in the presence of cooler underlying asthenosphere whereas active flow is due to forces external to the AAD.

Passive mantle flow (Pyle et al., 1992), represented by the fixed mantle coldspot (Hayes, 1976) and thin oceanic crust (Forsyth et al., 1987) models, implies a long-term relationship between the mantle dynamics responsible for the morphological and geophysical features of the AAD and the proposed Indian-Pacific Ocean isotopic boundary. Ideas involving passive flow may account for the long-lived features of the AAD, but they fail to explain the observed westward migration of both the residual negative depth anomaly (Marks et al., 1990) and the isotopic boundary (Pyle et al., 1992). Although the latter may represent a localised perturbation of a long-standing isotopic boundary in this region, Pyle et al. (1992) observed no transition zone between Indian and Pacific mantle west of the B4/B5 transform as would be expected with an oscillating contact. Transitional isotopic signatures in basalts dredged from the ridge immediately east of the B4/B5 transform may therefore reflect a certain amount of residual Indian Ocean upper mantle mixing with the westward migrating front of Pacific Ocean upper mantle.

According to the flow classifications of Pyle et al. (1992) active mantle flow would be represented by the direct convergence (Klein et al., 1988), channelled asthenospheric flow (Vogt and Johnson, 1973; Marks et al., 1990) and Pacific basin shrinkage (Alvarez, 1982; 1990) models, all of which propose relatively cold upper mantle beneath the AAD as a result of converging horizontal flow regimes. In each case, active flow could account for the progressive westward migration of the residual negative depth anomaly (Marks et al., 1990) and the isotopic boundary (Pyle et al., 1992). However, other more long-lived features of the AAD, including the morphotectonic depression extending between Australia and Antarctica (Veevers, 1982) and many of the geophysical and morphological characteristics of up to 25 Ma crust both north and south of the AAD (e.g. Vogt et al., 1983) must have been in existence prior to the recent (within the last 4 m.y. according to Pyle et al., 1992) arrival of the isotopic boundary beneath the AAD. This therefore implies that the current location of the isotopic boundary beneath such an anomalous region of mid-ocean ridge may be entirely coincidental.

8.3 SOUTHERN OCEAN SEAFLOOR RADIOGENIC ISOTOPE CHEMISTRY:

8.3.1 Radiogenic Isotope Data:

Radiogenic (Sr, Nd and Pb) isotope data for the Southern Ocean seafloor samples described in Chapter 7 are presented in Tables 8.2 and 8.3. Analytical methods, including descriptions of the acid-leaching technique used to minimise the effects of seafloor alteration processes, are described in Appendix 2. Initial isotopic ratios were calculated using the age of the closest magnetic seafloor lineation to each dredge site and the equations

Table 8.2: $^{87}Sr/^{86}Sr$ and $^{143}Nd/^{144}Nd$ data for the Southern Ocean seafloor samples; errors ($2\sigma_{mean}$) associated with individual measurements indicate within-run precision only. Inititial isotopic ratios were calculated using the N-MORB trace element values of Sun and McDonough (1989), as described in the text.

Sample No.	Age	$^{87}Sr/^{86}Sr$	±2σ	$(^{87}Sr/^{86}Sr)_i$	$(\varepsilon Sr)_i$	$^{143}Nd/^{144}Nd$	±2σ	$(^{143}Nd/^{144}Nd)_i$	$(\varepsilon Nd)_i$
Dredge 09:									
102/DR09-4A	53 Ma	0.703672	13	0.703658	-11.1	0.512898	49	0.512822	4.7
		0.703661	24	0.703647	-11.2	0.512953	10	0.512877	5.8
102/DR09-4B(i)	53 Ma	0.703172	12	0.703158	-18.2	-	-	-	-
		0.703199	13	0.703185	-17.8	0.513029	12	0.512953	7.2
102/DR09-4B(ii)	53 Ma	0.703176	15	0.703162	-18.1	0.513021	17	0.512945	7.1
		0.703182	20	0.703168	-18.0	0.513002	7	0.512926	6.7
102/DR09-4B4	53 Ma	0.703186	14	0.703172	-18.0	0.513031	8	0.512955	7.3
102/DR09-4B5	53 Ma	0.703189	15	0.703175	-17.9	-	-	-	-
		0.703198	27	0.703184	-17.8	0.513036	6	0.512960	7.4
Dredge 10:									
102/DR10-1B	36 Ma	0.702582	11	0.702573	-26.8	-	-	-	-
		0.702578	19	0.702569	-26.8	0.513120	8	0.513069	9.1
		0.702588	9	0.702579	-26.7	0.513140	4	0.513089	9.5
102/DR10-1C	36 Ma	0.703214	13	0.703205	-17.8	-	-	-	-
		0.703244	14	0.703235	-17.4	0.513093	13	0.513042	8.6
		0.703279	19	0.703270	-16.9	0.513107	8	0.513056	8.8
Dredge 11:									
102/DR11-2A	36 Ma	0.703235	5	0.703226	-17.5	0.512966	4	0.512915	6.1
102/DR11-2A(iii)	36 Ma	0.703249	11	0.703240	-17.3	0.512997	3	0.512946	6.7
102/DR11-2B	36 Ma	0.703333	11	0.703324	-16.1	0.512979	11	0.512928	6.3
Dredge 13:									
102/DR13-3(iii)	66 Ma	0.704325	7	0.704308	-1.6	0.512986	11	0.512892	6.4
		0.704343	19	0.704326	-1.7	0.513001	10	0.512907	6.7
102/DR13-3D	66 Ma	0.704592	16	0.704575	2.2	0.512997	11	0.512903	6.6
		0.704643	13	0.704626	2.5	0.512982	10	0.512888	6.3
102/DR13-3E	66 Ma	0.702645	21	0.702628	-25.5	0.513149	13	0.513055	9.6

Table 8.3: $^{206}Pb/^{204}Pb$, $^{207}Pb/^{204}Pb$ and $^{208}Pb/^{204}Pb$ data for the Southern Ocean seafloor samples. Initital isotopic ratios were calculated using the N-MORB trace element values of Sun and McDonough (1989), as described in the text.

Sample No.	Age	μ	$^{206}Pb/^{204}Pb$	$(^{206}Pb/^{204}Pb)_i$	$^{207}Pb/^{204}Pb$	$(^{207}Pb/^{204}Pb)_i$	$^{208}Pb/^{204}Pb$	$(^{208}Pb/^{204}Pb)_i$
Dredge 09:								
102/DR09-4A	53 Ma	9.72	17.641	17.561	15.475	15.471	37.651	37.584
102/DR09-4B(i)	53 Ma	9.78	17.988	17.907	15.488	15.484	37.791	37.723
102/DR09-4B(ii)	53 Ma	9.81	18.241	18.160	15.486	15.482	37.755	37.687
102/DR09-4B5	53 Ma	9.76	17.894	17.813	15.464	15.460	37.727	37.659
Dredge 10:								
102/DR10-1B	36 Ma	9.83	18.251	18.196	15.489	15.486	37.878	37.832
102/DR10-1C	36 Ma	9.79	18.117	18.062	15.464	15.461	37.737	37.691
Dredge 11:								
102/DR11-2A	36 Ma	9.79	17.965	17.910	15.494	15.491	37.867	37.821
102/DR11-2A(iii)	36 Ma	9.83	18.121	18.066	15.506	15.503	37.973	37.927
102/DR11-2B	36 Ma	9.79	17.908	17.853	15.499	15.496	37.888	37.842
Dredge 13:								
102/DR13-3(iii)	66 Ma	10.00	18.556	18.453	15.587	15.582	38.726	38.640
102/DR13-3D	66 Ma	10.00	18.542	18.439	15.586	15.581	38.721	38.635
102/DR13-3E	66 Ma	9.83	18.297	18.196	15.491	15.486	37.798	37.713

presented in Appendix 6. The methods used to calculate initial ε_{Nd} and ε_{Sr} (Table 8.2), μ (Table 8.3) and κ values are also presented in Appendix 6.

As discussed for the Balleny Plume samples (Section 3.7), acid-leaching (as described in Appendix 2) was used as a means of reducing, and hopefully negating, the effects of seafloor alteration processes on these old, and obviously altered, Southern Ocean samples. For the same reasons discussed in Section 3.7, REE and trace element abundances were not measured on the acid-leached sample aliquots used for isotopic analysis. Although ICP-MS data are available for a number of unleached Southern Ocean seafloor samples (Appendix 5), the possibility that they may be altered by the same seafloor processes suspected of affecting the isotopic ratios, means that they too are unsuitable for use in the calculation of initial isotopic ratios. In the absence of suitable measured REE and trace element abundances and ratios with which to age-correct the isotopic data, the N-type MORB elemental concentrations (ppm) of Sun and McDonough (1989: Table 1) have been adopted here: Rb = 0.56, Sr = 90, Sm = 2.63, Nd = 7.30, Pb = 0.30, Th = 0.12, U = 0.047; $^{87}Rb/^{86}Sr = 0.018, ^{147}Sm/^{144}Nd = 0.2179$, $\kappa = 2.64$.

As with the values calculated for the Balleny Plume samples (Section 3.7), it must be noted that the initial isotopic ratios calculated here for the Southern Ocean seafloor samples do not necessarily represent the correct initial isoptopic ratios, but are the best approximations possible under the circumstances. As the main purpose of this investigation is to compare these derived values with the range of isotopic data available in the literature for Pacific and Indian Ocean MORB, it is important to consider whether the use of different REE and trace element concentrations (such as the measured ICP-MS values) would significantly change the interpretation/s of the isotopic data presented in the following sections.

The measured and initial radiogenic isotope ratios of the Southern Ocean seafloor samples are compared in Figure 8.4. Differences between measured and initial $^{87}Sr/^{86}Sr$, $^{143}Nd/^{144}Nd$ and $^{207}Pb/^{206}Pb$ are negligible (Tables 8.2 and 8.3). The values most affected in all samples are $^{208}Pb/^{204}Pb$ and, particularly, $^{206}Pb/^{204}Pb$ which are also the most important isotopic parameters with which to distinguish Pacific and Indian Ocean MORB. Whereas μ ($^{238}U/^{204}Pb$) values presented in Table 8.3 are lower than the mean value of 11.2 calculated for MORB glasses by White (1993), μ values calculated for the Southern Ocean seafloor samples using the measured ICP-MS trace element data (Appendix 5: Table A5.1) range from 19.06 to 125.25 and are obviously the result of disrupted U/Pb contents. Assuming that these rocks would have possessed Ce/Pb values of 25±5 (Hofmann et al., 1986) at the time of crystallisation, it is possible to predict the cause of their current anomalously high μ values in terms of elemental variations resulting from seafloor alteration processes. The ICP-MS data presented in Appendix 5 yield Ce/Pb values within the 25±5 range for samples 09-4B(ii), 09-4B-5 and 10-1B. Samples 11-2A and 11-2A(iii) have slightly low Ce/Pb (~18.9) and samples 10-1C, 13-3D and 13-3E have high Ce/Pb (45.7, 30.8 and 76.2 respectively). This suggests that the high U/Pb values of samples with average Ce/Pb

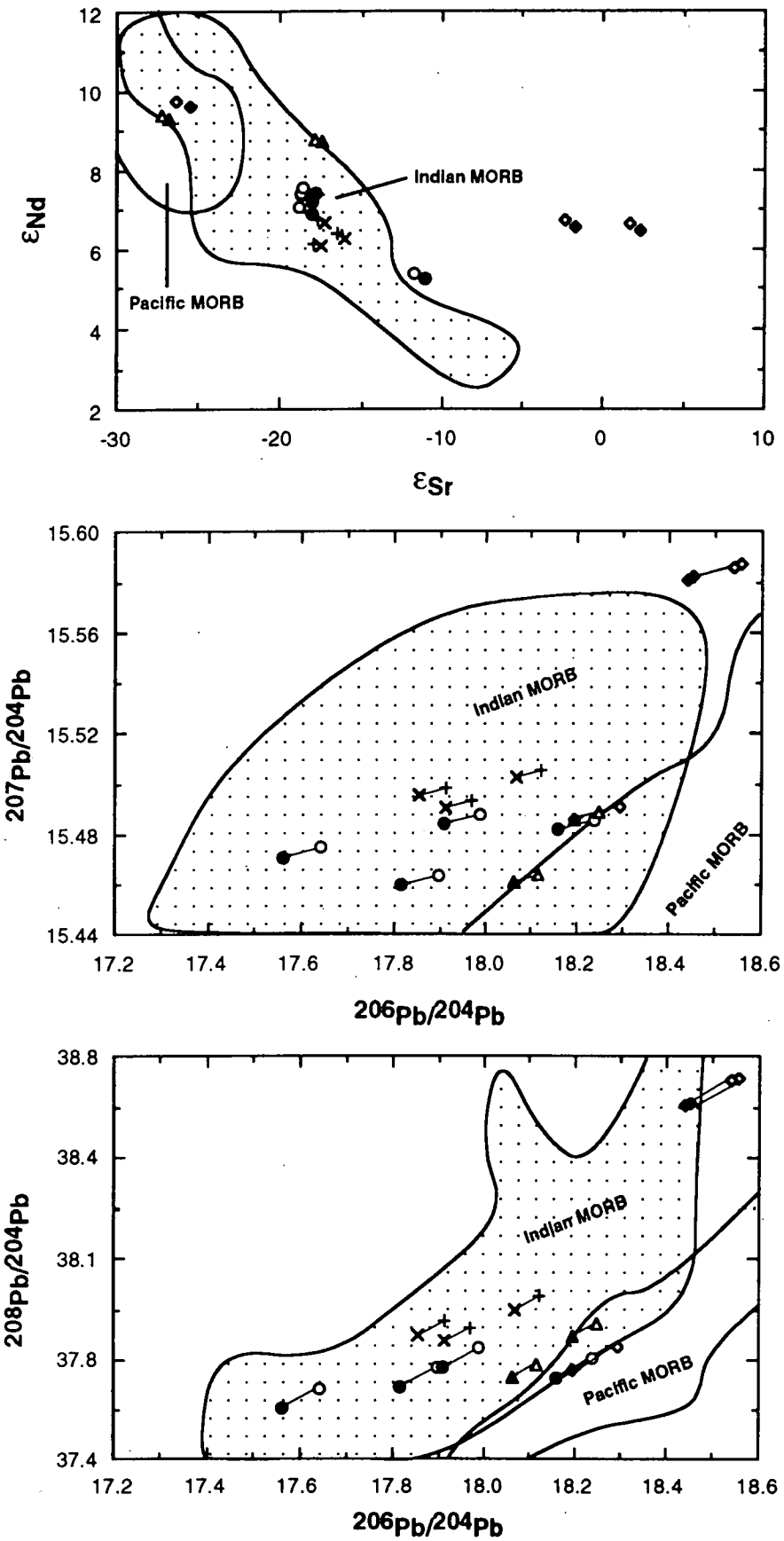

Figure 8.4: Comparison between the measured (open symbols) and initial (filled symbols) isotopic ratios for the Southern Ocean seafloor samples: dredge 102/DR09 (circles), dredge 102/DR10 (triangles), dredge 102/DR11 (crosses - oblique crosses represent the age-corrected data) and dredge 102/DR13 (diamonds); data from Tables 8.2 and 8.3. Data sources for the Indian and Pacific Ocean MORB isotopic fields are as for Table 8.1.

(ie. they have suffered no significant disruption to their Pb contents) or slightly lower than average Ce/Pb contents are primarily a function of U addition during seafloor alteration. The high μ value of sample 13-3D, with marginally higher than average Ce/Pb, may be a function of both Pb loss and U addition, whereas the extremely high Ce/Pb values of samples 10-1C and 13-3E imply that their high U/Pb is a product of quite significant Pb loss. An increase in U/Pb values of altered oceanic crust by U addition and/or Pb depletion has been documented by Michard and Albarède (1985) as a result of hydrothermal processes. Rather than being a function of seafloor age then, these results suggest that both the extent and type of seafloor alteration affecting these samples is varied, even on the scale of single dredge sites.

Using the measured ICP-MS trace element abundances to calculate the initial Pb isotopic ratios would therefore have produced anomalously high μ values and resultant over-correction in terms of $^{206}Pb/^{204}Pb$. However, even if values intermediate to the measured and the literature-derived concentrations were used to recalculate $^{206}Pb/^{204}Pb$, so as to acheive μ values closer to White's (1993) MORB average, calculated initial ratios would still plot within the same MORB isotopic field (Figure 8.4). This suggests, therefore, that the use of different elemental concentrations to calculate the initial isotopic ratios would not change the overall data interpretation, in terms of the aims of this study.

8.3.2 Interpretation of the Isotopic Data:

Despite the pervasive alteration evident in the Southern Ocean seafloor samples, the acid-leaching technique described in Appendix 2 has resulted in isotopic ratios which overlap with the MORB fields in general. This is particularly true in terms of their Pb isotopes, although two samples from dredge 102/DR13, probably from the same flow, have significantly higher $^{206}Pb/^{204}Pb$, $^{207}Pb/^{204}Pb$, $^{208}Pb/^{204}Pb$ and $^{87}Sr/^{86}Sr$ than the other samples. The relatively high Pb isotope ratios of samples 13-3(iii) and 13-3D overlap with the MORB ranges, but their Sr isotope values are significantly higher than MORB values.

The anomalous isotopic values, and T-MORB geochemical affinities (Chapter 7), of at least some samples from dredge 102/DR13 may be somehow related to its location within the Diamantina Fracture Zone (Figure 7.5) and/or its relative proximity (~70 km south of A34) to the continent-ocean boundary (COB) south of Western Australia. Very little is known about the Diamantina Fracture Zone. Its unusually rough topography, comprising a narrow series of ridges and troughs which extend for some 3000 km across the southern Indian Ocean to a longitude of 125°E south of Western Australia (Nicholls et al., 1981), is attributed to the unusually slow seafloor spreading rate between magnetic anomalies 34 (82 Ma) and 19 (45 Ma) (Cande and Mutter, 1982; Mutter et al., 1985). Possible sources of the high Sr and Pb isotopic ratios of these two dredge 102/DR13 samples may therefore include continental crust or lithospheric contamination, due to the proximity of the COB, and/or seafloor processes which were not negated by the acid-leaching process. The latter is particularly likely due to the advanced age (~66 Ma) and observed alteration (Chapter 7) of

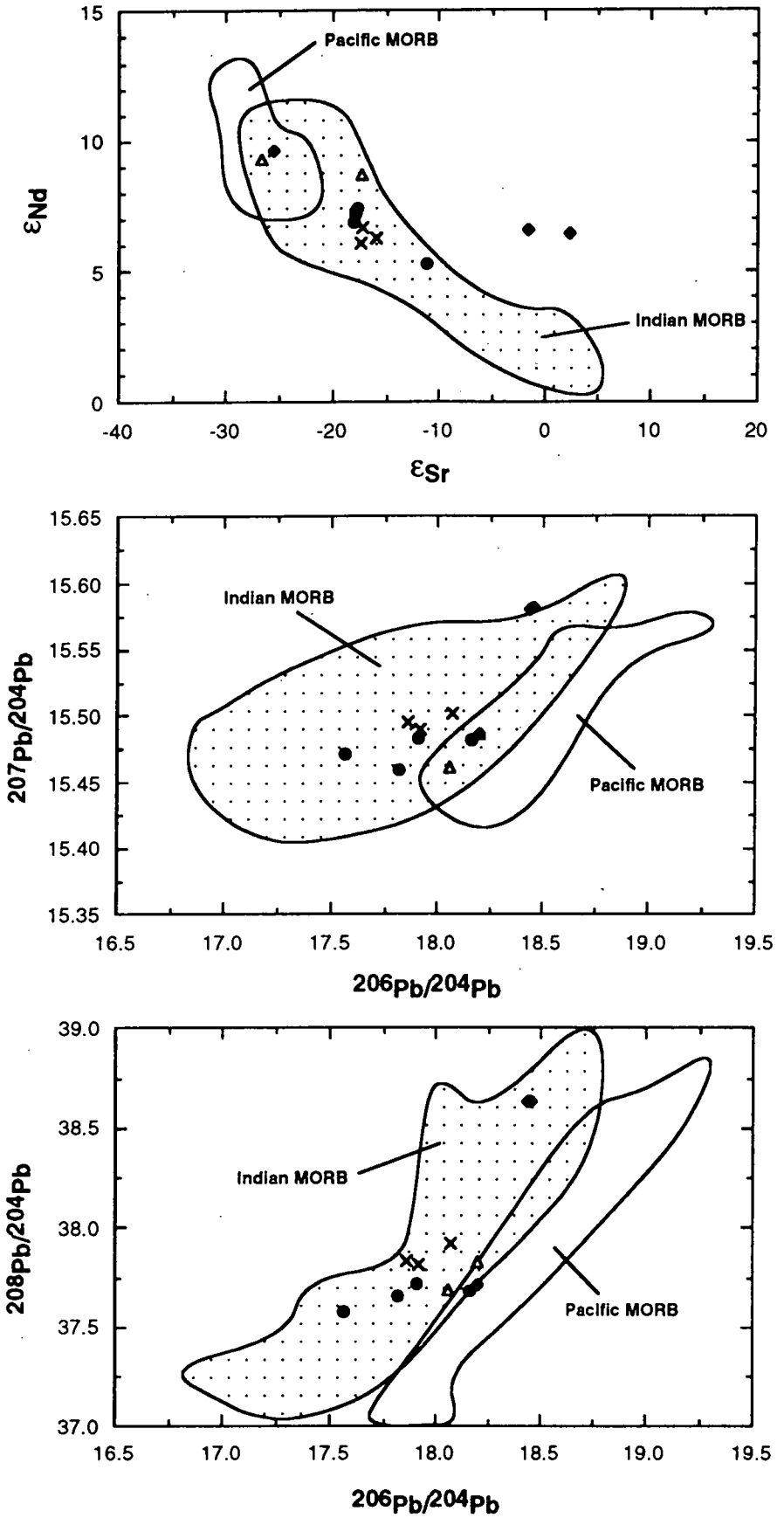

Figure 8.5: Plots of initial radiogenic isotope ratios as calculated for the Southern Ocean seafloor samples: dredge 102/DR09 (filled circles), dredge 102/DR10 (open triangles), dredge 102/DR11 (oblique crosses), and dredge 102/DR13 (filled diamonds); data from Tables 8.2 and 8.3 - average values are plotted for duplicate or triplicate analyses. Data sources for the Indian and Pacific Ocean MORB isotopic fields are as for Table 8.1.

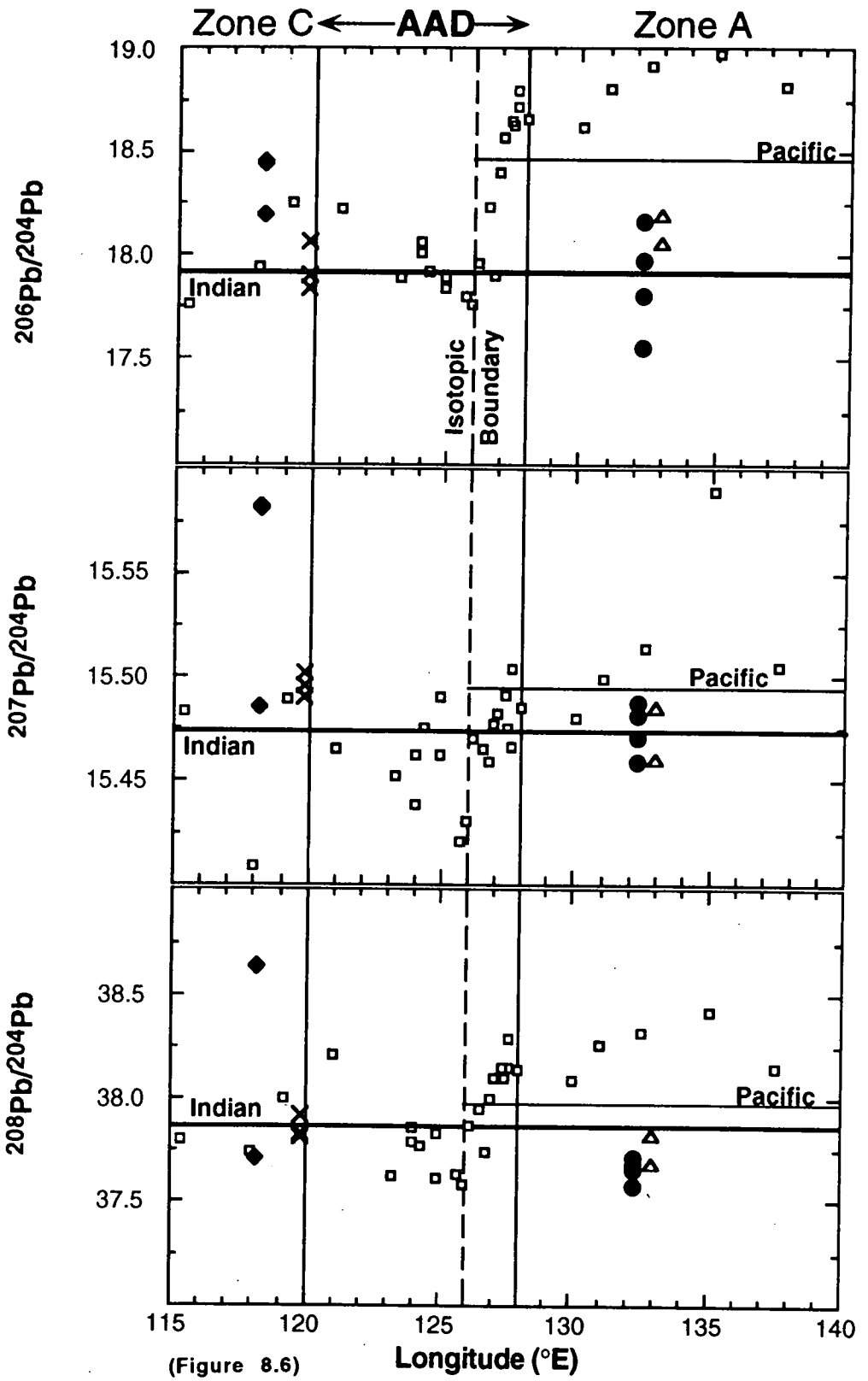
Zone C
AAD
Zone A
19.0
18.5
18.0
17.5
206Pb/204Pb
Pacific
Indian
Isotopic Boundary
15.55
15.50
15.45
207Pb/204Pb
Pacific
Indian
38.5
38.0
37.5
208Pb/204Pb
Pacific
Indian
115
120
125
130
135
140
Longitude (°E)

(Figure 8.6)

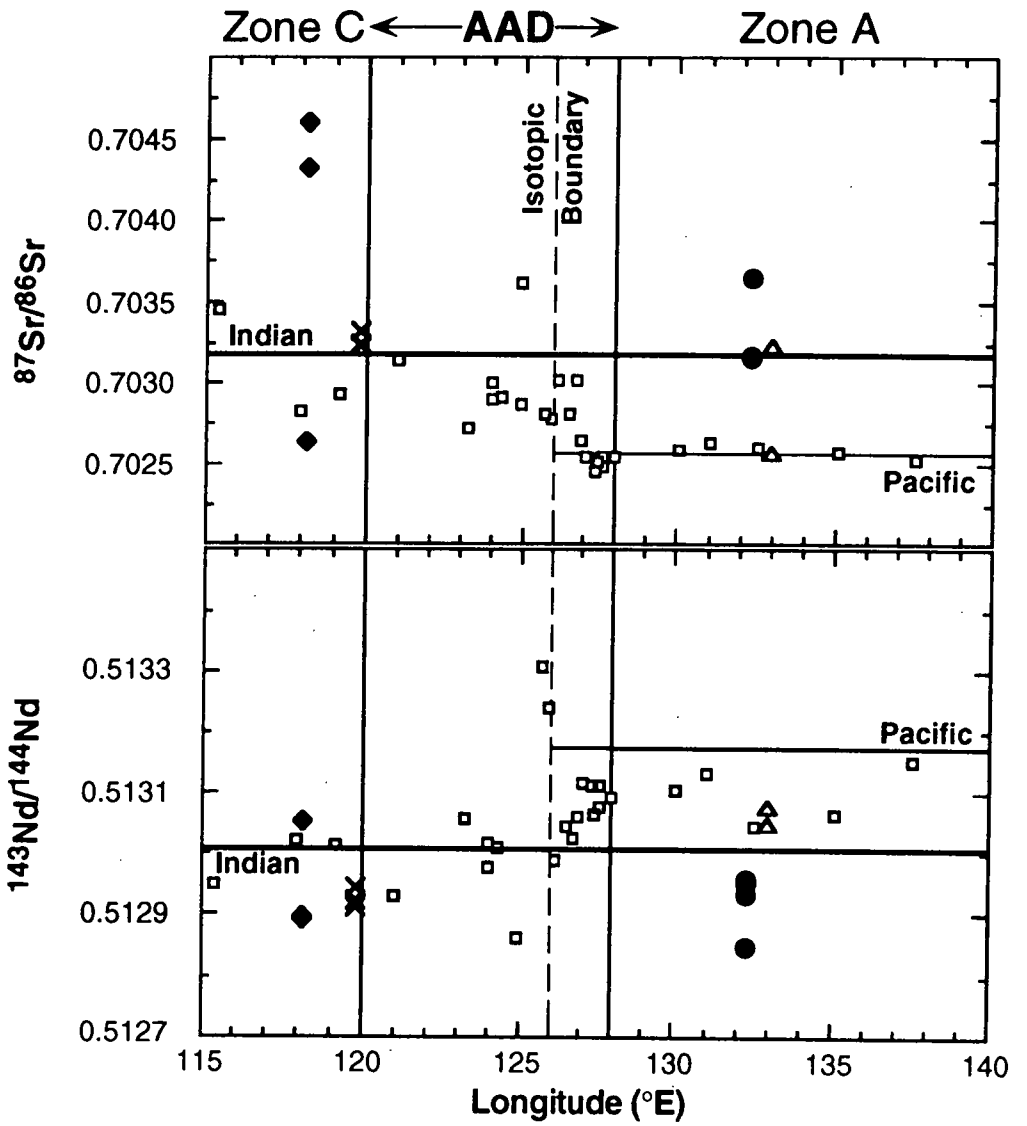

Figure 8.6: Plots of the initial radiogenic isotope values of the Southern Ocean seafloor samples from this study: dredge 102/DR09 (filled circles), dredge 102/DR10 (open triangles), dredge 102/DR11 (oblique crosses), and dredge 102/DR13 (filled diamonds), and the 0 to 4 Ma SEIR MORB data (open squares) of Klein et al. (1988) and Pyle et al. (1992) versus longitudinal position along the SEIR. Southern Ocean data from Tables 8.2 and 8.3; SEIR data are normalised as for Figure 8.3. Thick horizontal lines depict the average values for Indian and Pacific Ocean MORB samples as presented in Table 8.1.

these samples. As the post acid-leaching isotopic values measured for sample 13-3E are similar to those of the other Southern Ocean seafloor samples and MORB in general (Figure 8.5), and are therefore probably more representative of uncontaminated seafloor in this region.

The initial isotopic ratios claculated for samples from all four dredge sites plot within, or immediately adjacent to, the Indian Ocean MORB isotope fields in Figure 8.5. This is particularly evident on Pb-Pb plots, which generally provide the best distinction between Pacific and Indian Ocean MORB. Of the samples dredged from the two sites east of the northward extrapolation of the AAD, only sample 10-1B has a possible Pacific Ocean Sr isotopic signature, although it plots in a similar position to a western dredge site sample (13-3E). The two dredge 102/DR10 samples have Pb isotope values which plot within both the Indian and Pacific MORB fields, with similar values to eastern dredge site sample 09-4B(ii) and western dredge site sample 13-3E. All other samples, from dredge sites both east and west of the extrapolated AAD boundaries, are isotopically more like Indian Ocean than Pacific Ocean MORB.

The overall isotopic affinity between the Southern Ocean seafloor samples and Indian Ocean MORB is also evident in Figure 8.6. This is particularly true on plots of Pb isotopes versus longitude. The greatest distinction between zone A SEIR samples, with Pacific Ocean MORB affinities, and the dredge 102/DR09 and 102/DR10 rocks, sampling seafloor directly to the north, is evident in terms of $^{206}Pb/^{204}Pb$ and $^{208}Pb/^{204}Pb$ both of which are higher in the zero-age SEIR basalts.

One further observation to be made when comparing the isotopic compositions of samples from the eastern and western dredge sites is that basalts from site 102/DR09 extend to the lowest $^{206}Pb/^{204}Pb$, both in terms of measured and corrected values, the latter comparable to the most depleted values measured for Indian Ocean MORB. The possible implications of this will be discussed further in the following section.

8.4 IMPLICATIONS FOR THE LONGEVITY OF THE INDIAN-PACIFIC ISOTOPIC BOUNDARY WITHIN THE AAD:

The results of this study indicate that ≥36 Ma Southern Ocean seafloor north of zone A, and east of the northward extrapolation of the AAD, has an Indian Ocean isotopic signature, thereby supporting the suggestion of Pyle et al. (1992) that the Indian-Pacific Ocean isotopic boundary may be migrating steadily westwards beneath the Southern Ocean. The apparent migration along the ridge axis of both the isotopic boundary and the residual negative depth anomaly (Marks et al., 1990) imply that these features are linked and unrelated to the other anomalous features of the AAD which have been in existence for at least ~20 to 25 m.y. (Weissel and Hayes, 1974; Vogt et al., 1983).

Another indication that the on-axis location of the Indian-Pacific Ocean isotopic boundary within the AAD may be purely coincidental is provided by the major element chemistry of the AAD basalts (Chapter 7). Although Christie et al. (1988) propose that a major geochemical boundary is present along the SEIR axis, they suggest that it is coincident with the eastern boundary of the AAD rather than with the isotopically defined boundary of Klein et al. (1988). Klein et al. (1991) also concluded that there was no evidence for a major element discontinuity coinciding with the isotopic boundary beneath the AAD.

The limitations imposed by sampling at only two off-axis dredge sites (102/DR09 and 102/DR10) of similar longitudinal position east of the AAD are such that it is not possible to discern the actual location of the proposed Indian-Pacific isotopic boundary north of the SEIR. This means that it is also not possible, within the scope of this study, to distinguish between the various active mantle flow (Pyle et al., 1992) models proposed to explain the current location of the isotopic boundary within the AAD (Vogt and Johnson, 1973; Alvarez, 1982; Klein et al., 1988; Alvarez, 1990; Marks et al., 1990). The data obtained during this study do dictate, however, that the Indian-Pacific Ocean isotopic boundary must either be confined to the immediate vicinity of the ridge axis or, if it extends to older regions of the Southern Ocean seafloor north of the SEIR, it must be located east of ~133°E, at least within ≥36 Ma crust.

Of the various models discussed in Section 8.2.3, three could still be invoked to explain the presence and apparent westward migration of the Indian-Pacific upper mantle isotopic boundary in the Southern Ocean. The first of these confines the isotopic boundary to the immediate latitudinal vicinity of the SEIR as a result of convergence of hotspot-driven along-axis asthenospheric flow (Vogt and Johnson, 1973; Marks et al., 1990). The direct convergence model of Klein et al. (1988) also remains a possibility, but it must entail a progressive westward migration of the isotopic boundary with time and/or an arcuate shape to the boundary in order to account for the Indian Ocean isotopic signature in seafloor north of zone A. The third, and possibly most likely, model to be considered in light of this new data is that of Pacific basin shrinkage (Alvarez, 1982; 1990). This model could account for the apparent westward migration of the isotopic boundary with time, the occurrence of Indian Ocean MORB in ≥36 Ma seafloor north of zone A, and the probable arcuate or wedge-shaped surface trace of a boundary whose apex underlies the eastern AAD.

The observation that samples from the the eastern dredge site 102/DR09 extend to the lowest $^{206}Pb/^{204}Pb$ values of the Southern Ocean samples, and are similar to the most depleted values measured for Indian Ocean MORB, may have implications for the dynamics of mantle convection beneath the Indian Ocean. Mahoney et al. (1992) propose that the low $^{206}Pb/^{204}Pb$ values, characteristic of Indian Ocean MORB in general, may be a consequence of widespread upper mantle contamination by the Kerguelen, Marion and Crozet starting plume heads. If Australian-Antarctic rifting allowed the previously isolated Indian Ocean upper mantle (e.g. Klein et al., 1988) to migrate eastward into the gap formed by the opening of the Southern Ocean, contaminated sub-Indian Ocean asthenosphere

may have been flushed out into this gap (Mahoney et al., 1992) resulting in a more contaminated Indian Ocean isotopic signature in the more easterly SEIR eruptives.

8.5 OTHER PROPOSED LOCATIONS OF THE INDIAN-PACIFIC OCEAN ISOTOPIC BOUNDARY:

An apparent Indian-Pacific Ocean upper mantle isotopic boundary has also been recognised in association with island arc settings in the western Pacific Ocean. One example involves the transition from Pacific to Indian Ocean isotopic signatures with the southward propagation of the Valu Fa Ridge and the onset of true seafloor spreading within the Lau backarc basin. This has been attributed to slab rollback, whereby the ensuing advection, during the last ~5.5 m.y., of Indian Ocean asthenosphere into the sub-arc mantle has displaced the previously existing Pacific Ocean asthenosphere (Hergt and Hawkesworth, in press; Hergt and Nilsson-Farley, in press). This discovery places the Indian-Pacific Ocean isotopic boundary somewhere west of the Tonga Ridge, beneath the Indian-Australian Plate and west of the site of subduction of the Pacific Plate at the Tonga Trench. The apparent presence of Pacific Ocean asthenosphere beneath the Indian-Australian Plate is difficult to explain, although Hergt and Nilsson-Farley (in press) suggest that either an ancient trench jump or a reversal in the direction of subduction may have been involved.

Another recognised occurrence of both Pacific and Indian Ocean isotopic signatures in the western Pacific Ocean occurs within the central New Hebrides Arc (Briqueu et al., in press). Arc volcanism in this region was dominated by a Pacific Ocean isotopic signature until 3 Ma ago when collision of a submarine ridge, the D'Entrecasteaux Zone, with the central part of the Arc coincided with the introduction of an Indian Ocean isotopic signature, the latter characterised by higher $^{87}Sr/^{86}Sr$ and lower $^{206}Pb/^{204}Pb$ values in post-collisional arc volcanics. The radiogenic Pb isotope data from this region define surprisingly similar trends to that of the Lau basin samples analysed by Hergt and Hawkesworth (in press) (A.J. Crawford, pers. comm., 1993), both of which suggest the initial involvement of Pacific Ocean asthenosphere in arc volcanism, followed by the tapping of Indian Ocean asthenosphere in response to localised tectonic processes.

In a recent paper by Hickey-Vargas et al. (submitted) it is noted that the Western Pacific Marginal Basins, including the Sea of Japan, West Phillipine basin, Shikoku and Parece Vela basins, Mariana Trough and Sumisu Rift, South China Sea, Celebes Basin and Sulu Basin, are dominated by an Indian Ocean MORB isotopic signature and are assumed to have formed in continuity with Indian Ocean asthenosphere. In contrast, the arc magmas themselves indicate a source in the mantle wedge with Pacific Ocean MORB isotopic affinities. Clearly, the location of this apparent boundary between Indian and Pacific Ocean MORB mantle sources is close to that of the subduction zones in the western Pacific. This

has led these authors to suggest that subduction is geographically related to, and possibly even a consequence of downwelling at the Indian-Pacific upper mantle boundary.

8.6 CONCLUSIONS:

The radiogenic isotope data obtained for the Southern Ocean seafloor samples north of the SEIR indicate that, although a proposed isotopic boundary between Indian and Pacific Ocean upper mantle domains has been recognised within the eastern AAD (Klein et al., 1988; Pyle et al., 1992), it does not continue directly northwards towards the southern margin of Australia. This implies that the current location of the isotopic boundary at the SEIR is merely coincidental with, and not a long-term feature of, the AAD. Westward migration of the Indian-Pacific isotopic boundary (Pyle et al., 1992), possibly as a consequence of the separation of the South Tasman Rise from Antarctica, therefore seems likely.

Although the exact nature of the proposed boundaries between Indian and Pacific Ocean isotope domains is not yet understood, the relatively recent expression of Indian Ocean asthenosphere within island arc settings located at the contact between the Indian-Australian and Pacific Plates, and the apparent influx of Pacific Ocean upper mantle into the Southern Ocean in response to Australian-Antarctic rifting, suggests that the Indian-Pacific isotopic boundary was linked to the plate boundary prior to Gondwana break-up. Although this ties in with the proposal that deep sub-continental lithospheric roots may have impeded upper mantle convection beneath the Pacific Ocean (Alvarez, 1982; 1990), the actual explanation for the occurrence, location and current surface expressions of this apparent Indian-Pacific mantle reservoir boundary may be much more complicated than so far proposed and therefore requires more extensive investigation.

PART 3

U-Pb ZIRCON DATING OF A PROTEROZOIC MAFIC DYKE SWARM IN THE VESTFOLD HILLS, EAST ANTARCTICA

CHAPTER 9

THE PROTEROZOIC HISTORY OF THE VESTFOLD HILLS, EAST ANTARCTICA, AS DEDUCED FROM U-Pb ZIRCON DATING OF A MAFIC DYKE SWARM

9.1 INTRODUCTION:

Early to Middle Proterozoic mafic dyke swarms are relatively common within the Archaean blocks of the East Antarctic Shield, but are much less abundant in the adjoining, more extensive Proterozoic mobile zones (Sheraton et al., 1987). One such Archaean block, the Vestfold Hills, is intruded by numerous mafic dykes (Sheraton and Collerson, 1983; Sheraton et al., 1984; Collerson and Sheraton, 1986), which have been subdivided into at least nine distinct generations (Seitz, 1991). Obtaining emplacement ages for each of these dyke generations allows definition of the history of mafic magmatism of this region as well as elucidation of its Proterozoic crustal history. The latter is possible due to a sequence of deformational and metamorphic events, interspersed with the various episodes of mafic dyke intrusion (Oliver et al., 1982; Parker et al., 1983; Passchier et al., 1990; Hoek and Passchier, 1991; Passchier et al., 1991), which can be assigned absolute ages through the precise dating of the individual dyke generations.

Until now, dating of the Vestfold Hills dykes has been dominated by the Rb-Sr whole-rock isochron method. The SHRIMP (Sensitive High-Resolution Ion Microprobe) U-Pb zircon dating technique used in this study (Appendix 2), has significant advantages over the previously employed Rb-Sr isochron method in that individual parts of zircon crystals from a single rock sample can be analysed, and assigned to the appropriate generation of inheritance, crystallisation or recrystallisation. This method therefore eliminates the risk of combining isotopically unequilibrated or even geologically unrelated samples from various dykes in order to obtain a single age. The significantly higher blocking temperature of the U-Pb zircon system, compared to that of the Rb-Sr system of various minerals, and the highly refractory nature of zircon also ensures a greater probability that the crystallisation age will be retained.

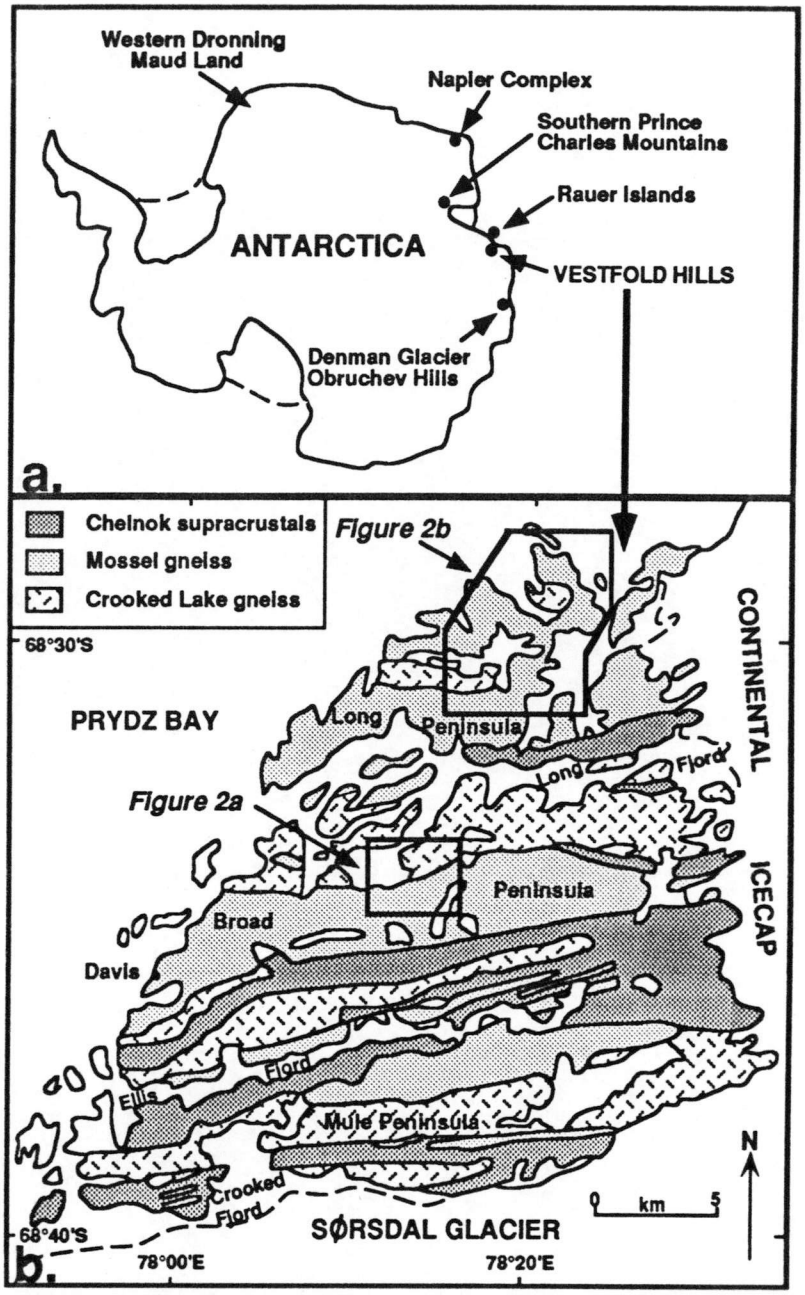

Figure 9.1: a) Map showing the location of the known Archaean nuclei within the East Antarctic Shield; b) Map of the Vestfold Hills (modified after Black et al., 1991b) showing the basement geology (except for the Grace Lake granodiorite, outcrops of which are not large enough to be shown at this scale) and the location of the sampling areas enlarged in Figure 9.2.

This study, in deriving new $^{207}Pb/^{206}Pb$ zircon ages for a number of Vestfold Hills dykes, not only confirms a zircon age obtained by Black et al. (1991a) for one of the dyke generations, but it also confirms the usefulness of zircons derived from felsic late-stage differentiates for the dating of mafic dykes (e.g. Heaman et al., 1986; Black et al., 1991a). Subsequent deductions about the Proterozoic crustal history of the Vestfold Hills from considerations of these new zircon ages, combined with information about the conditions of dyke emplacement, may also be applicable to the Proterozoic evolution of similar dyke-infested Archaean blocks of the East Antarctic Shield such as the Napier Complex and the

Southern Prince Charles Mountains. In a broader context, the potential to derive precise dyke emplacement ages by this method of U-Pb zircon dating has implications for the global correlation of Proterozoic dyke swarms and the reconstruction of supercontinents.

9.2 GEOLOGICAL SETTING:

The Vestfold Hills, a 400 km^2 ice-free area on the eastern shore of Prydz Bay, constitutes one of several Archaean cratonic blocks (James and Tingey, 1983; Collerson et al., 1983a) within the East Antarctic Shield (Figure 9.1). This block is separated from the other exposed Archaean nuclei, the Napier Complex of Enderby Land (Sheraton, 1979; Black and James, 1983), the Southern Prince Charles Mountains of MacRobertson Land (Tingey, 1982), the Obruchev Hills - Denman Glacier region of Queen Mary Land (Black et al., 1992) and western Dronning Maud Land (Barton et al., 1987) by an extensive Proterozoic high-grade metamorphic complex (e.g. James and Tingey, 1983). Geological contacts between the Vestfold block and the Archaean and Proterozoic rocks of the Rauer Islands (Kinny et al., 1993) to the southwest are hidden beneath the Sørsdal Glacier. Eastern geological contacts are covered by the continental icecap.

9.2.1 Archaean Basement Geology:

The basement geology of the Vestfold Hills (Figure 9.1b) was originally thought to comprise four strongly inter-folded, east-west striking gneissic units repeated from north to south throughout the area (Oliver, 1979; Collerson and Arriens, 1979; Collerson et al., 1983a; Sheraton and Collerson, 1983). Black et al. (1991b) revised the established basement geology of the region by retaining the Chelnok Supracrustal assemblage (dominated by garnetiferous paragneisses), the Mossel gneiss (mostly tonalitic orthogneiss with lesser trondhjemite, granodiorite and granite) and the Crooked Lake gneiss (a composite orthogneiss suite), while introducing a fourth unit, the Grace Lake granodiorite (leucocratic gneiss and granitoid outcropping in the northern Vestfold Hills). The oldest of Collerson et al.'s (1983a) original units, the Tryne metavolcanics (layered ultramafic, mafic, intermediate and minor felsic metavolcanics), which occurs mainly as either boudinaged xenoliths or tectonic intercalations within the Mossel and Crooked Lake gneisses, was not considered to be a separate mappable unit.

Although the proposed oldest units, the Tryne Metavolcanics and the Chelnok Supracrustal assemblage, contained no suitable zircons, ion microprobe (SHRIMP) zircon dating of the basement units of igneous origin defined the following series of Archaean to Early Proterozoic events (Black et al., 1991b). Precursors of the Mossel gneiss were emplaced between 2526 ± 6 Ma and 2501 ± 4 Ma, prior to emplacement of the Crooked

Lake gneiss between 2501 ± 4 Ma and 2484 ± 6 Ma. Earliest granulite facies metamorphism, M_1, (850° C, 7 kbars; Harley, 1989), probably occurred at 2501±4 Ma, and M_2 (similar P,T conditions to M_1) at 2487±6 Ma synchronous with the emplacement of the Grace Lake granodiorite. Following uplift, and preceding cratonisation, of the Vestfold block, a series of quartz diorite dykes were intruded in at least two areas of the northeastern Vestfold Hills. One of these dykes was dated at 2477±5 Ma. A subsequent amphibolite to granulite facies D_3,M_3 event produced southeasterly dipping mylonite zones within the basement gneisses (Parker et al., 1983; Passchier et al., 1991).

9.2.2 Emplacement and Classification of the Proterozoic Mafic Dyke Swarm:

Most of the Early to Middle Proterozoic dykes which intrude the Archaean basement of the Vestfold Hills are tholeiitic, although several volumetrically minor suites of lamprophyre dykes are also present. The dykes are generally unfolded, steeply dipping, and discordant to the east-west striking gneisses with which they display sharp contacts, often with parallel schlieren in the country rock. They range from a few cms or less to over 50 m in width (Collerson and Sheraton, 1986) and have aphanitic chilled margins. Most of the dykes are unmetamorphosed, except for those in the southwest Vestfold Hills, which experienced the peripheral effects of ~1000 Ma metamorphism in the adjoining Proterozoic complex (Collerson et al., 1983b) and display garnet-bearing crystal assemblages.

Several classifications have been applied to the various mafic dykes in the Vestfold Hills (Collerson and Sheraton, 1986; Kuehner, 1986; Kuehner,1987; Passchier et al., 1991; Seitz, 1991), and are summarised in Table 9.1. The classification scheme used in this study is based primarily on that of Seitz (1991), who subdivided the dykes in the Long Peninsula region (Figure 9.1b) into nine generations on the basis of their distinctive orientations, cross-cutting relationships, petrography and geochemistry. Seitz (1991) suggested that the various mafic magmatic episodes produced four distinct directional trends in the dykes which rotated clockwise with time, implying a continual rotation of the regional crustal stress field during the period of dyke emplacement. Characteristic dyke orientations are therefore considered to be a useful guide to identifying the various dyke suites in the field.

The major and trace element compositions of individual dykes from each suite which yielded zircons for this study are presented in Table 9.2. Italicised terms in the following descriptions refer to the dyke classifications used in this study; numbers in brackets refer to the relative ages of each generation, whereby (1) is the oldest.

9.2.2.1 High-Mg Tholeiite Dykes:

The SiO_2-oversaturated, hypersthene-normative High-Mg dykes of the Vestfold Hills are generally characterised by high SiO_2 (52-57 wt%), high MgO (7-18 wt%), low TiO_2 (0.38-0.74 wt%), ~9-13 % Fe_2O_3, enrichment in Platinum Group Elements (PGE), LILE (Ba, Rb and K) and LREE relative to the HFSE Nb and Ti, and pronounced negative Nb, P and Ti

Table 9.1: Classification schemes proposed for the mafic dykes of the Vestfold Hills.

	Collerson and Sheraton (1986)	Kuehner (1986; 1987)	Passchier et al. (1991)
First Magmatic Episode:	High-Mg tholeiite dykes	High-Mg tholeiite dykes - subgroup I	DT I
		High-Ti Fe-rich tholeiite dykes	
		High-Mg tholeiite dykes - subgroups II and III	DT II (?)
		Low-Ti and PM Fe-rich tholeiite dykes	
Second Magmatic Episode:	Group I tholeiite dykes	Fe-rich tholeiite dykes	DT II (?)
Third Magmatic Episode:	Group II and III tholeiite dykes	Subgroup 1 to 9 tholeiite dykes	DT III a, b and c
	Alkaline dykes	Alkaline dykes	Alkaline dykes

Table 9.1: (continued)

	Seitz (1991)	This Study
First Magmatic Episode:	Group I, Ia High-Mg tholeiite dykes	Group 1 High-Mg tholeiite dykes
	High-Ti Fe-rich tholeiite dykes	Group 1 Fe-rich tholeiite dykes - High-Ti subgroup
	Group II, IIa, III High-Mg tholeiite dykes; Norite ring complex	Group 2, 3 High-Mg tholeiite dykes; Norite
	Low-Ti and PM Fe-rich tholeiite dykes	Group 1 Fe-rich tholeiite dykes - Low-Ti and PM subgroups
Second Magmatic Episode:	Fe-rich tholeiite dykes	Group 2 Fe-rich tholeiite dykes
Third Magmatic Episode:	Lamprophyre dykes	Lamprophyre dykes
	Fe-rich tholeiite dykes	Group 3 Fe-rich tholeiite dykes
	Lamprophyre dykes	Lamprophyre dykes
	Fe-rich tholeiite dykes	Group 4 Fe-rich tholeiite dykes

anomalies (Seitz, 1991). Although Collerson and Sheraton (1986) originally considered the High-Mg tholeiite dykes to represent only one generation, Seitz (1991) expanded on the proposal of Kuehner (1986; 1987) that they actually represent three separate geochemical groups which cannot be simply related by crystal fractionation, crustal assimilation and/or partial melting. Geochemical differences between groups most probably reflect highly heterogeneous or different mantle source regions.

Group 1 High-Mg tholeiites (1) are E-W trending, olivine-orthopyroxene-phyric dykes. *Group 2 and 3 High-Mg tholeiites* (3) comprise NE-SW trending orthopyroxene-phyric dykes whose timing relationship is not yet understood due to a lack of visible cross-cut relationships between the two groups. Although both Group 2 and 3 High-Mg tholeiites have negative Sr anomalies, small negative Eu anomalies, and are slightly more enriched in LREE compared to Group 1 High-Mg tholeiites, Group 2 High-Mg tholeiites are geochemically distinguishable from Group 3 High-Mg tholeiites in that they are more enriched in Rb relative to Ba and K (Seitz, 1991).

A noritic ring dyke (3), recognised by Seitz (1991) in the northeastern Vestfold Hills (Figure 9.2b), was originally interpreted by Collerson et al. (1983a) as Tryne metavolcanics. It forms a semicircular complex with an average diameter of 7 to 8 kms and comprises three types of norite and associated fine-grained equivalents of the Group 2 High-Mg tholeiite dykes, with which it is therefore considered to be contemporaneous. The dominant lithology is the *Homogeneous Norite* (orthopyroxene-clinopyroxene-plagioclase), which has gradational contacts with smaller bodies of *Mottled Norite*, the latter characterised by cm-sized aggregates of plagioclase, quartz and K-feldspar. These presumably contemporaneous norites, and associated fine-grained High-Mg tholeiite dykes, are intruded by the minor *Rubbly Norite*, which is characterised by patches of bronzitic orthopyroxene, cognate and inherited xenoliths, and sulphide globules. Seitz (1991) attributed compositional differences between the three norites to orthopyroxene fractionation/accumulation, accompanied by Ni-Cu and Fe-sulphide accumulation in the case of the Rubbly Norite.

9.2.2.2 Fe-rich Tholeiite Dykes:

In general, the Fe-rich tholeiite dykes of the Vestfold Hills are characterised by lower SiO_2 (45-51 %) and MgO (4-8 %), and higher TiO_2 (1-3.5 %) and Fe_2O_3 (12-20 %) contents (based on analyses performed by Seitz, 1991) than the High-Mg tholeiite dykes. Kuehner (1986) considered the High-Mg and Fe-rich tholeiites to have been derived from different mantle source regions.

The NW-SE to E-W trending *Group 1 Fe-rich tholeiite* dykes (2 and 4), recognised by Kuehner (1986; 1987) to be contemporaneous with, but geochemically unrelated to, the High-Mg tholeiite dykes, are subdivided into three geochemical subgroups. Members of the *High-Ti(HiTi) subgroup* (2) postdate emplacement of the Group 1 High-Mg tholeiites and may be cross-cut by the Group 2 and 3 High-Mg tholeiites. The *Low-Ti (LoTi)* and *plagioclase*

megacryst-bearing (PM) subgroups (4) appear to be younger than all of the High-Mg tholeiites. Major and trace element differences between the High-Ti and Low-Ti subgroups, including the higher P, LREE and Zr, and lower TiO_2 contents of the Low-Ti dykes may be explained by open-system fractionation of a mutual source (Kuehner, 1986). Although the plagioclase megacryst-bearing subgroup may also have originated from this common parental liquid, it appears to have experienced a different P-T differentiation path than the other subgroups (Kuehner, 1986).

NW-SE trending *Group 2 Fe-rich tholeiite* dykes (5) are equivalent to the Group I dykes of Collerson and Sheraton (1986), and have a similar orientation to the Group 1 Fe-rich tholeiite dykes of this study. Due to the lack of observed dyke intersections, the relationship between the Low-Ti and plagioclase megacryst-bearing Group 1 Fe-rich tholeiites and the Group 2 Fe-rich tholeiites is poorly understood.

Younger Fe-rich tholeiite dykes in the Vestfold Hills were previously subdivided, into the Group II and III dykes of Collerson and Sheraton (1986) followed by the subgroup 1 to 9 tholeiite dykes of Kuehner (1987), on the basis of geochemistry alone. Extensive mapping of Long Peninsula dykes by Seitz (1991), however, revealed two separate generations displaying distinct orientations and a consistent cross-cut relationship, despite a lack of geochemical distinction: NNW-SSE trending *Group 3 Fe-rich tholeiite* dykes (7) are consistently cross-cut by NNE-SSW trending *Group 4 Fe-rich tholeiites* (9).

9.2.2.3 Lamprophyre Dykes:

Predominantly NNE-SSW to N-S *lamprophyre* dykes (6 and 8) both cross-cut, and are cross-cut by, the NNW-SSE Group 3 Fe-rich tholeiites. Seitz (1991) classified these compositionally variable dykes as ultramafic lamprophyres and alkaline lamprophyres, most probably derived from the melting of heterogeneous garnet lherzolite at pressures of more than 26 kbars. Ovoid-shaped, presumably pipe-like bodies, rich in ultramafic mantle- and more felsic crustal xenoliths are associated with some of the ultramafic lamprophyre dykes.

The suggestion that some lamprophyre dykes may be Phanerozoic in age (Collerson and Sheraton, 1986; Passchier et al., 1991) cannot be addressed here except to state that the only dyke known to cross-cut a Group 4 Fe-rich tholeiite dyke on Long Peninsula is a lamprophyre. This may either imply the presence of a tenth dyke generation or the approximately synchronous emplacement of at least some lamprophyre dykes (generation 8) with the Group 4 Fe-rich tholeiites (generation 9).

9.2.3 Proterozoic-Palaeozoic Thermotectonic Events:

Initial mafic dyke emplacement in the Vestfold Hills appears to have followed post-D_3,M_3 uplift. D_4,M_4 and D_5 occurred in between the emplacement of the Group 2 and Group 3 Fe-rich tholeiite dykes. The D_4,M_4 amphibolite facies event produced ductile mylonite zones, whereas D_5 resulted in sets of brittle fault-generated pseudotachylite veins (Passchier et al., 1991). The D_6,M_6 event, which produced ductile mylonite zones with

amphibolite facies mineral assemblages, postdates the intrusion of the Group 3 Fe-rich tholeiite dykes, but may be syngenetic with the emplacement of the Group 4 Fe-rich tholeiites (Passchier et al., 1991).

Garnet-bearing assemblages in dykes from the southwest Vestfold Hills are a product of amphibolite facies metamorphism (600-700° C; 6-7 kbars) peripheral to the widespread granulite facies metamorphic event at ~1100-1000 Ma within the adjacent Proterozoic complex (Collerson et al., 1983b). Passchier et al. (1991) propose that the repeated late brittle and ductile activity of D_7, evident in up to six generations of fault rock associated with and postdating emplacement of the lamprophyre dykes, is a Phanerozoic event.

An Early Palaeozoic event at ~500-600 Ma, contemporaneous with granite emplacement further south along the Prydz Bay coast, resulted in localized isotopic re-equilibration within at least some of the Vestfold Hills dykes (Collerson and Sheraton, 1986) as well as isotopic resetting within other areas of the East Antarctic Shield (Tingey, 1982; Yoshida and Kizaki, 1983) and other parts of Gondwana (Tilton, 1960).

9.3 PREVIOUS DYKE GEOCHRONOLOGY:

In an early attempt to obtain an emplacement age for the Vestfold Hills dykes, Harding and McLeod (1967) assumed that they were all produced by a single magmatic episode. They grouped together six samples collected from various dykes around the Heidemann Bay region, just south of Davis station on Broad Peninsula (Figure 9.1b), to produce a Rb-Sr whole-rock isochron age of 1030±220 Ma. This was originally regarded as an emplacement age, but now appears more likely to document isotopic resetting during ~1000 Ma granulite facies metamorphism within the adjacent Proterozoic complex.

On the basis of intrusive relationships, petrography and geochemistry, Collerson and Sheraton (1986) later subdivided the dykes into five generations (Table 9.1) which yielded Rb-Sr whole-rock isochron ages of 2424±72 Ma (High-Mg tholeiites), 1791±62 Ma (Group I tholeiites), 1374 ±125 Ma (Group II tholeiites) and 1362±108 Ma (Group II and III tholeiites). Group II and III tholeiites were therefore considered to have been derived contemporaneously from a similar mantle source region, and the conclusion was that three main episodes of mafic dyke formation occurred at approximately 2300-2400 Ma, 1800 Ma and 1200-1400 Ma, coincident with tensional periods within the relatively stable Archaean craton of the Vestfold block (Collerson and Sheraton, 1986; Sheraton et al., 1987). The Rb-Sr ages of Collerson and Sheraton (1986) were obtained by combining samples from various dykes of each of their geochemically-defined suites. As a consequence of the geographical spread of sample collection, and the probability that the samples might not have been in initial isotopic equilibrium, their data arrays were often highly scattered (MSWD as high as 323 for Group II tholeiites). The 2424±72 Ma age for the High-Mg tholeiites, in particular, is

unlikely to be meaningful because it was derived from samples of three petrographically and geochemically distinct subgroups (Kuehner, 1986).

A subsequent study by Black et al. (1991a), which applied ion microprobe U-Pb zircon dating to the problem of the Vestfold Hills dykes, demonstrated that one dyke, originally assigned to the 1374 Ma Group II tholeiite suite of Collerson and Sheraton (1986), contained 2483±9 Ma xenocrystic zircons, and reset 1025±56 Ma grains. An enclosed quartz diorite vein, of probable late magmatic origin, however, contained both xenocrystic zircon (2483±9 Ma) plus infrequent euhedral magmatic crystals that provided a precise minimum age of 1248±4 Ma for crystallisation of both the vein and enclosing dyke.

9.4 SAMPLE DESCRIPTION:

Most of the samples were collected from an area of Long Peninsula (Figures 9.1b and 9.2b) mapped in detail by Seitz (1991). Two additional samples were collected from the Brookes Hut region of Broad Peninsula (Figures 9.1b and 9.2a).

Felsic segregation veins within the dykes were sampled wherever possible. These veins range from a few mm to several cm in width, and are perpendicular to the margins of their host dykes. They vary greatly in abundance both within and between the various dyke suites and are intermediate (tonalitic to dioritic) in composition. The relatively sharp contacts between the felsic and mafic dyke components, the presence of en echelon structures within the veins, and the fact that they do not extend beyond the dyke margins, suggests that these felsic components are the result of late stage magmatic crystallisation within cooling cracks in the dykes.

If late-stage felsic segregations were not found within a particular dyke suite, large mafic dyke samples were collected to ascertain the presence or absence of magmatic baddeleyite (monoclinic ZrO_2), used by other workers (Davidson and van Breeman, 1988; LeCheminant and Heaman, 1989) for U-Pb dating of mafic igneous rocks. Baddeleyite is preferred for U-Pb dating because it usually provides more concordant results than zircon and its scarcity in crustal rocks means that inheritance is uncommon (LeCheminant and Heaman, 1989; Heaman and Parrish, 1991). High SiO_2 activity within the magma during the late stages of dyke crystallisation would have prevented the crystallisation of primary baddeleyite (Heaman and Parrish, 1991) and therefore the absence of baddeleyite from the felsic veins was to be expected. As no baddeleyite was detected in heavy mineral concentrates from the mafic dykes, dating of segregation-deficient dykes, the Group 1 and 3 High-Mg tholeiites, the Group 1 Fe-rich tholeiites and the lamprophyre dykes, which could only be attempted on the few zircons they contain, was often unsuccessful.

Of the twenty-nine samples examined for zircons and/or baddeleyite, only the fifteen which yielded zircons suitable for isotopic analysis will be discussed in detail. A list of sample localities is given in Appendix 1 (Table A1.3).

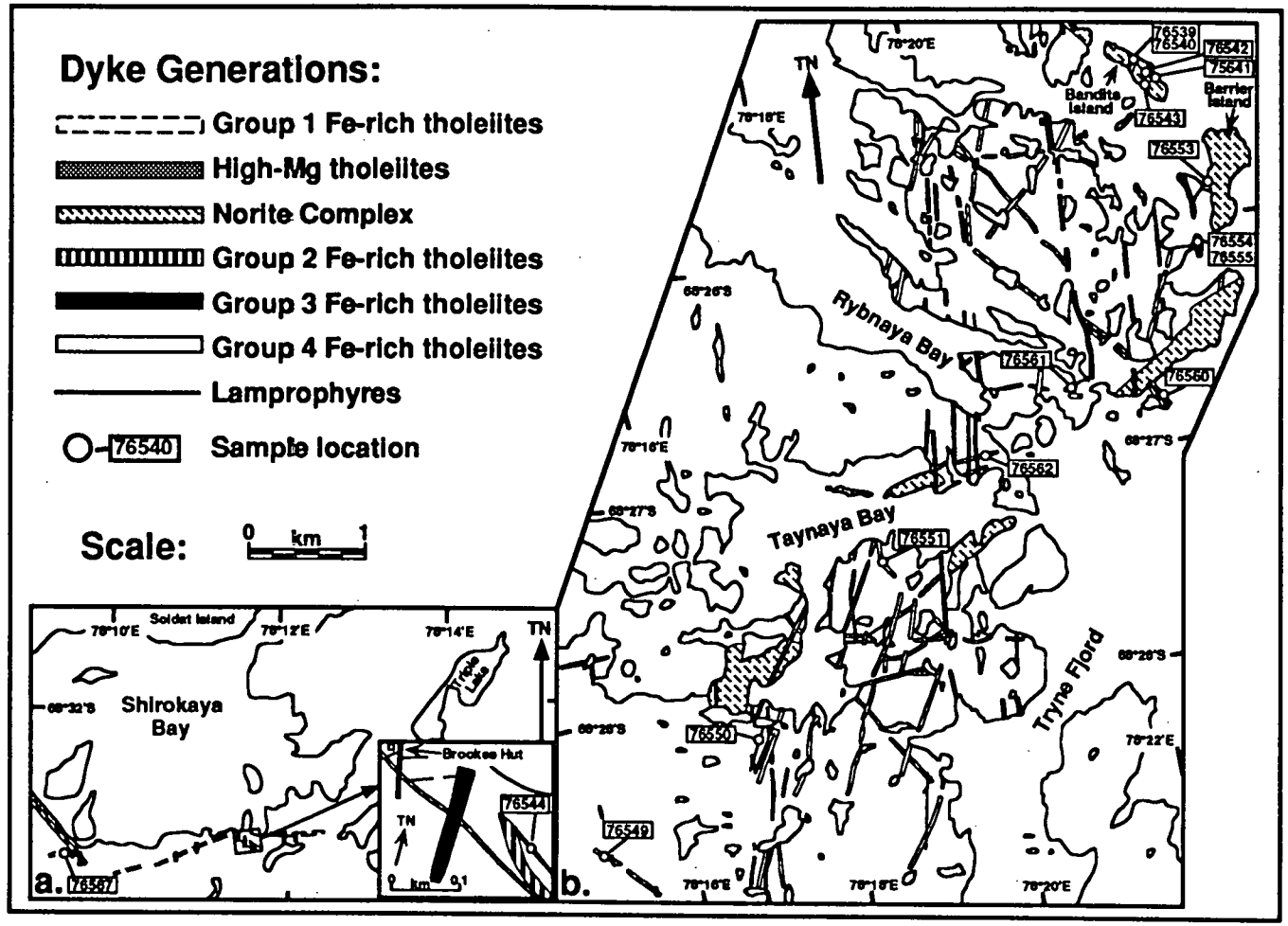

Figure 9.2: Maps of a) the Brookes Hut area of Broad Peninsula; and b) the Long Peninsula region, showing sample locations discussed in the text. Only representative dykes of each generation are shown.

9.4.1 High-Mg Tholeiite Dykes:

Two High-Mg tholeiite dyke samples collected from Long Peninsula were used in an attempt to ascertain the age of this suite. Felsic segregations are rare within these dykes and those sampled were found to contain no zircons. Sample 76562 is from a 10 m wide approximately E-W striking (082°) dyke crosscut further to the west by several Group 3 Fe-rich tholeiite dykes. The dyke itself belongs to the oldest olivine-orthopyroxene-phyric Group 1 High-Mg tholeiite suite. It has a porphyritic to glomeroporphyritic texture comprising anhedral to subhedral phenocrysts and glomerocrysts of orthopyroxene, often rimmed with clinopyroxene and with an average grainsize of 2-3 mm, plus less abundant anhedral remains of olivine phenocrysts (~5 %) rimmed with orthopyroxene. Clinopyroxene forms both microphenocrysts and groundmass crystals accompanied by plagioclase (andesine) laths and Fe-oxides. Minor groundmass phases include apatite and biotite.

Sample 76561 was collected from an E-W striking (093° strike at the site of collection) 2.5 m wide High-Mg tholeiite dyke east of Rybnaya Bay on Long Peninsula. Outcrop of this dyke terminates just short of a region of Homogeneous Norite outcrop. Although it cannot be traced into the norite, this represents one of the fine-grained Group 2 High-Mg tholeiite dykes associated with it This dyke is characterised by abundant anhedral orthopyroxene, up to 2 mm across, with narrow rims of clinopyroxene and subophitic inclusions of dusty plagioclase. Finer-grained phases include orthopyroxene, plagioclase, biotite, clinopyroxene, Fe-oxides, myrmekitic quartz-feldspar intergrowths and minor apatite.

9.4.2 Group 1 High-Ti Fe-rich Tholeiite Dykes:

Sample 76567 was collected from a NE-SW striking (067°) first generation Fe-rich tholeiite dyke west of Brookes Hut on Broad Peninsula. This sample included part of a thin tapering felsic vein with a maximum width of 3-4 mm which extended for ~1 m into the 8 m wide dyke from, and normal to, its southeastern margin. Felsic veins are rare within this dyke suite and where found they are so thin that both sample collection and separation of the vein from the mafic dyke is extremely difficult.

The medium-grained dyke sample, with an average grainsize of 0.5 to 1.5 mm, comprises abundant anhedral dusty plagioclase (andesine), orthopyroxene and clinopyroxene crystals. The two pyroxenes are often in close association and commonly have alteration rims of biotite, green amphibole and coarse Fe-oxides. Apatite needles are a relatively abundant accessory phase.

9.4.3 Homogeneous Norite:

The Homogeneous Norite is a medium- to coarse-grained, granular rock dominated by cumulus anhedral orthopyroxene (25-30 %) with external rims of amphibole, chlorite, biotite and Fe-oxides that are particularly pronounced immediately adjacent to felsic

segregation veins. Inverted pigeonite may also form a partial or complete internal rim around orthopyroxene. Abundant dusty plagioclase (andesine 30-40 %), minor clinopyroxene (~10 %) and partly chloritised and ragged biotite (~5 %), with elongate Fe-oxide inclusions or lamellae, occur as intercumulus phases. Late granophyric intergrowths of alkali feldspar and plagioclase (~5 %) often partially surround coarser-grained plagioclase near the dyke-vein contact. Accessory minerals include fine apatite needles and scattered Fe-oxides.

Felsic veins are common within the Homogeneous Norite on Barrier, Bandits, and other more westerly islands. Those on Bandits Island generally strike at 055-065° and dip 50-60° NW. Although felsic vein orientations within the Homogeneous Norite in other areas of the Vestfold Hills are more varied (trending between 043° and 087° on Barrier Island for instance), they are still generally perpendicular to the orientation of the norite at each location, reflecting the variation in the orientation of cooling cracks that could be expected within this ring complex. Three felsic segregation veins within the Homogeneous Norite on Bandits Island were sampled. Other felsic bodies within the norite, including irregular- and mushroom-shaped structures, were not sampled for dating.

Sample 76541, collected from a 15 cm wide felsic vein extending obliquely across a cliff face on the northern side of Bandits island (Figure 9.3a), is composed predominantly (79 %) of fine- to medium-grained plagioclase (andesine-oligoclase) and undulose quartz with irregular intergrown grain boundaries and an average grainsize of 0.5 to 1 mm. Abundant kinked plagioclase and finely recrystallised quartz reflect post-crystallisation deformation. Other phases, often forming fine-grained crystal aggregates, include pyroxene (18 %, predominantly clinopyroxene), biotite (<1 %), sphene (<1 % - often intimately associated with ilmenite), apatite (<1 %), alkali feldspar (1 %) and fine Fe-oxides (3 %). Intergrown sphene and ilmenite are also common within the dyke immediately adjacent to the felsic vein. The norite-vein contact is sharp and well-defined (Figure 9.4a), particularly on a macro-scale, although pyroxene and plagioclase crystals protrude into the vein from the norite. This feature, characteristic of all the various late-stage segregation samples, indicates that crystallisation or recrystallisation within the mafic host rock was concurrent with crystallisation of felsic material within the cooling cracks.

Sample 76542 is from a 25 m long felsic vein in the centre of Bandits Island (Figure 9.3b) crosscut by several discrete alkaline dykes. This vein, with an average width of 2 cm and a strike of 057°, has a granular, felsic (89 %) consertal texture dominated by fine- to medium-grained plagioclase (andesine-oligoclase) and quartz. Deformed plagioclase crystals plus branching bands and elongate domains of finely recrystallised quartz are common parallel to the vein margin, giving this sample a more sheared texture than that of sample 76541. Fine-grained mafic crystal aggregates, up to 1 mm in diameter, are dominated by clinopyroxene (5 %) and Fe-oxides (4 %). Biotite (1 %), apatite (1 %), sphene (<1 %), carbonate (<1 %) and perthite are minor phases.

Sample 76543 is from a felsic vein immediately adjacent to Bandits Hut. This 35 m long vein varies in width from 3 mm to 3 cm, trends towards 065°, and tapers to a fine point at

each end. It is also dominated (84 %) by deformed plagioclase (andesine-oligoclase) and medium-grained plus finely recrystallised quartz. Grain boundaries of the felsic minerals are irregular and intergrown. Mafic phases include biotite (<1 %), clinopyroxene (10 %), Fe-oxides (2 %) and intergrown sphene and ilmenite (<1 %). Fe-oxides occasionally form distinctive trellis structures. Alkali feldspar (4 %) and apatite (<1 %) are minor constituents.

9.4.4 Mottled Norite:

The Mottled Norite, a medium-grained orthocumulate with similar mineralogy to the Homogeneous Norite, is distinguished predominantly by large, evenly distributed, glomerocrysts of granophyric quartz and feldspar (Seitz, 1991), and bytownite rather than andesine plagioclase compositions. It occurs as a 70 m wide central east-west band within the Homogeneous Norite on Barrier Island.

Felsic segregations are less common within the Mottled Norite than within the Homogeneous Norite, and tend to be more irregular in shape with less well defined host rock contacts. Thin mm-wide late quartz veins crosscut both the Mottled Norite and the felsic segregations, often at right angles to the latter and extending for several metres through the norite.

A felsic segregation vein (sample 76553) within the Mottled Norite on Barrier Island has a strike of 020° and a variable width of up to 10 cm (Figure 9.3c). The felsic component (72 %) has a fine-grained, anhedral granular texture dominated by quartz and labradorite (plus minor alkali feldspar with irregular interlocking grain boundaries) with an average grainsize of 0.2 mm. Dominant mafic phases (20 %) (Figure 9.4b) include clinopyroxene (probably aegerine-augite) and fibrous amphibole (altered pyroxene) with fine zircon inclusions. Minor phases include Fe-oxides (6 %) biotite (<1 %), sphene (<1 %) and apatite (1 %). Within the felsic vein, fine bands rich in mafic minerals are interspersed with coarser-grained plagioclase and parallel the norite-vein contact, emphasizing its poorly defined nature (Figure 9.4c), and implying that norite crystallisation was incomplete at the time of felsic melt infiltration.Volatile activity associated with the formation of the felsic vein apparently resulted in hydration of immediately adjacent norite and the formation of abundant intergrown, medium-grained biotite and light green amphibole, similar to that within the vein itself. Very minor fibrous blue-green amphibole is also due to the uralitisation of pyroxene.

9.4.5 Group 2 Fe-rich Tholeiite Dykes:

Sample 76549 was collected from a NW-SE striking Group 2 Fe-rich tholeiite dyke located toward the southwest of Long Peninsula, and crosscut by two Group 3 Fe-rich tholeiite dykes near the sampling site. This dyke comprises abundant medium-grained dusty plagioclase (labradorite-andesine) subophitically enclosed by pyroxene (predominantly clinopyroxene), the latter altering to a combination of green amphibole, biotite and ilmenite.

Sample 76551 was collected from a sinuous NW-SE striking dyke characterised by a relatively shallow and variable dip of 30-40° NE, crosscut by later N-S striking lamprophyre dykes. This dyke is finer-grained than sample 76549, comprising anhedral clinopyroxene and orthopyroxene interspersed with interlocking ragged plagioclase (labradorite-andesine) laths. Biotite, amphibole and Fe-oxides form patches and rims of alteration associated with pyroxene. Apatite and myrmekite are present in minor amounts. Coarser-grained plagioclase crystals, up to 1 mm, may be kinked and partly surrounded by myrmekite.

A felsic segregation vein (sample 76560) within an 8 m wide steeply dipping Group 2 Fe-rich tholeiite dyke on Long Peninsula has an average thickness of 0.5 to 1.5 cm and extends from one chilled dyke margin to the other. The dyke itself is very similar petrographically to sample 76549. The felsic segregation has a sheared texture (Figure 9.4d) dominated by finely recrystallised quartz, and slightly coarser-grained irregular-shaped undulose quartz and plagioclase (84 % felsic minerals). Quartz-feldspar granophyre dominates the irregular vein-dyke contacts, which are paralleled by thin wispy bands of ragged biotite (14 %) throughout the vein. Sphene (<1 %), apatite (<1 %) and Fe-oxides (2 %) are also present. Uralitisation of pyroxene in the dyke is most pronounced within a few mm of the vein margin.

A WNW-ESE (110° strike) Group 2 Fe-rich tholeiite dyke adjacent to Brookes Hut on Broad Peninsula projects two mylonitised "horns" into the country rock. These linear projections parallel each of the dyke margins and are crosscut by NW-SE striking (160°) Fe-rich tholeiite dykes. Sample 76544, collected from the northernmost "horn", comprises alternating mm-wide felsic and mafic layers. Felsic bands are dominated by very fine, recrystallised, ribbon-like quartz with thin wisps of biotite parallel to layering. Scattered apatite, Fe-oxides and patches of carbonate are also present. Mafic layers consist of abundant very fine-grained hornblende (probably altered clinopyroxene), minor biotite, quartz, garnet and ilmenite. Scattered, coarser quartz and feldspar grains are anhedral and slightly strained.

9.4.6 Lamprophyre Dykes:

Sample 76550 was collected from a 0.5 m wide, approximately N-S (173°) striking alkaline dyke just south of Taynaya Bay on Long Peninsula. This dyke is crosscut by a NW-SE striking Fe-rich tholeiite dyke and therefore predates the intrusion of the Group 3 Fe-rich tholeiites. It falls into the olivine-poor (Delor and Rock, 1991) alkaline lamprophyre (Seitz, 1991) category and has a porphyritic texture, with subhedral oscillatory zoned phenocrysts of brown clinopyroxene up to 2 mm long. The texture is also slightly glomeroporphyritic due to occasional aggregates of coarse-grained clinopyroxene. Ocelli of carbonate and sieve-textured alkali feldspar are common and may also contain clots of fine-grained light green amphibole. Biotite, ilmenite and brown clinopyroxene comprise the fine- to medium -grained groundmass.

No felsic segregations were located in any of the alkaline dykes examined on Long Peninsula.

9.4.7 Group 3 Fe-rich Tholeiite Dykes:

Group 3 Fe-rich tholeiite dykes comprise medium- to coarse-grained, dusty brown labradorite-andesine laths subophitically enclosed by either single crystals or glomerocrysts of fine- to medium-grained anhedral to subhedral, commonly twinned, clinopyroxene. Some fine crystals of plagioclase are completely enclosed within pyroxene. Alteration rims around clinopyroxene include biotite, chlorite, green amphibole and coarse-grained ilmenite, and are most pronounced adjacent to the felsic segregation veins.

Sample 76554 was collected from an 037° striking felsic vein within a 12-15 m wide, 143° striking dyke on Long Peninsula, just southwest of Barrier Island. Both the dyke and the vein are crosscut by a younger, approximately N-S oriented, dyke (Figure 9.3d). The vein itself extends across the width of the dyke and ranges in thickness from <2 mm to 2 cm. It is dominated (90 %) by feldspar and quartz, the latter occurring as either medium-grained undulose interlocking grains or finely recrystallised domains, giving the rock a sheared texture. Common granophyric intergrowths of quartz and feldspar often surround andesine laths and dominate the vein-dyke contact. Scattered ragged biotite crystals (9 %), with abundant zircon inclusions, generally form thin elongate bands parallel to the dyke-vein contact. Minor phases include carbonate (<1 %, may enclose fine-grained biotite), apatite needles (1 %), Fe-oxides (<1 %) and sphene (<1 %).

Sample 76555, from a 3 cm wide vein within the same dyke (Figure 9.3e), was collected 10 m NNE of the previous sample. It is similar in terms of both field occurrence and petrography, but more commonly contains granophyric intergrowths of quartz and feldspar, often surrounding and/or radiating out from andesine crystals, and once again dominating the dyke-vein contact (Figure 9.4e). Coarser-grained euhedral apatite (1 %) plus minor amphibole (<1 %) intergrown with biotite (8 %) are also present.

9.4.8 Group 4 Fe-rich Tholeiite Dykes:

Group 4 Fe-rich tholeiite dykes have a medium-grained doleritic texture characterised by dusty brown plagioclase laths (labradorite-andesine) subophitically enclosed by 0.5 to 1 mm sized clinopyroxene crystals. The latter have alteration rims of amphibole, chlorite and biotite. Plagioclase glomerocrysts, of up to 8 mm, are scattered through the dyke. Ilmenite is often associated with alteration minerals, especially biotite, with which it is sometimes intergrown, particularly adjacent to the dyke-vein contact. Apatite needles are relatively rare.

Linear felsic segregations are common within a 15 m wide NNE-SSW (023°) striking dyke on Bandits Island, occurring at regular intervals of 4-5 m, and occasionally even less than 1 m. Sample 76540 was collected from one such segregation of variable width (2 mm to 3 cm) (Figure 9.3f), which extends from inside the eastern dyke margin to within 0.5 m of the

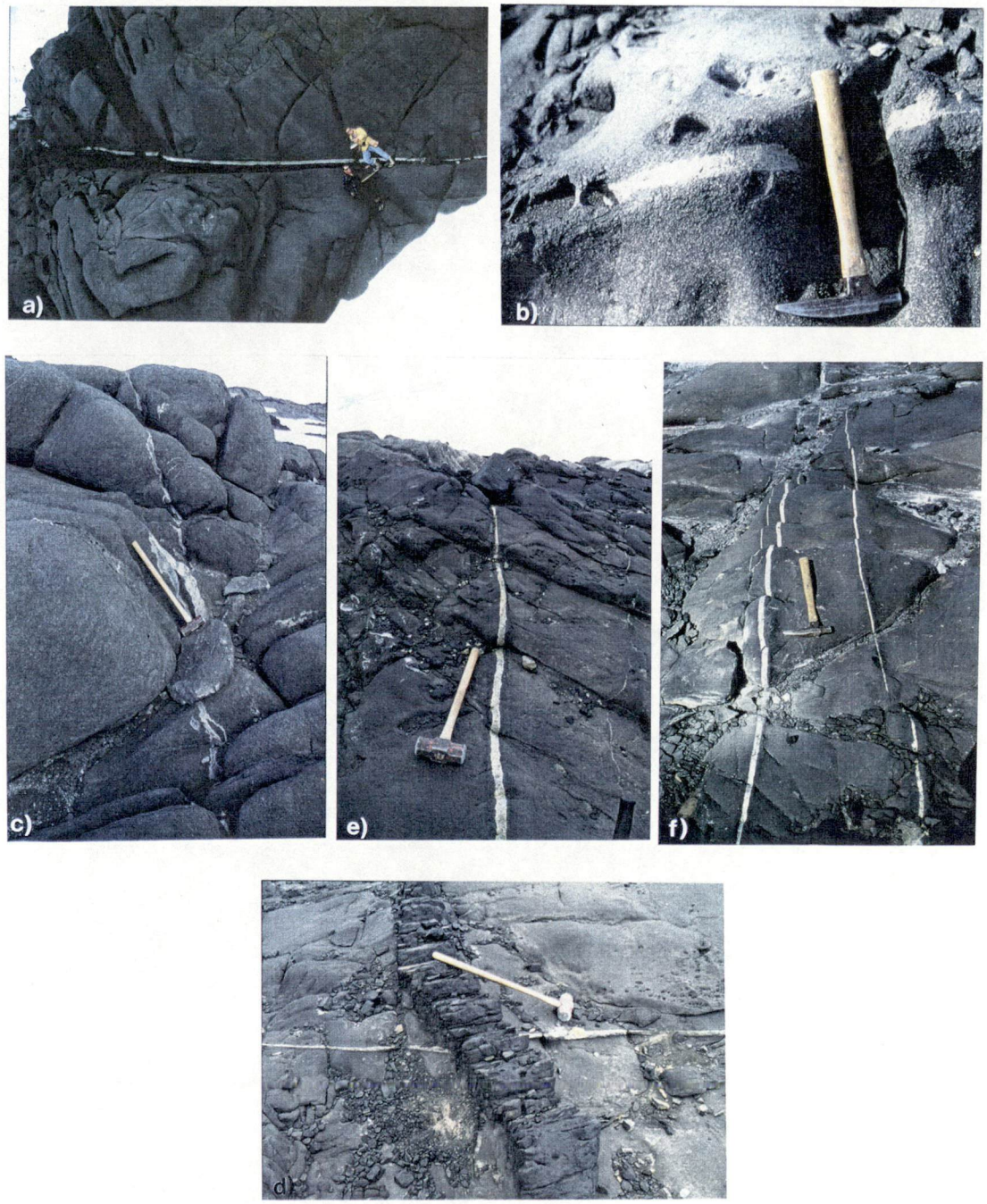

Figure 9.3: Sampling sites for the felsic segregation veins used in this study: a) & b) Samples 76541 and 76542 (respectively) crosscut the Homogeneous Norite on Bandits Island; c) Sample 76553 extends through the Mottled Norite of Barrier Island; d) & e) Samples 76554 and 76555 (respectively) were collected from a single Group 3 Fe-rich tholeiite dyke in the northeast of Long Peninsula. A Group 4 Fe-rich tholeiite dyke is shown crosscutting sample 76554; and f) Sample 76540 (left) is one of many felsic veins within a Group 4 Fe-rich tholeiite dyke located on Bandits Island.

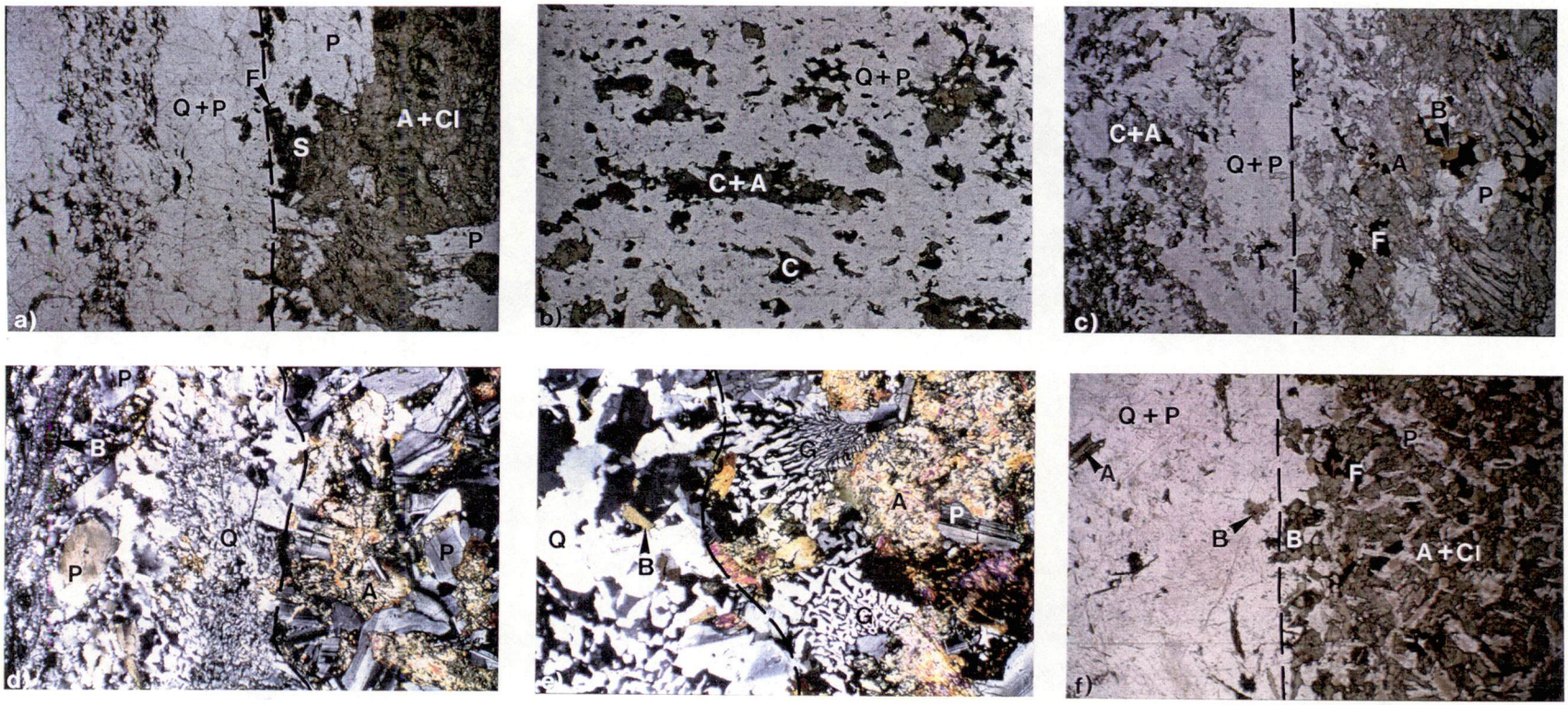

Figure 9.4: Photomicrographs of: a) the well-defined dyke (right)-vein (left) contact of sample 76541 from the Homogeneous Norite; b) mafic aggregates within the felsic segregation vein of sample 76553 from the Mottled Norite; c) the dyke (right)-felsic vein (left) contact of sample 76553 from the Mottled Norite, paralleled by fine bands of mafic aggregates within the felsic vein; d) the more irregular dyke (right)-vein (left) contact within the Group 2 Fe-rich tholeiite sample 76560 showing the sheared texture of the felsic segregation (crossed polars); e) the quartz-feldspar granophyre-dominated dyke (right)-felsic vein (left) contact of Group 3 Fe-rich tholeiite sample 76555 (crossed polars); and f) the sharp contact between the felsic vein (left) and enclosing dyke (right) of Group 4 Fe-rich tholeiite sample 76540. Approximate dyke-vein contacts are indicated by broken lines. Mineral abbreviations: Q = quartz; P = plagioclase; A = amphibole; B = biotite; C = clinopyroxene; G = granophyre; Cl = chlorite; F = Fe-oxide; S = sphene; Scale: 9 mm = 1 mm in all photos except b) where 9 mm = 0.5 mm.

western margin. Although it has numerous "steps" and "branches", dyke-vein contacts are always sharp and well-defined. The segregation vein comprises medium- to coarse-grained quartz and plagioclase (andesine) plus abundant granophyric intergrowths of quartz and feldspar (86 % felsic minerals). Mafic phases include green amphibole (3 %) which appears to be a product of pyroxene uralitisation and is often associated with fibrous chlorite (7 %), sphene (2 %) and ilmenite (<1 %) intergrowths, and lesser biotite (<1 %). Mafic aggregates range up to 3 mm across. Alkali feldspar and apatite needles (2 %) are minor constituents. Immediately adjacent to the felsic vein the dyke is extensively altered, with clinopyroxene crystals completely replaced by chlorite and amphibole. There is also a marked increase in the abundance of biotite (Figure 9.4f).

9.5 GEOCHEMISTRY OF THE FELSIC SEGREGATION VEINS:

The major and trace element geochemistry of the felsic segregation veins and their host dykes are presented in Table 9.2. The felsic veins are interpreted to be the differentiated products of the mafic dykes, formed when cooling cracks were infilled by interstitial melt drawn from the largely crystallised mafic dykes. The melt drawn into the cracks was probably in equilibrium with the crystallising phases, orthopyroxene and/or clinopyroxene and plagioclase, within the mafic dykes at the time of vein formation. Isolation of the melt and its progressive crystallisation in the cracks resulted in SiO_2 enrichment and the crystallisation of phases including quartz and plagioclase. Enrichment of the residual melt in incompatible components and volatile phases such as water resulted in the late-stage crystallisation of biotite and amphibole, due in part to reactions involving earlier formed pyroxenes, such as:

$$CaMgSi_2O_6 + CaAl_2Si_2O_8 + 3MgSiO_3 + H_2O = Ca_2(Mg_4Al)(Si_7AlO_{22})(OH)_2 \quad (1)$$

(clinopyroxene + plagioclase + orthopyroxene + water = amphibole)

$$3MgSiO_3 + KAlSi_3O_8 + H_2O = KMg_3(Si_3AlO_{10})(OH)_2 + 3SiO_2 \quad (2)$$

(orthopyroxene + K-feldspar + water = biotite + quartz)

The comparative chemistry of the veins and their host dykes (Table 9.2; Figure 9.5) is supportive of the idea that the felsic veins represent late stage differentiates. The veins are depleted in V, Sc, Ni and Cr, all of which are compatible elements with respect to the liquidus phases present in the dykes at the time of vein formation. Although they are also generally enriched in incompatible elements relative to their host dykes, as would be expected from the crystallisation of late-stage melt, there are some relative incompatible element depletions in the veins which require explanation, most probably by late-stage fluid loss.

Table 9.2: Major and trace element geochemistry of all mafic dyke and felsic vein samples which yielded zircons for ion microprobe analysis. Details of XRF analysis, using the Philips PW 1410 spectrometer, are outlined in Appendix 2. Due to a high Br content (450 ppm), which interfered with the XRF analysis of both U and Th, no U value is available for sample 76560 and its Th content (10 ppm) is only an approximate value.
Mg# = 100 atomic Mg/(Mg + Fe*) where FeO* = FeO + (0.89984 x Fe_2O_3); Fe_2O_3/FeO = 0.15 for the mafic dyke CIPW normative calculations; LOI = Loss on Ignition; (MS) after corresponding analysis sample numbers indicates that the geochemical results presented here were performed by Seitz (1991); corresponding samples are housed in the Geology Department, University of Tasmania rock collection.

Sample No:	**76562**	**76567**	**76561**		**76541**	**76542**	**76543**		**76553**	**76549**
Sample:	Group 1 High-Mg tholeiite	Group 1 High-Ti Fe-rich tholeiite	Group 2 High-Mg tholeiite	Homogeneous Norite	Segregation vein	Segregation vein	Segregation vein	Mottled Norite	Segregation vein	Group 2 Fe-rich tholeiite
Corresponding analysis (MS):	71874 (MS)	71853 (MS)	70709 (MS)	70801 (MS)				70755 (MS)		71964 (MS)
Major Elements (wt %):										
SiO_2	52.69	50.31	55.92	55.14	64.92	66.85	66.76	56.44	69.04	49.33
TiO_2	0.72	1.54	0.74	0.52	0.62	0.43	0.29	0.56	2.08	2.23
Al_2O_3	8.68	14.75	13.00	11.12	17.37	18.44	18.37	8.22	13.41	12.95
Fe_2O_3	12.04	14.84	11.39	12.42	3.88	2.17	2.10	11.91	4.84	15.82
FeO	0.00	0.00	0.00	0.00	0.00	0.00	0.00	0.00	0.00	0.00
MnO	0.18	0.20	0.17	0.19	0.05	0.04	0.04	0.17	0.04	0.24
MgO	12.52	4.55	7.56	11.00	0.93	0.60	0.65	15.27	1.65	5.80
CaO	9.10	9.72	7.93	7.45	2.45	2.59	1.72	5.18	4.74	9.94
Na_2O	1.95	2.57	1.72	1.71	8.81	8.15	9.80	1.06	3.29	2.36
K_2O	0.82	0.45	1.33	0.96	0.11	0.13	0.13	1.01	0.21	0.60
P_2O_5	0.12	0.33	0.13	0.09	0.17	0.26	0.07	0.10	0.31	0.24
LOI	0.65	0.06	0.16	-0.06	0.15	0.52	0.42	0.32	0.19	-0.39
Total	99.47	99.32	100.05	100.54	99.46	100.18	100.33	100.24	99.79	99.12
Mg#	67.31	37.78	56.79	63.69	32.19	35.38	37.82	71.74	40.33	42.06
FeO*	10.83	13.35	10.25	11.18	3.49	1.95	1.89	10.72	4.35	14.24
Trace Elements (ppm):										
Ba	286	155	292	202	168	299	144	212	475	166
Rb	31	13	72	40	2	2	2	44	19	27
Nb	3	7	6	5	15	10	13	9	21	12
Sr	214	145	115	98	134	211	156	69	202	148
Zr	72	130	122	78	251	165	231	89	249	172
Y	15	44	22	14	24	12	20	17	40	52
La	10	12	22	14	53	27	47	15	47	16
Ce	22	27	42	28	95	43	77	28	100	37
Nd	12	20	19	12	34	15	26	13	42	24
Ni	323	64	199	253	8	7	6	416	36	61
Cr	1358	88	524	836	16	6	7	1634	21	145
V	233	286	221	215	56	27	21	197	209	428
Sc	36	38	34	35	6	5	3	29	16	50
Pb	6	3	14	10	4	5	6	11	25	4
Th	3	4	12	6	14	14	21	11	16	7
U	2	<1.5	4	2	3	2	2	<1.5	7	2

Table 9.2: (continued)

Sample No:	76551	76544	76560	76560	76550	76554	76554	76555	76540	76540
Sample:	Group 2 Fe-rich tholeiite	Mylonitised Group 2 Fe-rich tholeiite	Group 2 Fe-rich tholeiite	Segregation vein	Lamprophyre	Group 3 Fe-rich tholeiite	Segregation vein	Segregation vein	Group 4 Fe-rich tholeiite	Segregation vein
Corresponding analysis (MS):	71912 (MS)		71975 (MS)						71979 (MS)	
Major Elements (wt %):										
SiO_2	52.06	70.44	50.81	69.34	41.50	49.52	74.59	74.22	49.54	74.41
TiO_2	1.64	0.55	1.17	0.36	4.94	0.84	0.20	0.18	1.33	0.53
Al_2O_3	13.70	12.82	14.46	13.01	7.75	13.69	13.12	13.35	14.53	13.10
Fe_2O_3	15.49	4.23	13.54	3.61	13.79	11.35	1.94	2.15	12.42	1.83
FeO	0.00	0.00	0.00	0.00	0.00	0.00	0.00	0.00	0.00	0.00
MnO	0.23	0.06	0.20	0.05	0.16	0.18	0.04	0.03	0.20	0.03
MgO	4.89	1.29	6.98	1.39	14.20	7.90	0.66	0.62	7.70	0.79
CaO	9.47	4.48	10.84	4.70	8.63	12.70	1.94	1.90	11.91	3.40
Na_2O	2.55	3.38	2.11	4.61	1.89	1.87	3.96	4.01	1.90	4.70
K_2O	0.77	0.62	0.17	0.75	3.98	0.24	2.77	2.69	0.35	0.15
P_2O_5	0.17	0.10	0.09	0.08	0.64	0.06	0.06	0.06	0.13	0.13
LOI	-0.27	1.75	-0.40	1.80	2.42	0.08	0.45	0.36	0.11	0.50
Total	100.70	99.70	99.97	99.68	99.90	98.43	99.69	99.56	100.12	99.57
Mg#	38.47	37.65	50.52	43.17	67.10	57.95	40.32	36.35	55.11	46.09
FeO*	13.94	3.81	12.18	3.25	12.41	10.21	1.74	1.93	11.18	1.65
Trace Elements (ppm):										
Ba	167	211	49	454	1262	52	1203	1754	127	186
Rb	39	19	5	28	106	7	24	24	14	2
Nb	8	9	4	9	79	3	9	7	8	13
Sr	146	179	104	215	897	124	173	183	158	212
Zr	123	165	70	149	419	50	200	208	90	223
Y	37	13	26	10	25	20	17	15	30	21
La	15	28	3	65	57	5	71	74	10	44
Ce	30	49	10	119	135	<5	127	138	22	84
Nd	20	16	9	37	67	7	44	48	14	31
Ni	26	16	95	27	503	65	7	16	88	4
Cr	24	17	201	21	663	215	4	5	378	7
V	359	75	361	68	284	295	24	28	306	45
Sc	46	9	50	10	20	49	4	4	51	6
Pb	6	6	2	9	14	2	9	2	3	20
Th	7	5	2	10	8	2	15	2	4	17
U	2	2	<1.5	-	2	1.5	2	1.5	<1.5	4

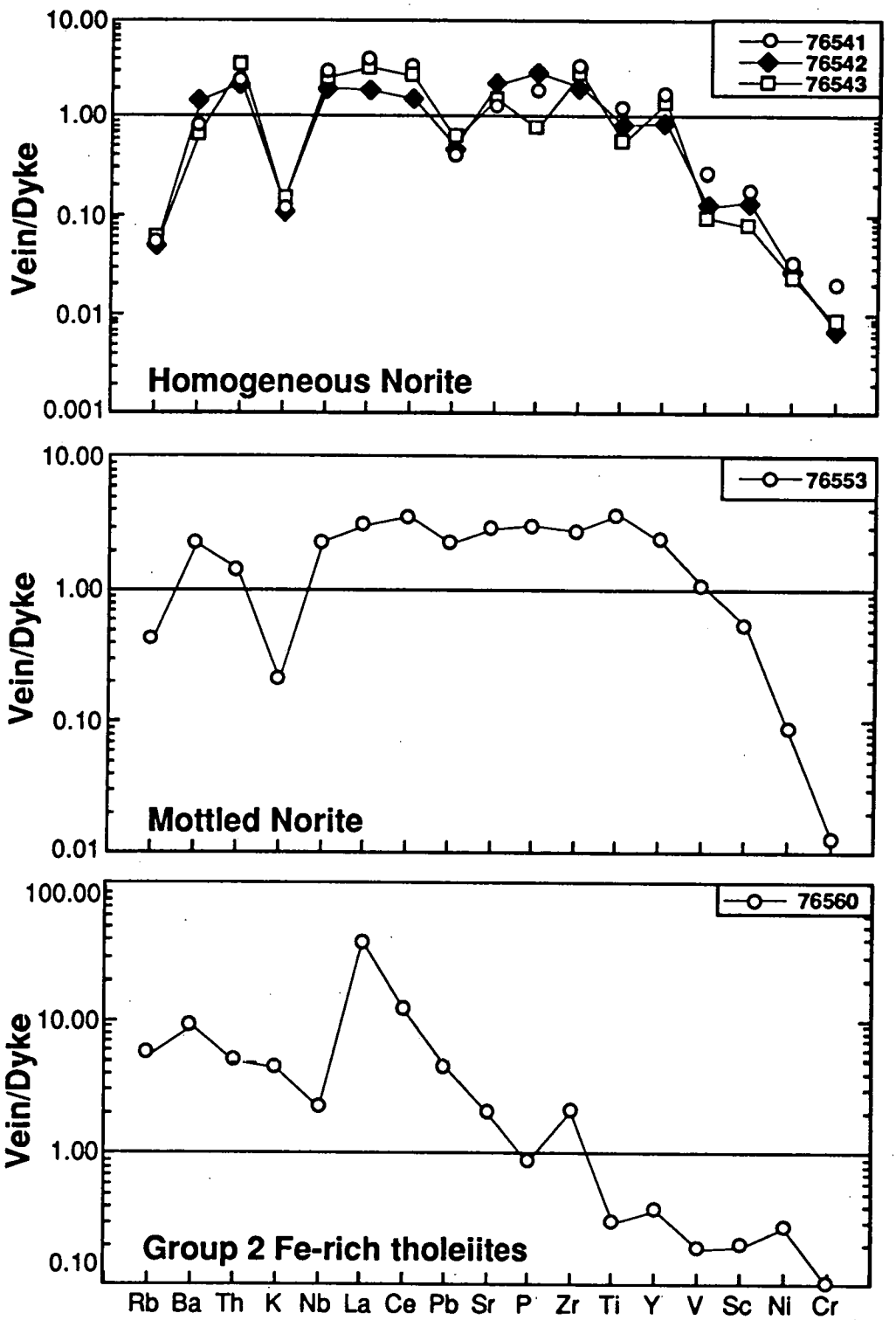
10.00
1.00
0.10
0.01
0.001
Vein/Dyke
76541
76542
76543
Homogeneous Norite
10.00
1.00
0.10
0.01
Vein/Dyke
76553
Mottled Norite
100.00
10.00
1.00
0.10
Vein/Dyke
76560
Group 2 Fe-rich tholeiites
Rb Ba Th K Nb La Ce Pb Sr P Zr Ti Y V Sc Ni Cr

(Figure 9.5)

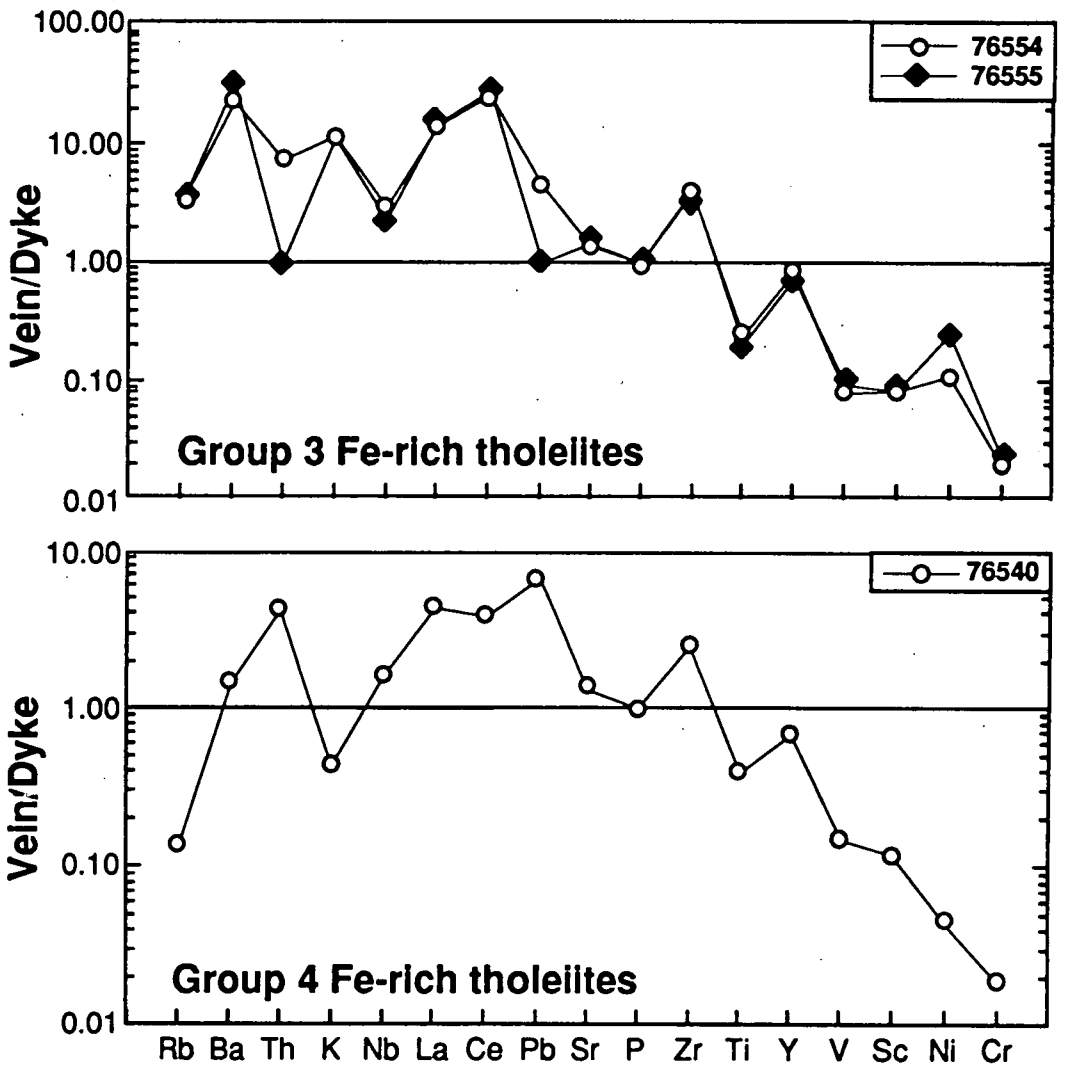

Figure 9.5: Trace element abundance patterns for the various late stage felsic segregation veins normalised to the relative abundances in the host dykes (data from Table 9.2).

The reaction of water-rich melt/fluid with the walls of the segregation veins can explain both the relative deficiency of certain incompatible elements in the veins and the occurrence of abundant hydrous and other late-stage mineral phases immediately adjacent to the dyke-vein contacts. The late-stage growth of biotite and amphibole in the wall-rocks adjacent to the segregation veins, the latter occurring mainly as a product of pyroxene alteration (equation 1), may account for relative Rb and K depletion within the segregation veins in all dyke generations. Slight Ba depletion in some segregation veins could also be attributable to biotite crystallisation. Abundant ilmenite, often intergrown with sphene and/or biotite at the dyke-vein contacts, could account for the relative Ti depletion of many segregations, except for those in the Mottled Norite. Late crystallisation of accessory apatite, also observed in the region of the dyke-vein contact, may have caused relative depletions of P in all dyke generations, and possibly Y depletion in the Fe-rich tholeiites. Alternatively, apatite crystallisation in the dykes prior to, and at the time of, vein formation may have been responsible for the removal of elements such as P and Y from the melt. Likewise, Th and Pb depletion, in segregation vein sample 76555 for example, plus Pb depletion in the Homogeneous Norite segregations could be related to sphene crystallisation. However, Pb and Ba depletion in the latter may also be related to the late-stage development of plagioclase - K-feldspar intergrowths representing late-stage exsolution textures within the norite immediately adjacent to the contact.

It should be noted that the separation of felsic vein material for analysis required that material immediately adjacent to the dyke-vein contact be discarded in order to avoid wall-rock contamination. This sampling bias may be responsible for some of the measured incompatible element depletions as the peripheral vein material is often dominated by very late-stage crystallisation products.

In summary, the petrology and geochemistry of the felsic veins, which occur within several generations of the Vestfold Hills dykes, is consistent with their derivation from the surrounding mafic magma. Primary magmatic zircons within the segregation veins therefore yield minimum ages for dyke crystallisation.

9.6 ISOTOPIC RESULTS:

Table 9.3 contains ^{204}Pb-corrected data for all analysed zircons. Errors associated with the $^{207}Pb/^{206}Pb$ ratios in Table 9.3 are the products of counting statistics, and are underestimated in certain cases, most notably in zircons with high U contents. Errors associated with the mean $^{207}Pb/^{206}Pb$ ages presented in the concordia diagrams (Figure 9.7) and text are the result of weighted mean calculations. Free-line regressions, performed on data sets used to derive dyke emplacement ages, all passed within error of the zero point of concordia indicating that any Pb loss occurred only in recent times, and that the samples

Table 9.3: Ion microprobe U-Th-Pb zircon data; SHRIMP analytical methods are described in Appendix 2.
Note: @ represents data excluded from the mean $^{207}Pb/^{206}Pb$ emplacement age calculations; # refers to data included in the mean $^{207}Pb/^{206}Pb$ xenocryst age calculation; * refers to xenocryst data excluded from the mean xenocryst age calculation; f_{206} is the proportion of common ^{206}Pb to total ^{206}Pb.

Grain area	U (ppm)	Th (ppm)	Th/U	$^{206}Pb/^{204}Pb$	f_{206}	$^{206}Pb/^{238}U$ (±1σ)	$^{207}Pb/^{235}U$ (±1σ)	$^{207}Pb/^{206}Pb$ (±1σ)	7/6 Pb age (± 1σ)
Group 1 High-Mg tholeiite (76562):									
62.2@	808	1274	1.58	67	0.2323	0.0533±0.0018	0.742±0.061	0.1010±0.0070	1644±136
Group 1 High-Ti Fe-rich tholeiite (76567):									
36.1@	120	56	0.47	19589	0.0009	0.1633±0.0055	1.707±0.079	0.0758±0.0021	1090±57
Group 2 High-Mg tholeiite (76561):									
61.1@	295	199	0.68	14631	0.0012	0.0639±0.0021	0.489±0.036	0.0560±0.0030	434±142
Homogeneous Norite (76541):									
1.1	4213	15631	3.71	401606	0.0000	0.4527±0.0149	8.783±0.291	0.1407±0.0001	2236±1
2.1	3457	7776	2.25	41237	0.0004	0.4332±0.0143	8.421±0.280	0.1410±0.0002	2240±2
3.1	2965	6633	2.24	510204	0.0000	0.4244±0.0140	8.245±0.273	0.1409±0.0002	2238±2
4.1	2669	5514	2.07	980392	0.0000	0.4335±0.0143	8.440±0.280	0.1412±0.0002	2242±2
5.1	2456	5551	2.26	172712	0.0001	0.4441±0.0147	8.669±0.288	0.1416±0.0002	2247±2
6.1	3473	10036	2.89	156006	0.0001	0.4473±0.0148	8.694±0.288	0.1410±0.0001	2239±2
7.1	3645	9442	2.59	406504	0.0000	0.4400±0.0145	8.587±0.285	0.1415±0.0002	2246±2
8.1	3551	7916	2.23	80906	0.0002	0.4536±0.0150	8.753±0.290	0.1400±0.0002	2227±2
9.1	2942	8448	2.87	46598	0.0003	0.4545±0.0150	8.862±0.294	0.1414±0.0002	2245±2
10.1	2913	5575	1.91	37879	0.0004	0.4507±0.0149	8.698±0.289	0.1400±0.0002	2227±2
109.1	2623	6571	2.51	1282051	0.0000	0.4381±0.0145	8.589±0.285	0.1422±0.0002	2254±2
Homogeneous Norite (76542):									
94.1	2541	8966	3.53	173310	0.0001	0.3860±0.0128	7.488±0.249	0.1407±0.0002	2236±3
95.1	2461	7780	3.16	540541	0.0000	0.4097±0.0135	7.990±0.266	0.1415±0.0002	2245±2
96.1	1316	3850	2.93	29630	0.0005	0.4318±0.0143	8.426±0.280	0.1415±0.0002	2246±3
97.1	4362	12688	2.91	24820	0.0006	0.4263±0.0141	8.317±0.276	0.1415±0.0002	2246±2
98.1	3256	14269	4.38	138504	0.0001	0.4274±0.0141	8.308±0.276	0.1410±0.0002	2239±2
99.1	2974	5272	1.77	156250	0.0001	0.4300±0.0142	8.386±0.278	0.1414±0.0002	2245±2
100.1	2365	8599	3.64	250000	0.0001	0.4380±0.0145	8.587±0.285	0.1422±0.0002	2254±2
101.1	2017	6836	3.39	123762	0.0001	0.4058±0.0134	7.904±0.263	0.1413±0.0002	2243±3
103.1	2351	8326	3.54	2272727	0.0000	0.4257±0.0141	8.334±0.276	0.1420±0.0002	2251±2
104.1	2044	5496	2.69	374532	0.0000	0.4464±0.0147	8.731±0.290	0.1419±0.0002	2250±2
105.1	5925	4871	0.82	1562500	0.0000	0.4456±0.0147	8.715±0.289	0.1419±0.0001	2250±1
106.1	5331	33906	6.36	161031	0.0001	0.4375±0.0144	8.365±0.277	0.1387±0.0001	2211±2
107.1	5249	7609	1.45	787402	0.0000	0.4498±0.0148	8.771±0.291	0.1414±0.0001	2245±2
108.1	1093	2753	2.52	33693	0.0004	0.4124±0.0136	8.040±0.268	0.1414±0.0003	2244±4

Table 9.3: (continued)

Grain area	U (ppm)	Th (ppm)	Th/U	$^{206}Pb/^{204}Pb$	f_{206}	$^{206}Pb/^{238}U$ (±1σ)	$^{207}Pb/^{235}U$ (±1σ)	$^{207}Pb/^{206}Pb$ (±1σ)	7/6 Pb age (± 1σ)
Homogeneous Norite (76543):									
88.1@	251	400	1.60	1824	0.0085	0.1829±0.0061	2.858±0.106	0.1133±0.0015	1853±24
89.1@	220	314	1.43	4797	0.0030	0.2733±0.0091	5.609±0.197	0.1489±0.0012	2333±14
90.1@	169	414	2.45	3205	0.0048	0.1300±0.0043	2.121±0.083	0.1183±0.0020	1931±30
91.1*	69	35	0.50	6416	0.0021	0.4612±0.0156	10.881±0.396	0.1711±0.0017	2568±17
92.1@	113	48	0.43	4725	0.0033	0.3039±0.0102	4.628±0.187	0.1104±0.0021	1807±35
93.1#	263	348	1.32	257732	0.0000	0.4684±0.0156	10.475±0.356	0.1622±0.0006	2479±7
Mottled Norite (76553):									
37.1	2291	2907	1.27	1333333	0.0000	0.4171±0.0138	8.077±0.269	0.1405±0.0002	2233±3
38.1	2168	1274	0.59	139665	0.0001	0.4017±0.0133	7.825±0.261	0.1413±0.0003	2243±3
39.1	3061	3008	0.98	45537	0.0003	0.4240±0.0140	8.209±0.273	0.1404±0.0002	2233±3
40.1	3541	3335	0.94	319489	0.0001	0.4119±0.0136	8.039±0.268	0.1415±0.0002	2246±3
41.1@	2108	4850	2.30	34294	0.0004	0.2193±0.0072	3.283±0.110	0.1086±0.0002	1776±4
42.1	2116	1299	0.61	117925	0.0001	0.3825±0.0126	7.456±0.249	0.1414±0.0003	2244±4
43.1	1553	1545	1.00	425532	0.0000	0.3802±0.0126	7.471±0.250	0.1425±0.0004	2258±5
44.1	3676	2787	0.76	3333333	0.0000	0.3918±0.0129	7.602±0.253	0.1407±0.0002	2236±3
45.1	1261	112	0.09	66934	0.0002	0.4625±0.0154	8.810±0.299	0.1381±0.0005	2204±7
46.1	5200	4985	0.96	164745	0.0001	0.4037±0.0133	7.804±0.259	0.1402±0.0002	2230±2
47.1@	830	284	0.34	43706	0.0003	0.3843±0.0127	7.167±0.242	0.1352±0.0005	2167±6
48.1	947	1061	1.12	110865	0.0001	0.4070±0.0135	7.818±0.261	0.1393±0.0003	2219±4
49.1	1999	929	0.47	102041	0.0001	0.4240±0.0140	8.310±0.278	0.1421±0.0003	2253±4
50.1	3255	931	0.29	309598	0.0001	0.4055±0.0134	7.923±0.263	0.1417±0.0002	2248±3
Group 2 Fe-rich tholeiite (76560):									
63.1#	182	103	0.56	101112	0.0001	0.4793±0.0160	10.766±0.373	0.1629±0.0009	2486±9
64.1#	172	98	0.57	49652	0.0003	0.4639±0.0156	10.411±0.372	0.1628±0.0014	2485±15
65.1*	163	63	0.38	8217	0.0017	0.5058±0.0170	12.487±0.436	0.1791±0.0011	2644±10
66.1#	1059	322	0.30	684932	0.0000	0.4799±0.0159	10.739±0.358	0.1623±0.0003	2480±3
67.1#	264	134	0.51	124378	0.0001	0.4691±0.0156	10.524±0.361	0.1627±0.0008	2484±8
68.1*	1341	252	0.19	73153	0.0002	0.5007±0.0166	12.277±0.410	0.1778±0.0003	2633±3
110.1	1001	353	0.35	3080	0.0050	0.2921±0.0096	4.251±0.144	0.1055±0.0004	1723±7
111.1	1088	233	0.21	2846	0.0055	0.2898±0.0096	4.238±0.143	0.1061±0.0004	1733±7
112.1	791	154	0.20	10255	0.0015	0.3232±0.0107	4.822±0.162	0.1082±0.0003	1769±5
113.1	1280	256	0.20	2953	0.0053	0.3061±0.0101	4.499±0.151	0.1066±0.0004	1742±6
114.1	715	122	0.17	1789	0.0087	0.3145±0.0104	4.651±0.160	0.1073±0.0007	1754±12

Table 9.3: (continued)

Grain area	U (ppm)	Th (ppm)	Th/U	$^{206}Pb/^{204}Pb$	f_{206}	$^{206}Pb/^{238}U$ (±1σ)	$^{207}Pb/^{235}U$ (±1σ)	$^{207}Pb/^{206}Pb$ (±1σ)	7/6 Pb age (± 1σ)
Group 2 Fe-rich tholeiite (76549):									
58.1	406	1023	2.52	37821	0.0004	0.3169±0.0105	4.743±0.165	0.1085±0.0007	1775±12
59.1	767	1182	1.54	505051	0.0000	0.3199±0.0106	4.782±0.162	0.1084±0.0005	1773±8
60.1	950	1308	1.38	64433	0.0002	0.3213±0.0160	4.779±0.161	0.1079±0.0004	1764±6
Group 2 Fe-rich tholeiite (76551):									
57.1@	67	46	0.69	6937	0.0023	0.3035±0.0104	4.104±0.189	0.0989±0.0026	1604±50
Mylonitised Group 2 Fe-rich tholeiite (76544):									
51.1@	339	243	0.72	35149	0.0005	0.0769±0.0025	0.594±0.027	0.0560±0.0015	454±60
51.2@	421	326	0.77	27847	0.0007	0.0817±0.0027	0.643±0.029	0.0571±0.0015	495±61
52.1	220	95	0.43	6328	0.0025	0.3321±0.0111	5.175±0.189	0.1130±0.0012	1849±20
53.1	465	204	0.44	840336	0.0000	0.3240±0.0108	4.947±0.169	0.1107±0.0006	1812±9
54.1	553	390	0.71	7035	0.0022	0.3120±0.0103	4.908±0.171	0.1141±0.0008	1866±13
55.1@	146	89	0.61	4696	0.0034	0.2606±0.0087	3.470±0.136	0.0966±0.0016	1559±32
56.1#	426	856	2.01	14678	0.0010	0.4629±0.0154	10.325±0.349	0.1618±0.0006	2474±6
Lamprophyre (76550):									
102.1@	108	73	0.68	5069	0.0033	0.1839±0.0061	1.872±0.101	0.0738±0.0028	1037±79
Group 3 Fe-rich tholeiite (76554):									
12.1#	326	509	1.56	53220	0.0003	0.4728±0.0157	10.502±0.357	0.1611±0.0007	2467±7
14.1*	843	612	0.73	14599	0.0009	0.5210±0.0172	13.639±0.456	0.1899±0.0004	2741±4
15.1*	631	40	0.06	19516	0.0007	0.4670±0.0155	11.038±0.371	0.1714±0.0005	2571±5
16.1	861	1655	1.92	31516	0.0005	0.2365±0.0078	2.852±0.097	0.0875±0.0004	1371±8
19.1	1415	3886	2.75	62461	0.0003	0.2373±0.0078	2.873±0.096	0.0878±0.0003	1378±6
20.1	745	2196	2.95	6667	0.0025	0.2401±0.0079	2.932±0.100	0.0886±0.0005	1395±10
21.1	1127	2664	2.36	4179	0.0039	0.2223±0.0073	2.659±0.091	0.0868±0.0004	1355±10
25.1	910	1821	2.00	6722	0.0024	0.2311±0.0076	2.768±0.095	0.0869±0.0005	1357±11
26.1	1566	4844	3.09	23815	0.0007	0.2240±0.0074	2.709±0.091	0.0877±0.0003	1376±7
28.1	1805	2357	1.31	61312	0.0003	0.2536±0.0084	3.076±0.103	0.0880±0.0002	1382±4
29.1	996	1957	1.96	16844	0.0010	0.2303±0.0076	2.814±0.095	0.0886±0.0004	1396±8
30.1	986	2660	2.70	29735	0.0005	0.2522±0.0083	3.075±0.104	0.0884±0.0003	1391±7
33.1@	795	1980	2.49	1235	0.0132	0.2190±0.0072	2.867±0.103	0.0950±0.0010	1527±20
34.1	1302	3707	2.85	17838	0.0009	0.2356±0.0078	2.883±0.097	0.0887±0.0003	1399±8
69.1#	310	485	1.57	4242	0.0033	0.4551±0.0152	10.131±0.351	0.1614±0.0010	2471±10
70.1#	176	207	1.18	62305	0.0002	0.4587±0.0154	10.263±0.362	0.1623±0.0012	2479±13
71.1#	227	93	0.41	26838	0.0005	0.4366±0.0146	9.765±0.339	0.1622±0.0010	2479±10
72.1*	868	19	0.02	14872	0.0009	0.5195±0.0172	13.520±0.452	0.1888±0.0004	2731±4
73.1*	1094	67	0.06	56022	0.0002	0.4744±0.0157	11.556±0.386	0.1767±0.0004	2622±4
74.1#	212	237	1.12	44248	0.0003	0.4660±0.0156	10.450±0.361	0.1626±0.0009	2483±9
75.1	1430	2488	1.74	761	0.0214	0.2491±0.0082	3.005±0.107	0.0875±0.0009	1372±19

Table 9.3: (continued)

Grain area	U (ppm)	Th (ppm)	Th/U	$^{206}Pb/^{204}Pb$	f_{206}	$^{206}Pb/^{238}U$ (±1σ)	$^{207}Pb/^{235}U$ (±1σ)	$^{207}Pb/^{206}Pb$ (±1σ)	7/6 Pb age (± 1σ)
Group 3 Fe-rich tholeiite (76555):									
76.1	972	1916	1.97	5901	0.0028	0.2363±0.0078	2.882±0.099	0.0885±0.0005	1393±11
77.1	1548	299	0.19	3381	0.0048	0.2233±0.0074	2.684±0.092	0.0872±0.0005	1364±12
78.1	2280	302	0.13	14162	0.0012	0.2587±0.0085	3.122±0.105	0.0875±0.0003	1372±7
79.1*	459	143	0.31	4030	0.0034	0.4298±0.0143	10.29±0.3497	0.1738±0.0007	2594±7
80.1	1813	299	0.17	4025	0.0041	0.2227±0.0074	2.694±0.091	0.0877±0.0004	1377±9
81.1*	887	1103	1.24	12607	0.0012	0.3852±0.0128	7.328±0.247	0.1380±0.0005	2202±6
82.1	1235	2702	2.19	4820	0.0034	0.2174±0.0072	2.667±0.091	0.0890±0.0005	1404±11
83.1	1905	1104	0.58	2084	0.0078	0.2340±0.0077	2.788±0.095	0.0864±0.0005	1347±11
84.1	988	1638	1.66	444	0.0368	0.2361±0.0078	2.738±0.107	0.0841±0.0014	1295±34
85.1	1719	231	0.13	2534	0.0064	0.2472±0.0082	2.959±0.101	0.0868±0.0005	1357±11
86.1	1426	2997	2.10	9560	0.0017	0.2484±0.0082	3.040±0.103	0.0888±0.0004	1399±8
87.1	1593	215	0.14	1466	0.0111	0.2339±0.0077	2.854±0.098	0.0885±0.0005	1393±11
Group 4 Fe-rich tholeiite (76540):									
11.1	1085	767	0.71	13759	0.0012	0.2143±0.0071	2.416±0.082	0.0818±0.0004	1240±9
13.1	1496	1414	0.95	17114	0.0010	0.2049±0.0068	2.288±0.077	0.0810±0.0003	1221±9
17.1@	1490	1365	0.92	132979	0.0001	0.2071±0.0068	2.311±0.078	0.0809±0.0002	1220±6
18.1	1973	1729	0.88	15936	0.0010	0.2103±0.0069	2.380±0.080	0.0821±0.0003	1248±7
22.1	1714	1465	0.86	4528	0.0037	0.1918±0.0063	2.132±0.074	0.0806±0.0006	1213±14
23.1	1534	1344	0.88	16787	0.0010	0.2039±0.0067	2.302±0.078	0.0819±0.0003	1243±8
24.1	1250	890	0.71	6985	0.0024	0.2082±0.0069	2.354±0.080	0.0820±0.0004	1245±10
27.1	1844	1698	0.92	549451	0.0000	0.2020±0.0067	2.274±0.076	0.0816±0.0003	1236±6
31.1	1410	1069	0.76	3028	0.0055	0.2016±0.0067	2.269±0.078	0.0816±0.0005	1236±13
32.1	1936	1731	0.89	32852	0.0005	0.2045±0.0067	2.304±0.077	0.0817±0.0003	1239±6
35.1@	2162	1679	0.78	6039	0.0028	0.1894±0.0063	2.105±0.072	0.0806±0.0004	1212±10
115.1	1734	1489	0.86	5579	0.0030	0.2066±0.0068	2.334±0.079	0.0819±0.0003	1244±7
116.1	1678	1467	0.87	31153	0.0005	0.2094±0.0069	2.371±0.080	0.0821±0.0002	1248±6
117.1	1658	1325	0.80	13714	0.0012	0.2103±0.0069	2.378±0.080	0.0820±0.0002	1245±5
118.1	11271	8011	0.71	4185	0.0040	0.3449±0.0114	3.882±0.133	0.0816±0.0005	1237±12

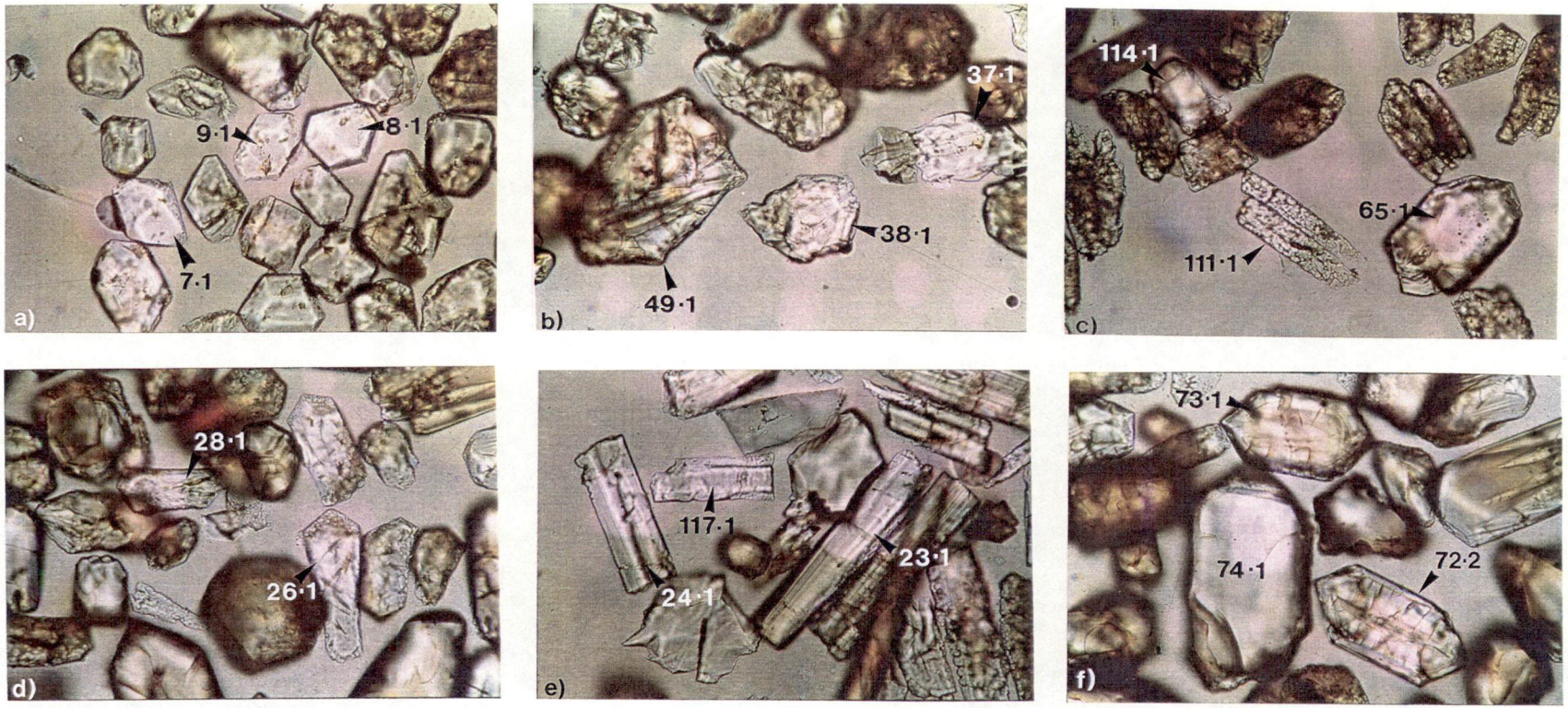

Figure 9.6: Photomicrographs of characteristic primary magmatic zircons used to date the following dyke suites: a) Homogeneous Norite (sample 76541); b) Mottled Norite (sample 76553); c) Group 2 Fe-rich tholeiites (sample 76560 - grain 65 is a xenocryst); d) Group 3 Fe-rich tholeiites (sample 76554); e) Group 4 Fe-rich tholeiites (sample 76540); plus f) Xenocrysts (sample 76554). Analysed zircons are numbered - refer to Table 9.3 for corresponding U-Th-Pb data; Scale: 16 mm = 100 μm.

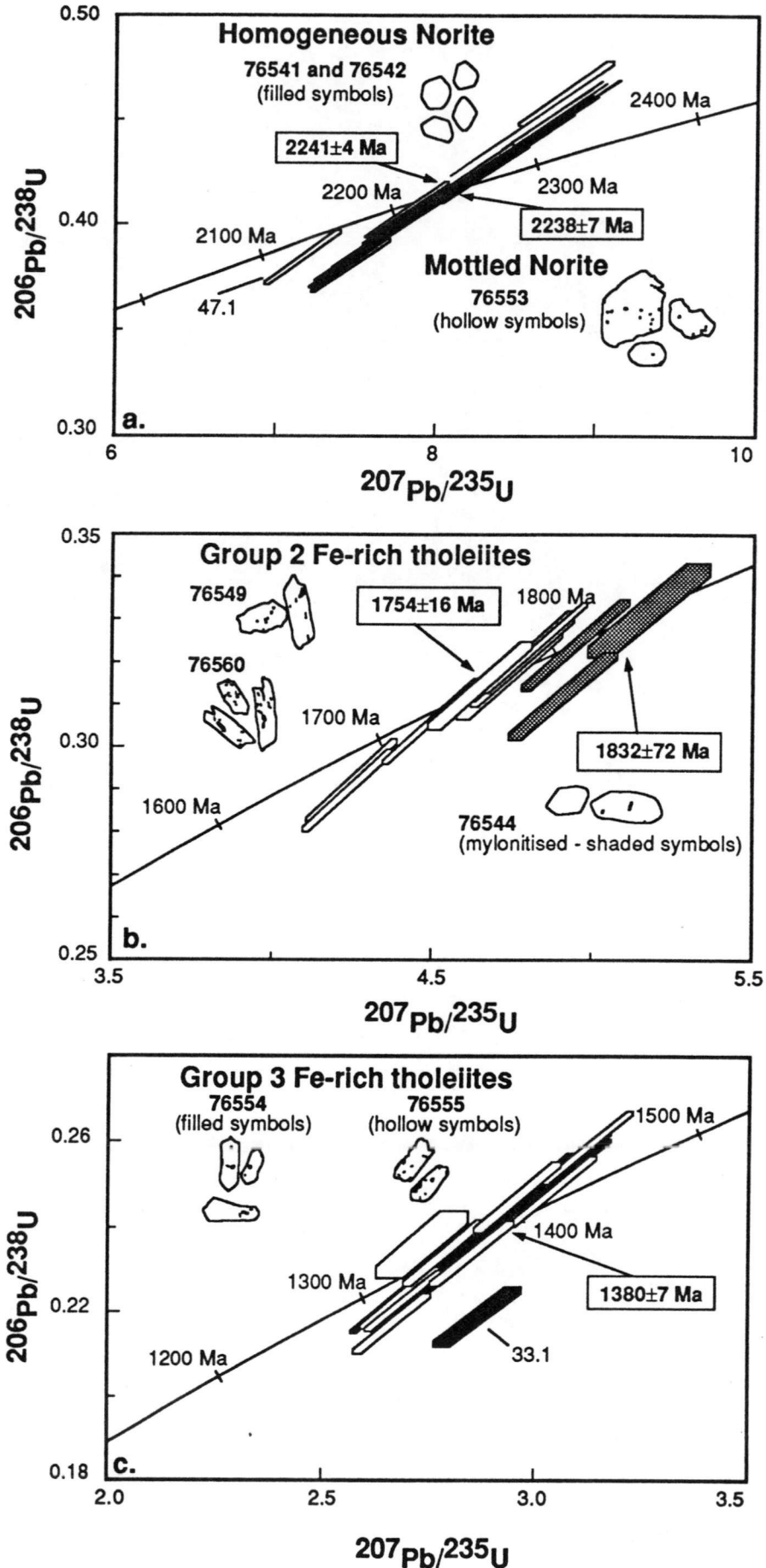
Homogeneous Norite
76541 and 76542
(filled symbols)
2241±4 Ma
2238±7 Ma
2400 Ma
2300 Ma
2200 Ma
2100 Ma
47.1
Mottled Norite
76553
(hollow symbols)
a.
0.50
0.40
0.30
6
8
10
$^{206}Pb/^{238}U$
$^{207}Pb/^{235}U$
Group 2 Fe-rich tholeiites
76549
76560
1754±16 Ma
1800 Ma
1700 Ma
1600 Ma
1832±72 Ma
76544
(mylonitised - shaded symbols)
b.
0.35
0.30
0.25
3.5
4.5
5.5
$^{206}Pb/^{238}U$
$^{207}Pb/^{235}U$
Group 3 Fe-rich tholeiites
76554
(filled symbols)
76555
(hollow symbols)
1500 Ma
1400 Ma
1300 Ma
1380±7 Ma
1200 Ma
33.1
c.
0.26
0.22
0.18
2.0
2.5
3.0
3.5
$^{206}Pb/^{238}U$
$^{207}Pb/^{235}U$

(Figure 9.7)

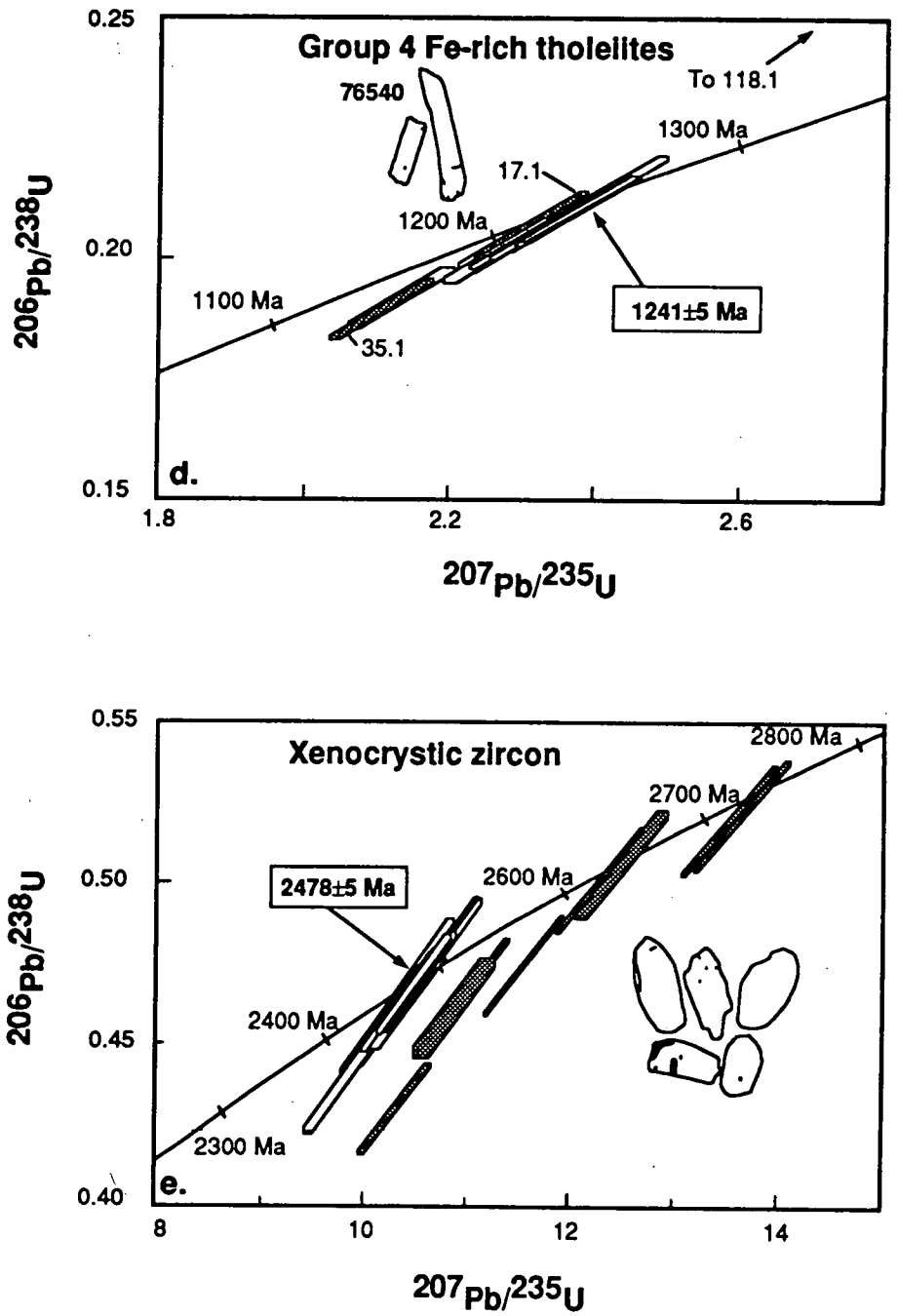

Figure 9.7: $^{207}Pb/^{235}U$ versus $^{206}Pb/^{238}U$ concordia plots for zircon analyses from: a) felsic segregation veins within the Homogeneous and Mottled Norites; b) a felsic segregation vein (76560), a mafic dyke sample (76549) and a mylonitised dyke sample (76544) from the Group 2 Fe-rich tholeiites; c) two felsic segregation veins within a Group 3 Fe-rich tholeiite dyke; d) a felsic segregation vein within a Group 4 Fe-rich tholeiite dyke; and e) xenocrystic zircons belonging to various dyke suites (refer to text) - shaded grains were not included in the calculation of the mean $^{207}Pb/^{206}Pb$ xenocryst age.
Data points are displayed as one sigma error boxes. Zircon outlines exhibit typical crystal shapes of grains used to obtain the quoted mean $^{207}Pb/^{206}Pb$ ages (± two sigma error).

can therefore be validly dated using the $^{207}Pb/^{206}Pb$ ages, quoted at the 95 % confidence level.

9.6.1 Successfully Dated Dyke Suites:

9.6.1.1 Homogeneous Norite:

Felsic segregation samples 76541 and 76542 contain colourless, relatively equidimensional, euhedral zircon crystals with a simple facetted morphology interpreted to be of primary magmatic origin, no visible internal zoning and only rare inclusions (Figure 9.6a). Zircons from sample 76541 range from ~60 to 80 μm, and those from sample 76542 range from ~70 to 100 μm in diameter. Sample 76542 also contains a number of more anhedral to subhedral zircons with length:breadth ratios ranging up to 2.5:1. Sample 76541 zircons have high U (2456 - 4213 ppm) and Th (5514 - 15631 ppm) contents; those from sample 76542 display an even greater range of U (1093 - 5925 ppm) and Th (2753 - 33906 ppm). All twenty-five zircon analyses from samples 76541 and 76542 cluster around concordia (Figure 9.7a) with a mean $^{207}Pb/^{206}Pb$ emplacement age of 2241±4 Ma. No zircon xenocrysts were found in either of these samples.

Zircons from felsic segregation sample 76543 lack the simple euhedral morphology of the previous two samples, ranging from rounded, anhedral or broken, irregular grains to complexly facetted crystals. Many display internal zoning with dark metamict cores, which were avoided during analysis; others are completely discoloured. Grainsize is highly variable (40 to 315 μm) with length:breadth ratios of up to 3.5:1. These zircons also have distinct chemistry, with low U (69 - 263 ppm) and Th (35 - 414 ppm) contents. Due to their morphology, low U and Th contents and Archaean or highly discordant younger ages, all of the analysed zircons from sample 76543 are considered to be xenocrystic and/or isotopically reset.

9.6.1.2 Mottled Norite:

Zircons from segregation vein sample 76553 are generally colourless to slightly discoloured, with irregular to subhedral shapes, ragged to slightly embayed edges and abundant inclusions (Figure 9.6b). Grainsize ranges from ~80 to 200 μm, with length:breadth ratios from 1:1 to 2.6:1. U (947 - 3676 ppm) and Th contents (112 - 4985 ppm) are highly variable.

Twelve of the fourteen zircon analyses define a mean $^{207}Pb/^{206}Pb$ age of 2238±7 Ma (Figure 9.7a), interpreted as the time of crystallisation of the felsic vein. This age, within error of the Homogeneous Norite zircon age, is consistent with an interpretation of contemporaneous Homogeneous and Mottled Norite intrusion, as indicated by their field relationships (Seitz, 1991).

The most euhedral grain (analysis 41.1; not shown in Figure 9.7a) is over 50 % discordant, and was excluded from the emplacement age calculation. It is a relatively clear zircon, with U (2108 ppm) and Th (4850 ppm) contents comparable to the more concordant

grains, but with the highest Th/U ratio (2.30) and common Pb content. Its $^{207}Pb/^{206}Pb$ age of 1776±4 Ma, lower concordia intercept of ~700-800 Ma and its position above the extension of the other analyses implies a more complex history of Pb loss.

Analysis 47.1 was also excluded from the age calculation. It is normally discordant (although to a lesser extent than analysis 41.1) and plots above the alignment defined by the remaining analyses. Although this irregular ragged grain is morphologically indistinct from the more concordant grains, it has the lowest U (830 ppm) and the second lowest Th (284 ppm) contents. This particular analysis was considered to be a statistical outlier and was excluded from the mean age calculation.

9.6.1.3 Group 2 Fe-rich Tholeiite Dykes:

Felsic segregation sample 76560 contains both xenocrystic and primary magmatic zircons, each of which has a distinctive morphology. The five analysed magmatic grains are generally small (~35 to 130 μm long), dark, and equant to elongate, with length:breadth ratios up to 3.6:1 and abundant inclusions (Figure 9.6c). Although most grains have frayed and broken ends, a few have pyramidal terminations. Abundant cracks may account for their apparent ease of breakage during mineral separation procedures. U contents range from 715 to 1280 ppm, Th contents from 122 to 353 ppm and Th/U ratios from 0.17 to 0.35. Xenocrystic zircons (Figure 9.6c) are larger (up to at least 180 μm) and more irregular in shape. Some have slightly corroded irregular edges, others are somewhat rounded. The six analysed xenocrysts have various U (163 - 1341 ppm) and Th (63 - 322 ppm) contents; common Pb is generally less than in the magmatic zircons.

Zircons from dyke sample 76549 are generally subhedral, slightly discoloured and/or cracked, and have pyramidal terminations. U contents (406 - 950 ppm) are generally lower whereas Th contents (1023 - 1308 ppm) and Th/U ratios(1.38 - 2.52) are higher than those of the magmatic zircons from the felsic segregation (sample 76560). All three analyses from this sample are relatively concordant, considered to be primary magmatic grains, and were used in the emplacement age calculation.

Eight zircon analyses from samples 76560 and 76549 yield a mean $^{207}Pb/^{206}Pb$ age of 1754 ±16 Ma (Figure 9.7b), which is regarded as the time of intrusion of the Group 2 Fe-rich tholeiite dykes.

Dyke sample 76551 yielded only one irregular shaped, complexly facetted zircon (130 x 60 μm) with very low U (67 ppm) and Th (46 ppm) contents. This reversely discordant grain, with a $^{207}Pb/^{206}Pb$ age of 1604±50 Ma, would plot to the left of the other analyses on Figure 9.7b, and was not included in the mean age calculation.

Seven analyses of five zircons from a mylonitised dyke (sample 76544) on Broad Peninsula show considerable isotopic complexity. Three analyses (52.1, 53.1 and 54.1) yield a mean $^{207}Pb/^{206}Pb$ age of 1832±76 Ma (Figure 9.7b), slightly older than, but within statistical uncertainty of, the 1754±16 Ma emplacement age obtained for Group 2 Fe-rich tholeiites on Long Peninsula. Two analyses of the complexly facetted, euhedral grain 51

provide a reasonably concordant age of ~500 Ma. This grain therefore appears to have formed at this later time. Grain 56, a rounded anhedral xenocryst, with a $^{207}Pb/^{206}Pb$ age of 2474±6 Ma, has a higher Th content (856 ppm) and Th/U ratio (2.0) than the other mylonite zircons, whereas the discordant, subhedral grain 55 has the lowest U (146 ppm) and Th (89 ppm) contents, the highest common Pb and a $^{207}Pb/^{206}Pb$ age of 1559±32 Ma.

9.6.1.4 Group 3 Fe-rich Tholeiite Dykes:

Thirty-three zircons were analysed from two felsic veins (samples 76554 and 76555) within the same Group 3 Fe-rich tholeiite dyke on Long Peninsula. Primary magmatic and xenocrystic zircon grains were identified, with the former displaying a similar morphology within both samples. Primary magmatic grains in sample 76554 are characteristically colourless, elongate grains with minor inclusions, pinched middles and bipyramidal terminations (Figure 9.6d). Average length:breadth ratios range from ~2:1 to 3.6:1, with lengths of ~70 to 130 µm. U (745 - 1805 ppm), Th (1655 - 4844 ppm) and Th/U ratios (1.31 - 3.09) are variable. Twelve of the twenty-one analysed zircons from sample 76554 are considered to represent primary magmatic grains. Eleven of these produce a mean $^{207}Pb/^{206}Pb$ emplacement age of 1381±8 Ma. The only analysis (33.1) excluded from the age calculation has a higher common Pb component and appears to be more cracked and to contain more opaque inclusions. Its discordant $^{207}Pb/^{206}Pb$ age (1527±30) may be indicative of a partially reset, xenocrystic origin.

Primary magmatic zircons from sample 76555 have a similar pinched morphology and grainsize to those of sample 76554, but are commonly more discoloured and often have broken or ragged ends. Although U (972 - 2280 ppm) and Th (215 - 2997 ppm) contents overlap with those of magmatic zircon from sample 76554, U contents tend to occupy the upper end of this range whereas Th contents are generally at or beyond the lower range of 76554 grains. This results in relatively low Th/U ratios (0.13 - 2.19) for sample 76555 zircons. The darker colour may reflect their slightly higher U contents and resultant radiation damage to the crystal lattices. A mean $^{207}Pb/^{206}Pb$ emplacement age of 1378±15 Ma was obtained for sample 76555.

Pooling of the indistinguishable data for primary magmatic zircons from the two felsic veins results in a mean $^{207}Pb/^{206}Pb$ age of 1380±7 Ma (Figure 9.7c) for Group 3 Fe-rich tholeiite dykes.

The nine xenocrysts from sample 76554 are larger (~70 to 180 µm), relatively equidimensional, subhedral to euhedral grains with more complex crystal facets than the magmatic grains. They are also characterised by very low Th (19 - 612 ppm) plus generally lower U (176 - 1094 ppm) and Th/U ratios (0.02 - 1.57), although there is some overlap of both U and Th/U with the lower ends of the U and Th/U spectra of the magmatic zircons. $^{207}Pb/^{206}Pb$ ages range from 2467 to 2741 Ma.

The morphology of the analysed xenocrysts, 79.1 and 81.1, from sample 76555 is not as obviously distinct from the magmatic zircon morphology as it is in sample 76554. Grain

81 is very anhedral whereas grain 79, although elongate and subhedral, lacks the pinched appearance typical of the magmatic crystals.

9.6.1.5 Group 4 Fe-rich Tholeiite Dykes:

A segregation vein from a Group 4 Fe-rich tholeiite dyke (sample 76540) yielded abundant primary magmatic zircons. No xenocrysts were found. Elongate, unzoned, zircon grains (Figure 9.6e), 90 - 250 μm long, have length:breadth ratios of up to ~7:1. As their ends are commonly broken, it is not possible to discern whether these grains originally possessed the bipyramidal terminations characteristic of many magmatic zircons. U (1085 - 11271 ppm) and Th (767 - 8011 ppm) are highly variable, the lowest values representing the most concordant grain (11). Th/U ratios range from 0.707 to 0.945.

Thirteen of the analyses from sample 76540 yield a mean $^{207}Pb/^{206}Pb$ age of 1241±5 Ma (Figure 9.7d). Two analyses (17.1 and 35.1), with significantly lower $^{207}Pb/^{206}Pb$ ages, were rejected from the mean age calculation. There is no independent reason for grain 17 to be excluded, but grain 35 has the second highest U content (2162 ppm) and is more cracked and slightly more discoloured that the other grains.

Grain 118, yields the most reversely discordant (~40 %) analysis and has by far the highest U content (11271 ppm). Although one would expect that the crystal lattice of such a high-U zircon would be subject to intense radiation damage, resulting in recent Pb loss and normal discordance, this is in fact a surprisingly clear grain with no obvious metamict zones or cracking. The reverse discordance of this analysis is most probably an analytical effect, whereby erroneous Pb/U ratios are obtained for high-U zircons on SHRIMP due to an inappropriate calibration with the low-U standard SL13 (Black et al., 1991a). Although this analytical bias may be a contributing factor to the Pb/U ratios of the reversely discordant analyses, it has no effect on the $^{207}Pb/^{206}Pb$ age measurements which are independent of machine-induced inter-element fractionation effects such as this. Therefore, reverse discordance alone is not a reason to exclude analyses such as 118.1 from mean $^{207}Pb/^{206}Pb$ age determinations.

Another felsic vein sample (76539) collected from the same dyke on Bandits Island, 10 m northeast of the previous sample site, was totally devoid of zircon.

9.6.2 Unsuccessfully Dated Dyke Suites:

9.6.2.1 High-Mg Tholeiite Dykes:

Two High-Mg mafic dyke samples (76562 and 76561) yielded one zircon each, neither of which provided an emplacement age for either the Group 1 or Group 2 High-Mg tholeiites, respectively.

Grain 62 (sample 76562) is a 200 x 86 μm, multiply facetted dark grain with a distinct metamict core and an extremely high common Pb content ($^{206}Pb/^{204}Pb$ = 67). No significance can be placed on its highly imprecise $^{207}Pb/^{206}Pb$ age of 1644±136 Ma.

Grain 61 (sample 76561), is a clear but broken euhedral crystal lacking both zoning and inclusions. It has low U (295 ppm) and Th (199 ppm) contents and a concordant $^{207}Pb/^{206}Pb$ age of 434±142 Ma. This grain may therefore have crystallised during the 500 Ma event.

9.6.2.2 Group 1 High-Ti Fe-rich Tholeiite Dykes:

No zircon was found in a thin felsic vein within Group 1 Fe-rich tholeiite dyke sample 76567. A clear, unzoned, euhedral zircon grain (36.1) from the mafic dyke has very low U (120 ppm) and Th (56 ppm) contents, a low Th/U ratio (0.47) and a $^{207}Pb/^{206}Pb$ age of 1090±57 Ma. Because of the low U, this analytical point is very imprecise but this zircon may have crystallised as a peripheral effect of Late Proterozoic metamorphism. The morphology and clarity of this zircon suggest that its age is due to late crystallisation rather than isotopic resetting.

9.6.2.3 Lamprophyre Dykes:

A euhedral zircon (102.1) from dyke sample 76550, containing low U (108 ppm), low Th (73 ppm) and substantial common Pb, has a slightly reversely discordant $^{207}Pb/^{206}Pb$ age of 1037±79. Its morphology and relative concordance indicate that it might also have grown during peripheral Late Proterozoic metamorphism.

9.6.3 Xenocrysts:

Eleven xenocryst analyses (discussed above) from the Homogeneous Norite (sample 76543), Group 2 Fe-rich tholeiite dykes (samples 76560 and 76544) and a Group 3 Fe-rich tholeiite dyke (sample 76554) - yield a mean $^{207}Pb/^{206}Pb$ age of 2478±5 Ma (Figure 9.7e). The xenocrysts are usually larger and commonly have more distinctively complex and multi-facetted morphologies (Figure 9.6f) than the primary magmatic grains.

The $^{207}Pb/^{206}Pb$ ages of nine other xenocrystic zircons range from 2202 Ma (sample 76555) to 2741 Ma (sample 76554) (Table 9.3), possibly defining at least three poorly constrained ages of ~2570-2590 Ma, 2630-2640 Ma and 2730-2740 Ma.

9.7 DISCUSSION:

9.7.1 Mafic Magmatic History of the Vestfold Hills:

This study has yielded a more tightly constrained Proterozoic mafic magmatic history for the Vestfold block through the derivation of new $^{207}Pb/^{206}Pb$ zircon ages for several generations of mafic dyke intrusion.

The 2241±4 Ma and 2238±7 Ma zircon ages derived for the Homogeneous and Mottled Norites, respectively, do not correspond to any previously reported isotopic ages for either felsic crustal rocks or mafic intrusives in the Vestfold Hills. As zircons from felsic

segregations (samples 76541, 76542 and 76553) within these norites are generally much higher in both U and Th (maximum U = 5925 ppm, maximum Th = 33906 ppm) than zircons from the basement gneisses (maximum U = 1396 ppm, maximum Th = 1705 ppm; Black et al., 1991a) they are unlikely to be crustal xenocrysts. These norites, and their associated fine-grained High-Mg tholeiite dykes, are younger than the 2424±72 Ma Rb-Sr age reported by Collerson and Sheraton (1986) for all high-Mg intrusives and the 2300-2400 Ma magmatic event age of Sheraton et al. (1987). Group 2 High-Mg intrusion occurred significantly later than the major Late Archaean - Early Proterozoic tectonothermal events (D_1,M_1 and D_2,M_2) recorded in the basement gneisses and may also significantly postdate intrusion of the Group 1 High-Mg tholeiites and the Group 1 High-Ti Fe-rich tholeiites for which no zircon ages have yet been obtained. Although the Low-Ti and plagioclase megacryst-bearing subgroups of the Group 1 Fe-rich tholeiite dyke suite may be younger than ~2240 Ma, it is not possible to ascribe an age to the Group 3 High-Mg tholeiite dykes, as their relationship to the Group 2 High-Mg tholeiites is still unclear.

Dating of the Group 2 Fe-rich tholeiite dykes is more problematic. A $^{207}Pb/^{206}Pb$ emplacement age of 1754±16 Ma for Long Peninsula Group 2 Fe-rich tholeiites is within error of the Rb-Sr 1791±62 Ma age of Collerson and Sheraton (1986) for their Group I tholeiites. Its relative imprecision is a result of both the limited number of analyses (8) and the scatter of isotopic data. This age was derived by pooling zircon analyses from a felsic segregation (76560) and a mafic dyke (76549). The latter is the only undeformed mafic sample analysed to contain what appear to be primary magmatic zircons. All other mafic dyke samples contained only xenocrysts, reset grains, or zircons which appear to have crystallised during either the 1000 or 500 Ma events. The crystallisation of these zircons in sample 76549 is also contrary to the findings of Black et al. (1991a) whose mafic dyke sample failed to yield any primary magmatic zircons. These apparent primary magmatic zircons are therefore not easily explained. Although sample 76549 does have a relatively high Zr content (172 ppm), compared to the other dykes (but an average composition for a comparable mafic intrusive; Poldervaart, 1956), its SiO_2 (49.33 %) and normative quartz (1.10 %) contents are as low as other dyke suites that did not crystallise zircon. Despite the fact that these zircons have low U contents (406 - 950 ppm), more like zircons from felsic crustal rocks than mafic magmas, and are by no means morphologically pristine or prismatic, a xenocrystic origin seems unlikely. If they were xenocrysts, their concordance would imply complete isotopic resetting due to an event at this time, for which there is no independent evidence (such as metamorphic mineral assemblages) in the dyke. In addition, a mylonitised Group 2 Fe-rich tholeiite dyke (76544) contains zircon xenocrysts which have retained their age.

The 1832±76 Ma zircon age for the mylonitised Group 2 Fe-rich tholeiite (sample 76544) from Broad Peninsula presents similar problems. If these zircons are a product of primary magmatic crystallisation, they once again suggest that it may be possible, in certain undefined cases, to derive mafic dyke emplacement ages directly from their constituent

zircons. Alternatively, D_4 mylonitisation may have been responsible for the crystallisation of these zircons due to the release of Zr and SiO_2 during the hydration of pyroxene, as evidenced by amphibole formation within this dyke. Yet another possibility is that the zircons formed by the breakdown of magmatic baddeleyite during D_4. Abundant recrystallised quartz indicates greatly increased SiO_2 activity at that time, and at least partial baddeleyite replacement by zircon during thermotectonic events has been documented (Davidson and van Breeman, 1988; Le Cheminant and Heaman, 1989). However, the expected polycrystalline nature of this replacement zircon (Davidson and van Breeman, 1988) was not observed.

Whatever the origin of the zircons within the Group 2 Fe-rich tholeiite mafic components (samples 76549 and 76544), their presence implies that an event occurred at ~1800 Ma that was capable of causing zircon formation. The fact that similar $^{207}Pb/^{206}Pb$ ages were obtained for several zircons from a felsic segregation vein (76560) in this same dyke generation indicates that the ages obtained are in fact dyke intrusion ages. Although the two proposed emplacement ages obtained for this dyke generation (1754±16 Ma and 1832±76 Ma) are within error of each other, it is also possible that Group 2 Fe-rich dyke emplacement occurred slightly later on Broad Peninsula than on Long Peninsula.

Although the younger Fe-rich tholeiite dykes of the Vestfold Hills were originally considered to represent two contemporaneous geochemical groups (Collerson and Sheraton, 1986), their subsequent subdivision by Seitz (1991), on the basis of distinct orientations and cross-cutting relationships throughout Long Peninsula, has now been confirmed with the determination of zircon emplacement ages of 1380±7 Ma and 1241±5 Ma for the Group 3 and 4 Fe-rich tholeiite dykes respectively. It appears to be merely coincidental that the 1374±125 Ma Rb-Sr whole-rock isochron age assigned by Collerson and Sheraton (1986) to their Group II dykes is within error of the 1380±7 Ma $^{207}Pb/^{206}Pb$ zircon age obtained for the Group 3 Fe-rich tholeiite dykes. The Rb-Sr age is extremely unlikely to be valid because at least one (sample 81285177) of the fifteen Group II tholeiites dated by Collerson and Sheraton (1986) is from a NNE-SSW trending (206°) dyke on Long Peninsula (J.W. Sheraton, pers. comm., 1992), consistent with the Group 4 Fe-rich tholeiite orientation. Therefore, the samples used in this previous study were probably a mixture of Group 3 and 4 Fe-rich tholeiite dykes, biased by the former to produce the older age.

The 1241±5 Ma $^{207}Pb/^{206}Pb$ zircon age obtained for the Group 4 Fe-rich tholeiites of Long Peninsula matches that of, and thereby confirms, the 1248±4 Ma zircon emplacement age of a similar dyke in the Platcha area of Broad Peninsula (Black et al., 1991a).

The 2478±5 Ma xenocrystic zircons appear to be crustal in origin with relatively low U and Th contents, similar to those analysed by Black et al. (1991a: 65 - 662 ppm U; 43 - 1170 ppm Th) which yielded an age of 2483±9 Ma. These xenocrysts were probably derived from the youngest orthogneisses in the region, which are of comparable age (Black et al., 1991b). The other analysed xenocrysts have $^{207}Pb/^{206}Pb$ ages up to 2741±4 Ma,

supporting previous proposals (Collerson et al., 1983a; Black et al., 1991b) that Archaean crustal source rocks at least 2700 to 2800 Ma underlie the Vestfold block.

The presence of a felsic segregation vein with no magmatic zircons within the same dyke as segregation veins containing abundant magmatic zircons may indicate some degree of crystal "clustering". Examples of this were found in the Homogeneous Norite and a Group 4 Fe-rich tholeiite dyke on Bandits Island. Felsic samples 76543 and 76539 within the norite and the Fe-rich tholeiite dyke, respectively, lack magmatic zircons but contain abundant xenocrysts. In contrast, Homogeneous Norite segregation samples 76541 and 76542 and Group 4 Fe-rich tholeiite felsic sample 76540 contain magmatic zircons but no xenocrysts. Whether these particular samples are representative of the felsic veins from which they were collected is not known but it does appear that there may be some preferential accumulation of different zircon generations either within different areas of individual segregation veins or between various segregations in the same mafic body. The latter would imply that felsic segregations in a single dyke may have different zircon components and therefore not all would be suitable for dating purposes.

Peripheral ~1000 Ma metamorphism, most evident in the southwest Vestfold Hills, was only detected by Black et al. (1991a) in zircons from the mafic dyke, dated at 1025±56 Ma. The 1090±57 Ma (sample 76567) and 1037±79 Ma (sample 76550) zircons analysed during the course of this study were also obtained from mafic dyke samples; no felsic segregation zircons yielded any evidence of this Late Proterozoic metamorphic event. These results are consistent with the suggestion of Black et al. (1991a), that conversion of baddeleyite (which originally crystallised only in the SiO_2-poor mafic parts of the dykes) to zircon occurred as a result of increased SiO_2 activity during metamorphism.

Sparse evidence of probable hydrothermal zircon growth associated with the widespread 500 Ma isotopic resetting event was also confined to the mafic dyke samples.

9.7.2 Proterozoic Crustal History of the Vestfold Hills:

The timing and pressure/temperature conditions of mafic dyke emplacement can be used to provide a framework for the various interspersed thermotectonic events which define the Proterozoic crustal history of the Vestfold Hills (Table 9.4).

Kuehner's (1986) estimate of a 7-8 kbar emplacement pressure for the High-Mg tholeiites of the Vestfold Hills was revised to 3-5 kbars, or possibly as low as 1-2 kbars, by Seitz (in press) on the basis of a study of Al exchange between clinopyroxene and plagioclase and the recognition that the chilled margin phenocryst assemblages (olivine and orthopyroxene) used by Kuehner may have been transported from greater depths. This relatively shallow emplacement implies uplift and reburial between the medium- to high-grade ductile events D_3,M_3 and D_4,M_4 (Passchier et al., 1991), which bracket the intrusion of the Group 1 Fe-rich tholeiites, the High-Mg tholeiites and norite complex, and the Group 2 Fe-rich tholeiite dykes. D_3,M_3 therefore occurred after 2487±6 Ma (the time of D_2,M_2; Black et al., 1991b), but before ~2240 Ma, which corresponds to Group 2 High-Mg tholeiite and

Table 9.4: Conditions and timing of dyke intrusion based on data from Collerson et al. (1983b), Kuehner (1986), Harley (1989); Seitz (1991), Black et al. (1991b), Passchier et al. (1991) and this study.

Approximate U-Pb Zircon Age (Ma)	Event	P,T conditions
2526 - 2501	Mossel gneiss emplacement	
	D1,M1 - granulite facies metamorphism	7 kbars, 850° C
2501 - 2484	Crooked Lake gneiss emplacement	
2487	Grace Lake granodiorite emplacement/ D2,M2 - granulite facies metamorphism	7 kbars, 850° C
2477	Intrusion of quartz diorite dykes	
	D3,M3 - amphibolite to granulite facies metamorphism / mylonite zones	
?	Intrusion of Group 1 High-Mg tholeiite dykes	3-5 kbars (maybe as low as 1-2 kbars)
?	Intrusion of Group 1 Fe-rich tholeiite dykes - High-Ti subgroup	
2240	Intrusion of Group 2, (?3) High-Mg tholeiite dykes; Norite	3-5 kbars (maybe as low as 1-2 kbars)
?	Intrusion of Group 1 Fe-rich tholeiite dykes - Low-Ti and PM subgroups	
1754	Intrusion of Group 2 Fe-rich tholeiite dykes	
	D4,M4 - ductile mylonite zones / amphibolite facies	
	D5 brittle deformation / pseudotachylites	≤4-5 kbars
?	Lamprophyre dyke intrusion	
1380	Intrusion of Group 3 Fe-rich tholeiite dykes	4-5 kbars
?	Lamprophyre dyke intrusion	
1241	Intrusion of Group 4 Fe-rich tholeiite dykes / D6,M6 amphibolite facies metamorphism	4-5 kbars
(~1000)	Amphibolite facies metamorphism in SW	6-7 kbars, 600-700° C
(?Phanerozoic)	? Late alkaline dykes	
	D7 brittle / ductile deformation events	

norite emplacement. D_4,M_4 postdates Group 2 Fe-rich tholeiite emplacement at 1754±16 Ma (at least in the Long Peninsula area).

Subsequent D_5 deformation and pseudotachylite formation, at pressures ≤4-5 kbars (Passchier et al., 1991), followed by the emplacement, at 1380±7 Ma and similar depths (Kuehner, 1986), of the Group 3 Fe-rich tholeiite dykes, would have required post-D_4,M_4 uplift. Evidence for reburial, following the emplacement of the Group 4 Fe-rich tholeiites at 1241±5 Ma and pressures of 4-5 kbars (Kuehner, 1986), is provided by the ductile conditions responsible for D_6,M_6, and the subsequent amphibolite facies peak metamorphic conditions associated with ~1000 Ma metamorphism in the southwest Vestfold Hills (Passchier et al., 1991).

The repeated ductile and brittle deformation of D_7, which postdates the 1000 Ma event (Passchier et al., 1991), implies subsequent further uplift.

9.7.3 History of the East Antarctic Shield:

Refinement of the ages of the Vestfold Hills mafic dykes, and confirmation that this ion microprobe zircon technique is a suitable method by which to date mafic intrusives, may have implications for other dyke swarms within the East Antarctic Shield, as well as for previously adjoining regions of Gondwana.

The hypersthene-rich, olivine-normative High-Mg dykes of the Napier Complex, Enderby Land, are petrographically and geochemically virtually identical to the Vestfold Hills High-Mg tholeiites and yield a Rb-Sr whole rock isochron age of 2350±48 Ma (Sheraton and Black, 1981; Sheraton et al., 1987), similar to the 2424±72 Ma Rb-Sr age previously applied to all of the Vestfold Hills High-Mg tholeiite dykes (Collerson and Sheraton, 1986). The new 2240 Ma age of the Vestfold Hills Group 2 High-Mg tholeiites (the Homogeneous and Mottled Norites and their associated fine-grained dykes) may therefore indicate that the 2350±48 Ma Rb-Sr isochron age could also be too old for at least some of the Napier Complex High-Mg tholeiite dykes.

Group I Amundsen dykes of the Napier Complex, dated by the Rb-Sr isochron method at 1190±200 Ma (Sheraton and Black, 1981) and Group II Amundsen dykes are thought (Sheraton and Black, 1981; Sheraton et al., 1987) to be similar in age to the Vestfold Hills Group II and III tholeiites of Collerson and Sheraton (1986), although the large associated error makes meaningful age comparison difficult. These Napier Complex dykes may be coeval with either the Vestfold Hills ~1380 Ma Group 3 Fe-rich tholeiites, the ~1240 Ma Group 4 Fe-rich tholeiites, or even the ~1000 Ma granulite facies metamorphism within the adjacent Proterozoic Rayner Complex. Alternatively, their age might be meaningless, reflecting a combination of events, as did the 1374±125 Ma Group II age of Collerson and Sheraton (1986).

Recent Sm-Nd dating of dolerite dykes in the Bunger Hills region of East Antarctica, ~1000 km east of the Vestfold Hills (Sheraton et al., 1990), has produced an age of ~1140 Ma with a maximum emplacement age of 1151 Ma provided by zircon dating of a crosscut quartz monzodiorite. These dykes are therefore somewhat younger than both the Group 3 and 4 Fe-rich tholeiite dyke suites of the Vestfold Hills.

Deformed, amphibolitized dykes of the Southern Prince Charles Mountains are chemically similar to the Vestfold Hills Group II tholeiites of Collerson and Sheraton (1986) and, on this basis, are thought to be of a similar age (Sheraton et al., 1987); they are yet to be dated. The Borgmassivet Intrusions of western Dronning Maud Land, another major group of Antarctic mafic intrusives comprising dolerite to diorite sills and layered bodies with poorly constrained Middle to Late Proterozoic ages (Tingey, 1991), are another possible target for this method of zircon dating.

Further U-Pb zircon geochronological work in the Vestfold Hills should be directed towards locating felsic segregations within Group 1 Fe-rich tholeiite dykes, Group 1 and 3 High-Mg dykes and the various lamprophyre dykes, although the latter seem unlikely to yield suitable felsic material. Knowledge about the dyke swarms and geological histories of other East Antarctic Archaean nuclei could also benefit from zircon dating of late-stage felsic segregations within mafic intrusives and subsequent comparison with the Vestfold Hills data.

9.7.4 Application on a Global Scale:

It has been shown in the context of this and numerous other studies (e.g. Heaman et al., 1986; Krogh et al., 1987; Heaman and Tarney, 1989; Kamo et al., 1989; Black et al., 1991a) that U-Pb zircon and/or baddeleyite dating represents the most successful means of determining the emplacement ages of individual mafic dykes. The confirmation that primary magmatic zircon can crystallise within late-stage felsic differentiates of mafic magmas, coupled with the ability to analyse individual zircons, provides the potential for extensive and accurate U-Pb dating of mafic material, thereby helping to resolve many global controversies involving poorly constrained or unconstrained mafic dyke emplacement ages.

As mafic dyke swarms are a common feature of continental rifted plate margins, the ability to obtain precise age determinations for them is necessary if accurate global plate reconstructions are to be made. In theory, it should be possible to use mafic dyke ages to correlate the Vestfold Hills and the region of India with which it was contiguous prior to the breakup of Gondwana. However, this may well prove impossible due to the probable location of the latter beneath the extensive deltaic sediments of the Ganges and Brahmaputra Rivers (Black et al., 1991b). Mafic dyke swarms within other Precambrian cratons may in fact provide better opportunities for this type of supercontinent reconstruction. For example, U-Pb bulk zircon and baddeleyite dating has been used to determine the emplacement age of a mafic dyke in southeastern Labrador in an attempt to constrain the time of opening of the proto-Atlantic Ocean (Kamo et al., 1989). However, confirmation must await U-Pb dating of the other mafic dyke swarms (Kamo et al., 1989) thought to be related to this rifting event.

Definition of the Proterozoic histories of numerous dyke-infested cratons could also derive potential benefit from this method of zircon dating. The Scourie dyke swarm, for example, represents a marker horizon emplaced between two major Archaean-Proterozoic tectonothermal events within the Archaean Lewisian Complex of northwest Scotland (e.g. Chapman, 1990). Although U-Pb bulk zircon and baddeleyite dating of these dykes has indicated two periods of Proterozoic dyke emplacement at ~2400 and ~2000 Ma (Heaman and Tarney, 1989), controversy still surrounds conflicting Rb-Sr whole rock ages, Sm-Nd mineral ages and U-Pb baddeleyite ages derived for the various dyke suites, and a reliable age has yet to be determined for the norite suite (Chapman, 1990). Although Heaman and Tarney (1989) only attempted bulk zircon analyses on the norite suite, they did report petrological variations within individual dykes of other suites which were consistent with late stage fluids concentrating in the central parts of the dykes, and which may therefore yield primary magmatic zircon on further examination. Ion microprobe U-Pb dating of individual zircons from each of the four Scourie dyke suites has the potential to solve the problem of their emplacement ages, and thereby define the timing of the Archaean-Proterozoic tectonothermal events.

The Archaean craton of West Greenland is also characterised by Proterozoic dyke swarms whose relative emplacement ages have not been successfully defined through Rb-Sr whole-rock dating (e.g. Kalsbeek and Taylor, 1985). However, the age of one noritic dyke in the Isukasia area has been determined using ion microprobe (SHRIMP) U-Pb dating of two zircons recovered from a co-magmatic felsic igneous segregation (AP Nutman, pers. comm., 1993).

9.8 CONCLUSIONS:

Although the importance of accurately dating mafic dyke swarms has long been recognised, the inherent difficulties associated with determining precise radiometric ages for mafic rocks have resulted in a paucity of precise dyke emplacement ages on a global scale. The results of this study suggest that future mafic dyke sampling programs should be directed towards locating late-stage felsic differentiates, with an awareness that their form may vary from the well-defined linear veins observed in the Vestfold Hills dykes to the more diffuse and coarser-grained granophyric patches sampled in Canada and West Greenland (Heaman et al., 1986; A.P. Nutman, pers. comm., 1993).

REFERENCES

Adams C.J. 1980 New K-Ar age data for South Island lamprophyre dyke swarms in the Buller-S. Westland and Haast-Wanaka areas. *Geological Society of New Zealand Conference*, Christchurch (abstract): 14.

Adams C.J. 1983 Age of the volcanoes and granite basement of the Auckland Islands, Southwest Pacific. *New Zealand Journal of Geology and Geophysics.*, 26: 227-237.

Adams C.J., Morris P.A. and Beggs J.M. 1979 Age and correlation of volcanic rocks of Campbell Island and metamorphic basement of the Campbell Plateau, south-west Pacific. *New Zealand Journal of Geology and Geophysics.*, 22: 679-691.

Adams R.D. 1962 Thickness of the Earth's crust beneath the Campbell Plateau. *New Zealand Journal of Geology and Geophysics.*, 5: 74-85.

Albarede F. 1992 How deep do common basaltic magmas form and differentiate? *Journal of Geophysical Research.*, 97: 10997-11009.

Allègre C.J. 1982 Chemical geodynamics. *Tectonophysics.*, 81: 109-132.

Allègre C.J. and Turcotte D.L. 1985 Geodynamic mixing in the mesosphere boundary layer and the origin of oceanic islands. *Geophysical Research Letters.*, 12: 207-210.

Allègre C.J. and Turcotte D.L. 1986 Implications of a two-component marble-cake mixture. *Nature.*, 323: 123-127.

Allègre C.J., Staudacher T. and Sarda P. 1987 Rare gas systematics: formation of the atmosphere, evolution and structure of the Earth's mantle. *Earth and Planetary Science Letters.*, 81: 127-150.

Alvarez W. 1982 Geological evidence for the geographical pattern of mantle return flow and the driving mechanism of plate tectonics. *Journal of Geophysical Research.*, 87: 6697-6710.

Alvarez W. 1990 Geologic evidence for the plate-driving mechanism: the continental undertow hypothesis and the Australian-Antarctic Discordance. *Tectonics.*, 9: 1213-1220.

Anderson D.L. 1979 Chemical stratification of the mantle. *Journal of Geophysical Research.*, 84: 6297-6298.

Anderson D.L. 1982 Isotopic evolution of the mantle: a model. *Earth and Planetary Science Letters.*, 57: 13-24.

Anderson R.N., McKenzie D., and Sclater J.G. 1973 Gravity, bathymetry and convection in the Earth. *Earth and Planetary Science Letters.*, 18: 391-407.

Anderson R.N., Spariosu D.J., Weissel J.K. and Hayes D.E. 1980 The interrelation between variations in magnetic anomaly amplitudes and basalt magnetization and chemistry along the Southeast Indian Ridge. *Journal of Geophysical Research.*, 85: 3883-3898.

Armstrong R.L. 1978 K-Ar dating: Late Cenozoic McMurdo Volcanic Group and dry valley glacial history, Victoria Land, Antarctica. *New Zealand Journal of Geology and Geophysics.*, 6: 685-698.

Baillie P.W. 1987 A Palaeocene radiometric age for basalt at Bream Creek, south-eastern Tasmania. *Tasmanian Department of Mines Report.*, 1987/21.

Barling J. and Goldstein S.L. 1990 Extreme isotopic variations in Heard Island lavas and the nature of mantle reservoirs. *Nature.*, 348: 59-62.

Barnes C.E. and Cochran J.K. 1990 Uranium removal in oceanic sediments and the oceanic U balance. *Earth and Planetary Science Letters.*, 97: 94-101.

Barreiro B.A. and Cooper A.F. 1987 A Sr, Nd and Pb isotope study of alkaline lamprophyres and related rocks from Westland and Otago, South Island, New Zealand. *Geological Society of America Special Paper.*, 215: 115-125.

Barton J.M. Jr., Klemd R., Allsopp H.L., Auret S.H. and Copperthwaite Y.E. 1987 The geology and geochronology of the Annandagstoppane granite, western Dronning Maud Land, Antarctica. *Contributions to Mineralogy and Petrology.*, 97: 488-496.

Bentley C.R. 1983 Crustal structure of Antarctica from geophysical evidence: a review. In Oliver R.L., James P.R. and Jago J.B. (Editors) *Antarctic Earth Science.*, 491-497. Australian Academy of Science, Canberra.

Black L.P. and James P.R. 1983 Geological history of the Archaean Napier Complex of Enderby Land. In Oliver R.L., James P.R. and Jago J.B. (Editors) *Antarctic Earth Science.*, 11-15. Australian Academy of Science, Canberra.

Black L.P., Kinny P.D. and Sheraton J.W. 1991a The difficulties of dating mafic dykes: An Antarctic example. *Contributions to Mineralogy and Petrology.*, 109: 183-194.

Black L.P., Kinny P.D., Sheraton J.W. and Delor C.P. 1991b Rapid production and evolution of late Archaean felsic crust in the Vestfold Block of East Antarctica. *Precambrian Research.*, 50: 283-310.

Black L.P., Sheraton J.W., Tingey R.J. and McCulloch M.T. 1992 New U-Pb zircon ages from the Denman Glacier area, East Antarctica, and their significance for Gondwana reconstruction. *Antarctic Science.*, 4: 447-460.

Bougault H., Dmitriev L., Schilling J.G., Sobolev A., Joron J.L. and Needham H.D. 1988 Mantle heterogeneity from trace elements: MAR triple junction near 14° N. *Earth and Planetary Science Letters.*, 88: 27-36.

Bradshaw J.D. 1989 Cretaceous geotectonic patterns in the New Zealand region. *Tectonics.*, 8: 803-820.

Briqueu L., Laporte C., Crawford A.J., Hasenaka T., Baker P. and Coltorti M. (in press) Temporal magmatic evolution of the Aoba Basin - central New Hebrides Arc: Pb, Sr and Nd isotopic evidence for the coexistence of two mantle components beneath the arc: ODP leg 143, sites 832 and 833. *Proceedings ODP Scientific Results.*, (134): College Station, TX, (Ocean Drilling Program).

Bryan W.B., Thompson G. and Ludden J.N. 1981 Compositional variation in normal MORB from 22° - 25°N: Mid-Atlantic Ridge and Kane Fracture Zone. *Journal of Geophysical Research.*, 86: 11815-11836.

Buck W.R. 1985 When does small-scale convection begin beneath oceanic lithosphere? *Nature.*, 313: 775-777.

Budahn J.R. and Schmitt R.A. 1985 Petrogenetic modeling of Hawaiian tholeiitic basalts: A geochemical approach. *Geochimica et Cosmochimica Acta.*, 49: 67-87.

Campsie J., Neumann E.R. and Johnson L. 1983 Dredged volcanic rocks from the southern oceans: the Eltanin collection. *New Zealand Journal of Geology and Geophysics.*, 26: 31-45.

Cande S.C. and Mutter J.C. 1982 A revised identification of the oldest sea-floor spreading anomalies between Australia and Antarctica. *Earth and Planetary Science Letters.*, 58: 151-160.

Chaffey D.J., Cliff R.A. and Wilson B.M. 1989 Characterization of the St Helena magma source, In Saunders A.D. and Norry M.J. (Editors) Magmatism in the ocean basins. *Geological Society Special Publication.*, 42: 257-276.

Chapman H.J. 1990 Scourie dyke isotope controversy. *Third International Archaean Symposium*, Perth (abstract): 119-120.

Chase C.G. 1981 Oceanic island Pb: two-stage histories and mantle evolution. *Earth and Planetary Science Letters.*, 52: 277-284.

Chauvel C., Hofmann A.W. and Vidal P. 1992 HIMU-EMI: The French Polynesian connection. *Earth and Planetary Science Letters.*,110: 99-119.

Chen C.-Y., Frey F.A. and Garcia M.O. 1990 Evolution of alkalic lavas at Haleakala Volcano, east Maui, Hawaii. *Contributions to Mineralogy and Petrology.*, 105: 197-218.

Chen C.-Y., Frey F.A., Garcia M.O., Dalrymple G.B. and Hart S.R. 1991 The tholeiite to alkalic basalt transition at Haleakala Volcano, Maui, Hawaii. *Contributions to Mineralogy and Petrology.*, 106: 183-200.

Chen J.H. and Wasserburg G.J. 1983 The least radiogenic Pb in iron meteorites. *Fourteenth Lunar and Planetary Science Conference,* Lunar and Planetary Science Institute, Houston, Texas (abstract): 103-104.

Chen Y. and Morgan J. 1990 Rift valley/no rift valley transition at mid-ocean ridges. *Journal of Geophysical Research.*, 95: 17571-17581.

Christie D.M., Pyle D., Sempéré J.-C., Morgan J.P. and Shor A. 1988 Petrologic and Tectonic Observations in and adjacent to the Australian-Antarctic Discordance. *EOS: Transactions, American Geophysical Union.*, 69: 1426.

Christoffel D.A. and Falconer R.K. 1972 Marine magnetic measurements in the southwest Pacific Ocean and the identification of new tectonic features. In Hayes D.E. (Editor) Antarctic Oceanology II: The Australian-New Zealand sector. *Antarctic Research Series.*, 19: 197-209. American Geophysical Union, Washington D.C.

Clague D.A., Weber W.S. and Dixon J.E. 1991 Picritic glasses from Hawaii. *Nature.*, 353: 553-556.

Class C., Goldstein S.L., Galer S.J.G. and Weis D. 1993 Young formation age of a mantle plume source. *Nature.*, 362: 715-721.

Coffin M.F. and Eldholm O. 1992 Volcanism and continental break-up: a global compilation of large igneous provinces. In Storey B.C., Alabaster T. and Pankhurst R.J. (Editors) Magmatism and the causes of continental break-up. *Geological Society Special Publication.*, 68: 17-30.

Cohen R.S. and O'Nions R.K. 1982 The lead, neodymium and strontium isotopic structure of ocean ridge basalts. *Journal of Petrology.*, 23: 299-324.

Cohen R.S., Evensen N.M., Hamilton P.J. and O'Nions R.K. 1980 U-Pb, Sm-Nd and Rb-Sr systematics of mid-ocean ridge basalt glasses. *Nature.*, 283: 149-153.

Collerson K.D. and Arriens P.A. 1979 Rb-Sr isotope systematics in high-grade gneisses from the Vestfold Hills, East Antarctica. *Journal of the Geological Society of Australia.*, 26: 267-268.

Collerson K.D. and Sheraton J.W. 1986 Age and geochemical characteristics of a mafic dyke swarm in the Archaean Vestfold Block, Antarctica: inferences about Proterozoic dyke emplacement in Gondwana. *Journal of Petrology.*, 27: 853-886.

Collerson K.D., Reid E., Millar D. and McCulloch M.T. 1983a Lithological and Sr-Nd isotopic relationships in the Vestfold Block: implications for Archaean and Proterozoic crustal evolution in the East Antarctic. In Oliver R.L., James P.R. and Jago J.B. (Editors) *Antarctic Earth Science.*, 77-84. Australian Academy of Science, Canberra.

Collerson K.D., Sheraton J.W. and Arriens P. 1983b Granulite facies metamorphic conditions during the Archaean evolution and Late Proterozoic reworking of the Vestfold block, eastern Antarctica. In Lithosphere dynamics and evolution of continental crust. *Geological Society of Australia conference,* Canberra (abstract): 53-54.

Compston W., McDougall I. and Heier K.S. 1968 Geochemical comparison of the Mesozoic basaltic rocks of Antarctica, South Africa, South America and Tasmania. *Geochimica et Cosmochimica Acta.*, 32: 129-149.

Compston W., Williams I.S. and Meyer C. 1984 U-Pb geochronology of zircons from lunar breccia 73217 using a sensitive high mass-resolution ion microprobe. Proceedings of the 14th Lunar Science Conference - *Journal of Geophysical Research.*, 89: B525-534.

Coombs D.S., Cas R.A., Kawachi Y., Landis C.A., McDonough W.F. and Reay A. 1986 Cenozoic volcanism in north, east and central Otago. In Smith I.E.M (Editor) Late Cenozoic Volcanism in New Zealand. *Royal Society of New Zealand - Bulletin.*, 23: 279-312.

Cooper A.F. 1986 A carbonatitic lamprophyre dike swarm from the Southern Alps, Otago and Westland. In Smith I.E.M (Editor) Late Cenozoic Volcanism in New Zealand. *Royal Society of New Zealand - Bulletin.*, 23: 313-336.

Cooper J.A. and Green D.H. 1969 Lead isotope measurements on lherzolite inclusions and host basanites from western Victoria, Australia. *Earth and Planetary Science Letters.*, 6: 69-76.

Cousens B.L. and Ludden J.N. 1991 Radiogenic isotope studies of oceanic basalts: a window into the mantle. In Heaman L. and Ludden J.N. (Editors) Applications of radiogenic isotope systems to problems in geology. *Mineralogical Association of Canada Short Course Handbook.*, 19: 225-257.

Cox K.G., Bell J.D. and Pankhurst R.J. 1979 *The interpretation of igneous rocks.* Unwin Hyman Ltd., U.K., 450 pp.

Cullen D.J. 1969 Quaternary volcanism at the Antipodes Islands: its bearing on structural interpretation of the Southwest Pacific. *Journal of Geophysical Research.*, 74: 4213-4220.

Cullen D.J. 1970 A tectonic analysis of the south-west Pacific. *New Zealand Journal of Geology and Geophysics.*, 13: 7-20.

Cumming G.L. and Richards J.R. 1975 Ore lead isotope ratios in a continuously changing Earth. *Earth and Planetary Science Letters.*, 28: 155-171.

Cundari A. 1989 East Australian leucitite suite. In Johnson R.W. (Editor) *Intraplate Volcanism in Eastern Australia and New Zealand.*, 131. Cambridge University Press, Cambridge, U.K.

Dalrymple G.B. and Clague D.A. 1976 Age of the Hawaiian - Emperor bend. *Earth and Planetary Science Letters.*, 31: 313-329.

Davidson A. and van Breeman O. 1988 Baddeleyite - zircon relationships in coronitic metagabbro, Grenville Province, Ontario: implications for geochronology. *Contributions to Mineralogy and Petrology.*, 100: 291-299.

Davies G.F. 1988 Ocean bathymetry and mantle convection 1. large-scale flow and hotspots. *Journal of Geophysical Research.*, 93: 10467-10480.

Davies G.F. 1990 Mantle plumes, mantle stirring and hotspot chemistry. *Earth and Planetary Science Letters.*, 99: 94-109.

Davies G.F. and Richards M.A. 1992 Mantle convection. *Journal of Geology.*, 100: 151-206.

Day R.A. 1983 Petrology and geochemistry of the Older Volcanics, Victoria. Unpublished PhD thesis, Monash University, Melbourne, Australia.

Day R.A. 1989 Older Volcanics. In Johnson R.W. (Editor) *Intraplate Volcanism in Eastern Australia and New Zealand.*, 133-135. Cambridge University Press, Cambridge, U.K.

Deer W.A., Howie R.A. and Zussman J. 1992 *An introduction to the rock-forming minerals*, (2nd edition). Longman Group Limited, U.K., 696 pp.

Delor C.P. and Rock N.M.S. 1991 Alkaline - ultramafic lamprophyre dykes from the Vestfold Hills, Princess Elizabeth Land (East Antarctica): primitive magmas of deep mantle origin. *Antarctic Science.*, 3: 419-432.

DePaolo D.J. 1988 *Neodymium isotope geochemistry - an introduction.* Springer-Verlag, New York, 187 pp.

DePaolo D.J. and Wasserburg G.J. 1976 Inferences about magma sources and mantle structure from variations of $^{143}Nd/^{144}Nd$. *Geophysical Research Letters.*, 3: 743-746.

Devey C.W., Albarede F., Cheminee J.-L., Michard A., Muhe R. and Stoffers P. 1990 Active submarine volcanism on the Society Hotspot swell (west Pacific): A geochemical study. *Journal of Geophysical Research.*, 95: 5049-5066.

Diebold J., Carpenter G., Hayes D.E., Weissel J.K. and Anderson R.N. 1977 Seismic refraction investigations of the depth anomaly south of Australia. *EOS: Transactions, American Geophysical Union.*, 58: 505.

Diraison C. 1991 Le volcanisme aerien des archipels polynesiens de la Societe, des Marquises et des Australes-Cook. Tephrostratigraphie, datation isotopique et geochemie comparees. Contribution a l'etude des origines du volcanisme intraplaque du Pacifique Central. Unpublished PhD thesis, L'Universite de Bretagne Occidentale.

Doell R.R. and Dalrymple G.B. 1973 Potassium-argon ages and palaeomagnetism of the Waianae and Koolau volcanic series, Oahu, Hawaii. *Geological Society of America Bulletin.*, 84: 1217-1242.

Dosso L., Bougault H., Beuzart P., Calvez J.-Y. and Joron J.-L. 1988 The geochemical structure of the South-East Indian Ridge. *Earth and Planetary Science Letters.*, 88: 47-59.

Dostal J., Dupuy C. and Liotard J.M. 1982 Geochemistry and origin of basaltic lavas from Society Islands, French Polynesia (south central Pacific Ocean). *Bulletin Volcanologique.*, 45-1: 51-62.

Duncan R.A. 1975 Linear volcanism in French Polynesia. Unpublished PhD thesis, The Australian National University, Canberra, Australia.

Duncan R.A. 1981 Hotspots in the southern oceans - an absolute frame of reference for motion of the Gondwana continents. *Tectonophysics.*, 74: 29-42.

Duncan R.A. and Compston W. 1976 Sr-isotopic evidence for an old mantle source region for French Polynesian volcanism. *Geology.*, 4: 728-732.

Duncan R.A. and McDougall I. 1989 Volcanic time-space relationships. In Johnson R.W. (Editor) *Intraplate Volcanism in Eastern Australia and New Zealand.*, 43-54. Cambridge University Press, Cambridge, U.K.

Duncan R.A. and Varne R. 1988 The age and distribution of the igneous rocks of Macquarie Island. *Papers and Proceedings of the Royal Society of Tasmania.*, 122: 45-50.

Duncan R.A., McCulloch M.T., Barsczus H.G. and Nelson D.R. 1986 Plume versus lithospheric sources for melts at Ua Pou, Marquesas Islands. *Nature.*, 322: 534-538.

Dupré B. and Allègre C.J. 1980 Pb-Sr-Nd isotopic correlation and the chemistry of the North Atlantic mantle. *Nature.*, 286: 17-22.

Dupré B. and Allègre C.J. 1983 Pb-Sr isotope variation in Indian Ocean basalts and mixing phenomena. *Nature.*, 303: 142-146.

Dupuy C., Barsczus H.G, Liotard J.M. and Dostal J. 1988 Trace element evidence for the origin of ocean island basalts: an example from the Austral Islands (French Polynesia). *Contributions to Mineralogy and Petrology.*, 98: 293-302.

Dupuy C., Barsczus H.G., Dostal J., Vidal P. and Liotard J.M. 1989 Subducted and recycled lithosphere as the mantle source of ocean island basalts from southern Polynesia, central Pacific. *Chemical Geology.*, 77: 1-18.

Dupuy C., Vidal P., Barsczus H.G. and Chauvel C. 1987 Origin of basalts from the Marquesas Archipelago (south central Pacific Ocean): isotope and trace element constraints. *Earth and Planetary Science Letters.*, 82: 145-152.

Edwards A.B. 1938 The age and physiographical relationships of some Cainozoic basalts in central and eastern Tasmania. *Papers and Proceedings of the Royal Society of Tasmania.*, 175-199.

Eggins S.M., Green D.H. and Falloon T.J. 1991 The Tasmantid Seamounts: shallow melting and contamination of an EMI mantle plume. *Earth and Planetary Science Letters.*, 107: 448-462.

Ellerman P.J. and Kyle P.R. 1990 Franklin Island. In LeMasurier W.E. and Thomson J.W. (Editors) Volcanoes of the Antarctic plate and Southern Oceans. *Antarctic Research Series.*, 48: 91-93. American Geophysical Union, Washington D.C.

Embleton B.J.J. 1984 Magnetic properties of oriented rock samples from Sturge Island and Sabrina Island in the Balleny Group. In Lewis D. (Author) *Voyage to the ice. The Antarctic expedition of Solo.*, 128-131. Australian Broadcasting Commission, Sydney.

Etheridge M.A., Symonds P.A. and Lister G.S. 1989 Application of the detachment model to reconstruction of conjugate passive margins. In Tankard A.J. and Balkwill H.R. (Editors) Extensional tectonics and stratigraphy of the north Atlantic margins. *American Association of Petroleum Geologists Memoir.*, 46: 23-40.

Everard J.L. 1984 Appendix A: Petrography of Tertiary basalt, altered dolerite and tuff samples. In Gulline A.B. Sorell, Tasmania. *Tasmanian Department of Mines Geological Atlas 1 Mile Series Explanatory Report*, Sheet 38 (82155).

Evernden J.F. and Richards J.R. 1962 Potassium-argon ages in eastern Australia. *Journal of the Geological Society of Australia.*, 9: 1-49.

Ewart A. and Menzies M.A. 1989 Isotope Geochemistry. In Johnson R.W. (Editor) *Intraplate Volcanism in Eastern Australia and New Zealand.*, 235-284. Cambridge University Press, Cambridge, U.K.

Ewart A., Chappell B.W. and Menzies M.A. 1988 An overview of the geochemical and isotopic characteristics of the eastern Australian Cainozoic volcanic provinces. *Journal of Petrology., Special Lithosphere Issue*: 225-273.

Falconer R.K. 1972 The Indian-Antarctic-Pacific Triple Junction. *Earth and Planetary Science Letters.*, 17: 151-168.

Falloon T.J. and Green D.H. 1987 Anhydrous partial melting of MORB pyrolite and other peridotite compositions at 10 kbar: implications for the origin of primitive MORB glasses. *Mineralogy and Petrology.*, 37: 181-219.

Falloon T.J., Green D.H., Hatton C.J. and Harris K.L. 1988 Anhydrous partial melting of a fertile and depleted peridotite from 2 to 30 kb and application to basalt petrogenesis. *Journal of Petrology.*, 29: 1257-1282.

Falloon T.J., Varne R., Hart S.R. and Duncan R.A. (in prep.) The age and petrogenesis of alkaline volcanic rocks from Christmas Island and Vening Meinesz seamounts, NE Indian Ocean.

Fitzgerald P.G., Sandiford M, Barrett P.J. and Gleadow A.J.W. 1987 Asymmetric extension associated with uplift and subsidence in the Transantarctic Mountains and Ross Embayment. *Earth and Planetary Science Letters.*, 81: 67-78.

Flower M.F.J. 1981 Thermal and kinematic control on mid-ocean ridge magma fractionation: contrasts between Atlantic and Pacific spreading axes. *Journal of the Geological Society of London.*, 138: 695-712.

Fodor R.V., Husler J.W., Kumar N. 1977 Petrology of volcanic rocks from an aseismic ridge: implications for the origin of the Rio Grande Rise, South Atlantic Ocean. *Earth and Planetary Science Letters.*, 35: 225-233.

Ford R.J. 1983 The alkaline rocks of Port Cygnet, Tasmania. Unpublished PhD thesis, University of Tasmania.

Ford R.J. 1989 Cretaceous alkaline rocks. In Burrett C.F. and Martin E.L. (Editors) Geology and mineral resources of Tasmania. *Special Publication Geological Society of Australia.*, 15: 381-383.

Forsyth D.W., Ehrenbard R.L. and Chapin S. 1987 Anomalous upper mantle beneath the Australian-Antarctic Discordance. *Earth and Planetary Science Letters.*, 84: 471-478.

Francheteau J. and Ballard R.D. 1983 The East Pacific Rise near 21°N, 13°N and 20°S: inferences for along-strike variability of axial processes of the mid-ocean ridge. *Earth and Planetary Science Letters.*, 64: 93-116.

Frey F.A., Bryan W.B. and Thompson G. 1974 Atlantic ocean floor: geochemistry and petrology of basalts from legs 2 and 3 of the Deep Sea Drilling Project. *Journal of Geophysical Research.*,79: 5507-5527.

Frey F.A., Dickey J.S. Jnr., Thompson G., Bryan W.B. and Davies H.L. 1980 Evidence for heterogeneous primary MORB and mantle sources, northwest Indian Ocean. *Contributions to Mineralogy and Petrology.*, 74: 387-402.

Frey F.A., Garcia M.O. and Roden M.F. (in press) Geochemical characteristics of Koolau Volcano: Implications of intershield geochemical differences among Hawaiian volcanoes. *Geochimica et Cosmochimica Acta.*

Frey F.A., Green D.H. and Roy S.D. 1978 Integrated models of basalt petrogenesis: a study of quartz tholeiites to olivine melilitites from south eastern Australia utilizing geochemical and experimental petrological data. *Journal of Petrology.*, 19: 463-513.

Frey F.A., Jones W.B., Davies H. and Weis D. 1991 Geochemical and petrologic data for basalts from sites 756, 757 and 758: implications for the origin and evolution of ninetyeast ridge. *Proceedings of the Ocean Drilling Program, Scientific Results.*, 121: 611-659.

Frey F.A., Wise W.S., Garcia M.O., West H., Kwon S.-T. and Kennedy A. 1990 Evolution of Mauna Kea Volcano, Hawaii: petrologic and geochemical constraints on postshield volcanism. *Journal of Geophysical Research.*, 95: 1271-1300.

Fujii T. and Scarfe C.M. 1985 Composition of liquids coexisting with spinel lherzolite at 10 kbar and the genesis of MORB. *Contributions to Mineralogy and Petrology.*, 90: 18-28.

Futa K. and LeMasurier W.E. 1983 Nd and Sr isotopic studies on Cenozoic mafic lavas from West Antarctica: another source for continental alkali basalts. *Contributions to Mineralogy and Petrology.*, 83: 38-44.

Gamble J.A. and Adams C.J. 1990 Antipodes Islands. In LeMasurier W.E. and Thomson J.W. (Editors) Volcanoes of the Antarctic plate and Southern Oceans. *Antarctic Research Series.*, 48: 468-469. American Geophysical Union, Washington D.C.

Gamble J.A., Morris P.A. and Adams C.J. 1986 The geology, petrology and geochemistry of Cenozoic volcanic rocks from the Campbell Plateau and Chatham Rise. In Smith I.E.M (Editor) Late Cenozoic Volcanism in New Zealand. *Royal Society of New Zealand - Bulletin.*, 23: 345-365.

Garfunkel Z. 1975 Growth, shrinking, and long-term evolution of plates and their implications for the flow pattern in the mantle. *Journal of Geophysical Research.*, 80: 4425-4432.

Gariépy C. and Dupré B. 1991 Pb isotopes and crust-mantle evolution. In Heaman L. and Ludden J.N. (Editors) Applications of radiogenic isotope systems to problems in geology. *Mineralogical Association of Canada Short Course Handbook.*, 19: 191-224.

Gill C.P. and Collerson K.D. 1992 Origin of the HIMU geochemical signature: constraints from the Balleny Islands, Ross Sea, Antarctica. *EOS: Transactions, American Geophysical Union.*, 73: 375.

Gill C.P. and Collerson K.D. (in prep.) The origin of the HIMU geochemical signature by carbonate melt metasomatism: constraints from the Balleny Islands, Ross Sea, Antarctica.

Glazner A.F. 1984 Activities of olivine and plagioclase components in silicate melts and their application to geothermometry.*Contributions to Mineralogy and Petrology.*, 88: 260-268.

Goldich S.S., Treves S.B., Suhr N.H. and Stuckless J.S. 1975 Geochemistry of the Cenozoic volcanic rocks of Ross Island and vicinity, Antarctica. *The Journal of Geology.*, 83: 415-435.

Gordon R.D. and Jurdy D.M. 1986 Cenozoic global plate motions. *Journal of Geophysical Research.*, 91: 12389-12406.

Govindaraju K. 1989 1989 compilation of working values and sample description for 272 geostandards. *Geostandards Newsletter, special issue.*,13: 1-113.

Graham D., Lupton J., Klein E., Christie D. and Pyle D. 1990 Helium isotope geochemistry of the Australian-Antarctic Discordance. Seventh International Conference on Geochronology, Cosmochronology and Isotope Geology, Canberra. *Geological Society of Australia abstracts.*, 27: 41.

Graham D.W., Humphris S.E., Jenkins W.J. and Kurz M.D. 1992 Helium isotope geochemistry of some volcanic rocks from Saint Helena. *Earth and Planetary Science Letters.*, 110: 121-131.

Graham D.W., Zindler A., Kurz M.D., Jenkins W.J., Batiza R. and Staudigel H. 1988 He, Pb, Sr and Nd isotope constraints on magma genesis and mantle heterogeneity beneath young Pacific seamounts. *Contributions to Mineralogy and Petrology.*, 99: 446-463.

Green T.H. 1992 Petrology and geochemistry of basaltic rocks from the Balleny Islands, Antarctica. *Australian Journal of Earth Sciences.*, 39: 603-617.

Griffin B.J. and Varne R. 1980 The Macquarie Island ophiolite complex: Mid-Tertiary oceanic lithosphere from a major ocean basin. *Chemical Geology.*, 30: 285-308.

Griffiths J.R. and Varne R. 1972 Evolution of the Tasman Sea, Macquarie Ridge and Alpine Fault. *Nature.*, 235: 83-86.

Griffiths R.W. and Campbell I.H. 1990 Stirring and structure in mantle starting plumes. *Earth and Planetary Science Letters.*, 99: 66-78.

Griffiths R.W. and Campbell I.H. 1991 On the dynamics of long-lived plume conduits in the convecting mantle. *Earth and Planetary Science Letters.*, 103: 214-227.

Griffiths R.W. and Richards M.A. 1989 The adjustment of mantle plumes to changes in plate motion. *Geophysical Research Letters.*, 16: 437-440.

Grindley G.W. and Oliver P.J. 1983 Palaeomagnetism of Cretaceous volcanic rocks from Marie Byrd Land, Antarctica. In Oliver R.L., James P.R. and Jago J.B. (Editors) *Antarctic Earth Science.*, 573-578. Australian Academy of Science, Canberra.

Grindley G.W., Adams C.J.D., Lumb J.T. and Watters W.A. 1977 Palaeomagnetism, K-Ar dating and tectonic interpretation of Upper Cretaceous and Cenozoic volcanic rocks of the Chatham Islands, New Zealand. *New Zealand Journal of Geology and Geophysics.*, 20: 425-467.

Halliday A.N., Davidson J.P., Holden P., DeWolf C., Lee D.-C. and Fitton J.G. 1990 Trace-element fractionation in plumes and the origin of HIMU mantle beneath the Cameroon line. *Nature.*, 347: 523-528.

Hamelin B. and Allègre C.J. 1985 Large-scale regional units in the depleted upper mantle revealed by an isotope study of the South-West Indian Ridge. *Nature.*, 315: 196-199.

Hamelin B., Dupré B. and Allègre C.J. 1984 Lead-strontium isotopic variation along the East Pacific Rise and the Mid-Atlantic Ridge: a comparative study. *Earth and Planetary Science Letters.*, 67: 340-350.

Hamelin B., Dupré B. and Allègre C.J. 1986 Pb-Sr-Nd isotopic data of Indian Ocean ridges: new evidence of large-scale mapping of mantle heterogeneities. *Earth and Planetary Science Letters.*, 76: 288-298.

Hamelin B., Manhes G., Albarede F. and Allègre C.J. 1985 Precise lead isotope measurements by the double spike technique: A reconsideration. *Geochimica et Cosmochimica Acta.*, 49: 173- 182.

Hamilton W. 1972 The Hallett Volcanic Province. *United States Geological Survey Professional Paper.*, 456-C: 1-62.

Harding R.R. and McLeod I.R. 1967 Age of dolerite dykes in the Vestfold Hills, Antarctica. *Nature.*, 215: 149-151.

Harley S.L. 1989 The origins of granulites: a metamorphic perspective. *Geological Magazine.*, 126: 215-247.

Harrington H.J, Wood B.L., McKellar I.C. and Lensen G.J. 1967 Topography and geology of the Cape Hallett district, Victoria Land, Antarctica. *New Zealand Geological Survey Bulletin.*; 80: 100 pp.

Harrington H.J. 1958 Nomenclature of rock units in the Ross Sea region, Antarctica. *Nature.*, 182: 290.

Hart S.R. 1984 A large-scale isotope anomaly in the Southern Hemisphere mantle. *Nature.*, 309: 753-757.

Hart S.R. 1988 Heterogeneous mantle domains: signatures, genesis and mixing chronologies. *Earth and Planetary Science Letters.*, 90: 273-296.

Hart S.R., Gerlach D.C. and White W.M. 1986 A possible new Sr-Nd-Pb mantle array and consequences for mantle mixing. *Geochimica et Cosmochimica Acta.*, 50: 1551-1557.

Hart S.R., Hauri E.H., Oschmann L.A. and Whitehead J.A. 1992 Mantle plumes and entrainment: isotopic evidence. *Science.*, 256: 517-520.

Hatherton T., Dawson E.W. and Kinsky F.C. 1965 Balleny Islands reconnaissance expedition, 1964. *New Zealand Journal of Geology and Geophysics.*, 8: 164 -179.

Hauri E. H. and Hart S.R. 1993 Re-Os isotope systematics of HIMU and EMII oceanic island basalts from the south Pacific Ocean. *Earth and Planetary Science Letters.*, 114: 353-371.

Hauri E.H., Shimizu N., Dieu J.J. and Hart S.R. 1993 Evidence for hotspot-related carbonatite metasomatism in the oceanic upper mantle. *Nature.*, 365: 221-227.

Hawkesworth C.J., Rogers N.W., van Calsteren P.W.C. and Menzies M.A. 1984 Mantle enrichment processes. *Nature.*, 311: 331-335.

Hayes D.E. 1976 Nature and implications of asymmetric sea-floor spreading - "Different rates for different plates". *Geological Society of America Bulletin.*, 87: 994-1002.

Hayes D.E. 1988 Age-depth relationships and depth anomalies in the southeast Indian Ocean and south Atlantic Ocean. *Journal of Geophysical Research.*, 93: 2937-2954.

Hayes D.E. and Conolly J.R. 1972 Morphology of the southeast Indian Ocean. In Hayes D.E. (Editor) Antarctic Oceanology II: The Australian - New Zealand Sector. *Antarctic Research Series.*, 19: 125-145. American Geophysical Union, Washington D.C.

Hayes D.E. and Ringis J. 1973 Seafloor spreading in the Tasman Sea. *Nature.*, 243: 454-458.

Hayes D.E. and Talwani M. 1972 Geophysical investigation of the Macquarie Ridge complex. In Hayes D.E. (Editor) Antarctic Oceanology II: The Australian-New Zealand sector. *Antarctic Research Series.*, 19: 211-234. American Geophysical Union, Washington D.C.

Hayes D.E., Heirtzler J.R., Herron E.M. and Pitman W.C. III 1969 Preliminary report of volume 21 U.S.N.S. Eltanin cruises 22-27. *Lamont Doherty Geological Observatory of Columbia University Technical Report*: 2-CU-2-69.

Heaman L. and Parrish R. 1991 U-Pb geochronology of accessory minerals. In Heaman L. and Ludden J.N. (Editors) Applications of radiogenic isotope systems to problems in geology. *Mineralogical Association of Canada short course handbook*, 19: 59-102.

Heaman L.M. and Tarney J. 1989 U-Pb baddeleyite ages for the Scourie dyke swarm, Scotland: evidence for two distinct intrusion events. *Nature.*, 340: 705-708.

Heaman L.M., Machado N., Krogh T.E. and Weber W. 1986 Precise U-Pb zircon ages for the Molson dyke swarm and the Fox River sill: constraints for Early Proterozoic crustal evolution in northeastern Manitoba, Canada. *Contributions to Mineralogy and Petrology.*, 94: 82-89.

Hedge C.E., Futa K., Engel C.G. and Fisher R.L. 1979 Rare earth abundances and Rb-Sr systematics of basalts, gabbro, anorthosite and minor granitic rocks from the Indian Ocean Ridge system, western Indian Ocean. *Contributions to Mineralogy and Petrology.*, 68: 373-376.

Hedge C.E., Watkins N.D., Hildreth R.A. and Doering W.P. 1973 $^{87}Sr/^{86}Sr$ ratios in basalts from islands in the Indian Ocean. *Earth and Planetary Science Letters.*, 21: 29-34.

Hergt J.M and Hawkesworth C.J. (in press) The Pb, Sr and Nd isotopic evolution of the Lau Basin: implications for mantle dynamics during back-arc opening. *Proceedings ODP Scientific Results.*, (135): College Station, TX, (Ocean Drilling Program).

Hergt J.M. and Nilsson-Farley K. (in press) Major, trace element, and isotope (Pb, Sr, and Nd) variations in site 834 basalts: implications for the initiation of backarc opening. *Proceedings ODP Scientific Results.*, (135): College Station, TX, (Ocean Drilling Program).

Hergt J.M., Chappell B.W., McCulloch M.T., McDougall I. and Chivas A.R. 1989a Geochemical and isotopic constraints on the origin of the Jurassic dolerites of Tasmania. *Journal of Petrology.*, 30: 841-883.

Hergt J.M., McDougall I., Banks M.R. and Green D.H. 1989b Jurassic dolerite. In Burrett C.F. and Martin E.L. (Editors) Geology and mineral resources of Tasmania. *Special Publication Geological Society of Australia.*, 15: 375-381.

Hey R. and Vogt P. 1977 Spreading center jumps and sub-axial asthenosphere flow near the Galapagos Hotspot. *Tectonophysics.*, 37: 41-52.

Hey R.N., Naar D.F., Kleinrock M.C., Phipps Morgan W.J., Morales E. and Schilling J.-G. 1985 Microplate tectonics along a superfast seafloor spreading system near Easter Island. *Nature.*, 317: 320-325.

Hickey-Vargas R., Hergt J.M. and Spadea P. (submitted) The Indian Ocean isotopic signature in western Pacific marginal basins: origin and significance. *A.G.U. Monograph Series.*

Hill R.I. 1991 Starting plumes and continental break-up. *Earth and Planetary Science Letters.*, 104: 398-416.

Hirose K. and Kushiro T. 1993 Partial melting of dry peridotites at high pressures: determinations of compositions of melts segregated from peridotite using aggregates of diamond. *Earth and Planetary Science Letters.*, 114: 477-489.

Hoek J.D. and Passchier C.W. 1991 The Proterozoic structural evolution of the Vestfold Hills, an Archaean craton in a Proterozoic metamorphic belt, East Antarctic Shield. *Sixth International Symposium on Antarctic Earth Sciences*, Japan (abstract): 231.

Hoernle K. and Schmincke H-U. 1993 The role of partial melting in the 15-Ma geochemical evolution of Gran Canaria: a blob model for the Canary Hotspot. *Journal of Petrology.*, 34: 599-626.

Hofmann A.W. and White W.M. 1982 Mantle plumes from ancient oceanic crust. *Earth and Planetary Science Letters.*, 57: 421-436.

Hofmann A.W., Jochum K.P., Seufert M. and White W.M. 1986 Nb and Pb in oceanic basalts; new constraints on mantle evolution. *Earth and Planetary Science Letters.*, 79: 33-45.

Huang T.C., Watkins N.D. and Shaw D.M. 1975 Atmospherically transported volcanic glass in deep-sea sediments: Volcanism in sub-Antarctic latitudes of the South Pacific during Late Pliocene and Pleistocene time. *Geological Society of America Bulletin.*, 86: 1305-1315.

Hubble T.C.T., Robson A.D., Jenkins C.J., Garces J. and Packham G.H. 1987 Geophysical and geological results of the Cook 17-86 (seamap 4) cruise: Sydney to Cook Strait. *Ocean Sciences Institute, University of Sydney, report.*, 24: 60 pp.

Humphris S.E. and Thompson G. 1983 Geochemistry of rare earth elements in basalts from the Walvis Ridge: implications for its origin and evolution. *Earth and Planetary Science Letters.*, 66: 223-242.

Irving A.J. and Green D.H. 1976 Geochemistry and petrogenesis of the Newer Basalts of Victoria and South Australia. *Journal of the Geological Society of Australia.*, 23: 45-66.

Irving A.J. and Price R.C. 1981 Geochemistry and evolution of lherzolite-bearing phonolitic lavas from Nigeria, Australia, East Germany and New Zealand. *Geochimica et Cosmochimica Acta.*, 45: 1309-1320.

Ito E., White W.M. and Gopel C. 1987 The O, Sr, Nd and Pb isotope geochemistry of MORB. *Chemical Geology.*, 62: 157-176.

Jacobsen S.B. and Wasserburg G.J. 1984 Sm-Nd isotopic evolution of chondrites and achondrites, II. *Earth and Planetary Science Letters.*, 67: 137-150.

James P.R. and Tingey R.J. 1983 The Precambrian geological evolution of the East Antarctic metamorphic shield - a review. In Oliver R.L., James P.R. and Jago J.B. (Editors) *Antarctic Earth Science.*, 5-10. Australian Academy of Science, Canberra.

Jenkins C.J. 1985 Geological/geophysical results of the seamap 1 (Cook 1/84) cruise, south Tasman Sea and New Zealand region with some derived acoustic models. *Ocean Sciences Institute, University of Sydney, report.*, 13: 39 pp.

Jenkins C.J., Packham G.H., Hubble T.C., Quilty P.G. and Adams C.J. 1992 Trace of the Balleny hotspot in the Tasman Sea and Southern Ocean from 70 Ma to present. *First Australian Marine Geoscience Meeting, Canberra* (abstract).

Jenkins C.J., Packham G.H., Hubble T.C., Quilty P.G. and Adams C.J. (in prep.) Trace of the Balleny Hotspot in the Tasman SEa and Southern Ocean from 70 Ma to present.

Jenner G.A. and Hertogen J. 1986 Constraints on processes affecting the origin of oceanic crust: geochemical evidence from the 0 - 35 M.y. age basalts between 30°N and 40°N, MAR. *Journal of Geodynamics.*, 5: 49-78.

Jenner G.A., Longerich H.P., Jackson S.E. and Fryer B.J. 1990 ICP-MS - A powerful tool for high-precision trace-element analysis in earth sciences: evidence from analysis of selected U.S.G.S. reference samples. *Chemical Geology.*, 83: 133-148.

Jochum K.P., Seufert H.M. and Thirlwall M.F. 1990 Multi-element analysis of 15 international standard rocks by isotope-dilution spark source mass spectrometry. *Geostandards Newsletter.*, 14: 469-473.

Johnson G.L., Kyle P.R., Vanney J.R. and Campsie J. 1982 Geology of Scott and Balleny Islands, Ross Sea, Antarctica and morphology of adjacent seafloor. *New Zealand Journal of Geology and Geophysics.*, 25: 427-436.

Johnson H.P., Karsten J.L. and Delaney J.R. 1983 A detailed study of the Cobb offset of the Juan de Fuca Ridge: evolution of a propagating rift. *Journal of Geophysical Research.*, 88: 2297-2315.

Jones L.M. and Walker R.L. 1972 Geochemistry of the McMurdo Volcanics, Victoria Land Part 1. Strontium isotope composition. *Antarctic Journal of the United States.*, 7: 142-144.

Jones L.M., Faure G., Taylor K.S. and Corbato C.E. 1983 The origin of salts on Mount Erebus and along the coast of Ross Island, Antarctica. *Isotope Geoscience.*, 1: 57-64.

Joyce E.B. and Day R.A. 1989 Victoria and South Australia - Introduction. In Johnson R.W. (Editor) *Intraplate Volcanism in Eastern Australia and New Zealand.*, 132-133. Cambridge University Press, Cambridge, U.K.

Kalsbeek F. and Taylor P.N. 1985 Age and origin of early Proterozoic dolerite dykes in South-West Greenland. *Contributions to Mineralogy and Petrology.*, 89: 307-316.

Kamo S.L., Gower C.F. and Krogh T.E. 1989 Birthdate for the Iapetus Ocean? A precise U-Pb zircon and baddeleyite age for the Long Range dikes, southeast Labrador. *Geology.*, 17: 602-605.

Kay R., Hubbard N.J. and Gast P.W. 1970 Chemical characteristics and origin of oceanic ridge volcanic rocks. *Journal of Geophysical Research.*, 75: 1585-1613.

Kay R.W. and Gast P.W. 1973 The rare earth content and origin of alkali-rich basalts. *Journal of Geology.*, 81: 653-682.

Kempe D.R.C. 1973 Rocks from Antarctica: The Discovery collection in the British Museum (Natural History). *Bulletin of the British Museum of Natural History, Mineralogy.*, 2: 337-376.

Kinny P.D., Black L.P. and Sheraton J.W. 1993 Zircon ages and the distribution of Archaean and Proterozoic rocks in the Rauer Islands. *Antarctic Science.*, 5: 193-206.

Klein E.M. and Langmuir C.H. 1987 Global correlations of ocean ridge basalt chemistry with axial depth and crustal thickness. *Journal of Geophysical Research.*, 92: 8089-8115.

Klein E.M. and Langmuir C.H. 1989 Local versus global variations in ocean ridge basalt composition: a reply. *Journal of Geophysical Research.*, 94: 4241-4252.

Klein E.M., Langmuir C.H. and Staudigel H. 1991 Geochemistry of basalts from the Southeast Indian Ridge. *Journal of Geophysical Research.*, 96: 2089-2107.

Klein E.M., Langmuir C.H., Zindler A., Staudigel H. and Hamelin B. 1988 Isotope evidence of a mantle convection boundary at the Australian-Antarctic Discordance. *Nature.*, 333: 623-629.

Knutson J., Sun S.-S. and Ewart A. 1989 Comparison with other intraplate areas. In Johnson R.W. (Editor) *Intraplate Volcanism in Eastern Australia and New Zealand.*, 313-321. Cambridge University Press, Cambridge, U.K.

Krogh T.E., Corfu F., Davis D.W., Dunning G.R., Heaman L.H., Kamo S.L., Machado N., Greenough J.D. and Nakamura E. 1987 Precise U-Pb isotopic ages of diabase dykes and mafic to ultramafic rocks using trace amounts of baddeleyite and zircon. In Halls H.C. and Fahrig W.F. (Editors) Mafic Dyke Swarms. *Geological Association of Canada Special Paper.*, 34: 147-152.

Kuehner S.M. 1986 Mafic dykes of the East Antarctic Shield: experimental, geochemical and petrological studies focusing on the Proterozoic evolution of the crust and mantle. Unpublished PhD thesis, University of Tasmania.

Kuehner S.M. 1987 Mafic dykes of the East Antarctic Shield: a note on the Vestfold Hills and Mawson Coast occurrences. In Halls H.C. and Fahrig W.F. (Editors) Mafic Dyke Swarms. *Geological Association of Canada Special Paper.*, 34: 429-430.

Kuo B-Y. 1993 Thermal anomalies beneath the Australian-Antarctic Discordance. *Earth and Planetary Science Letters.*, 119: 349-364.

Kurz M.D. 1991 Noble gas isotopes in oceanic basalts: controversial constraints on mantle models. In Heaman L. and Ludden J.N. (Editors) Applications of radiogenic isotope systems to problems in geology. *Mineralogical Association of Canada Short Course Handbook.*, 19: 259-286.

Kyle P.R. 1976 Geology, mineralogy and geochemistry of the Late Cenozoic McMurdo Volcanic Group, Victoria Land, Antarctica. Unpublished PhD thesis, Victoria University of Wellington, New Zealand.

Kyle P.R. 1981 Mineralogy and geochemistry of a basanite to phonolite sequence at Hut Point Peninsula, Antarctica, based on core from Dry Valley Drilling Project drillholes 1, 2 and 3. *Journal of Petrology.*, 22: 451-500.

Kyle P.R. 1990a McMurdo Volcanic Group, western Ross Embayment: Introduction. In LeMasurier W.E. and Thomson J.W. (Editors) Volcanoes of the Antarctic plate and Southern Oceans. *Antarctic Research Series.*, 48: 19-25. American Geophysical Union, Washington D.C.

Kyle P.R. 1990b Vulcan Hills. In LeMasurier W.E. and Thomson J.W. (Editors) Volcanoes of the Antarctic plate and Southern Oceans. *Antarctic Research Series.*, 48: 69-71. American Geophysical Union, Washington D.C.

Kyle P.R. and Cole J.W. 1974 Structural control of volcanism in the McMurdo Volcanic Group, Antarctica. *Bulletin Volcanologique.*, 38: 16-25.

Kyle P.R. and McIntosh W.C. 1990 Adare Peninsula. In LeMasurier W.E. and Thomson J.W. (Editors) Volcanoes of the Antarctic plate and Southern Oceans. *Antarctic Research Series.*, 48: 32-35. American Geophysical Union, Washington D.C.

Kyle P.R. and Noll M.R. 1990 Mount Overlord. In LeMasurier W.E. and Thomson J.W. (Editors) Volcanoes of the Antarctic plate and Southern Oceans. *Antarctic Research Series.*, 48: 65-68. American Geophysical Union, Washington D.C.

Kyle P.R. and Rankin P.C. 1976 Rare earth element geochemistry of Late Cenozoic lavas of the McMurdo Volcanic Group, Antarctica. *Geochimica et Cosmochimica Acta.*, 40: 1497-1507.

Kyle P.R., Adams J. and Rankin P.C. 1979 Geology and petrology of the McMurdo Volcanic Group at Rainbow Ridge, Brown Peninsula, Antarctica. *Geological Society of America Bulletin.*, 90: 676-688.

Langmuir C.H. and Hanson G.N. 1980 An evaluation of major element heterogeneity in the mantle sources of basalts. *Philosophical Transactions of the Royal Society London.*, A297: 383-407.

Langmuir C.H., Bender J.F., Bence A.E., Hanson G.N. and Taylor S.R. 1977 Petrogenesis of basalts from the FAMOUS area: Mid-Atlantic Ridge. *Earth and Planetary Science Letters.*, 36: 133-156.

Langmuir C.H., Klein E.M. and Plank T. 1992 Petrological systematics of mid-ocean ridge basalts: constraints on melt generation beneath ocean ridges. In Phipps Morgan J., Blackman D.K. and Sinton J.M. (Editors) Mantle Flow and Melt Generation at Mid-Ocean Ridges. *Geophysical Monograph.*, 71: 183-280.

Lanyon R., Varne R. and Crawford A.J. 1993 Tasmanian Tertiary basalts, the Balleny plume and, opening of the Tasman Sea (southwest Pacific Ocean). *Geology.*, 21: 555-558.

le Roex A.P., Dick H.J.B. and Fisher R.L. 1989 Petrology and geochemistry of MORB from 25°E to 46°E along the Southwest Indian Ridge: evidence for contrasting styles of mantle enrichment. *Journal of Petrology.*, 30: 947-986.

le Roex A.P., Dick H.J.B., Reid A.M., Frey F.A., Erlank A.J. and Hart S.R. 1985 Petrology and geochemistry of basalts from the American-Antarctic Ridge, Southern Ocean: implications for the westward influence of the Bouvet mantle plume. *Contributions to Mineralogy and Petrology.*, 90: 367-380.

LeBas M.J., Le Maitre R.W., Streckeisen A. and Zanettin B. 1986 A chemical classification of volcanic rocks based on the total alkali-silica diagram. *Journal of Petrology.*, 27: 745-750.

LeCheminant A.N. and Heaman L.M. 1989 Mackenzie igneous events, Canada: Middle Proterozoic hotspot magmatism associated with ocean opening. *Earth and Planetary Science Letters.*, 96: 38-48.

LeMasurier W.E. and Rex D.C. 1982 Volcanic record of Cenozoic glacial history in Marie Byrd Land and Western Ellesworth Land: revised chronology and evaluation of tectonic factors. In Craddock C.C. (Editor) *Antarctic Geoscience.*, 725-734. Madison: University of Wisconsin Press.

LeMasurier W.E. and Rex D.C. 1989 Evolution of linear volcanic ranges in Marie Byrd Land, West Antarctica. *Journal of Geophysical Research.*, 94: 7223-7236.

LeMasurier W.E. and Rex D.C. 1991 The Marie Byrd Land volcanic province and its relation to the Cainozoic West Antarctic rift system. In Tingey R.J. (Editor) The Geology of Antarctica. *Oxford Monographs on Geology and Geophysics.*, 17: 249-284., Oxford Science Publications, Clarendon Press, Oxford.

Lewis D. 1984 *Voyage to the ice. The Antarctic expedition of Solo.* Australian Broadcasting Commission, Sydney.

Lin J. and Phipps Morgan J. 1992 The spreading rate dependence of three-dimensional mid-ocean ridge gravity structure. *Geophysical Research Letters.*, 19: 13-16.

Lin J., Purdy G.M., Schouten H., Sempere J.-C. and Zervas C. 1990 Evidence from gravity data for focussed magmatic accretion along the Mid-Atlantic Ridge. *Nature.*, 344: 627-632.

Liotard J.M., Barsczus H.G., Dupuy C. and Dostal J. 1986 Geochemistry and origin of basaltic lavas from Marquesas Archipelago, French Polynesia. *Contributions to Mineralogy and Petrology.*, 92: 260-269.

Lister G.S., Etheridge M.A. and Symonds P.A. 1986 Detachment faulting and the evolution of passive continental margins. *Geology.*, 14: 246-250.

Loper D.E. and Stacey F.D. 1983 The dynamical and thermal structure of deep mantle plumes. *Physics of the Earth and Planetary Interiors.*, 33: 304-317.

Lugmair G.W. and Marti K. 1978 Lunar initial $^{143}Nd/^{144}Nd$: differential evolution of the lunar crust and mantle. *Earth and Planetary Science Letters.*, 39: 349-357.

Macdonald G.A. and Katsura T. 1964 Chemical composition of Hawaiian lavas. *Journal of Petrology.*, 5: 82-133.

Macdonald K.C. 1982 Mid-ocean ridges: fine scale tectonic, volcanic and hydrothermal processes within the plate boundary zone. *Annual Review of Earth and Planetary Sciences.*, 10: 155-190.

Macdougall J.D. and Lugmair G.W. 1986 Sr and Nd isotopes in basalts from the East Pacific Rise: significance for mantle heterogeneity. *Earth and Planetary Science Letters.*, 77: 273-284.

Mahoney J., le Roex A.P., Peng Z., Fisher R.L. and Natland J.H. 1992 Southwestern limits of Indian Ocean ridge mantle and the origin of low $^{206}Pb/^{204}Pb$ mid-ocean ridge basalt: isotope systematics of the central Southwest Indian Ridge (17°-50°E). *Journal of Geophysical Research.*, 97: 19771-19790.

Mahoney J.J. 1987 An isotopic survey of Pacific oceanic plateaus: implications for their nature and origin. In Keating B., Fryer P., Batiza R. and Boehlert G. (Editors) Seamounts, Islands and Atolls. *A.G.U. Monograph.*, 43: 207-220.

Mahoney J.J. and Spencer K.J. 1991 Isotopic evidence for the origin of the Manihiki and Ontong Java oceanic plateaus. *Earth and Planetary Science Letters.*, 104: 196-210.

Mahoney J.J., Natland J.H., White W.M., Poreda R., Bloomer S.H., Fisher R.L. and Baxter A.N. 1989 Isotopic and geochemical provinces of the western Indian Ocean spreading centers. *Journal of Geophysical Research.*, 94: 4033-4052.

Mahoney J.J., Storey M., Duncan R.A., Spencer K.J. and Pringle M. 1993 1. Geochemistry and geochronology of Leg 130 basement lavas: nature and origin of the Ontong Java Plateau. *Proceedings ODP Scientific Results.*, (130): 3-22., College Station, TX, (Ocean Drilling Program).

Marks K.M., Sandwell D.T., Vogt P.R. and Hall S.A. 1991 Mantle downwelling beneath the Australian-Antarctic discordance zone: evidence from geoid height versus topography. *Earth and Planetary Science Letters.*, 103: 325-338.

Marks K.M., Vogt P.R. and Hall S.A. 1990 Residual depth anomalies and the origin of the Australian-Antarctic Discordance Zone. *Journal of Geophysical Research.*, 95: 17325-17337.

Marsh J.G., Brenner A.C., Beckley B.D. and Martin T.V. 1986 Global mean sea surface based upon the Seasat altimeter data. *Journal of Geophysical Research.*, 91: 3501-3506.

Mawson D. 1950 Basaltic lavas of the Balleny Islands A.N.A.R.E. report. *Transactions of the Royal Society of South Australia.*, 73: 223-231.

McCulloch M.T. 1993 The role of subducted slabs in an evolving earth. *Earth and Planetary Science Letters.*, 115: 89-100.

McDonough W.F. 1987 Chemical and isotopic systematics of basalts and peridotite xenoliths: implications for the composition and evolution of the Earth's mantle. Unpublished PhD thesis, The Australian National University, Canberra, Australia.

McDonough W.F. and Chauvel C. 1991 Sample contamination explains the Pb isotopic composition of some Rurutu island and Sasha seamount basalts. *Earth and Planetary Science Letters.*, 105: 397-404.

McDonough W.F., McCulloch M.T. and Sun S.S. 1985 Isotopic and geochemical systematics in Tertiary-Recent basalts from southeastern Australia and implications for the evolution of sub-continental lithosphere. *Geochimica et Cosmochimica Acta.*, 49: 2051-2067.

McDonough W.F., McCulloch M.T., Duncan R.A., Gamble J.A., McDougall I., Morris P.A. and Briggs R.M. 1986 Geochemical and isotopic systematics of Cenozoic intraplate basalts from continental and oceanic regions in the South Pacific. *IAVCEI General Assembly, Canberra* (abstract): 180.

McDougall I. and Coombs D.S. 1973 Potassium-argon ages for the Dunedin Volcano and outlying volcanics. *New Zealand Journal of Geology and Geophysics.*, 16: 179-188.

McDougall I. and Duncan R.A. 1988 Age progressive volcanism in the Tasmantid Seamounts. *Earth and Planetary Science Letters.*, 89: 207-220.

McDougall I. and Green D.C. 1982 In McClenaghan M.P., Turner N.J., Baillie P.W., Brown A.V., Williams P.R. and Moore W.R. Geology of the Ringarooma - Boobyalla area. *Geological Survey of Tasmania Bulletin.*, 61: appendix 3.

McDougall I. and Harrison T.M. 1988 Geochronology and thermochronology by the $^{40}Ar/^{39}Ar$ method. *Oxford Monographs of Geology and Geophysics.*, 9: 212 pp.

McDougall I. and Leggo P.J. 1965 Isotopic age determinations on granitic rocks from Tasmania. *Journal of the Geological Society of Australia.*, 12: 295-332.

McDougall I. and Schmincke H.-U. 1977 Geochronology of Gran Canaria, Canary Islands: Age of shield building volcanism and other magmatic processes. *Bulletin Volcanologique.*, 40: 57-77.

McDougall I., Allsopp H.L. and Chamalaun F.H. 1966 Isotopic dating of the Newer Volcanics of Victoria, Australia and geomagnetic polarity epochs. *Journal of Geophysical Research.*, 71: 6107-6118.

McDougall I., Embleton B.J.J. and Stone D.B. 1981 Origin and evolution of Lord Howe Island, southwest Pacific Ocean. *Journal of the Geological Society of Australia.*, 28: 155-176.

McGinnis L.D., Bowen R.H., Erickson J.M., Allred B.J. and Kreamer J.L. 1985 East - West Antarctic boundary in McMurdo Sound. In Husebye E.S., Johnson G.L. and Kristoffersen Y. (Editors) Geophysics of the Polar Regions. *Tectonophysics.*, 114: 341-356.

McGinnis L.D., Wilson D.D., Burdelik W.J. and Larson T.H. 1983 Crust and upper mantle study of McMurdo Sound. In Oliver R.L., James P.R. and Jago J.B. (Editors) *Antarctic Earth Science.*, 204-208. Australian Academy of Science, Canberra.

McKenzie D. and O'Nions R.K. 1983 Mantle reservoirs and ocean island basalts. *Nature.*, 301: 229-231.

McKenzie D. and O'Nions R.K. 1991 Partial melt distributions from inversion of rare earth element concentrations. *Journal of Petrology.*, 32: 1021-1091.

McKenzie D., Roberts J. and Weiss N. 1973 Numerical models of convection in the Earth's mantle. *Tectonophysics.*, 19: 89-103.

McKenzie D.P. 1978 Some remarks on the development of sedimentary basins. *Earth and Planetary Science Letters.*, 40: 25-32.

Meijer A., Kwon T.-T. and Tilton G.R. 1990 U-Th-Pb partitioning behaviour during partial melting in the upper mantle: implications for the origin of high-mu components and the "Pb paradox". *Journal of Geophysical Research.*, 95: 433-448.

Menard H.W. 1967 Seafloor spreading, topography and the second layer. *Science.*, 157: 923-924.

Menard H.W. 1973 Depth anomalies and the bobbing motion of drifting islands. *Journal of Geophysical Research.*, 78: 5128-5137.

Michard A. and Albarède F. 1985 Hydrothermal uranium uptake at ridge crests. *Nature.*, 317: 244-245.

Michard A., Montigny R. and Schlich R. 1986 Geochemistry of the mantle beneath the Rodriguez Triple Junction and the South-East Indian Ridge. *Earth and Planetary Science Letters.*, 78: 104-114.

Minster J.B. and Jordan T.H. 1978 Present-day plate motions. *Journal of Geophysical Research.*, 83: 5331-5354.

Molnar P., Atwater T., Mammerickx J. and Smith S.M. 1975 Magnetic anomalies, bathymetry and the tectonic evolution of the South Pacific since the Late Cretaceous. *Geophysical Journal of the Royal Astronomical Society.*, 40: 383-420.

Monnereau M. and Cazenave A. 1988 Variation of the apparent compensation depth of hotspot swells with age of plate. *Earth and Planetary Science Letters.*, 91: 179-197.

Moore J.A. and Kyle P.R. 1987 Volcanic geology of Mt. Erebus, Ross Island, Antarctica. *Proceedings of the National Institute of Polar Research on Antarctic Geosciences.*, 1: 48-65.

Morgan W.J. 1971 Convection plumes in the lower mantle. *Nature.*, 230: 42-42.

Morgan W.J. 1972 Hot spots, plate motions and polar wandering. *Geological Society of America Abstracts.*, 4: 202.

Morris J.D. and Hart S.R. 1983 Isotopic and incompatible element constraints on the genesis of island arc volcanics from Cold Bay and Amak Island, Aleutians, and implications for mantle structure. *Geochimica et Cosmochimica Acta.*, 47: 2015-2030.

Morris P.A. 1984 Petrology of the Campbell Island volcanics, southwest Pacific Ocean. *Journal of Volcanology and Geothermal Research.*, 21: 119-148.

Morris P.A. 1985 Petrology of Late Cretaceous alkaline volcanic rocks from the Chatham Islands, New Zealand. *New Zealand Journal of Geology and Geophysics.*, 28: 253-266.

Mutter J.C., Hegarty K.A., Cande S.C. and Weissel J.K. 1985 Breakup between Australia and Antarctica: a brief review in the light of new data. *Tectonophysics.*, 114: 255-279.

Nakamura Y. and Tatsumoto M. 1988 Pb, Nd, and Sr isotopic evidence for a multicomponent source for rocks of Cook-Austral Islands and heterogeneities of mantle plumes. *Geochimica et Cosmochimica Acta.*, 52: 2909-2924.

Nathan S. and Schulte F.J. 1968 Geology and petrology of the Campbell-Aviator Divide, Northern Victoria Land, Antarctica. *New Zealand Journal of Geology and Geophysics.*, 11: 940-975.

Newsom H.E., White W.M., Jochum K.P. and Hofmann A.W. 1986 Siderophile and chalcophile element abundances in oceanic basalts, Pb isotope evolution and growth of the Earth's core. *Earth and Planetary Science Letters.*, 80: 299-313.

Nicholls I.A. and Joyce E.B. 1989 Newer Volcanics. In Johnson R.W. (Editor) *Intraplate Volcanism in Eastern Australia and New Zealand.*, 137-140. Cambridge University Press, Cambridge, U.K.

Nicholls I.A., Ferguson J., Jones H., Marks G.P. and Mutter J.C. 1981 Ultramafic blocks from the ocean floor southwest of Australia. *Earth and Planetary Science Letters.*, 56: 362-374.

Nielsen R.L. and Dungan M.A. 1983 Low pressure mineral-melt equilibria in natural anhydrous mafic systems.*Contributions to Mineralogy and Petrology.*, 84: 310-326.

Nielsen R.L., Davidson P.M. and Grove T.L. 1988 Pyroxene-melt equilibria: an updated model. *Contributions to Mineralogy and Petrology.*, 100: 361-373.

Niu Y. and Batiza R. 1991 An empirical method for calculating melt compositions produced beneath mid-ocean ridges: application for axis and off-axis (seamounts) melting. *Journal of Geophysical Research.*, 96: 21753-21777.

Niu Y. and Batiza R. 1993 Chemical variation trends at fast and slow spreading mid-ocean ridges. *Journal of Geophysical Research.*, 98: 7887-7902.

Norman M.D., Leeman W.P., Blanchard D.P., Fitton J.G. and James D. 1989 Comparison of major and trace element analyses by ICP - XRF, INAA and ID methods. *Geostandards Newsletter.*, 13: 283-290.

Norrish K. and Chappell B.W. 1977 X-ray fluorescence spectrometry. In Zussman J. (Editor) *Physical Methods in Determinative Mineralogy*, (2nd edition)., 254-272. Academic Press Inc., London.

Norrish K. and Hutton J.T. 1969 An accurate X-ray spectrographic method for analysis of a wide range of geological samples. *Geochimica et Cosmochimica Acta.*, 33: 431-454.

Norton I.O. and Sclater J.G. 1979 A model for the evolution of the Indian Ocean and the breakup of Gondwanaland. *Journal of Geophysical Research.*, 84: 6803-6830.

Nye C.J. and Reid M.R. 1986 Geochemistry of primary and least fractionated lavas from Okmok Volcano, central Aleutians: implications for arc magmagenesis. *Journal of Geophysical Research.*, 91: 10271-10287.

Officer C.B. 1955 Southwest Pacific crustal structure. *Transactions, American Geophysical Union.*, 36: 449-459.

Oliver R.L. 1979 Aspects of the basement geology of the Vestfold Hills, Antarctica. *Journal of the Geological Society of Australia.*, 26: 268-269.

Oliver R.L., James P.R., Collerson K.D. and Ryan A.B. 1982 Precambrian geological relationships in the Vestfold Hills, Antarctica. In Craddock C.C. (Editor) *Antarctic Geoscience.*, 435-444. Madison: University of Wisconsin Press.

Palacz Z.A. and Saunders A.D. 1986 Coupled trace element and isotope enrichment in the Cook-Austral-Samoa islands, southwest Pacific. *Earth and Planetary Science Letters.*, 79: 270-280.

Palmer J., Sempéré J.-C., Christie D.M. and Phipps Morgan J. 1993 Morphology and tectonics of the Australian-Antarctic Discordance between 123°E and 128°E. *Marine Geophysical Researches.*, 15: 121-152.

Parker A.J., James P.R., Oliver R.L. and Mielnik V. 1983 Structure, fabric development and metamorphism in Archaean gneisses of the Vestfold Hills, East Antarctica. In Oliver R.L., James P.R. and Jago J.B. (Editors) *Antarctic Earth Science.*, 85-90. Australian Academy of Science, Canberra.

Parmentier E.M. and Phipps Morgan J. 1990 Spreading rate dependence of three-dimensional structure in oceanic spreading centres. *Nature.*, 348: 325-328.

Passchier C.W., Bekendam R.F., Hoek J.D., Dirks P.H.G.M. and de Boorder H. 1991 Proterozoic geological evolution of the northern Vestfold Hills, Antarctica. *Geological Magazine.*, 128: 307-318.

Passchier C.W., Hoek J.D., Bekendam R.F. and De Boorder H. 1990 Ductile reactivation of Proterozoic brittle fault rocks; an example from the Vestfold Hills, East Antarctica. *Precambrian Research.*, 47: 3-16.

Pearce J.A., Thirlwall M.F., Ingram G., Murton B.J., Arculus R.J. and van der Laan S.R. 1992 Isotopic evidence for the origin of boninites and related rocks drilled in the Izu-Bonin (Ogasawara) Forearc, Leg 125. *Proceedings of the Ocean Drilling Program, Scientific results.*, 125: 237-261.

Phipps Morgan J., Parmentier E.M. and Lin J. 1987 Mechanisms for the origin of mid-ocean ridge axial topography: implications for the thermal and mechanical structure of accreting plate boundaries. *Journal of Geophysical Research.*, 92: 12823-12836.

Phipps Morgan J., Sempéré J.-C., Christie D. and Shor A. 1988 Propagating rifts along the Southeast Indian Ridge. *EOS: Transactions, American Geophysical Union.*, 69: 1430.

Poldervaart A . 1956 Zircon in rocks. 2. Igneous Rocks. *American Journal of Science.*, 254: 521-554.

Price R.C. and Chappell B.W. 1975 Fractional crystallisation and the petrology of Dunedin Volcano. *Contributions to Mineralogy and Petrology.*, 53: 157-182.

Price R.C. and Compston W. 1973 The geochemistry of the Dunedin Volcano: strontium isotope chemistry. *Contributions to Mineralogy and Petrology.*, 42: 55-61.

Price R.C. and Taylor S.R. 1973 The geochemistry of the Dunedin Volcano, East Otago, New Zealand: rare earth elements. *Contributions to Mineralogy and Petrology.*, 40: 195-205.

Price R.C. and Taylor S.R. 1980 Petrology and geochemistry of the Banks Peninsula Volcanoes, South Island, New Zealand. *Contributions to Mineralogy and Petrology.*, 72: 1-18.

Price R.C., Kennedy A.K., Riggs-Sneeringer M. and Frey F.A. 1986 Geochemistry of basalts from the Indian Ocean triple junction: implications for the generation and evolution of Indian Ocean ridge basalts. *Earth and Planetary Science Letters.*, 78: 379-396.

Prior G.T. 1907 Report on the rock specimens collected during the "Discovery" Antarctic Expedition, 1901-1904. *National Antarctic Expedition 1901-1904, Natural History 1, Geology.*, 101-140.

Pyle D.G., Christie D.M. and Mahoney J.J. 1992 Resolving an isotopic boundary within the Australian-Antarctic Discordance. *Earth and Planetary Science Letters.*, 112: 161-178.

Quilty P.G., Rubenach M. and Wilcoxon J.A. 1973 Miocene ooze from Macquarie Island. *Search.*, 4: 163-164.

Rautenschlein M., Jenner G.A., Hertogen J., Hofmann A.W., Kerrich R., Schmincke H.-U. and White W.M. 1985 Isotopic and trace element composition of volcanic glasses from the Akaki Canyon, Cyprus: implications for the origin of the Troodos ophiolite. *Earth and Planetary Science Letters.*, 75: 369-383.

Rees D.G. 1989 *Essential Statistics*, (2nd edition). Chapman and Hall, London, 258pp.

Reinemund J.A. 1984 Plate-tectonic map of the Circum-Pacific Region, scale 1:17 000 000. *Circum-Pacific Council for Energy and Mineral Resources*, AAPG, Tulsa, Oklahoma, U.S.A.

Renard V., Hekinian R., Francheteau J., Ballard R.D. and Backer H. 1985 Submersible observations at the axis of the ultra-fast-spreading East Pacific Rise (17°30' to 21°30'S). *Earth and Planetary Science Letters.*, 75: 339-353.

Rhodes J.M., Dungan M.A., Blanchard D.P. and Long P.E. 1979 Magma mixing at Mid-Ocean Ridges: evidence from basalts drilled near 22°N on the Mid-Atlantic Ridge. *Tectonophysics.*, 55: 35-61.

Richards M.A. and Griffiths R.W. 1988 Deflection of plumes by mantle shear flow: experimental results and a simple theory. *Geophysical Journal.*, 94: 367-376.

Richards M.A. and Griffiths R.W. 1989 Thermal entrainment by deflected mantle plumes. *Nature.*, 342: 900-902.

Richardson S.H., Erlank A.J., Duncan A.R. and Reid D.L. 1982 Correlated Nd, Sr and Pb isotope variation in Walvis Ridge basalts and implications for the evolution of their mantle source. *Earth and Planetary Science Letters.*, 59: 327-342.

Richardson S.H., Erlank A.J., Reid D.L. and Duncan A.R. 1984 Major and trace elements and Nd and Sr isotope geochemistry of basalts from the deep sea drilling project leg 74 Walvis Ridge transect. In Moore T.C. Jr. and Rabinowitz P.D. et al. (Editors) *Initial Reports of the Deep Sea Drilling Project.*, 74: 739-754. U.S. government printing office, Washington D.C.

Richter F.M. and Parsons B. 1975 On the interaction of two scales of convection in the mantle. *Journal of Geophysical Research.*, 80: 2529-2541.

Ringwood A.E. 1982 Phase transformations and differentiation in subducted lithosphere: implications for mantle dynamics, basalt petrogenesis, and crustal evolution. *The Journal of Geology.*, 90: 611-643.

Ringwood A.E. and Irifune T. 1988 Nature of the 650-km seismic discontinuity: implications for mantle dynamics and differentiation. *Nature.*, 331: 131-136.

Robinson P., Higgins N.C. and Jenner G.A. 1986 Determination of rare-earth elements, yttrium and scandium in rocks by ion exchange X-ray fluorescence technique. *Chemical Geology.*, 55: 121-137.

Roden M.F., Frey F.A. and Clague D.A. 1984 Geochemistry of tholeiitic and alkalic lavas from the Koolau Range, Oahu, Hawaii: implications for Hawaiian volcanism. *Earth and Planetary Science Letters.*, 69: 141-158.

Roden M.F., Trull T., Hart S.R. and Frey F.A. (in press) New He, Nd, Pb and Sr isotopic constraints on the constitution of the Hawaiian plume: results from Koolau Volcano, Oahu, Hawaii. *Geochimica et Cosmochimica Acta.*

Roeder P.L. and Emslie R.F. 1970 Olivine-liquid equilibrium. *Contributions to Mineralogy and Petrology.*, 29: 275-289.

Royer J.-Y. and Sandwell D.T. 1989 Evolution of the eastern Indian Ocean since the Late Cretaceous: constraints from Geosat altimetry. *Journal of Geophysical Research.*, 94: 13755-13782.

Saunders A.D., Norry M.J. and Tarney J. 1988 Origin of MORB and chemically-depleted mantle reservoirs: trace element constraints. *Journal of Petrology, Special Lithospheric Issue*: 415-445.

Saunders A.D., Storey M., Kent R.W. and Norry M.J. 1992 Consequences of plume-lithosphere interaction. In Storey B.C., Alabaster T. and Pankhurst R.J. (Editors) Magmatism and the causes of continental break-up. *Geological Society Special Publication.*, 68: 41-60.

Schmidt-Thomé M., Mueller P. and Tessensohn F. 1990 Malta Plateau. In LeMasurier W.E. and Thomson J.W. (Editors) Volcanoes of the Antarctic plate and Southern Oceans. *Antarctic Research Series.*, 48: 53-59. American Geophysical Union, Washington D.C.

Sclater J.G., Fisher R.L., Patriat P., Tapscott C. and Parsons B. 1981 Eocene to Recent development of the South-west Indian Ridge, a consequence of the evolution of the Indian Ocean Triple Junction. *Geophysical Journal of the Royal Astronomical Society.*, 64: 587-604.

Seitz H.-M. (in press) Estimation of emplacement pressures for 2350 Ma high-Mg tholeiite dykes, Vestfold Hills, East Antarctica. *European Journal of Mineralogy.*

Seitz H.-M. 1991 Geochemistry and petrogenesis of High-Mg tholeiites and lamprophyres in the Vestfold Hills, Antarctica. Unpublished PhD thesis, University of Tasmania, Tasmania, Australia.

Sempéré J.-C., Palmer J., Christie D.M., Phipps Morgan J. and Shor A.N. 1991 Australian-Antarctic Discordance. *Geology.*, 19: 429-432.

Sewell R.J. and Weaver S.D. 1989 South Island. In Johnson R.W. (Editor) *Intraplate Volcanism in Eastern Australia and New Zealand.*, 162-169. Cambridge University Press, Cambridge, U.K.

Sheraton J.W. 1979 The metamorphic geology of Enderby Land, Antarctica. *Journal of the Geological Society of Australia.*, 26: 269.

Sheraton J.W. and Black L.P. 1981 Geochemistry and geochronology of Proterozoic dykes of East Antarctica: evidence for mantle metasomatism. *Contributions to Mineralogy and Petrology.*, 78: 305-317.

Sheraton J.W. and Collerson K.D. 1983 Archaean and Proterozoic geological relationships in the Vestfold Hills - Prydz Bay area, Antarctica. *BMR Journal of Australian Geology and Geophysics.*, 8: 119-128.

Sheraton J.W., Black L.P. and McCulloch M.T. 1984 Regional geochemical and isotopic characteristics of high-grade metamorphics of the Prydz Bay area: the extent of Proterozoic reworking of Archaean continental crust in East Antarctica. *Precambrian Research.*, 26: 169-198.

Sheraton J.W., Black L.P., McCulloch M.T. and Oliver R.L. 1990 Age and origin of a compositionally varied mafic dyke swarm in the Bunger Hills, East Antarctica. *Chemical Geology.*, 85: 215-246.

Sheraton J.W., Thomson J.W. and Collerson K.D. 1987 Mafic dyke swarms of Antarctica. In Halls H.C. and Fahrig W.F. (Editors) Mafic Dyke Swarms. *Geological Association of Canada Special Paper.*, 34: 419-428.

Shirey S.B. 1991 The Rb-Sr, Sm-Nd and Re-Os isotopic systems: a summary and comparison of their applications to the cosmochronology and geochronology of igneous rocks. In Heaman L. and Ludden J.N. (Editors) Applications of radiogenic isotope systems to problems in geology. *Mineralogical Association of Canada Short Course Handbook.*, 19: 103-166.

Shirey S.B., Bender J.F. and Langmuir C.H. 1987 Three-component isotopic heterogeneity near the Oceanographer transform, Mid-Atlantic Ridge. *Nature.*, 325: 217-223.

Sinton J.M. and Detrick R.S. 1992 Mid-ocean ridge magma chambers. *Journal of Geophysical Research.*, 97: 197-216.

Skilbeck J.N. and Whitehead J.A. Jr. 1978 Formation of discrete islands in linear island chains. *Nature.*, 272: 499-501.

Sleep N.H. 1990 Hotspots and mantle plumes: some phenomenology. *Journal of Geophysical Research.*, 95: 6715-6736.

Sleep N.H. 1992 Hotspot volcanism and mantle plumes. *Annual Review in Earth and Planetary Science.*, 20: 19-43.

Sleep N.H. and Rosendahl B.R. 1979 Topography and tectonics of mid-ocean ridge axes. *Journal of Geophysical Research.*, 84: 6831-6839.

Smith A.G. and Drewry D.J. 1984 Delayed phase change due to hot asthenosphere causes Transantarctic uplift? *Nature.*, 309: 536-538.

Staudacher T. and Allègre C.J. 1989 Noble gases in glass samples from Tahiti: Teahitia, Rocard and Mehetia. *Earth and Planetary Science Letters.*, 93: 210-222.

Staudigel H., Park K.-H., Pringle M., Rubenstone J.L., Smith W.H.F. and Zindler A. 1991 The longevity of the South Pacific isotopic and thermal anomaly. *Earth and Planetary Science Letters.*, 102: 24-44.

Steiger R.H. and Jäger E. 1977 Subcommission on geochronology: convention on the use of decay constants in geo- and cosmochronology. *Earth and Planetary Science Letters.*, 36: 359-362.

Stille P., Unruh D.M. and Tatsumoto M. 1983 Pb, Sr, Nd and Hf isotopic evidence of multiple sources for Oahu, Hawaii basalts. *Nature.*, 304: 25-29.

Storey M., Saunders A.D., Tarney J., Gibson I.L., Norry M.J., Thirlwall M.F., Leat P., Thompson R.N. and Menzies M.A. 1989 Contamination of Indian Ocean asthenosphere by the Kerguelen - Heard mantle plume. *Nature.*, 338: 574-576.

Stork A.L., Smith D.K. and Gill J.B. 1987 Evaluation of geochemical reference standards by X-ray fluorescence analysis. *Geostandards Newsletter.*, 11: 107-113.

Stuckless J.S. and Ericksen R.L. 1976 Strontium isotopic geochemistry of the volcanic rocks and associated megacrysts and inclusions from Ross Island and vicinity, Antarctica. *Contributions to Mineralogy and Petrology.*, 58: 111-126.

Subbarao K.V. and Hedge C.E. 1973 K, Rb, Sr and $^{87}Sr/^{86}Sr$ in rocks from the Mid-Indian Ocean Ridge. *Earth and Planetary Science Letters.*, 18: 223-228.

Sun S.-S. 1980 Lead isotopic study of young volcanic rocks from mid-ocean ridges, ocean islands and island arcs. *Philosophical Transactions of the Royal Society London.*, A297: 409-445.

Sun S.-S. and Hanson G.N. 1975a Evolution of the mantle: Geochemical evidence from alkali basalt. *Geology.*, 3: 297-302.

Sun S.-S. and Hanson G.N. 1975b Origin of Ross Island basanitoids and limitations upon the heterogeneity of mantle sources for alkali basalts and nephelinites. *Contributions to Mineralogy and Petrology.*, 52: 77-106.

Sun S.-S. and Hanson G.N. 1976 Rare earth element evidence for differentiation of McMurdo Volcanics, Ross Island, Antarctica. *Contributions to Mineralogy and Petrology.*, 54: 139-155.

Sun S.-S. and McDonough W.F. 1989 Chemical and isotopic systematics of oceanic basalts: implications for mantle composition and processes. In Saunders A.D. and Norry M.J. (Editors) Magmatism in the Ocean Basins. *Geological Society Special Publication.*, 42: 313-345.

Sun S.-S., McDonough W.F. and Ewart A. 1989 Four component model for east Australian basalts. In Johnson R.W. (Editor) *Intraplate Volcanism in Eastern Australia and New Zealand.*, 333-347. Cambridge University Press, Cambridge, U.K.

Sun S.-S., Nesbitt R.W. and Sharaskin A.Y. 1979 Geochemical characteristics of mid-ocean ridge basalts. *Earth and Planetary Science Letters.*, 44: 119-138.

Sutherland F.L 1989 Tasmania and Bass Strait. In Johnson R.W. (Editor) *Intraplate Volcanism in Eastern Australia and New Zealand.*, 143-149. Cambridge University Press, Cambridge, U.K.

Sutherland F.L. 1991 Cainozoic volcanism, Eastern Australia: a predictive model based on migration over multiple 'hotspot' magma sources. In Williams M.A.J., De Deckker P. and Kershaw A.P. (Editors) The Cainozoic in Australia: a re-appraisal of the evidence. *Special Publication Geological Society of Australia.*, 18: 15-43.

Sutherland F.L. and Wellman P. 1986 Potassium-Argon ages of Tertiary volcanic rocks, Tasmania. *Papers and Proceedings of the Royal Society of Tasmania.*, 120: 77-86.

Tatsumoto M. 1978 Isotopic composition of lead in oceanic basalt and its implication to mantle evolution. *Earth and Planetary Science Letters.*, 38: 63-87.

Thompson G. and Humphris S.E. 1984 Petrology and geochemistry of rocks from the Walvis Ridge: Deep Sea Drilling Project 74, sites 525, 527 and 528. In Moore T.C. Jr. and Rabinowitz P.D. et al. (Editors) *Initial Reports of the Deep Sea Drilling Project.*, 74: 755-764. U.S. government printing office, Washington D.C.

Thompson G., Humphris S. and Schilling J.G. 1983 Petrology and geochemistry of basaltic rocks from Rio Grande Rise, South Atlantic: Deep Sea Drilling Project leg 72, hole 516F. In Barker P.F., Carlson R.L. and Johnson D.A. et al. (Editors) *Initial Reports of the Deep Sea Drilling Project.*, 72: 457-466. U.S. government printing office, Washington D.C.

Thomson A.A. and Evison F.F. 1962 Thickness of the Earth's crust in New Zealand. *New Zealand Journal of Geology and Geophysics.*, 5: 29-45.

Tilton G.R. 1960 Volume diffusion as a mechanism for discordant Pb ages. *Journal of Geophysical Research.*, 65: 2933-2945.

Tingey R.J. 1982 The geologic evolution of the Prince Charles Mountains - An Antarctic Archaean cratonic block. In Craddock C.C. (Editor) *Antarctic Geoscience.*, 455-464. University of Wisconsin Press, Madison.

Tingey R.J. 1991 The regional geology of Archaean and Proterozoic rocks in Antarctica. In Tingey R.J. (Editor) The Geology of Antarctica. *Oxford Monographs on Geology and Geophysics* 17: 1-73. Clarendon Press, Oxford.

Turcotte D.L. and Schubert G. 1982 *Geodynamics applications of continuum physics to geological problems.* John Wiley and Sons, Inc., U.S.A., 450 pp.

Vanney J.R., Falconer R.K.H. and Johnson G.L. 1981 Geomorphology of the Ross Sea and adjacent oceanic provinces. *Marine Geology.*, 41: 73-102.

Varne R. 1989 Macquarie Island. In Burrett C.F. and Martin E.L. (Editors) Geology and mineral resources of Tasmania. *Special Publication Geological Society of Australia.*, 15: 398-402.

Varne R. and Rubenach M.J. 1972 Geology of Macquarie Island and its relationship to oceanic crust. In Hayes D.E. (Editor) Antarctic Oceanology II: The Australian-New Zealand sector. *Antarctic Research Series.*, 19: 251-266. American Geophysical Union, Washington D.C.

Varne R., Gee R.D. and Quilty P.G.J. 1969 Macquarie Island and the cause of oceanic linear magnetic anomalies. *Science.*, 166: 230-233.

Veevers J.J. 1977 Paleobathymetry of the crest of spreading ridges related to the age of ocean basins. *Earth and Planetary Science Letters.*, 34: 100-106.

Veevers J.J. 1982 Australian-Antarctic depression from the mid-ocean ridge to adjacent continents. *Nature.*, 295: 315-317.

Veevers J.J. and Li Z.X. 1991 Review of seafloor spreading around Australia. II. Marine magnetic anomaly modelling. *Australian Journal of Earth Sciences.*, 38: 391-408.

Veevers J.J., Powell C. McA. and Roots S.R. 1991 Review of seafloor spreading around Australia. I. Synthesis of the patterns of spreading. *Australian Journal of Earth Sciences.*, 38: 373-389.

Veevers J.J., Stagg H.M.J., Willcox J.B. and Davies H.L. 1990 Pattern of slow seafloor spreading (<4 mm/year) from breakup (96 Ma) to A20 (44.5 Ma) off the southern margin of Australia. *BMR Journal of Australian Geology and Geophysics.*, 11: 499 - 507.

Vidal P. and Dosso L. 1978 Core formation: catastrophic or continuous? Sr and Pb isotope geochemistry constraints. *Geophysical Research Letters.*, 5: 169-172.

Vidal Ph. 1992 Mantle: More HIMU in the future? *Geochimica et Cosmochimica Acta.*, 56: 4295-4299.

Vidal Ph., Chauvel C. and Brousse R. 1984 Large mantle heterogeneity beneath French Polynesia. *Nature.*, 307: 536-538.

Vogt P.R. and Conolly J.R 1971 Tasmantid guyots, the age of the Tasman Basin, and motion between the Australia plate and the mantle. *Geological Society of America Bulletin.*, 82: 2577-2584.

Vogt P.R. and Johnson G.L. 1973 A longitudinal seismic reflection profile of the Reykjanes Ridge: Part II - Implications for the mantle hotspot hypothesis. *Earth and Planetary Science Letters.*, 18: 49-58.

Vogt P.R., Cherkis N.Z. and Morgan G.A. 1983 Project Investigator - I: evolution of the Australian-Antarctic Discordance deduced from a detailed aeromagnetic study. In Oliver R.L., James P.R. and Jago J.B. (Editors) *Antarctic Earth Science.*, 608-613. Australian Academy of Science, Canberra.

Vollmer R. 1977 Terrestrial lead isotopic evolution and formation time of the Earth's core. *Nature.*, 270: 144-147.

Ware N.G. 1991 Combined energy-dispersive - wavelength-dispersive quantitative electron microprobe analysis. *X-Ray Spectrometry.*, 20: 73-79.

Watson S. 1993 Rare earth element inversions and percolation models for Hawaii. *Journal of Petrology.*, 34: 763-783.

Weaver B.L. 1991 The origin of ocean island basalt end-member compositions: trace element and isotopic constraints. *Earth and Planetary Science Letters.*, 104: 381-397.

Weaver B.L., Wood D.A., Tarney J. and Joron J.L. 1986 Role of subducted sediment in the genesis of ocean-island basalts: Geochemical evidence from South Atlantic Ocean islands. *Geology.*, 14: 275-278.

Weaver B.L., Wood D.A., Tarney J. and Joron J.L. 1987 Geochemistry of ocean island basalts from the South Atlantic: Ascension, Bouvet, St. Helena, Gough and Tristan da Cunha. In Fitton J.G. and Upton B.G.J. (Editors) Alkaline Igneous Rocks., *Geological Society Special Publication.*, 30: 253-267.

Weaver S.D., Smith I.E.M., Sewell R.J., Gamble J.A. and Pankhurst R.J. 1989 Isotope geochemistry. In Johnson R.W. (Editor) *Intraplate Volcanism in Eastern Australia and New Zealand.*, 185-187. Cambridge University Press, Cambridge, U.K.

Weissel J.K. and Hayes D.E. 1971 Asymmetric seafloor spreading south of Australia. *Nature.*, 231: 518-522.

Weissel J.K. and Hayes D.E. 1972 Magnetic anomalies in the southeast Indian Ocean. In Hayes D.E. (Editor) Antarctic Oceanology II: The Australian - New Zealand Sector. *Antarctic Research Series.*, 19: 165-196. American Geophysical Union, Washington D.C.

Weissel J.K. and Hayes D.E. 1974 The Australian-Antarctic Discordance: new results and implications. *Journal of Geophysical Research.*, 79: 2579-2587.

Weissel J.K. and Hayes D.E. 1977 Evolution of the Tasman Sea reappraised. *Earth and Planetary Science Letters.*, 36: 77-84.

Weissel J.K., Hayes D.E. and Herron E.M. 1977 Plate tectonics synthesis: the displacements between Australia, New Zealand, and Antarctica since the Late Cretaceous. *Marine Geology.*, 25: 231-277.

Wellman P. and McDougall I. 1974 Cainozoic igneous activity in eastern Australia. *Tectonophysics.*, 23: 49-65.

Wernicke B. 1981 Low angle normal faults in the Basin and Range Province: nappe tectonics in an extending orogen. *Nature.*, 291: 645-648.

Wernicke B. 1985 Uniform-sense normal simple shear of the continental lithosphere. *Canadian Journal of Earth Sciences.*, 22: 108-125.

West H.B., Garcia M.O., Gerlach D.C. and Romano J. 1992 Geochemistry of tholeiites from Lanai, Hawaii. *Contributions to Mineralogy and Petrology.*, 112: 520-542.

White R. and McKenzie D. 1989 Magmatism at rift zones: the generation of volcanic continental margins and flood basalts. *Journal of Geophysical Research.*, 94: 7685-7729.

White R.S. 1992 Magmatism during and after continental break-up. In Storey B.C., Alabaster T. and Pankhurst R.J. (Editors) Magmatism and the causes of continental break-up. *Geological Society Special Publication.*, 68: 1-16.

White W.M. 1985 Sources of oceanic basalts: Radiogenic isotopic evidence. *Geology.*, 13: 115-118.

White W.M. 1993 $^{238}U/^{204}Pb$ in MORB and open system evolution of the depleted mantle. *Earth and Planetary Science Letters.*, 115: 211-226.

White W.M. and Hofmann A.W. 1982 Sr and Nd isotope geochemistry of oceanic basalts and mantle evolution. *Nature.*, 296: 821-825.

White W.M., Hofmann A.W. and Puchelt H. 1987 Isotope geochemistry of Pacific mid-ocean ridge basalt. *Journal of Geophysical Research.*, 92: 4881-4893.

Whitehead J.A. Jr. 1982 Instabilities of fluid conduits in a flowing earth - are plates lubricated by the asthenosphere? *The Geophysical Journal of the Royal Astronomical Society.*, 70: 415-433.

Williams I.S. and Claesson S. 1987 Isotopic evidence for the Precambrian provenance and Caledonian metamorphism of high grade paragneisses from the Seve Nappes, Scandinavian Caledonides. II Ion microprobe zircon U-Th-Pb. *Contributions to Mineralogy and Petrology.*, 97: 205-217.

Williams I.S., Compston W., Black L.P., Ireland T.R. and Foster J.J. 1984 Unsupported radiogenic Pb in zircon: a cause of anomalously high Pb-Pb, U-Pb and Th-Pb ages. *Contributions to Mineralogy and Petrology.*, 88: 322-327.

Williamson P.E. 1988 Origin, structural and tectonic history of the Macquarie Island region. *Papers and Proceedings of the Royal Society of Tasmania.*, 122: 27-43.

Wood D.A., Tarney J. and Weaver B.L. 1981 Trace element variations in Atlantic Ocean basalts and Proterozoic dykes from northwest Scotland: their bearing upon the nature and geochemical evolution of the upper mantle. *Tectonophysics.*, 75: 91-112.

Woodhead J.D. 1992 Temporal geochemical evolution in oceanic intra-plate volcanics: a case study from the Marquesas (French Polynesia) and comparison with other hotspots. *Contributions to Mineralogy and Petrology.*, 111: 458-467.

Woodhead J.D. and Devey C.W. 1993 Geochemistry of the Pitcairn seamounts I: source character and temporal trends. *Earth and Planetary Science Letters.*, 116: 81-99.

Woodhead J.D. and McCulloch M.T. 1989 Ancient seafloor signals in Pitcairn Island lavas and evidence for large amplitude, small length-scale mantle heterogeneities. *Earth and Planetary Science Letters.*, 94: 257-273.

Woodhead J.D., Greenwood P., Harmon R.S. and Stoffers P. 1993 Oxygen isotope evidence for recycled crust in the source of EM-type ocean island basalts. *Nature.*, 362: 809-813.

Woodhead J.D., Volker F. and McCulloch M.T. (submitted) Routine Pb isotope determinations using a ^{207}Pb-^{204}Pb double spike: a long-term assessment of analytical precision and accuracy. *Chemical Geology.*

Woodhouse J.H. and Dziewonski A.M. 1984 Mapping of the upper mantle: three-dimensional modeling of Earth structure by inversion of seismic waveforms. *Journal of Geophysical Research.*, 89: 5953-5986.

Wörner G. and Viereck L. 1990 Mount Melbourne. In LeMasurier W.E. and Thomson J.W. (Editors) Volcanoes of the Antarctic plate and Southern Oceans. *Antarctic Research Series.*, 48: 72-78. American Geophysical Union, Washington D.C.

Wright A.C. and Kyle P.R. 1990a Balleny Islands. In LeMasurier W.E. and Thomson J.W. (Editors) Volcanoes of the Antarctic plate and Southern Oceans. *Antarctic Research Series.*, 48: 449-451. American Geophysical Union, Washington D.C.

Wright A.C. and Kyle P.R. 1990b Mason Spur. In LeMasurier W.E. and Thomson J.W. (Editors) Volcanoes of the Antarctic plate and Southern Oceans. *Antarctic Research Series.*, 48: 128-130. American Geophysical Union, Washington D.C.

Wright A.C. and Kyle P.R. 1990c Mount Discovery. In LeMasurier W.E. and Thomson J.W. (Editors) Volcanoes of the Antarctic plate and Southern Oceans. *Antarctic Research Series.*, 48: 120-123. American Geophysical Union, Washington D.C.

Wright A.C. and Kyle P.R. 1990d Scott Island. In LeMasurier W.E. and Thomson J.W. (Editors) Volcanoes of the Antarctic plate and Southern Oceans. *Antarctic Research Series.*, 48: 452-453. American Geophysical Union, Washington D.C.

Wright E. and White W.M. 1987 The origin of Samoa: new evidence from Sr, Nd, and Pb isotopes. *Earth and Planetary Science Letters.*, 81: 151-162.

Yan C.-Y. 1991 Indo-Australian counterpart of the Hawaiian-Emperor: Tasmania bend. *EOS: Transactions, American Geophysical Union.*, 71: 1640.

Yoder H.S. Jr. and Tilley C.E. 1962 Origin of basalt magmas. *Journal of Petrology.*, 3: 343-532.

Yoshida M. and Kizaki K. 1983 Tectonic situation of Lutzow-Holm Bay in East Antarctica and its significance in Gondwanaland. In Oliver R.L., James P.R. and Jago J.B. (Editors) *Antarctic Earth Science.*, 36-39. Australian Academy of Science, Canberra.

Zhu B.Q. and Fan C.Y. 1989 K-Ar ages, Pb and Sr isotopic features and the mantle anomaly. In Li H.M. and Wang S.Y. (Editors) *Geology and Geochemistry of the Transantarctic Mountains and Ross Island, Antarctica.*, 120-124. Science Press, Beijing.

Zindler A. and Hart S. 1986 Chemical Geodynamics. *Annual Reviews in Earth and Planetary Science.*, 14: 493-571.

Zindler A., Jagoutz E. and Goldstein S. 1982 Nd, Sr and Pb isotopic systematics in a three-component mantle: a new perspective. *Nature.*, 298: 519-523.

APPENDICES

APPENDICES - LIST OF TABLES

Appendix 1

Appendix 2

Appendix 3

Appendix 4

Appendix 5

APPENDICES - LIST OF FIGURES

Appendix 1

Appendix 2

Appendix 3

Appendix 4

Appendix 5

APPENDIX 1

SAMPLE LOCALITIES

The localities of all samples analysed during the course of this study are listed in Appendix 1. They have been subdivided into the following three groups: dredged oceanic igneous rocks (Table A1.1); Australian basalts, including Macquarie Island samples (Table A1.2); and rocks collected from the mafic dyke swarms of the Vestfold Hills, East Antarctica (Table A1.3). All samples are housed in the rock collection of the Geology Department, University of Tasmania; portions of some samples are also retained by the institute of origin, as listed in the table captions. Seafloor topography for the *USNS Eltanin* dredge sites is depicted in Figure A1.1.

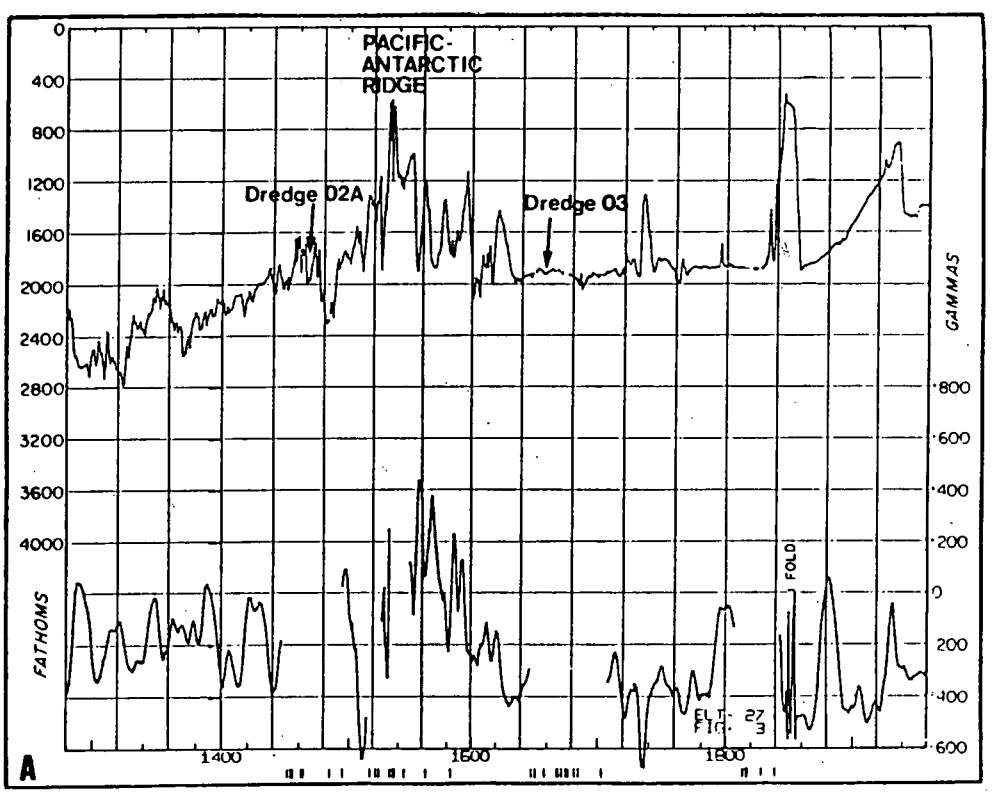

(Figure A1.1)

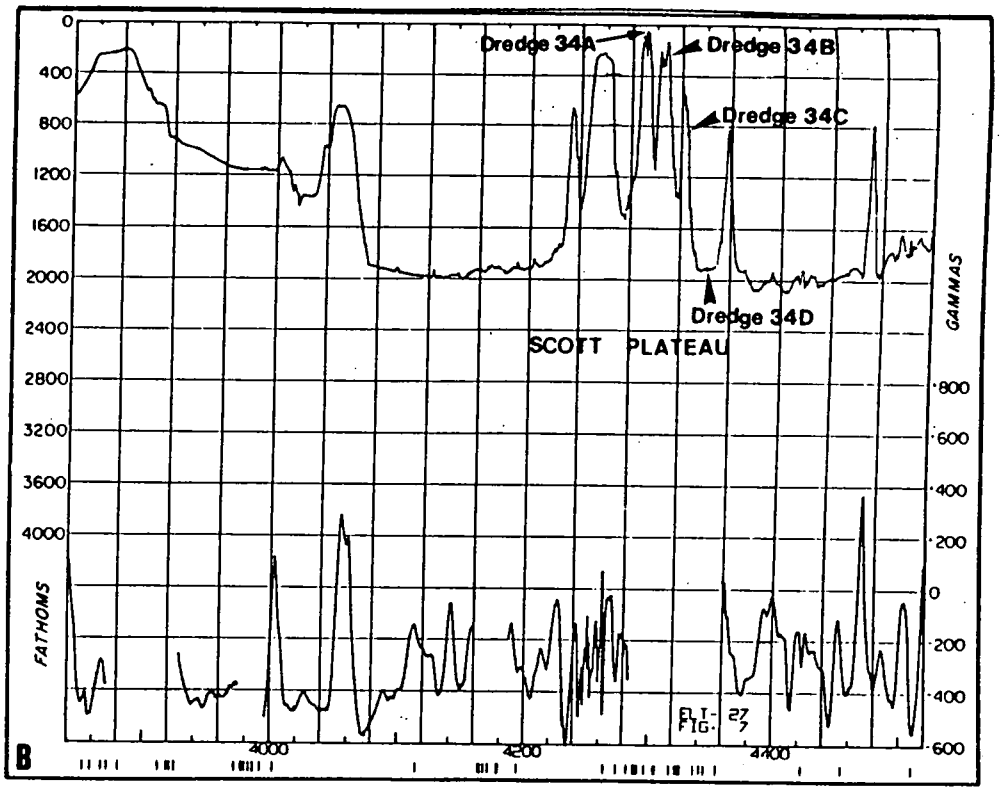
Dredge 34A
Dredge 34B
Dredge 34C
Dredge 34D
SCOTT PLATEAU
FATHOMS
GAMMAS
B

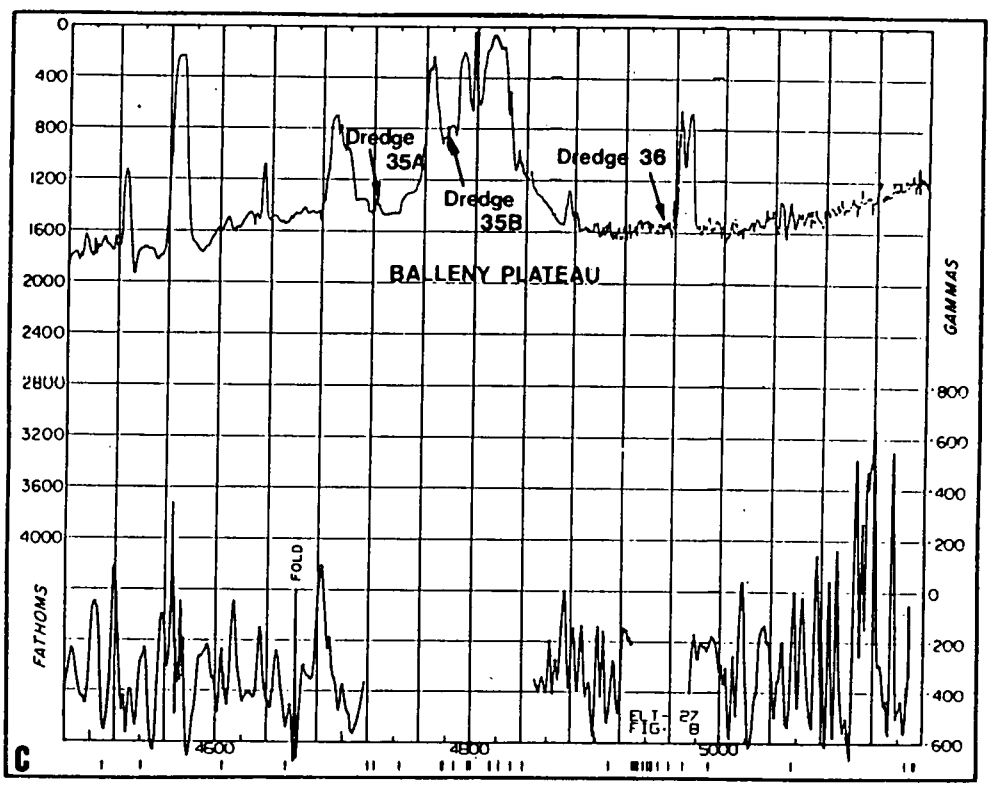
Dredge 35A
Dredge 35B
Dredge 36
RALLENY PLATEAU
FOLD
FATHOMS
GAMMAS
C

(Figure A1.1)

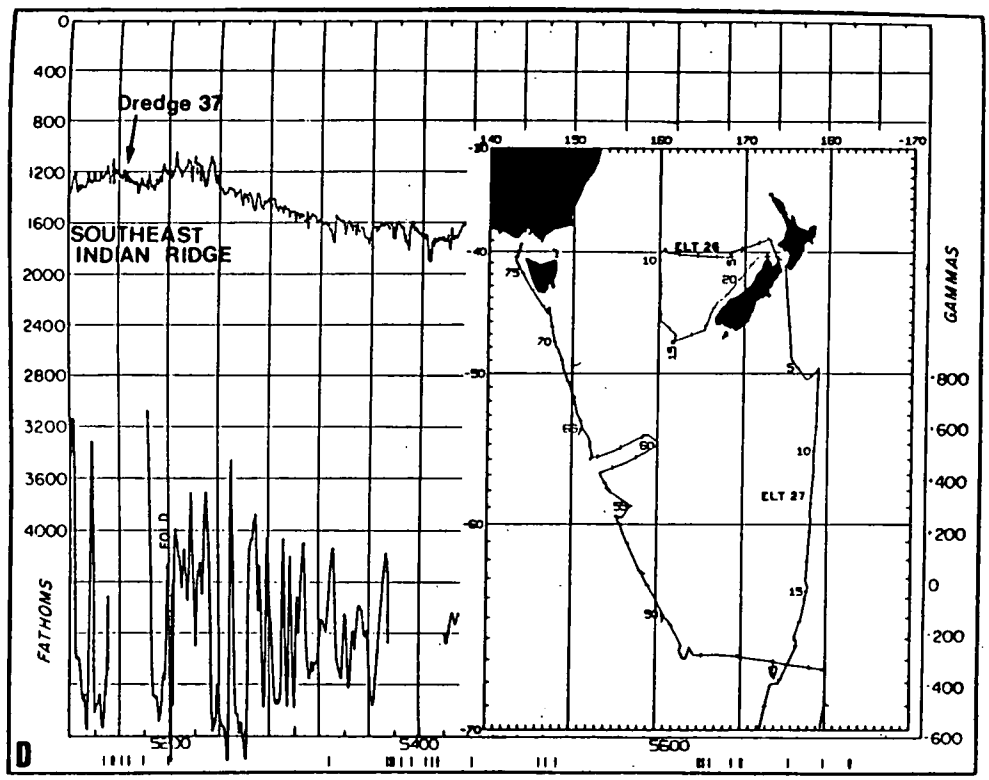

Figure A1.1: Topographic (upper) and magnetic (lower) profiles (Hayes et al., 1969) showing the location of *USNS Eltanin* cruise 27 dredge sites for samples listed in Table A1.1 (1 fathom = 1.83 metres). Inset in D shows the route taken by cruise E27.

Table A1.1: Sample localities of dredged oceanic rocks analysed during this study. The Antarctic Marine Geology Research Facility, Florida State University, supplied samples dredged during the 1967 cruise E27 of the *USNS Eltanin*. Soela Seamount samples were supplied by CSIRO division of Fisheries, the Australian Maritime College and local Tasmanian deep-sea fishermen. The south Tasman Sea seamount samples, furnished by the Ocean Sciences Institute, University of Sydney, were dredged during two cruises of the *HMAS Cook*: Leg 2 of cruise 1/84 dredged Janszoon Seamount (Jenkins, 1985); *HMAS Cook* cruise 17/86 dredged Heemskirk and Zeehan Seamounts (Hubble et al., 1987). Samples from the 1991 Southern Margins cruise 102 of the *R/V Rig Seismic* were provided by the Australian Geological Survey Organisation (AGSO).

Catalogue No. (Tas Uni.)	Sample No. (as dredged)	Rock Classification	Latitude	Longitude	Water Depth	Location
USNS Eltanin dredges:						
78351	E27-02A-2	Trachybasalt	63°13.8'S	177°40.5'E	3660 m	~150 km N of Pacific-Antarctic ridge crest
78353	E27-03	Phonotephrite	66°07.0'S	176°18.1'E	3541 m	~120 km SW of Pacific-Antarctic ridge crest
78354	E27-34A-1	Phonolite	67°24.7'S	179° 54.5'W	220 m	Submarine flanks of Scott Island, Scott Plateau
78355	E27-34A-2	Phonolite	67°24.7'S	179° 54.5'W	220 m	Submarine flanks of Scott Island, Scott Plateau
78357	E27-34A-4	Phonolite	67°24.7'S	179° 54.5'W	220 m	Submarine flanks of Scott Island, Scott Plateau
78358	E27-34B-1	Phonolite	67°23.8'S	179°57.5'W	611 m	Submarine flanks of Scott Island, Scott Plateau
78359	E27-34B-2	Phonolite	67°23.8'S	179°57.5'W	611 m	Submarine flanks of Scott Island, Scott Plateau
78360	E27-34B-3	Phonolite	67°23.8'S	179°57.5'W	611 m	Submarine flanks of Scott Island, Scott Plateau
78361	E27-34B-4	Phonolite	67°23.8'S	179°57.5'W	611 m	Submarine flanks of Scott Island, Scott Plateau
78364	E27-34C-1	Phonotephrite	67°32.0'S	179°57.0'W	1519 m	Submarine flanks of Scott Island, Scott Plateau
78365	E27-34C-2	Phonotephrite	67°32.0'S	179°57.0'W	1519 m	Submarine flanks of Scott Island, Scott Plateau
78366	E27-34D-1	Phonolite	67°35.5'S	179°37.0'E	3495 m	Submarine flanks of Scott Island, Scott Plateau
78368	E27-35A-1	Phonotephrite	66°48.0'S	164°24.0'E	2580 m	~50 km ENE of Buckle Island, Balleny Group
78369	E27-35A-2	Trachyte	66°48.0'S	164°24.0'E	2580 m	~50 km ENE of Buckle Island, Balleny Group
78370	E27-35A-3	Basanite	66°48.0'S	164°24.0'E	2580 m	~50 km ENE of Buckle Island, Balleny Group
78371	E27-35A-4	Trachybasalt	66°48.0'S	164°24.0'E	2580 m	~50 km ENE of Buckle Island, Balleny Group
78372	E27-35A-5	Alkali olivine basalt	66°48.0'S	164°24.0'E	2580 m	~50 km ENE of Buckle Island, Balleny Group
78373	E27-35A-6	Trachybasalt	66°48.0'S	164°24.0'E	2580 m	~50 km ENE of Buckle Island, Balleny Group
78374	E27-35A-7	Basanite	66°48.0'S	164°24.0'E	2580 m	~50 km ENE of Buckle Island, Balleny Group
78375	E27-35B-1	Basanite	67°00.0'S	163°41.5'E	1587 m	~20 km SE of Buckle Island, Balleny Group
78376	E27-35B-2	Basanite	67°00.0'S	163°41.5'E	1587 m	~20 km SE of Buckle Island, Balleny Group
78378	E27-36-2	Basanite	65°02.2'S	160°44.5'E	2837 m	~240 km SW of Southeast Indian Ridge crest
78380	E27-36-4	Basanite	65°02.2'S	160°44.5'E	2837 m	~240 km SW of Southeast Indian Ridge crest
78381	E27-36-5	Basanite	65°02.2'S	160°44.5'E	2837 m	~240 km SW of Southeast Indian Ridge crest
78383	E27-36-7	Basanite	65°02.2'S	160°44.5'E	2837 m	~240 km SW of Southeast Indian Ridge crest
78384	E27-36-8	Trachybasalt	65°02.2'S	160°44.5'E	2837 m	~240 km SW of Southeast Indian Ridge crest
78386	E27-37-2	Alkali olivine basalt	62°50.4'S	158°21.01'E	2342 m	Southern flank of Southeast Indian Ridge
78387	E27-37-3	Tephriphonolite	62°50.4'S	158°21.01'E	2342 m	Southern flank of Southeast Indian Ridge
Soela Seamount dredges:						
78400	SS1-1	Basaltic trachyandesite clast	43°56.0'S - 43°56.8'S	150°21.0'E - 150°31.73'E	895 - 990 m	Soela Seamount, East Tasman Plateau
78405	SS2-4	Alkali olivine basalt clast	43°56.0'S - 43°56.8'S	150°21.0'E - 150°31.73'E	895 - 990 m	Soela Seamount, East Tasman Plateau
78407	SS2-6	Alkali olivine basalt clast	43°56.0'S - 43°56.8'S	150°21.0'E - 150°31.73'E	895 - 990 m	Soela Seamount, East Tasman Plateau
78410	SS3	Alkali olivine basalt	43°56.0'S - 43°56.8'S	150°21.0'E - 150°31.73'E	895 - 990 m	Soela Seamount, East Tasman Plateau
78411	SS4-1	Alkali olivine basalt clast	43°56.0'S - 43°56.8'S	150°21.0'E - 150°31.73'E	895 - 990 m	Soela Seamount, East Tasman Plateau
78412	SS4-2	Alkali olivine basalt clast	43°56.0'S - 43°56.8'S	150°21.0'E - 150°31.73'E	895 - 990 m	Soela Seamount, East Tasman Plateau
78413	SS4-3	Trachybasalt clast	43°56.0'S - 43°56.8'S	150°21.0'E - 150°31.73'E	895 - 990 m	Soela Seamount, East Tasman Plateau

Table A1.1: (continued)

Catalogue No. (Tas Uni.)	Sample No. (as dredged)	Rock Classification	Latitude	Longitude	Water Depth	Location
Soela Seamount Dredges:						
78414	SS4-4	Trachybasalt clast	43°56.0'S - 43°56.8'S	150°21.0'E - 150°31.73'E	895 - 990 m	Soela Seamount, East Tasman Plateau
78415	SS4-5	Transitional alkali basalt clast	43°56.0'S - 43°56.8'S	150°21.0'E - 150°31.73'E	895 - 990 m	Soela Seamount, East Tasman Plateau
78416	SS4-6	Trachybasalt clast	43°56.0'S - 43°56.8'S	150°21.0'E - 150°31.73'E	895 - 990 m	Soela Seamount, East Tasman Plateau
78417	SS4-7	Trachybasalt clast	43°56.0'S - 43°56.8'S	150°21.0'E - 150°31.73'E	895 - 990 m	Soela Seamount, East Tasman Plateau
78418	SS4-8	Alkali olivine basalt clast	43°56.0'S - 43°56.8'S	150°21.0'E - 150°31.73'E	895 - 990 m	Soela Seamount, East Tasman Plateau
78419	SS5	Trachybasalt	43°56.0'S - 43°56.8'S	150°21.0'E - 150°31.73'E	895 - 990 m	Soela Seamount, East Tasman Plateau
HMAS Cook dredges:						
78389	C1/84 (2) 2DB 10	Trachybasalt	39°34.4'S	154°13.6'E	2215 m	Janszoon Seamount, south Tasman Sea
78390	C1/84 (2) 2DB 14	Basanite	39°34.4'S	154°13.6'E	2215 m	Janszoon Seamount, south Tasman Sea
78391	C17/86 8DB 2/1	Trachyandesite	36°17.1'S - 36°16.2'S	159°33.6'E - 159°36.5'E	2560 - 3800 m	Zeehan Seamount, south Tasman Sea
78392	C17/86 8DB 2/2	Trachyandesite	36°17.1'S - 36°16.2'S	159°33.6'E - 159°36.5'E	2560 - 3800 m	Zeehan Seamount, south Tasman Sea
78393	C17/86 8DB 2/5	Trachyandesite	36°17.1'S - 36°16.2'S	159°33.6'E - 159°36.5'E	2560 - 3800 m	Zeehan Seamount, south Tasman Sea
78394	C17/86 8DB 3/4	Trachyandesite	36°17.1'S - 36°16.2'S	159°33.6'E - 159°36.5'E	2560 - 3800 m	Zeehan Seamount, south Tasman Sea
78396	CK17/86 7DB 1/10	Trachybasalt	36°21.5'S - 36°23.4'S	159°51.0'E - 159°53.0'E	3700 - 4000 m	Heemskirk Seamount, south Tasman Sea
78398	CK17/86 7DB 1/13	Trachybasalt	36°21.5'S - 36°23.4'S	159°51.0'E - 159°53.0'E	3700 - 4000 m	Heemskirk Seamount, south Tasman Sea
Rig Seismic dredges:						
78435	102/DR09-4A	Olivine tholeiite basalt	37°46.87'S - 37°48.78'S	132°19.98'E - 132°18.00'E	4940 - 5550 m	~53 Ma old oceanic crust, E of AAD, Southern Ocean
78436	102/DR09-4B(i)	Transitional tholeiite basalt	37°46.87'S - 37°48.78'S	132°19.98'E - 132°18.00'E	4940 - 5550 m	~53 Ma old oceanic crust, E of AAD, Southern Ocean
78437	102/DR09-4B(ii)	Olivine tholeiite basalt	37°46.87'S - 37°48.78'S	132°19.98'E - 132°18.00'E	4940 - 5550 m	~53 Ma old oceanic crust, E of AAD, Southern Ocean
78439	102/DR09-4B4	Transitional tholeiite basalt	37°46.87'S - 37°48.78'S	132°19.98'E - 132°18.00'E	4940 - 5550 m	~53 Ma old oceanic crust, E of AAD, Southern Ocean
78440	102/DR09-4B5	Olivine tholeiite basalt	37°46.87'S - 37°48.78'S	132°19.98'E - 132°18.00'E	4940 - 5550 m	~53 Ma old oceanic crust, E of AAD, Southern Ocean
78441	102/DR09-4C	Transitional tholeiite basalt	37°46.87'S - 37°48.78'S	132°19.98'E - 132°18.00'E	4940 - 5550 m	~53 Ma old oceanic crust, E of AAD, Southern Ocean
78443	102/DR10-1B	Olivine tholeiite gabbro	39°55.28'S - 39°55.12'S	131°58.59'E - 131°58.97'E	5241 - 5550 m	~36 Ma old oceanic crust, E of AAD, Southern Ocean
78444	102/DR10-1C	Metagabbro	39°55.28'S - 39°55.12'S	131°58.59'E - 131°58.97'E	5241 - 5550 m	~36 Ma old oceanic crust, E of AAD, Southern Ocean
78445	102/DR10-3A	Metadolerite	39°55.28'S - 39°55.12'S	131°58.59'E - 131°58.97'E	5241 - 5550 m	~36 Ma old oceanic crust, E of AAD, Southern Ocean
78450	102/DR10-4	Andesite	39°55.28'S - 39°55.12'S	131°58.59'E - 131°58.97'E	5241 - 5550 m	~36 Ma old oceanic crust, E of AAD, Southern Ocean
78451	102/DR11-2A	Olivine tholeiite basalt	39°45.92'S - 39°46.75'S	119°46.02'E - 119°44.70'E	5050 - 5240 m	~36 Ma old oceanic crust, W of AAD, Southern Ocean
78452	102/DR11-2A(iii)	Olivine tholeiite basalt	39°45.92'S - 39°46.75'S	119°46.02'E - 119°44.70'E	5050 - 5240 m	~36 Ma old oceanic crust, W of AAD, Southern Ocean
78453	102/DR11-2A(iv)	Olivine tholeiite basalt	39°45.92'S - 39°46.75'S	119°46.02'E - 119°44.70'E	5050 - 5240 m	~36 Ma old oceanic crust, W of AAD, Southern Ocean
78454	102/DR11-2B	Olivine tholeiite basalt	39°45.92'S - 39°46.75'S	119°46.02'E - 119°44.70'E	5050 - 5240 m	~36 Ma old oceanic crust, W of AAD, Southern Ocean
78459	102/DR13-3(iii)	Olivine tholeiite dolerite	37°14.62'S - 37°10.00'S	118°09.35'E - 118°09.35'E	3950 - 4480 m	~66 Ma old oceanic crust, W of AAD, Southern Ocean
78460	102/DR13-3D	Olivine tholeiite dolerite	37°14.62'S - 37°10.00'S	118°09.35'E - 118°09.35'E	3950 - 4480 m	~66 Ma old oceanic crust, W of AAD, Southern Ocean
78461	102/DR13-3E	Tholeiite basalt	37°14.62'S - 37°10.00'S	118°09.35'E - 118°09.35'E	3950 - 4480 m	~66 Ma old oceanic crust, W of AAD, Southern Ocean

Table A1.2: Sample localities for Australian continental and Macquarie Island basalts analysed during the course of this study. Victorian Older Volcanics samples were collected by the author. Suppliers of Tasmanian samples, and the maps used to derive grid references for sample localities are as follows: Cape Portland - G.M. Yaxley, University of Tasmania Geology Department (Cape Portland 8416 1:100 000 map); Weldborough basalt - A.J. Crawford, University of Tasmania Geology Department and S.M. Eggins, RSES, Australian National University (Forester 8415 1:100 000 map); and Bream Creek basalt - F.L. Sutherland, Australian Museum, Sydney (Prosser 8412 1:100 000 map). Note that sample number DR 13516 is an Australian Museum registration number. Macquarie Island samples from the University of Tasmania Geology Department collection were sampled by M.Rubenach and R. Varne in 1970-71 (sample 38287), and R.A. Duncan, J. Cocker, B. Griffin and R. Varne in 1979 (samples 47963, 47978 and 47979). Macquarie Island samples 25601 and 25637 were supplied by the Geology Department at the Australian National University.

Catalogue No. (Tas Uni.)	Sample No. (as collected)	Rock Classification	Location	Grid Reference	Latitude	Longitude
Victorian Older Volcanics:						
78421	OV 1	Transitional alkali basalt	Foreshore on western side of Cape Schank, Victoria - Flinders Province		144°59'E	38°30'S
78422	OV 2	Basanite	Swans Rd,~2.8 km WNW of Links Rd, Pentland Hills, Victoria - Ballan Graben Province		144°20'E	37°37'S
78423	OV 3	Basanite	Swans Rd, W of Bald Hill, Pentland Hills, Victoria - Ballan Graben Province		144°20'E	37°37'S
78424	OV 4	Transitional alkali basalt	Disused quarry opposite Tullamarine airport, Victoria - Melbourne Province		144°51'E	37°44'S
78425	OV 5	Quartz tholeiite basalt	~2 km SE of Ford's Bridge, Tolmie-Tatong Rd, Victoria - Toombullup Province		146°18'E	37°44'S
78426	OV 6	Olivine tholeiite basalt	~0.7 km N of Ford's Bridge, Tolmie-Tatong Rd, Victoria - Toombullup Province		146°18'E	37°44'S
Tasmanian Tertiary basalts:						
78427	2	Alkali basalt	Weldborough, Tasmania	791365		
78428	DR 13516	Alkali olivine basalt	16 m below top of Benders Hill, Bream Creek, Tasmania	EN685602		
Cape Portland hypabyssal assemblage:						
78429	10	Appinite	Cape Portland, Tasmania			
78430	11	Appinite	Cape Portland, Tasmania	EQ811884		
78431	13	Appinite	Cape Portland, Tasmania	EQ811884		
				EQ811884		
Macquarie Island basalts:						
	25601	Alkali basalt	Macquarie Island			
	25637	Transitional tholeiite basalt	Macquarie Island			
38287		Quartz tholeiite basalt	Plateau, ENE of Mt. Merlin, Macquarie Island			
47963		Trachybasalt	Overland track ~0.25 km E of Prion Lake, Macquarie Island			
47978		Trachybasalt	Catch Me Point, Macquarie Island			
47979		Olivine tholeiite basalt	Catch Me Point, Macquarie Island			

Table A1.3: Localities of analysed mafic dyke and felsic segregation samples collected by the author from the Vestfold Hills region of East Antarctica during the austral summer of 1990-1991. Ozchron numbers refer to samples housed by AGSO. Grid references relate to the second edition 1:50 000 Vestfold Hills map (NATMAP).

Sample No. (Tas Uni.)	Ozchron No. (A.G.S.O.)	Sample Description	Location	Grid Reference
76539	-	Late stage segregation in Group 4 Fe-rich tholeiite dyke	Bandits Island	LK924077
76540	91286551	Late stage segregation in Group 4 Fe-rich tholeiite dyke	Bandits Island	LK924078
76541	91286552	Late stage segregation in Homogeneous Norite	Bandits Island	LK926077
76542	91286553	Late stage segregation in Homogeneous Norite	Bandits Island	LK925077
76543	91286554	Late stage segregation in Homogeneous Norite	Bandits Island	LK925076
76544	91286555	Mylonitised Group 2 Fe-rich tholeiite dyke	Brookes Hut	LJ854939
76549	91286556	Group 2 Fe-rich tholeiite dyke	S of Taynaya Bay	LK872014
76550	91286557	Lamprophyre dyke	S of Taynaya Bay	LK897023
76551	91286558	Group 2 Fe-rich tholeiite dyke	E of Taynaya Bay	LK899037
76553	91286559	Late stage segregation in Mottled Norite	Barrier Island	LK930066
76554	91286560	Late stage segregation in Group 3 Fe-rich tholeiite dyke	W of Tryne Sound	LK929062
76555	91286561	Late stage segregation in Group 3 Fe-rich tholeiite dyke	W of Tryne Sound	LK929062
76560	91286562	Late stage segregation in Group 2 Fe-rich tholeiite dyke	W of Tryne Fjord	LK924048
76561	91286563	Group 2 High-Mg tholeiite dyke	E of Rybnaya Bay	LK915052
76562	91286564	Group 1 High-Mg tholeiite dyke	SE of Rybnaya Bay	LK908046
76567	91286565	Group 1 High-Ti Fe-rich tholeiite dyke	W of Brookes Hut	LJ839939

Table A2.1: X-ray fluorescence major and trace element data for two 'in-house' standard rocks, TasBas and TasGran, measured on two different spectrometers at the University of Tasmania Geology Department. Standard detection limits are for 3σ (99 %) confidence levels.

	Philips PW1410 spectrometer: Detection limits	TasBas	±1σ	σ %	n	TasGran	±1σ	σ %	n
Major Elements (wt %):									
SiO_2	0.037	44.91	0.25	0.6	11	72.42	0.11	0.2	3
TiO_2	0.015	2.29	0.04	1.8	11	0.28	0.02	7.1	3
Al_2O_3	0.028	14.14	0.10	0.7	11	13.54	0.01	0.1	3
Fe_2O_3	0.014	12.51	0.09	0.7	11	2.32	0.06	2.4	3
MnO	0.009	0.17	0.01	5.9	11	0.04	0.00	0.0	3
MgO	0.050	8.12	0.13	1.6	11	0.59	0.03	5.1	3
CaO	0.015	7.81	0.06	0.8	11	1.83	0.01	0.3	3
Na_2O	0.200	5.48	0.07	1.3	11	2.77	0.03	0.9	3
K_2O	0.013	1.91	0.04	2.1	11	4.56	0.06	1.3	3
P_2O_5	0.028	0.97	0.02	2.1	11	0.11	0.01	5.5	3
Trace Elements (ppm):									
Ba	3	203.8	4.2	2.1	9	467.0			1
Rb	1	16.3	2.0	12.3	7	259.8	2.0	0.8	4
Nb	1	59.2	1.1	1.8	7	19.7	0.1	0.4	2
Sr	1	1012.9	10.3	1.0	7	151.5	1.0	0.7	4
Zr	1	259.7	3.2	1.2	7	160.5	2.1	1.3	2
Y	1.5	23.3	1.0	4.3	7	34.7	1.1	3.3	2
Ni	1	149.1	2.6	1.8	8	4.0			1
Cr	2	191.0	2.4	1.3	8	11.0			1
V	3	160.1	2.6	1.6	8	26.0			1
Sc	1	12.1	1.8	14.8	6	7.0			1
Zn	1	119.1	1.2	1.0	5	41.0			1
Cu	1	62.6	1.3	2.1	5	2.0			1
La	2.5	41.8	1.0	2.5	3	38.5	0.7	1.8	2
Ce	5	88.7	4.0	4.6	3	79.5	5.0	6.2	2
Nd	3	42.0	1.7	4.1	3	33.5	0.7	2.1	2
U	2					3.5	0.7	20.3	2
Th	2					19.1	0.1	0.7	2
Pb	3					27.6	0.1	0.5	2

	Philips PW1480 spectrometer: Detection limits	TasBas	±1σ	σ %	n	TasGran	±1σ	σ %	n
Major Elements (wt %):									
SiO_2	0.0020	44.68	0.08	0.2	5	73.05	0.27	0.4	3
TiO_2	0.0060	2.32	0.01	0.4	5	0.29	0.01	3.4	3
Al_2O_3	0.0080	14.19	0.02	0.1	5	13.70	0.06	0.4	3
Fe_2O_3	0.0041	12.69	0.16	1.3	5	2.25	0.05	2.2	3
MnO	0.0035	0.16	0.01	3.1	5	0.04	0.00	0.0	3
MgO	0.0110	8.32	0.06	0.7	5	0.69	0.01	0.9	3
CaO	0.0009	7.84	0.03	0.4	5	1.83	0.01	0.5	3
Na_2O	0.0240	5.42	0.03	0.6	5	2.73	0.02	0.7	3
K_2O	0.0004	1.93	0.00	0.0	5	4.61	0.01	0.2	3
P_2O_5	0.0026	0.95	0.01	1.1	5	0.12	0.01	5.0	3
Trace Elements (ppm):									
Ba	4	206.0	2.3	1.1	15				
Rb	1	16.5	0.1	0.6	11				
Nb	1	54.2	0.4	0.7	15				
Sr	1	1010.0	6.0	0.6	15				
Zr	1	260.0	1.8	0.7	15				
Y	1	21.4	0.4	1.9	11				
Ni	1	150.0	1.3	0.9	11				
Cr	1	190.3	0.6	0.3	15				
V	1.5	154.0	1.0	0.7	15				
Sc	2	13.2	0.4	3.0	15				
La	2	44.2	1.4	3.2	15				
Ce	4	89.2	1.2	1.4	15				
Nd	2	40.8	0.8	1.9	15				
Th	1	4.8	0.4	8.3	11				
Pb	1.5	4.4	0.4	9.1	11				

APPENDIX 2

ANALYTICAL TECHNIQUES

A2.1 WHOLE-ROCK MAJOR AND TRACE ELEMENT ANALYSES:

Two methods of major and and trace element analysis were employed, depending on the amount of sample available:

1. X-ray fluorescence (XRF) spectrometry major and trace element analyses were performed at the University of Tasmania Geology Department, using Philips PW1410 and Philips PW1480 spectrometers. Spectrometer calibration was maintained using international standards, blanks and specpure compounds (silica and oxides). Data precision was monitored by repeated analysis of several internal standards including TasBas and TasGran (Table A2.1). Results for two international rock standards, BIR-1 and BHVO-1 (Table A2.2) measured on the Philips PW1410 spectrometer, provide an indication of the accuracy of trace element data measured by this method. Instrumental conditions are presented in Table A2.3.

Sample preparation included soaking Soela Seamount conglomerates SS1, SS2 and SS4 in concentrated HCl to dissolve carbonate matrix material, followed by washing constituent clasts with distilled water prior to crushing. Other samples were prepared by removing all weathered and cut surfaces with an hydraulic splitter. All samples for major and trace element analysis were crushed in a steel jaw crusher to produce ~0.5 cm-sized chips. Selected chips (50-100 g) were then powdered in a tungsten carbide swing mill.

Major elements were analysed on fused glass discs (1.5 g flux, 0.28 g sample, 0.02 g $LiNO_3$) following the method described by Norrish and Hutton (1969). Loss on ignition (LOI) was measured as the weight percent loss of 1 g of powdered sample heated to 1000° C for ~15 hours, followed by ~5 hours at 400° C. Trace elements were analysed on 5 g pressed powder pellets coated with boric acid using the method described by Norrish and Chappell (1977) and mass absorption coefficients calculated from major element XRF analyses.

Cs, Hf, Ta and Th data were obtained by instrumental neutron activation analysis (INAA) performed by Becquerel Laboratories on samples (~1 g) powdered in a chrome steel swing mill to avoid Ta contamination. Analytical methods are described in section A2.2.

2. Samples of insufficient quantity for XRF techniques were analysed for major element concentrations on the Cameca SX50 electron microprobe, at the University of Tasmania Central Science Laboratories, using whole-rock powders fused to glass by Ir-strip heating. Results are presented as the mean of six analyses, with the microprobe operating at a beam current of 20 nA and accelerating voltage of 15 kV.

Table A2.2: X-ray fluorescence trace element data for two international standard rocks, BIR-1 and BHVO-1, as measured on the Philips PW1410 spectrometer at the University of Tasmania Geology Department, compared to accepted values collated from the literature (W.F. McDonough; pers. comm.) Literature sources include Sun et al. (1979), Rautenschlein et al. (1985), Nye and Reid (1986), Robinson et al. (1986), Stork et al. (1987), Govindaraju (1989), Norman et al. (1989), Chen et al. (1990), Frey et al. (1990), Jenner et al. (1990), Jochum et al. (1990), Chen et al. (1991), Frey et al. (1991) and West et al. (1992).

	BIR-1: accepted	measured	BHVO-1: agreed	measured
Ba			133	145
Rb	0.24	<2	9.5	10.8
Nb	0.50	<1	19.5	20.8
Sr	110	111	390	402
Zr	14	17	175	178
Y	16	15.7	28	28.3
Ni	166	158.6	120	121.3
Cr	382	393	289	303
V	313	315.7	320	319.5
Sc			31.8	32.2
Zn			105	106.8
Cu			136	150

Table A2.3: Instrumental conditions for routine XRF trace element analysis at the University of Tasmania Geology Department. The X-ray tube was operated at 60 kV 40 mA for all elements except Ba, Sc, La, Ce and Nd where 50 kV 50 mA was used; a LiF crystal was used for all analyses.

Element	Emission line	X-ray Tube PW1410	X-ray Tube PW1480	Precision PW1410
Ba	L (α)	Cr	Au	500±5, 1200±5
Rb	K (α)	Rh	Mo/Sc	10±1, 70±1, 170±2
Nb	K (α)	Rh	Au	10±0.5, 20±1
Sr	K (α)	Rh	Au	10±1, 200±2, 500±5
Zr	K (α)	Rh	Au	100±2, 250±4, 500±10
Y	K (α)	Rh	Mo/Sc	10±2, 20±1, 100±2
Ni	K (α)	Au	Mo/Sc	3±0.5, 20±0.5, 200±2
Cr	K (α)	Au	Au	10±2, 400±4
V	K (α)	Au	Au	30±2, 100±1
Sc	K (α)	Cr	Au	10±1, 30±1
Zn	K (α)	Au	Mo/Sc	40±1
Cu	K (α)	Au	Mo/Sc	5±1, 50±1
La	L (α)	Au	Au	20±1, 40±2, 100±2
Ce	L (β)	Au	Au	30±2, 80±3, 150±1
Nd	L (α)	Au	Au	15±1, 30±2, 50±2
U	L (α)	Mo	Mo/Sc	5±1, 40±1
Th	L (α)	Mo	Mo/Sc	25±1, 100±2
Pb	L (β)	Mo	Mo/Sc	20±1, 50±1

The trace element, including rare earth elements, contents of these samples were analysed by inductively coupled plasma-mass spectrometry (ICP-MS)on the VG PlasmaQuad II STE at the Research School of Earth Sciences, the Australian National University. Samples for ICP-MS analysis were crushed in an agate mortar, following hand selection of rock chips devoid of weathered and/or cut surfaces. Approximately 50 mg of each sample (whole-rock powder or fine chips) was dissolved in 1 ml HF plus 0.015 ml concentrated HNO_3. Following

Table A2.4: ICP-MS trace element data for three international rock standards, AGV-1, BIR-1 and BCR-1, as measured at the Research School of Earth Sciences, The Australian National University, compared to the accepted values used in this laboratory. Machine calibration is based on the accepted values for the international rock standard BHVO-1 presented here.

	BHVO-1: accepted	AGV-1: accepted	measured	% difference	BIR-1: accepted	measured	% difference	BCR-1: accepted	measured	% difference
Trace Elements (ppm):										
Rb	9.5	68	67.80	0.3	0.22	0.20	9.1	46.9	48.25	2.9
Sr	390	660	660.00	0.0	110	111.00	0.9	330	335.00	1.5
Y	28	20	21.10	5.5	16.5	16.60	0.6	35	40.10	14.6
Zr	175	225	243.00	8.0	15	15.00	0.0	187	199.00	6.4
Nb	19.5	14	15.60	11.4	0.6	0.70	16.7	13.5	13.40	0.7
Cs	0.1	1.25	1.25	0.3	0.007	0.01	28.6	0.956	0.97	1.6
Ba	133	1200	1178.00	1.8	6	7.00	16.7	675	674.00	0.1
La	15.5	39	38.64	0.9	0.58	0.61	5.2	24.9	25.98	4.3
Ce	38	70	68.43	2.2	1.85	1.91	3.2	53.6	53.90	0.6
Pr	5.45	8	8.43	5.4	0.37	0.38	2.7	6.8	7.01	3.1
Nd	24.7	32	31.69	1.0	2.35	2.41	2.6	28.8	29.03	0.8
Sm	6.17	5.9	5.86	0.7	1.1	1.09	0.9	6.59	6.79	3.0
Eu	2.06	1.55	1.60	3.2	0.52	0.51	1.9	1.98	1.93	2.5
Gd	6.22	4.7	4.57	2.8	1.97	1.94	1.5	6.72	6.92	3.0
Tb	0.99	0.7	0.69	1.4	0.38	0.39	2.6	1.13	1.15	1.8
Dy	5.25	3.8	3.54	6.8	2.5	2.56	2.4	6.42	6.66	3.7
Ho	1	0.7	0.68	2.9	0.55	0.57	3.6	1.35	1.35	0.0
Er	2.56	1.9	1.84	3.2	1.7	1.71	0.6	3.7	3.80	2.7
Tm	0.34	0.28	0.27	3.6	0.25	0.26	4.0	0.51	0.55	7.8
Yb	1.98	1.75	1.61	8.0	1.6	1.55	3.1	3.38	3.34	1.2
Lu	0.28	0.27	0.25	7.4	0.25	0.24	4.0	0.5	0.51	2.0
Hf	4.3	5.17	4.91	5.0	0.56	0.57	1.8	4.97	4.89	1.6
Pb	2.1	37	36.20	2.2	3	3.00	0.0	13.5	13.80	2.2
Th	1.26	6.5	6.28	3.4	0.03	0.03	0.0	5.91	5.97	1.0
U	0.42	1.9	1.82	4.1	0.01	0.01	10.0	1.7	1.61	5.5

evaporation, samples were heated in 4 mls 6N HNO_3 for one hour and redried. Each sample was then combined with 5g of internal standard (200 ppb ^{7}Li, 200 ppb ^{77}Se, 200 ppb ^{115}In, 50 ppb ^{187}Re and 200 ppb ^{209}Bi), to monitor drift in mass response, and diluted with 2 % HNO_3 to form 100 g of solution (ie. 2000 x dilution). Instrument calibration was performed using solutions of the international rock standard BHVO-1, accepted values for which are given in Table A2.4. All analyses were blank (chemistry blanks) subtracted, and various laboratory and international standards were interspersed with sample analysis to monitor accuracy (Table A2.4) and precision (Table A2.5). Interference corrections were made for $^{144}Nd^{16}O$ and ^{160}Dy on ^{160}Gd, and $^{135}Ba^{16}O$ on ^{151}Eu; all other interferences were negligible.

Table A2.5: Mean and 1s trace element data for repeated analyses of two international rock standards, AGV-1 and BHVO-1, as measured by ICP-MS at the Research School of Earth Sciences, the Australian National University.

	AGV-1: mean	± 1σ	σ %	n	BHVO-1: mean	± 1σ	σ %	n
Trace Elements (ppm):								
Rb	68.03	1.120	1.6	5	9.35	0.208	2.2	6
Sr	658.5	9.657	1.5	5	394.04	5.038	1.3	6
Y	20.86	0.628	3.0	5	28.52	0.445	1.6	6
Zr	237.05	7.561	3.2	5	177.52	5.803	3.3	6
Nb	14.99	0.661	4.4	5	19.84	0.861	4.3	6
Cs	1.17	0.146	12.5	5	0.091	0.012	13.2	5
Ba	1191	10.034	0.8	5	131.87	3.229	2.4	6
La	38.68	0.458	1.2	5	15.49	0.341	2.2	6
Ce	69.33	0.872	1.3	5	38.17	0.801	2.1	6
Pr	8.39	0.229	2.7	5	5.45	0.112	2.1	6
Nd	31.81	0.300	0.9	5	24.63	0.467	1.9	6
Sm	5.88	0.082	1.4	5	6.16	0.178	2.9	6
Eu	1.55	0.045	2.9	5	2.07	0.051	2.5	6
Gd	4.63	0.070	1.5	5	6.14	0.161	2.6	6
Tb	0.696	0.007	1.0	5	1.00	0.013	1.3	6
Dy	3.64	0.106	2.9	5	5.3	0.102	1.9	6
Ho	0.696	0.011	1.6	4	1.02	0.029	2.8	3
Er	1.88	0.025	1.3	5	2.58	0.050	1.9	6
Tm	0.272	0.006	2.2	4	0.344	0.006	1.6	3
Yb	1.66	0.052	3.1	5	1.96	0.040	2.0	6
Lu	0.254	0.009	3.5	5	0.28	0.007	2.5	6
Hf	5.07	0.112	2.2	5	4.33	0.116	2.7	6
Ta	0.9	0.064	7.1	5	1.17	0.094	8.0	6
Pb	36.18	1.006	2.8	5	2.07	0.065	3.1	6
Th	6.42	0.096	1.5	5	1.29	0.059	4.6	6
U	1.87	0.072	3.9	5	0.44	0.023	5.2	5

A2.2 WHOLE-ROCK RARE EARTH ELEMENT ANALYSES:

Two methods of rare earth element (REE) analysis were employed for samples whose major and trace element compositions were determined by XRF spectrometry:

1. Instrumental neutron activation analysis (INAA) was performed by Helen Waldron at Becquerel Laboratories Pty. Ltd. using the Australian Nuclear Science and Technology Organisation's HIFAR irradiation facility at Lucas Heights. Powdered samples (~1 g) were

Table A2.6: Details of isotopes, photopeaks and detection limits for REE and trace elements measured by instrumental neutron activation analysis at Becquerel Laboratories Pty. Ltd. Routine analytical precision for REE and certain trace elements determined on the Becquerel 'in-house' granite standard is indicated by % CV (= % coefficient of variation = 100 x standard deviation/mean).

Target isotope	Product isotope	Thermal neutron capture cross section (barn)	Half-life	Analytical photopeak KeV	Detection Limits (ppm)	% CV
La 139	La 140	9	40.3 h	1596.2	0.10	1
Ce 140	Ce 141	0.57	32.4 d	145.5	1.00	3
Nd 146	Nd 147	1.3	11.1 d	91.1	2.00	3
Sm 152	Sm 153	206	46.8 d	103.2	0.05	1
Eu 151	Eu 152	5900	12.7 y	1408.1	0.10	3
Tb 159	Tb 160	25.5	72.1 d	879.4	0.50	5
Ho 165	Ho 166	63	26.8 h	80.6	0.50	5
Yb 174	Yb 175	65	4.19 d	396.3	0.10	2
Lu 176	Lu 177	2050	6.71 d	208.4	0.05	2
Cs 133	Cs 134	27	2.06y	595.8	0.50	3
Hf 180	Hf 181	12.6	42.4d	482.1	0.20	2
Ta 181	Ta 182	21	115d	1221.4	0.50	5
Th 232	Th 233	7.4	27d	311.9	0.20	2

Table A2.7: REE data obtained for two 'in-house' standard rocks, TasBas and TasGran, by ion exchange - XRF spectrometry (PW1410 spectrometer - L(α) line, Au X-ray tube, LiF 200 crystal) at the University of Tasmania Geology Department; detection limits are for 3σ (99 %) confidence levels (data from Robinson et al., 1986).

Element	Detection limit (µg)	TasBas	±1σ	σ %	TasGran	±1σ	σ %
La	0.35	43.20	1.25	2.9	38.80	0.93	2.4
Ce	0.33	89.10	2.58	2.9	86.90	2.00	2.3
Pr	0.31	10.34	0.28	2.7	9.96	0.25	2.5
Nd	0.26	41.80	0.79	1.9	37.40	0.56	1.5
Sm	0.23	8.15	0.10	1.2	7.09	0.11	1.6
Eu	0.22	2.61	0.11	4.3	0.83	0.10	12.5
Gd	0.20	7.01	0.10	1.5	6.14	0.23	3.8
Dy	0.19	4.89	0.10	2.0	5.98	0.16	2.6
Er	0.17	2.05	0.15	7.2	3.78	0.06	1.5
Yb	0.17	1.26	0.06	4.6	3.40	0.06	1.7

weighed and heat sealed in 1 cm^2 polyethylene bags. Samples, with attached flux monitor labels to measure flux variations, were irradiated for 30-60 minutes at a thermal flux of 2.5-3.5 $ncm^2 s^{-1}$. This bombardment with thermal neutrons resulted in certain target isotopes (Table A2.6) becoming radioactive through neutron capture. Specific radioisotopes are recognised by the characteristic energy of their emitted gamma ray(s) as they decay with specific half-lives (Table A2.6). The concentrations of the desired elements can therefore be determined by measuring the area of the analytical photopeaks for each of the radioisotopes. The gamma spectrum of each radioactive sample, and attached monitor, was measured simultaneously after decay times of 6 days for the determination of La, Sm, Ho, Yb and Lu, and 2-4 weeks for the determination of Ce, Nd, Eu,Tb, Hf, Cs, Ta and Th. Irradiated samples were tested for the amount of activity to adjust sample-detector geometries so that no dead time corrections were necessary. Samples were then mounted on automatic sample changer tables and counted for 60-90 minutes for the earlier count and 2-3 hours for the later count.

Gamma ray spectra were measured using Princeton Gamma-tech hyperpure Ge coaxial detectors linked to Nuclear data multichannel analysers.

The sensitivity to which each element can be measured depends on the magnitude of its thermal neutron capture cross section and the intensity of the gamma photopeak measured (Table A2.6), plus the overall background activity level in the sample. Detection limits for each of the elements analysed by INAA are also given in Table A2.6. Accuracy was monitored using international and 'in-house' rock standards; synthetic Becquerel standards were used for initial flux-element calibrations and routine monitoring. Precision was monitored by repeated analyses of samples and in-house standards both within and between different sample batches. Precision on the flux monitors (Table A2.6) attached to each sample was generally better than 5 % CV (% coefficient of variation) for each element analysed.

2. REE contents of other samples were measured at the University of Tasmania Geology Department using the ion exchange - XRF spectrometry method of Robinson et al. (1986). Precision was monitored by repeated analysis of internal standards. Detection limits and REE data for two 'in-house' standard rocks using this method are given in Table A2.7.

A2.3 MINERAL ANALYSES:

The majority of analyses of individual minerals in polished thin section were obtained using wavelength-dispersive spectrometry (WDS) on the Cameca SX50 electron microprobe at the University of Tasmania Central Science Laboratories. The microprobe was operated at a beam current of 20 nA and accelerating voltage of 15 kV.

The remainder of the mineral analyses were performed using energy-dispersive spectrometry (EDS - peak integration with background subtraction) on the Cameca Microbeam electron microprobe at the Australian National University Research School of Earth Sciences, operated at an accelerating voltage of 15 kV and calibrated on pure Cu as described by Ware (1991).

A2.4 WHOLE-ROCK RADIOGENIC ISOTOPE ANALYSES:

A2.4.1 Strontium and Neodymium:

Isotope analyses were performed at the Research School of Earth Sciences, Australian National University, using a Finnigan MAT 261 mass spectrometer operated in static multi-collector mode. Individual analytical results represent the mean (following the removal of obvious outliers) and $2\sigma_{mean}$ errors (where σ_{mean} is the standard error of the

mean) of 10 blocks comprising 12 measurements at each of 5 mass stations for Sr (^{84}Sr, ^{85}Sr, ^{86}Sr, ^{87}Sr and ^{88}Sr) and 7 mass stations for Nd (^{142}Nd, ^{143}Nd, ^{144}Nd, ^{145}Nd, ^{146}Nd, ^{149}Nd and ^{150}Nd). To correct for mass fractionation effects measured $^{87}Sr/^{86}Sr$ and $^{143}Nd/^{144}Nd$ values are normalised to $^{86}Sr/^{88}Sr = 0.1194$ and $^{146}Nd/^{144}Nd = 0.7219$ respectively. Mean and $2\sigma_{pop}$ error values (where σ_{pop} is the population standard deviation) for NBS 987, nNd-1 and La Jolla standards analysed during the course of this study are given in Table A2.8. Individual standard measurements made during this study are plotted in Figure A2.1.

Table A2.8: Mean and $2\sigma_{pop}$ values measured by various operators for the NBS 987, nNd-1, La Jolla and NBS 981 standards during the period of this study. The expected precision (or reproducibility) of values obtained for analysed samples during this study, indicated by the $2\sigma_{pop}$ values obtained for the standards, is greater than, and should not be confused with, the $2\sigma_{mean}$ errors associated with individual sample measurements which indicate within-run precision only.

Standard	Mean	± 2σ	n
NBS 987	$^{87}Sr/^{86}Sr = 0.710209$	35	39
nNd-1	$^{143}Nd/^{144}Nd = 0.512189$	19	54
La Jolla	$^{143}Nd/^{144}Nd = 0.511897$	18	9
NBS 981	$^{206}Pb/^{204}Pb = 16.939$	10	8
	$^{207}Pb/^{204}Pb = 15.494$	11	8
	$^{208}Pb/^{204}Pb = 36.712$	31	8

Rock chips (0.1 to 0.15 g) for radiogenic isotope analysis were first crushed in an agate mortar to ≤0.2 cm (predominantly fine chips <0.05 cm), and then hand-picked under a binocular microscope, excluding chips with weathered or cut surfaces as well as phenocrysts where possible. The latter were avoided in case they were xenocrystic, as concluded for at least some of the phenocrysts in the Balleny Plume samples (Appendix 3). To minimise the effects of low temperature seawater alteration, the chips were acid-leached before dissolution. Initially, the acid-leaching method adopted and described by Mahoney (1987) was attempted. This method involves multiple-step leaching using 6N HCl and an ultrasonic bath, each step being repeated until the acid no longer changes colour. Unfortunately, Mahoney (1987) fails to mention whether or not the ultrasonic bath should be set at any specific temperature. Attempts to use this method at room temperature failed to produce any change in the colour of the acid whatsoever and no results were obtained using this leaching method. As a result, a different method was adopted using a hotplate to heat successive additions of 6N HCl, but omitting the ultrasonic bath. Limited experimentation, due to limited laboratory and mass spectrometer access, indicated no consistent differences (relative to the $2\sigma_{pop}$ errors of the NBS 987 and nND-1 standard measurements - Table A2.8) between the isotopic shifts produced by the different leaching regimes tested (Table A2.9), although the results of leached and unleached samples were significantly different. Old seafloor and

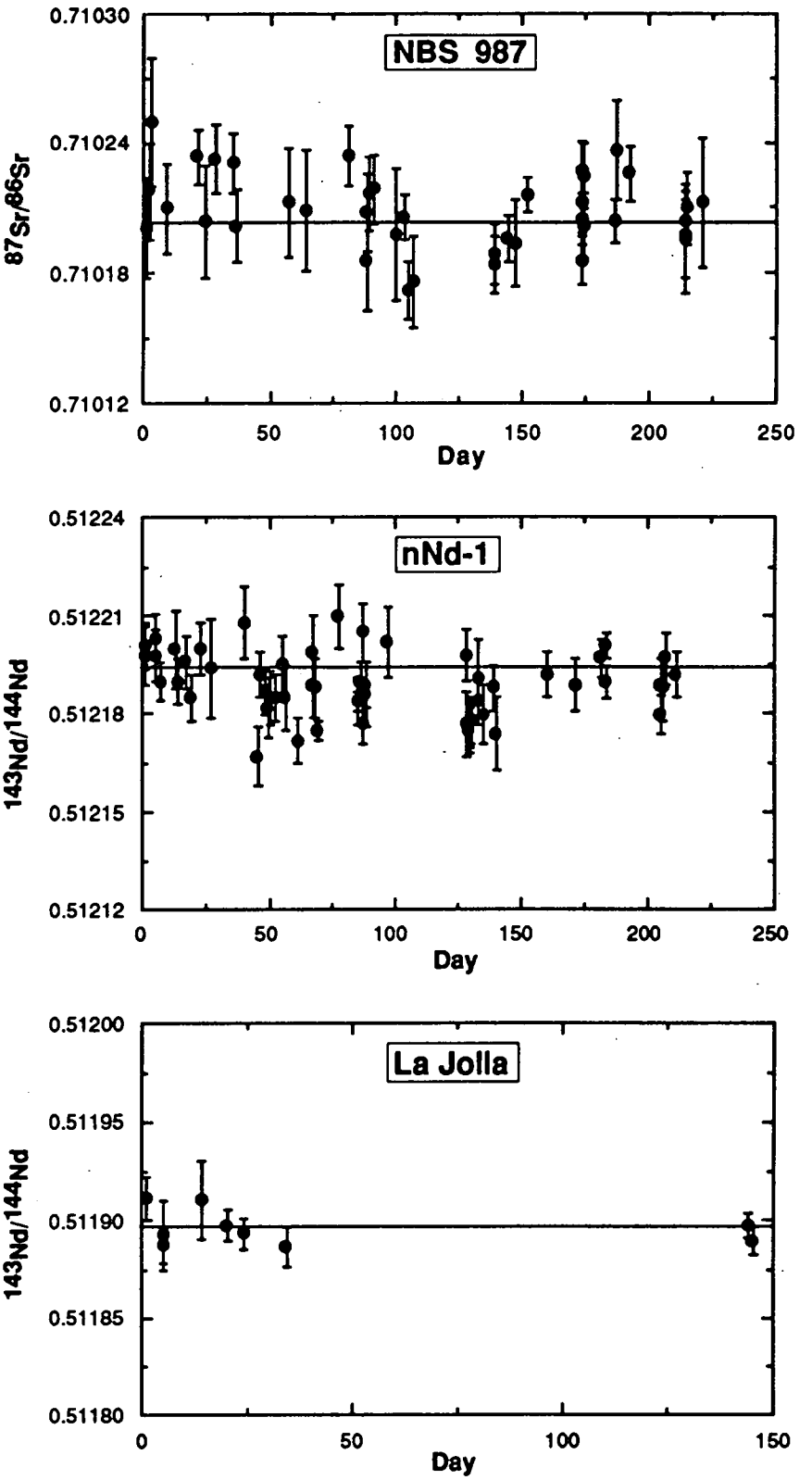

Figure A2.1: Time versus isotopic ratio plots for Sr and Nd standards analysed during the course of this study. Horizontal lines indicate mean values. Error bars associated with individual data points represent $2\sigma_{mean}$ errors and indicate within-run precision.

continental basalts were therefore leached twice in hot 6N HCl for one hour, and rinsed thoroughly with milli-Q ultrapure water (≥18 MΩ.cm) after each leaching step. Younger samples, such as the Macquarie Island glasses, were subjected to less severe leaching in hot 4N or 6N HCl for approximately 20 minutes or until the acid had just changed colour.

Despite an inability to check the leached residues for remnant alteration phases using X-ray diffraction (XRD), as described by Mahoney (1987), the leaching method adopted here is considered to have produced reliable and reproducible isotopic results. This inference is based on the fact that the vast majority of sample repeats, involving entirely different aliquots subjected separately to the selection, leaching, dissolution and analytical processes described here produced results that are within analytical error (2σ)of each other (e.g. Table 3.11) despite the quite extensive degree of alteration present within some samples. Samples for which the results of repeated analyses are not quite within analytical error include SS4-7 (Sr and Nd), E27-02A-2 (Nd), 102/DR09-4B(i) (Sr), 102/DR10-1C (Sr), 102/DR13-3D (Sr), 102/DR10-1B (Nd). It must be noted, however, that the fact that these Sr and/or Nd isotopic data may be slightly imprecise in the fifth or sixth decimal place will not affect the various interpretations discussed throughout this thesis. The similarity of the isotopic data obtained here for the submarine Balleny Province samples to that presented in the literature for subaerial Balleny Islands rocks (Chapter 3) also supports the viability of the described techniques.

Sample dissolution was achieved in 1 ml HF plus 0.015 ml concentrated HNO_3 heated for 3 to 12 hours. Samples were evaporated to dryness, avoiding baking and the formation of insoluble fluoride phases. HF-HNO_3 dissolution was repeated if necessary, particularly in the presence of undissolved spinel residue. Samples were redissolved in 1 ml 4N HCl and heated overnight in order to completely convert fluoride phases to chlorides and thereby prevent interference from any HF residues during subsequent chemistry in a hydrochloric acid medium. Samples were then evaporated to dryness, redissolved in 4 mls cold 1N HCl, centrifuged, and loaded onto cation exchange columns avoiding any solid residue.

Rb, Sr and the REE were initially separated from the other matrix elements using pre-calibrated 3 g cation (Dowex AG 50W-X8; 200-400#) exchange columns equilibrated with 1N HCl. Rb and Sr were eluted with 2.5N HCl, the REE with 4N HCl, prior to drying down. Secondary clean-up stages of ion exchange chemistry were performed in two separate stages: Sr was collected with 2.5N HCl using 1.6 g cation (Dowex AG 50W-X8; 200-400#) exchange columns equilibrated with 1N HCl; Nd was collected with 0.2N HCl using HDEHP (Kel-F teflon powder coated with di(2-ethylhexyl)orthophosphoric acid) cation exchange columns equilibrated with 0.2N HCl. Samples were dried down prior to filament loading.

Sr samples were loaded onto outgassed Ta single filaments in 1 µl 0.3N H_3PO_4. Nd samples were loaded in 1 µl 1N HNO_3 (with a trace of H_3PO_4) onto the outgassed Ta filament of a Re-Ta pair.

Procedural blanks, included at regular intervals, were spiked with ~0.07 pmol ^{150}Nd and ~5.7 pmol ^{84}Sr prior to HF-HNO_3 dissolution. Results for procedural blanks were: ≤3319 pg for Sr; ≤407 pg for Nd.

Table A2.9: Isotopic results for the unleached fractions and leached residues of three samples subjected to two different acid-leaching regimes. Leach 1 involved two episodes of leaching for one hour in hot 6N HCl; leach 2 involved repeated leachings for one hour at a time in hot 4N HCl until there was no further colour change with the addition of fresh acid. $2\sigma_{mean}$ errors indicate within-run precision only.

	Unleached	Leach 1	Leach 2
SS4-7:			
$^{87}Sr/^{86}Sr$	0.703248 ± 21	0.703171 ± 13	0.703153 ± 10
$^{143}Nd/^{144}Nd$	0.512880 ± 6	0.512904 ± 6	0.512874 ± 6
102/DR09-4B4:			
$^{87}Sr/^{86}Sr$	0.703525 ± 12	0.703186 ± 14	0.703224 ± 12
$^{143}Nd/^{144}Nd$	0.512995 ± 8	0.513031 ± 8	0.513005 ± 10
102/DR11-2B:			
$^{87}Sr/^{86}Sr$	0.703627 ± 11	0.703333 ± 11	0.703358 ± 11
$^{143}Nd/^{144}Nd$	0.513011 ± 8	0.512979 ± 11	0.512962 ± 6

A2.4.2 Lead:

Pb isotopes were analysed on the Finnigan MAT 261 mass spectrometer at the Research School of Earth Sciences, Australian National University, operating in static multi-collector mode.

Initial crushing and selection of rock chips for Pb isotope analysis followed the method described above for Sr and Nd. Leaching, particularly of old seafloor basalts, was performed in order to rid the samples of alteration phases resulting from possible hydrothermal processes. The results of limited Pb leaching experiments are shown in Table A2.10. Unleached samples proved unexpectedly difficult to analyse on the mass spectrometer, therefore the results for only one unleached sample are given in Table A2.10. Small differences (relative to the $2\sigma_{pop}$ errors of the NBS 981 standard measurements - Table A2.8) between the two types of leaching tested are mainly evident in the $^{206}Pb/^{204}Pb$ and $^{208}Pb/^{204}Pb$ results. The former could support the idea that ^{206}Pb is more readily affected by alteration than ^{207}Pb due to the high present-day $^{238}U/^{235}U$ ratio (Pearce et al., 1992). As the two types of leaching produced similar results - differences between them are neither consistent (for example, leach 2 produced higher Pb isotope ratios than leach 1 in sample E27-35A-1) or sufficient to alter data interpretation - leach 1 was chosen in preference to leach 2 to save both time and reagents. Old seafloor and continental basalts were leached twice in hot 6N HCl for one hour, and rinsed thoroughly with milli-Q ultrapure water (≥18 MΩ.cm) after each leaching step. Younger samples, such as the Macquarie Island glasses, were again subjected to less severe leaching in hot 6N HCl for approximately 10 minutes until a change occurred in the colour of the acid.

Sample dissolution was performed by heating in 1 ml HF and ~0.015 ml concentrated HNO_3 for one hour twice, followed each time by evaporation to dryness. Samples were then redissolved in ~1 ml hot 6N HCl for one hour, evaporated to dryness and soaked in cold 0.8N HBr overnight. Procedural blanks, included with each batch of five samples, were spiked with ~60 pmol ^{208}Pb spike ($^{206}Pb/^{204}Pb$ = 59.640; $^{206}Pb/^{207}Pb$ = 0.29952; $^{206}Pb/^{208}Pb$ = 0.00208) prior to dissolution.

Ion exchange chemistry was performed in two stages using 250 µl teflon resin reservoirs and anion resin (Dowex AG 1-X8; 200-400#), ~125 µl for the first stage and ~50 µl for the second stage, discarded after each elution. Reagent volumes used were approximately equivalent to the amount of resin. Resin was cleaned repeatedly with H_2O and 6N HCl prior to equilibration with 0.8N HBr. Samples were loaded in 0.8N HBr avoiding any solid residue. Pb was eluted with H_2O, 6N HCl twice and H_2O prior to evaporating the sample to dryness. Following collection of the second purified Pb fraction, ~0.03 ml concentrated HNO_3 was added prior to drying to destroy any organic material. Samples were then evaporated with ~0.03-0.06 ml 0.3N H_3PO_4 and ~0.1 ml 6N HCl in order to avoid complete dryness and to ensure that all phases were in chloride form respectively.

All samples for Pb analysis were loaded onto outgassed Re single filaments. Individual analytical results represent the mean (following the removal of obvious outliers) and $2\sigma_{mean}$ errors (where σ_{mean} is the standard error of the mean) of 3 blocks comprising 12 measurements at each of 4 mass stations (^{204}Pb, ^{206}Pb, ^{207}Pb and ^{208}Pb). To correct for the effects of mass fractionation, the double spike technique described in Hamelin et al. (1985) and Woodhead et al. (submitted) was used. This technique requires each sample to be analysed twice. All samples were mixed with silica gel and ~0.03 ml 0.3N H_3PO_4. Two thirds of each sample solution was used for the 'composition run', which measures the isotopic composition of the sample itself. The other third was used for the 'double spike run' following mixing with an appropriate amount of a mixed ^{207}Pb-^{204}Pb spike (74 DSR) enriched in ^{204}Pb (2.3854 ppm) and ^{207}Pb (20.787 ppm). The known ratio for these two isotopes in the spike ($^{207}Pb/^{204}Pb$ = 8.714) permits the calculation of a mass fractionation correction for the composition run. The choice of an appropriate amount of spike for each sample is dependent on the Pb content of the sample. However, due to the fact that the samples were acid leached prior to ion exchange chemistry, the precise Pb contents of the samples were not known. Therefore, the Q mixing ratio, where

$$Q = \frac{(^{207}Pb/^{204}Pb)_{mix} - (^{207}Pb/^{204}Pb)_{spike}}{(^{207}Pb/^{204}Pb)_{sample} - (^{207}Pb/^{204}Pb)_{mix}}$$

was calculated for each sample following analysis to check that an appropriate amount of 74 DSR ($0.02 < Q < 1$; Hamelin et al., 1985) had been added to the double spike run. When the calculated Q ratio lay outside these limits, sample chemistry and analysis was repeated due to the possibility of error magnification associated with the double spike correction (Hamelin et al., 1985). Despite the fact that some samples were found to be repeatedly overspiked, even with the use of decreasing amounts of spike, due to their low and somewhat variable

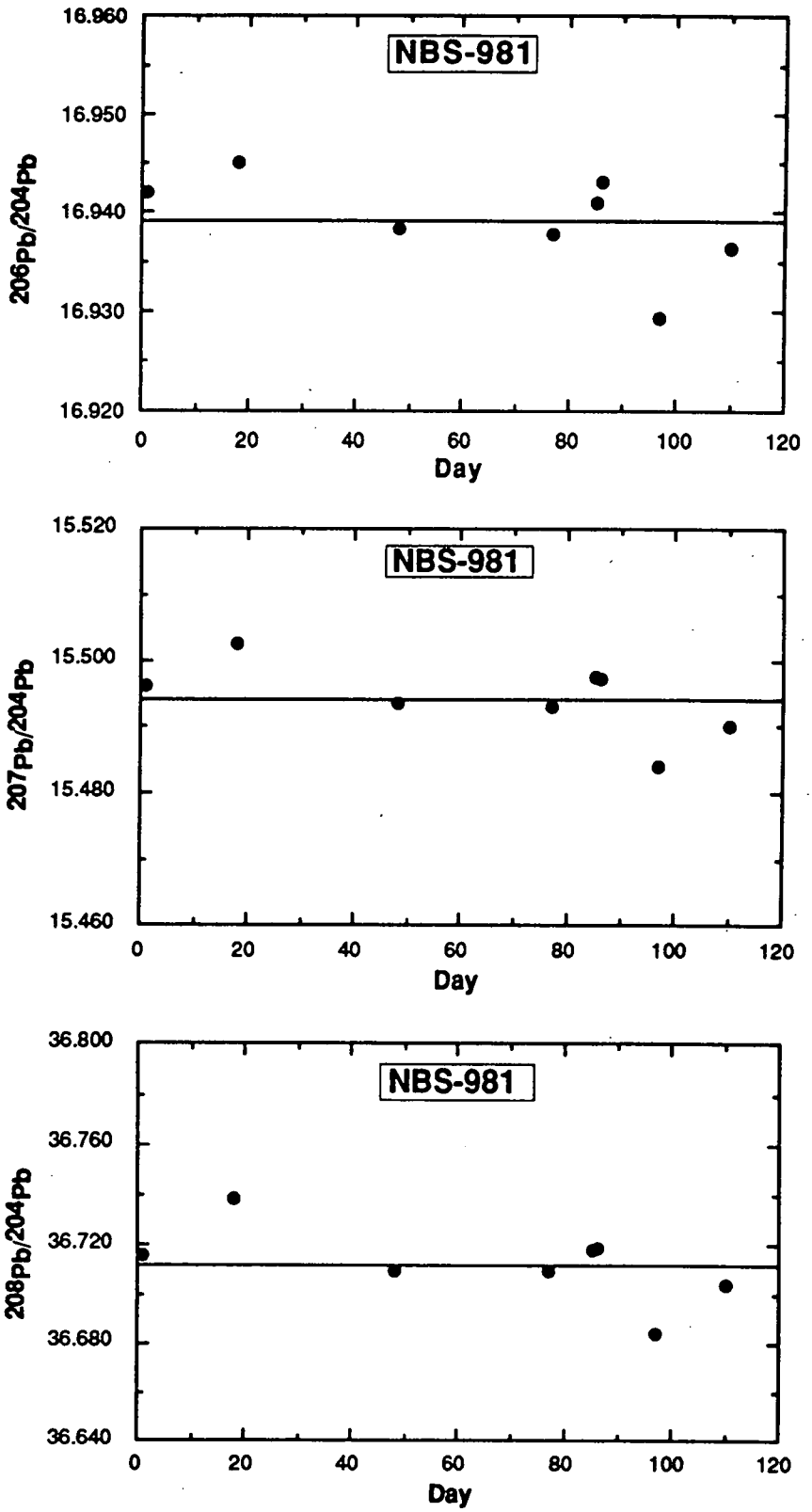

Figure A2.2: Time versus isotopic ratio plots for the NBS 981 Pb standard measurements made during the course of this study. Horizontal lines indicate mean values.

Pb contents as a result of leaching, the results of two or more analyses generally indicated good precision and are therefore included in the data tables.

NBS 981 standards were also analysed using the double spike technique. One standard run was included with each batch of 12 sample runs. The concentration run comprised NBS 981, 0.3N H_3PO_4 and silica gel; ^{207}Pb-^{204}Pb spike was added to the double spike run. Mean and $2\sigma_{pop}$ error values for NBS 981 standard analyses performed during the course of this study are presented in Table A2.8; individual results are plotted in Figure A3.2.

Procedural blanks, loaded in 0.3N H_3PO_4 and silica gel, were considered to be negligible: ≤117 pg.

Table A2.10: Isotopic results for the unleached fractions and leached residues of three samples subjected to two different acid-leaching regimes. Leach 1 involved two episodes of leaching for one hour in hot 6N HCl; leach 2 involved repeated leachings for one hour at a time in hot 6N HCl until there was no further colour change with the addition of fresh acid. $2\sigma_{mean}$ errors indicate within-run precision only.

	Unleached	Leach 1	Leach 2
SS3:			
$^{206}Pb/^{204}Pb$	20.044	20.015	19.998
$^{207}Pb/^{204}Pb$	15.645	15.649	15.643
$^{208}Pb/^{204}Pb$	39.913	39.856	39.813
SS5:			
$^{206}Pb/^{204}Pb$	-	20.039	19.996
$^{207}Pb/^{204}Pb$	-	15.638	15.632
$^{208}Pb/^{204}Pb$	-	39.868	39.824
E27-35A-1:			
$^{206}Pb/^{204}Pb$	-	19.736	19.747
$^{207}Pb/^{204}Pb$	-	15.604	15.612
$^{208}Pb/^{204}Pb$	-	39.436	39.468

A2.5 URANIUM-THORIUM-LEAD ZIRCON ANALYSES:

Zircons were extracted from 2 to 3 kg dyke and 0.2 to 0.3 kg late-stage felsic segregation samples by Australian Geological Survey Organisation (AGSO) technicians, using the following heavy liquid and magnetic separation techniques and attempting to minimise the risk of contamination. All cut and weathered surfaces were removed from the rocks and ~1 cm-sized chips were produced using an hydraulic splitter. Rock chips were rinsed in water in an ultrasonic bath to remove dust, crushed in a rotary disc mill to produce a coarse powder and washed with water on a Wilfley table to concentrate the heavy minerals and remove powder and light minerals such as quartz and feldspar. Dried samples were then subjected to heavy liquid mineral separation using tetrabromoethane (D = 2.96), washed with alcohol and redried prior to the removal of magnetics with a permanent magnet. An isodynamic separator was used to remove mildly magnetic minerals such as biotite, prior to

another heavy liquid separation step using methylene iodide (D = 3.3). Isodynamic separation was repeated on samples containing sufficient zircons to warrant it, in an attempt to expel 'contaminated' zircons containing inclusions or attachments of other material. Initial isodynamic separation was at full power and low tilt (5° side tilt), gradually reducing the tilt angle until only pristine zircons were left. All recovered zircons were set in an epoxy mount which was polished so that ~50 % of each grain was removed, in order to best expose their cores. This grain mount was coated with Au for conductive purposes.

U-Th-Pb zircon analyses were performed on the Sensitive High-Resolution Ion Microprobe (SHRIMP) at the Research School of Earth Sciences, Australian National University, operated at a mass resolution in excess of 6500 to eliminate significant spectral interferences. An 11 kV primary beam of negative oxygen ions was used to sputter positive secondary ions from a 25 μm diameter spot on the zircon surface. Individual zircons were chosen for analysis on the basis of their clarity and morphology, avoiding obvious cracks, inclusions or metamict zones. Each analysis comprises a set of seven regressed scans (from which obvious outliers have been removed) through each of nine mass stations ($^{196}Zr_2O^+$, $^{204}Pb^+$, $^{204.1}$background Pb, $^{206}Pb^+$, $^{207}Pb^+$, $^{208}Pb^+$, $^{238}U^+$, $^{248}ThO^+$ and $^{254}UO^+$) measured by cyclic magnetic field stepping using a single ion collector. SHRIMP analytical procedures are based on the techniques described in Compston et al. (1984), Williams et al. (1984) and Williams and Claesson (1987).

U and Th decay constants used are as recommended by the IUGS Subcommission on Geochronology: $\lambda(^{238}U) = 1.55125 \times 10^{-10}$ / yr; $\lambda(^{235}U) = 9.8485 \times 10^{-10}$ / yr; $\lambda(^{232}Th) = 4.9475 \times 10^{-11}$ / yr (Steiger and Jäger, 1977). Inter-element fractionation was monitored by repeated analysis (every fifth or sixth analysis) of the SL13 standard zircon fragment, which has a $^{206}Pb/^{238}U$ ratio of 0.0928, equivalent to an age of 572 Ma, to which measured Pb/U values in the unknowns were referenced. Th/U ratios were derived using a known fixed discrimination of 1.11 between actual Th/U ratios and measured ThO^+/UO^+ ratios. Systematic inter-element fractionation during each analysis was corrected by means of a quadratic relationship between Pb^+/U^+ and UO^+/U^+ measured on the standard zircon. Uncertainties of 20 %, associated with the absolute concentrations of U, Th and Pb, are governed by the observed range in the U concentration of the zircon standard (Williams and Claesson, 1987). This does not, however, affect the relative concentrations of these elements as measured in the unknowns, which are accurate to ~1 %.

The observed standard error of 3.3 % for twenty-nine analyses of the standard (interspersed between the analyses reported in this study) is included in the quoted errors for the Pb/U ratios of the unknowns. Radiogenic Pb compositions were determined by subtracting contemporaneous initial common Pb (Cumming and Richards, 1975) from measured compositions.

APPENDIX 3

MINERAL CHEMISTRY AND PHASE EQUILIBRIA CALCULATIONS

A3.1 MINERAL CHEMISTRY:

Representative electron microprobe analyses of silicate phenocryst and/or microphenocryst phases within the Balleny Province (Table A3.1), Soela Seamount (Table A3.3), south Tasman Sea seamount (Table A3.5), Scott Island (Table A3.6) and southwest Pacific seafloor samples (Table A3.7) were analysed by electron microprobe using either wavelength-dispersive spectrometry (WDS) or energy-dispersive spectrometry (EDS), as described in Appendix 2 and noted in individual table captions. Total iron was measured as Fe^{2+}; Fe^{3+} was calculated by stoichiometry for clinopyroxene and plagioclase. The following notation is used throughout this thesis for the silicate phases:

$Mg\# = \frac{100\ Mg}{(Mg + Fe^{2+})}$;

pyroxene end-members: Di = diopside, Hd = hedenbergite, $En = \frac{100\ Mg}{(Ca + Fe^{2+} + Mg)}$ $Fs = \frac{100\ Fe^{2+}}{(Ca + Fe^{2+} + Mg)}$ $Wo = \frac{100\ Ca}{(Ca + Fe^{2+} + Mg)}$

feldspar end-members: $An = \frac{100\ Ca}{(Ca + Na + K)}$ $Ab = \frac{100\ Na}{(Ca + Na + K)}$ $Or = \frac{100\ K}{(Ca + Na + K)}$

Representative oxide phenocryst/microphenocryst phases and inclusions for Balleny Province (Table A3.2), Soela Seamount (Table A3.4) and southwest Pacific seafloor samples (Table A3.8) were also analysed by electron microprobe, using either WDS or EDS, as described in Appendix 2 and noted in individual table captions. Total Fe was measured as Fe^{2+}; Fe^{3+} was calculated to produce a cation total of 3. The following notation is used throughout this thesis for the oxide minerals:

$Mg\# = \frac{100\ Mg}{(Mg + Fe^{2+})}$ $Cr\# = \frac{100\ Cr}{(Cr + Al)}$ $Fe^{3+}\# = \frac{100\ Fe^{3+}}{(Fe^{3+} + Fe^{2+})}$

Accompanying olivine Mg# data have been measured within olivine phenocrysts close to the contact with spinel. Spinel classification is based on the method described in Deer et al. (1992; p. 560) using the dominant R^{3+} and R^{2+} constituents and modified Johnston spinel prisms.

A3.2 EQUILIBRIUM MINERAL COMPOSITIONS:

Calculated equilibrium compositions of olivine, clinopyroxene and feldspar with respect to host whole-rock major element compositions for all Balleny Plume samples whose mineral chemistry was ascertained by electron microprobe (WDS) analysis are presented in

Table A3.1: Mineral chemistry (WDS) of representative silicate phenocryst and microphenocryst phases within submarine Balleny Province samples.
Analyses include: 1. disequilibrium core of olivine phenocryst; 2. rim of olivine phenocryst; 3. core of previous olivine phenocryst - reverse zoning; 4. rim of olivine phenocryst; 5. disequilibrium core of previous olivine phenocryst - normal zoning; 6. Fe-rich olivine microphenocryst; 7. clinopyroxene phenocryst (diopside); 8. rim of clinopyroxene phenocryst (augite); 9. core of previous clinopyroxene phenocryst (salite) - reverse zoning; 10. rim of clinopyroxene microphenocryst (salite); 11. core of previous clinopyroxene microphenocryst (diopside) - normal zoning; 12. rim of clinopyroxene microphenocryst (salite); 13. core of previous clinopyroxene microphenocryst (salite) - reverse zoning; 14. rim of clinopyroxene microphenocryst (ferrosalite); 15. core of previous clinopyroxene microphenocryst (ferrosalite) - reverse zoning; 16. rim of plagioclase phenocryst (bytownite); 17. partly resorbed rim of plagioclase phenocryst (labradorite); 18. core of previous plagioclase phenocryst (labradorite) - reverse zoning; 19. rim of plagioclase microphenocryst (bytownite) in plagioclase + clinopyroxene + spinel glomerocryst; 20. core of previous plagioclase microphenocryst (labradorite) - reverse zoning; 21. rim of feldspar phenocryst (anorthoclase); and 22. core of previous feldspar phenocryst (oligoclase) - normal zoning.

	Olivine:						Clinopyroxene:						
Analysis	1	2	3	4	5	6	7	8	9	10	11	12	13
Sample No.	E27-35A-7	E27-35B-2	E27-35B-2	E27-35B-1	E27-35B-1	E27-35A-2	E27-35B-2	E27-35A-3	E27-35A-3	E27-35B-1	E27-35B-1	E27-35A-4	E27-35A-4
SiO_2	39.72	38.97	38.73	37.42	39.12	31.97	48.12	47.71	43.29	45.89	49.15	49.91	43.63
TiO_2							1.88	2.01	3.95	2.48	0.81	1.68	3.84
Al_2O_3							7.15	6.82	10.94	8.01	7.80	3.20	7.53
Cr_2O_3	0.03	0.00	0.02	0.10	0.06	0.00	0.60	0.22	0.37	0.31	0.12	0.02	0.00
Fe_2O_3							0.02	0.03	0.01	0.01	0.01	0.01	0.01
FeO	12.52	17.26	18.53	22.77	13.34	52.83	5.24	7.28	7.12	7.04	4.77	8.34	9.83
MnO	0.09	0.18	0.14	0.47	0.11	3.95	0.05	0.17	0.23	0.09	0.10	0.13	0.22
NiO	0.32	0.10	0.15	0.15	0.25	0.00							
MgO	45.91	42.53	41.34	37.45	45.30	10.37	14.19	14.05	11.22	12.18	15.00	14.17	11.34
CaO	0.21	0.26	0.30	0.26	0.26	1.03	22.60	19.76	20.42	22.57	21.03	21.46	21.57
Na_2O							0.50	0.52	0.66	0.47	0.70	0.36	0.49
K_2O							0.00	0.02	0.02	0.01	0.01	0.00	0.06
Total	98.80	99.30	99.21	98.62	98.44	100.15	100.35	98.59	98.23	99.06	99.50	99.27	98.32
Cations													
Si	1.000	0.998	0.999	0.994	0.993	0.999	1.774	1.793	1.647	1.734	1.808	1.876	1.689
Ti							0.052	0.057	0.113	0.070	0.022	0.048	0.106
Al							0.311	0.302	0.491	0.357	0.338	0.142	0.344
Cr	0.000	0.000	0.000	0.001	0.000	0.000	0.017	0.007	0.011	0.009	0.003	0.001	0.000
Fe^{3+}							0.000	0.001	0.000	0.000	0.000	0.000	0.000
Fe^{2+}	0.263	0.369	0.399	0.506	0.283	1.380	0.162	0.229	0.227	0.222	0.147	0.262	0.318
Mn	0.002	0.004	0.003	0.011	0.002	0.105	0.002	0.005	0.007	0.003	0.003	0.004	0.007
Ni	0.007	0.002	0.004	0.004	0.006	0.000							
Mg	1.722	1.622	1.588	1.483	1.714	0.483	0.780	0.787	0.638	0.688	0.823	0.794	0.654
Ca	0.006	0.007	0.008	0.007	0.007	0.034	0.893	0.796	0.832	0.914	0.829	0.864	0.895
Na							0.036	0.038	0.049	0.035	0.050	0.026	0.037
K							0.000	0.001	0.001	0.000	0.000	0.000	0.003
Total	3.000	3.002	3.001	3.006	3.005	3.001	4.027	4.015	4.014	4.030	4.024	4.018	4.053
Mg#	86.75	81.47	79.92	74.56	85.83	25.93	82.83	77.48	73.75	75.55	84.87	75.19	67.30
En							42.52	43.45	37.54	37.66	45.75	41.35	35.06
Fs							8.81	12.63	13.36	12.19	8.15	13.64	17.03
Wo							48.67	43.92	49.10	50.15	46.09	45.01	47.91
An													
Ab													
Or													

Table A3.1: (continued)

	Clinopyroxene:		Feldspar:						
Analysis	14	15	16	17	18	19	20	21	22
Sample No.	E27-35A-2	E27-35A-2	E27-35A-7	E27-35B-1	E27-35B-1	E27-35A-4	E27-35A-4	E27-35A-2	E27-35A-2
SiO_2	56.15	49.54	49.20	50.95	55.12	50.10	51.65	63.49	61.41
TiO_2	0.17	0.24							
Al_2O_3	11.37	1.13	31.32	30.80	28.06	30.13	29.24	21.71	23.63
Cr_2O_3	0.00	0.00							
Fe_2O_3	0.00	0.00	0.00	0.00	0.01	0.03	0.08	0.00	0.01
FeO	8.77	17.89	0.66	0.41	0.21	0.63	0.55	0.43	0.23
MnO	0.41	1.10							
NiO									
MgO	3.88	7.21	0.25	0.00	0.02	0.09	0.09	0.01	0.00
CaO	11.60	21.99	15.02	14.18	10.80	14.67	13.27	2.81	4.80
Na_2O	4.34	0.49	2.86	3.48	5.12	3.08	3.80	8.20	7.91
K_2O	2.24	0.01	0.19	0.17	0.36	0.19	0.29	2.51	1.12
Total	98.93	99.60	99.50	99.99	99.70	98.91	98.97	99.16	99.11
Cations									
Si	2.052	1.960	2.268	2.324	2.494	2.317	2.378	2.849	2.755
Ti	0.005	0.007							
Al	0.490	0.053	1.700	1.656	1.496	1.642	1.587	1.148	1.249
Cr	0.000	0.000							
Fe^{3+}	0.000	0.000	0.000	0.000	0.000	0.001	0.003	0.000	0.000
Fe^{2+}	0.268	0.592	0.025	0.016	0.008	0.024	0.021	0.016	0.009
Mn	0.013	0.037							
Ni									
Mg	0.211	0.425	0.017	0.000	0.001	0.008	0.006	0.001	0.000
Ca	0.454	0.932	0.741	0.693	0.524	0.727	0.655	0.135	0.231
Na	0.307	0.000	0.255	0.308	0.449	0.276	0.339	0.713	0.688
K	0.105	0.001	0.011	0.010	0.021	0.011	0.017	0.144	0.064
Total	3.904	4.007	5.017	5.007	4.993	5.005	5.005	5.006	4.996
Mg#	44.09	41.81							
En	22.64	21.82							
Fs	28.72	30.36							
Wo	48.64	47.82							
An			73.55	68.56	52.70	71.67	64.76	13.61	23.48
Ab			25.34	30.48	45.20	27.23	33.55	71.90	70.00
Or			1.11	0.98	2.09	1.11	1.68	14.49	6.53

Table A3.2: Mineral chemistry of representative oxide phases within submarine Balleny Province samples. Analyses 4, 5 and 6 were analysed by EDS, all others by WDS.

Analyses include: 1. Cr-pleonaste inclusion within an olivine phenocryst; 2. pleonaste inclusion within a clinopyroxene microphenocryst; 3. Mg-Al-titanomagnetite inclusion within a clinopyroxene microphenocryst; 4. Cr-pleonaste inclusion within an olivine phenocryst ($Mg\#_{84.4}$); 5. pleonaste inclusion within an olivine phenocryst ($Mg\#_{82.2}$); 6. Cr-Al-titanomagnetite inclusion within an olivine phenocryst ($Mg\#_{81.0}$); 7. Cr-pleonaste inclusion within an olivine microphenocryst; and 8. Cr-Al-titanomagnetite inclusion within an olivine microphenocryst.

	Spinel:							
Analysis	**1**	**2**	**3**	**4**	**5**	**6**	**7**	**8**
Sample No.	**E27-35A-7**	**E27-35A-7**	**E27-35A-7**	**E27-35A-5**	**E27-35A-5**	**E27-35B-2**	**E27-35A-3**	**E27-35A-3**
SiO_2	0.13	0.09	0.13	0.00	0.00	0.00	0.07	0.90
TiO_2	0.59	1.83	14.91	1.49	2.30	16.25	1.38	15.35
Al_2O_3	41.38	52.21	12.69	33.92	53.34	6.98	40.98	7.12
Cr_2O_3	20.50	0.01	0.00	25.67	0.13	8.81	13.73	5.90
Fe_2O_3	5.58	11.36	27.49	8.07	10.60	21.56	10.31	25.27
FeO	14.54	20.36	37.62	18.13	16.10	39.61	17.45	37.89
MnO	0.04	0.22	0.24	0.00	0.13	0.63	0.20	0.70
NiO	0.15	0.00	0.00				0.28	0.00
MgO	15.59	13.87	5.77	13.63	17.07	4.36	13.83	4.60
Total	98.50	99.95	98.85	100.91	99.67	98.20	98.22	97.73
Cations								
Ti	0.013	0.038	0.386	0.0326	0.0464	0.4374	0.030	0.418
Al	1.393	1.690	0.516	1.1670	1.6906	0.2952	1.401	0.305
Cr	0.462	0.000	0.000	0.5909	0.0028	0.2493	0.314	0.169
Fe^{3+}	0.120	0.234	0.712	0.1769	0.2139	0.5806	0.224	0.689
Fe^{2+}	0.346	0.466	1.083	0.4413	0.3612	1.1857	0.422	1.148
Mn	0.001	0.005	0.007	0.0000	0.0030	0.0191	0.005	0.021
Ni	0.003	0.000	0.000				0.007	0.000
Mg	0.662	0.566	0.296	0.5913	0.6823	0.2326	0.596	0.248
Total	3.000	3.000	3.000	3.0000	3.0000	3.0000	3.000	3.000
Mg#	65.65	54.84	21.46	57.27	65.39	16.40	58.55	17.79
Cr#	79.41	0.09	0.00	76.96	1.27	30.04	58.33	19.70
Fe^{3+}#	25.69	33.43	39.67	28.61	37.19	32.87	34.70	37.51
End-members								
Mg_2TiO_4	0.83	2.07	8.28	1.87	3.03	7.17	1.76	7.44
$MgAl_2O_4$	45.73	46.34	5.54	33.41	55.27	2.42	41.03	2.71
$MgCr_2O_4$	15.16	0.01	0.00	16.92	0.09	2.04	9.20	1.50
$MgFe_2O_4$	3.93	6.42	7.64	5.06	6.99	4.76	6.57	6.13
Fe_2TiO_4	0.43	1.70	30.31	1.39	1.61	36.57	1.24	34.40
$FeAl_2O_4$	23.93	38.17	20.27	24.94	29.26	12.34	29.04	12.54
$FeCr_2O_4$	7.93	0.00	0.00	12.63	0.05	10.42	6.51	6.95
$FeFe_2O_4$	2.06	5.29	27.96	3.78	3.70	24.27	4.65	28.33

Table A3.3: Mineral chemistry (WDS) of representative silicate phenocryst and microphenocryst phases within Soela Seamount samples.
Analyses include: 1. rim of olivine microphenocryst; 2. rim of olivine microphenocryst; 3. core of previous olivine microphenocryst - normal zoning; 4. core of olivine microphenocryst; 5. rim of clinopyroxene phenocryst (salite); 6. core of previous clinopyroxene phenocryst (augite) - normal zoning; 7. rim of clinopyroxene phenocryst (salite); 8. core of previous clinopyroxene phenocryst (diopside) - normal zoning; 9. rim of clinopyroxene microphenocryst (salite); 10. core of previous clinopyroxene microphenocryst (salite) - normal zoning; 11. rim of clinopyroxene phenocryst (salite); 12. rim of plagioclase phenocryst (bytownite); 13. core of previous plagioclase phenocryst (bytownite) - normal zoning; 14. core of plagioclase phenocryst (bytownite); 15. core of plagioclase microphenocryst (labradorite); 16. rim of plagioclase phenocryst (bytownite); and 17. core of previous plagioclase phenocryst (bytownite) - normal zoning.

	Olivine:				Clinopyroxene:							Plagioclase:					
Analysis	1	2	3	4	5	6	7	8	9	10	11	12	13	14	15	16	17
Sample No.	SS3	SS4-1	SS4-1	SS2-4	SS4-1	SS4-1	SS2-4	SS2-4	SS5	SS5	SS1-1	SS2-4	SS2-4	SS2-6	SS5	SS1-1	SS1-1
SiO_2	39.05	38.56	39.00	39.64	47.33	50.79	47.00	49.62	47.84	48.55	48.97	50.34	48.32	47.90	50.93	49.38	48.00
TiO_2					2.87	1.14	2.64	1.71	2.04	1.75	1.28						
Al_2O_3					4.45	3.15	6.57	5.07	6.02	5.20	4.81	30.75	32.42	32.80	29.48	29.95	30.83
Cr_2O_3	0.09	0.02	0.09	0.16	0.00	0.10	0.48	0.37	0.47	0.40	0.35						
Fe_2O_3					0.09	0.03	0.01	0.01	0.00	0.01	0.03	0.01	0.01	0.01	0.03	0.01	0.00
FeO	18.00	18.29	16.75	16.73	8.34	6.33	7.33	5.70	6.83	6.40	6.33	0.57	0.50	0.51	0.62	0.52	0.54
MnO		0.21	0.35		0.33	0.07	0.12	0.04	0.15	0.05	0.09						
NiO	0.23	0.16	0.20	0.18													
MgO	41.97	40.57	42.46	42.63	12.91	15.80	12.55	14.38	13.78	13.91	14.25	0.09	0.11	0.11	0.09	0.03	0.06
CaO	0.24	0.37	0.36	0.30	22.57	21.77	21.72	22.79	22.81	22.65	21.89	14.34	16.25	16.56	14.33	14.96	16.17
Na_2O					0.45	0.26	0.39	0.35	0.41	0.36	0.85	3.21	2.21	2.12	3.56	2.97	2.35
K_2O					0.00	0.00	0.06	0.05	0.03	0.01	0.00	0.22	0.11	0.08	0.20	0.23	0.11
Total	99.58	98.18	99.21	99.64	99.34	99.44	98.87	100.09	100.38	99.29	98.85	99.53	99.93	100.09	99.23	98.05	98.06
Cations																	
Si	1.000	1.004	0.999	1.008	1.797	1.887	1.776	1.835	1.781	1.819	1.840	2.312	2.220	2.200	2.347	2.307	2.249
Ti					0.082	0.032	0.075	0.048	0.057	0.049	0.036						
Al					0.199	0.138	0.292	0.221	0.264	0.230	0.213	1.664	1.755	1.775	1.601	1.649	1.703
Cr	0.001	0.000	0.001	0.001	0.000	0.004	0.014	0.011	0.014	0.012	0.010						
Fe^{3+}					0.003	0.001	0.000	0.000	0.000	0.000	0.001	0.001	0.000	0.000	0.001	0.000	0.000
Fe^{2+}	0.385	0.398	0.359	0.356	0.265	0.197	0.232	0.176	0.212	0.201	0.200	0.022	0.019	0.020	0.024	0.020	0.021
Mn		0.005	0.008		0.011	0.002	0.004	0.001	0.005	0.002	0.003						
Ni	0.005	0.004	0.005	0.004													
Mg	1.602	1.574	1.620	1.615	0.731	0.875	0.707	0.793	0.765	0.777	0.798	0.004	0.008	0.008	0.006	0.002	0.004
Ca	0.007	0.010	0.010	0.008	0.918	0.867	0.879	0.903	0.910	0.909	0.881	0.705	0.800	0.815	0.707	0.749	0.812
Na					0.033	0.019	0.029	0.025	0.030	0.026	0.062	0.286	0.197	0.189	0.318	0.269	0.213
K					0.000	0.000	0.003	0.002	0.001	0.000	0.000	0.013	0.006	0.005	0.012	0.014	0.007
Total	3.000	2.995	3.002	2.992	4.037	4.021	4.011	4.015	4.039	4.025	4.044	5.005	5.005	5.010	5.017	5.010	5.009
Mg#	80.62	79.82	81.86	81.94	73.39	81.66	75.31	81.80	78.26	79.49	79.97						
En					38.18	45.15	38.89	42.35	40.53	41.19	42.47						
Fe					13.84	10.14	12.75	9.42	11.26	10.63	10.64						
Wo					47.98	44.70	48.36	48.23	48.21	48.18	46.89						
An												70.26	79.74	80.82	68.20	72.60	78.68
Ab												28.47	19.62	18.72	30.66	26.07	20.68
Or												1.27	0.64	0.46	1.13	1.33	0.64

Table A3.4: Mineral chemistry of representative oxide phases within Soela Seamount samples. Analyses 2, 3, 4, 7 and 8 were measured by EDS, all others by WDS. Analyses include: 1. Mg-Al-titanomagnetite inclusion within a clinopyroxene phenocryst; 2. Cr-titanomagnetite inclusion within an olivine phenocryst ($Mg\#_{75.2}$); 3. titanian chromite inclusion within an olivine phenocryst ($Mg\#_{73.8}$); 4. aluminous chromite inclusion within an olivine phenocryst ($Mg\#_{80.4}$); 5. Mg-titanomagnetite inclusion within an olivine microphenocryst; 6. Mg-Al chromite inclusion within an olivine microphenocryst ($Mg\#_{81.9}$); 7. Mg-Al chromite inclusion within the same olivine microphenocryst ($Mg\#_{81.9}$); 8. Al-Mg-titanomagnetite microphenocryst; and 9. Cr-Mg-Al-titanomagnetite inclusion within an olivine microphenocryst.

	Spinel:								
Analysis	1	2	3	4	5	6	7	8	9
Sample No.	SS3	SS3	SS3	SS3	SS4-1	SS4-1	SS4-1	SS5	SS5
SiO_2	0.03	0.26	0.12	0.00	0.08	0.00	0.00	0.11	0.03
TiO_2	14.02	11.68	8.47	6.65	26.49	4.14	2.53	15.54	21.18
Al_2O_3	6.01	6.62	9.83	17.09	1.42	12.83	23.00	7.18	4.79
Cr_2O_3	3.00	18.13	29.89	21.70	0.04	36.76	29.96	2.91	6.14
Fe_2O_3	32.14	23.11	15.39	18.90	14.04	12.14	11.64	28.64	17.94
FeO	34.65	36.85	32.09	29.00	50.26	28.25	20.87	37.53	43.98
MnO	0.23	0.37	0.00	0.00	0.67	0.00	0.00	0.40	1.02
NiO	0.15							0.14	0.04
MgO	5.79	4.17	6.25	7.74	2.27	6.23	10.85	5.17	4.15
Total	96.02	101.19	102.04	101.08	95.27	100.35	98.85	97.62	99.28
Cations									
Ti	0.385	0.308	0.214	0.162	0.764	0.104	0.060	0.420	0.570
Al	0.259	0.274	0.390	0.656	0.064	0.509	0.857	0.305	0.203
Cr	0.087	0.502	0.793	0.557	0.001	0.976	0.747	0.083	0.174
Fe^{3+}	0.884	0.609	0.389	0.462	0.405	0.307	0.276	0.774	0.483
Fe^{2+}	1.058	1.079	0.901	0.788	1.613	0.793	0.550	1.127	1.317
Mn	0.007	0.011	0.000	0.000	0.022	0.000	0.000	0.012	0.031
Ni	0.004				0.000			0.004	0.001
Mg	0.315	0.218	0.313	0.375	0.130	0.312	0.510	0.277	0.221
Total	3.000	3.000	3.000	3.000	3.000	3.000	3.000	3.000	3.000
Mg#	22.95	16.78	25.76	32.23	7.45	28.21	48.10	19.71	14.39
Cr#	25.04	64.69	67.04	45.93	1.85	65.72	46.57	21.33	46.17
Fe^{3+}#	45.50	36.08	30.14	36.96	20.09	27.88	33.42	40.71	26.85
End-members									
Mg_2TiO_4	8.84	5.16	5.51	5.23	5.69	2.95	2.89	8.27	8.21
$MgAl_2O_4$	2.98	2.30	5.02	10.57	0.24	7.18	20.61	3.00	1.46
$MgCr_2O_4$	0.99	4.21	10.22	8.98	0.00	13.76	17.96	0.81	1.25
$MgFe_2O_4$	10.14	5.11	5.01	7.44	1.51	4.32	6.64	7.62	3.48
Fe_2TiO_4	29.68	25.60	15.88	11.01	70.75	7.50	3.11	33.69	48.81
$FeAl_2O_4$	10.00	11.40	14.48	22.23	2.98	18.27	22.24	12.23	8.67
$FeCr_2O_4$	3.34	20.89	29.45	18.88	0.06	35.02	19.38	3.32	7.44
$FeFe_2O_4$	34.04	25.34	14.43	15.65	18.76	11.00	7.17	31.06	20.69

Table A3.5: Mineral chemistry (EDS) of representative silicate phenocryst and microphenocryst phases within Zeehan (C17/86 8DB) and Heemskirk (C17/86 7DB) Seamount samples.
Analyses include: 1. rim of olivine microphenocryst; 2. core of previous olivine microphenocryst - reverse zoning; 3. rim of olivine phenocryst; 4. core of previous olivine phenocryst - normal zoning; 5. rim of clinopyroxene microphenocryst (augite); 6. core of previous clinopyroxene microphenocryst (ferroaugite) - reverse zoning; and 7. clinopyroxene lath (augite).

	Olivine:				Clinopyroxene:		
Analysis	1	2	3	4	5	6	7
Sample No.	C17/86 8DB 2/1	C17/86 8DB 2/1	C17/86 8DB 2/2	C17/86 8DB 2/2	C17/86 8DB 2/1	C17/86 8DB 2/1	C17/86 7DB 1/13
SiO_2	32.16	31.91	32.20	32.93	48.94	47.88	49.39
TiO_2					0.65	0.83	1.71
Al_2O_3					1.25	1.69	3.15
Cr_2O_3	0.00	0.00	0.00	0.00	0.00	0.17	0.11
Fe_2O_3					0.01	0.01	0.01
FeO	51.96	52.50	51.32	50.04	16.12	19.73	12.99
MnO	1.29	1.29	1.37	1.03	0.41	0.54	0.24
NiO							
MgO	13.91	13.71	14.32	16.05	9.34	7.07	12.03
CaO	0.34	0.28	0.38	0.31	20.88	20.64	19.94
Na_2O					0.45	0.61	0.65
K_2O					0.00	0.00	0.00
Total	99.66	99.69	99.59	100.36	98.05	99.17	100.22
Cations							
Si	0.990	0.985	0.989	0.992	1.937	1.910	1.875
Ti					0.019	0.025	0.049
Al					0.058	0.080	0.141
Cr	0.000	0.000	0.000	0.000	0.000	0.005	0.003
Fe^{3+}					0.000	0.000	0.000
Fe^{2+}	1.337	1.356	1.318	1.260	0.533	0.658	0.412
Mn	0.034	0.034	0.036	0.026	0.014	0.018	0.008
Ni							
Mg	0.638	0.631	0.656	0.720	0.551	0.420	0.681
Ca	0.011	0.009	0.013	0.010	0.885	0.882	0.811
Na					0.034	0.047	0.048
K					0.000	0.000	0.000
Total	3.010	3.015	3.011	3.008	4.032	4.046	4.028
Mg#	32.30	31.76	33.21	36.37	50.82	38.97	62.28
En					27.98	21.44	35.75
Fs					27.08	33.58	21.65
Wo					44.94	44.98	42.60

Table A3.6: Mineral chemistry (WDS) of representative silicate phenocryst and microphenocryst phases within submarine Scott Island samples. Analyses include: 1. olivine microphenocryst; 2. core of olivine microphenocryst; 3. rim of olivine microphenocryst; 4. core of previous olivine phenocryst - normal zoning; 5. olivine microphenocryst; 6 olivine microphenocryst; 7. groundmass feldspar lath (oligoclase); 8. feldspar microphenocryst (anorthoclase); 9. feldspar microlite (anorthoclase); 10. groundmass feldspar lath (oligoclase-anorthoclase); 11. rim of plagioclase microphenocryst (labradorite); 12. core of previous plagioclase microphenocryst (labradorite); 13. groundmass feldspar lath (anorthoclase); and 14. kaersutite microphenocryst.

	Olivine:						Feldspar:							Amphibole:
Analysis	1	2	3	4	5	6	7	8	9	10	11	12	13	14
Sample No.	E27-34B-1	E27-34B-2	E27-34C-2	E27-34C-2	E27-34D-1	E27-34D-1	E27-34A-4	E27-34A-4	E27-34B-1	E27-34B-2	E27-34C-2	E27-34C-2	E27-34D-1	E27-34B-2
SiO_2	30.80	30.14	36.47	35.95	31.13	30.95	61.44	65.20	63.97	64.07	55.16	54.49	63.44	39.25
TiO_2														4.78
Al_2O_3							23.00	20.94	20.12	22.61	28.00	28.02	22.04	13.13
Cr_2O_3	0.02	0.00	0.00	0.00	0.00	0.00								0.05
Fe_2O_3														
FeO	56.87	57.83	35.37	34.55	56.01	54.93	0.30	0.55	1.76	0.85	0.49	0.55	0.71	16.11
MnO	3.83	3.72	0.98	1.03	4.27	3.84								0.21
NiO	0.02	0.00	0.01	0.04	0.00	0.00								
MgO	7.07	6.52	27.63	28.08	6.82	7.10	0.00	0.04	0.06	0.00	0.04	0.05	0.00	9.22
CaO	0.94	1.08	0.47	0.66	0.95	1.43	4.37	2.11	2.29	4.09	10.37	10.59	3.34	10.98
Na_2O							8.05	8.51	7.34	7.68	5.40	5.16	8.01	2.63
K_2O							1.21	2.93	3.97	1.99	0.29	0.31	2.27	0.89
Total	99.55	99.29	100.93	100.31	99.18	98.25	98.37	100.28	99.51	101.29	99.75	99.17	99.81	97.25
Cations														
Si	0.994	0.983	1.006	0.997	1.005	1.005	2.778	2.899	2.913	2.827	2.500	2.488	2.840	5.966
Ti														0.546
Al							1.229	1.100	1.082	1.179	1.500	1.512	1.166	Al (tet) - 2.034
														Al (oct) - 0.325
Cr	0.000	0.000	0.000	0.000	0.000	0.000								0.006
Fe^{2+}	1.534	1.577	0.816	0.801	1.512	1.491								2.048
Mn	0.105	0.103	0.023	0.024	0.117	0.106								0.027
Ni	0.001	0.000	0.000	0.001	0.000	0.000								
Mg	0.340	0.317	1.136	1.160	0.328	0.344								2.090
Ca	0.032	0.038	0.014	0.020	0.033	0.050	0.212	0.101	0.112	0.193	0.504	0.518	0.160	1.788
Na							0.706	0.734	0.648	0.657	0.475	0.457	0.695	(M4) - 0.189
														(A) - 0.606
K							0.070	0.168	0.231	0.112	0.017	0.018	0.130	0.173
Total	3.006	3.018	2.995	3.003	2.995	2.996	4.995	5.000	4.986	4.968	4.996	4.993	4.991	15.778
Mg#	18.14	16.74	58.20	59.15	17.83	18.75								50.51
An							21.46	10.09	11.30	20.06	50.60	52.17	16.24	
Ab							71.46	73.33	65.39	68.30	47.69	46.02	70.56	
Or							7.09	16.58	23.31	11.64	1.71	1.81	13.20	

Table A3.7: Mineral chemistry (WDS) of representative silicate phenocryst and microphenocryst phases within southwest Pacific Ocean seafloor samples. Analyses include: 1. olivine microphenocryst rim; 2. core of previous olivine microphenocryst - normal zoning; 3. olivine microphenocryst rim; 4. core of previous olivine microphenocryst - normal zoning; 5. rim of olivine phenocryst with salite overgrowth rim (analysis 23); 6. olivine phenocryst rim; 7. core of previous olivine phenocryst - reverse zoning; 8. olivine microphenocryst rim; 9. core of previous olivine microphenocryst - reverse zoning; 10 olivine microphenocryst rim; 11. core of previous olivine microphenocryst - normal zoning; 12. olivine overgrowth rim around previous olivine; 13. olivine microphenocryst rim; 14. core of previous olivine microphenocryst - normal zoning and rimmed by salite overgrowth (analysis 34); 15. olivine microphenocryst rim; 16. core of previous olivine microphenocryst - reverse zoning; 17. olivine phenocryst rim; 18. core of previous olivine phenocryst - homogeneous grain; 19. olivine rim; 20. core of previous olivine; 21. clinopyroxene microphenocryst rim (salite)

	Olivine:												
Analysis	1	2	3	4	5	6	7	8	9	10	11	12	13
Sample No.	E27-03	E27-03	E27-36-2	E27-36-2	E27-36-2	E27-36-4	E27-36-4	E27-36-5	E27-36-5	E27-36-7	E27-36-7	E27-36-7	E27-36-8
SiO_2	34.39	35.34	39.8	40.41	39.19	40.02	39.52	39.54	38.98	38.82	39.91	38.57	39.34
TiO_2													
Al_2O_3													
Cr_2O_3	0.00	0.00	0.00	0.00	0.10	0.00	0.00	0.00	0.00	0.00	0.00	0.00	0.00
Fe_2O_3													
FeO	39.66	35.92	15.08	11.37	15.99	14.19	18.81	15.08	20.24	18.37	13.28	24.27	15.78
MnO	1.14	0.85	0.26	0.04	0.26	0.15	0.24	0.15	0.19	0.28	0.18	0.40	0.29
NiO	0.02	0.00	0.08	0.26	0.19	0.23	0.11	0.20	0.29	0.17	0.10	0.05	0.18
MgO	23.6	27.13	43.69	47.13	43.06	45.31	40.98	44.02	40.43	41.05	44.88	36.71	42.88
CaO	0.57	0.37	0.29	0.20	0.29	0.25	0.22	0.27	0.08	0.34	0.37	0.39	0.30
Na_2O													
K_2O													
Total	99.38	99.61	99.27	99.41	99.08	100.15	99.88	99.26	100.21	99.03	98.72	100.39	98.77
Cations													
Si	0.992	0.994	1.008	1.004	1.001	1.000	1.011	1.002	1.002	1.002	1.008	1.009	1.005
Ti													
Al													
Cr					0.001								
Fe^{3+}													
Fe^{2+}	0.956	0.845	0.319	0.236	0.341	0.297	0.402	0.319	0.435	0.397	0.280	0.531	0.337
Mn	0.028	0.020	0.006	0.001	0.006	0.003	0.005	0.003	0.004	0.006	0.004	0.009	0.006
Ni	0.001	0.000	0.002	0.006	0.005	0.005	0.003	0.005	0.007	0.004	0.002	0.001	0.004
Mg	1.014	1.137	1.649	1.744	1.638	1.688	1.562	1.662	1.548	1.579	1.688	1.431	1.633
Ca	0.018	0.011	0.008	0.005	0.008	0.007	0.006	0.007	0.002	0.009	0.010	0.011	0.008
Na													
K													
Total	3.009	3.007	2.992	2.996	3.000	3.000	2.989	2.998	2.998	2.997	2.992	2.992	2.993
Mg#	51.47	57.37	83.79	88.08	82.77	85.04	79.53	83.9	78.06	79.91	85.77	72.94	82.89
En													
Fs													
Wo													
An													
Ab													
Or													

Table A3.7: (continued) 22. core of previous clinopyroxene microphenocryst (salite); 23. salite rim around olivine phenocryst (analysis 5); 24. salite inclusion in olivine phenocryst; 25. clinopyroxene microphenocryst rim (salite); 26. core of previous clinopyroxene microphenocryst (salite) - reverse zoning; 27. clinopyroxene phenocryst rim (salite); 28. core of previous clinopyroxene phenocryst (diopside) - normal zoning; 29. clinopyroxene microphenocryst rim (salite); 30. apple-green core of previous clinopyroxene microphenocryst (salite) - reverse zoning; 31. salite rim around olivine microphenocryst (analyses 13 and 14); 32. clinopyroxene microphenocryst rim (diopside); 33. core of previous clinopyroxene microphenocryst (salite); 34. clinopyroxene phenocryst rim (salite); 35. core of previous clinopyroxene phenocryst (salite) - reverse zoning; 36. diopside inclusion in olivine phenocryst; 37. plagioclase phenocryst rim (labradorite); 38. core of previous plagioclase phenocryst (labradorite); 39. plagioclase phenocryst rim (bytownite); 40. core of previous plagioclase phenocryst (labradorite) - reverse zoning; 41. plagioclase microphenocryst rim (labradorite); and 42. core of previous plagioclase microphenocryst (bytownite) - normal zoning.

	Olivine :							Clinopyroxene:					
Analysis	14	15	16	17	18	19	20	21	22	23	24	25	26
Sample No.	E27-36-8	E27-36-8	E27-36-8	E27-37-2	E27-37-2	E27-37-3	E27-37-3	E27-03	E27-03	E27-36-2	E27-36-2	E27-36-4	E27-36-4
SiO_2	40.08	40.01	39.71	39.56	39.32	32.47	32.38	49.75	47.23	46.63	47.52	47.25	44.93
TiO_2								1.64	2.60	2.55	1.74	2.18	2.89
Al_2O_3								3.05	5.22	7.75	7.33	6.72	10.3
Cr_2O_3	0.04	0.00	0.01	0.04	0.00	0.00	0.00	0.00	0.06	0.04	0.29	0.37	0.19
Fe_2O_3													
FeO	13.11	17.47	18.04	16.33	16.61	51.08	51.99	11.63	10.48	9.18	6.50	6.86	6.93
MnO	0.09	0.29	0.39	0.26	0.14	2.43	2.27	0.35	0.30	0.31	0.05	0.06	0.00
NiO	0.32	0.16	0.16	0.12	0.29	0.10	0.00						
MgO	45.44	42.96	42.42	43.24	43.11	13.68	13.11	10.83	11.14	11.3	13.43	13.25	12.27
CaO	0.23	0.28	0.26	0.35	0.34	0.58	0.57	22.08	21.86	21.26	22.19	22.83	21.6
Na_2O								0.70	0.55	0.79	0.63	0.41	0.72
K_2O								0.01	0.01	0.00	0.00	0.00	0.00
Total	99.31	101.17	100.99	99.90	99.81	100.34	100.32	100.04	99.45	99.81	99.68	99.93	99.83
Cations													
Si	1.005	1.004	1.002	1.002	0.998	0.993	0.994	1.891	1.802	1.758	1.773	1.767	1.679
Ti								0.047	0.075	0.072	0.049	0.061	0.081
Al								0.137	0.235	0.344	0.322	0.296	0.454
Cr									0.002	0.001	0.009	0.011	0.006
Fe^{3+}													
Fe^{2+}	0.275	0.367	0.381	0.346	0.353	1.306	1.335	0.374	0.334	0.289	0.203	0.214	0.217
Mn	0.002	0.006	0.008	0.006	0.003	0.063	0.059	0.011	0.010	0.010	0.002	0.002	0.000
Ni	0.007	0.004	0.004	0.003	0.007	0.003	0.000						
Mg	1.698	1.607	1.595	1.632	1.631	0.623	0.600	0.613	0.633	0.635	0.747	0.738	0.683
Ca	0.006	0.008	0.007	0.009	0.009	0.019	0.019	0.899	0.894	0.859	0.887	0.914	0.865
Na								0.052	0.041	0.058	0.046	0.030	0.052
K								0.000	0.000	0.000	0.000	0.000	0.000
Total	2.993	2.996	2.997	2.998	3.001	3.007	3.007	4.024	4.026	4.026	4.038	4.033	4.037
Mg#	86.06	81.41	80.72	82.51	82.21	32.30	31.01	62.11	65.46	68.72	78.63	77.52	75.89
En								32.5	34.01	35.61	40.66	39.55	38.70
Fs								19.83	17.95	16.21	11.05	11.47	12.29
Wo								47.67	48.04	48.18	48.29	48.98	49.01
An													
Ab													
Or													

Table A3.7: (continued)

	Clinopyroxene:										Feldspar:		
Analysis	27	28	29	30	31	32	33	34	35	36	37	38	39
Sample No.	E27-36-7	E27-36-7	E27-36-7	E27-36-7	E27-36-8	E27-36-8	E27-36-8	E27-37-2	E27-37-2	E27-37-2	E27-03	E27-03	E27-36-4
SiO_2	48.72	48.41	47.01	50.24	46.35	49.03	45.98	50.06	47.89	50.44	52.61	54.13	49.50
TiO_2	1.86	1.63	2.56	0.79	2.39	1.84	2.60	1.26	2.05	1.21			
Al_2O_3	6.47	6.59	5.74	3.51	8.08	5.26	8.08	3.79	5.08	3.99	29.31	28.48	31.14
Cr_2O_3	0.08	0.71	0.09	0.00	0.13	0.43	0.02	0.30	0.17	1.24			
Fe_2O_3													
FeO	6.11	5.37	6.83	11.79	7.93	5.86	6.69	6.58	8.12	5.05	0.31	0.33	0.78
MnO	0.08	0.12	0.00	0.57	0.22	0.10	0.15	0.23	0.15	0.15			
NiO													
MgO	13.69	13.78	13.26	10.69	11.85	14.30	12.49	14.88	13.43	15.14	0.02	0.04	0.00
CaO	22.78	23.23	22.43	21.75	21.54	22.91	22.54	22.45	22.35	22.67	11.71	10.93	15.05
Na_2O	0.56	0.49	0.33	1.00	0.77	0.47	0.60	0.33	0.38	0.44	4.64	5.37	2.81
K_2O	0.00	0.00	0.02	0.00	0.00	0.01	0.00	0.00	0.00	0.02	0.31	0.32	0.18
Total	100.35	100.33	98.27	100.34	99.26	100.21	99.15	99.88	99.62	100.35	98.91	99.6	99.46
Cations													
Si	1.801	1.790	1.786	1.903	1.749	1.817	1.732	1.862	1.804	1.858	2.413	2.462	2.287
Ti	0.052	0.045	0.073	0.022	0.068	0.051	0.074	0.035	0.058	0.034			
Al	0.282	0.287	0.257	0.157	0.359	0.230	0.359	0.166	0.226	0.173	1.589	1.531	1.700
Cr	0.002	0.021	0.003	0.000	0.004	0.013	0.001	0.009	0.005	0.036			
Fe^{3+}													
Fe^{2+}	0.189	0.166	0.217	0.373	0.250	0.182	0.211	0.205	0.256	0.156			
Mn	0.003	0.004	0.000	0.018	0.007	0.003	0.005	0.007	0.005	0.005			
Ni													
Mg	0.754	0.759	0.751	0.603	0.666	0.790	0.701	0.825	0.754	0.831			
Ca	0.902	0.920	0.913	0.883	0.871	0.909	0.910	0.895	0.902	0.895	0.575	0.533	0.745
Na	0.040	0.035	0.024	0.073	0.056	0.034	0.044	0.024	0.028	0.031	0.413	0.474	0.252
K	0.000	0.000	0.001	0.000	0.000	0.000	0.000	0.000	0.000	0.001	0.018	0.019	0.011
Total	4.025	4.027	4.025	4.032	4.030	4.029	4.037	4.028	4.038	4.020	5.008	5.019	4.995
Mg#	79.96	82.05	77.58	61.78	72.71	81.28	76.86	80.10	74.65	84.19			
En	40.87	41.14	39.93	32.44	37.27	42.00	38.47	42.86	39.44	44.16			
Fs	10.24	9.00	11.54	20.06	13.99	9.68	11.58	10.65	13.39	8.29			
Wo	48.89	49.86	48.54	47.50	48.74	48.32	49.95	46.49	47.18	47.56			
An											57.16	51.95	73.91
Ab											41.05	46.2	25.00
Or											1.79	1.85	1.09

Table A3.7: (continued)

Analysis	Feldspar: 40	41	42
Sample No.	E27-36-4	E27-37-2	E27-37-2
SiO_2	51.71	52.09	47.15
TiO_2			
Al_2O_3	29.82	28.68	31.79
Cr_2O_3			
Fe_2O_3			
FeO	0.79	0.81	0.60
MnO			
NiO			
MgO	0.01	0.10	0.07
CaO	13.54	13.34	17.34
Na_2O	3.78	3.92	1.85
K_2O	0.22	0.24	0.09
Total	99.87	99.18	98.89
Cations			
Si	2.370	2.405	2.205
Ti			
Al	1.615	1.565	1.757
Cr			
Fe^{3+}			
Fe^{2+}			
Mn			
Ni			
Mg			
Ca	0.665	0.660	0.869
Na	0.336	0.351	0.168
K	0.013	0.014	0.005
Total	4.999	4.995	5.004
Mg#			
En			
Fs			
Wo			
An	65.58	64.39	83.4
Ab	33.14	34.24	16.12
Or	1.28	1.37	0.48

Table A3.8: Mineral chemistry (WDS) of representative oxide phases within southwest Pacific Ocean seafloor samples.
Analyses include: 1. Cr-pleonaste inclusion within an olivine microphenocryst; 2. Mg-Al-titanomagnetite groundmass crystal; 3. Cr-pleonaste inclusion within an olivine phenocryst; 4. pleonaste inclusion within a clinopyroxene phenocryst; 5. pleonaste microphenocryst rim; 6. core of previous microphenocryst; 7. pleonaste inclusion within an olivine phenocryst; 8. Cr-Al-titanomagnetite inclusion within an olivine microphenocryst; 9. Cr-pleonaste inclusion within an olivine microphenocryst; 10. Cr-Al-titanomagnetite groundmass crystal; 11. Cr-pleonaste inclusion within an olivine phenocryst; and 12. Al-titanomagnetite microphenocryst.

	Spinel:											
Analysis	1	2	3	4	5	6	7	8	9	10	11	12
Sample No.	E27-36-2	E27-36-2	E27-36-2	E27-36-4	E27-36-5	E27-36-5	E27-36-7	E27-36-7	E27-36-7	E27-36-8	E27-37-2	E27-37-3
SiO_2	0.35	0.08	0.14	0.10	0.05	0.03	0.08	0.03	0.12	0.19	0.08	0.15
TiO_2	1.87	23.54	1.47	1.11	0.09	1.00	1.97	21.18	2.08	17.41	2.26	20.44
Al_2O_3	31.90	2.92	27.70	54.74	49.42	49.35	47.12	4.79	23.01	6.03	24.11	4.08
Cr_2O_3	27.53	0.23	31.88	0.00	9.29	9.29	3.68	6.14	33.13	7.77	28.72	0.00
Fe_2O_3	7.80	19.81	6.86	11.00	7.92	6.04	12.94	17.94	9.69	21.10	12.11	24.47
FeO	16.14	46.67	15.43	14.40	16.71	18.80	18.38	43.98	18.69	39.95	18.08	46.83
MnO	0.16	1.13	0.24	0.41	0.28	0.02	0.14	1.02	0.23	1.01	0.05	1.10
NiO	0.22	0.05	0.19	0.09	0.19	0.23	0.11	0.04	0.15	0.09	0.13	0.05
MgO	14.54	3.12	13.76	17.24	14.51	13.88	14.46	4.15	11.76	4.31	12.27	1.49
Total	100.51	97.54	97.67	99.09	98.46	98.63	98.88	99.28	98.86	97.85	97.81	98.61
Cations												
Ti	0.041	0.656	0.034	0.022	0.002	0.021	0.042	0.570	0.049	0.473	0.053	0.570
Al	1.106	0.128	1.002	1.733	1.626	1.627	1.562	0.203	0.852	0.258	0.894	0.179
Cr	0.639	0.007	0.772	0.000	0.204	0.205	0.082	0.174	0.821	0.222	0.713	0.000
Fe^{3+}	0.172	0.553	0.158	0.222	0.166	0.127	0.273	0.483	0.229	0.574	0.286	0.682
Fe^{2+}	0.396	1.447	0.395	0.323	0.389	0.438	0.431	1.317	0.490	1.208	0.475	1.451
Mn	0.004	0.035	0.006	0.009	0.007	0.000	0.003	0.031	0.006	0.031	0.001	0.035
Ni	0.005	0.001	0.005	0.002	0.004	0.005	0.002	0.001	0.004	0.003	0.003	0.001
Mg	0.638	0.172	0.628	0.688	0.602	0.577	0.605	0.221	0.549	0.232	0.574	0.082
Total	3.000	3.000	3.000	3.000	3.000	3.000	3.000	3.000	3.000	3.000	3.000	3.000
Mg#	61.61	10.65	61.38	68.09	60.74	56.82	58.37	14.39	52.86	16.13	54.73	0.05
Cr#	36.60	5.01	43.50	0.00	11.17	11.19	4.97	46.17	49.07	46.30	44.35	0.00
Fe^{3+}#	30.30	27.64	28.58	40.74	29.90	22.41	38.77	26.85	31.82	32.21	37.60	0.32
End-members												
Mg_2TiO_4	2.54	6.99	2.08	1.52	0.11	1.19	2.43	8.21	2.59	7.63	2.92	3.06
$MgAl_2O_4$	34.08	0.68	30.76	59.01	49.38	48.21	45.59	1.48	22.53	2.08	24.48	0.48
$MgCr_2O_4$	19.68	0.04	23.69	0.00	6.21	5.82	2.38	1.25	21.70	1.79	19.51	0.00
$MgFe_2O_4$	5.31	2.94	4.85	7.55	5.04	3.60	7.97	3.48	8.04	4.63	7.83	1.83
Fe_2TiO_4	1.58	58.65	1.31	0.71	0.07	0.91	1.73	48.81	2.31	39.69	2.42	53.90
$FeAl_2O_4$	21.23	5.72	19.35	27.68	31.91	35.12	32.52	8.67	20.09	10.80	20.24	8.45
$FeCr_2O_4$	12.26	0.30	14.90	0.00	4.01	4.42	1.70	7.44	19.35	9.31	16.13	0.00
$FeFe_2O_4$	3.31	24.69	3.05	3.54	3.26	2.74	5.68	20.69	5.39	24.06	6.47	32.28

Table A3.9: Olivine, clinopyroxene and feldspar equilibrium compositions for Balleny Plume samples as calculated via the methods of A) Nielsen and Dungan (1983); B) Nielsen et al. (1988); C) Glazner (1984); and D) Roeder and Emslie (1970). Apart from aphyric samples (SS4-4 and 7DB 1/13) and samples with no phenocryst plagioclase (35A-5 and SS3), calculated data are presented only for fresh phenocryst phases for which electron microprobe analyses are available.

BALLENY PROVINCE:	Olivine	Clinopyroxene	Plagioclase
E27-35A-1			
A	$Mg\#_{65}$	$Mg\#_{79.73}$	An_{58}
C	$Mg\#_{90}$	$Mg\#_{77.52}$	An_{63}
D	$Mg\#_{67}$		
E27-35A-2			
A	$Mg\#_{33}$	$Mg\#_{47.76}$	An_{59}
B		$Mg\#_{50.59}$	
C			An_{85}
D	$Mg\#_{36}$		
E27-35A-3			
A	$Mg\#_{80}$	$Mg\#_{89.02}$	An_{58}
B		$Mg\#_{87.75}$	
C	$Mg\#_{97}$		An_{74}
D	$Mg\#_{81}$		
E27-35A-4			
A		$Mg\#_{79.55}$	An_{48}
B		$Mg\#_{78.43}$	
C			An_{62}
E27-35A-5			
A	$Mg\#_{84}$	$Mg\#_{91.14}$	An_{59}
B		$Mg\#_{90.31}$	
C	$Mg\#_{98}$		An_{74}
D	$Mg\#_{85}$		
E27-35A-7			
A	$Mg\#_{82}$	$Mg\#_{89.74}$	An_{67}
B		$Mg\#_{88.26}$	
C	$Mg\#_{99}$		An_{77}
D	$Mg\#_{83}$		
E27-35B-1			
A	$Mg\#_{76}$	$Mg\#_{86.57}$	An_{67}
B		$Mg\#_{84.69}$	
C	$Mg\#_{95}$		An_{75}
D	$Mg\#_{78}$		
E27-35B-2			
A	$Mg\#_{83}$	$Mg\#_{90.44}$	An_{55}
B		$Mg\#_{89.36}$	
C	$Mg\#_{98}$		An_{76}
D	$Mg\#_{84}$		

SOELA SEAMOUNT:	Olivine	Clinopyroxene	Plagioclase
SS1-1			
A		$Mg\#_{83.25}$	An_{62}
B		$Mg\#_{81.01}$	
C			An_{67}
SS2-4			
A	$Mg\#_{81}$	$Mg\#_{87.87}$	An_{69}
B		$Mg\#_{85.21}$	
C	$Mg\#_{96}$		An_{83}
D	$Mg\#_{82}$		
SS2-6			
A		$Mg\#_{83.72}$	An_{62}
B		$Mg\#_{81.90}$	
C			An_{71}
SS3			
A	$Mg\#_{83}$	$Mg\#_{89.91}$	An_{63}
B		$Mg\#_{88.19}$	
C	$Mg\#_{96}$		An_{76}
D	$Mg\#_{84}$		
SS4-1			
A	$Mg\#_{82}$	$Mg\#_{88.50}$	An_{66}
B		$Mg\#_{86.09}$	
C	$Mg\#_{95}$		An_{80}
D	$Mg\#_{83}$		
SS4-2			
A		$Mg\#_{85.89}$	An_{69}
B		$Mg\#_{83.58}$	
C			An_{79}
SS4-4			
A		$Mg\#_{83.28}$	An_{66}
B		$Mg\#_{80.79}$	
C			An_{73}
SS5			
A		$Mg\#_{83.35}$	An_{68}
B		$Mg\#_{82.09}$	
C			An_{75}

SOUTH TASMAN SEA SEAMOUNTS:	Olivine	Clinopyroxene	Plagioclase
8DB 2/1			
A	$Mg\#_{81}$	$Mg\#_{57.07}$	An_{71}
B		$Mg\#_{56.16}$	
C	$Mg\#_{72}$		An_{58}
D	$Mg\#_{42}$		
8DB 2/2			
A	$Mg\#_{58}$	$Mg\#_{58.04}$	An_{63}
B		$Mg\#_{55.69}$	
C	$Mg\#_{88}$		An_{57}
D	$Mg\#_{41}$		
8DB 2/5			
A	$Mg\#_{62}$	$Mg\#_{53.87}$	An_{71}
B		$Mg\#_{54.24}$	
C	$Mg\#_{74}$		An_{54}
D	$Mg\#_{41}$		
8DB 3/4			
A	$Mg\#_{81}$	$Mg\#_{54.74}$	An_{70}
B		$Mg\#_{54.78}$	
C	$Mg\#_{76}$		An_{58}
D	$Mg\#_{41}$		
7DB 1/13			
A		$Mg\#_{57.63}$	An_{68}
B		$Mg\#_{55.35}$	
C			An_{55}

Table A3.9. In the absence of melt composition data (ie. groundmass compositions), the best results would be expected for those samples with the least number of phenocrysts so that whole-rock composition most closely approximates the composition of the liquid. Graphical comparisons of measured and calculated mineral compositions are presented in Figures A3.1, A3.2 and A3.3.

Calculated equilibrium olivine compositions for the submarine Scott Island and southwest Pacific Ocean seafloor samples are compared with measured values in Table A3.10.

Table A3.10: Olivine compositions (Mg-values) in equilibrium with whole-rock compositions were calculated via the method of Roeder and Emslie (1970), and are here compared to the most Mg-rich olivines measured in each of the submarine Scott Island and southwest Pacific Ocean seafloor samples for which electron microprobe data are available.

	Calculated Olivine Composition	Measured Olivine Composition
Scott Island:		
E27-34B-1	$Mg\#_{19.9}$	$Mg\#_{19.2}$
E27-34B-2	$Mg\#_{19.8}$	$Mg\#_{20.0}$
E27-34C-2	$Mg\#_{55.1}$	$Mg\#_{59.3}$
E27-34D-1	$Mg\#_{17.0}$	$Mg\#_{18.7}$
Southwest Pacific Ocean:		
E27-02A-2	$Mg\#_{66.3}$	$Mg\#_{60.5}$
E27-03	$Mg\#_{59.7}$	$Mg\#_{60.7}$
E27-36-2	$Mg\#_{84.0}$	$Mg\#_{88.1}$
E27-36-4	$Mg\#_{84.4}$	$Mg\#_{86.4}$
E27-36-5	$Mg\#_{83.7}$	$Mg\#_{87.5}$
E27-36-7	$Mg\#_{83.5}$	$Mg\#_{86.7}$
E27-36-8	$Mg\#_{81.8}$	$Mg\#_{87.0}$
E27-37-2	$Mg\#_{76.9}$	$Mg\#_{85.7}$
E27-37-3	$Mg\#_{37.9}$	$Mg\#_{33.7}$

A3.2.1 Olivine:

Three methods were used to calculate equilibrium olivine compositions, as described by Roeder and Emslie (1970), Nielsen and Dungan (1983) and Glazner (1984). The olivine compositions predicted by the activity-composition relationship method of Glazner (1984) are significantly more Mg-rich than the results produced via the methods of Roeder and Emslie (1970) and Nielsen and Dungan (1983) which are generally in close agreement, at least for the Balleny Province and Soela Seamount samples (Figures A3.1 and A3.2), despite the differences in their methodology. Nielsen and Dungan (1983) prescribe the use of temperature-dependent mineral-melt distribution coefficients, calculated by regressing the results of equilibrium experiments, whereas Roeder and Emslie (1970) present a fixed, temperature-independent, distribution coefficient: (K_D = 0.30). Their poor correlation with compositions predicted by Glazner's (1984) method is probably a function of the calibration of the latter being inappropriate to the Balleny Plume magmas, as a result of the limited data set upon which the model has been based.

Equilibrium olivine compositions calculated by the Roeder and Emslie (1970) and Nielsen and Dungan (1983) methods indicate that most of the Balleny samples contain olivine phenocrysts and/or microphenocrysts which are too Mg-rich to be in equilibrium with their host rock melt compositions. In some samples (e.g. sample 35B-1 - Table 3.2) it is evident that these Mg-rich cores are rimmed by less magnesian olivine of equilibrium composition. Calculated equilibrium olivine compositions within the Zeehan Seamount samples vary greatly according to the method used (Figure A3.3). Those values obtained using the method of Roeder and Emslie (1970) are closest to the observed compositions. Despite the sparseness of phenocryst phases within these samples, the Roeder and Emslie (1970) method results in equilibrium olivine compositions inconsistent with measured olivine compositions. These more Mg-rich calculated compositions may be due to the relatively evolved whole-rock compositions of these rocks for which none of the methods used may be entirely appropriate.

A3.2.2 Clinopyroxene:

Equilibrium clinopyroxene compositions have been calculated via the methods of Nielsen and Dungan (1983) and Nielsen et al. (1988) and are in close agreement. Measured Balleny, Soela and south Tasman Sea seamount clinopyroxene compositions are generally similar to calculated equilibrium compositions. However, clinopyroxene phenocrysts and/or microphenocrysts within Balleny basanite (except for the most evolved sample 35B-1) and alkali basalt samples have Mg#s well below calculated equilibrium compositions (Figure A3.1). Although these samples contain substantial phenocryst components, which may be expected to affect correlations between observed and calculated compositions, sample 35A-2, with the greatest phenocryst content of the Balleny samples, contains clinopyroxene crystals of similar composition to that calculated. Soela Seamount samples which demonstrate this same disagreement between measured and calculated clinopyroxene compositions (Figure A3.2) include the relatively densely-phyric alkali basalts SS3 and SS4-1. However, other equally porphyritic alkali basalts, such as sample SS2-4, have clinopyroxenes which range in composition up to calculated Mg values. In contrast, Heemskirk sample 7DB 1/13 contains some clinopyroxene which is more magnesian than the calculated equilibrium composition (Figure A3.3). Although this lack of correlation between measured and calculated compositions in some samples may therefore be indicative of some degree of mineral-melt disequilibrium, it should also be considered as a possible effect of limited microprobe analyses.

A3.2.3 Plagioclase:

The methods of Nielsen and Dungan (1983) and Glazner (1984) yield very different equilibrium plagioclase compositions for the majority of samples. The reason for this is not clear; however, the results produced by the Glazner (1984) method are consistently closer

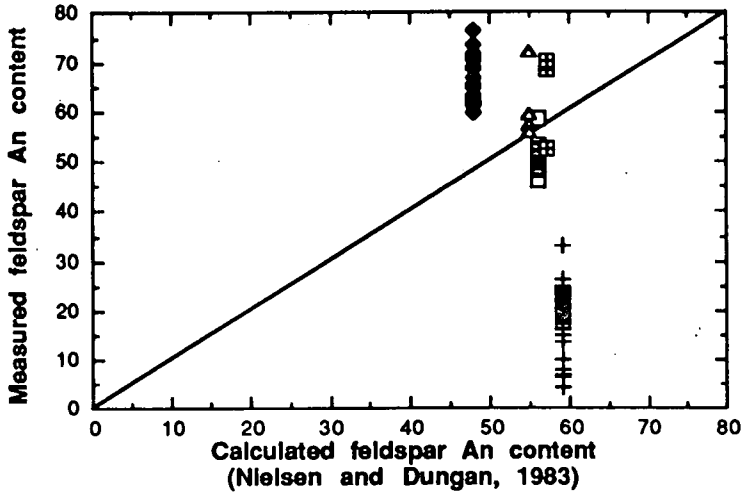
Measured feldspar An content
Calculated feldspar An content
(Nielsen and Dungan, 1983)

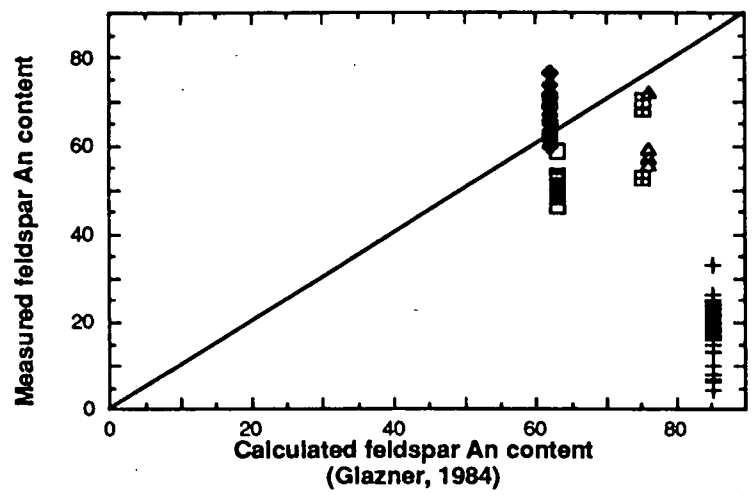
Measured feldspar An content
Calculated feldspar An content
(Glazner, 1984)

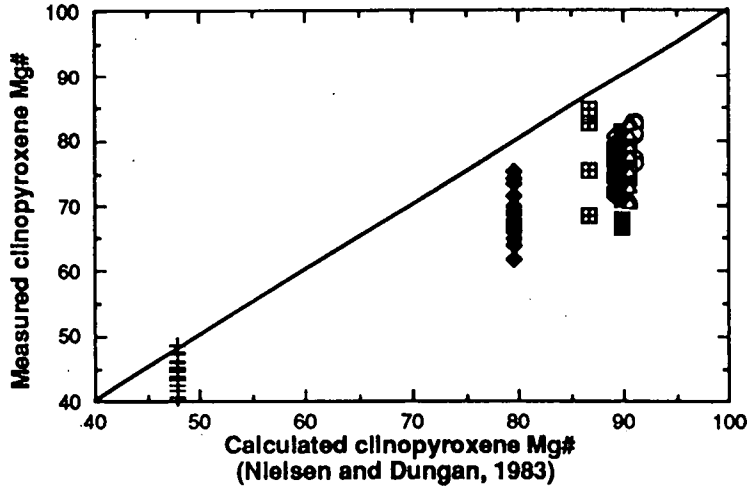
Measured clinopyroxene Mg#
Calculated clinopyroxene Mg#
(Nielsen and Dungan, 1983)

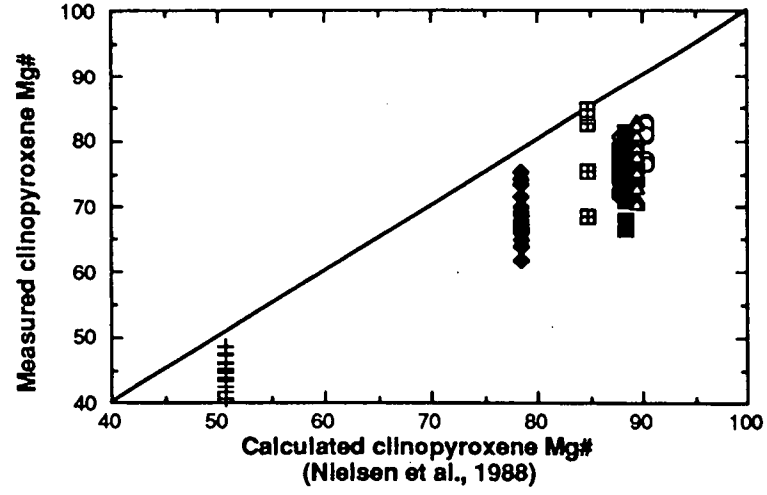
Measured clinopyroxene Mg#
Calculated clinopyroxene Mg#
(Nielsen et al., 1988)

(Figure A3.1)

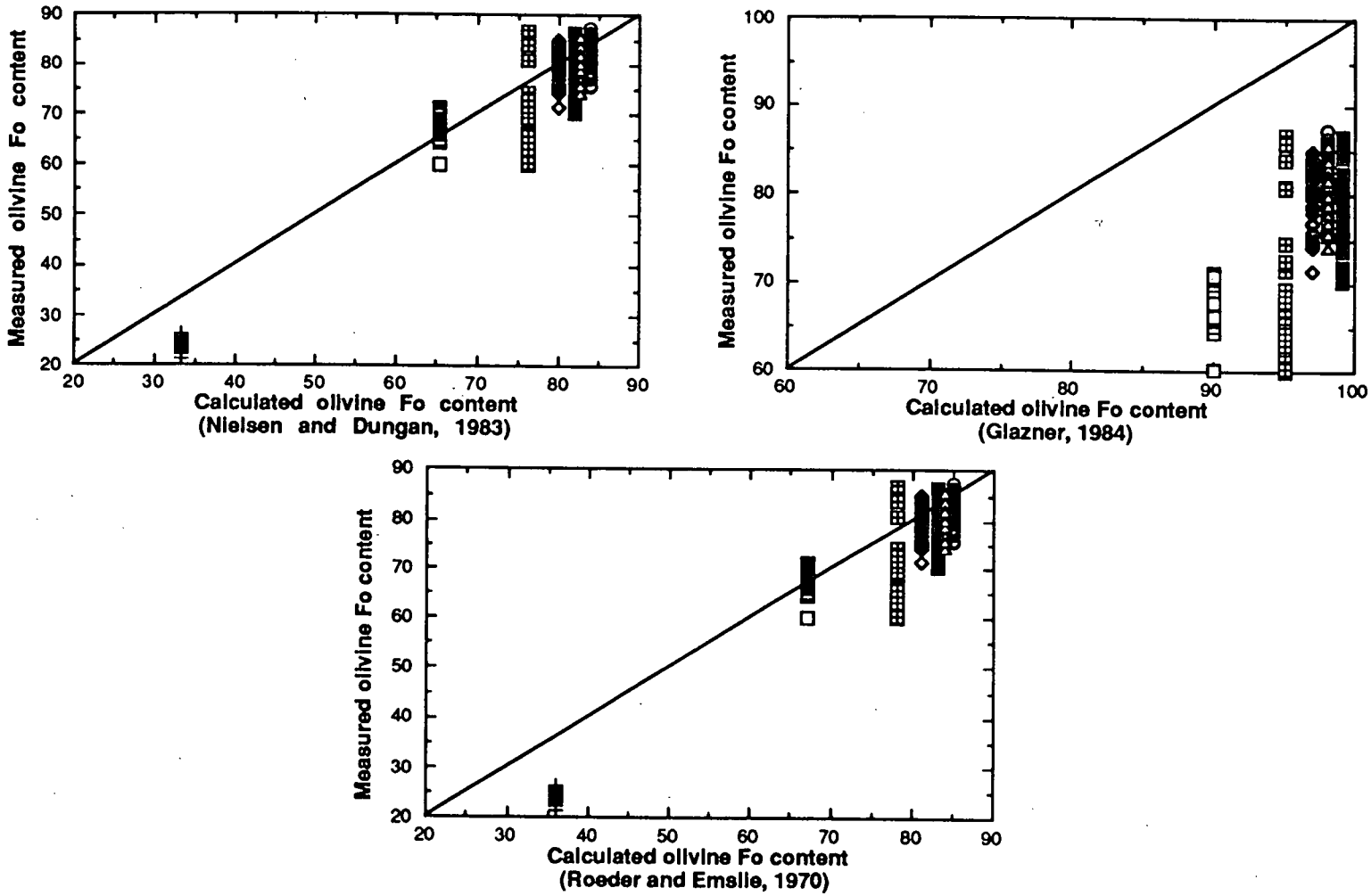

Figure A3.1: Measured mineral compositions versus equilibrium mineral compositions (Table A3.9) as calculated by the various methods described in the text for submarine Balleny Province samples 35A-1 (open squares), 35A-2 (crosses), 35A-3 (open diamonds), 35A-4 (filled diamonds), 35A-5 (open circles), 35A-7 (filled squares), 35B-1 (crosses within squares) and 35B-2 (open triangles).

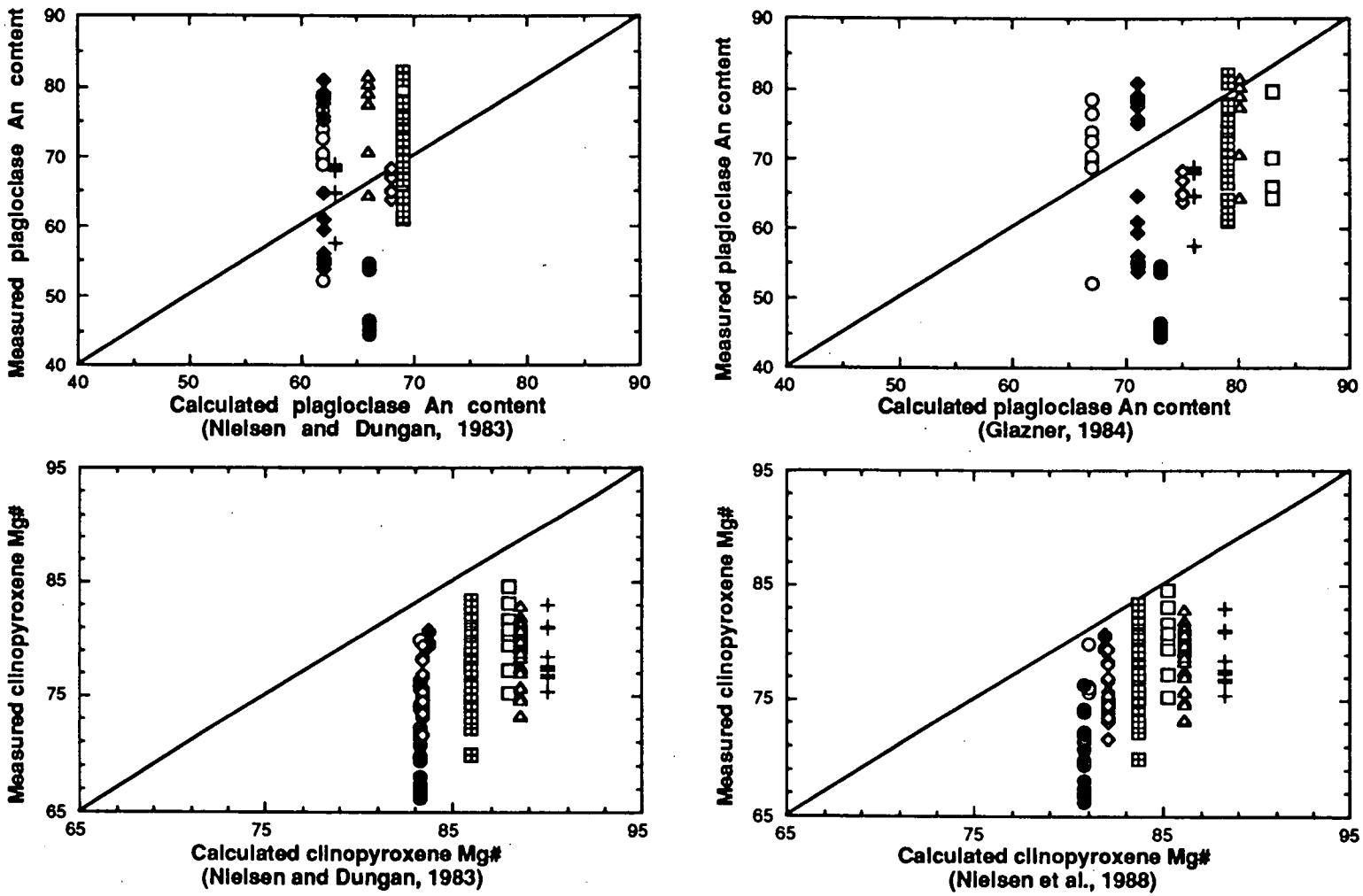
Measured plagioclase An content
Calculated plagioclase An content
(Nielsen and Dungan, 1983)
Calculated plagioclase An content
(Glazner, 1984)
Measured clinopyroxene Mg#
Calculated clinopyroxene Mg#
(Nielsen and Dungan, 1983)
Calculated clinopyroxene Mg#
(Nielsen et al., 1988)

(Figure A3.2)

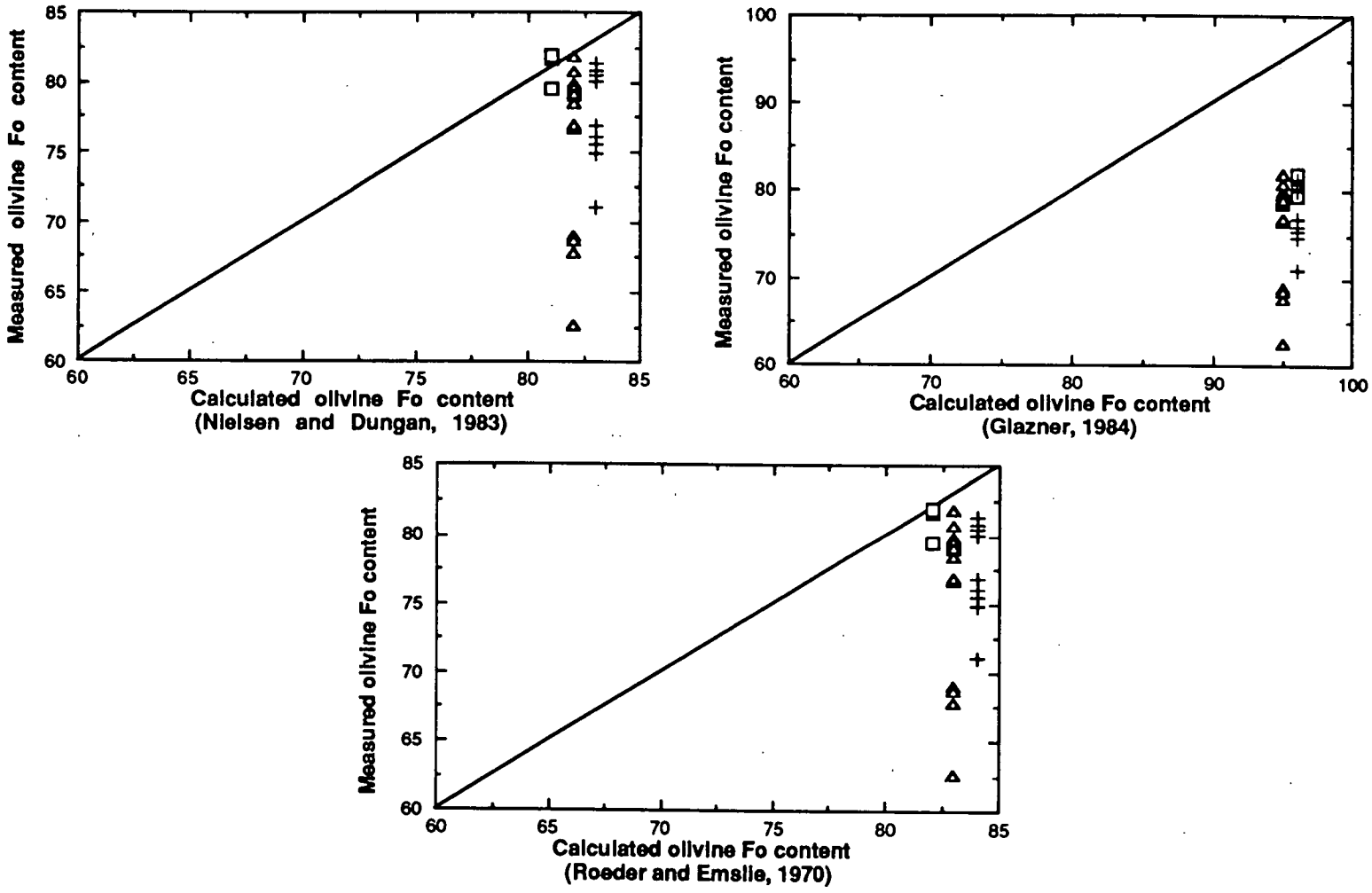

Figure A3.2: Measured mineral compositions versus equilibrium mineral compositions (Table A3.9) as calculated by the various methods described in the text for Soela Seamount samples SS1-1 (open circles), SS2-4 (open squares), SS2-6 (filled diamonds), SS3 (crosses), SS4-1 (open triangles), SS4-2 (crosses within squares), SS4-4 (filled circles) and SS5 (open diamonds).

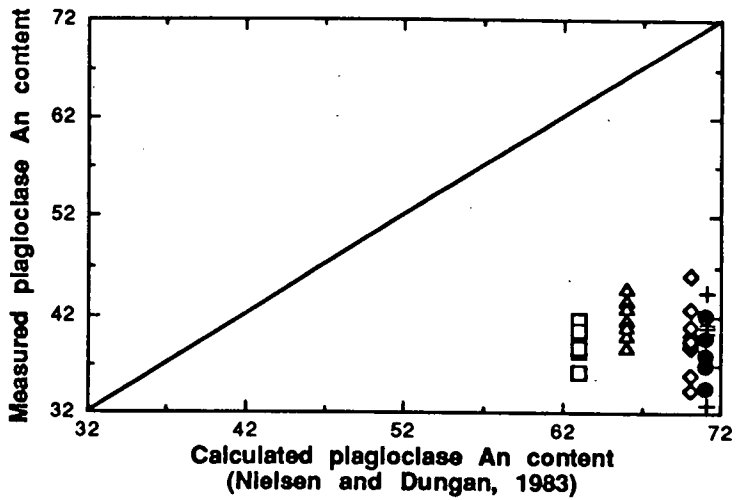
Measured plagioclase An content
72
62
52
42
32
32
42
52
62
72
Calculated plagioclase An content
(Nielsen and Dungan, 1983)

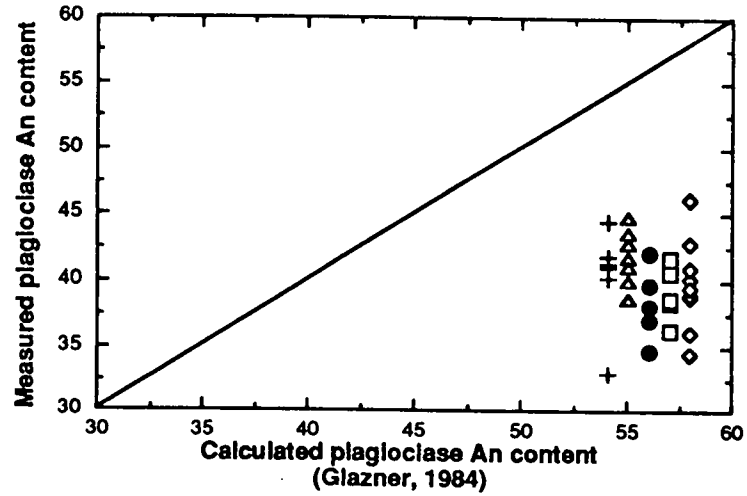
Measured plagioclase An content
60
55
50
45
40
35
30
30
35
40
45
50
55
60
Calculated plagioclase An content
(Glazner, 1984)

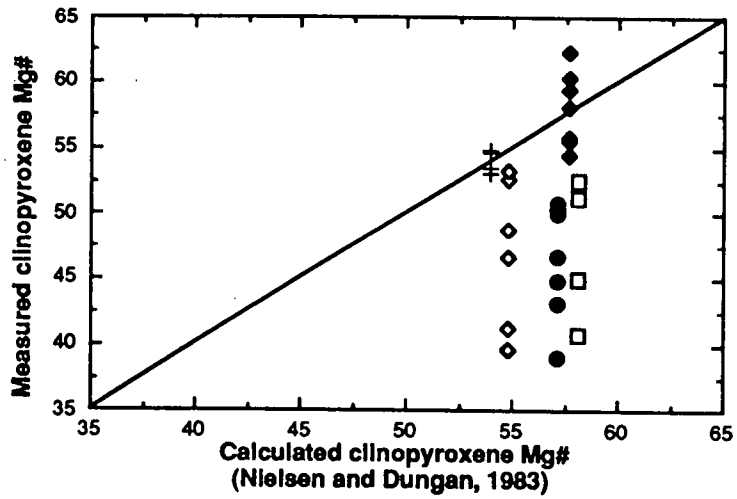
Measured clinopyroxene Mg#
65
60
55
50
45
40
35
35
40
45
50
55
60
65
Calculated clinopyroxene Mg#
(Nielsen and Dungan, 1983)

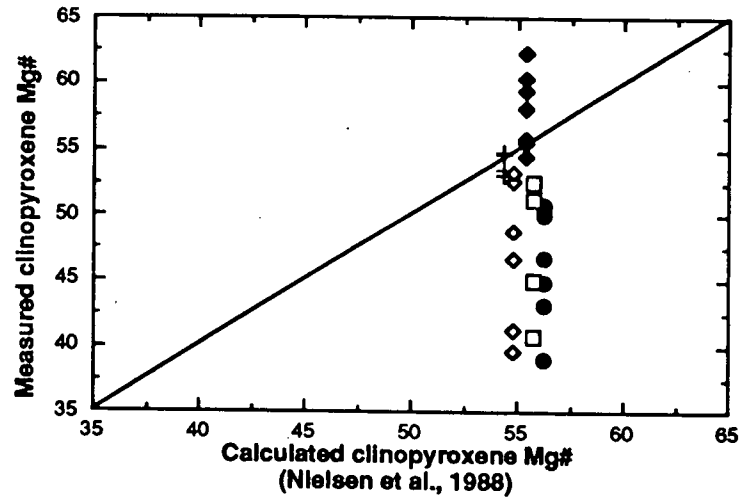
Measured clinopyroxene Mg#
65
60
55
50
45
40
35
35
40
45
50
55
60
65
Calculated clinopyroxene Mg#
(Nielsen et al., 1988)

(Figure A3.3)

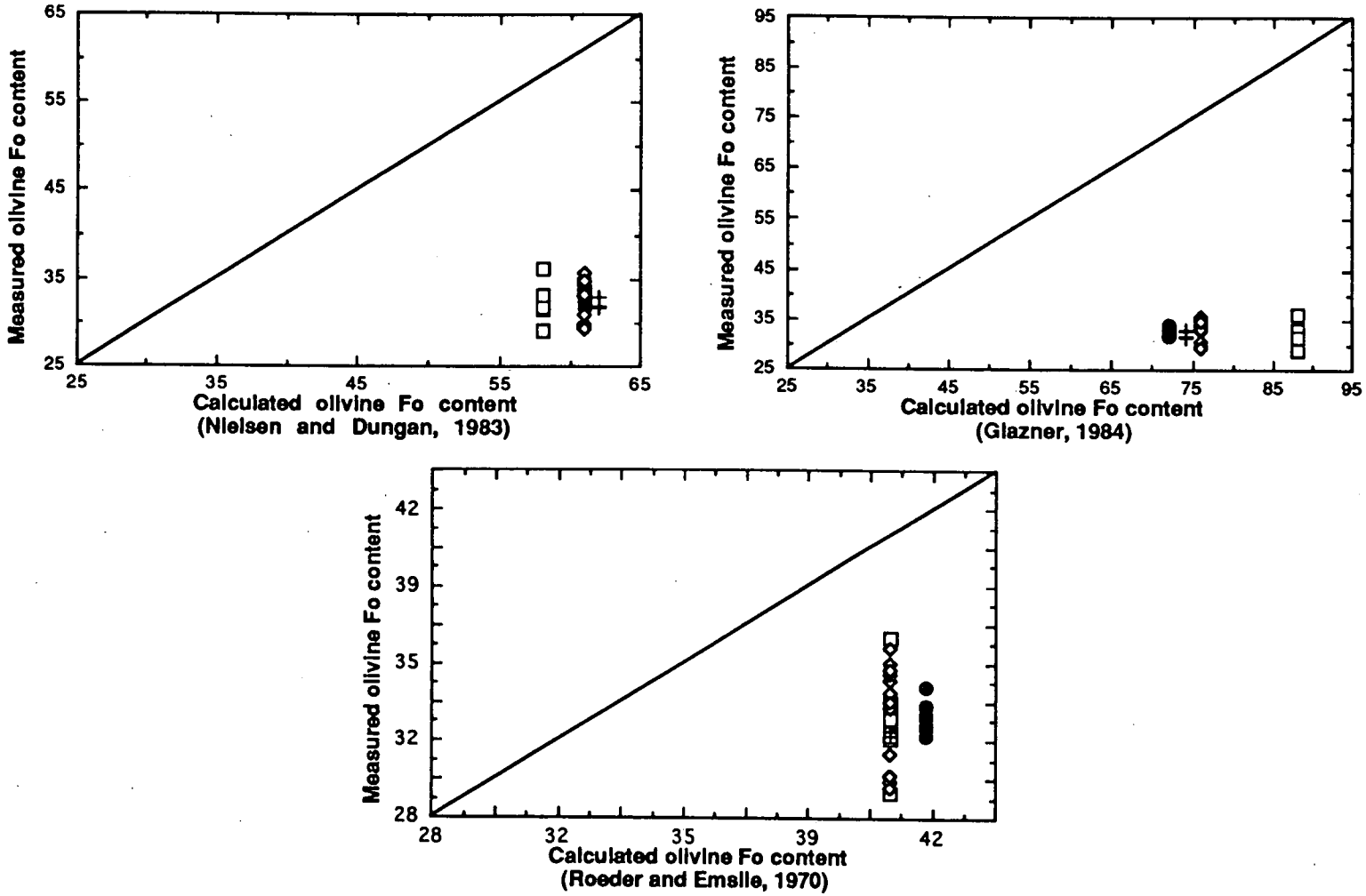

Figure A3.3: Measured mineral compositions versus equilibrium mineral compositions (Table A3.9) as calculated by the various methods described in the text for Zeehan - 8DB 2/1 (filled circles), 8DB 2/2 (open squares), 8DB 2/5 (crosses), 8DB 3/4 (open diamonds) and Heemskirk - 7DB 1/13 (filled diamonds) Seamount samples.

to the measured values, resulting in less feldspar of apparently disequilibrium composition in both the Balleny and Soela samples (Figures A3.1 and A3.2).

A3.2.4 Summary:

The results presented here combine with petrographic observations (Chapter 3) to suggest that some mineral-melt disequilibrium is present in many of the Balleny Plume samples. This is particularly evident in the Mg-rich olivine crystals or crystal cores present in Balleny Province samples, which may therefore have either a cumulate or xenocrystic origin. Disequilibrium may also be responsible for the unexpectedly low Mg# of some Balleny and Soela clinopyroxenes and the resorption textures observed in all of the major mineral phases. The cause of this disequilibrium, whether it involves crystal contamination and/or high-level magma chamber processes is, however, beyond the scope of this study.

APPENDIX 4

RADIOMETRIC DATING OF SOELA SEAMOUNT

Four Soela Seamount samples have been dated using the K-Ar and ^{40}Ar-^{39}Ar techniques. This work was not performed by the author, however, the results have not been published elsewhere and are presented here with the permission of I. McDougall and R.A. Duncan.

K-Ar analyses of two Soela Seamount samples, SS1 and SS3, were performed by I. McDougall at the Research School of Earth Sciences, The Australian National University, following the procedure of McDougall and Schmincke (1977). The results are presented in Table A4.1.

Table A4.1: K-Ar radiometric age data for two Soela Seamount samples. Ages were calculated using the decay constants $\lambda(^{40}K_{\beta}\text{-}) = 4.962 \times 10^{-10}$/year and $\lambda(^{40}K_e) + \lambda'(^{40}K_e) = 0.581 \times 10\text{-}10$/year (Steiger and Jäger, 1977); $^{40}K/K = 1.167 \times 10^{-4}$ mol/mol; and

$$\% \text{ radiogenic } ^{40}Ar = \frac{\text{radiogenic } ^{40}Ar \times 100}{\text{Total } ^{40}Ar}.$$

Sample No.	% K	Radiogenic ^{40}Ar (X 10-10 mol/g)	% Radiogenic ^{40}Ar	Age	$\pm 1\sigma$
SS1	2.245	1.232	82.9	31.6	0.5
	2.216	1.229	80.2	31.5	0.5
SS3	1.204	0.705	73.4	33.4	0.3
	1.205				

^{40}Ar-^{39}Ar analysis of two other Soela Seamount samples was performed by R.A. Duncan at the College of Oceanic and Atmospheric Sciences, Oregon State University, U.S.A. (Table A4.2). Figure A4.1 depicts the apparent $^{40}Ar^*/^{39}Ar_K$ plateau ages for the two samples as a function of the cumulative proportion of ^{39}Ar released during incremental heating after sample irradiation. These ages assume that trapped Ar has an atmospheric $^{40}Ar/^{36}Ar$ ratio of 295.5 (Steiger and Jäger, 1977). The inverse isochron diagrams of Figure A4.2 plot measured $^{36}Ar/^{40}Ar$ versus $^{39}Ar_K/^{40}Ar^*$. The y-intercept gives the measured composition of the pure trapped Ar component; the x-intercept represents the pure radiogenic Ar component and provides the age of the sample. Further information on the ^{40}Ar-^{39}Ar dating method used is available in McDougall and Harrison (1988).

The inverse isochron plots (Figure A4.2) indicate that the trapped Ar component in the Soela Seamount samples has a composition close to atmospheric. This is also reflected in the agreement, within error, of the ^{40}Ar-^{39}Ar plateau and isochron ages for both samples. The slightly younger ages produced by the K-Ar method may be due to either geological variation or minor Ar loss (as observed in the age spectra produced by the ^{40}Ar-^{39}Ar

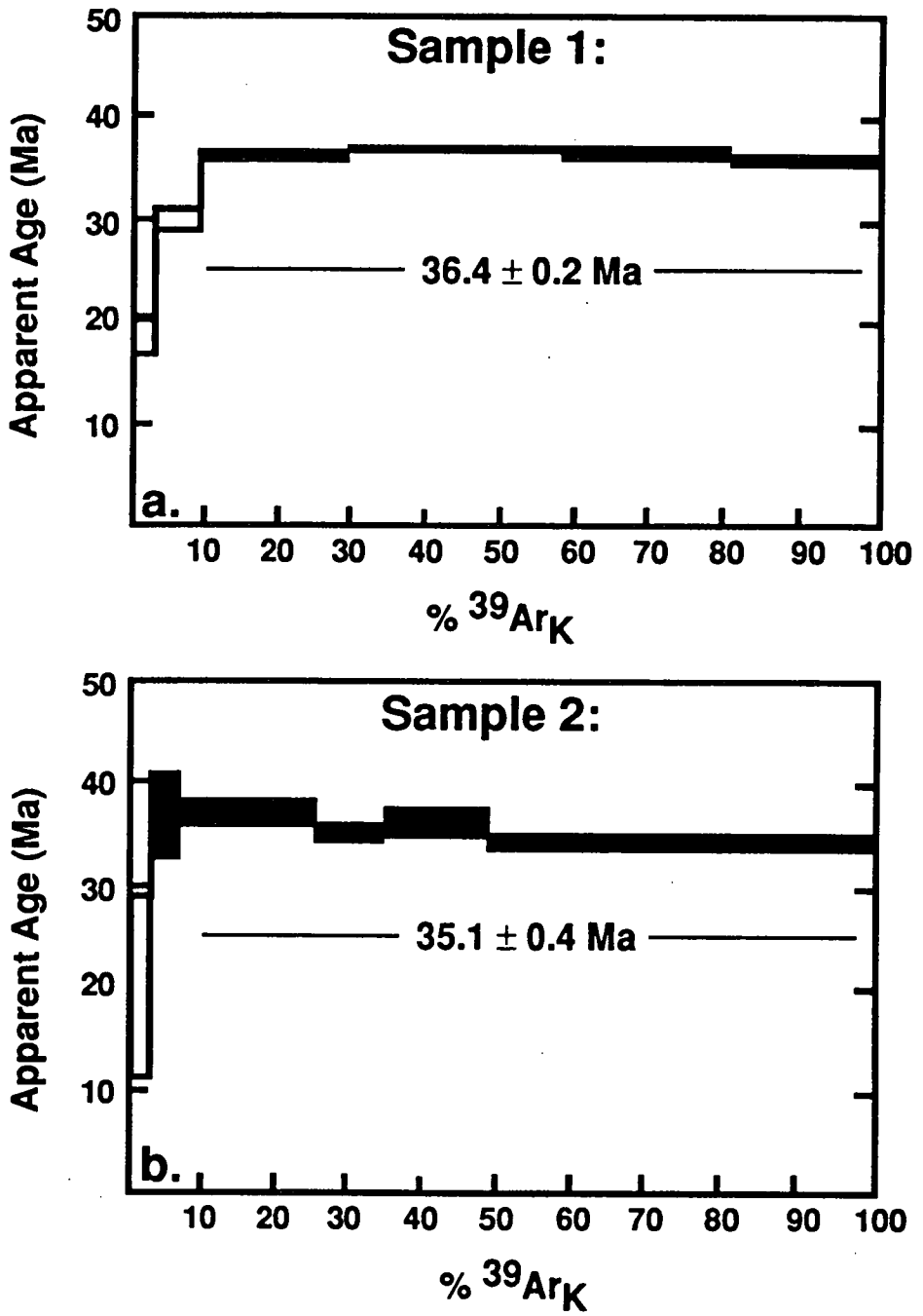

Figure A4.1: Plots of % ^{39}Ar released during the incremental heating of two Soela Seamount samples versus apparent $^{40}Ar^*/^{39}Ar_K$ age; presented sample ages represent model plateau ages ± 1σ error calculated according to the equation:

$t = \frac{1}{\lambda} \ln (1 + J \frac{^{40}Ar^*}{^{39}Ar_K})$ where J is the irradiation parameter (McDougall and Harrison, 1988); decay constants as for Table A4.1.

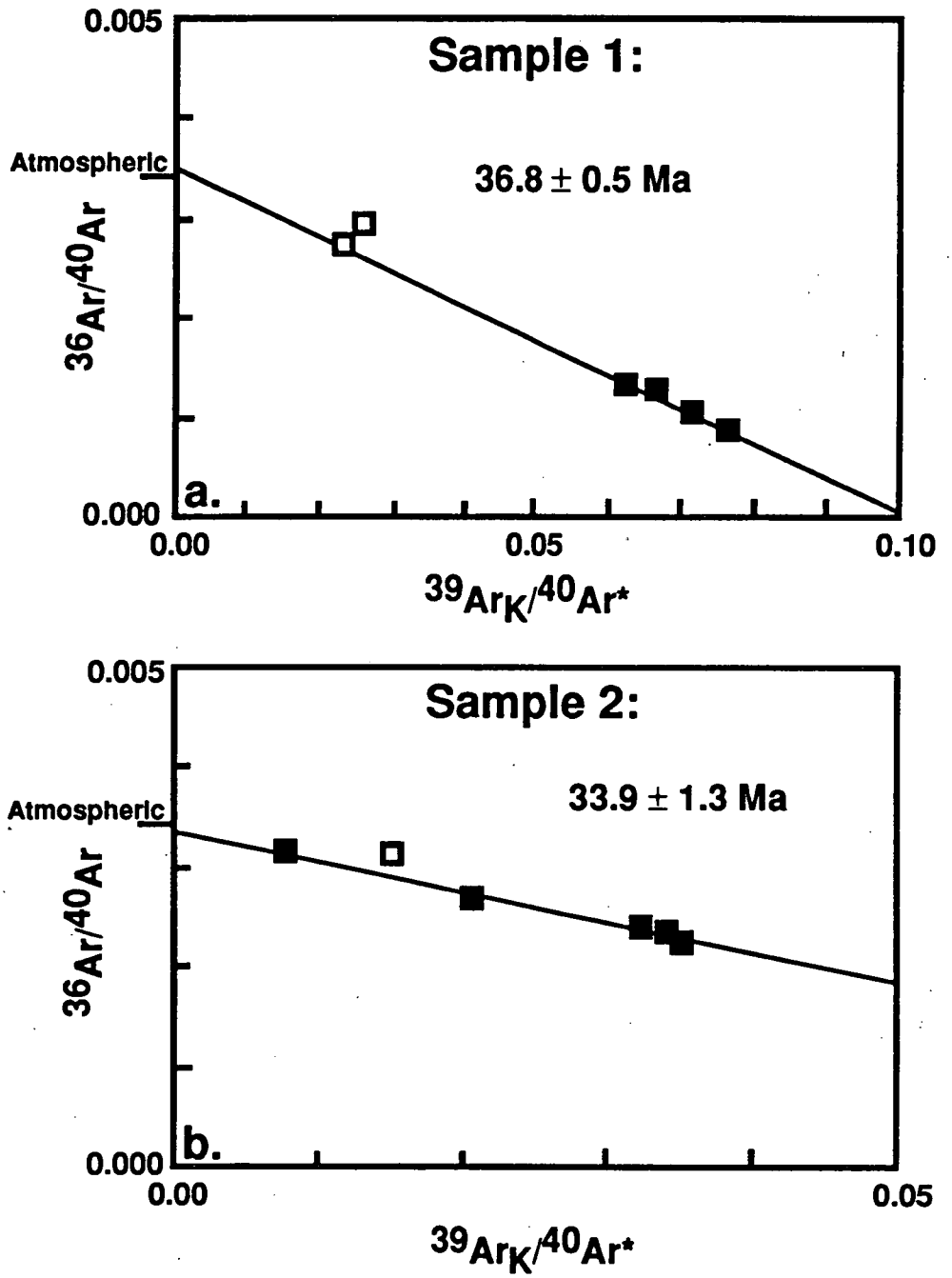

Figure A4.2: Inverse isochron plots of $^{39}Ar_K/^{40}Ar^*$ versus $^{36}Ar/^{40}Ar$; presented sample ages ± 1σ error are calculated as for Figure A4.1 ages; open symbols represent non-plateau data whereas filled symbols represent plateau data used for the final age calculation.

measurements). The ^{40}Ar-^{39}Ar ages are therefore considered to provide the best estimate for the age of the Soela Seamount.

Table A4.2: Results of ^{40}Ar-^{39}Ar analyses performed on two Soela Seamount basalts on an MS-10 mass spectrometer with a sensitivity of ~6 x 10^{-4} cc/pico-amp. Units of measurement for Ar isotope data are pico-amps; ^{37}Ar and ^{39}Ar are corrected for post-irradiation decay and all isotope measurements are corrected for mass fractionation; Δ values represent 1σ errors on intercept values after regressing peak height versus time.

Step	Age	±1σ	^{36}Ar	Δ36	^{37}Ar	Δ37	^{39}Ar	Δ39	^{40}Ar	Δ40
Sample 1:										
1	18.9	1.7	0.006270	0.0000829	0.060	0.001	0.005443	0.000269	2.1167	0.76
2	30.0	1.1	0.012340	0.0001040	0.185	0.002	0.010490	0.000283	4.4574	1.41
3	36.4	0.3	0.007596	0.0000676	0.738	0.007	0.034360	0.000420	5.4790	3.13
4	36.7	0.2	0.006093	0.0000638	0.934	0.009	0.050690	0.000566	6.6243	1.99
5	36.3	0.6	0.006100	0.0002000	0.962	0.010	0.039490	0.000403	5.4994	0.98
6	35.7	0.3	0.007517	0.0000902	4.053	0.041	0.033460	0.000240	5.0165	1.06
Sample 2:										
1	20.3	8.8	0.004516	0.0001730	0.125	0.001	0.002203	0.000176	1.4406	0.44
2	36.4	4.1	0.010900	0.0001000	0.159	0.002	0.002735	0.000189	3.4679	2.41
3	36.9	1.1	0.020000	0.0001500	1.656	0.017	0.015120	0.000213	7.2384	0.18
4	35.0	0.7	0.006000	0.0000500	1.164	0.012	0.007830	0.000238	2.3938	2.26
5	36.0	1.2	0.007350	0.0001210	0.775	0.008	0.011100	0.000264	3.1573	1.85
6	34.3	0.6	0.030100	0.0002000	6.425	0.065	0.041450	0.000167	12.0837	4.43

APPENDIX 5

ICP-MS Rare Earth and Trace Element Data

Inductively coupled plasma-mass spectrometry (ICP-MS) REE and trace element data have been obtained for most of the samples analysed for Sr, Nd and Pb isotopes during the course of this study. Analytical methods are described in Appendix 2. The ICP-MS data presented in Table A5.1 are not, however, necessarily representative of whole-rock compositions as the samples used for analysis were taken from the same fractions of fine rock chips used for the radiogenic isotope analyses. These fractions were chosen, using a binocular microscope, to be relatively free of phenocryst phases and were less likely to include areas of alteration than the larger chips hand-picked (with the naked eye) for XRF/INAA analysis. They were also quite limited in volume and therefore more at risk of not producing entirely representative whole-rock values in heterogeneous samples than the larger fractions crushed for analysis by XRF and/or INAA procedures.

The main objectives of performing the ICP-MS analyses were to gain a range of REE and trace element data for the south Tasman Sea seamount samples, which were too small to analyse by other methods, as well as to gain elemental (such as Pb) data not available to the same level of precision using the other analytical methods. Despite the fact that the actual elemental abundances obtained by the different analytical methods vary slightly, the trace element abundance ratios are considered to be more representative of whole-rock values. A comparison between Rb/Sr and Sm/Nd values measured by the various analytical methods (Figure A5.1) indicates that the former are very similar by both methods. However, some of the REE ratios measured by INAA are significantly higher or lower than those measured by ICP-MS. This is particularly true for the most altered samples, such as the Southern Ocean dredge samples, and therefore appears to be due to the more selective hand-picking of the ICP-MS samples. The poorer precision of the INAA method as compared to ICP-MS analysis (Appendix 2) may also be a contributing factor.

Due to the above limitations, interpretations and discussions in this thesis involving ICP-MS REE and trace element data have been limited to the use of ratios involving U or Pb (Th/U, Nb/U, Nb/Pb and Ce/Pb) in the characterisation of trace element systematics on the basis of elemental abundance ratios.

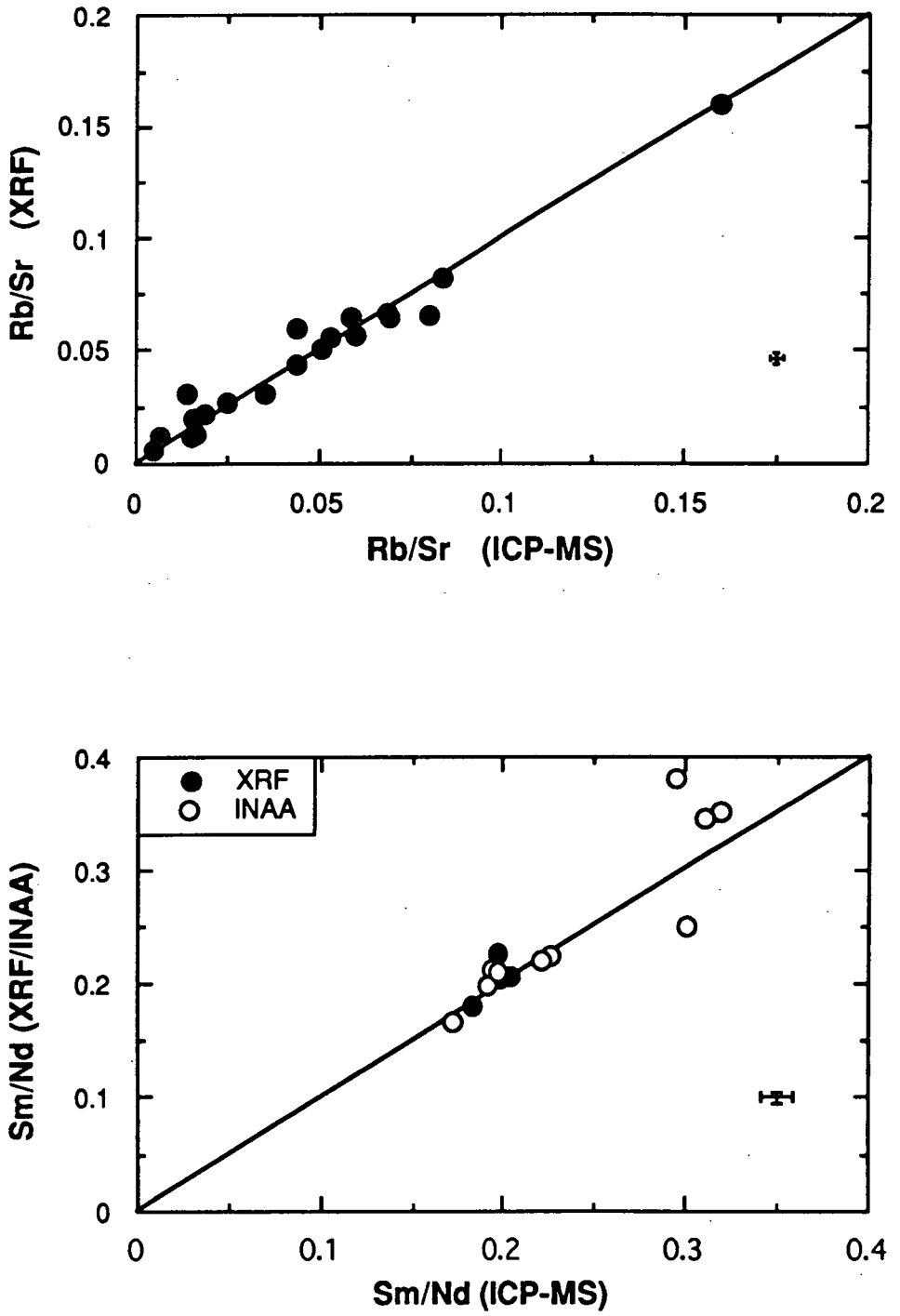

Figure A5.1: Plots of a) ICP-MS versus XRF Rb/Sr measurements b) ICP-MS versus XRF or INAA Sm/Nd measurements. One sigma error bars were calculated using the error propagation equation presented in Chapter 2 (Section 2.2.2) and the following data: a) ICP-MS errors for BHVO-1 Rb and Sr data in Table A2.5 and XRF (1410) errors for TasBas Rb and Sr in Table A2.1; ICP-MS errors for BHVO-1 Sm and Nd data in Table A2.5 and XRF errors for TasBas Sm and Nd in Table A2.7; no error bar could be calculated for the INAA Sm/Nd measurements.

Table A5.1: ICP-MS REE and trace element data for samples analysed for radiogenic Sr, Nd and Pb isotopes.

	Balleny Province:				Scala Seamount:		Janszoon Seamount:			Zeehan Seamount:		
	E27-35A-1	E27-35A-4	E27-35A-5	E27-35B-2	SS3	SS4-7	SS5	2DB 10	2DB 14	8DB 2/1	8DB 2/2	8DB 3/4
Isotope												
Li 7		8.80	5.43	4.84	8.11	33.64	29.81				8.78	9.54
Be 9		2.56	2.12	2.48	1.82	2.60	2.06				5.37	4.99
B 11		7.23	6.55	5.54	40.46	64.25	50.26				23.51	26.36
Sc 45		24.52	31.89	30.26	31.72	19.45	21.40				13.50	13.14
V 51		358.35	266.86	265.73	249.18	335.91	262.32				1.30	1.10
Cr 53		15.05	401.09	287.28	441.74	14.19	63.70				6.64	18.26
Co 59		42.79	49.82	48.10	74.99	36.00	36.95				6.67	6.83
Ni 60		15.85	238.12	170.13	383.83	52.90	84.28				1.85	8.86
Cu 63		30.48	63.57	48.31	127.06	27.43	60.61				10.80	10.95
Zn 66		134.88	88.85	91.63	124.88	136.83	149.35				138.77	141.28
Ga 71		23.78	18.85	19.05	20.34	26.50	24.95				30.65	31.17
Rb 85	65.24	40.50	30.40	35.20	32.10	64.80	50.20	37.25	10.57	47.38	43.90	42.90
Sr 86	950.89	582.88	692.92	656.61	536.56	808.14	853.15	937.39	1011.56	299.80	274.17	272.00
Y 89	39.26	40.47	31.17	30.98	23.80	34.83	32.42	44.90	91.68	84.54	80.88	82.38
Zr 91	459.50	312.51	222.88	257.65	253.86	347.55	361.24	435.09	355.76	641.35	650.98	656.86
Nb 93	123.83	78.95	73.23	78.34	62.60	87.46	89.78	103.17	97.98	90.25	91.07	91.05
Cs 133	0.60	0.38	0.35	0.42	0.69	1.37	2.27	0.52	0.25	1.25	0.52	0.53
Ba 137	581.54	385.37	372.85	390.00	343.99	442.07	466.05	461.18	454.91	481.79	458.21	464.62
La 139	76.63	45.22	41.37	42.52	40.39	53.68	58.54	65.05	89.76	61.32	58.45	59.19
Ce 140	147.49	93.27	81.93	82.58	82.12	107.59	116.66	129.80	126.91	130.25	122.49	123.24
Pr 141	16.64	11.44	9.80	9.74	9.69	13.00	13.96	15.29	18.62	16.14	15.39	15.55
Nd 146	59.24	45.83	38.51	37.68	37.68	50.45	53.25	57.83	70.50	63.61	61.41	61.96
Sm 147	10.85	9.41	7.69	7.49	7.34	9.98	10.22	11.30	13.47	14.37	13.71	13.77
Eu 151	3.32	2.93	2.45	2.34	2.27	3.04	3.11	3.54	3.87	4.10	3.89	3.91
Tb 159	1.39	1.36	1.08	1.05	0.94	1.31	1.25	1.54	1.97	2.46	2.36	2.41
Gd 160	8.76	8.68	6.90	6.66	6.27	8.60	9.39	9.71	12.68	14.18	13.75	13.87
Dy 163	7.12	7.30	5.69	5.64	4.75	6.59	6.32	8.10	10.97	14.05	13.48	13.78
Ho 165		1.38	1.08	1.06	0.85	1.19	1.11				2.75	2.83
Er 167	3.64	3.59	2.79	2.81	2.10	2.96	2.74	3.97	6.22	8.13	7.74	7.91
Tm 169		0.49	0.39	0.39	0.27	0.40	0.37				1.17	1.15
Yb 174	3.10	2.85	2.27	2.30	1.53	2.17	1.99	3.26	5.00	7.36	6.94	7.04
Lu 175	0.45	0.42	0.33	0.35	0.22	0.32	0.27	0.48	0.77	1.11	1.05	1.08
Hf 178	9.51	6.33	4.62	5.25	5.42	7.07	7.23	9.19	8.23	14.15	13.25	13.57
Ta 181	7.76	4.21	3.70	4.12	3.43	4.64	4.69	6.13	5.63	5.23	4.66	4.73
Pb 208	4.51	2.31	1.95	2.56	3.72	3.09	3.43	13.65	14.74	5.36	4.94	5.05
Th 232	11.56	4.79	4.47	5.63	4.96	6.63	6.89	8.15	7.73	7.57	6.84	7.37
U 238	3.19	0.96	1.17	1.43	1.15	1.64	2.07	2.20	2.64	2.13	1.88	1.97

Table A5.1: (continued)

		Heemskirk Seamount:		Tasmania:			Southern Ocean Dredges:					
	8DB 2/5	7DB1/10	7DB1/13	10	2	DR 13516	DR09-4B(II)	DR09-4B5	DR10-1B	DR10-1C	DR11-2A	DR11-2A(III)
Isotope												
Li 7			27.42									
Be 9			1.75									
B 11			165.59									
Sc 45			17.80									
V 51			132.49									
Cr 53			16.25									
Co 59			8.10									
Ni 60			20.76									
Cu 63			72.80									
Zn 66			195.94									
Ga 71			23.73									
Rb 85	48.06	25.24	20.00	61.54	23.04	24.75	3.68	9.95	0.82	0.20	2.35	2.84
Sr 86	267.24	477.26	366.21	734.64	649.57	902.88	217.37	224.72	117.17	138.96	168.13	150.32
Y 89	77.76	147.34	169.17	28.59	28.66	35.21	44.00	45.00	16.20	21.69	33.73	32.68
Zr 91	601.32	257.19	367.01	172.41	223.75	196.43	175.53	162.43	31.12	12.49	101.84	92.88
Nb 93	84.08	47.53	68.84	20.82	67.36	73.12	6.67	7.36	0.44	0.20	3.54	3.92
Cs 133	0.45	0.57	0.53	0.59	0.62	0.30	0.13	0.27	0.05	0.01	0.10	0.14
Ba 137	453.84	350.88	364.67	458.99	339.61	581.88	32.23	33.70	7.70	6.32	17.72	17.32
La 139	57.41	110.73	91.33	33.93	40.22	50.06	8.09	8.29	1.13	3.84	4.62	4.39
Ce 140	122.51	94.28	92.76	66.02	78.01	87.74	22.17	23.47	3.93	10.58	12.74	12.05
Pr 141	15.25	22.84	23.66	8.06	9.13	10.06	3.51	3.66	0.72	1.58	2.08	1.95
Nd 146	60.01	90.91	99.41	31.14	34.38	36.78	17.40	17.82	3.99	7.62	10.65	9.92
Sm 147	13.45	19.17	20.53	6.35	6.62	6.92	5.18	5.34	1.50	2.25	3.41	3.13
Eu 151	3.83	5.20	6.19	1.70	2.10	2.17	1.82	1.86	0.68	0.89	1.28	1.24
Tb 159	2.34	3.29	3.76	0.87	0.94	1.01	1.17	1.21	0.40	0.57	0.84	0.82
Gd 160	13.35	20.62	23.45	5.33	5.82	6.27	6.49	6.71	2.14	3.02	4.52	4.29
Dy 163	13.34	18.60	21.99	4.65	5.17	5.52	7.11	7.26	2.53	3.51	5.10	5.02
Ho 165			4.83				1.53	1.58		0.76	1.14	1.13
Er 167	7.73	11.30	13.91	2.66	2.66	2.97	4.37	4.47	1.57	2.14	3.18	3.15
Tm 169			2.03				0.63	0.64		0.31	0.45	0.45
Yb 174	6.94	9.62	12.03	2.45	2.21	2.51	3.89	3.93	1.39	1.90	2.86	2.78
Lu 175	1.04	1.50	1.93	0.38	0.33	0.38	0.60	0.60	0.21	0.29	0.44	0.44
Hf 178	13.24	7.19	8.49	3.96	4.57	3.81	4.00	3.81	0.81	0.48	2.39	2.29
Ta 181	4.99	3.56	3.66	1.21	3.78	3.69	0.46	0.48	0.05	0.02	0.23	0.25
Pb 208	4.84	18.51	2.92	7.16	2.21	3.19	0.97	0.97	0.18	0.23	0.67	0.64
Th 232	7.17	4.92	4.96	8.16	5.12	5.93	0.48	0.50	0.02	0.09	0.27	0.28
U 238	2.04	1.92	1.24	2.55	1.42	1.55	0.85	0.59	0.01	0.07	0.28	0.36

Table A5.1: (continued)

	Southern Ocean Dredges:		Older Volcanics:				Macquarie Island:					
	DR13-3D	DR13-3E	OV1	OV3	OV4	OV5	38287	47979	25637	25601	47963	47978
Isotope												
Li 7												
Be 9												
B 11												
Sc 45												
V 51												
Cr 53												
Co 59												
Ni 60												
Cu 63												
Zn 66												
Ga 71												
Rb 85	2.66	1.01	15.65	6.66	27.49	3.28	19.54	3.43	11.67	28.91	50.93	41.74
Sr 86	169.42	109.80	623.17	1379.47	542.90	200.83	250.58	156.43	252.72	411.49	706.29	767.45
Y 89	25.96	43.75	24.32	34.29	32.90	46.66	46.14	23.25	24.86	29.52	28.03	28.43
Zr 91	62.03	91.58	171.74	276.14	200.76	101.16	185.86	66.21	94.44	169.88	196.00	177.14
Nb 93	8.36	1.63	34.95	105.22	42.06	11.26	43.00	7.97	25.59	57.16	101.48	86.52
Cs 133	0.07	0.11	0.35	0.82	0.23	2.14	0.21	0.04	0.12	0.33	0.57	0.43
Ba 137	87.05	3.53	237.31	684.81	393.08	52.36	186.15	35.48	124.20	291.28	542.21	388.89
La 139	5.32	3.49	20.56	78.29	36.16	8.11	20.70	4.55	12.97	26.93	46.10	39.26
Ce 140	12.62	12.16	42.42	149.93	64.00	21.63	42.50	10.65	25.90	50.31	81.78	71.05
Pr 141	1.83	2.16	5.21	16.88	8.96	3.35	5.39	1.56	2.18	5.84	8.95	7.90
Nd 146	8.85	11.71	21.48	61.46	36.90	16.57	23.13	7.62	13.21	22.79	33.23	29.83
Sm 147	2.67	4.22	4.90	10.59	8.28	5.17	5.69	2.34	3.15	4.80	6.04	5.74
Eu 151	1.09	1.48	1.67	3.24	2.63	1.76	1.91	0.92	1.14	1.68	2.04	1.91
Tb 159	0.68	1.13	0.78	1.24	1.25	1.23	1.21	0.57	0.66	0.85	0.88	0.87
Gd 160	3.64	5.89	4.84	8.62	7.98	6.70	6.70	3.12	3.68	5.06	5.63	5.40
Dy 163	4.13	6.84	4.27	6.26	6.56	7.59	7.19	3.59	3.86	4.91	4.81	4.77
Ho 165	0.90		0.87	1.15	1.23	1.65	1.56	0.79	0.84	1.03	0.97	0.98
Er 167	2.56	4.24	2.22	2.79	3.06	4.60	4.49	2.25	2.38	2.82	2.53	2.64
Tm 169	0.37		0.32	0.36	0.41	0.66	0.65	0.33	0.33	0.39	0.35	0.36
Yb 174	2.27	3.80	1.90	2.05	2.42	4.06	3.95	2.03	2.09	2.44	2.18	2.24
Lu 175	0.34	0.55	0.28	0.29	0.34	0.60	0.63	0.32	0.33	0.38	0.34	0.35
Hf 178	1.69	2.50	3.50	4.91	4.52	3.03	4.09	1.63	2.05	3.47	3.91	3.65
Ta 181	0.48	0.13	1.97	4.57	2.45	0.68	2.31	0.44	0.98	2.99	5.31	4.33
Pb 208	0.41	0.16	1.90	5.96	4.18	0.98	1.24	0.39	0.89	1.71	2.45	2.42
Th 232	0.57	0.09	2.36	9.93	4.25	0.77	3.22	0.57	2.07	4.78	8.34	7.02
U 238	0.13	0.32	0.75	2.31	0.95	0.20	0.80	0.16	0.51	1.22	2.06	1.71

APPENDIX 6

RADIOGENIC ISOTOPE CALCULATIONS

A6.1 INITIAL RATIOS:

The following equations were used to calculate the initial Sr, Nd and Pb isotope ratios quoted throughout this thesis, where t = age (years) cited in the text, *Ab* = isotopic abundance and *W* = atomic weight.

A6.1.1 Strontium:

$(^{87}Sr/^{86}Sr)_{initial} = (^{87}Sr/^{86}Sr)_{measured} - {}^{87}Rb/^{86}Sr\ (e^{\lambda t} - 1)$

where the Rb-Sr decay constant is $\lambda = 1.42 \times 10^{-11}\ y^{-1}$ (Steiger and Jäger, 1977) and

$$^{87}Rb/^{86}Sr = \left(\frac{Rb}{Sr}\right)_{measured} \times \left(\frac{Ab^{87}Rb \times WSr}{Ab^{86}Sr \times WRb}\right)$$

A6.1.2 Neodymium:

$(^{143}Nd/^{144}Nd)_{initial} = (^{143}Nd/^{144}Nd)_{measured} - {}^{147}Sm/^{144}Nd\ (e^{\lambda t} - 1)$

where the Sm-Nd decay constant is $\lambda = 6.54 \times 10^{-12}\ y^{-1}$ (Lugmair and Marti, 1978) and

$$^{147}Sm/^{144}Nd = \left(\frac{Sm}{Nd}\right)_{measured} \times \left(\frac{Ab^{147}Sm \times WNd}{Ab^{144}Nd \times WSm}\right)$$

A6.1.3 Lead:

$(^{206}Pb/^{204}Pb)_{initial} = (^{206}Pb/^{204}Pb)_{measured} - {}^{238}U/^{204}Pb\ (e^{\lambda 8 t} - 1)$

where the U-Pb decay constant $\lambda_8 = 1.55125 \times 10^{-11}\ y^{-1}$, (Steiger and Jäger, 1977) and

$$^{238}U/^{204}Pb = \mu = \left(\frac{U}{Pb}\right)_{measured} \times \left(\frac{Ab^{238}U \times WPb}{Ab^{204}Pb \times WU}\right)$$

$(^{207}Pb/^{204}Pb)_{initial} = (^{207}Pb/^{204}Pb)_{measured} - {}^{235}U/^{204}Pb\ (e^{\lambda 5 t} - 1)$

where the U-Pb decay constant $\lambda_5 = 9.8485 \times 10^{-10}\ y^{-1}$ (Steiger and Jäger, 1977) and

$$^{235}U/^{204}Pb = \frac{\mu}{137.88}$$

$(^{208}Pb/^{204}Pb)_{initial} = (^{208}Pb/^{204}Pb)_{measured} - {}^{232}Th/^{204}Pb\ (e^{\lambda 2 t} - 1)$

where the Th-Pb decay constant $\lambda_2 = 4.9475 \times 10^{-11}\ y^{-1}$ (Steiger and Jäger, 1977) and

$$^{232}Th/^{204}Pb = \left(\frac{Th}{Pb}\right)_{measured} \times \left(\frac{Ab^{232}Th \times WPb}{Ab^{204}Pb \times WTh}\right)$$

$$\kappa = {}^{232}Th/^{238}U = \left(\frac{Th}{U}\right)_{measured} \times \left(\frac{Ab^{232}Th \times WU}{Ab^{238}U \times WTh}\right)$$

A6.2 EPSILON Nd and Sr VALUES:

Initial epsilon ε_{Nd} and ε_{Sr} values were calculated using:

$$(\varepsilon Nd)_i = \left[\frac{(^{143}Nd/^{144}Nd)_{sample\ at\ time\ t}}{(^{143}Nd/^{144}Nd)_{CHUR\ at\ time\ t}} - 1\right] \times 10^4$$

where:

$$(^{143}Nd/^{144}Nd)_{CHUR\ at\ time\ t} = (^{143}Nd/^{144}Nd)_{CHUR} - (^{147}Sm/^{144}Nd)_{CHUR}\ (e^{\lambda t} - 1)$$

$$(\varepsilon Sr)_i = \left[\frac{(^{87}Sr/^{86}Sr)_{sample\ at\ time\ t}}{(^{87}Sr/^{86}Sr)_{UR\ at\ time\ t}} - 1\right] \times 10^4$$

where:

$$(^{87}Sr/^{86}Sr)_{UR\ at\ time\ t} = (^{87}Sr/^{86}Sr)_{UR} - (^{87}Rb/^{86}Sr)_{UR}\ (e^{\lambda t} - 1)$$

Present-day epsilon ε_{Nd} and ε_{Sr} values were calculated using:

$$\varepsilon Nd = \left[\frac{(^{143}Nd/^{144}Nd)_{measured}}{(^{143}Nd/^{144}Nd)_{CHUR}} - 1\right] \times 10^4$$

$$\varepsilon Sr = \left[\frac{(^{87}Sr/^{86}Sr)_{measured}}{(^{87}Sr/^{86}Sr)_{UR}} - 1\right] \times 10^4$$

Bulk Earth values used are:

$(^{143}Nd/^{144}Nd)_{CHUR} = 0.51265$ (equivalent to accepted value for BCR-1 at RSES)

$(^{147}Sm/^{144}Nd)_{CHUR} = 0.1966$ (Jacobsen and Wasserburg, 1984)

$(^{87}Sr/^{86}Sr)_{UR} = 0.7045$ (DePaolo, 1988)

$(^{87}Rb/^{86}Sr)_{UR} = 0.0827$ (DePaolo, 1988)

APPENDIX 7

ACRONYMS AND ABBREVIATIONS

The following is a list of the acronyms and abbreviations used throughout the main text of this thesis. Other abbreviations associated with mineral chemistry or radiogenic isotope data can be found in Appendices 3 and 6 respectively.

AAD	Australian-Antarctic Discordance
Ab	albite content of feldspar = 100 Na/(Na + Ca + K)
An	anorthite content of feldspar = 100 Ca/(Na + Ca + K)
BE	Bulk Earth
D_1	first deformational event
DMM	Depleted MORB Mantle end-member component
CHUR	CHondritic Uniform Reservoir
E-MORB	Enriched MORB
EDS	Energy-Dispersive Spectrometry
EMI	Enriched Mantle 1 end-member component
EMII	Enriched Mantle 2 end-member component
EPR	East Pacific Rise
F	extent of partial melting
f_{206}	proportion of common ^{206}Pb to total ^{206}Pb
FeO*	(0.9 x Fe_2O_3) + FeO
FOZO	isotopic FOcal ZOne
HFSE	High Field Strength Elements (ionic potential >2.0)
HIMU	High-μ ($^{238}U/^{204}Pb$) end-member component
HREE	Heavy Rare Earth Elements
ICP-MS	Inductively Coupled Plasma-Mass Spectrometry
INAA	Instrumental Neutron Activation Analysis
K_D	FeO-MgO partition coefficient between olivine and the melt
K_d	mineral - melt partition coefficient
LILE	Large Ion Lithophile Elements (ionic potential <2.0)
LIP	Large Igneous Province
LLD	Liquid Lines of Descent
LOI	Loss On Ignition
LoNd	HIMU - EMI mixing array
LREE	Light Rare Earth Elements
LVZ	Low Velocity Zone

M_1	first metamorphic event
MAR	Mid-Atlantic Ridge
Mg#	100 Mg/(Mg+Fe^{2+})
MORB	Mid-Ocean Ridge Basalt/s
MREE	Middle Rare Earth Elements
N-MORB	Normal MORB
$Na_{8.0}$	Na_2O normalised to 8 wt % MgO to correct for low P (1 atm) fractionation
NHRL	Northern Hemisphere Reference Line
No-EM	HIMU - DMM mixing array
OIB	Ocean Island Basalt/s
Or	orthoclase content of feldspar = 100 K/(Na + Ca + K)
P	Pressure
PGE	Platinum Group Elements
PREMA	PREvalent MAntle end-member
R_A	atmospheric $^3He/^4He = 1.39 \times 10^{-6}$
REE	Rare Earth Elements or lanthanides (La^{3+} to Lu^{3+})
SEIR	Southeast Indian Ridge
SHRIMP	Sensitive High-Resolution Ion Microprobe
SOPITA	South Pacific Isotopic and Thermal Anomaly
T	Temperature
T-MORB	Transitional MORB
TAS	Total Alkalis versus Silica
UR	Uniform Reservoir
WDS	Wavelength-Dispersive Spectrometry
XRF	X-Ray Fluorescence

This article has been removed for copyright or proprietary reasons.

Lanyon R., Black L.P., Seitz H.-M., 1993, U-Pb zircon dating of mafic dykes and its application to the Proterozoic geological history of the Vestfold Hills, East Antarctica, Contributions to mineralogy and petrology, 115, 184-203

This article has been removed for copyright or proprietary reasons.

Lanyon R., Varne R. and Crawford A.J., 1993, Tasmanian Tertiary basalts, the Balleny Plume, and opening of the Tasman Sea (southwest Pacific Ocean), Geology, 21, 555-558.